

# **Unitary renormalization group for correlated electrons**

*A thesis submitted in partial fulfilment  
for the requirements of the degree of*

**Doctor of Philosophy**

by

**Anirban Mukherjee**

14RS016

under the supervision of

**Dr. Siddhartha Lal**

to the

Department of Physical Sciences



**Indian Institute of Science Education  
and Research–Kolkata**

September, 2020



# **Declaration by the student**

I, Mr. Anirban Mukherjee, Registration No. 14RS016, August, 2014, a student of Department of Physical Sciences of the Doctoral Program of IISER Kolkata, hereby declare that this thesis is my own work and, to the best of my knowledge, it neither contains materials previously published or written by any other person, nor it has been submitted for any degree/diploma or any other academic award anywhere before. I also declare that all copyrighted material incorporated into this thesis is in compliance with the Indian Copyright (Amendment) Act, 2012 and that I have received written permission from the copyright owners for my use of their work. This work was done under the guidance of Dr. Siddhartha Lal, at Indian Institute of Science Education and Research Kolkata (IISER Kolkata).

Anirban Mukherjee  
Department of Physical Sciences  
Indian Institute of Science Education and Research  
Mohanpur 741246, West Bengal, India



# Certificate from the supervisor

This is to certify that the work contained in this thesis entitled "**Unitary renormalization group for correlated electrons**" has been carried out by **Anirban Mukherjee (14RS016)** under my supervision from August 2014 to September 2020 and that in my opinion is fully adequate, in scope and quality, as a dissertation for the degree of **Doctor of Philosophy** in **Indian Institute of Science Education and Research-Kolkata**.

Dr. Siddhartha Lal  
Associate Professor Department of Physical Sciences  
Indian Institute of Science Education and Research  
Mohanpur 741246, West Bengal, India



# Acknowledgement

**Dr. Siddhartha Lal** I would like to express my deepest gratitude to my supervisor Prof. Siddhartha Lal for his invaluable guidance, encouragement and support throughout my doctoral studies at Indian Institute of Science Education and Research, Kolkata. It has been a worthwhile experience working under his supervision, from which I have gained valuable insight on several matters.

**IISER-Kolkata** I would like to thank my institute IISER-Kolkata for providing me scholarship, computing facility, contingency throughout my Ph.D. period.

**Ananda Dasgupta and Ritesh Singh** I would like to thank Ananda Dasgupta and Ritesh Singh for being members of my “Research Progress committee” and evaluating my research progress. The discussion in the seminars helped me a lot in carrying out my research. I learnt a lot from your courses too.

**Pinaki Mazumdar** I would like to thank Prof. Pinaki Mazumdar for giving me a platform to present my research work and helping me with critical discussions during a short visit to HRI, Allahabad, India.

**NS Vidhyadhiraja** I would like to thank Prof. NS Vidhyadhiraja for discussing with me, quizzing me about the unitary renormalization group formalism and motivating me for presenting the formalism with more clarity and detail.

**Arghya Taraphder** I would like to thank Prof. Arghya Taraphder for mentoring me with critical discussions, suggestions and feedback on various strongly correlated problems from the beginning.

**Santanu Pal and Siddhartha Patra** I would like to thank my senior postdoc Santanu Pal and PhD student Siddhartha Patra for being friends with whom I discussed about various aspects of the unitary renormalization group method. They have asked a lot of questions which made me rethink about various assumptions, which I later on dropped thanks to them. All of these suggestions solidified the methodology.

Finally, much love and thanks to my wife **Mahashweta** and my son **Ritwik**: their love and presence rocketed me towards my goal.



# Abstract

This thesis reports the development of an analytic unitary tensor network renormalization group (URG) for models of strongly correlated electrons/spins. The RG proceeds via an iterative procedure involving the unitary disentanglement of the highest energy (UV) electronic degree of freedom from its low energy (IR) counterparts in a single step. The unitary transformations generate RG flow in the space of effective Hamiltonians, manifested in a hierarchy of RG flow equations for the  $2n$ -point scattering vertex tensors. The flow equations support a non-trivial dependence on the renormalized self/correlation energy of the many-body configurations. All orders of loop expansion are non-perturbatively resummed in the vertex flows via the denominator of the RG flow functions; this is seen to lead to a non-trivial stable fixed point at which the RG flows are arrested. Further, the denominator of the RG flow equations possess an additional frequency dependence originating in the non-commutativity between different parts of the many-body Hamiltonian. Contributions from relevant higher-order scattering diagrams generated at every RG step can be tracked in a controlled manner. At weak coupling, the URG flow equations match those obtained from the perturbative truncations involved in the continuous unitary transformation (CUT) RG and functional RG (FRG) treatments of models of strongly correlated electrons such as the 2D Hubbard model on the square lattice. Importantly, the URG flows yield stable field points in the IR that are not accessible from other RG approaches.

URG is constructed by a collection of nonlocal unitary gates arranged sequentially from UV to IR, forming a quantum circuit/tensor network encoded via two-point and higher-order correlators. The circuit is composed of two-local universal gates and single-qubit rotation gates. From the URG analysis, we identify the dominant scattering diagrams and selectively construct an optimal arrangement of quantum gates. The depth of quantum circuit ( $D$ ) will then be naturally optimized to obtain the desired ground state. URG corresponds to an interacting version of the entanglement holographic mapping (EHM) network: the URG flow generates an emergent holographic spacetime in the bulk of the tensor network. We have verified the Ryu-Takayanagi entropy bound for the many-body states generated by the tensor network RG. As the URG method distils the dominant scattering diagrams at low energies, its analytic framework enables the optimization of the numerical procedure by which to obtain the effective Hamiltonian and its eigenspectrum at the stable fixed points. From the ground state, we can obtain the interacting Green's function over the entire frequency and momentum domains. Further, the unitaries can also be employed in reconstructing, say, the unknown ground state wavefunction in the UV by reversing the URG flow by starting from its form at the IR fixed point. Reverse RG flow implements the controlled inclusion of the scattering diagrams in order of RG relevance, and its reliability of the reconstructed states obtained from such a reverse RG can be checked by computing the energy fluctuations for the parent Hamiltonian. In this way, the complete Green's

---

function can also be obtained in the UV.

We have applied the URG technique to various paradigmatic models of correlated electrons and spins, including the 2d Hubbard model on the square lattice at and away from half-filling, the XXZ spin-1/2 antiferromagnet on the 2d Kagome lattice, a general one-band problem of interacting fermions in 2d, the generalised Sachdev Ye model for electrons, the 1d Hubbard model and the single impurity Kondo model. In these models, we have obtained a variety of stable fixed point theories and analysed their low-energy spectrum and eigenstates. In this way, the unitary RG formalism has revealed a multitude of exotic quantum many-body phenomena in these models: quantum criticality, topologically ordered spin and charge quantum liquids, pseudogapped phases, marginal Fermi liquids, charge fractionalization of excitations, many-body localization and thermalisation. We now list a set of important questions whose answers we attempt in the thesis. First, can we construct a non-perturbative unitary renormalization group for correlated electrons on a lattice? Does such a formulation generate a Hamiltonian renormalization group and an entanglement renormalization group concomitantly? Does the RG flow generically lead to a stable fixed point with an analytically tractable effective Hamiltonian? As the RG procedure is unitary, can we demonstrate dynamical spectral weight transfer (even as we show that the total spectral weight, or the f-sum rule, is conserved)? Specifically, can we show that the propagating degrees of freedom emergent from an instability of Fermi surface (e.g., Cooper pairs) help account for the spectral weight lost by the gapless excitations of the normal state (e.g., Landau quasiparticles)? By reconstructing the URG flow backwards from the IR ground state, can we track the evolution of correlation functions and entanglement features towards the UV?

We now offer short descriptions of the primary content in various chapters. In the introductory chapter of the thesis, we motivate the many-electron problem originating from the interplay of electronic correlations, band topology, lattice geometry, disorder, multi-orbital effects etc., resulting in a wide array of exotic quantum phenomena lying beyond Fermi liquid theory and the Landau-Ginzburg-Wilson paradigm. We survey briefly several well established methods for studies of systems of correlated electrons. We then motivate the renormalization group approach and review the existing literature. Next, we motivate the URG approach, and provide a list of major questions to be answered in the thesis. Following this, we layout the novel features of the URG program. Finally, we provide a detailed review of the phenomenology of various paradigmatic problems studied in this thesis.

In chapter 2, we develop the unitary RG formalism and present a unified framework for the renormalisation of the Hamiltonian and its eigenbasis for a system of correlated electrons, unveiling thereby the interplay between electronic correlations and many-particle entanglement. We recast the RG as a discrete flow of the Hamiltonian tensor network, i.e., the collection of various  $2n$ -point scattering vertex tensors comprising the Hamiltonian. The renormalisation progresses via unitary transformations that block diagonalize the Hamiltonian iteratively via the disentanglement of single-particle eigenstates. This procedure incorporates naturally the role of quantum fluctuations. The RG flow equations possess a non-trivial structure, displaying a feedback mechanism through frequency-dependent dynamical self-energies and correlation energies. The interplay between various UV energy scales enables the coupled RG equations to flow towards a stable fixed point in the IR. The effective Hamiltonian at the IR fixed point generically has a reduced parameter space, as well as the number of degrees of freedom, compared to the microscopic Hamiltonian. Importantly, the vertex tensor network is observed to govern the RG

---

flow of the tensor network that denotes the coefficients of the many-particle eigenstates. The RG evolution of various many-particle entanglement features of the eigenbasis are, in turn, quantified through the coefficient tensor network. In this way, we show that the URG framework provides a microscopic understanding of holographic renormalisation: the RG flow of the vertex tensor network generates an eigenstate coefficient tensor network possessing a many-particle entanglement metric. We find that the eigenstate tensor network accommodates sign factors arising from the exchange of fermions and that the IR fixed point reached generically involves a trivialisation of the fermion sign factor. In chapter 3, we present several results for the emergence of composite excitations in the neighbourhood of a gapless Fermi surface, as well as for the condensation phenomenon involving the gapping of the Fermi surface.

In chapter 4, we present the URG phase diagram for the electronic Hubbard model in two dimensions on the square lattice at half-filling. The phase diagram possesses the quantum fluctuation energy scale ( $\omega$ ) as one of its axes. A relation is derived between  $\omega$  and the effective temperature scale up to which gapless, as well as emergent gapped, phases can be obtained. We find that the normal and insulating phases of the half-filled Hubbard model correspond, for any on-site repulsion, to a marginal Fermi liquid normal phase and a topologically-ordered gapped Mott insulating liquid respectively. The marginal Fermi liquid is found to arise from singular forward scattering in directions normal to the nested Fermi surface, while singular backscattering events lead to Mott liquid state. The transition between these two phases involves passage through a pseudogapped phase bookended by Fermi surface topology-changing Lifshitz transitions. The pseudogap phase is observed to arise from the electronic differentiation encoded within the nested Fermi surface and involves the gradual gapping of the Fermi surface from antinodes to nodes via charge and spin excitations that are mutually entangled. We obtain effective Hamiltonians for various phases, as well as wavefunctions for the low-energy many-body eigenstates of the Mott liquid. Benchmarking of the ground-state energy per particle and the double-occupancy fraction for the Mott liquid against existing numerical results yields excellent agreement. Presence of an Néel ordering symmetry-breaking perturbation in the RG leads to an antiferromagnetic spin-ordered charge insulating Mott state. Our results thus offer novel insights on a variety of aspects of the Mott-Hubbard problem and can be extended to the doped system.

In chapter 5, we present a  $T = 0K$  renormalization group (RG) phase diagram for the hole-doped 2D Hubbard model on the square lattice. Using effective Hamiltonians and wavefunctions for the low-energy many-body eigenstates for the doped Mott liquid obtained from the stable fixed point of the RG flows, we demonstrate the collapse of the pseudogap for charge excitations (Mottness) at a quantum critical point (QCP) possessing a nodal non-Fermi liquid with superconducting fluctuations, and spin-pseudogapping near the antinodes. The QCP is characterised using both thermodynamic and quantum information-theoretic measures. d-wave Superconducting order is shown to arise from this quantum critical state of matter. The pseudogap phase possesses a variety of fluctuations that lead to several symmetry-broken phases at low-energies. Benchmarking of the ground state energy per particle and the double-occupancy fraction obtained from a finite-size scaling analysis against existing numerical results yields excellent agreement. We present a detailed insight into the  $T = 0$  origin of several experimentally observed findings in the cuprates, including Homes law and Planckian dissipation. We also establish that the hierarchy of temperature scales for the pseudogap ( $T_{PG}$ ), onset temperature for pairing ( $T_{ons}$ ), the formation of the Mott liquid ( $T_{ML}$ ) and superconductivity ( $T_C$ ) obtained from our analysis is quantitatively

---

consistent with that observed experimentally for some members of the cuprates. Our results offer insight on the ubiquitous origin of superconductivity in doped Mott insulating states and pave the way towards a systematic search for higher superconducting transition temperatures in such systems.

In chapter 6, we apply the unitary renormalization group (URG) to study two archetypal models of strongly correlated lattice electrons, one with translation invariance and one without. We obtain detailed insight into the emergence of various gapless and gapped phases of quantum electronic matter by computing effective Hamiltonians from numerical evaluation of the various RG equations, as well as their entanglement signatures through their respective tensor network descriptions. For the translationally invariant model of a single-band of interacting electrons, this includes results on gapless metallic phases such as the Fermi liquid and Marginal Fermi liquid, as well as gapped phases such as the reduced Bardeen-Cooper-Schrieffer, pair density-wave and Mott liquid phases. Additionally, a study of a generalised Sachdev-Ye model with disordered four-fermion interactions offers detailed results on many-body localised phases, as well as the thermalised phase. We emphasise the distinctions between the various phases based on a combined analysis of their dynamical (obtained from the effective Hamiltonian) and entanglement properties. Importantly, the RG flow of the Hamiltonian vertex tensor network is shown to lead to emergent gauge theories for the gapped phases. Taken together with results on the holographic spacetime generated from the RG of the many-particle eigenstate (seen through, for instance, the holographic upper bound of the one-particle entanglement entropy), our analysis offers an ab-initio perspective of the gauge-gravity duality for quantum liquids that are emergent in systems of correlated electrons.

In chapter 7, we introduce a novel momentum-space entanglement renormalization group (MERG) scheme for the topologically ordered ground state of the 2D Hubbard model on a square lattice using a unitary quantum circuit comprised of non-local unitary gates. At each MERG step, the unitary quantum circuit disentangles a set of electronic states, thereby transforming the tensor network representation of the many-particle state. By representing the non-local unitary gate as a product of two-qubit disentangler gates, we provide an entanglement holographic mapping (EHM) representation for MERG. Using entanglement based measures from quantum information theory and complex network theory, we study the emergence of topological order in the bulk of the EHM. We also demonstrate that the MERG is equivalent to a stabiliser quantum error-correcting code. The MERG reveals distinct holographic entanglement features for the normal metallic, topologically ordered insulating quantum liquid and Ne l antiferromagnetic symmetry-broken ground states of the 2D Hubbard model at half-filling, clarifying the essence of the entanglement phase transitions that separates the three phases. A MERG analysis of the quantum critical point of the hole-doped 2D Hubbard model reveals the evolution of the many-particle entanglement of the quantum liquid ground state with hole-doping, as well as how the collapse of Mottness is responsible for the emergence of d-wave superconductivity. We perform an information-theoretic analysis of the EHM network, demonstrating that the information bottleneck principle is responsible for the distillation of entanglement features in the hierarchical structure of the EHM network. As a result, we construct a deep neural network (DNN) architecture based on our EHM network and employ it for predicting the onset of topological order. We also demonstrate that the DNN is capable of distinguishing between the topologically ordered and gapless normal metallic phases.

---

In chapter 8, we perform a URG study of the 1D fermionic Hubbard model. The formalism generates a family of effective Hamiltonians and many-body eigenstates arranged holographically across the tensor network from UV to IR. The URG is realized as a quantum circuit, leading to the entanglement holographic mapping (EHM) tensor network description. A topological  $\Theta$ -term of the projected Hilbert space of the degrees of freedom at the Fermi surface are shown to govern the nature of RG flow towards either the gapless Tomonaga-Luttinger liquid or gapped quantum liquid phases. This results in a nonperturbative version of the Berezinskii-Kosterlitz-Thouless (BKT) RG phase diagram, revealing a line of intermediate coupling stable fixed points, while the nature of RG flow around the critical point is identical to that obtained from the weak-coupling RG analysis. This coincides with a phase transition in the many-particle entanglement, as the entanglement entropy RG flow shows distinct features for the critical and gapped phases depending on the value of the topological  $\Theta$ -term. We demonstrate the Ryu-Takayanagi entropy bound for the many-body eigenstates comprising the EHM network, concretizing the relation to the holographic duality principle. The scaling of the entropy bound also distinguishes the gapped and gapless phases, implying the generation of very different holographic spacetimes across the critical point. Finally, we treat the Fermi surface as a quantum impurity coupled to the high energy electronic states. A thought-experiment is devised to study entanglement entropy generated by isolating the impurity and propose ways by which to measure it by studying the quantum noise and higher-order cumulants of the full counting statistics.

In chapter 9, we study the single-channel Kondo problem using the URG approach. We present non-perturbative RG scaling equations for the Kondo problem. The strong coupling IR fixed point for antiferromagnetic Kondo exchange coupling is represented by an effective Hamiltonian, and from which we also obtain the singlet ground state formed from the impurity spin and the Kondo cloud that screens it. Starting from the effective Hamiltonian, our analysis reproduces the well-known impurity thermodynamics for the Kondo problem, including Wilson ratio of 2 and the variations of the specific heat coefficient and spin susceptibility with temperature. Then, employing the reverse RG approach of chapter 7, we also track the flow of mutual information between electronic qubits in the Kondo cloud as well as four-point correlations. Our findings reveal the non-Fermi liquid character of the Kondo cloud, indicated by strong off-diagonal two-particle correlations and non-trivial entanglement content. We also show that the well-known local Fermi liquid description of the Kondo effect corresponds to the correlations among the decoupled electrons lying outside the Kondo cloud.

We conclude in Chapter 10 by presenting the important outcomes of the thesis, both in terms of the development of the URG method as well as the results obtained from its application to various paradigmatic models of interacting electrons. We also outline various open directions for future work.



# Contents

<b>Acknowledgement</b>	<b>7</b>
<b>1 Introduction</b>	<b>19</b>
1.1 The many-electron problem . . . . .	19
1.1.1 A brief review of some methods used for the study of correlated electrons .	20
1.1.2 The renormalization group approach . . . . .	22
1.1.3 Motivating the unitary renormalization group approach . . . . .	24
1.1.4 Features of the Unitary RG program . . . . .	26
1.2 Phenomenology of models studied in the thesis . . . . .	41
1.2.1 Th 2d Hubbard model . . . . .	43
1.2.2 Four-fermionic interaction and generalized Sachdev-Ye models . . . . .	46
1.2.3 1D Hubbard model . . . . .	47
1.2.4 Kondo model . . . . .	49
1.3 Layout of following chapters . . . . .	51
<b>2 Unitary Renormalization Group Method</b>	<b>53</b>
2.1 Unitary disentanglement transformation . . . . .	54
2.2 Hamiltonian Block Diagonalization . . . . .	56
2.3 Correspondence between $\omega$ and an emergent thermal scale $T$ . . . . .	57
2.4 Vertex tensor network renormalization . . . . .	58
2.5 Geometry of Eigenbasis Renormalization . . . . .	63
2.5.1 Eigenbasis renormalization scheme . . . . .	64
2.5.2 RG flow of entanglement within subspace $\mathcal{A}_j$ . . . . .	67
2.5.3 Mitigating the fermion sign problem through URG flow . . . . .	70
2.5.4 Relation between geometric measure of entanglement and composite p-h residues . . . . .	75
2.5.5 Evolution of the Fubini Study metric under RG flow . . . . .	76
2.5.6 Change in entanglement entropy generated in disentangling one electronic state per RG step . . . . .	77
<b>3 Perturbing the Fermi surface: insights into fermionic criticality</b>	<b>79</b>
3.1 The gapless Fermi surface: Fermi liquid and beyond . . . . .	79
3.1.1 RG flow from Nearly Free Fermi gas to Tight binding Metal . . . . .	80
3.1.2 Fate of single-particle excitations . . . . .	83
3.1.3 One-particle self-energy . . . . .	87

3.1.4	Partial Luttinger sum and Luttinger points . . . . .	89
3.1.5	Oshikawa's topological argument . . . . .	91
3.1.6	Preservation of partial Luttinger's count . . . . .	92
3.2	RG for bound state condensation: gapping the Fermi surface . . . . .	92
3.2.1	Outcome of two-particle excitations . . . . .	94
3.2.2	Dynamical mixing between ee/hh, eh/he pairs . . . . .	97
3.2.3	Self-energy hybridized by ee-eh pair mixing . . . . .	98
3.2.4	Bound-state formation near the Fermi surface . . . . .	99
3.2.5	Bound-state condensation, Friedel's phase shift and RG flows . . . . .	100
<b>4</b>	<b>Scaling theory for Mott-Hubbard transitions - I :</b>	
	<b><math>T = 0</math> phase diagram of the 1/2-filled Hubbard model</b>	<b>103</b>
4.1	The model and the RG scheme . . . . .	103
4.1.1	RG via the decoupling of single-particle occupation states . . . . .	104
4.1.2	Fermi surface instabilities . . . . .	105
4.1.3	RG flow equations for Longitudinal and Tangential scattering processes .	106
4.2	Mott MIT at 1/2-filling: the normal state . . . . .	110
4.2.1	Normal state for the Mott insulator . . . . .	115
4.2.2	Marginal Fermi liquid in the IR . . . . .	116
4.3	RG flow through the Pseudogap . . . . .	118
4.4	Properties of the Mott liquid . . . . .	120
4.4.1	Low energy eigenstates of the Mott liquid . . . . .	120
4.4.2	Topological features of the Mott liquid . . . . .	123
4.4.3	Benchmarking against existing numerical results . . . . .	124
4.4.4	Symmetry breaking of the Mott Liquid: Néel Antiferromagnetism . . . .	125
4.4.5	Cooper-pair fluctuations within the Mott liquid . . . . .	125
4.5	Conclusions and perspectives . . . . .	126
<b>Appendices</b>		<b>129</b>
4.A	The Hamiltonian renormalization group flow . . . . .	129
4.B	The renormalized Hamiltonian at RG step $j$ . . . . .	131
4.C	Benchmarking results for $2 \leq U/t \leq 12$ . . . . .	131
<b>5</b>	<b>Scaling theory for Mott-Hubbard transitions - II :</b>	
	<b>Quantum Criticality of the doped Mott insulator</b>	<b>133</b>
5.1	Hubbard model with finite chemical potential . . . . .	133
5.2	Mottness Collapse and quantum criticality with hole-doping . . . . .	136
5.2.1	Low energy eigenstates of the doped Mott liquid and the QCP . . . . .	137
5.2.2	Signature of QCP in ground state fidelity susceptibility with doping . . .	141
5.2.3	Theory for the vicinity of the QCP . . . . .	142
5.2.4	$T = 0$ origin of Homes Law: Planckian dissipation and preformed Cooper pairs . . . . .	145
5.2.5	Mixed optical conductivity of the Correlated Fermi liquid . . . . .	148
5.3	Symmetry breaking Orders and superconductivity . . . . .	149
5.4	Conclusions and perspectives . . . . .	155

---

<b>Appendices</b>	<b>159</b>
5.A RG equation of the symmetry breaking orders . . . . .	159
5.B Benchmarking results for $2 \leq U/t \leq 12$ . . . . .	162
<b>6 Tensor RG theory for four-fermi interacting models</b>	<b>165</b>
6.1 URG scaling of the Ryu-Takayanagi entanglement entropy bound . . . . .	166
6.2 Four Fermi interacting model with translational invariance . . . . .	168
6.2.1 Derivation of the RG equation for 1 particle self energy $\Sigma_{\mathbf{k}\sigma}(\omega)$ . . . . .	169
6.2.2 Derivation of RG flow equations for $\Gamma_{\alpha\beta}^4$ and $\Gamma_{\alpha\beta}^6$ . . . . .	170
6.2.3 RG flows towards Fermi liquid and BCS fixed points . . . . .	172
6.2.4 The Marginal Fermi liquid . . . . .	187
6.2.5 RG flow into the spin/charge hybridized pseudospin-pairing force models .	194
6.2.6 RG Phase diagram for $H_{SFIM}$ . . . . .	197
6.2.7 Scaling features of holographic entanglement entropy bound for gapless and gapped quantum liquids . . . . .	198
6.3 Gauge theories and Topological order for emergent gapped quantum liquids . . .	201
6.4 RG analysis of the generalized Sachdev-Ye <sub>4</sub> model . . . . .	206
6.5 Conclusions . . . . .	215
<b>Appendices</b>	<b>221</b>
6.A 1-particle self-energy RG for three-particle MFL Hamiltonian . . . . .	221
6.B RG equations for SY <sub>4</sub> model . . . . .	222
<b>7 Holographic entanglement renormalisation of topological order in a quantum liquid</b>	<b>225</b>
7.1 Normal and topologically ordered (T.O.) insulating phases of the 2D Hubbard model at 1/2-filling . . . . .	226
7.2 MERG construction for the topologically ordered insulating ground state of the 2D Hubbard model . . . . .	227
7.2.1 Quantum circuit network representation of the T.O. ground state and its renormalization . . . . .	232
7.2.2 Eigenstate reconstruction within the MERG scheme . . . . .	234
7.2.3 Entanglement holographic mapping (EHM) representation for the topolog- ically ordered phase . . . . .	235
7.2.4 Emergence of T.O. ground state and quantum error correcting code . . .	240
7.3 Entanglement RG flow towards the topologically ordered ground state . . . .	241
7.3.1 Definitions and Computation method . . . . .	242
7.3.2 Results on emergence of strongly entangled short-distance pairs . . . .	243
7.3.3 Entanglement scaling features for the Mott liquid, normal metal and Neel antiferromagnetic insulating phases . . . . .	245
7.4 Probing the entanglement of the QCP in a hole-doped Mott liquid . . . . .	249
7.5 A Deep Neural Network based on EHM . . . . .	253
7.5.1 Demonstrating the IB principle for EHM based on MERG . . . . .	254
7.5.2 Constructing a DNN model for classifying <i>entangledness</i> of a pair . . . .	255
7.6 Conclusions and discussions . . . . .	258

<b>Appendices</b>	<b>263</b>
7.A Derivation of the unitary operator . . . . .	263
7.B Derivation of the normal phase Hamiltonian in pseudospin subspace . . . . .	264
7.C URG study for the symmetry broken Neel SDW state . . . . .	265
7.D Effective Cooper pair Hamiltonian obtained from the Mott liquid fixed point at half filling . . . . .	267
7.E Effective Hamiltonian and eigenstates at critical doping . . . . .	268
<b>8 Fermionic criticality is shaped by Fermi surface topology: a case study of the Tomonaga-Luttinger liquid</b>	<b>269</b>
8.1 Symmetries and Topology of the Fermi surface . . . . .	270
8.2 Topological constraints on condensation . . . . .	275
8.3 Structure of the Fermi surface pseudospin Hilbert space . . . . .	279
8.4 URG for Fermi surface instabilities: a topological viewpoint . . . . .	282
8.5 Holographic entanglement scaling towards the Fermi surface . . . . .	289
8.6 Observing the instability of the Fermi surface . . . . .	291
8.7 Topological order and its observables . . . . .	296
8.8 Discussions and Outlook . . . . .	300
<b>Appendices</b>	<b>307</b>
8.A RG equation for the BCS instability . . . . .	307
<b>9 URG study of the Kondo model: unveiling the Kondo cloud</b>	<b>309</b>
9.1 The Model . . . . .	309
9.2 URG Theory for the Kondo model . . . . .	310
9.3 RG flow to the IR fixed point . . . . .	312
9.3.1 Variation of the Kondo cloud size $\xi_K$ and effective Kondo coupling $J^*$ as function of bare coupling $J_0$ . . . . .	315
9.4 Derivation of the local Fermi liquid effective Hamiltonian . . . . .	316
9.4.1 Wilson ratio ( $R$ ) for the local Fermi liquid . . . . .	318
9.5 Impurity susceptibility at finite temperatures . . . . .	319
9.6 Excitations of the Kondo cloud and the Sommerfeld coefficient . . . . .	322
9.7 Many body correlations and entanglement properties of the Kondo cloud . . . . .	324
9.8 Conclusions . . . . .	327
<b>Appendices</b>	<b>329</b>
9.A Calculation of effective Hamiltonian from URG . . . . .	329
<b>10 Conclusion and Future Directions</b>	<b>333</b>

# Chapter 1

## Introduction

### 1.1 The many-electron problem

The quantum many-body problem originating from the interplay of electronic correlations [1, 2], dimensionality of the system [3–8], electronic band topology [9], disorder [10, 11], multiorbital physics and spin-exchange interactions [12, 13] is host to a wide range of exotic quantum phenomena whose description lies beyond the paradigmatic Fermi liquid [14] and BCS [15] theories. This includes high- $T_c$  superconductivity [5], spin liquids [16], non-Fermi liquids [17–20], topological order and fractional statistics [21, 22], many-body localization [23]. The inherent complexity in solving a given model Hamiltonian  $H$  for a system of interacting electrons arises from the presence of multiple parameters that complicate the problem: tight-binding hopping coefficients, inter- and intra-orbital two-particle interaction strengths, disordered one- and two-body potential etc. Further, another source of complexity arises from the many-particle entanglement content [24–26] within the many-body eigenstates of  $H$ . This complicates the construction of variational ansatz eigenstates for  $H$ . Indeed, Laughlin’s wavefunction for the fractional quantum hall effect [27] and the Bardeen Cooper Schrieffer (BCS) [15] wavefunction for s-wave superconductivity are two outstanding achievements where the variational wavefunction successfully describes the wide phenomenology of the respective problems.

Phenomenological theories belonging to the Landau-Ginzburg-Wilson (LGW) [28, 29] paradigm are typically formulated in terms of bosonic order parameters, and describe a wide range of quantum phases with different symmetries across a critical point. For instance, the BCS theory of superconductivity[15] and Hertz-Millis-Moriya theory of itinerant ferromagnetism [30–32] are prime examples of the success of LGW theories in explaining experimentally observed phenomena. However, over the last four decades, we have observed a new family of exotic quantum many-body phenomenon emerging from quantum criticality [33–35], such as non-Fermi liquid metals [36, 37], long-range entangled states of matter and topological order [21, 22] where the concept of a real space local order parameter is invalidated. Here, the concept of degrees of freedom emergent at a critical point becomes important. For instance, such emergent degrees of freedom are associated with charge fractionalization [38, 39], changes in a topological invariant [40–42], etc. They also have well-documented experimentally observable effects, for example, a T-linear resistivity at low energies, Planckian dissipation [43] and Homes law [44] in the strange metallic phase of the doped cuprate Mott insulators, a jump in bulk compressibility in the fractional quantum Hall

ground state at  $\nu = 1/3$ [45, 6] etc. The primary goal of this thesis is to develop a renormalisation group (RG) formalism that can, by beginning with the study of some paradigmatic models of interacting electrons, pave the way towards unveiling the effective theories that govern such exotic phenomena.

We now lay out the plan for the rest of the introduction. To begin with, in Sec.1.1.1, we survey some state-of-the-art methods that are popular for the study of electronic correlations. This is followed, in by Sec.1.1.2, by a motivation for a renormalization group (RG) approach, together with a review of the existing literature for various RG approaches including functional RG, Hamiltonian RG, entanglement RG etc. In Sec.1.1.3, we motivate the unitary renormalization group approach and list the major questions answered within this thesis. Sec.1.1.4 lays out the novel features of the unitary RG program, including the connections to other Hamiltonian and entanglement RG methods. Finally, Sec.1.2 offers a review of the phenomenology of various paradigmatic models studied in this thesis.

### 1.1.1 A brief review of some methods used for the study of correlated electrons

In order to study the phases of interacting fermionic quantum matter lying beyond the LGW paradigm, a variety of methods have been developed in which quantum fluctuations have been incorporated at low energies. This includes the dynamical mean-field theory (DMFT) and its variants, quantum monte Carlo (QMC), functional renormalization group (FRG), density matrix renormalization group (DMRG), density matrix embedding theory (DMET) etc. Below, we briefly review several of these methods (except for FRG, which is reviewed in the next subsection). The auxiliary-field quantum Monte Carlo (AFQMC) [46–48] is a non-perturbative approach based on the principle that as the inverse temperature  $\beta \rightarrow \infty$ , the imaginary-time evolution of an initial state ( $|\Psi\rangle$ ) via a Hamiltonian  $H$  leads to the ground state  $|\Psi_g\rangle$ : i.e.,  $|\Psi_g\rangle = \lim_{\beta \rightarrow \infty} \exp(-\beta H)|\Psi(\beta = 0)\rangle$ . This evolution is simulated via stochastic evaluation of the imaginary-time path integral in terms of an auxiliary field obtained via a Hubbard Stratonovich transformation of  $H$ . On a finite-sized lattice, if the computation converges to the ground state energy, the ground state wavefunction can then be obtained. This can be followed by a finite-size scaling of the ground state energy towards the thermodynamic limit. The major advantage of the AFQMC method is that, upon introducing the parent symmetries of the model Hamiltonian, various properties (e.g., ground state energy density) can be computed accurately. Included among the recent successes of this method are the benchmarking studies for the 2d Hubbard model on a square lattice [49] and the hydrogen chain [50]. The essential limitations of AFQMC are the convergence of the stochastic imaginary-time evolution and the fermion-sign problem. In this method, the fermion exchange signatures are handled via a path constrained summation, naturally introducing thereby an error bound.

The single-site DMFT method [51–54] is a Green’s function based method in which a correlated electrons model Hamiltonian is mapped to a quantum impurity problem: e.g., the Hubbard model is mapped onto an Anderson impurity model (i.e., a single impurity site with on-site repulsion and a hybridization coupling to a bath of non-interacting fermions) that must be solved self-consistently. A convergent self-consistent solution of the problem is reached when the impurity Green’s function equals the local Green’s function at every real-space site. The

primary approximation within DMFT is the assumption of the  $\mathbf{k}$ -independence of the electronic self-energy. The loss of momentum-space sensitivity within DMFT, however, prevents it from capturing novel phenomena such as the Fermi arcs in the pseudogap phase of the 2d Hubbard model. On the other hand, the momentum-space cluster embedding of DMFT, i.e., the dynamical cluster approximation (DCA) [55–59] reintroduces momentum-space resolution, thereby assisting in the study of the pseudogap phase, the superconducting phase [60], the non-Fermi liquid [58] etc. of the hole-doped 2d Hubbard model. DCA is an embedding technique in which the electronic self-energy is approximated by mapping a cluster of momentum space sites  $N_c$  to a quantum impurity problem. The Brillouin zone is partitioned into tiles, and the self energy is approximated within each tile. The four-fermion interaction among the members of each cluster are those of the parent model, and the one-particle terms are determined from the self-consistency relation equating the impurity Green's function to the lattice Green's function. In order to solve the impurity problem with  $N_c$  sites, a diagrammatic Monte Carlo (diag MC) method is implemented. At high temperatures, diag MC has good convergence and the coordination number increases for increasing cluster sizes, making DCA exact. On the other hand, for low temperatures, the fermion-sign problem leads to convergence issues in diag MC, restricting the accuracy of this calculation. Similarly, cellular DMFT (cDMFT), a real space cluster embedding extension of DMFT, has also been employed extensively in the study of the 2D Hubbard model [61–68].

The density matrix renormalization group (DMRG) [69–72] is a variational method for representing the ground state of a Hamiltonian via an iterative construction of the basis. The optimal representation of the basis (e.g., using the matrix product states (MPS) for 1D systems [73, 74, 25]) is attained via iterative Schmidt decomposition across several partitions, thereby generating a diagonalized Hamiltonian within a subspace. Within this construction, quantum entanglement is restricted between subparts of the many-body state. The error originates from the convergence of the ground state energy for a finite system size, and its extrapolation to large system sizes. 2d tensor network states like projected entangled pair states (PEPS) and infinite PEPS (iPEPS) [75, 76] are restricted in being able to represent short-range entangled states, i.e., they cannot capture the more complex longer-ranged entanglement features that may appear near quantum criticality. To extend this idea to two spatial dimensions for a  $L_x \times L_y$  rectangular grid requires us to consider periodic boundary conditions along (say) the  $L_y$  direction and open boundary along  $L_x$ . Essentially, we obtain in this way a cylindrical geometry of finite length  $L_x$  and circumference  $L_y$ . Next, the sites on the cylinder are re-indexed along a path that covers all sites, with the one obvious difficulty is that nearby sites on a 2d grid are now separated by an extra circumference distance. Due to this, the number of states in the optimal DMRG basis increases exponentially with increasing cylinder circumference. This severely limits the system size along one direction, and the thermodynamic limit for DMRG is restricted to thin cylinders:  $L_x \rightarrow \infty$ ,  $L_y$  is a small finite number (for simulating 2D Hubbard model  $L_y = 6$ ). In recent times two dimensional DMRG has been used to study the low energy phases of the pure 2d Hubbard model on a square lattice revealing dominance of stripes[77–79] in the intermediate hole doped regime (around 12.5%) and with moderate to strong Hubbard coupling.

Density matrix embedding theory (DMET) [80–84] is a ground state wavefunction based cluster embedding method that maps the problem of correlated electrons onto an impurity-bath problem. The mapping is carried out by accounting for the many-body entanglement between impurity clusters ( $N_c$  sites) and the bath states, i.e., from a Schmidt decomposition of the wavefunction

$|\Psi\rangle$  into a cluster of sites ( $N_c$ ) and the remaining sites. However, the many-body state is not known a priori and is chosen as an ansatz, followed by the self-consistent treatment of the coupled impurity-bath problem. DMRG is implemented as an intermediate step as an impurity solver. Among the recent successes within the DMET approach is the ground state energy benchmarking studies of the 2d Hubbard model[49] and the equation of the state benchmarking for the hydrogen chain[50]. Further, DMET calculations for the frustrated 2d Hubbard model with hole doping reveals a ground state phase diagram with antiferromagnetism, metallic phase, d-wave superconductivity. On the otherhand for the pure 2d Hubbard model with nearest neighbor hopping DMET finds the metal insulator transition. In this manner DMET results are broadly consistent with regards to ground state energy, correlations functions as obtained from other methods[80, 85]. The sources of error within this approach are the convergence of the self-consistency condition, and any limitations arising from the DMRG solution of the impurity problem.

Finally, we also note the importance of spectral flow arguments for correlated electron and spin systems. This approach is based on the sensitivity of the ground state to changes boundary conditions through the application of twist operators ( $\hat{O}$ ). Several non-perturbative results have been obtained over the years using such methods, including the Lieb-Schultz-Mattis (LSM) theorem [86] for the 1D Heisenberg antiferromagnetic (HAFM) spin-1/2 chain at zero external field, and the Oshikawa-Yamanaka-Affleck (OYA) criterion for HAFM spin-1/2 chains and ladders at finite field [87]. In the presence of a spectral gap, the ground state expectation value  $\langle \Psi_g | \hat{O} | \Psi_g \rangle$  acts as a topological parameter that predicts ground state degeneracies, magnetization plateaus, fractional excitations etc. [42]. By following a similar line of arguments for the stability of the gapless Fermi surface, Luttinger's sum is found to act as a topological invariant [40, 41, 88]. An instability of the Fermi surface leading to a gapped insulating ground state generates a Luttinger surface of zeros. These findings are very different from the LGW paradigm of symmetry broken phases, indicating the need for a different paradigm of quantum criticality for systems of interacting fermions and spins.

### 1.1.2 The renormalization group approach

Renormalization group (RG) theory plays an important role in developing our understanding of the emergent energy/length scales at a critical point. Indeed, the RG formalism has enabled the description of complex microscopic models in terms of tractable effective theories [89–96] across energy and length scales. As RG theory allows for the emergence of new composite degrees of freedom (or the physics of new scattering processes) at a given scale (which often corresponds to the infra-red in the context of condensed matter physics), the method is also apt for studying a variety of exotic quantum phases. RG thus aids in studying critical phenomena, as well as the classification of many body phases [97, 98]. As RG scaling theory was formulated in Refs. [99–102] for system of weakly interacting fermions, demonstrating the Fermi liquid fixed point theory of Landau quasiparticles as well as the Bardeen Cooper Schreiffer (BCS) instability of the Fermi liquid for attractive interactions.

Strongly correlated electron systems on a lattice in two spatial dimensions and higher are known to host several exotic emergent quantum phenomena that are yet to be understood clearly, e.g., high- $T_c$  superconductivity, non-Fermi liquids, topological order, many- body localization etc. [103, 2, 104–107, 23]. Considerable effort has been made towards the development of

functional renormalisation group (FRG) approaches to the understanding of these phenomena [108, 109]. FRG deals with the RG flow of the Grassmannian many-body action [110–114], and incorporates (in principle) all orders of quantum fluctuations by accounting for the entire hierarchy of  $2n$ -point scattering vertex RG flow equations [115, 116]. This approach has provided deeper insights into various emergent phases of quantum matter via effective descriptions derived from parent models of strongly correlated electrons. Recent developments in FRG involve the inclusion of frequency dependence within the self-energy [117, 118] and vertices [119–121], allowing the RG flows to reach theories closer to stable fixed points. Another important development has been the resummation of multiloop diagrams in FRG equations, yielding the parquet approximation [122]. Such careful computations has led to a better quantification of the effective theories in terms of measurables like the susceptibility, spectral function etc. [108, 116, 123] This formalism has been successful in capturing a wide variety of strongly correlated phases of electronic quantum matter, e.g., the pseudogap, strange metal, d-wave superconductivity etc. [124, 125, 120, 126–128] While the method is in principle nonperturbative, numerical implementations of FRG have however typically needed truncations at finite orders in the loop expansion. Thus, despite much success, FRG is limited thus far to studying weak-to-intermediate values of the interaction coupling, and effective Hamiltonians or actions at IR stable fixed points is not obtainable.

There have also been Hamiltonian approaches to the RG theory, namely the continuous unitary transformation (CUT) based RG formulation [129, 130, 98, 131, 132]. In this version of the RG, connectivity elements between different energy levels are removed via the transformation, rendering the Hamiltonian more band diagonal. In this scheme, a loop expansion becomes difficult and the renormalization group structure remains perturbative. CUT RG method based stability analysis for the 2d Hubbard model on the square lattice reveal the antiferromagnetic phase transition, d-wave pomeranchuk phases etc.[133]. There is another Hamiltonian RG approach[134–136] based on the unitary transformations of Refs.[137–140]. Further, in Refs.[141, 142], a Hamiltonian RG scheme is constructed using a coupled cluster based similarity transformation. However, in both these methods, the complication arises primarily from the presence of a nontrivial many-body Hermitian operator in the denominator of the effective Hamiltonian.

Another approach towards classifying many-body phases stems from the study of many-particle quantum entanglement [143, 22, 144, 145]. It has emerged as an important feature for quantum many-body systems with strong correlations, e.g., quantum spin liquids, fractional quantum hall phases, high Tc superconductors etc. [105–107]. A complete classification along these lines is an outstanding challenge, with implications for many-body theory, quantum information theory and quantum field theory [146–154]. In the systems mentioned just above, a marked (and sometimes dramatic) change in the nature of many-particle entanglement is observed as a signature of quantum criticality [155–157, 146, 158, 151]. For studying the scaling property of many particle entanglement features, entanglement renormalization group (ERG) approaches based on tensor network (TN) states has emerged as an indispensable tool [149, 159, 160, 25, 161]. For instance, TN states such as matrix product states (MPS) (developed initially in DMRG [69]) have been shown as being highly accurate for studying the ground state properties of 1D gapped phases. In 2D, tree tensor network states (TTN) [162, 163] and projected entangled pair states (PEPS) are useful for studying gapped phases (see references in [25]). The multiscale entanglement renormalization group ansatz (MERA) is yet another tensor network RG program in which each layer of RG transformations are organized as a stacking of (one or several) layer(s) of tensor

products of two-local unitary operations (i.e., that perform the entanglement renormalization) together with a layer composed of isometries that remove the disentangled qubits (i.e., that carry out the process of coarse-graining). MERA has been used for studying both quantum criticality [164–166], as well as gapped topological quantum liquids [167–171].

A diverse array of gapped and gapless quantum liquids can be studied via entanglement renormalization (ER) [167, 164, 172–174, 169–171]. It is thus imperative to ask the question: can we classify various quantum liquids solely based on the attributes of entanglement features generated via ER? An outstanding challenge for entanglement renormalization group (ERG) has been in its application to strongly correlated electronic systems [175, 176]. Although there are several works on constructing tensor networks, e.g., MERA and its variants for systems of noninteracting fermions [175, 177, 178], there are only a few on systems of interacting fermions [179, 163]. Thus, by and large, the implementation of ERG on long-range entangled systems (resulting from strong electronic correlations) remains an unresolved challenge.

### 1.1.3 Motivating the unitary renormalization group approach

In this section, we list a set of outstanding questions that constitute the primary goals for the development of a new RG method in this thesis.

1. *Can we construct a nonperturbative Hamiltonian RG flow formalism for the many-electron problem by the iterative decoupling high energy degrees of freedom, such that it enables the access to stable fixed points of the RG flow? The Hamiltonian RG flow should generate, in principle, a family of RG flow equations for the parameters (e.g., hopping, two-body interactions, etc.). What is the nature of the nonperturbative RG flow equations for various couplings? Can they account for quantum fluctuations to all orders of a loop expansion? Hamiltonian decoupling schemes generally take account of retardation or quantum fluctuation effects arising from the non-commutativity between different parts of the Hamiltonian. Can we construct frequency-dependent effective Hamiltonians within the Hamiltonian RG approach? Finally, can we obtain phase diagrams from the Hamiltonian RG scheme in a suitable parameter space depicting the various phases and phase boundaries?*
2. *Low energy effective Hamiltonians at stable RG fixed points are expected to be more tractable than the parent models. If such effective theories can be obtained from the RG, can we analytically construct the low energy eigenspectrum and eigenbasis from here? If this can be done efficiently, we should be able to simulate on a classical computer various low-energy properties like the ground state energy density, resistivity, spin- and charge-susceptibility, the nature of many-particle entanglement etc. Such a study should also enable the benchmarking pf various measurables of a many-body state obtained via the RG with those obtained from other state-of-the-art numerical methods.*
3. *Can a Hamiltonian renormalization group be based purely on unitary disentangling transformations, such that at each RG step, high-energy (UV) degrees of freedom are disentangled from their low-energy (IR) counterparts. Such transformations would necessarily preserve total spectral weight, and display dynamical spectral weight redistribution (or UV-IR mixing) through the RG flow. If the low-energy eigenstates of the effective Hamiltonian can then be obtained analytically, the RG flow of the many-body eigenstates can be obtained by*

*inverting the action of unitary maps on the IR eigenstates. Further, this would also enable tracking the RG flow of various many-body entanglement features, e.g., entanglement entropy, mutual information etc.*

*Further, any RG based on unitary transformations should possess a quantum circuit representation of the ground state in terms of the universal gates: one qubit rotation and two-qubit rotation gates. If this can be obtained, the entire unitary RG flow circuit can be represented as a holographic tensor network: a collection of layers of unitary gates arranged holographically from UV (boundary) to IR (bulk). Each layer of such a tensor network should be composed of universal two-qubit and one qubit gates. The highest energy qubits lying at the boundary layer of the tensor network would be disentangled at first, while scaling towards the bulk of the tensor network would indicate the disentangling of the IR degrees of freedom. Can such a tensor network representation be constructed for the Hamiltonian RG framework?*

4. *The Hamiltonian RG framework may well lead to effective Hamiltonians with a low-energy spectral gap. Can we then probe such emergent theories for topological order in the ground state manifold by combining the RG framework with spectral flow arguments? Upon tracking the RG flow for entanglement features (e.g., entanglement entropy), can we distinguish between symmetry-preserved topologically ordered, symmetry-broken and gapless phases?*
5. *Gapped effective Hamiltonians can emerge from the IR fixed points of RG flow. Can we provide gauge theoretic constructions for them in terms of non-local emergent degrees of freedom, e.g., Wilson loops? This should serve as a complementary route of deriving gauge theories that are obtained otherwise from the effective action approach.*
6. *Can we account for the fermion exchange signatures in the RG flow of many-body eigenstates? If yes, can we show how RG theory leads to certain effective Hamiltonians (e.g., the reduced BCS Hamiltonian) where the fermion signs are mitigated.*
7. *An RG theory built out of unitary transformations will naturally preserve the fundamental symmetries of the parent model, e.g.,  $U(1)$  phase-rotation symmetry, spin-rotation symmetry, translation invariance, etc. By incorporating infinitesimal explicit symmetry-breaking terms, can we redo the RG formalism and obtain the effective low-energy theories where symmetry-broken phases are attained as eigensolutions?*
8. *Unitary transformations will preserve the total spectral weight such that the f-sum rule will be preserved. Starting from a unitary RG flow formalism, can we demonstrate the preservation of the f-sum rule (whilst demonstrating the emergence of bound states or composite degrees of freedom)? Similarly, can we show that parent Hamiltonians that lead to effective theories with a gapless Fermi surface under RG flow encode the Luttinger's sum rule? On the other hand, can we show within a unitary RG flow formalism that the gapping of the Fermi surface is consistent with the appearance of a surface of Luttinger zeros in the single-particle Green function?*

In this thesis, we present a novel unitary renormalisation group (URG) program shown in Fig.1.1 for electronic states that block diagonalizes the Hamiltonian at each RG step in the occupation-number basis of an electronic state. The electronic states are arranged with respect to their

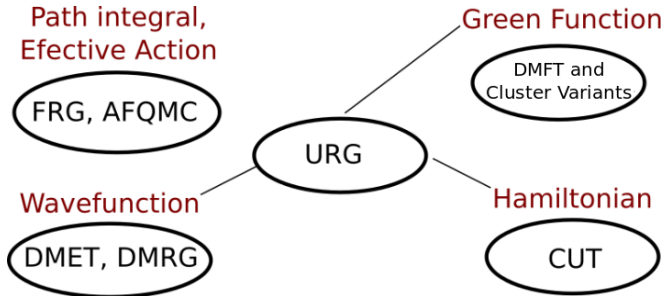


Figure 1.1: Comparison between different many-body methods, including Hamiltonian, effective action, Green’s function and wavefunction based approaches. In this thesis, we present the URG method incorporating aspects of Hamiltonian, wavefunction and Green’s function based approaches.

bare dispersion energies in the following order of precedence: the highest energy states are disentangled first, scaling gradually towards those at lower energies. The Hamiltonian RG evolution generates nonperturbative RG flows equations for the 1-particle self-energy, various 2-particle and 3-particle scattering vertices (i.e, the couplings of various four-fermionic and six-fermionic scattering terms) and all higher-order  $n$ -particle scattering vertices. Concomitantly, upon acting the unitary transformations on the eigenstates of the Hamiltonian, we obtain rotated eigenstates where the highest energy electronic qubits are disentangled. The many-body coefficients comprising the eigenstates are renormalized, thereby renormalizing the many-particle entanglement content as well. In this way, URG leads in a unified manner to both the vertex RG flow equations together with the entanglement renormalization group.

The nonperturbative nature of the URG flow equations originates from the fact that, in obtaining them, the expansion in vertex loops to all orders has been resummed into closed-form expressions. Further, the denominator in the right-hand side of the RG equations for the scattering vertices contains the renormalized 1-particle self-energy, as well as higher-order correlation energies for composites of electrons and holes [180–183]. Importantly, we find that the vertex URG flow happens across a family of quantum fluctuation scales ( $\omega$ ) that arise from the noncommutativity between the kinetic energy and the four-fermionic interactions in the bare model. Indeed, this non-commutativity leads to number-density fluctuations of the single-particle electronic states in momentum-space. As a direct outcome of the nonperturbative nature of the RG equations, we obtain stable fixed points of the flows at any given fluctuation scale  $\omega$ . In this way, we have performed the RG analysis of various models of correlated electrons with the effective dimensionless coupling strength (i.e., the ratio of kinetic and potential energy couplings) ranging all the way from weak to strong: the 2d Hubbard model [180, 181, 184], the XXZ kagome antiferromagnet [185], a general problem of four-fermionic interactions without and with disorder (i.e., a generalized Sachdev-Ye model) [183]. The effective Hamiltonian and associated low-energy eigenstates obtained at various stable IR fixed points then provides further avenues for analyses.

#### 1.1.4 Features of the Unitary RG program

URG is carried out via a sequence of unitary disentanglement operations on a graph, each of whose nodes corresponds to one electronic state. Each unitary operation on the graph disentangles an

electronic state  $|N\rangle$  from the rest (the coupled subspace), resulting in a block diagonalizing the Hamiltonian in the occupation number basis states  $|1_N\rangle$  and  $|0_N\rangle$ . This involves the removal of off-diagonal terms with respect to a given electronic state  $|N\rangle$ , and the creation of good quantum numbers of the occupation numbers (1 and 0) of that state. Below, we list the essential features of the URG program.

- 1. Unitary operator** Given a bare Hamiltonian  $H$  and an ordering of the bare electronic onsite energy  $\epsilon_1 \leq \epsilon_2 \leq \dots \leq \epsilon_N$  (for states  $|1\rangle, \dots |N\rangle$ ), the unitary operator  $U_{(N)}$  for disentangling  $|N\rangle$  is determined as shown below (see Fig.1.2)

$$U_{(N)} = \frac{1}{\sqrt{2}}[1 + \eta_{(N)} - \eta_{(N)}^\dagger] , \quad \{\eta_{(N)}, \eta_{(N)}^\dagger\} = 1 . \quad (1.1)$$

Electron-hole transition operators  $\eta_{(N)}$  and  $\eta_{(N)}^\dagger$  are determined from the off-diagonal and diagonal parts of the Hamiltonian  $H$ . The rotated Hamiltonian  $H' = U_{(N)} H U_{(N)}^\dagger$  satisfies the decoupling equation

$$[H', \hat{n}_N] = 0 , \quad (1.2)$$

whereas  $[H, \hat{n}_N] \neq 0$ . The quantum fluctuations in the occupation subspace of  $\hat{n}_N$  arises from the off-diagonal terms  $\hat{n}_N \hat{H}(1 - \hat{n}_N)$  and its hermitian conjugate, such that these are removed via the unitary rotation:  $\hat{n}_N H'(1 - \hat{n}_N) = 0$ , resulting in a block diagonal Hamiltonian. An iterative application of the unitary transformations  $H_{(j-1)} = U_{(j)} H_{(j)} U_{(j)}^\dagger$  leads to the Hamiltonian renormalization group (see Fig.1.3).

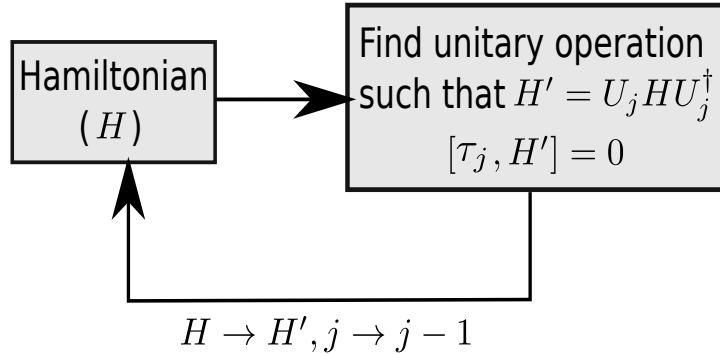


Figure 1.2: Schematic representation of the Hamiltonian RG flow. The feedback loop  $j \rightarrow j - 1$  depicts the iterative RG process. Each RG step involves the creation of one integral of motion  $\tau_j$  that commutes with the rotated Hamiltonian.

Below, we compare the form of the unitary operator  $U_{(j)}$  with those that have appeared in the literature. First,  $U_{(j)}$  can be cast in the familiar van Vleck form [186]

$$U_{(j)} = \exp\left[\frac{\pi}{4}(\eta_{(j)}^\dagger - \eta_{(j)})\right] , \quad (1.3)$$

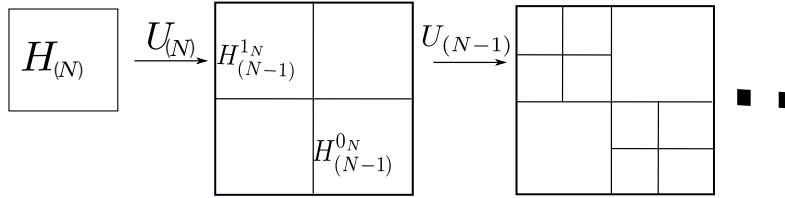


Figure 1.3: Representation of the Hamiltonian as a block matrix in the occupation number basis of single-electron states, and where the unitary rotation removes the off-diagonal blocks.

providing a geometric representation of a rotation angle (whose value here is  $\pi/4$ ) between the old and new configuration subspaces [187]. The  $\pi/4$  unitary gate has the following property:  $(U_{(N)})^4 = -I$ . In this form, it can be compared to the unitary exponential wave-operator investigated in the context of coupled cluster theory [188–191]. We further note that the form of eq.(1.3) is a simplified version of the canonical transformation advocated first by Shavitt and Redmond [137] (see also [140, 139]). Unlike the wave-operator of coupled cluster theory, however, it is clear from the relations given earlier in eqs.(7.8) that the unitary operator  $U_{(N)}$  does not involve a infinite series expansion.

Recently, in the context of the phenomenon of many-body localisation in systems with both strong correlations as well as disorder (see, e.g., [192]), several variants of the strong disorder RG studied in the past (see Refs.[193–199]) have been proposed. These involve a RG flow arising from the diagonalization of Hamiltonians via the iterative application of unitary operators [200–204]. A similar renormalisation scheme for Hamiltonians had also been proposed earlier by White [205] in the context of the quantum chemistry of molecular clusters. These schemes rely essentially on Jacobi’s method for the iterative diagonalisation of Hermitian matrices [206]. This involves the application of a unitary displacement operator that removes the largest off-diagonal element in the Hamiltonian matrix. A comparison with our unitary operator reveals that the generator of the transformation  $i(\eta_{(j)} - \eta_{(j)}^\dagger)$  in our unitary map (eq.(1.3)) satisfies the same properties as the generator in the aforementioned method, along with an extra property that  $\{\eta, \eta^\dagger\} = 1$ . The latter leads, however, to an important difference in terms of the results obtained from the two approaches. The strong-disorder style RG schemes lead to an effective Hamiltonian at low energies that is an expansion in terms of products of the emergent local integrals of motion ( $\tau_i$ ) generated along the RG flow, i.e.,  $H_{eff} = \sum_i \epsilon_i \tau_i + \sum_{ij} V_{ij} \tau_i \tau_j + \sum_{ijk} V_{ijk} \tau_i \tau_j \tau_k + \dots$ . On the other hand, we will see below that the effective Hamiltonian reached from our RG scheme involves only a small number of such terms, as the rest can be shown to be irrelevant under the RG transformations. Another important difference is that in our RG, the iterative decoupling procedure can be inhibited if a stable fixed point theory (involving residual occupation number quantum fluctuations due to the remaining coupled states) is attained. This leads to breakdown of the adiabatic continuity between the states at higher and lower energies, signalling instead the emergent condensation of composite degrees of freedom at low energies. This, as we shall see later, is a non-perturbative outcome of the UV-IR mixing. In this case, the local integrals of motion will not form a complete set.

It is also worth noting the efforts of Wilson [89], who attempted the partitioning of the Hamiltonian into low and high energy subspaces. To decouple the blocks at a particular

step of the RG flow, Wilson proposed an operator  $R$  that mixes states between the two subspaces. The effective Hamiltonian then obtained possesses a Bloch-Brandow form [207–209], which can be seen as the action of a unitary transformation  $U_W = \exp(\operatorname{arctanh}(R - R^\dagger))$  on  $H$  [186, 210, 137, 188, 139, 187] :  $H_{\text{eff}} = U_W H U_W^\dagger$ . The  $\eta_{(N)}$  transition operator obtained by in this thesis is analogous to Wilson's  $R$  operator, with the important difference that, in our case, the partitioning (or decoupling procedure) is carried out in the fermion occupation number (i.e., Fock) basis of the state  $N$ . The relations in eqs.(7.8) then allow for a simplification of both the unitary operator, as well as the effective Hamiltonian, at every step of the RG procedure.

2. **Quantum fluctuation scales** Within the unitary RG formalism, we find a quantum fluctuation operator  $\hat{\omega}_N = H'_D + \Delta H'_X$  written in terms of the number diagonal part of the rotated Hamiltonian ( $H'_D$ ) and the additional renormalization contribution of the off-diagonal terms ( $\Delta H'_X$ ). The RG evolution of the spectral component  $H^j(\omega)$  of the rotated Hamiltonian  $U_j H U_j^\dagger - H = \Delta H$  takes place along each of the eigendirections  $|\omega\rangle$  of  $\hat{\omega}_N$  (tagged by an eigenvalue  $\omega$ ). The RG evolution of Hamiltonians from high energy (UV) to low energy (IR) can be considered as a holographic network of eigenstates and eigenvalues in theory space from boundary to bulk [211]. The RG dynamics of the Hamiltonian naturally feeds into that of the quantum fluctuations  $\Delta\omega_N$ . In this way, we realize the bulk of the Hamiltonian network as manifestly possessing non-trivial quantum as well as RG dynamics [212–214]. For instance, the renormalized diagonal Hamiltonian is given by

$$H'_D(\omega) = \sum_i \epsilon'(\omega) \hat{n}_i + V'_{ij}(\omega) \hat{n}_i \hat{n}_j , \quad (1.4)$$

where  $\epsilon'(\omega) = \epsilon + \Sigma(\omega)$  is the one-particle term renormalized by the self-energy ( $\Sigma(\omega)$ ). Similarly, the renormalization of the off-diagonal Hamiltonian is given by

$$\Delta H_X = H'_X - H_X = \Delta V_{i,j}(\omega) c_i^\dagger c_j + \Delta V_{ijkl}(\omega) c_i^\dagger c_j^\dagger c_k c_l , \quad (1.5)$$

where  $H' = U H U^\dagger$  is the rotated Hamiltonian and  $H$  is the bare Hamiltonian. The two components of  $\hat{\omega}_j$  thus encode the renormalization of different aspects of the coupled degrees of freedom: the first ( $\Delta H_X$ ) corresponds to the renormalization of various off-diagonal scattering vertices, and the second ( $H_D$ ) to the renormalization of various  $n$ -particle self-/correlation energies.

The spectral decomposition of  $\hat{\omega}_{(j)}$  in the various eigendirections  $|\omega\rangle$  (and with eigenvalue  $\omega$ ) leads to that of the electron-hole transition operator  $\eta_{(j)}(\omega)$ . Here,  $|\omega\rangle$  for RG step  $j$  belong to the  $2^{j-1}$  dimensional Hilbert space of remaining quantum fluctuation-entangled single-particle states.  $\eta_{(j)}^\dagger(\omega_{(j)}^i)$  represents the collection of all scattering processes that take the electronic state  $j$  between the unoccupied and occupied configurations, in turn causing quantum fluctuations involving many-body configurations of the coupled  $\{0, j-1\}$  single-particle states (see Fig.1.4). Apart from the unitary operator in eq.(1.3), we can also define a wave-operator  $\Omega_{(j)} = \exp(-\eta_{(j)}^\dagger)$ , such that  $|\Psi_{(j)}^{1,j,i}\rangle = \Omega_{(j)} |\Psi_{(j),i}\rangle$ . This wave-operator is an equivalent non-unitary transformation that can be employed in solving the decoupling equation eq.(1.2), and obtaining the effective Hamiltonian [134]. A similar wave-operator appears in the generalized Bloch equations and multireference coupled-cluster

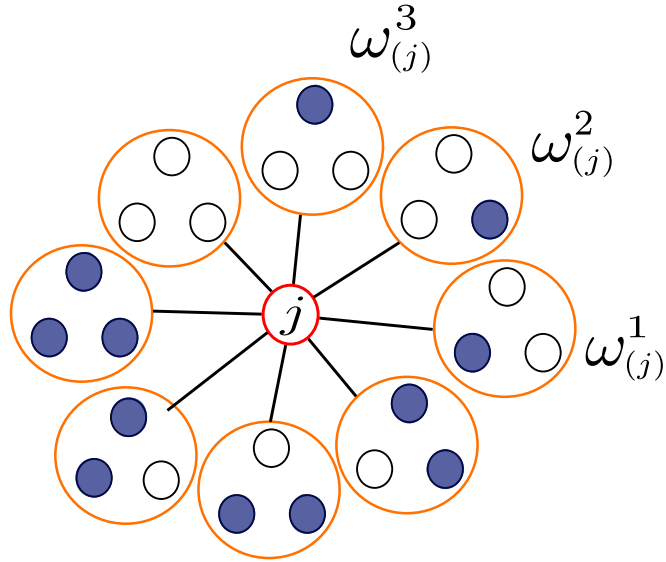


Figure 1.4: An example describing the quantum fluctuations originate from the coupling of 3 electronic states with the state  $j$  via off-diagonal Hamiltonian blocks. The fluctuation operator  $\hat{\omega}$  then describes the energy scales  $\omega_{(3)}^1, \dots, \omega_{(3)}^8$  for occupation number fluctuations generated about the  $2^3 = 8$  number diagonal configurations of the coupled states, with blue/white filled circles representing occupied/unoccupied states respectively.

methods [215–217] for solving the decoupling equations between two subspaces of many-body configurations.

Further, the spectral decomposition of  $\hat{\eta}$  in terms of the  $\hat{\eta}(\omega)$  can be used to recast the decoupling equation eq.(1.2) in the form employed in multireference Brillouin-Wigner perturbation theory [217, 218]. In this form,  $\hat{\eta}(\omega)$  connects many-body states with single-particle state  $j$  either occupied ( $|1_j\rangle$ ) or unoccupied ( $|0_j\rangle$ ). The multi-reference nature of the approach allows for the treatment of dynamical fluctuations associated with the  $2^{j-1}$  occupation number configurations of the  $\{1, j\}$  coupled states. Thus, it enables the exploration of the ground state as well as excited states of the Hamiltonian spectrum [219–221]. An important distinction can now be made. In the standard Brillouin-Wigner method, the denominator of the frequency-resolved e-h transition operator  $\eta_{(j)}^\dagger(\omega_{(j)}^i)$  contains a many-body Hamiltonian with off-diagonal terms (indicated by  $H_X$  in our formalism). This leads to a Dyson series-like expansion of the propagator, whose truncation makes the approach perturbative. On the other hand, we have recast the denominator in  $\eta_{(j)}^\dagger(\omega_{(j)}^i)$  such that it contains only the number diagonal many-body operator  $H_{(j)}^D$  at every RG step. This resolves the problem associated with the inversion of a large many-body matrix, allowing the closed-form derivation of flow equations along multiple many-body configuration channels without the need for truncation of any series expansion.

We can also use the spectral representations of  $\hat{\omega}_{(j)}$  and  $\eta_{(j)}^\dagger$  to obtain the spectral components of the Hamiltonian flow equation  $\Delta H(\omega) = |\omega\rangle\langle\omega|(H' - H)|\omega\rangle\langle\omega|$ . The dependence on  $\omega$  reflects retardation effects in the effective Hamiltonian at multiple energy scales. Such frequency-dependent effects dates back to the early work of Breit [222]. Recently,

they have also been taken account of within the functional RG approach to strongly correlated condensed matter systems [223], as well as in QCD in the form of the dynamical renormalization group formalism of Refs.[224–226].

A multi-reference formalism leading to effective Hamiltonians at various energy scales deserves to be contrasted with the single-reference Wilsonian approach to RG. In the latter, we typically obtain only the effective Hamiltonian at low-energies via the application of projection operators. In our formalism, however, the lowest energy state for the effective Hamiltonian  $H_{(j)}(\omega_{(j)}^i)$  can be obtained from the asymptotic imaginary time ( $\tau$ ) evolution operation  $\exp(-\tau H_{(j)}(\omega_{(j),i}))$  on any arbitrary state  $|\Psi(\omega_{(j),i})\rangle$  belonging to its Hilbert space [227, 228]. As a fixed point is reached for the Hamiltonian RG flow (i.e.,  $H_{(j)}(\omega_{(j)}^i) \rightarrow H_{(j)}(\omega_{(j^*)}^i)$ ), the lowest energy state for the spectrum  $|\Psi_{(j)}^0(\omega_{(j)}^i)\rangle$  is also obtained concomitantly. In this way, we can explore the spectrum around any fluctuation scale  $\omega_{(j)}^i$ . Fig.(1.4) illustrates the 8 configurations of three electronic states labelled by the associated quantum fluctuation energy scales  $\omega_{(j)}^i$  of a fourth state's (labelled  $j$ ). In this way, we demonstrate that the renormalization procedure developed in this thesis is a multi-reference method [217], i.e., the RG steps resolve the multiple energyscales for quantum fluctuations in an iterative fashion.

As discussed above, eigenvalues of the quantum fluctuation operator  $\hat{\omega}$  correspond to emergent quantum fluctuation scales  $\omega$ . The retardation effects associated with  $\omega$  leads to a frequency-dependent self-energy in the effective Hamiltonian. From the Kramers-Kronig relations, we obtain the imaginary part of the single-particle self-energy, in turn revealing the associated thermal scale up to which the one-particle excitations can survive. We show in the following chapters that the URG transformations lead generically to two possible scenarios: the first involves the iterative block diagonalization procedure reaching a fixed point with a gapless Fermi surface, and the second the reaching of a fixed point involving the gapping of the Fermi surface via the formation and condensation of bound states. The temperature scale associated with  $\omega$  has meaning for both scenarios. For the first, it indicates the lifetime of the gapless excitations in the neighbourhood of the Fermi surface. On the other hand, it indicates the regime of validity for the emergence of two-particle bound states at finite temperatures for the second scenario.

3. **Heirarchy of RG flow equations** The Hamiltonian operator's diagonal ( $H_{(j)}^D$ ) and off-diagonal ( $H_{(j)}^X$ ) parts at any given RG step ( $j$ ) can be written as a closed-form cluster decomposition: the sum constitutes one-particle off-diagonal, two-particle scattering, three-particle scattering terms etc., upto the highest off-diagonal  $n$ -particle vertex

$$H_{(j)}(\omega_{(j)}^i) = H_{(j)}^2(\omega_{(j)}^i) + H_{(j)}^4(\omega_{(j)}^i) + H_{(j)}^6(\omega_{(j)}^i) + \dots \quad (1.6)$$

As the RG proceeds, certain electronic states are disentangled and do not participate any further in the off-diagonal scattering processes, thereby rendering smaller the string length of remnant off-diagonal scattering terms. To obtain the vertex RG flow equations from the renormalized Hamiltonian, we decompose it into a sum of strings comprised of number-diagonal and off-diagonal operators. This decomposition is carried out as follows. First, we write one spectral component of the rotated Hamiltonian  $H_{(j)}(\omega)$  as a *cluster expansion*

of 2-point, 4-point, 6-point and higher order vertices:

$$H_{(j)}(\omega) = H_{(j)}^2(\omega) + H_{(j)}^4(\omega) + H_{(j)}^6(\omega) + \dots . \quad (1.7)$$

Each cluster component, say  $H_{(j)}^{2l}(\omega^i)$ , has both diagonal as well as off-diagonal parts, and involve  $2l$ -point off-diagonal scattering vertices and correlation energies with contributions from all the various  $2n$ -point vertices. This vertex RG flows can thus be represented in a compact manner as a hierarchy of RG flow expressions.

Each of the RG flow expressions, arising from the analytic structure of  $\eta$ , depends upon denominators containing various renormalized correlation energies and the retardation self-energy. This leads to two non-perturbative features of the RG transformations. First, the interplay of the multi-reference quantum fluctuation scale  $\omega_{(j)}^i$  and the correlation energies within the denominator distils the relevant vertices from the irrelevant ones. Second, the stable IR fixed points of the RG equations are associated with the poles of the two-particle (or higher order composite) propagator, depicting the emergence of new degrees of freedom. From these fixed point solutions, the effective Hamiltonian for the two-particle composite (or other electron-hole composite) objects can then be derived. In the following chapters, we will demonstrate explicitly the derivation of fixed point effective Hamiltonians that arise from the RG treatment of various microscopic models.

It should be noted that the feedback from correlation energies, and the hierarchical nature of RG flow equations, are also features of the FRG scheme [223, 108]. For instance, the recent multiloop functional RG scheme [115, 116] contains a systematic way of dealing with various  $2n$ -point vertices, but the heirarchy of flow equations therein typically requires a truncation. The unitary RG formulation for the Hamiltonian presented here, however, does not. Instead, its non-perturbative nature overcomes the limitations of both a coupling expansion [229] as well as a cluster expansion [200] prevalent in other Hamiltonian RG formulations. Further, symmetry-broken orders can be efficiently tracked within the FRG approach by studying the RG flow for bosonic order parameter functionals obtained from a Hubbard-Stratonovich transformation[230, 112]. However, in the URG scheme, the symmetries of the parent Hamiltonian are maintained manifestly via the unitary mappings. We instead obtain the symmetry-broken phases upon including the respective symmetry breaking fields and re-performing the unitary RG analysis.

#### 4. Vertex tensor network description of URG

The electronic Hamiltonian obtained from URG can be realized as a vertex tensor network: as shown in Fig.1.5, the scattering vertices are represented as tensors where the blue legs of the tensors represent the electronic states. The black dashed/solid edges represents the outgoing/incoming electronic states respectively. The number of  $2n$  denoting the vertex is the total number of incoming and outgoing lines. Similar to the case of spectrum bifurcation renormalization group (SBRG) [229], URG preserves the Hilbert space and the spectrum of Hamiltonian. Thus, following the finding in Ref.[231, 177], URG has a holographic [212] interpretation in the form of an emergent vertex tensor network (see Fig.1.6). Further, in Ref.[184], we have also shown that the entanglement renormalization group flow generated by the unitary transformations  $U_{(j)}$  also describes an entanglement holographic mapping

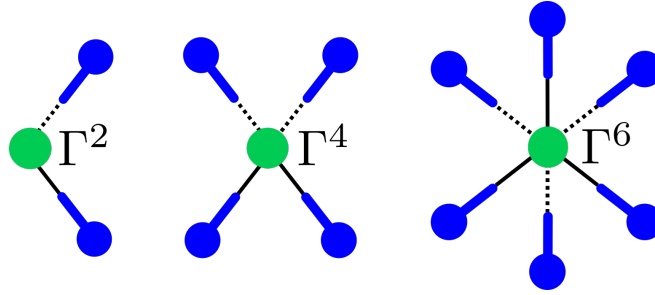


Figure 1.5: The 2-point  $\Gamma^2$ , 4-point  $\Gamma^4$  and 6-point  $\Gamma^6$  scattering vertex tensors. The blue legs represent electronic states, while the dashed/solid lines represent the outgoing/incoming electrons respectively.

(EHM) network [232]. In keeping with this, we will discuss the RG flow of many-body coefficient tensor comprising the eigenbasis RG flow in a point below.

In the RG step  $j$ , the unitary transformation  $U_{(j)}$  (yellow block in Fig.1.6) causes the disentanglement of exactly one electronic state (blue leg enclosed by a dotted rectangle) from the rest of the electronic states (blue legs). In this process,  $U_{(j)}$  leads to the renormalization of the Hamiltonian and its associated eigenbasis. This causes the (blue) physical electronic states (i.e., the occupied/unoccupied basis of fermionic qubits) from the left of the *holographic boundary* to be mapped onto the red *emergent bulk physical qubits*. The initially entangled boundary qubits (blue legs) are arranged in descending order of the single-electron energy contribution  $\epsilon_i$  from left to right, i.e.,  $\epsilon_N \geq \dots \geq \epsilon_1$ . The Hilbert space of the bulk electronic qubits is spanned by the Pauli gates:  $\tau_z = \hat{n} - \frac{1}{2}$ ,  $\tau_x = \frac{1}{2}(c^\dagger + c)$ ,  $\tau_y = \frac{1}{2i}(c^\dagger - c)$ .

Thus, the color variation of the disentangled qubits from light (high energy) to deep red (low energy) in proceeding between the various layers of the tensor network in Fig.1.6 represents the RG flow from UV (high energy physical qubits) to IR (low energy physical qubits). This also reflects the fact that, due to the nonlocal nature of the unitary transformations, the nature of entanglement within the remnant coupled electronic states morphs along with the disentanglement of the boundary qubits. We also note that the unitary gates we have presented here belong to a generalized notion of the Clifford gates discussed in Ref.[233]: at every RG step, the Pauli group transforms under the unitary map. In this way, the tensor network structure of Fig.1.6 represents the RG flow of the entire set of  $2n$ -point vertex tensors.

5. **Analytic construction of low energy theory** The effective Hamiltonian constructed from the stable fixed points of the URG method can be solved exactly for the ground state in certain cases, for instance, the 2d Hubbard model at half-filling and with hole-doping [180, 181], the 1d Hubbard model [234] etc. From the ground state, we obtain correlation functions, ground state energy, single-particle lifetime, etc. Further, by studying the excited states (obtained from various spectral components of the Hamiltonian  $H(\omega)$ ), we also obtain the finite frequency parts of the observables like resistivity, charge and spin susceptibilities etc. Upon accounting for the low energy spectrum at the IR fixed point, we can also obtain the finite-temperature partition function in certain cases (e.g., Kondo

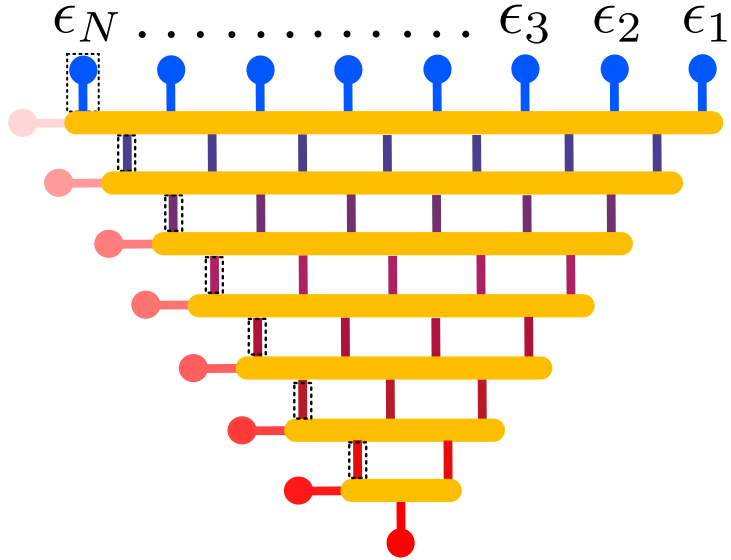


Figure 1.6: Hamiltonian (or vertex) tensor network representation of URG. The blue legs represent the holographic boundary composed of the physical fermionic qubits coupled via the bare  $2n$ -point vertex tensors. The yellow blocks represent nonlocal unitary disentanglers that iteratively map the boundary qubits to the bulk decoupled qubits (on left of each yellow block) with energies varying from high (light red) to low (deep red). Color variation of the input legs into each subsequent unitary operator (yellow block) depicts the variation in the nonlocal structure of the vertex tensor network within the remnant coupled states as the RG flows from UV to IR.

problem [235]), enabling a pathway towards extending the  $T = 0$  results obtained from URG to finite temperature.

**6. Eigenbasis renormalization** The bare (or initial) Hamiltonian  $H_{(N)}$  of the RG flow has  $N$  coupled electronic degrees of freedom, with an eigenbasis comprising of  $2^N$  eigenstates  $\mathcal{B}_{(N)} = \{|\Psi^i\rangle, i \in [1, 2^N]\}$  that satisfy the eigenvalue relation  $H_{(N)}|\Psi^i\rangle = E^i|\Psi^i\rangle$ . The elements of the eigenbasis are renormalized via the same unitary rotation that block diagonalizes the Hamiltonian, thereby preserving the spectrum. The renormalization of the eigenbasis partitions the basis into a direct sum of two halves (see Fig.1.7) labelled by the occupation number of the decoupled state  $j+1$ . Further, such a partitioning is carried out at every RG step. Along with this, the entanglement content within the remnant coupled nodes in the many-body states is also modified. The subparts of the renormalized eigenbasis can be denoted by the occupation number configurations of the decoupled single-particle states. The configurations of the separable subspace are visualized in Fig.(1.7) in terms of the filled (occupied)/unfilled (unoccupied) circles on the handles attached to any one given subpart (shown in light blue). The collection of the separable electronic state occupation numbers is composed of a string of 1's and 0's, and can be represented as a tensor. This tensorial representation is visualized in Fig. 1.8 by treating the occupied electronic state configurations as legs of the object marked 1 in red. The iterative decoupling of the eigenbasis into smaller sub-bases (Fig.1.7) indicates that the renormalized eigenstates at RG step  $j$  possess an interaction-driven many-body entanglement that is limited to within the

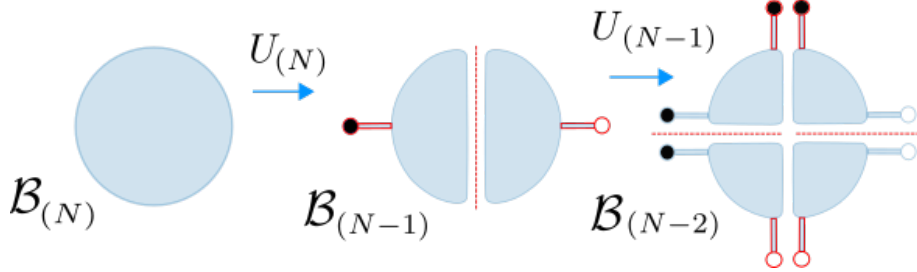


Figure 1.7: The RG evolution of the Hamiltonian's eigenbasis  $\mathcal{B}_{(N)}$  (blue disk, top left) via the disentangling unitary operations. Upon the application of the first unitary operation  $U_{(N)}$ ,  $\mathcal{B}_{(N)}$  bifurcates into two blue semicircular disks representing the eigenbasis of the entangled electronic states  $\mathcal{B}_{(N-1)}$  labeled by the occupation of the disentangled state. The red handles (on the blue semicircular disks) with filled (black)/unfilled (white) circles represent the occupied ( $1_N$ )/unoccupied ( $0_N$ ) configurations of the disentangled state. Upon subsequent application of the next unitary operation  $U_{(N-1)}$ , the blue disk further bifurcates into four quadrants, and so on.

subspace of coupled states. On the other hand, the entanglement of the decoupled state is limited to that arising from the Pauli exclusion principle for fermions. Such a decoupling allows us to write the many-body state as a tensor product of decoupled and entangled nodes, and reflects the many-body disentangling procedure in the unitary renormalization group formalism.

$$|\Psi_{(j)}^{i,r}\rangle = \sum \left( \underbrace{\left( \begin{array}{c} l_3 & l_2 & l_1 \\ \vdots & \vdots & \vdots \\ l_s & & l_m \\ l_{m-1} & & l_m \end{array} \right)^{(j)}}_{\text{entangled subspace}} C_\alpha^{i,(j)} \otimes \left( \begin{array}{c} t_2 & t_1 \\ \vdots & \vdots \\ t_3 & & t_p \end{array} \right)^{(j)} \underbrace{\text{separable subspace}}_{\text{separable subspace}} \right)$$

Figure 1.8: The eigenstate of the renormalized Hamiltonian is represented as a sum over tensor coefficients, where the legs of tensors represents various occupied states. This state is represented as a tensor product of (i) a state comprising electronic qubits belonging to the entangled subspace of states, and (ii) a separable state comprising of the disentangled qubits.

Each of the coefficients comprising the entangled state is a tensor with  $m$  legs representing the occupied single-particle states  $|l\rangle$  ( $l = 0, \dots, m - 1$ ), and is renormalized via the unitary operation thereby generating the RG flow for the many-body entanglement. The wave function at RG step  $(j)$  (Fig.1.8c) is a sum of all such tensors chosen from among the coupled states. To account for the fermion exchange signatures, an even/odd permutation of the indices ordering is made explicit as a signature in the coefficient tensors. It should be noted that similar disentanglement procedures are also employed in the Tensor

Network Renormalization, the Multiscale Entangled Renormalization Ansatz (MERA) approaches [236–238] and the entanglement holographic mapping (EHM) network of Ref.[231], albeit for removing short-ranged many-body entanglement in the bare problem. In contrast, the unitary operators of the URG remove every type of entanglement between a given electronic state  $j$  and all others. The unitary operations comprising the corresponding tensor network are thus non-local in nature.

An important feature of the tensor network shown in Fig.1.6 [184] can now be discussed. Implicit to the construction of this tensor network is another holographic dimension given by the eigenspectrum of quantum fluctuations  $\{\omega_i\}$ , i.e., the set of  $2^N$  eigenvalues of the quantum fluctuation operator  $\hat{\omega}$ ,  $\hat{\omega}|\Psi_i\rangle = \omega_i|\Psi_i\rangle$ , corresponding to the  $2^N$  orthogonal directions  $\{|\Psi_i\rangle\}$  encoding the entire many-body eigenbasis  $\mathcal{B}$ . Separate tensor networks are then generated by projecting the master tensor network shown in Fig.1.6 along each of these  $2^N$  directions. The nature of any individual projected tensor network encodes the entanglement content of the corresponding many-body eigenstate  $|\Psi_i\rangle$  that it describes. For instance, a projected tensor network corresponding to a gapless eigenstate will possess equal numbers of boundary and emergent bulk qubits [177]. On the other hand, a projected tensor network corresponding to a gapped eigenstate will possess a lesser number of emergent bulk qubits than the boundary qubits, with the former forming an emergent tensor network with finite entanglement [184]. In geometrizing these projected tensor networks, we employ quantum information-theoretic measures such as mutual information [239] for computing the information geodesics (shortest distance) between any pair of boundary qubits [184, 240, 241, 161].

7. **Entanglement RG flow** The ground state wavefunction of a parent many-particle model is, in general, difficult to obtain. However, once available, it allows the simulation of various low-energy properties such as susceptibility, self-energy, resistivity, as well as an investigation of the nature of many-particle entanglement. URG can lead to effective theories at stable fixed point Hamiltonians that are comparatively tractable analytically when compared to their parent model counterparts, and have been observed to enable such computations with the ground state wavefunction [181]. As shown in Fig.9.7.2, upon reversing the unitary transformations of the URG [241, 242], we can holographically reconstruct the (a priori unknown) ground eigenstate  $|\Psi\rangle$  of the parent model. In this manner, we can also study the entire RG flow for the many-body ground state of a given parent Hamiltonian model.

### Quantum Circuit representation of unitary RG

If the many-body ground state at an IR RG fixed point is analytically obtainable (as we have shown for, e.g., the 2d Hubbard model [180, 181]), its quantum circuit representation can be determined as follows. First, the entanglement content is restricted only to nodes comprising the coupled subspace, given that the decoupled nodes are separable and have fixed occupation number configurations. We can find the optimal collection of universal one-qubit (e.g., Hadamard gates) and two-qubit gates (controlled Not (CNOT) gates) that generate the required state from a generic separable state [243]. In this manner, we generate the quantum circuit representation of the ground state  $|\Psi_g\rangle$ . Note that the Hadamard gate puts a input single-particle state, say an occupied state  $|1_j\rangle$ , into a equal superposition state

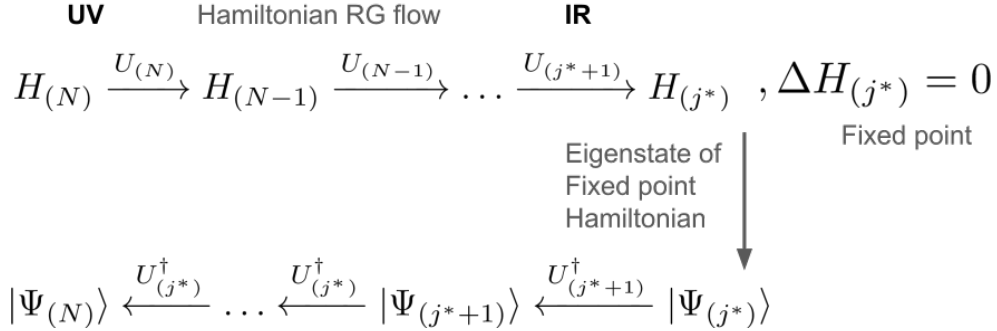


Figure 1.9: Upper line: URG flow scheme for Hamiltonians, terminating at fixed point Hamiltonian. Lower line: entanglement renormalization RG flow constructed via the inverse unitary transformations  $U^\dagger$ 's on the eigenstate  $|\Psi^*\rangle$  of  $H^*$ .

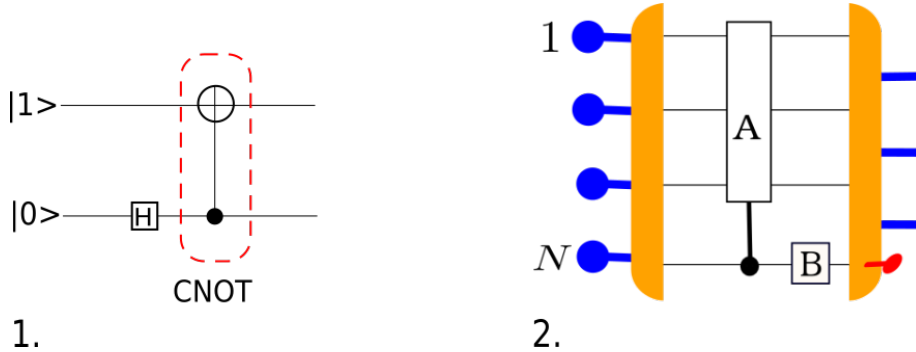


Figure 1.10: 1. A two-qubit entangler quantum circuit.  $|1\rangle$  and  $|0\rangle$  represent the input configurations of the two qubits.  $H$  is a Hadamard gate that acts on a single qubit, and the red rounded circuit element is a CNOT gate. The control qubit is marked by black dot. 2. The quantum circuit representation of the unitary gate, comprising a nonlocal controlled unitary rotation ( $A$ ) on qubits  $|1\rangle, \dots, |N-1\rangle$ , and a single-qubit rotation ( $B$ ) acting on qubit  $|N\rangle$ .

$\frac{1}{\sqrt{2}}(|1_j\rangle + |0_j\rangle)$ . The C-NOT gate is a two-qubit gate acting on a target bit  $|a\rangle$  and control bit  $|b\rangle$ . If the control bit ( $|b\rangle$ ) is in configuration  $|0_b\rangle$ , the target bit is left unmodified. In the other hand, if the control bit is  $|1_b\rangle$ , the target bit is swapped  $|1_a\rangle \leftrightarrow |0_a\rangle$  (see Fig.1.10(1)). The disentangled states (red qubits in Fig.9.7.2) have either up- or down-spin configurations. Similarly, the unitary disentangler in URG eq.(7.8) can be represented as a nonlocal CNOT operation. In order to disentangle qubit  $|N\rangle$ , the unitary operation  $A$  acts upon a many-body configuration of qubits  $1, \dots, N-1$ , followed by a single-qubit rotation gate  $B$ . The single-qubit rotation gate orients the electronic states in the occupation-number configuration post disentanglement (see Fig.1.10(2)).

Upon performing reverse RG by operating the inverse unitary operations on  $|\Psi_g\rangle$ , i.e.,  $U_j^\dagger|\Psi_g\rangle$ , we can obtain the quantum circuit descriptions of the many-body states by rescaling from IR to UV. This is obtained by decomposing the net unitary operation  $U_j^\dagger$  as a tensor product of two-qubit and single-qubit gates [244, 25]. Similarly, the quantum circuits arranged holographically from IR to UV [182] allows the description of the entire

RG procedure as a grand quantum circuit. Importantly, the fact that the unitary circuits employed in URG can be decomposed in terms of universal gates (i.e., CNOT gates, Hadamard gates, and phase gates belonging to the normalizer of the Pauli group for the system of electronic qubits) implies that URG is a version of a Clifford stabilizer code [233] that obeys the Gottesman-Knill theorem. By this, we mean that such a quantum circuit can be simulated on a classical computer in polynomial time. We note that similar reverse RG approaches that involve the re-entangling of hitherto disentangled degrees of freedom have been discussed for some tensor network RG approaches [241, 242].

The reconstruction method within URG is validated by computing a reduction in the uncertainty of the energy eigenvalue of the reconstructed state at UV. By representing the many-body states at each RG step as quantum circuits/tensor network [244, 25], and by further representing each unitary transformation step as a product of two-local universal gates [243], we obtain an equivalent entanglement holographic mapping (EHM) [232] description for the URG. The reverse RG can be visualized as an entanglement RG flow along the reverse holographic direction [241, 177]. Much like the EHM, URG is a version of MERA that preserves spectral weight during the RG flow [177]; this is precisely why we can implement both forward and reverse RG constructions. Importantly, note that at each RG step, the  $U$  transformations are not determined variationally as in MERA [160] or EHM [232]. Also, note that in MERA, the input qubits at the boundary (high energy or UV) layer are gradually transformed by a holographic arrangement of transformation layers. Each of the layers has two parts: the first a tensor product of (real-space) local unitary disentangler gates with two input and two output legs each, and the second a product of isometries with two input legs and one output leg each (which removes the disentangled qubits generated at each RG step from the complete Hilbert space). As a result, the number of legs at the output from each layer is exactly half of the number of input legs. MERA and its variants [245–247] allow the holographic generation of spatial geometry along the RG direction [161, 211, 241, 232, 177, 240], starting from a tensor network representation of the many-body state it acts on [26, 25, 244]. On the other hand, in the entanglement holographic mapping (EHM) [232, 177] network, each transformation layer is comprised of only unitaries (i.e., layer 1 discussed above). Consequently, the EHM (and therefore the URG) is also a tensor network formed from a collection of the unitary transformation layers.

### Measures of many-particle entanglements

An important feature of tensor network renormalization approaches like MERA is related to the entanglement entropy ( $S = -Tr_R(\rho \log \rho)$ ,  $\rho = |\Psi\rangle\langle\Psi|$ ) generated upon isolating a UV block  $R$  in the boundary of the tensor network. It was shown in Refs.[241, 160] that the entanglement entropy is bounded from above by the number of legs that must be cut for the isolation of the region  $R$  from its complementary part. At each RG step in the MERA framework, half of the input qubit legs are disentangled and isolated from the rest. Therefore, upon descending further into the IR region of the tensor network, the number of legs that need to be cut are reduced exponentially. The depth of the MERA/EHM quantum circuit/tensor network quantifies the circuit complexity of the state  $|\Psi\rangle$ , i.e., the minimum number of two-local and one-local universal gates required to obtain the entangled state from a separable state [248]. Similarly, upon disentangling qubits within the URG program,

the circuit complexity is greatly reduced in the bulk of the EHM. While the MERA and EHM networks remove only the local entanglement content between qubits, the long-ranged entanglement content (if any) between a given qubit and the rest of the qubits is perfectly removed within the URG program. For these various tensor networks, the gain in efficiency in obtaining the entanglement features of a region  $R$  in  $|\Psi\rangle$  is tied to the reduction in circuit complexity of the state  $|\Psi\rangle$  and the unitary transformation  $U$ . This attribute of the EHM conforms to the Ryu-Takayanagi formula [148], where the entanglement entropy of a region is determined by the minimal surface (whose length is the number of links cut) of the causal cone enveloping it [241, 249].

Another essential feature of tensor networks such as EHM and MERA is that they encode the entanglement content of the many-body state geometrically [177, 240], as measured by the information distance ( $d_{ij} = -\log \frac{I(i:j)}{2 \log 2}$ ): negative logarithm of the quantum mutual information  $I(i:j)$  (MI) between pairs of qubits  $(i,j)$ . MI measures the total amount of quantum and classical correlations in a system [239]. In the present context, the *MI* between pairs of qubits characterizes the *strength of entanglement* [239, 240, 177] among the members  $i$  and  $j$

$$I(i:j) = -Tr(\rho_i \ln \rho_i) - Tr(\rho_j \ln \rho_j) + Tr(\rho_{ij} \ln \rho_{ij}) , \quad (1.8)$$

where  $\rho_i$  or  $\rho_j$  and  $\rho_{ij}$  are the 1- and 2-pseudospin reduced density matrices respectively. If pseudospins  $(i,j)$  are individually strongly entangled with the rest of the pseudospins,  $\rho_{ij}$  has a wide-tailed distribution leading to a enhanced joint entropy  $S(\rho_{ij})$  and low MI. On the other hand, if  $\rho_{ij}$  has a sharper distribution, and the MI content is high. As an illustrative example, consider the 2-spin singlet state  $|\psi\rangle = \sqrt{2^{-1}}(|\uparrow_1\downarrow_2\rangle - |\downarrow_1\uparrow_2\rangle)|\uparrow_3\rangle$ . Here, the MI between spins 1 and 2 is high  $I(1:2) = 2 \log 2$  as the joint entropy vanishes  $S(\rho_{1,2}) = 0$ , and the individual entropies  $S(\rho_1) = S(\rho_2) = \log 2$ .

Within this definition, we find that the lower the entanglement of the qubit pair  $(i,j)$ , the higher is the information distance  $d_{ij}$  and vice-versa. Note that the information-theoretic distance between a pair of qubits  $(i,j)$  obtained from the bulk of EHM is, in general, different from that obtained at the boundary, implying that a curved space-time geometry can be encoded into the tensor network. For instance, an information-theoretic distance proportional to the logarithm of the physical distance indicates the generation of hyperbolic space-time geometry from the entanglement along the RG holographic direction [240]. We further note that while Ref.[250] established that the mutual information is an upper bound for various two-point correlation functions, it has been shown that the entanglement geometry generated asymptotically from MI of the EHM (i.e. deep within the tensor network) can also encode the single-particle bulk correlation function [177]. Further, for the EHM of a gapped ground state obtained from URG, the MI between pairs of qubits  $i$  and  $j$  corresponds to the two-particle correlation function written in terms of composite two-particle degrees of freedom.

8. **Topological order and emergent gauge theories** Topological order is one of the important findings of from studies beyond LGW theories that has received experimental verification [42, 251–254]. Essentially, it refers to a degenerate ground state manifold

that is protected via a many-body gap, and whose degeneracy is related to the topological properties of the spatial manifold on which the system is embedded. Such a state of matter is relatively robust against weak thermal and quantum fluctuations. Importantly, it arises from the interplay of strong correlations and fermion exchange signatures, and can be broadly categorized into two classes: one possessing time-reversal symmetry breaking, and the other not. Fractional quantum hall phases [251–253] are an example where the interplay of electronic correlations and a strong transverse magnetic field lead to topologically ordered ground states on a torus. These systems show other classic signatures of topological order, including gapless edge states and excitations displaying charge fractionalization. On the other hand, Kitaev’s Toric code [255] and the topological Haldane model [256, 257] are examples of topological order without time-reversal symmetry breaking. The  $U(1)$  symmetry-broken superconductor coupled to a dynamical gauge field is yet another example of a time-reversal symmetric topologically ordered state of quantum matter [258].

In the Chern-Simons effective gauge theory for Abelian topologically ordered ground states, the standard approach involves integrating out the massive Dirac fermions living on an anholonomic background [259]. The  $K$  matrices [260] defining the Chern-Simons action can then be used to compute topological entanglement entropy, ground-state degeneracy, charge fractionalization etc. Similarly modular matrices acts as a order parameter to describe topological order [261]. However, an important challenge lies in obtaining analytically such effective Chern Simons actions and modular matrix order parameters for strongly correlated electronic systems starting from a microscopic approach. This is due to the lack of a weak-coupling parameter around which a perturbative renormalization group treatment can be carried out. However, in the URG approach, the effective Hamiltonian can be written in terms of composite and nonlocal degrees of freedom at the IR fixed points. There, we can construct a twist operator [41, 42] that reveal the fractional excitations generated in interpolating between the topologically ordered ground states. Further, we find that a network of the emergent composite degrees of freedom described in terms of dual nonlocal objects, i.e. Wilson lines, can lead to formulating an emergent gauge theory. In certain cases, such a gauge theory shows signatures of topological order, seen from ground state degeneracy, charge fractionalization etc.

Finally, topological stabilizer codes can also be constructed for quantum error correction involving the ground state manifold obtained from URG. Indeed, both MERA and EHM have interpretations as a quantum error-correcting codes [262–265]: along the reverse holographic direction from IR to UV, the unitary transformation layer acts as an *encoding map* that re-entangles the stabilizer codeword (IR fixed point) with the (hitherto) disentangled degrees of freedom [266]. Conversely, the passage from UV to IR involves the disentanglement of qubits at the UV scale and acts as a *decoder* of the stabilizer codeword in the IR. This has implications for fault-tolerant quantum computing and topological quantum error correction codes [255, 266, 267]. Thus, the entanglement URG flow provides a platform for designing noise-resilient topological quantum error correction [268, 269, 247].

9. **Mitigating the fermion sign problem** Fermion sign problems plague certain well-known numerical methods like quantum Monte Carlo and limit their accuracy in determining

ground state properties [270, 271]. Path constrained Monte Carlo techniques [47, 272] are sometimes implemented in these cases such that the fermion exchange signatures can be numerically accounted for in a manageable manner. In Ceperley's approach [272–274], the odd number of fermions exchange signatures appears as a geometric constraint acting on the residual hard-core bosons. On the other hand, within the URG approach, the passage to gapped phases involves dominant RG flows along particular channels, thereby mitigating the fermion sign in the low energy subspace [180–183]. The effective Hamiltonians for gapped ground states are described in terms of a composite object made of pairs of electrons, such that exchanging them does not generate a fermion sign. For the gapless phases, on the other hand, URG leads to number-diagonal fixed point effective Hamiltonians written in terms of number operators  $\hat{n}_{\mathbf{k}\sigma}$  (where  $\mathbf{k}$  is a momentum-space label). The eigenstates of such effective Hamiltonian are represented purely in terms of occupation numbers, and the fermion exchange signatures aren't important in their description. However, it is important to note that fermion exchange signatures resurface in the excitation spectrum upon perturbing away even slightly from the fixed point theories for gapless states with RG irrelevant non-zero momentum transfer scattering processes.

10. **Sum rules and spectral weight redistribution** The preservation of total spectral weight (e.g., the content of the f-sum rule) is a fundamental attribute of any unitary operator based formalism. However, keeping track of the redistribution of spectral weight during the formation of emergent states of matter is no simple task. For instance, CDMFT approaches have shown the conversion from pole to zero in the single-particle Green's function, signalling an instability of the Fermi surface [275]. This is also related to a violation of the Luttinger's sum rule, i.e., appearance of Luttinger surface of zeros [276, 277] and the gapping of the Fermi surface. In order to study the effect of an instability, the Friedel's scattering phase shift [278, 279] needs to be considered. It accounts for the formation of bound states, and is essentially the node counting content of Levinson's theorem[280]. The manifest preservation of total spectral weight in the renormalized theory obtained from functional RG is difficult. On the other hand, the URG approach is manifestly unitary, such that spectral weight redistribution can be reconstructed by tracking the simultaneous pole to zero conversion in the single-particle Green's function and the appearance of poles in the corresponding two-particle Green's function (for the emergent condensate). For cases of gapless IR ground states obtained from a URG treatment of electronic correlations, we find either adiabatic continuity towards the Fermi liquid (where Luttinger's sum is preserved), or a flow towards the marginal Fermi liquid with a vanishing quasiparticle residue. In the latter case, Luttinger's sum is violated when represented purely in terms one-particle Green's function, and compensated by the inclusion of the Green's function for a 2-electron 1-hole composite propagating degree of freedom.

## 1.2 Phenomenology of models studied in the thesis

In this thesis, we study a variety of paradigmatic models of correlated electron across dimensionalities: the Kondo impurity models [281], the 1d Hubbard model [282], the 2d Hubbard model [49], the single-band four-fermion interacting model and the generalized electronic

Sachdev-Ye model [283]. Of these, the Hubbard model is one of the simplest models for studying strong correlations in 2d, involving hopping on a 2d square lattice and an onsite Hubbard repulsion. Despite its simplicity, the model exhibits a variety of phenomena: metal-insulator transitions, d-wave superconductivity, pseudogap, strange metallicity, and antiferromagnetism. An analytically exact solution to this model exists only in one and infinite spatial dimensions. However, in 2d, only certain rigorous analytical bounds of the ground state energy are available. Perturbation theory, on the other hand, suffers from the requirement of either very strong or weak repulsion. In the intermediate coupling regime, one generally resorts to numerical techniques for solving the problem, e.g., DCA [284, 60, 285], CDMFT [286], QMC [287, 288] etc. In this thesis, we study the 2d Hubbard model by an analytic unitary RG method at half-filling and upon doping with holes, obtaining effective Hamiltonians at various energy scales and for various doping and interaction parameters. By then solving the effective Hamiltonian for eigenstates and eigenvalues, we simulate the low energy properties and entanglement features for various quantum phases of matter obtained.

The Hubbard model also represents a paradigm for studying the primary instabilities of the Tomonaga Luttinger liquid (TLL) metallic phase in one spatial dimensions [282]. A wide range of analytical methods like bosonization and Bethe Ansatz [3, 4] and numerical techniques like DMRG [71] reveal a variety of low-energy gapped quantum liquid states of matter with topological properties, e.g., the Luther-Emery (LE) and the Mott insulating (MI) liquids. Importantly, the matrix product state (MPS) [289–293] representation and MERA [157, 175], provides a distinguishing criterion for classifying gapped and gapless low-dimensional quantum liquids respectively. In this thesis, we take a unified approach to Hamiltonian as well as entanglement renormalization groups based on the tensor network representation of the URG. This helps us obtain, on one hand, the RG phase diagram with effective Hamiltonians at fixed points and, on the other, eigenstates and their RG evolution of their entanglement features.

The translationally invariant single-band four-fermionic interacting model represents a family of parent model Hamiltonians hosting a variety of effective Hamiltonian based theories: the Fermi liquid [14], the reduced BCS model [15], the effective Hamiltonian for pair density waves [294], non-Fermi liquid metals [295, 296], a Mott instability via nesting [227] etc. However, a systematic identification of the parameter space regimes leading to various effective Hamiltonian remains open. Similarly, the generalised Sachdev-Ye model [283] is host to a wide range of quantum phases arising from the interplay of electronic correlations and disorder, e.g., many-body localized [192, 297, 298, 201] and thermalized [299] phases. In the thesis, we use the URG approach to analyze the RG flow equations for various scattering vertices, self energies etc., and obtain therefrom the parameter subspaces and effective Hamiltonians for such novel states of quantum matter. This helps realize an RG phase diagram in the parameter subspace, as well as unveil the tensor network representations leading to various effective Hamiltonians.

Finally, the Kondo model [300, 301] is a paradigmatic quantum impurity model where local interactions between the spin impurity and its itinerant electronic host can lead to a macroscopic quantum phenomenon of the spin-exchange mediated resistivity minimum at low temperatures. Here, spin-exchange interactions leads to the formation of a Kondo cloud that arises from the entanglement between the electrons and the spin impurity [302, 303]. Although a vast literature exists on studies of this problem, analytic insight into the effective Hamiltonian and eigenstates that describe the Kondo cloud is missing. In this thesis, we obtain a low-energy effective Hamil-

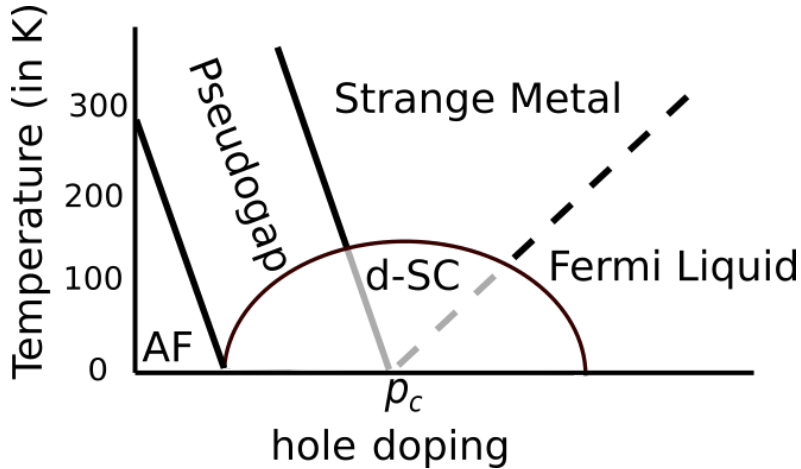


Figure 1.11: Phase diagram for the hole-doped Mott insulating cuprate materials, with temperature ( $T$ ) on the  $y$ -axis and hole-doping level on the  $x$ -axis. AF represents the Neél antiferromagnetic, and d-SC d-wave superconductivity.  $p_c$  indicates the doping level at which the pseudogap phase is expected to terminate, and the Fermi liquid phase arises, in the absence of d-SC. The line between the AF and Pseudogap phases is a transition, as is the dome-like border of the d-SC phase. The bold and dashed lines between the Strange Metal and the Pseudogap and Fermi liquid phases respectively are crossovers.

tonian and its eigenstates from the URG approach. We then employ these to compute various well-known thermodynamic quantities and zero temperature results of this system, and benchmarking them against the literature.

### 1.2.1 Th 2d Hubbard model

The nature of, and the transition into, the Mott insulating state by tuning the bandwidth defines a central problem in strongly correlated quantum matter. An analytically exact solution for the electronic Mott-Hubbard metal-insulator transition (MIT) exists only in one spatial dimension [304], while the status of the problem remains open in general. While the Mott insulator is often associated with a ( $T = 0$ ) first order transition leading to a Neél antiferromagnetic (AFM) ground state [2], the search continues for quantum liquid-like ground states corresponding to an insulating state that breaks no lattice or spin-space symmetries and is reached via a continuous transition. Indeed, there exist some theoretical proposals [305–308] as well as some experimental evidence for insulating spin-liquid ground states in layered organic conductors [309] and Herbertsmithite [310]. Recently, the metal-organic compound  $Cu(DCOO)_2 \cdot 4D_2O$ , an unfrustrated quasi two-dimensional antiferromagnet, was found to contain features of a resonating valence bond (RVB) like spin-liquid ground state [311].

Theoretical studies have not, however, identified unambiguously the order parameter for such correlation-driven metal-insulator transitions. The difficulties appear to be associated with an interplay of several complications: the fermion-sign problem limits some nonperturbative numerical investigations at low-temperatures [312], while many other numerical methods are either limited to small sizes or certain ranges in the coupling  $U/t$  (the ratio of the Hubbard repulsion to the

nearest-neighbour hopping amplitude). It is, therefore, remarkable that a benchmarking exercise conducted on the 2D Hubbard model identified ranges in the values for the ground state energy per particle and the double occupancy fraction at specific values of the filling and  $U/t$  [49]. At the same time, a lack of an identifiable small parameter makes most analytic approaches beyond various mean-field schemes intractable when studying the problem at strong coupling.

Amidst these difficulties, several important questions related to the nature of the  $T = 0$  phase diagram of the Mott-Hubbard transition, as well as the nature of the ground state, continue to be debated. For instance, we may ask: is there a critical value of the ratio  $U/t$  for the  $T = 0$  Mott transition in the half-filled unfrustrated (i.e., with nearest neighbour hopping only) Hubbard model on a square lattice that corresponds to a paramagnetic state (i.e., with no magnetic order)? Studies using dynamical mean field theory (DMFT) [313–315] and quantum Monte Carlo [316] approaches indicate a first order transition at  $T > 0$  ending at a critical  $(U/t)_c$  at finite  $T$ . The status of the  $T = 0$  metal-insulator transition remains to be understood. Further, the paramagnetic calculations can be interpreted as solutions for the case of vanishing inter-site correlations, and can presumably be trusted within only the (single-site) DMFT framework for the case of infinite dimensions.

The question, therefore, of whether the ground state of the two-dimensional Mott insulator at  $T = 0$  possesses magnetic ordering or not needs further consideration. A reduction in the value of  $(U/t)_c$  has also been observed in dynamical cluster approximation (DCA) studies [284, 60, 285] as well as in cluster DMFT (CDMFT) studies [286]. Recent studies involving the dynamical vertex approximation (DΓA) [317, 318, 288], auxillary field quantum Monte Carlo (AFQMC) [287, 288], density matrix embedding theory (DMET) [84] and ladder dual-fermion approach (LDFA) [319] have instead supported the existence of a gapped antiferromagnetic Néel state for all  $U > 0$ . Variational Monte Carlo studies using Gutzwiller projected wavefunctions have shown that a symmetry-preserved resonating valence bond (RVB) state is energetically close to the symmetry-broken Néel antiferromagnetic state [306]. At the same time, a better view of the quantum metal-insulator transition involves understanding the nature of parent metallic state of the Mott insulator: is it a Fermi liquid with coherent Landau quasiparticle excitations, or some form of non-Fermi liquid involving collective excitations?

We now turn to the case of the Mott transition driven by tuning the filling [2]. Upon doping with holes, for instance, the physics behind charge localization competes strongly with hopping-induced electronic delocalization. Further, the theoretical effort towards understanding the physics of the hole-doped 2D Hubbard model is given prominence by the experimentally rich phenomenology of the cuprate doped Mott insulators (see schematic diagram in Fig.1.11, and Ref.[5] for a review). It is widely believed that the physics of the cuprates is associated with that of (almost) decoupled Cu-O planes in which the doped holes (or electrons) pair into a d-wave superconducting state. Indeed, a very recent experimental study [320] has shown that the phase diagram of the cuprate system can be obtained with both qualitative, as well as quantitative, accuracy from a monolayer crystal of  $\text{Bi}_2\text{Sr}_2\text{CaCu}_2\text{O}_{8+\delta}$  containing only two Cu-O planes. This presents strong evidence that the phase diagram encapsulates the  $T = 0$  symmetry-broken phases of a single Cu-O plane that is stabilised at finite temperatures by weak inter-layer tunnelling [321] (and would have otherwise been forbidden by the Mermin-Wagner-Hohenberg theorem). While the overall positioning of different phases in this phase diagram are quite universal, certain features like the width and height of the superconducting dome, critical doping  $p_c$  etc. are not

universal across different compounds.

While this complex phenomenology has been studied extensively within the realms of the 2D Hubbard model on the square lattice with a finite chemical potential away from 1/2-filling, an overarching understanding of the mechanisms responsible for it remains elusive. The challenges here include understanding a non-Fermi liquid (NFL) metallic phase with a striking resistivity that varies linearly with temperature [322, 323]. Another enduring puzzle involves the pseudogap (PG): a phase in which parts of the Fermi surface (FS) are gapped, and whose origin and role remain unknown [324]. The mystery of the pseudogap is reinforced by conflicting experimental findings, some of which suggest that it is the origin of the observed superconductivity in the form of pre-formed Cooper pairs, while others report fluctuations of various orders that are inimical to superconductivity [5]. Much debate has also ensued over the existence of a quantum critical point (QCP) lying hidden within the superconducting dome [325, 326]. That these phases are reached experimentally by exiting the Mott insulating state suggest that their origins lie therein [327], highlighting the need for understanding the Mott transition in generality.

Not surprisingly, a large number of numerical methods have been brought to bear on this problem. These include, for instance, quantum Monte Carlo simulations at finite-temperature (QMC) [328–336, 282], density matrix renormalization group (DMRG) [337–339], dynamical cluster approximation [55–59], cluster DMFT (CDMFT)[61–67] and the variational cluster approximation VCA [340, 341]. Together with several others, these techniques suggest a rich and detailed temperature-doping phase diagram shown in Fig.1.11, including numerous phases including the antiferromagnetic Mott insulator, d-wave superconductivity, the pseudogap (or nodal-antinodal dichotomy) arising from electronic differentiation, non-Fermi liquid, stripes etc. [332, 333, 55–59, 61–67, 342–346, 111, 347–352, 127, 353, 354]. These findings are, by and large, in keeping with the experimental phenomenology of the doped cuprate Mott insulators (see [5] for a recent review). A significant drawback remains, however, in the fact that detailed resolution of the low-energy neighbourhood of the Fermi surface is not available from these theoretical methods. Unfortunately, this leaves several critical questions unanswered on the nature and origins of the  $T = 0$  phenomenology of the doped Mott-Hubbard insulator.

Noteworthy among efforts towards resolving this problem involves the application of the functional renormalization group (FRG) technique to the Mott transitions in the 2D Hubbard model (for reviews, see Refs.[108, 116] and references therein). Results from FRG studies provide evidence for nodal-antinodal dichotomy, as well as spectral weight transfer between Hubbard bands in the half-filled Hubbard model [355]. For the case of doping-induced Mott transitions, FRG studies show the co-existence and interplay of antiferromagnetism with  $d$ -wave superconductivity [127, 128] over a wide doping range, in agreement with results obtained from CDMFT [356]. In this range of doping, signatures of stripes [357] and nematicity [358] have also been reported, as well as their interplay with  $d$ - wave superconductivity. These findings are also in consensus with results from diagrammatic mean field theory [359] and CDMFT [360]. Signatures of the strange metal, the pseudogap, and a quantum critical region have also been reported within the FRG scheme [357, 358, 360, 359, 361, 362, 120]. While the method is non-perturbative in principle, numerical implementations of the FRG have typically needed truncations at finite orders in the loop expansion. Thus, despite much success, the FRG is limited thus far to studying weak-to-intermediate values of  $U/t$ .

## 1.2.2 Four-fermionic interaction and generalized Sachdev-Ye models

The four-fermionic interaction model with a single tight-binding band ( $\epsilon_{\mathbf{k}\sigma}\hat{n}_{\mathbf{k}\sigma}$ ) is a translationally invariant multi-parameter model, in which the interactions are described as

$$H_{\text{int}} = \sum_{k,k',q,\sigma,\sigma'} V_{\sigma\sigma'}(\mathbf{k}, \mathbf{k}', \mathbf{q}) c_{\mathbf{k}\sigma}^\dagger c_{\mathbf{k}'\sigma'}^\dagger c_{\mathbf{k}+\mathbf{q}\sigma'} c_{\mathbf{k}'-\mathbf{q}\sigma} , \quad (1.9)$$

where  $\mathbf{k}$  and  $\mathbf{k}'$  are individual momenta and  $\mathbf{q}$  is the momentum transfer. This model constitutes parameter subspaces leading to several well known phenomenological models. For instance, for a system of electrons with repulsive interactions, a fully connected and non-nested Fermi surface,  $V(\mathbf{k}, \mathbf{k}', \mathbf{q} = 0) = V(\mathbf{k}, \mathbf{k}')$  and  $V(\mathbf{k}, \mathbf{k}', \mathbf{q} \neq 0) = 0$ , the Fermi liquid Hamiltonian  $H_{FL}$  can be obtained. On the other hand, the reduced BCS Hamiltonian is obtained for a finite attractive interaction for zero net-momentum pairs  $\mathbf{k} + \mathbf{k}' = 0$ ,  $V(\mathbf{k}, -\mathbf{k}, \mathbf{q}) = V(\mathbf{k}, \mathbf{q})$  and zero interaction for all non-zero momentum pairs. The Fermi liquid [363] and reduced BCS [15] Hamiltonian models are paradigms in quantum condensed matter, describing a family of gapless metallic and s-wave superconducting phases respectively. These models have been extensively studied via perturbative renormalization group approaches. The low energy properties of the Fermi liquid Hamiltonian [14], e.g., the quasiparticle residue, and the temperature dependences of the resistivity, specific heat, spin and charge susceptibility provide a universal description of a large class of conventional Fermi liquid metals. Thus, can a URG study reveal the flow towards the effective Fermi liquid model starting from a parent interacting model of electrons? If so, can we obtain the quasiparticle residue and confirm the existence of the Landau quasiparticle excitation of the Fermi liquid? How does screening takes place, such that all the non-zero momentum transfer ( $\mathbf{q} \neq 0$ ) vertices become less RG relevant compared to  $\mathbf{q} = 0$  vertices that form the effective Fermi liquid Hamiltonian?

On the other hand, for the reduced BCS model, both mean-field theory [15] and renormalization group studies of quantum fluctuations provide an efficient description for the phenomenology of its low energy physics [364, 100–102]. Low energy properties like pairing susceptibility, resistivity, Meissner effect, a gap in the one-particle density of states, magnetic susceptibility etc. [365] obtained from the effective BCS mean-field model are in good agreement with experimental observations. Despite the tremendous success for BCS and Fermi liquid theory, however, some outstanding questions remain: what is the universal parent model underlying the reduced BCS and Fermi liquid Hamiltonians? RG theory was constructed to study the flow towards effective models that display the emergence and condensation of effective degrees of freedom (e.g., Cooper pairs). Further, Wilsonian [92, 364, 100–102] and similarity transformation [366] based Hamiltonian RG procedures have reproduced the mean-field results from a one-loop perturbative RG. Despite this success, however, the parent reduced BCS model Hamiltonian, has not been derived from existing RG frameworks. Can URG meet this aim? Further, can we show the zero in the single-particle Green's function, signalling an instability of the Fermi surface? Can we obtain insight into the pairing instability by showing that zero pair-momentum scattering vertices dominates at the IR RG fixed point?

Among the various unconventional quantum phases that are possible, can we understand the phenomenology of marginal Fermi liquid metals from the URG approach? Can we reach other models with strong correlations, e.g., the Hubbard model? What happens if we add disorder to the mix? By studying a generalised Sachdev-Ye model with disordered intersite hopping, onsite

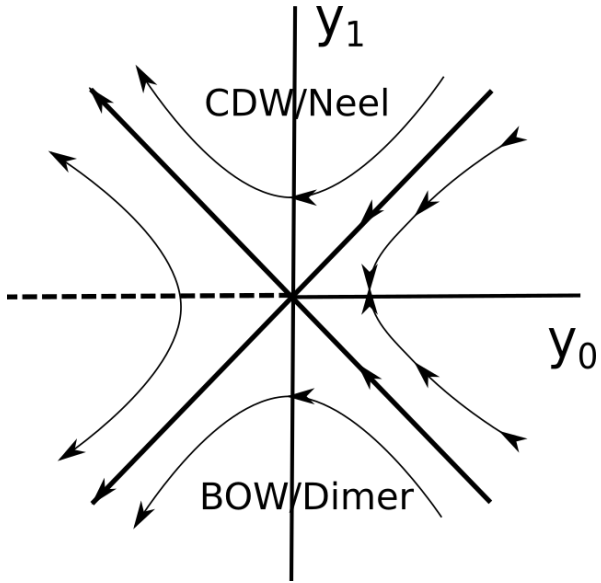


Figure 1.12: RG flow diagram for the sine Gordon model, where  $y_1/y_0$  are the Umklapp scattering/Gaussian couplings respectively. The RG flows leading to  $y_1 = y_0 = 0$  describe the trivial noninteracting fixed point.  $|y_1| = y_0 > 0$  are the BKT trajectories leading to the strong coupling fixed point, while the flows to  $y_1 \rightarrow 0$ ,  $y_0 > 0$  are towards a line of Tomonaga-Luttinger liquid gapless metallic fixed points.

energies and four-fermionic interactions, can we observe RG flows towards electron glass many-body localised (MBL) [192, 297, 298, 201] and thermalised [299] phases? Can this enable insight into the extensive local integrals of motion that comprise the MBL states, and the exponential growth in the complexity of the many-particle entanglement that leads to the thermalised state?

### 1.2.3 1D Hubbard model

Electronic correlations in one dimension are generically observed to lead to exotic quantum liquids that either remain critical (and belong to the universality class of the Tomonaga Luttinger liquid (TLL) [367, 38], or possess a gapped spectrum [3, 4]. Careful studies involving a host of analytical and numerical methods reveal a variety of low-energy gapped quantum liquids including the Luther Emery (LE) liquid and the Mott insulating liquid (MI). One dimensional gapped quantum liquids can be classified via their emergent topological properties [368, 291, 369, 292, 370–375], and are notably different from the tenfold classification of gapped non-interacting systems [376, 377]. Transitions from the TLL to various gapped phases are described by the Berezinski-Kosterlitz-Thouless (BKT) universality class. Further, the universality has been shown to extend to a variety of models in 1D, e.g., the Schwinger model, massive Thirring model, quantum sine-Gordon model etc. Fig.1.12 displays the BKT RG phase diagram for the sine-Gordon model. The figure shows that a line of stable fixed point theories corresponding to the TLL are reached for couplings  $y_0 > 0, y_1 \rightarrow 0\pm$ , charge density waves (CDW) or Neel antiferromagnetic (AFM) low-energy phases for charge/spin degrees of freedom respectively are reached for repulsive Umklapp interactions (coupling  $y_1 > 0$ ). On the other hand, for attractive

interactions (coupling  $y_1 < 0$ ), bond density wave (BOW) or dimer phases are reached for charge/spin degrees of freedom respectively.

Extensive studies have shown that the physics of the BKT transitions that describe instabilities of the TLL reflect the binding-unbinding transitions of vortices, and can be studied from the spin and charge vertex operators of the associated sine-Gordon field theory [38, 4]. Topological aspects of the zero mode of these vertex operators [378] are understood from their connection to non-local gauge transformations [379, 86] arising from boundary condition changes on the Hilbert space [380]. Indeed, such boundary condition changes are associated with Berry phases that characterize the various phases in the BKT renormalization group (RG) phase diagram [380]. These insights inspire the following questions. Instabilities of a gapless state such as the TLL are outcomes of divergent quantum fluctuations that begin with scatterings events at the Fermi surface, and lead to the gapping of its neighbourhood. Can we relate such scattering processes to topological properties of the fermionic Hilbert space at the Fermi surface? Can we build a skeletal phase diagram by studying this Fermi surface scattering problem, and if yes, how closely does this resemble the phase diagram obtained from a RG study of the divergent quantum fluctuations? An affirmative answer would indicate that the topological features of degrees of freedom at the Fermi surface can track the low-energy physics arising from UV-IR mixing.

At the same time, the nature of many-body entanglement analyzed via tensor network methods [25, 26, 244] provides another important pathway for classifying low dimensional quantum liquids. This includes, for instance, the matrix product state (MPS) representation for gapped states [289–293] and multiscale entanglement RG (MERA) [157, 175] for gapless states. The entanglement entropy (EE) of critical 1D quantum liquids has also been studied extensively using field theory methods [146, 381–384], and is consistent with other calculations for the EE arising from a finite Fermi surface in higher spatial dimensions that show a violation of the area law [385, 386, 152]. Given the extensive developments in the understanding the physics of interacting fermions in 1D, a unified view is needed of the emergence of the effective low-energy Hamiltonians of quantum liquids and the associated entanglement content of their many-particle Hilbert space. This will surely provide deeper insights into the interplay of electronic correlations, low spatial dimensions and many-body entanglement.

With this as our goal, we turn to the unitary RG (URG) for fermionic systems [180, 181, 184, 182, 183], as this method generates the RG flow of both Hamiltonians and their eigenbasis along the holographic RG direction [387–389, 212, 390–392]. As discussed at length earlier in this chapter, the URG can be realized as a quantum circuit [149, 393, 394, 184]. Importantly, as the RG can be implemented on a 1D momentum-space lattice, we will clarify the role played by the topological properties of electronic states near the Fermi surface in guiding the RG flow towards a variety of gapped or gapless fixed points. The interplay between Fermi surface topology and electronic correlations has been recently demonstrated by us for the nested Fermi surface of the tight-binding model on the square lattice in a study of the 2D Hubbard model [180, 181]. There, we took careful account of the singular nature of the Fermi surface, as it contained van Hove singularities at half-filling. Here, we aim is to study the simplest possible Fermi surface, i.e., the two-point Fermi surface of the tight-binding chain, in the hope of gleaning insights on higher dimensional systems with regular connected (non-singular) [183] or Dirac point-like [185] Fermi surfaces. Even as we apply the URG to the 1D fermionic Hubbard Hamiltonian, our conclusions are relevant to the case of translation invariant four-fermionic interactions. Further, our analysis

requires neither the linearisation of the electronic dispersion near the Fermi surface, nor relies on any emergent phenomenon such as the separation of charge and spin excitations.

This leads us to ask the following questions in the present work. First, can the URG procedure show the emergence of nonlocal constraints associated with the Hilbert space topology of degrees of freedom residing at (and near the) Fermi surface, and how this leads to the condensation of composite degrees of freedom? As our starting point is a lattice version of the sine-Gordon model, we expect that an affirmative answer to this question will likely yield a non-perturbative version of the BKT phase diagram. The BKT phase diagram has separatrices that separate relevant from irrelevant flows, while the flows along the separatrices meet at a critical point [93]. Is it possible to reconcile the partitioning of the coupling space diagram obtained from analysis of topological objects living at the Fermi surface with the partitioning of the BKT RG phase diagram via the separatrices? Can we diagonalise the effective Hamiltonians obtained from the stable fixed points of the URG flow to obtain the low-energy spectrum and the associated eigenstates? If yes, we can perform a reverse URG on by the low-energy eigenstates of the fixed point Hamiltonian by re-entangling the UV degrees of freedom, generating thereby many-body eigenstates at higher energy scales. In this way, we aim to obtain the EHM tensor network representation of the URG, and study the entanglement RG for the various phases in the BKT RG phase diagram. Will the critical and gapped fixed points reveal distinct entanglement entropy scaling features from such a study? We verified the Ryu-Takayanagi entanglement entropy bound [148, 147, 184] for the ML and MFL ground states of the 2D Hubbard model, concretizing the connection between entanglement renormalization and holographic duality for the unitary quantum circuit/tensor network of the URG. In a similar fashion, can we construct the entanglement holographic mapping tensor network for the entanglement RG flow of correlated electrons in 1D, and verify the entropy bound in this case as well? Finally, can we provide a quantum circuit description of the RG flow in terms of two-local unitary disentangling maps? While a quantum circuit model for the entanglement scaling of massless Dirac fermions [394] was recently achieved in the continuum field theory for gapless phases, we aim instead to construct quantum circuit models for both gapped as well as gapless phases arising from a Hamiltonian of lattice-based electrons.

### 1.2.4 Kondo model

Quantum impurity models (see [281] for a review) and the Kondo effect [300] are paradigms of low-dimensional quantum many-body physics [8, 282]. In the Kondo model, a local interaction  $J$  between a magnetic quantum impurity and the non-interacting metallic host (with a tight binding hopping parameter  $t$ ) leads to a macroscopic quantum phenomenon, i.e., a resistivity minimum at low temperatures [395, 396]. For antiferromagnetic Kondo coupling  $J > 0$ , this is associated with a crossover from local moment formation to a screened local moment, arising out of spin-dependent scattering between the conduction electron cloud and the impurity spin. The spin-flip scattering rate defines a temperature scale: the Kondo temperature ( $T_K$ ). Perturbation theory in  $J/t \ll 1$  breaks down at temperatures below the Kondo temperature, and all orders in perturbation theory the impurity-electron scattering contribute log-divergence to the resistivity. Anderson, Yuval and Hamman [397, 398] formulated a perturbative RG study by mapping the problem onto a 1+1D Coulomb gas model. Later, a T matrix-based “poor man’s” (Wilsonian) RG scaling theory was also formulated for the Kondo problem by Anderson [301]. These RG analyses showed that an unscreened local moment is formed for ferromagnetic Kondo couplings

$(J < 0)$ , while the runaway RG flow to strong coupling for an antiferromagnetic coupling ( $J > 0$ ) leads to the formation of a bound state between the Kondo impurity and the conduction electron cloud.

The numerical renormalization group (NRG) approach introduced by Wilson [93, 281] offers a more general treatment for impurity problems: it accounts for the spin-flip scattering based quantum fluctuations by mapping the Kondo model to a (so-called Wilson) effective 1D tight-binding chain in many-body configuration space in which the tight-binding hopping parameters fall off exponentially with distance. Iterative RG scaling of the Wilson chain leads to a strong coupling solution of the Kondo problem. Further, the NRG method allows the computation of the impurity contribution to various thermodynamic quantities, e.g., the impurity specific heat and magnetic susceptibility. Importantly, these quantities are found to be free from the log-singularities that plagued the perturbation theory solutions.

Although perturbative RG approaches cannot be trusted beyond the magnitude of coupling  $J/t$  of the order  $O(1)$ , the works by Anderson et al. [397, 398] argue for the simplest possibility of the RG flow towards strong coupling, i.e., the coupling constant diverges at the attractive fixed point,  $J/t \rightarrow \infty$ . These studies conjecture the following results for the strong coupling theory: the Kondo singlet is paramagnetic, the magnetic susceptibility time-independent and the specific heat linear in temperature. Wilson's nonperturbative NRG solution to the Kondo problem does indeed show all these features. Importantly, it obtains the Wilson ratio, i.e., the ratio of the magnetic susceptibility and the coefficient of the  $T$ -linear impurity specific heat, as a universal number of  $W = 2$  (note that  $W = 1$  for the non-interacting Fermi gas).

As renormalization group studies connect the weak coupling theory ( $J/t \ll 1$ ) to the strong coupling theory ( $J/t \gg 1$ ), Nozieres [399] provided an alternate solution of the Kondo problem from the strong coupling limit itself. In this approach, the Hamiltonian is a tight binding semi-infinite chain at whose origin resides the impurity spin. At the strong coupling limit  $J \gg t$ , a singlet is formed between the impurity spin and an electronic state at the origin. Nozieres argued that the capture of one electron at the origin is associated with a Friedel scattering phase shift of  $\delta = \pi/2$ . This lowers the Luttinger's sum by a count of  $\frac{2\delta}{\pi} = 1$  [278]. Virtual hopping of an electron between the origin and the next site of the tight-binding chain constitutes the simplest perturbation to the Kondo singlet, and leads to a repulsive local interaction on the first site. This leads to the local Fermi liquid theory of weakly interacting electrons around the impurity. The thermodynamic features of the local Fermi liquid theory reveal a  $T$ -linear specific heat, temperature-independent magnetic susceptibility and a Wilson ratio 2, all of which are in agreement with NRG.

The Kondo problem has also been independently studied via the Bethe ansatz (BA) approach [400, 401], revealing the integrability of the model and the entire diagonalized many-body spectrum. The results of the BA calculations are in good agreement with the forms of the specific heat and impurity susceptibility obtained from NRG. Importantly, the BA reveals an analytic form for the Wilson number  $\tilde{W} = T_k k / T_0$  in terms of the Euler constant, agreeing well with the  $\tilde{W} \simeq 0.413$  from NRG. Here,  $T_0$  is the dynamical Kondo scale signaling the entry into the strong coupling regime of the Kondo problem, such that for  $T < T_0$ , a saturation is reached by both the impurity magnetic susceptibility and specific heat coefficient. Finally, the conformal field theory (CFT) approach to the Kondo model by Affleck and Ludwig [402, 403] mapped the problem, via bosonization, to independent problems of spin and charge degrees of freedom. The CFT

methods lead to results in agreement with those obtained from Bethe ansatz and NRG. From a calculation of the impurity thermodynamic entropy, the CFT method further shows a lowering in ground state degeneracy under RG flow for  $J > 0$  from the local moment to the singlet regime, in agreement with Zamalodchikov's c-theorem.

As discussed at the beginning of this subsection, despite the extensive literature on this problem, a description of the Kondo effect in terms of an effective Hamiltonian and its eigenstates have remained elusive. In this thesis, we use the URG approach to meet this goal: we obtain an effective low-energy Hamiltonian and its eigenspectrum for the Kondo problem. We then benchmark the impurity specific heat and magnetic susceptibility obtained from the effective theory against results from NRG and Bethe Ansatz. In this way, we display that URG is able to capture all the universal features of the Kondo problem from a Hamiltonian RG approach.

### **1.3 Layout of following chapters**

Put in a single paragraph lay out of the following chapters of the thesis here. Or you can fold in the lines (with citations) in the respective sections and subsections above.



# Chapter 2

## Unitary Renormalization Group Method

In this chapter, we formulate the unitary RG framework for a general electronic Hamiltonian defined on a graph comprised of nodes. The nodes represent electronic states labeled by their respective bare single-particle energies. Edges connecting the nodes represent the off-diagonal scattering vertices. At each URG step, the highest energy node is disentangled via a unitary rotation, such that all its edges are removed. In Sec.2.1, we provide analytical derivation of the disentangling unitary transformation [180, 182]. This is followed by a derivation of the block-diagonal Hamiltonian resulting from such a rotation [180] in Sec.2.2. The URG approach reveals a range of retardation energyscales ( $\omega$ ) arising from the non-commutativity between the number diagonal and number off-diagonal parts of the renormalized Hamiltonian. These energyscales track the RG evolution of various subparts of the many-body spectrum, and altogether describe the Hamiltonian RG evolution. In Sec.2.3, we derive a finite-temperature thermal scale associated with a given retardation energyscale [180], such that this thermal scale acts as a high energy cutoff upto which a given  $T = 0$  quantum phase will persist.

In Sec.2.4, we show how the unitary RG flow of Hamiltonians from UV to IR renormalizes the entire hierarchy of  $2n$ -point scattering vertex tensors [182]. This allows us to interpret the Hamiltonian RG as a vertex tensor network formed from the  $2n$ -point scattering vertices. URG is a unified formalism in which the effects of Hamiltonian block diagonalization are incorporated on its eigenbasis. In Sec.2.5, we carry out an eigenbasis renormalization by applying the unitary transformations of the URG to perform disentanglement of UV degrees of freedom. Subsequently, this generates the entanglement renormalization of the remnant IR degrees of freedom [182]. In this way, the Hamiltonian (vertex) tensor network is shown to govern the eigenstate coefficient tensor network (that corresponds an exact holographic mapping (EHM) network [184]). We demonstrate that the eigenstate tensor network accommodates fermion-exchange sign factors arising from the vertex renormalizations, and that the IR fixed point reached generically involves a trivialization of the fermion sign factor. Additionally, we show that the Hilbert space geometry quantified by a many-particle entanglement metric also undergoes an RG flow.

## 2.1 Unitary disentanglement transformation

Single-electron states constituting an electronic system with  $N$  degrees of freedom (d.o.f) can be assigned indices ranging from 1 to  $N$ . The index  $j \in (1, \dots, N)$  refers to a collection of attributes that label the electron creation ( $c_j^\dagger$ ), annihilation ( $c_j$ ) and occupation number ( $\hat{n}_j = c_j^\dagger c_j$ ) operators in the second-quantized representation. For example,  $j \equiv \{n, \mathbf{r}, \sigma\}$  refers to band index ( $n$ ), position vector ( $\mathbf{r}$ ) and spin ( $\sigma$ ). The electron creation and annihilation operators satisfy the usual on-site commutation and anti-commutation relation dictated by the Pauli exclusion principle

$$\{c_j, c_k^\dagger\} = 1, [c_j^\dagger, c_k] = 2\hat{n}_{jk} - 1. \quad (2.1)$$

The numerical ordering of the indices 1 to  $N$  describe the single-particle energy eigenvalues sorted in ascending order. (For degenerate energy values the states are labelled via a specified random choice.) The Hamiltonian  $H$  governing the dynamics of this system will contain two kinds of terms: (i) scattering terms that are off-diagonal in occupation number basis, i.e., causing fluctuations in the occupancy of a electronic state, and (ii) self/correlation energy terms that are diagonal in occupation number basis, i.e., causing a shift in energy associated with a given electronic occupancy configuration. Such a partitioning of the Hamiltonian matrix was formalised in the context of quantum mechanical perturbation theory by Lowdin [404–406], and independently by Feshbach [407, 408]. Via this technique, the Hamiltonian( $H$ ) is represented as a block matrix, in the occupation number basis of the state  $N$ :  $\{|0_N\rangle, |1_N\rangle\}$ ,

$$H = \hat{n}_N H \hat{n}_N + (1 - \hat{n}_N) H (1 - \hat{n}_N) + (1 - \hat{n}_N) H \hat{n}_N + \hat{n}_N H (1 - \hat{n}_N) \quad (2.2)$$

$$= \begin{bmatrix} Tr_N(H \hat{n}_N) & Tr(H c_N) \\ Tr(c_N^\dagger H) & Tr_N(H(1 - \hat{n}_N)) \end{bmatrix}. \quad (2.3)$$

The occupation number operators  $\hat{n}_N = c_N^\dagger c_N$  and  $1 - \hat{n}_N = c_N c_N^\dagger$  represent electron and hole subspace projections in the second quantized notation respectively. We define the unitary transformation  $U_{(N)}$  as that which decouples state  $N$  from all others, i.e, it block diagonalises  $H$  by removing the off-diagonal quantum fluctuation blocks, resulting in the new Hamiltonian  $H_{N-1} = U_{(N)} H U_{(N)}^\dagger$  (see fig(1.3b)).  $U_{(N)}$  is determined by the *decoupling equation*,

$$\hat{n}_N \hat{U}_{(N)} H U_{(N)}^\dagger (1 - \hat{n}_N) = 0. \quad (2.4)$$

In this way, the label ( $N$ ) (representing the decoupling of state  $N$ ) is the first step of the RG transformations. Below we recollect the steps from Ref.[180] for deriving  $U_{(N)}$  for a general fermionic Hamiltonian  $H$ .

The fermionic Hamiltonian  $H_{(N)} = H$  can, very generally, be decomposed as

$$H_{(N)} = H_{(N)}^D + H_{(N)}^{X,N} + H_{(N)}^{X,\bar{N}}, \quad (2.5)$$

where the number diagonal part of the Hamiltonian ( $H_{(N)}^D$ ) is associated with n-particle self/correlation energies, and the term  $H_{(N)}^{X,\bar{N}}$  represents coupling only among the other degrees of freedom  $\{1, \dots, N-1\}$ . These comprise the diagonal blocks in the block matrix representation of  $H$

eq.(2.3).  $H_{(N)}^{X,N} = c_N^\dagger \text{Tr}(H_{(N)}c_N) + h.c.$  represents the off-diagonal blocks in  $H$  eq.(2.3) that are responsible for quantum fluctuations in the occupation number of state  $N$ . We are searching for a rotated many-body basis of states  $|\Psi\rangle$ 's in which the old Hamiltonian  $H_{(N)}$  attains a block diagonal form  $H_{(N-1)} = H_{(N-1)}^D + H_{(N-1)}^{X,\bar{N}}$

$$(H_{(N)}^D + H_{(N)}^{X,N} + H_{(N)}^{X,\bar{N}})|\Psi\rangle = (H_{(N-1)}^D + H_{(N-1)}^{X,\bar{N}})|\Psi\rangle . \quad (2.6)$$

To proceed further in solving this equation, we write  $|\Psi\rangle$  in the occupation number basis of states  $|0_N\rangle$  and  $|1_N\rangle$

$$|\Psi\rangle = a_1|\Psi_1, 1_N\rangle + a_0|\Psi_0, 0_N\rangle , \quad (2.7)$$

where the pair of states  $|\Psi_1\rangle$  and  $|\Psi_0\rangle$  belong to the remnant  $2^{N-1}$  dimensional Hilbert space of  $1, \dots, N-1$  single electron degrees of freedom. The 2 dimensional Hilbert space of the electron  $N$  is spanned by  $|1_N\rangle$  and  $|0_N\rangle$ . Replacing eq.(2.7) in eq.(2.6), we obtain a set of simultaneous equations

$$\begin{aligned} a_{1_N}(\hat{\omega}_{(N)} - \text{Tr}_N(\hat{n}_N H_{(N)}^D) \hat{n}_N)|\Psi_1, 1_N\rangle &= a_{0_N} c_N^\dagger \text{Tr}_N(H_{(N)}c_N) |\Psi_0, 0_N\rangle , \\ a_{0_N}(\hat{\omega}_{(N)} - \text{Tr}((1 - \hat{n}_N) H_{(N)}^D)(1 - \hat{n}_N))|\Psi_0, 0_N\rangle &= a_{1_N} \text{Tr}_N(c_N^\dagger H_{(N)}) c_N |\Psi_1, 1_N\rangle , \end{aligned} \quad (2.8)$$

where

$$\hat{\omega}_{(N)} = H_{(N-1)}^D + H_{(N-1)}^{X,\bar{N}} - H_{(N)}^{X,\bar{N}} . \quad (2.9)$$

From equation set 2.8, we deduce the following equations

$$\eta_{(N)}^\dagger \eta_{(N)} |\Psi_1, 1_N\rangle = |\Psi_1, 1_N\rangle \implies \eta_{(N)}^\dagger \eta_{(N)} = \hat{n}_N , \quad (2.10)$$

$$\eta_{(N)} \eta_{(N)}^\dagger |\Psi_0, 0_N\rangle = |\Psi_0, 0_N\rangle \implies \eta_{(N)} \eta_{(N)}^\dagger = 1 - \hat{n}_N , \quad (2.11)$$

where  $\eta_{(N)}^\dagger$  and  $\eta_{(N)}$  are defined as

$$\eta_{(N)}^\dagger = \frac{1}{\hat{\omega}_{(N)} - \text{Tr}_N(H_{(N)}^D \hat{n}_N) \hat{n}_N} c_N^\dagger \text{Tr}_N(H c_N) , \quad (2.12)$$

$$\eta_{(N)} = \frac{1}{\hat{\omega}_{(N)} - \text{Tr}_N(H_{(N)}^D (1 - \hat{n}_N)) (1 - \hat{n}_N)} \text{Tr}_N(c_N^\dagger H) c_N . \quad (2.13)$$

Finally, the above equations enable us to relate  $|\Psi\rangle$  and  $|\Psi_1, 1_N\rangle$  via a similarity transformation as follows

$$|\Psi\rangle = a_1(1 + \eta_{(N)})|\Psi_1, 1_N\rangle = a_1 \exp(\eta_{(N)})|\Psi_1, 1_N\rangle . \quad (2.14)$$

The similarity transformation  $\exp(\eta_{(N)})$  can be used to construct a unitary operator  $U_{(N)}$  [137, 139],

$$U_{(N)} = \exp \frac{\pi}{4} (\eta_{(N)}^\dagger - \eta_{(N)}) = \frac{1}{\sqrt{2}} (1 + \eta_{(N)}^\dagger - \eta_{(N)}) . \quad (2.15)$$

The property of a unitary transformation  $U_{(N)} U_{(N)}^\dagger = U_{(N)}^\dagger U_{(N)} = I$  can be immediately checked from the anti-commutation relation  $\{\eta_{(N)}, \eta_{(N)}^\dagger\} = 1$ . Via applying the unitary operator  $U_{(N)}$  on  $H$ , we will obtain the form of the rotated Hamiltonian in the next section.

## 2.2 Hamiltonian Block Diagonalization

We note that the rotated Hamiltonian should be purely diagonal in the occupation-number basis states  $1_N$  and  $0_N$ . In order to verify this, we decompose the rotated Hamiltonian into diagonal and off-diagonal components

$$\begin{aligned} U_N H U_N^\dagger &= H_1 + H_2, \\ H_1 &= \frac{1}{2} \left[ H + [\eta_N^\dagger - \eta_N, H] + \eta_N H \eta_N^\dagger + \eta_N^\dagger H \eta_N \right], \\ H_2 &= \frac{1}{2} \left[ H_N^X - \eta_N^\dagger \text{Tr}_N(c_N^\dagger H) c_N \eta_N^\dagger - \eta_N c_N^\dagger \text{Tr}_N(H c_N) \eta_N \right], \end{aligned} \quad (2.16)$$

where the off-diagonal component  $H_2$  must vanish. To show that, we first set up the preliminaries(using eq.(2.12) and eq.(2.13))

$$\begin{aligned} \eta_N^\dagger \eta_N = \hat{n}_N &\implies \hat{\omega} - \text{Tr}_N(H^D \hat{n}_N) \hat{n}_N = c_N^\dagger \text{Tr}_N(H c_N) \eta_N, \\ &\implies \eta_N c_N^\dagger \text{Tr}_N(H c_N) \eta_N = \text{Tr}_N(c_N^\dagger H) c_N. \end{aligned} \quad (2.17)$$

The definition of  $H_N^X = c_N^\dagger \text{Tr}_N(H c_N) + h.c.$ , along with eq.(2.17), then implies that  $H_2 = 0$ . In the other component,  $H_1$ , we first unravel the terms  $\eta_N H \eta_N^\dagger$  and  $\eta_N^\dagger H \eta_N$ . Using eq.(2.9), eq.(2.12) and eq.(2.13), we obtain

$$\begin{aligned} \frac{1}{\hat{H}' - \text{Tr}_N(H \hat{n}_N) \hat{n}_N} c_N^\dagger \text{Tr}_N(H c_N) &= c_N^\dagger \text{Tr}_N(H c_N) \frac{1}{\hat{H}' - \text{Tr}_N(H(1 - \hat{n}_N))(1 - \hat{n}_N)}, \\ \implies \text{Tr}_N(H \hat{n}_N) \hat{n}_N c_N^\dagger \text{Tr}_N(H c_N) &= c_N^\dagger \text{Tr}_N(H c_N) \text{Tr}_N(H(1 - \hat{n}_N))(1 - \hat{n}_N). \end{aligned} \quad (2.18)$$

The above relation then allows us to simplify  $\eta_N H \eta_N^\dagger$  and  $\eta_N^\dagger H \eta_N$  as follows

$$\begin{aligned} \eta_N H \eta_N^\dagger &= \text{Tr}_N(H(1 - \hat{n}_N))(1 - \hat{n}_N), \\ \eta_N^\dagger H \eta_N &= \text{Tr}_N(H \hat{n}_N) \hat{n}_N. \end{aligned} \quad (2.19)$$

Next, we deduce  $[\eta_N^\dagger - \eta_N, H]$ , i.e., the renormalization of the Hamiltonian using the relations obtained above

$$[\eta_N^\dagger - \eta_N, H] = 2\tau_N \{c_N^\dagger \text{Tr}_N(H c_N), \eta_N\}. \quad (2.20)$$

Finally, by combining the result  $H_2 = 0$  together with eqs.2.19 and 7.12, we obtain the form of the rotated  $H$

$$U_N H U_N^\dagger = \frac{1}{2} \text{Tr}_N(H) + \tau_N \text{Tr}_N(H \tau_N) + \tau_N \{c_N^\dagger \text{Tr}_N(H c_N), \eta_N\}. \quad (2.21)$$

One can easily check that the rotated Hamiltonian  $[U_N H U_N^\dagger, \hat{\tau}_N] = 0$ , i.e.,  $\tau_N$  is an integral of motion.

For a given RG step  $j$  the form of the unitary operator is given similar to eq.(2.15)

$$U_{(j)} = \frac{1}{\sqrt{2}} [1 + \eta_{(j)} - \eta_{(j)}^\dagger], \quad \{\eta_{(j)}^\dagger, \eta_{(j)}\} = 1, \quad (2.22)$$

Here,  $\eta_{(j)}$  and  $\eta_{(j)}^\dagger$  are the electron-hole (e-h) transition operators associated with the  $j$ th RG step, they possess the usual anti-commutation relation as well as satisfy the following relations

$$\begin{aligned} (1 - \hat{n}_j)\eta_{(j)}\hat{n}_j &= \eta_{(j)}, \quad \hat{n}_j\eta_{(j)}(1 - \hat{n}_j) = 0 \\ \eta_{(j)}^2 &= 0, \quad [\eta_{(j)}^\dagger, \eta_{(j)}] = 2\hat{n}_j - 1. \end{aligned} \quad (2.23)$$

It can be easily seen that the operators  $\eta_{(N)}$  and  $\eta_{(N)}^\dagger$  defined in eqs.(2.12, 2.13) satisfies the above properties. Using the above relations we obtain an simplified form for the Hamiltonian flow equation,

$$\hat{H}_{(j-1)} = U_{(j)} H_{(j)} U_{(j)}^\dagger = \frac{1}{2} Tr_j(\hat{H}_{(j)}) + Tr_j(\hat{H}_{(j)}\tau_j) + \tau_j\{c_j^\dagger Tr_j(H_{(j)}c_j), \eta_{(j)}\}. \quad (2.24)$$

Here, the off-diagonal term  $c_j^\dagger Tr_j(H_{(j)}c_j)$  is a compact representation of the multi-particle scattering terms via which the state labeled  $j$  is coupled to the remaining  $j - 1$  d.o.f. Importantly, this compact representation of the off-diagonal block respects the signatures arising from fermion exchanges[182]. It is evident from the expression eq.(2.24) that the renormalization of the Hamiltonian blocks marked by the two values of the occupation number of the  $j$ th state ( $\hat{H}_{(j-1)}^{1,j}$  and  $\hat{H}_{(j-1)}^{0,j}$ ) take place in an opposite manner. Finally we discuss an important outcome of our RG transformation scheme  $H \rightarrow U_N H U_N^\dagger$  :- if along the RG flow, one of the energy eigenvalues of  $\hat{\omega}$  operator matches with an eigenvalue of the diagonal operator  $H^D$ , we obtain a stable fixed point of the RG transformations that is signalled via the vanishing of the off-diagonal blocks in the occupation basis of the electronic state being disentangled at that step. This can be seen by starting from equation eq.(2.13), with  $\eta_N$  acting on any one of the eigenstates of the  $\hat{\omega}$  operator (say  $|\Phi_1, 1_{\mathbf{k}\sigma}\rangle$ ) with eigenvalue  $\omega$

$$\begin{aligned} (\omega - Tr_N(H^D\hat{n}_N)|\Phi_1, 1_N\rangle &= c_N^\dagger Tr(Hc_N)\eta_N|\Phi_1, 1_N\rangle \\ \text{Det}(\omega - Tr_N(H^D\hat{n}_N)) = 0 &\implies H_N^X|\Phi_1, 1_N\rangle = 0. \end{aligned} \quad (2.25)$$

This shows that if one of the eigenenergies of  $H^D$  becomes equal to fluctuation energy scale  $\omega$ , a stable fixed point is reached due to a vanishing off-diagonal block [409].

## 2.3 Correspondence between $\omega$ and an emergent thermal scale $T$

In the above RG scheme, the renormalized Hamiltonian can be decomposed over all fluctuation scales as follows:  $H_{(j)} = \sum_\omega (H_{(j)}(\omega)\hat{O}(\omega))_{(j)}$ , where  $\hat{O}(\omega)_{(j)}$  projects onto a eigensubspace of  $\hat{\omega}$  with fluctuation energy eigenvalue  $\omega$ . A variety of many body correlations can be encoded within the various  $H_{(j)}(\omega)$ 's describing different subspaces of the many body spectrum. Can the effects of  $\omega$  dependent many-body correlations on the non-interacting Fermi gas at  $T = 0$ K be manifested in a finite temperature  $T$ -scale?

We now proceed to find the relation between the thermal energy  $k_B T$  and energy broadening due to the virtual excitations of the quasiparticle. These virtual excited states drive the RG flow. Resultingly an effective Hamiltonian  $H_{>j} = Tr_{1,\dots,j}(H_{(j)})$  comprising the excited states decoupled

under RG flow is obtained by partial tracing  $H_{(j)}$  over the remnant coupled degrees of freedom ( $\tau_j = \hat{n}_j - \frac{1}{2}$ ),

$$H_{>j}(\omega_i) = \sum_{j_1 > j} \tilde{\epsilon}_{j_1}(\omega_i) \tau_{j_1} + \sum_{j_1, j_2 > j} \Gamma_{j_1, j_2}^4(\omega_i) \tau_{j_1} \tau_{j_2} + \sum_{j_1, j_2, j_3 > j} \Gamma_{j_1, j_2, j_3}^6(\omega_i) \tau_{j_1} \tau_{j_2} \tau_{j_3} + \dots . \quad (2.26)$$

where  $\tilde{\epsilon}_j(\omega_i) = \epsilon_j + \Sigma_j(\omega_i)$  with  $\Sigma_j$  composed of all higher order correlations. Given that we are unitarily disentangling precisely one single-particle state at every RG step, a thermal scale arises by limiting our perspective to many-body correlations within the single-particle Hamiltonian  $\sum_{j_1} \epsilon_j(\omega_i) \tau_{j_1}$ .

For this Hamiltonian, we introduce the imaginary-time evolution operator

$$U_{(j)}^1(\tau) = \exp(-\tau \sum_{j_1 > j} \tilde{\epsilon}_{j_1}(\omega_i) \tau_{j_1}) \quad (2.27)$$

fulfilling the Kubo-Martin-Schwinger(KMS) condition  $U_{(j)}^1(\tau) = -U_{(j)}^1(\tau + \beta)$  for fermions [410],  $\beta = (k_B T)^{-1}$  is the imaginary-time period. The KMS condition allows us to attain a Matsubara spectral representation for  $U_{>j}^1$  (where  $\tilde{\omega}_m = \frac{\pi(2m+1)}{\beta}$  are the harmonics)

$$U_{>j}^1(i\tilde{\omega}_m, \omega) = \sum_{\beta} e^{\tau\tilde{\omega}_m} \tilde{U}_{>j}^1(\tau, \omega) = \sum_{l=j+1}^N \frac{|l\rangle\langle l|}{i\tilde{\omega}_m - \epsilon_l \tau_l - \Sigma_l(\omega) \tau_l} . \quad (2.28)$$

We can define a complex self-energy,  $\bar{\Sigma}_l(\omega) = \Sigma_l(\omega) - i\tilde{\omega}_m$ , where  $\tilde{\omega}_m$  is the Matsubara frequency. As the single-particle states are disentangled, any mixedness in the state of the effective non-interacting metal can be attributed to a thermal scale  $\tilde{\omega}_0 = 2\pi\beta^{-1}$ . The Matsubara frequencies  $\tilde{\omega}_m = \pi(2m+1)\beta^{-1}$  are defined as the  $m$ th harmonics of  $\beta = 1/k_B T$ . Here we choose  $m = 0$ , i.e.,  $\tilde{\omega}_0 = \pi\beta^{-1}$  in order to find the largest temperature scale  $T$  upto which the poles will persist. By writing the imaginary part of the self energy as a Kramers-Kronig partner of the real self-energy, we obtain an equivalent temperature scale

$$\frac{\hbar}{\tau} = \frac{1}{\pi} \mathcal{P} \int_{-\infty}^{\infty} \frac{\Sigma_{j+1}(\bar{\omega})}{\bar{\omega} - \tilde{\omega}_0} d\bar{\omega} \equiv \hbar\tilde{\omega}_0 , \quad (2.29)$$

upto which the one-particle excitations can survive. Beyond it, they are replaced by 2e-1h composite excitations. The above relation shows the finite lifetime  $\tau$  of the single-particle states can be viewed as an effective temperature scale arising out of the unitary disentanglement.

## 2.4 Vertex tensor network renormalization

The Hamiltonian operator's diagonal ( $H_{(j)}^D$ ) and off-diagonal ( $H_{(j)}^X$ ) parts at a given RG step ( $j$ ) can be written as a closed-form cluster decomposition

$$H_{(j)} = H_{(j)}^D + H_{(j)}^X . \quad (2.30)$$

$$H_{(j)}^D = \sum_{i=1}^{2^{j-1}} \sum_{n=1}^N \sum_{\alpha, \alpha'} \{ \tilde{c}_{\alpha}^{\dagger} \frac{\Gamma_{\alpha\alpha'}^{2n}(\omega^i)}{2^n} \tilde{c}_{\alpha'} \hat{O}(\omega^i) \}_{(j)} ,$$

$$H_{(j)}^X = \sum_{i=1}^{2^{j-1}} \sum_{n=1}^{a_j^{max}} \sum_{\alpha, \beta} \{ \tilde{c}_{\alpha}^{\dagger} \Gamma_{\alpha\beta}^{2n}(\omega^i) \tilde{c}_{\beta} \hat{O}(\omega^i) \}_{(j)} . \quad (2.31)$$

We now clarify the various terms and notations appearing in these equations. The index  $i$  is associated with the  $2^{j-1}$  configurations of the coupled  $j - 1$  single-particle states. The index  $n$  labels the various  $n$ -particle (or  $2n$ -point) scattering process, and runs from 1 to  $N$  for the contributions to  $H_{(j)}^D$  for a system of  $N$  particles. On the other hand,  $n$  runs from 1 to an upper limit  $a_j^{max} = \min\{2^j a_0 - 2^{j+1} + 2, j\}$ , indicating the largest off-diagonal  $n$ -particle vertex string present in  $H_{(j)}^X$ . The indices  $\alpha, \alpha'$  and  $\beta$  are defined as follows:  $\alpha := \{(l, \mu)\}$  is an ordered set of  $n$  pairs of indices  $l$  and  $\mu$ , where the index  $0 \leq l \leq j$  (the subspace of coupled single-particle states) and  $\mu = 0, 1$  refers to either unoccupied (0) or occupied (1) state. Thus, the operator  $\tilde{c}_\alpha^\dagger$  refers to a string of  $n$  fermionic creation and annihilation operators for the  $0, \dots, n$  states in product. The index  $\alpha' := \{(l, \bar{\mu})\}$ , where  $0 \leq l \leq j$  once again but  $\bar{\mu}$  is the complement of  $\mu$ , i.e.,  $\bar{\mu} = 1, 0$  refers to unoccupied (1) and occupied (0). Thus, by construction, the operator  $\tilde{c}_{\alpha'}$  also refers to a string of  $n$  fermionic creation and annihilation operators for the  $0, \dots, j$  states in product, and which are the complement to the string given by  $\tilde{c}_\alpha^\dagger$ . In this way, the product  $\tilde{c}_\alpha^\dagger \tilde{c}_{\alpha'}$  defines a product of  $n$  number operators. Thus, the vertex function associated with this term,  $\Gamma_{\alpha\alpha'}^{2n}(\omega^i)$ , denotes the magnitude of the diagonal  $n$ -particle correlation energy  $H_{(j)}^D$ . The presence of the projection operator  $\hat{O}$  ensures a sum over each member of  $2^{j-1}$  many-body configurations. The closed form representation of  $H$  eq.(2.31) can be interpreted as a tensor network formed from the  $2n$ -point vertex tensors. As shown in Fig.1.5, the node of each such vertex tensor  $\Gamma_{\alpha\alpha'}^{2n,(j)}(\omega^i)$  represents the scattering process, while the blue legs of the tensors represents the electronic states. The black dashed/solid edges represents the outgoing/incoming electronic states respectively. The number  $2n$  is the total number of incoming and outgoing lines.

The sum over the indices  $\alpha$  and  $\alpha'$  is an anti-symmetrised summation over the indices  $\mu$  and  $\bar{\mu}$ , as can be seen from the following. Under interchange of  $\alpha$  and  $\alpha'$ ,  $\Gamma_{\alpha\alpha'}^{2n}$  satisfies the relation

$$\Gamma_{\alpha\alpha'}^{2n} = (-1)^{\sum_{i=1}^n (\bar{\mu}_i - \mu_i)} \Gamma_{\alpha'\alpha}^{2n}. \quad (2.32)$$

This allows the recasting of  $H_{(j)}^D$  as a sum over various  $n$ -particle vertex terms

$$\tilde{c}_\alpha^\dagger \frac{\Gamma_{\alpha\alpha'}^{2n}(\omega^i)}{2^n} \tilde{c}_{\alpha'} = \Gamma_{\alpha\alpha'}^{2n} \prod_{s=1}^n \tau_{l_s}, \quad (2.33)$$

where  $\tau_{l_s} = (\hat{n}_{l_s} - \frac{1}{2})$  is the occupation number operator defined in an electron-hole symmetric fashion, and  $0 \leq l_s \leq j$ . We illustrate this representation in an example of a 2-particle correlation energy

$$\Gamma_{\alpha\alpha'}^4 \tau_{l_1} \tau_{l_2} = \frac{1}{4} \Gamma_{\alpha\alpha'}^4 \left[ \hat{n}_{l_1} \hat{n}_{l_2} - \hat{n}_{l_1} (1 - \hat{n}_{l_2}) - (1 - \hat{n}_{l_1}) \hat{n}_{l_2} + (1 - \hat{n}_{l_1})(1 - \hat{n}_{l_2}) \right]. \quad (2.34)$$

In the same way, the index  $\beta := \{(l', \mu')\}$  refers to an ordered set of  $n$  pairs of indices  $l'$  and  $\mu'$ , where the index  $0 \leq l' \leq j$  (the subspace of coupled single-particle states) and  $\mu' = 0, 1$  refers to either unoccupied (0) or occupied (1) state, *but* with  $l'$  and  $\mu'$  being distinct from  $l$  and  $\mu$ . Then, the product  $\tilde{c}_\alpha^\dagger \tilde{c}_\beta$  appearing in  $H_{(j)}^X$  defines a product of fermionic annihilation and creation operators that transfer electrons between the sets of states given by  $\{(l, \mu)\}$  and  $\{(l', \mu')\}$ . Naturally, the vertex function associated with this term,  $\Gamma_{\alpha\beta}^{2n}(\omega^i)$ , denotes the magnitude of the off-diagonal element for  $n$ -particle (or  $2n$ -point) scattering.

In the off-diagonal  $n$ -particle terms within  $H_{(j)}^X$ , the ordering of any given creation and annihilation operator string can be seen as a permutation of the normal ordered form arranged in an ascending sequence of the entries of the labels  $\alpha$  and  $\beta$ . The sign of this permutation can be accommodated within the  $n$ -particle vertex

$$\Gamma_{\alpha\beta}^{2n} = \text{sgn}(\mathcal{P}_{\alpha\beta}) \Gamma_{(\alpha_0\beta_0)}^{2n}, \quad (2.35)$$

where  $(\alpha_0\beta_0)$  represents a two-level sorting of the indices  $\alpha$  and  $\beta$ .  $\mathcal{P}_{\alpha\beta}$  represents the permutation operation on the sorted list. The first involves a sorting of the labels  $\mu$  and  $\mu'$  in a descending fashion: this creates a normal ordered string, i.e.,  $c^\dagger$  operators followed by  $c$  operators. The second sorting involves a further arrangement of the labels  $l$  and  $l'$  in ascending order. The sign of the permutation generated in this process,  $\text{sgn}(\mathcal{P}_{\alpha\beta})$ , nullifies the fermion sign of the unsorted list. It can also be seen that the largest off-diagonal operator string has a length of  $a_j$ . We have shown in Fig.(2.2) that  $a_j$  has a non-monotonic behaviour with the RG step  $j$ : it increases initially, peaks and then falls till the fixed point is reached. A similar behaviour is displayed in for the total number of off-diagonal terms with RG step  $j$ . Further, the off-diagonal parts of the Hamiltonian can be seen to describe both number conserving as well as non-conserving terms. For example, the  $n = 1$  vertices with  $\alpha = (l_1, 1), \beta = (l_2, 0)$  and  $\alpha' = (l_1, 1), \beta' = (l_2, 1)$  correspond to the following number conserving and non-conserving terms respectively

$$\tilde{c}_\alpha^\dagger \Gamma_{\alpha\beta}^2 \tilde{c}_\beta = \Gamma_{\alpha\beta}^2 c_{l_1}^\dagger c_{l_2}, \quad \tilde{c}_{\alpha'}^\dagger \Gamma_{\alpha'\beta'}^2 \tilde{c}_{\beta'} = \Gamma_{\alpha'\beta'}^2 c_{l_1}^\dagger c_{l_2}^\dagger. \quad (2.36)$$

In order to obtain the vertex RG flow equations from the renormalized Hamiltonian, we decompose it into a sum of strings comprised of number diagonal and off-diagonal operators. This decomposition is carried out as follows. First, we write one spectral component of the rotated Hamiltonian  $H_{(j)}$  using eq.(2.31), i.e.,  $H_{(j)}(\omega_{(j)}^i)$  as a *cluster expansion* of 2-point, 4-point, 6-point and higher order vertices

$$H_{(j)}(\omega_{(j)}^i) = H_{(j)}^2(\omega_{(j)}^i) + H_{(j)}^4(\omega_{(j)}^i) + H_{(j)}^6(\omega_{(j)}^i) + \dots. \quad (2.37)$$

The term  $H_{(j)}^2(\omega^i)$  can, very generally, be decomposed into diagonal and off-diagonal parts,  $H_{(j)}^2 = H_{(j)}^{2,D} + H_{(j)}^{2,X}$ , and each of the two parts renormalized via contributions from all  $2n$ -point vertices. For instance, the contribution to  $H_{(j)}^{2,D}$  is given by

$$\begin{aligned} H_{(j)}^{2,D} &= \left( \sum_l \Gamma_{\alpha\alpha'}^{2,(j)}(\omega_{(j)}^i) \sigma_l + 2 \sum_{\alpha,\gamma} \{\Gamma_{\alpha\gamma}^2 G_{\gamma\gamma'}^2 \Gamma_{\gamma\alpha'}^2\}^{(j)}(\omega_{(j)}^i) \tau_j \sigma_l + 8 \sum_{\alpha,\gamma} \{\Gamma_{\alpha\gamma}^4 G_{\gamma\gamma'}^6 \Gamma_{\gamma\alpha'}^4\}^{(j)}(\omega_{(j)}^i) \tau_j \sigma_{j_1} \sigma_{j_2} \sigma_l \right. \\ &\quad \left. + 32 \sum_{\alpha,\gamma} \{\Gamma_{\alpha\gamma}^6 G_{\gamma\gamma'}^{10} \Gamma_{\gamma\alpha'}^6\}^{(j)}(\omega_{(j)}^i) \tau_j \sigma_{j_1} \sigma_{j_2} \sigma_{j_3} \sigma_{j_4} \sigma_l + \dots \right) \times \left( 1 + \sum_{k_1=j+1}^N \tau_{k_1} + \sum_{\substack{k_1 \neq k_2 \\ \in \{j+1, N\}}}^N \tau_{k_1} \tau_{k_2} + \dots \right) \\ &= \sum_l \Gamma_{\alpha\alpha'}^{2,(j-1)} \tau_l \left( \sum_{\substack{i=1, \\ \{k_1, \dots, k_i\}}}^{N-j+1} \prod_{l=1}^i \tau_{k_l} \right), \end{aligned} \quad (2.38)$$

where

$$\Gamma_{\alpha\alpha'}^{2,(j-1)}(\omega_{(j)}^i) = \Gamma_{\alpha\alpha'}^{2,(j)}(\omega_{(j)}^i) + \sum_{\alpha,\gamma} \{\Gamma_{\alpha\gamma}^{p_1} G_{\gamma\gamma'}^{2p_1-2} \Gamma_{\gamma\alpha'}^{p_1}\}^{(j)}(\omega_{(j)}^i), \quad (2.39)$$

$G_{\gamma\gamma'}^{2p_1-2}$  is the Green's function containing the correlation energies of  $p_1 - 1$  particle labelled  $j_1, \dots, j_{p_1-1}$

$$G_{\gamma\gamma'}^{2p_1-2} = \frac{2^{p_1-1} \prod_{s=1}^{p_1-1} \sigma_{j_s} \tau_j}{\omega_{(j)}^i - \sum_{\alpha,l=1}^{p_1-1} (\Gamma_{\alpha\alpha'}^{2l,(j)}(\omega_{(j)}^i) + \Gamma_{\alpha\alpha'}^{2l+2,(j)}(\omega_{(j)}^i) \tau_j) \prod_{s=1}^l \sigma_{n_s}} , \quad (2.40)$$

and the operators  $\tau_{k_i} = n_{k_i} - \frac{1}{2}$  in eq.(2.38) represent decoupled degrees of freedom that commute with the Hamiltonian  $H_{(j)}$ . Note, however, that the operators  $\sigma_{n_s} = n_{n_s} - \frac{1}{2}$  do not commute with  $H_{(j)}$  as they belong to the coupled space, and the labels  $n_1, \dots, n_l \in j_1, \dots, j_j$  lie within  $1, \dots, j$ . Similarly, the contribution to  $H_{(j)}^{2,X}$  is given by

$$\begin{aligned} H_{(j)}^{2,X} &= \left( \sum_l \Gamma_{\alpha\beta}^{2,(j)}(\omega_{(j)}^i) c_l^\dagger c_{l'} + 2 \sum_{\alpha,\gamma} \{\Gamma_{\alpha\gamma}^2 G_{\gamma\gamma'}^2 \Gamma_{\gamma\beta}^2\}^{(j)}(\omega_{(j)}^i) \tau_j c_l^\dagger c_{l'} \right. \\ &+ 8 \sum_{\alpha,\gamma} \{\Gamma_{\alpha\gamma}^4 G_{\gamma\gamma'}^6 \Gamma_{\gamma\beta}^4\}^{(j)}(\omega_{(j)}^i) \tau_j \sigma_{j_1} \sigma_{j_2} c_l^\dagger c_{l'} + 2 \sum_{\alpha,\gamma} \{\Gamma_{\alpha\gamma}^6 G_{\gamma\gamma'}^{10} \Gamma_{\gamma'\beta}^6\}^{(j)}(\omega_{(j)}^i) \tau_j \sigma_{j_1} \sigma_{j_2} \sigma_{j_3} \sigma_{j_4} c_l^\dagger c_{l'} + \dots \left. \right) \\ &\times \left( 1 + \sum_{k_1=j+1}^N \tau_{k_1} + \sum_{\substack{k_1 \neq k_2 \\ \in \{j+1, N\}}}^N \tau_{k_1} \tau_{k_2} + \dots \right) \\ &= \sum_{l,l'} \Gamma_{\alpha\beta}^{2,(j-1)} c_l^\dagger c_{l'} \left( \sum_{\substack{i=1, \\ \{k_1, \dots, k_i\}}}^{N-j+1} \prod_{l=1}^i \tau_{k_l} \right) , \end{aligned} \quad (2.41)$$

where

$$\Gamma_{\alpha\beta}^{2,(j-1)}(\omega_{(j)}^i) = \Gamma_{\alpha\beta}^{2,(j)}(\omega_{(j)}^i) + 2^{p_1-1} \sum_{\alpha,\gamma} \{\Gamma_{\alpha\gamma}^{p_1} G_{\gamma\gamma'}^{p_1+p_2-2} \Gamma_{\gamma'\beta}^{p_2}\}^{(j)}(\omega_{(j)}^i) . \quad (2.42)$$

Similarly, the renormalisations of  $H_{(j)}^4$  and  $H_{(j)}^6$  are given by

$$H_{(j)}^4 = \left[ \sum_{l_1, l_2} \Gamma_{\alpha\alpha'}^{4,(j-1)} \sigma_{l_1} \sigma_{l_2} + \sum_{\substack{l_1, l_2, \\ l_3, l_4}} \Gamma_{\alpha\beta}^{4,(j-1)} c_{l_1}^\dagger c_{l_2}^\dagger c_{l_3} c_{l_4} \right] \left( \sum_{\substack{i=1, \\ \{k_1, \dots, k_i\}}}^{N-j+1} \prod_{l=1}^i \tau_{k_l} \right) , \quad (2.43)$$

$$H_{(j)}^6 = \left( \sum_{l_1, l_2} \Gamma_{\alpha\alpha'}^{6,(j-1)} \sigma_{l_1} \sigma_{l_2} \sigma_{l_3} + \sum_{\substack{l_1, l_2, l_3 \\ l_4, l_5, l_6}} \Gamma_{\alpha\beta}^{6,(j-1)} c_{l_1}^\dagger c_{l_2}^\dagger c_{l_3}^\dagger c_{l_4} c_{l_5} c_{l_6} \right) \left( \sum_{\substack{i=1, \\ \{k_1, \dots, k_i\}}}^{N-j+1} \prod_{l=1}^i \tau_{k_l} \right) , \quad (2.44)$$

where  $\Gamma_{\alpha\beta}^{4,(j-1)}$  and  $\Gamma_{\alpha\beta}^{6,(j-1)}$  are given by

$$\Gamma_{\alpha\beta}^{4,(j-1)}(\omega_{(j)}^i) = \Gamma_{\alpha\beta}^{4,(j)}(\omega_{(j)}^i) + 2^{p_1-1} \sum_{\alpha,\gamma} \{\Gamma_{\alpha\gamma}^{p_1} G_{\gamma\gamma'}^{p_1+p_2-4} \Gamma_{\gamma'\beta}^{p_2}\}^{(j)}(\omega_{(j)}^i) , \quad (2.45)$$

$$\Gamma_{\alpha\beta}^{6,(j-1)}(\omega_{(j)}^i) = \Gamma_{\alpha\beta}^{6,(j)}(\omega_{(j)}^i) + 2^{p_1-1} \sum_{\alpha,\gamma} \{\Gamma_{\alpha\gamma}^{p_1} G_{\gamma\gamma'}^{p_1+p_2-6} \Gamma_{\gamma'\beta}^{p_2}\}^{(j)}(\omega_{(j)}^i) . \quad (2.46)$$

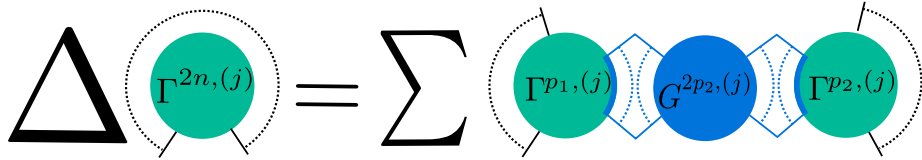


Figure 2.1: The RG evolution of the  $2n$ -point vertices  $\Gamma^{2n,(j)}$ . The green disk with multiple legs in black/blue (shown via a span of dots) on the left hand side of the equation represents a  $2n$ -point vertex( $\Gamma^{2n,(j)}$ ), while on the right, it represents a  $p_1$ -point ( $\Gamma^{p_1,(j)}$ ) and a  $p_3$ -point vertex ( $\Gamma^{p_3,(j)}$ ) respectively. The blue disk (sandwiched between the two green disks) represents a  $2p_2$ -point Green's function ( $G^{2p_2,(j)}$ ) in which the blue legs represent the states involved in the scattering process. The blue legs of the Green's function  $G^{2p_2,(j)}$  are shown to be contracted with the legs of the green disks (also marked in blue), so as to generate the tensor legs of the  $2n$ -point vertex. The index  $p_1$  and  $p_3$  are summed over, as discussed in the main text.

We now present one of the important results of our work. Using the method of induction, we generalize the expressions for the 2-, 4- and 6-point vertex RG flow eqns. eq.(2.39), eq.(2.41), eq.(2.45) and eq.(2.46) in order to recast the Hamiltonian flow equation in terms of an entire hierarchy of  $2n$ -point vertex RG equations  $\Gamma_{\alpha\beta}^{2n}$  (see Fig.(2.1))

$$\Delta\Gamma_{\alpha\beta}^{2n,(j)}(\omega^i) = \sum_{p_1,p_3} \sum_{\gamma}^{2a_j^{max}} \{\Gamma_{\alpha\gamma}^{p_1} G_{\gamma\gamma'}^{2p_2} \Gamma_{\gamma'\beta}^{p_3}\}^{(j)}(\omega^i), \quad (2.47)$$

where  $\alpha := \{(l, \mu)\}$  is an ordered set of  $p_1 - p_2$  pairs of indices, and  $l$  and  $\mu$  are defined precisely as earlier. The indices  $\gamma := \{(l', \mu')\}$  and  $\gamma' := \{(l', \bar{\mu}')\}$  are ordered sets of  $p_2$  pairs of indices, where  $l'$  and  $\mu'$  are defined similarly to  $l$  and  $\mu$ , and  $\bar{\mu}'$  is the complement of  $\mu'$ . The index  $\beta := \{(l'', \mu'')\}$  is also an ordered set of  $p_3 - p_2$  pairs of indices, where  $l''$  and  $\mu''$  are defined similarly to  $l$  and  $\mu$ . The indices  $p_1$  and  $p_3$  take value from the set of even positive integers lying in  $[n + 1, 2a_j^{max}]$  and  $[2, 2a_j^{max}]$  respectively while  $p_2$  takes values among the set of all positive integers lying in  $[1, 2a_j^{max} - n]$ , such that  $p_1 + p_3 - 2p_2 = 2n$ .

The Green's function  $G_{\gamma\gamma'}^{2p_2,(j)}(\omega_{(j)}^i)$  contains all correlation energies ( $\Gamma_{\delta\delta'}^{2k,(j)}$ ) for  $1 \leq k \leq p_2$  particles

$$G_{\gamma\gamma'}^{2p_2,(j)} = \left( \omega_{(j)}^i - \sum_{k=1}^{p_2} \sum_{\delta\delta'} \Gamma_{\delta\delta'}^{2k,(j)} \prod_{s=1}^k (\hat{n}_{l_s} - \frac{1}{2}) \right)^{-1} 2^{p_2} \prod_{s=1}^{p_2} (\hat{n}_{l_s} - \frac{1}{2}), \quad (2.48)$$

where the indices  $\delta := \{(l, \mu)\}$  and  $\delta' := \{(l, \bar{\mu})\}$  are ordered sets of  $k$  pairs of indices,  $l$  and  $\mu$  are defined as earlier, and  $\bar{\mu}$  is the complement of  $\mu$ . The index  $l_s$  denotes the entries of  $l$  that appear within  $\delta$ . As shown in the diagrammatic representation of Fig.(2.1), various  $2p_2$ -point Green's functions connect the  $p_1$ - and  $p_3$ -point interaction vertices in renormalising the  $2n$ -point vertex. The appearance of the frequency dependent correlation energies within the Green's function leads to two non-perturbative features of the RG transformations. First, the interplay of the multireference quantum fluctuation scale  $\omega_{(j)}^i$  and the correlation energies in the vertex RG flows eq.(2.47) enables the distillation of the relevant vertices from the irrelevant

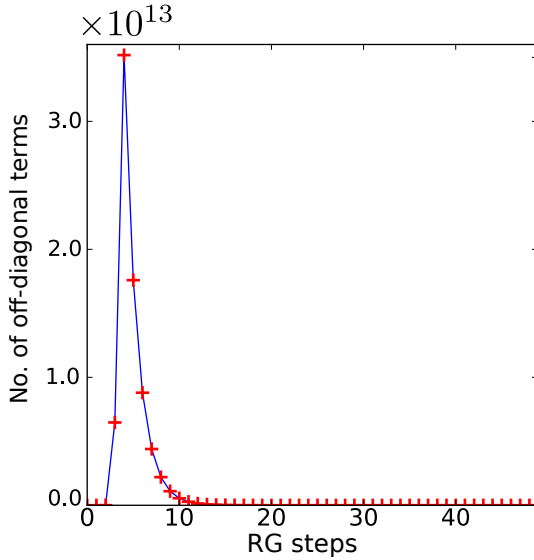


Figure 2.2: Variation of the total number of off-diagonal terms  $K_j$  with RG step  $j$ . The analysis has been carried out for  $N = 50$  electronic states and  $a_0 = 4$ . The dimensionality is given by  $\dim(\mathcal{C}^{50} = 2^{50})$ .

ones. Second, following the discussion of eq.(2.25), the fixed points of the RG equations are given by the poles of eq.(2.48) and allows the fixed point effective Hamiltonians to be derived. In subsequent sections, we will demonstrate the fixed point effective Hamiltonians that arise from the RG treatment of various microscopic models.

It should be noted that the feedback from correlation energies and the hierarchical nature of RG flow equations are also features of the FRG scheme [223]. For instance, the recent multiloop functional RG scheme [115, 116] contains a systematic way of dealing with various  $2n$ -point vertices, but the hierarchy of flow equations typically requires a truncation. The unitary RG formulation for the Hamiltonian presented here does not, however, need any truncation. Instead, its non-perturbative nature overcomes the limitations of both a coupling expansion [229] as well as a cluster expansion [200] prevalent in other Hamiltonian RG formulations.

## 2.5 Geometry of Eigenbasis Renormalization

Having formulated the RG procedure for the Hamiltonian, we will now provide a geometric view of many-body eigenbasis renormalization in terms of the RG flow of Fubini-Study quantum distances [411] between many body states. As discussed earlier, the bare (or starting) Hamiltonian  $H_{(N)}$  of the RG flow has  $N$  coupled electronic degrees of freedom, with an eigenbasis of  $2^N$  eigenstates  $\mathcal{B}_{(N)} = \{|\Psi^i\rangle, i \in [1, 2^N]\}$  that satisfy the eigenvalue relation

$$H_{(N)}|\Psi^i\rangle = E^i|\Psi^i\rangle . \quad (2.49)$$

The eigenbasis  $\mathcal{B}_{(N)}$  is renormalized via the same unitary rotation that block diagonalizes  $H_{(N)}$  (eq.(2.4))

$$H_{(j-1)} = U_{(j)} H_{(j)} U_{(j)}^\dagger , \quad \mathcal{B}_{(j)} = U_{(j+1)} \mathcal{B}_{(j+1)} . \quad (2.50)$$

This ensures the *spectrum preserving* nature of RG flow

$$H_{(j)}|\Psi_{(j)}^i\rangle = E^i|\Psi_{(j)}^i\rangle \Rightarrow H_{(j-1)}|\Psi_{(j-1)}^i\rangle = E^i|\Psi_{(j-1)}^i\rangle . \quad (2.51)$$

We have already seen that the Hamiltonian is block diagonalized in the occupation number basis of  $j$ , i.e.,  $[H_{(j-1)}, \hat{n}_j] = 0$ , such that the occupation eigenvalues of  $\hat{n}_j$  ( $1_j$  and  $0_j$ ) are good quantum numbers that label the renormalized eigenstates. By writing the Hamiltonian in terms of diagonal ( $H^D$ ) and off-diagonal ( $H^X$ ) parts as before, the renormalized eigenstates will have a renormalized value of the *quantum distance* measured with respect to the separable eigenstates ( $\phi_l$ ) of  $H^D$ . This allows us to observe the *geometry of eigenbasis renormalization*. In this way, by using Shimony's geometric measure of entanglement [412], we will show that the quantum distance RG will guide the renormalization flow of many-body entanglement.

### 2.5.1 Eigenbasis renormalization scheme

The iterative block diagonalization of the Hamiltonian and concomitant renormalisation of the eigenbasis (eq.(2.50)) partitions  $\mathcal{B}_{(j)}$  into a direct sum of two halves (see Fig.1.7) labelled by the occupation number of the decoupled state  $j + 1$

$$\mathcal{B}_{(j)} = \mathcal{B}_{(j)}^{0_{j+1}} \oplus \mathcal{B}_{(j)}^{1_{j+1}} . \quad (2.52)$$

As the RG procedure is iterative, every RG step halves the sub-bases obtained at the earlier step into two equal parts. As observed earlier, the subparts of the renormalized eigenbasis  $\mathcal{B}_{(j)}$  can be denoted by the collection of occupation numbers of all the decoupled states ( $\mathcal{Q}_j$ ,  $\{j + 1, N\}$ ), represented by blue and red handles with filled ( $1_l$ )/ unfilled ( $0_l$ ) circles in Fig.(1.7)). These subspaces satisfy the following completeness relation:  $\mathcal{B}_{(j)} = \bigoplus_{\mathcal{Q}_j} \mathcal{B}_{(j)}^{\mathcal{Q}_j}$ , where  $\mathcal{Q}_j$  labels the  $2^{N-j}$  number diagonal configurations that complete the *separable subspace*. The configurations of the separable subspace is visualised in Fig.(1.7) in terms of the filled/unfilled circles on the handles attached to any one light blue subpart. The state  $|\mathcal{Q}_j\rangle$  which is a collection of the separable electronic state occupation numbers is composed of a string of 1's and 0's, and can be represented as a tensor. This tensorial representation is visualised in Fig. 1.8(c) by treating the occupied electronic state configurations as legs of the object marked 1 in red.

The iterative decoupling of the eigenbasis into smaller sub-bases (Fig.1.7) indicates that the renormalized eigenstates at RG step  $j$  possess an interaction-driven many-body entanglement that is limited to within the subspace of coupled states labelled  $\{1, j\}$  (shown by light blue filled regions in Fig.(1.7)). On the other hand, the entanglement of the decoupled states  $\{j + 1, N\}$  is limited to that arising from the Pauli exclusion principle for fermions. This allows us to write a many-body eigenstate at RG step  $(j)$ ,  $|\Psi_{(j)}^{i,r}\rangle$ , labelled by pair of indices  $(i, r)$ . Here, the index  $r$  indicates the configurations belonging to the separable (or decoupled) subspace  $(\mathcal{Q}_j^r)$ , and  $i$  indicates the many-body configuration involving the states  $\{1, j\}$  that are still coupled. The configuration of coupled states is then described uniquely by the index  $\alpha_1$  (defined similarly to  $\alpha$  in (eq.(2.47)),  $\alpha_1 := \{(l, \mu)\}$  is an ordered set of  $m$  pairs of indices,  $1 \leq l \leq j$  and  $\mu = 1$  throughout. Thus,  $\alpha_1$  denotes the set of coupled occupied single-particle states  $\{l_1, \dots, l_m\}$ , as shown in Fig. 1.8c.

Thus, very generally, we can write the eigenstates  $|\Psi_{(j)}^{i,r}\rangle$  as a sum over all  $\alpha_1$  configurations

$$|\Psi_{(j)}^{i,r}\rangle = \sum_{\alpha_1} C_{\alpha_1}^{i,(j)} |\alpha_1\rangle |\mathcal{Q}_j^r\rangle . \quad (2.53)$$

The coefficient  $C_{\alpha_1}^{i,(j)}$  is a tensor with  $m$  legs representing the superposition weight of the configuration of occupied single-electron states. The wave function at RG step  $(j)$  (Fig.1.8c) is therefore a summation of all such tensors chosen from among the remaining  $j$  coupled states. The index  $\alpha_1$  is arranged as  $l_1 < l_2 < \dots < l_m$ , such that an even/odd permutation of this order due to electron exchanges will be compensated by a signature  $(+1/-1)$  in the coefficient  $C_{\alpha_1}^{i,(j)}$

$$C_{\mathcal{P}\alpha_1}^{i,(j)} = e^{i\pi n_{\mathcal{P}}} C_{\alpha_1}^{i,(j)}, \quad (2.54)$$

where  $n_P$  is the no. of electron exchanges in the permutation. The subspace of coupled states  $\mathcal{A}_{(j)}$  (Fig.(1.8)(a)) can be removed from eigenbasis partitions  $\mathcal{B}_{(j)}$  obtained at RG step  $j$  by taking a *partial inner product* of  $|\Psi_{(j)}^{i,r}\rangle$  with the configurations of the decoupled states ( $|\mathcal{Q}_j^i\rangle$ )

$$\mathcal{A}_{(j)} = \{|\Phi_{(j)}^i\rangle := \langle \mathcal{Q}_j^r | \Psi_{(j)}^{i,r}\rangle, \ r = [1, 2^{N-j}], \ i = [1, 2^j]\} . \quad (2.55)$$

This partial inner product procedure preserves orthogonality between the basis elements of  $\mathcal{A}_{(j)}$  (Fig.(1.8)(a)).

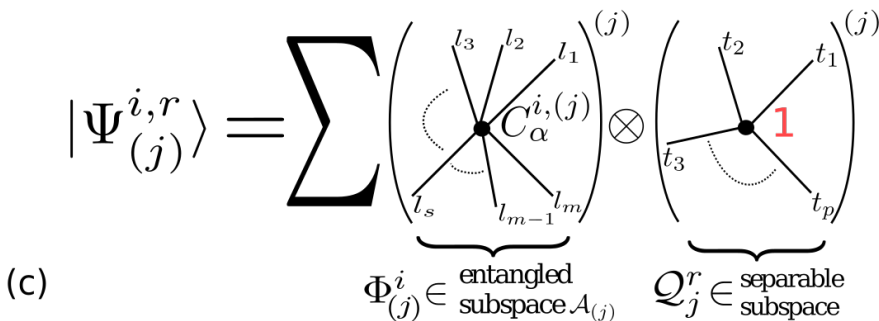
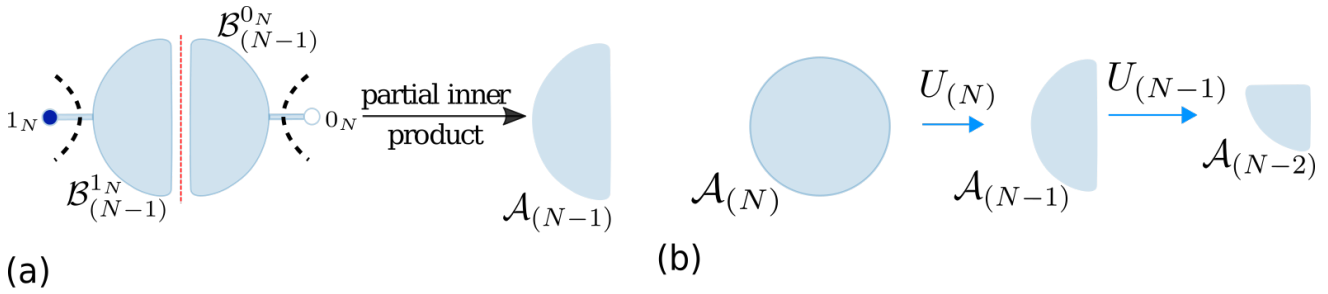


Figure 2.3: (a) The entangled subspace  $\mathcal{A}_{N-1}$  resulting from the partial inner product of the eigenstates in  $\mathcal{B}_{(N-1)}$  with the occupation states  $1_N, 0_N$  of the disentangled electronic state  $N$ . (b) The shrinking *entangled subspace*  $\mathcal{A}_{(N)} \rightarrow \mathcal{A}_{(N-1)} \rightarrow \mathcal{A}_{(N-2)}$  upon the action of successive unitary operations. (c) The eigenstate of renormalized Hamiltonian  $|\Psi_{(j)}^{i,r}\rangle$  is represented as a sum over tensor coefficients  $C_\alpha^{i,(j)}$ , where  $\alpha := (l_1,..l_m)$  are the legs of tensors labelling the occupied states. This state is represented as a direct product of  $|\Phi_{(j)}^i\rangle \in \mathcal{A}_j$  belonging to the space of entangled states, and  $|Q_j^r\rangle$  belonging to the separable subspace.

In this way, at every RG step, one single-electron state is decoupled from the coupled subspace  $\mathcal{A}_j$  (Fig. 1.8b) and added to the separable subspace  $\mathcal{Q}_j$ . This leads to the partitioning of the

occupation number eigenbasis  $\mathcal{B}$  (Fig.1.7), such that there is no superposition between states belonging to different occupation number sub-bases of the decoupled single-electron state. This is the many-body disentangling procedure in our renormalization group formalism. It should be noted that similar disentanglement procedures are employed in the Tensor Network Renormalization and the Multiscale Entangled Renormalization Ansatz approaches [236–238], albeit for removing short-ranged many-body entanglement. In contrast, the unitary decoupling operation eq.(2.4) in our method removes every type of entanglement between a given electronic state  $j$  and all others, and the unitary operations comprising the corresponding tensor network are thus non-local in nature. This will be presented in the section below.

An important feature of the vertex tensor network shown in Fig.1.6 and the EHM network (generated from entanglement RG of correlated electron systems)[184] must now be discussed. Implicit to the construction of this tensor network is the fact that it has another holographic dimension  $\omega_i$ , i.e., an eigenvalue of the quantum fluctuation operator  $\hat{\omega}|\Psi_i\rangle = \omega_i|\Psi_i\rangle$  corresponding to the eigenstate  $\Psi_i$ . The  $2^N$  eigenvalues of  $\hat{\omega}$  correspond to the  $2^N$  orthogonal directions encoding the entire many-body eigenbasis  $\mathcal{B}$ . Separate tensor networks are then generated by projecting the master tensor network shown in Fig.1.6 along each of these  $2^N$  directions. The nature of the individual projected tensor network encodes the entanglement content of the many-body eigenstate  $|\Psi_i\rangle$  it describes. For instance, a projected tensor network corresponding to a gapless eigenstate will possess equal numbers of boundary and emergent bulk qubits[177]. On the other hand, a projected tensor network corresponding to a gapped eigenstate will possess a lesser number of emergent bulk qubits than the boundary qubits and the remnant will form a emergent tensor network with finite entanglement [184]. In geometrising these projected tensor networks, one can employ quantum information theoretic measures such as mutual information in computing the information geodesics (shortest distance) between any pair of boundary qubits [184, 240, 241, 161].

### Disentangling single-electron occupation number states

The many-body eigenstate  $|\Phi_{(j)}^i\rangle$  within the coupled subspace  $\mathcal{A}_j$  is transformed at RG step  $j$  via the unitary evolution equation

$$|\Phi_{(j-1)}^i\rangle = U_{(j)}|\Phi_{(j)}^i\rangle. \quad (2.56)$$

Inspired by the exponential form of the unitary operator  $U_{(j)} = \exp(\frac{\pi}{4}(\eta_{(j)}^\dagger - \eta_{(j)}))$ , we write the state  $|\Phi_{(j)}^i\rangle$  as

$$|\Phi_{(j)}^i\rangle = \frac{1}{\sqrt{2}}\Omega_{(j)}|\Phi_{(j)}^{i,0_j}\rangle, \quad (2.57)$$

where  $\Omega_{(j)} = \exp(-\eta_{(j)}^\dagger)$  is the wave operator and  $|\Phi_{(j)}^{i,0_j}\rangle$  denotes the many-body state with the decoupled electronic state  $j$  being unoccupied. The normalization factor above can be determined from the e-h transition operator relations given in eq.(2.23). Further, the e-h transition operator relations  $(\eta_{(j)}^\dagger)^2 = 0$  and  $\hat{n}_j\eta_{(j)}^\dagger(1 - \hat{n}_j) = \eta_{(j)}^\dagger$  allow a remarkable simplification of the wave operator:  $\Omega_{(j)} = 1 - \eta_{(j)}^\dagger$ . Thus, we find that  $\Omega_{(j)}$  contains the entanglement content of the state  $j$  with the rest of the coupled states.

Further, using eq.(1.3) and the form of the wave operator obtained just above, eq.(2.56) simplifies to

$$|\Phi_{(j-1)}^i\rangle = \frac{1}{\sqrt{2}} U_{(j)} \hat{\Omega}_j |\Phi_{(j)}^{i,0_j}\rangle = |\Phi_{(j)}^{i,0_j}\rangle . \quad (2.58)$$

This confirms the disentanglement procedure from the action of the unitary operator on the eigenstates, and is a complementary view of basis partitioning (eq.(2.50)). Finally, we can use eq.(2.58) together with eq.(2.57) to obtain the renormalisation of the many-body eigenstate  $|\Phi_{(j)}^{i,0_j}\rangle$  in going from RG step  $j$  to step  $j - 1$

$$|\Phi_{(j-1)}^{i,0_{j-1}}\rangle = \sqrt{2} \Omega_{(j)}^{-1} |\Phi_{(j)}^{i,0_j}\rangle , \quad (2.59)$$

where  $\Omega_{(j-1)}^{-1} = e^{\eta^\dagger} = 1 + \eta^\dagger$ . A renormalisation of the eigenstate  $|\Phi_{(j)}^{i,1_j}\rangle$  can be obtained similarly

$$|\Phi_{(j-1)}^{i,1_{j-1}}\rangle = \sqrt{2} (\Omega_{(j)}^\dagger)^{-1} |\Phi_{(j)}^{i,1_j}\rangle . \quad (2.60)$$

## 2.5.2 RG flow of entanglement within subspace $\mathcal{A}_j$

We will now quantify the RG flow of entanglement through measures like Shimony's geometric measure and entanglement entropy. The flow is manifested in the renormalization of the tensors comprising the configuration space expansion of the states  $|\Phi_{(j)}^i\rangle$  belonging to the coupled (or *entangled*) subspace ( $\mathcal{A}_j$ )

$$|\Phi_{(j)}^i\rangle = \sum_{\alpha_1} C_{\alpha_1}^{i,(j)} |\alpha_1\rangle + \sum_{\beta_1} C_{\beta_1}^{i,(j)} |\beta_1\rangle , \quad (2.61)$$

where  $\alpha_1 := \{(l, \mu)\}$  is an ordered set of  $m$  pairs of indices,  $1 \leq l \leq j$ ,  $\mu = 1$  throughout, and one of the occupied single-particle states is the state  $j$ . Similarly,  $\beta_1 := \{(l, \mu)\}$  is an ordered set of  $m$  pairs of indices,  $1 \leq l \leq j - 1$ ,  $\mu = 1$  throughout, i.e., the occupied states do not include the state  $j$ . The tensor coefficients  $C_{\alpha_1/\beta_1}^{i,(j)}$  fulfil the normalization condition:

$\langle \Phi_{(j)}^i | \Phi_{(j)}^i \rangle = \sum_{\alpha_1, \beta_1} \left( |C_{\alpha_1}^{i,(j)}|^2 + |C_{\beta_1}^{i,(j)}|^2 \right) = 1$ . The renormalization of tensor coefficients  $C_{\alpha_1/\beta_1}^{i,(j)}$  proceeds via the wave operator operating on the eigenstates. Using the decomposition of the wave operator  $\Omega_{(j)}$  in terms of eqs.2.31 in eq.(2.60), we obtain we obtain a set of tensor flow equations for  $\Delta C_{\beta_1}^{i,(j)} = C_{\beta_1}^{i,(j-1)} - C_{\beta_1}^{i,(j)}$

$$\Delta C_{\beta_1}^{i,(j)} = (\sqrt{N^{(j)}} - 1) C_{\beta_1}^{i,(j)} - \sqrt{N^{(j)}} \sum_{n=1}^{a_j^{max}} \sum_{\alpha_1, \alpha'_1, \beta'_1} \text{sgn}(\alpha_1, \alpha'_1, \beta'_1) \{ \Gamma_{\beta'_1 \alpha_1}^{2n} G_{\alpha_1 \alpha'_1}^{2\bar{p}} C_{\alpha'_1}^i \}^{(j)}, \quad (2.62)$$

where  $N^{(j)}$  is the normalization coefficient for the RG step  $j$  given by

$$(N^{(j)})^{-1} = \sum_{\beta_1} \frac{1}{2} \left[ C_{\beta_1}^{i,(j)} - \sum_{n=1}^{a_j^{max}} \sum_{\bar{p}=1}^{2n} \sum_{\alpha_1, \alpha'_1, \beta'_1} \text{sgn}(\alpha_1, \alpha'_1, \beta'_1) \{ \Gamma_{\beta'_1 \alpha_1}^{2n} G_{\alpha_1 \alpha'_1}^{2\bar{p}} C_{\alpha'_1}^i \}^{(j)} \right]^2 , \quad (2.63)$$

$\text{sgn}(\alpha_1, \alpha'_1, \beta'_1)$  is a fermion sign function arising from electron exchanges due to  $n$ -particle scattering processes, and the various indices are described as follows. The index  $\alpha'_1 := \{(l, \mu)\}$  is an ordered set of  $\bar{m} + \bar{p}$  pairs of indices,  $1 \leq l \leq j$ ,  $\mu = 1$  throughout, and one of the occupied single-particle states is the state  $j$ . On the other hand,  $\alpha_1 := \{(l, \mu)\}$  is an ordered set of  $\bar{p}$  pairs of indices,  $1 \leq l \leq j$ ,  $\mu = 0$  throughout. Clearly, the set of values of  $l$  taken within  $\alpha_1$  is contained within the set of values of  $l$  taken within  $\alpha'_1$ . In this way, the indices  $\alpha_1 \alpha'_1$  in the Green's function  $G_{\alpha_1 \alpha'_1}^{2\bar{p}}$  indicates the  $\bar{p}$  single-electron states undergoing a scattering via the vertex  $\Gamma_{\beta'_1 \alpha_1}^{2n}$ , and the sum over the index  $\alpha_1$  involves only these  $\bar{p}$  single-electron states. In turn, the index  $\beta'_1$  within the vertex  $\Gamma_{\beta'_1 \alpha_1}^{2n}$  is an ordered set  $\beta'_1 := \{(l, \mu)\}$  of  $p = 2n - \bar{p}$  pairs of indices,  $1 \leq l \leq j-1$ ,  $\mu = 1$  throughout, such that the occupied single-particle states do not include the state  $j$ . Finally, the index that labels the flow equation of the tensor coefficient,  $\beta_1 := \{(l, \mu)\}$ , is an ordered set of  $\bar{m} + p$  pairs of indices,  $1 \leq l \leq j-1$ ,  $\mu = 1$  throughout, such that the occupied single-particle states do not include the state  $j$ . The index  $\beta_1$  emerges from the convolution of the indices  $\alpha_1, \alpha'_1$  and  $\beta'_1$ , i.e., it is defined as  $\beta_1 := (\beta'_1 \cup \alpha'_1) - \bar{\alpha}_1$ , i.e., a set formed from the union of the sets  $\beta'_1$  and  $\alpha'_1$  and from which a set  $\bar{\alpha}_1$  has been removed, where  $\bar{\alpha}_1 := \{(l, \bar{\mu})\}$  is an ordered set of  $\bar{p}$  pairs of indices,  $1 \leq l \leq j$ ,  $\bar{\mu} = 1$  throughout. Note that the set of values of  $l$  with  $\alpha_1$  is the same as those within  $\bar{\alpha}_1$ . However  $\bar{\mu}$  values in  $\bar{\alpha}_1$  are different from  $\mu$  in  $\alpha_1$ .

We will now describe the fermion sign function  $\text{sgn}(\alpha_1, \alpha'_1, \beta_1)$ . For this, we write the state  $|\alpha'_1\rangle$  (that contributes to the coefficient tensor flow eq.(2.62)) in second quantized notation as

$$|\alpha'_1\rangle = |l_{\bar{m}+\bar{p}} \dots l_1\rangle = c_{l_{\bar{m}+\bar{p}}}^\dagger \dots c_{l_1}^\dagger |0\rangle , \quad (2.64)$$

where  $l_1 < l_2 < \dots < l_{\bar{m}+\bar{p}-1} < l_{\bar{m}+\bar{p}}$  belong to the ordered set  $\alpha'_1$ . Similarly, the set  $\alpha_1 = \{(b_{\bar{p}}, 0), \dots, (b_1, 0)\}$  and  $\beta'_1 = \{(a_p, 1), \dots, (a_1, 1)\}$  (see also below eq.(2.62)). As  $\alpha_1 \subset \alpha'_1$ , the label  $b_i$  in  $\alpha_1$  corresponds to a label  $l_k$  in the list  $\beta'_1$ . This information will be useful below in counting the electron exchanges. Now, the phase collected from counting the electron exchanges in the  $n$ -particle scattering process is accounted for as follows

$$\begin{aligned} & \Gamma_{\beta'_1 \alpha_1}^{2n, (j)} c_{a_p}^\dagger \dots c_{a_1}^\dagger c_{b_{\bar{p}}} \dots c_{b_1} |\alpha'_1\rangle, \\ &= \exp \left( i\pi \sum_{i=1}^{b_1} n_i \right) \Gamma_{\beta'_1 \alpha_1}^{2n, (j)} c_{a_p}^\dagger \dots c_{a_1}^\dagger c_{b_{\bar{p}}} \dots c_{b_2} |l_{\bar{m}+\bar{p}} \dots l_{k+1} l_{k-1} \dots l_1\rangle, \\ &= \exp \left( i\pi \sum_{\substack{i=1, \\ i \neq b_1}}^{b_2} n_i \right) \exp \left( i\pi \sum_{i=1}^{b_1} n_i \right) \Gamma_{\beta'_1 \alpha_1}^{2n, (j)} c_{a_p}^\dagger \dots c_{a_1}^\dagger c_{b_{\bar{p}}} \dots c_{b_3} |l_{\bar{m}+\bar{p}} \dots l_{k'+1} l_{k'-1} \dots l_{k+1} l_{k-1} \dots l_1\rangle \end{aligned} \quad (2.65)$$

In the expression for the phase  $\exp \left( i\pi \sum_{i=1}^{b_1} n_i \right)$ , the number  $n_i = 1$  if  $i \in \alpha'_1$  and  $n_i = 0$  otherwise. The labels  $b_1$  and  $b_2$  in set  $\alpha_1$  correspond to labels  $k$  and  $k''$  in set  $\alpha'_1$ . In this way, the state resulting from the operation of the entire string of annihilation operators comprising the  $2n$ -point scattering vertex is given by

$$\Gamma_{\beta'_1 \alpha_1}^{2n, (j)} c_{a_p}^\dagger \dots c_{a_1}^\dagger c_{b_{\bar{p}}} \dots c_{b_1} |\alpha'_1\rangle = \prod_{k=1}^{\bar{p}} P_k \Gamma_{\beta'_1 \alpha_1}^{2n, (j)} c_{a_p}^\dagger \dots c_{a_1}^\dagger |\alpha''_1\rangle , \quad (2.66)$$

where index  $\alpha''_1 = \{(l, \mu)\}$  is an ordered set of  $\bar{m}$  pairs of indices with  $\mu = 1$ . The net phase comprising the operation of  $\bar{p}$  annihilation operators is given by  $\prod_{k=1}^{\bar{p}} P_k$ , where

$$P_k = \exp \left( i\pi \sum_{i \in \alpha'_1 - \rho}^{b_k} n_i \right), \quad \rho = \{b_1, \dots, b_{k-1}\}. \quad (2.67)$$

In the above summation, the index  $i$  is restricted to the set  $\alpha'_1 - \rho$ , as electrons in set  $\rho$  are annihilated. Finally, the net electron exchange phase generated by the string of electron creation and annihilation operators is

$$\text{sgn}(\alpha_1, \alpha'_1, \beta'_1) = \prod_{k=1}^p Q_k \prod_{k=1}^{\bar{p}} P_k, \quad (2.68)$$

where  $Q_k$  is given by

$$Q_k = \exp(i(k-1)\pi) \exp \left( i\pi \sum_{\substack{i=1, \\ i \notin \gamma \cup \alpha_1}}^{a_k} n_i \right), \quad (2.69)$$

and the index  $\gamma = \{a_1, \dots, a_k\}$  is a set of labels for the states where electrons are created. In the expression for  $Q_k$ , the number  $n_i = 1$  if  $i \in \alpha''_1$  and  $n_i = 0$  otherwise.

We have seen earlier that the action of the unitary operator  $U_{(j)}$  on state  $|\Phi_{(j)}^i\rangle$  (eq.(2.56)) led to a subspace rotation of the state onto one of the occupation number configurations of state  $j$ , such that the projection along the other occupation number configuration axis is precisely zero

$$\begin{aligned} |\Phi_{(j)}^{i,0_j}\rangle &= \frac{1}{\sqrt{2}}(1 + \eta_{(j)}^\dagger - \eta_{(j)})|\Phi_{(j)}^i\rangle \\ &= \frac{1}{\sqrt{2}}(1 + \eta_{(j)}^\dagger) \sum_{\gamma'_1} C_{\gamma'_1}^{i,(j)} |\gamma'_1\rangle + \frac{1}{\sqrt{2}}(1 - \eta_{(j)}) \sum_{\rho'_1} C_{\rho'_1}^{i,(j)} |\rho'_1\rangle \\ \Rightarrow \quad \eta_{(j)}^\dagger \sum_{\gamma'_1} C_{\gamma'_1}^{i,(j)} |\gamma'_1\rangle + \sum_{\rho'_1} C_{\rho'_1}^{i,(j)} |\rho'_1\rangle &= 0, \end{aligned} \quad (2.70)$$

where  $\rho'_1$  and  $\gamma'_1$  are defined identically to the indices  $\alpha'_1$  and  $\beta'_1$  defined earlier respectively. The index  $\rho'_1 = \{(l, \mu)\}$  is, similar to  $\alpha_1$ , an ordered set of  $\bar{p}$  elements with state  $j$  occupied. This leads to a constraint on the value of tensor coefficient  $C_{\alpha'_1}^{i,(j)}$  given by

$$C_{\alpha'_1}^{i,(j)} = - \sum_{k=1}^{a_j^{\max}} \sum_{\gamma_1, \gamma'_1, \rho'_1} \text{sgn}(\gamma_1, \gamma'_1, \rho'_1) \{ \Gamma_{\rho'_1 \gamma_1}^{2k} G_{\gamma_1 \gamma'_1}^{4k-2\bar{p}} C_{\gamma'_1}^i \}^{(j)}, \quad (2.71)$$

where the index  $\gamma_1$  are defined in the same way as  $\alpha_1$ . The index  $\gamma_1 := \{(l, \mu)\}$  is an ordered set of  $2k - \bar{p}$  indices with all  $\mu = 0$  and the state  $j$  excluded. This comprises the  $(2k = \bar{p} + 2k - \bar{p})$ -point off-diagonal vertex  $\Gamma_{\rho'_1 \gamma_1}^{2k,(j)}$ . The index  $\gamma'_1 = \{(l, \mu)\}$  is an ordered set of  $\bar{m} + 2k - \bar{p}$  indices with all

$\mu = 1$  and the state  $j$  is excluded. Similar to  $\alpha_1$  and  $\alpha'_1$  we observe  $\gamma_1$  is a subset of  $\gamma'_1$ . So the indices  $\gamma_1\gamma'_1$  in the Green's function  $G_{\gamma_1\gamma'_1}^{4k-2\bar{p}}$  represents only the  $2k - \bar{p}$  single electron states which get scattered by the vertex  $\Gamma_{\rho'_1\gamma_1}^{2k,(j)}$ . Similar to  $\beta_1$ , the index  $\alpha'_1$  emerges from the convolution of the indices  $\gamma_1, \gamma'_1$  and  $\alpha'_1$ :  $\alpha'_1 := (\rho'_1 \cup \gamma'_1) - \gamma_1$ . In other words,  $\alpha'_1$  corresponds to a set formed from the union of the sets  $\rho'_1$  and  $\gamma'_1$ , and from which a set  $\gamma_1$  has been removed.

Using the constraint eq.(2.71) together with the  $n$ -particle vertex flow eq.(2.47), the tensor flow eq.(2.62) can be written as

$$\Delta C_{\beta_1}^{i,(j)} = (\sqrt{N^{(j)}} - 1)C_{\beta_1}^{i,(j)} + \sqrt{N^{(j)}} \sum_{\bar{k}=1}^{a_j^{\max}} \sum_{\gamma_1, \gamma'_1, \beta'_1} sgn(\gamma_1, \gamma'_1, \beta'_1) \{\Delta \Gamma_{\beta'_1\gamma_1}^{2\bar{k}} G_{\gamma_1\gamma'_1}^{4\bar{k}-2p} C_{\gamma'_1}^i\}^{(j)}, \quad (2.72)$$

where the RG flow for  $2\bar{k}$ -point vertex ( $2\bar{k} = 2n + 2k - 2\bar{p}$ ) is given by

$$\Delta \Gamma_{\beta'_1\gamma_1}^{2\bar{k}} = \sum_{n,k}^{2a_j^{\max}} \sum_{\rho_1} \{\Gamma_{\beta'_1\rho_1}^{2n} G_{\rho_1\rho_1}^{2\bar{p}} \Gamma_{\rho_1\gamma'_1}^{2k}\}^{(j)}. \quad (2.73)$$

As observed previously, the phase  $sgn(\gamma_1, \gamma'_1, \beta'_1)$  in eq.(2.72) is obtained via counting the electrons exchanged via the  $2\bar{k}$  point scattering vertex. Importantly, eq.(2.72) relates the RG flow of the many-body state space to that of the effective Hamiltonian (through the vertex flow equation). We now arrive at an important result. When the final fixed point of the vertex tensor network RG flow is reached, i.e., when  $\Delta \Gamma_{\beta'_1\gamma_1}^{2\bar{k},(j*)} = 0$ ,  $N^{(j*)} = 1$ , the RG flow of the coefficient tensor also ceases,  $\Delta C_{\beta_1}^{i,(j*)} = 0$ . Note that the renormalization of the coefficient tensors is responsible for the renormalization of the many-particle entanglement features; this implies that the vertex tensor network RG flow guides the entanglement RG. Thus, the entanglement RG fixed points and vertex tensor RG fixed points are attained concurrently. In a recent work [184], we have shown the connection between the nonlocal unitary disentangler based entanglement renormalization group and the entanglement holographic mapping (EHM) of Ref.[232]. An EHM is a tensor network formed via a stacking of unitary transformation layers, where each such layer disentangles a certain set of qubits. The input electronic states/nodes comprise the boundary layer describing the UV theory, and the unitary map generates the bulk of the EHM such that the IR fixed point theory is obtained deep in the bulk. In this way, eq.(2.72) above shows that the vertex tensor network RG generates the EHM.

### 2.5.3 Mitigating the fermion sign problem through URG flow

In this section, we will show that by applying the URG to models of interacting electrons, certain classes of stable fixed points are obtained from the RG flow in the IR that are free from the signatures that arise from electronic exchanges. A system of interacting electrons with translational invariance can very generally be described by the Hamiltonian

$$\hat{H} = \sum_{\mathbf{k}} (\epsilon_{\mathbf{k}} - \mu) \hat{n}_{\mathbf{k}\sigma} + \sum_{\mathbf{k}, \mathbf{k}', \mathbf{p}} V_{\mathbf{k}-\mathbf{k}'}^{\sigma\sigma'} c_{\mathbf{k},\sigma}^\dagger c_{\mathbf{p}-\mathbf{k},\sigma'}^\dagger c_{\mathbf{p}-\mathbf{k}',\sigma'} c_{\mathbf{k}',\sigma}. \quad (2.74)$$

The  $\mathbf{k}$  are wave-vectors belonging to the first Brillouin zone. We consider that the Fermi surface of the non-interacting part, defined as a collection of wave-vectors  $\mathbf{k}_F$  such that  $\epsilon_{\mathbf{k}_F} = E_F = \mu$ ,

to be described as an extended object in the Brillouin zone. Further, we explore the sub-parameter space of  $H$  where (i) all opposite-spin electron exchange scattering vertices are attractive:  $V_{\mathbf{k}-\mathbf{k}' \neq 0}^{\sigma, -\sigma} < 0$ , as well as Hartree terms  $V_0^{\sigma, \sigma'} > 0$  and the same-spin electron exchange scattering vertices  $V_{\mathbf{k}-\mathbf{k}' \neq 0}^{\sigma, \sigma'} > 0$  are repulsive.

In applying the URG method to this problem, we adopt a RG scheme where the states farthest away from the Fermi surface are disentangled first. Following Refs.[180, 181], this is carried out by defining curves *parallel* to the Fermi surface. The wave-vectors  $\mathbf{k}_{\Lambda\hat{s}} = \mathbf{k}_F(\hat{s}) + \Lambda\hat{s}$  are represented in terms of the distance ( $\Lambda$ ) normal from the Fermi surface and the unit normal vector,  $\hat{s} = \nabla\epsilon_{\mathbf{k}}/|\nabla\epsilon_{\mathbf{k}}|_{\epsilon_{\mathbf{k}}=E_F}$ . At each RG step, the entire isogeometric curve at a distance  $\Lambda_j$  from the Fermi surface is disentangled via a product of unitary operations  $U_j = \prod_l U_{(j,l)}$ , such that  $U_{j,l} = \sqrt{2^{-1}}[1 + \eta_{j,l} - \eta_{j,l}^\dagger]$  disentangles the electronic state  $|j, l\rangle = |\mathbf{k}_{\Lambda_j\hat{s}}, \sigma\rangle$  from the rest. This iterative disentanglement procedure leads to the URG flow equation  $H_{(j-1)} = U_{(j)} H_{(j)} U_{(j)}^\dagger$ . URG generates the  $2n$ -point vertex tensor RG equation hierarchy eq.(2.47). We initially restrict ourselves to studying just the four-point vertex RG flow equations

$$\Delta\Gamma_{\mathbf{q},\mathbf{p}}^{\sigma,\sigma',(j)} = \frac{\Gamma_{\mathbf{q}_1,\mathbf{p}}^{\sigma,\sigma',(j)} \Gamma_{\mathbf{q}_2,\mathbf{p}}^{\sigma,\sigma',(j)}}{\omega - \epsilon_{j,a} - \epsilon_{j,a'} - \frac{1}{4}\Gamma_{0,\mathbf{p}}^{(j)}} \quad (2.75)$$

where the labels  $(j, a) := \mathbf{k}_{\Lambda_j\hat{s}}, \sigma$ ,  $(j, a') := \mathbf{p} - \mathbf{k}_{\Lambda_j\hat{s}}, \sigma'$ . The momentum transfer wave-vectors  $\mathbf{q}_1 = \mathbf{k} - \mathbf{k}_{\Lambda_j\hat{s}}$  and  $\mathbf{q}_2 = \mathbf{k}_{\Lambda_j\hat{s}} - \mathbf{k}'$ , such that  $\mathbf{q} = \mathbf{q}_1 + \mathbf{q}_2$ . In the discussion below, we will be asking the following question: can a excited pair of electrons with momenta  $\mathbf{k}$  and  $\mathbf{p} - \mathbf{k}$  residing outside the Fermi surface ( $\epsilon_{\mathbf{k}}, \epsilon_{\mathbf{p}-\mathbf{k}} > E_F$ ) have a condensation energy lower than the Fermi energy? This is the primary ingredient for bound-state condensation. If the answer is yes, can the effective theories describing the IR fixed points reached from URG analysis be free of fermion exchange signatures?

To proceed further, we work in the regime of quantum fluctuation energyscales:  $\omega < 2^{-1}(\epsilon_{\mathbf{k}} + \epsilon_{\mathbf{p}-\mathbf{k}})$ . As the electronic states  $\mathbf{k}$  and  $\mathbf{p} - \mathbf{k}$  are both occupied and are the primary two-particle excitations with  $\epsilon_{\mathbf{k}}, \epsilon_{\mathbf{p}-\mathbf{k}} > E_F$ , we have

$$|\omega - 2^{-1}(\epsilon_{\mathbf{k}} + \epsilon_{-\mathbf{k}})| < |\omega - 2^{-1}(\epsilon_{\mathbf{k}} + \epsilon_{\mathbf{p}-\mathbf{k}})| < 0 . \quad (2.76)$$

Along the URG flow within the regime of eq.(2.76), the  $\mathbf{p} = 0$ -momentum electron exchange scattering vertex tensors  $|\Delta\Gamma_{\mathbf{q},0}^{(j)}|$  are the most dominant among all finite-momentum pairs

$$|\Delta\Gamma_{\mathbf{q},0}^{(j)}| > |\Delta\Gamma_{\mathbf{q},\mathbf{p}}^{(j)}| . \quad (2.77)$$

As a resulting, the RG flow of the 6-point vertices  $\Gamma^{6,(j)}$  in eq.(2.47) are also sub-dominant, as they arise from the interplay between different pair-momentum vertices. On the other hand, the repulsive Hartree terms and the same-spin electron exchange scattering vertices are RG irrelevant:  $\Delta\Gamma_{0,\mathbf{p}}^{\sigma,\sigma',(j)}, \Delta\Gamma_{\mathbf{q},\mathbf{p}}^{\sigma,\sigma',(j)} < 0$ .

Armed with this insight, we now explore the wavefunction coefficient tensor flow equation (eq.(2.72)) while taking into account only the RG dominant four-point vertices. For this, we define the ordering scheme of the electronic states shown in Fig.2.4. The electronic state on the isogeometric curve farthest from the Fermi surface is defined as  $N := \mathbf{k}_{\Lambda_0,\hat{s}_0}, \uparrow$ , while the electronic state with opposite-spin residing on the diametrically opposite position (and on the same

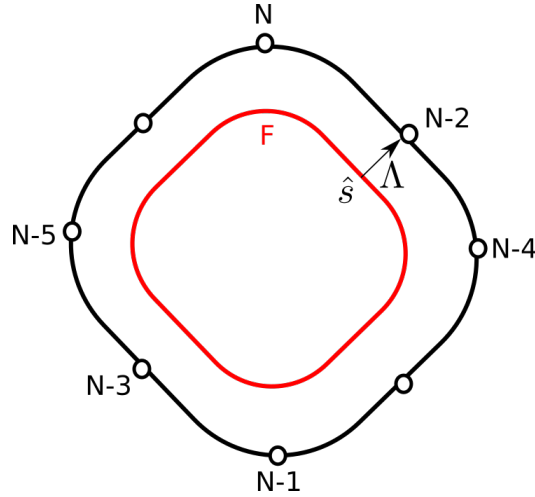


Figure 2.4: Schematic representation of Fermi sea for representing the electron counting scheme. The labels  $N$  and  $N - 1$  correspond to the partner electronic states  $\mathbf{k}_{\Lambda\hat{s}}, \uparrow$  and  $-\mathbf{k}_{\Lambda\hat{s}}, \downarrow$  of the opposite-spin zero momentum pair.  $N - 1, N - 2$  are the next pair of such electronic states. The red curve represents the Fermi surface.

isogeometric curve) is labelled  $N - 1 := \mathbf{k}_{\Lambda_0, -\hat{s}_0}, \downarrow$ . The electronic state along the next normal direction on the same isogeometric curve  $\Lambda_0$  is labelled  $N - 2 := \mathbf{k}_{\Lambda_0, \hat{s}_1}, \uparrow$ , while the diametrically opposite state is labelled  $N - 3 := \mathbf{k}_{\Lambda_0, -\hat{s}_1}, \downarrow$ , and so on. In this way, all the states are labelled by progressively decreasing integers as they approach the Fermi surface. The states on the Fermi surface (red curve in Fig.2.4) are marked as  $2N_F : k_{F, \hat{s}_0}, \uparrow$ ,  $2N_F - 1 : k_{F, -\hat{s}_0}, \downarrow$ , leading down to the last two state  $2 : k_{F, \hat{s}_{N_F}}, \uparrow$  and  $1 : k_{F, -\hat{s}_{N_F}}, \downarrow$ . Here,  $N_F$  is the number of normal directions  $\hat{s}$ 's on the Fermi surface. The coefficient tensor flow equation for the eigenstates  $|\Psi_{(j)}^i\rangle$  of  $H_{(j)}$  is then given by

$$\Delta C_{\beta_1}^{i,(j)} = (\sqrt{N^{(j)}} - 1)C_{\beta_1}^{i,(j)} + \sqrt{N^{(j)}} \sum_{\gamma_1, \gamma'_1, \beta'_1} \frac{\text{sgn}(\beta'_1, \gamma_1, \gamma'_1) \Delta \Gamma_{\mathbf{q}, \mathbf{p}}^{\sigma, \sigma', (j)}}{\omega - \frac{1}{2}(\epsilon_{\mathbf{k}_{\Lambda\hat{s}}} + \epsilon_{\mathbf{p} - \mathbf{k}_{\Lambda\hat{s}}}) - \frac{1}{4}\Gamma_{0, \mathbf{p}}^{(j), \sigma, \sigma'}} C_{\gamma'_1}^{i,(j)}, \quad (2.78)$$

where the index  $\gamma'_1 = \{l\}$  refers to a collection of labels where the electronic state is occupied. The indices  $\gamma_1 = \{a := (\mathbf{k}_{\Lambda\hat{s}}, \sigma), b := (\mathbf{p} - \mathbf{k}_{\Lambda\hat{s}}, \sigma')\}$  and  $\beta'_1 = \{c := (\mathbf{k}_{\Lambda\hat{s}} + \mathbf{q}, \sigma), d := (\mathbf{p} - \mathbf{k}_{\Lambda\hat{s}} - \mathbf{q}, \sigma')\}$  respectively. Keeping only the dominant RG flow contribution from  $\Delta \Gamma_{\mathbf{q}, 0}^{\sigma, -\sigma, (j)}$  in eq.(2.77), the coefficient RG equation simplifies to

$$\Delta C_{\beta_1}^{i,(j)} = (\sqrt{N^{(j)}} - 1)C_{\beta_1}^{i,(j)} + \sqrt{N^{(j)}} \sum_{\mathbf{q}, \mathbf{k}_{\Lambda\hat{s}}} \frac{\text{sgn}(\beta'_1, \gamma_1, \gamma'_1) \Delta \Gamma_{\mathbf{q}, 0}^{\sigma, -\sigma, (j)}}{\omega - \epsilon_{\mathbf{k}_{\Lambda\hat{s}}} - \frac{1}{4}\Gamma_{0, 0}^{(j), \sigma, -\sigma}} C_{\gamma'_1}^{i,(j)}. \quad (2.79)$$

Here,  $\gamma'_1$  reduces to a special class of sequences comprised of only consecutive pairs of integers  $(l, l + 1)$ . This marks the pair of electronic states with opposite-spins and zero net-momentum:  $\gamma'_1 = \{(l_1, l_1 + 1), (l_2, l_2 + 1), \dots\}$ , and  $\gamma_1 = \{(m, m + 1)\}$ ,  $\beta'_1 = \{(n, n + 1)\}$ .

Importantly, for this case, the fermion exchange sign function  $\text{sgn}(\beta'_1, \gamma_1, \gamma'_1)$  trivializes to 1, as

can be seen by recalling eq.(2.68)

$$\begin{aligned} \text{sgn}(\beta'_1, \gamma_1, \gamma'_1) &= Q_2 Q_1 P_2 P_1 \\ &= \exp(i\pi \sum_{i=1}^{m-1} n_i) \exp(i\pi \sum_{i=1}^{m-1} n_i) \exp(i\pi \sum_{i=1}^{n-1} n_i) \exp(i\pi \sum_{i=1}^{n-1} n_i) = 1 . \end{aligned} \quad (2.80)$$

In this way, we observed that in this case, the fermion string essentially counts an even number of electron exchanges for any configuration, rendering the  $\mathbf{p} = 0$  pair-momentum subspace free of fermion signatures. As a result, we obtain a reduced BCS effective Hamiltonian for this subspace obtained at the fixed point  $\omega = \max_{\hat{s}} \epsilon_{\mathbf{k}_{\Lambda^* \hat{s}}}$  given by

$$H_{\text{eff}} = \sum_{\mathbf{k}} \epsilon_{\mathbf{k}} A_{\mathbf{k}}^z - \sum_{\mathbf{q}, \mathbf{k}} |V_{\mathbf{q}, 0}^*| A_{\mathbf{k}}^+ A_{\mathbf{k}+\mathbf{q}}^- , \quad (2.81)$$

where  $A_{\mathbf{k}}^+ = c_{\mathbf{k}\uparrow}^\dagger c_{-\mathbf{k}\downarrow}^\dagger$  and  $A_{\mathbf{k}}^- = c_{-\mathbf{k}\downarrow} c_{\mathbf{k}\uparrow}$ ,  $A_{\mathbf{k}}^z = 2^{-1} [A_{\mathbf{k}}^+, A_{\mathbf{k}}^-]$  are Anderson pseudospins [413]. Very generally, we can redefine a pair of legs  $l := (l, l+1)$  as the Anderson pseudospin  $l$ . The eigenstates of Hamiltonian  $H_{\text{eff}}$  can be written as

$$|\Phi^i\rangle = \sum_{\rho} C_{\rho}^{i,*} A_{l_1}^+ \dots A_{l_n}^+ |\Downarrow \dots \Downarrow\rangle , \quad (2.82)$$

where  $\rho = \{l\}$  is the label for the set of Anderson pseudospins which are in the  $|1_l 1_{l+1}\rangle = |\uparrow \uparrow\rangle$  configuration. We stress that exchanging the legs of the coefficient tensor  $C_{\rho}^{i,*}$  here is free of fermion exchange signatures. In this way, we have mitigated the problem of fermion exchange signatures via the URG flow to the reduced BCS theory obtained in the IR.

### RG flow of a geometric measure of entanglement and its relation to bound state spectral weight

The Fubini-Study distances (represented by black lines in Fig.(2.5))  $d(\beta_1, \Phi_{(j)}^i)$  between the separable states  $|\beta_1\rangle$  (black disk in figure) and the renormalized eigenstates  $|\Phi_{(j)}^i\rangle$  (green disk in figure) of  $H_{(j)}$  belonging to  $\mathcal{A}_{(j)}$  is defined as [414, 415]

$$d^2(\beta_1, \Phi_{(j)}^i) = 1 - |\langle \beta_1 | \Phi_{(j)}^i \rangle|^2 = 1 - |C_{\beta_1}^{i,(j)}|^2 , \quad (2.83)$$

where  $C_{\beta_1}^{i,(j)}$  is the fidelity between the entangled state  $|\Phi_{(j)}^i\rangle$  and a separable state  $|\beta_1\rangle$  [414]. If  $|\Phi_{(j)}^i\rangle$  lies in the UV and  $|\beta_1\rangle$  lies in the IR, the fidelity corresponds to a transition amplitude obtained from the RG flow between UV and IR [177]. In general,  $C_{\beta_1}^{i,(j)} = W_{(j)} e^{iF_{(j)}}$ , i.e.,  $0 \leq W_{(j)} \leq 1$  and  $F_{(j)}$  correspond to the magnitude and phase of the fidelity respectively. Across a quantum critical point,  $W_{(j)}$  is expected to display a non-monotonic behaviour [416]. We will now obtain the RG evolution of the distance  $d$ , and observe its behaviour as the stable fixed point is obtained.

The RG equation for the Fubini-Study distances  $d(\beta_1, \Phi_{(j)}^i)$  (eq.(2.83)) is obtained using the RG flow of tensor coefficient (eq.(2.72))

$$\begin{aligned} \Delta d^2(\beta_1, \Phi^i)^{(j)} &= -\Delta |C^{i,(j)}|^2 = |C_{\beta_1}^{i,(j)}|^2 - |C_{\beta_1}^{i,(j-1)}|^2 \\ &= |C_{\beta_1}^{i,(j)}|^2 - |C_{\beta_1}^{i,(j)} + \Delta C_{\beta_1}^{i,(j)}|^2 \\ &= -|\Delta C_{\beta_1}^{i,(j)}|^2 - 2\text{Re}(\bar{C}_{\beta_1}^{i,(j)} \Delta C_{\beta_1}^{i,(j)}) , \end{aligned} \quad (2.84)$$

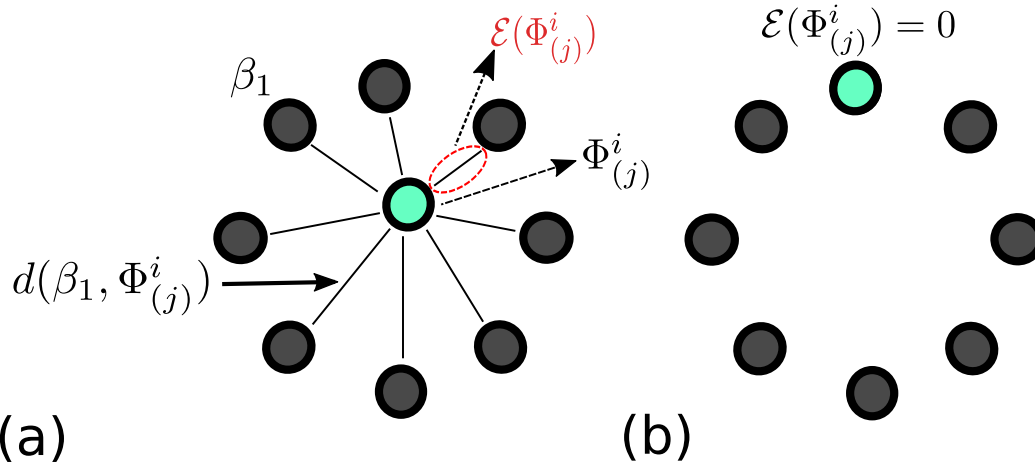


Figure 2.5: (a) The figure represents a collection of orthogonal separable states labelled  $\beta_1$  (black disks), and where the green disk is an entangled state. The quantum distances between the green disk and black disks  $d^2(\beta_1, \Phi)$  are represented by the lines connecting them. The red dashed line encircling the minimum non-zero quantum distance is a geometric measure of entanglement  $\mathcal{E}(\Phi_{(j)}^i)$ . (b) The figure shows the situation where the state (green disk) is not entangled.

where  $\bar{C}_{\beta_1}^{i,j}$  are the complex conjugate tensor coefficients. The RG flow of the geometric measure of entanglement  $(\mathcal{E}(\Phi_{(j)}^i))$ [412, 415, 414] for an eigenstate  $|\Phi_{(j)}^i\rangle$  can now be obtained from the quantum distance RG equations (eq.(2.84)) by computing the minimum distance (red dashed circle in Fig.(2.5)) of the state  $|\Psi_{(j)}^i\rangle$  from the product states  $|\phi_l^{(j)}\rangle$

$$\Delta\mathcal{E}(\Phi_{(j)}^i) = \Delta(\min_{\beta_1} d^2(\beta_1, \Phi_{(j)}^i)). \quad (2.85)$$

The RG flow of the entanglement content  $\mathcal{E}_{(j)}$  within the *entire* energy eigenbasis (eq.(2.50)) is defined as  $\mathcal{E}_{(j)} = \{\mathcal{E}(\Phi_{(j)}^1), \dots, \mathcal{E}(\Phi_{(j)}^{2^{N-j}})\}$  is represented by the variation in the colour of the legs of tensor network from blue to red in Fig.(1.6).

We can see from eq.(2.84) that the quantum distance  $d^2(\beta_1, \Phi_{(j^*)}^i)$  and the geometric measure of entanglement  $\mathcal{E}(\Phi_{(j^*)}^i)$  will reach a fixed point  $j^*$  under RG flow,  $\Delta d^2(\beta_1, \Phi_{(j^*)}^i) = 0 = \Delta\mathcal{E}(\Phi_{(j^*)}^i)$ , simultaneously along with the tensor coefficients  $\Delta C_{\beta_1}^{i,(j^*)} = 0$ . Given a fluctuation scale  $\omega$ , the RG relevance and irrelevance of various  $n$ -particle vertices are guided by the signature in the denominator of the Green's function present in the vertex flow eq.(2.73). Figure 2.5(a) represents the quantum geometric distances ( $d(\beta_1, \Phi_{(j)}^i)$ ) and entanglement measure ( $\mathcal{E}(\Phi_{(j)}^i)$ ) for RG flow that leads to an emergent subspace with finite entanglement content at the final fixed point. On the other hand, Fig.2.5(b) represents the case when the final low-energy subspace is disentangled. As discussed in an earlier section, the fixed point is determined among the various RG flow equations by considering those in which there is a signature change in the denominator coming from level crossing of fluctuation scale  $\omega$  and the renormalized  $n$ -particle self/correlation energies. In eq.(2.25), we saw that the fixed point condition is accompanied by vanishing of the off-diagonal block with respect to state  $j^*$  (i.e., those terms that change the occupation number of state  $j$ ). At the final fixed point  $j^*$ , there are  $2^{j^*}$  configurations in  $\mathcal{A}_{(j^*)}$ . A non trivial fixed point with remnant fluctuation in  $\mathcal{A}_{(j^*)}$  implies that these configurations describe a condensate

of composite degrees of freedom protected by a many body gap. The Fubini-Study distances between separable states  $|\phi_l^{(j*)}\rangle$  projected onto the subspace of coupled states  $\{1, \dots, j^*\}$  and the entangled eigenstate configurations  $|\Phi_{(j^*)}^i\rangle \in \mathcal{A}_{(j^*)}$  of  $H_{(j^*)}(\omega)$  form a *squared-distance* matrix  $D$ , whose elements are  $D_{(l)_m^1, \Phi_{(j^*)}^i} = d^2((l)_m^1, \Phi_{(j^*)}^i)$ .  $D$  has dimensions  $\text{dim}(D) = 2^{j^*} \times 2^{j^*}$ , and accounts for the dynamical spectral weight transfer at the fixed point (i.e., the electronic spectral weight that has converted to bound states). This can be seen from the following relation connecting the net Friedel's phase shift (or change in Luttinger volume  $\Delta N$  for systems with translational invariance, as will be discussed in more detail in Sec.3.2) to  $\text{dim}(D)$

$$\Delta N = \log_2 \sqrt{\text{dim}(D)} = j^*. \quad (2.86)$$

#### 2.5.4 Relation between geometric measure of entanglement and composite p-h residues

The squared minimum distance between separable states  $|\phi_{(l)_m^1}\rangle$  and eigenstate  $|\Phi_{(j)}^i\rangle \in \mathcal{A}_{(j)}$  (in the  $m$  particle- $(p-m)$  hole projected subspace) is given by

$$\mathcal{E}(\kappa, \Phi_{(j)}^i) = \min_{\beta} (1 - |\langle \beta | \prod_{i=1}^m n_{l_i} \prod_{i=m+1}^p (1 - n_{l_i}) |\Phi_{(j)}^i \rangle|^2), \quad (2.87)$$

where  $\kappa = \{(l_1, 1), \dots, (l_m, 1), (l_{m+1}, 0), \dots, (l_p, 0)\}$  is a collection of pairwise indices defined similarly to  $\alpha$ . By decomposing the projection operator as a product of composite excitation and de-excitation operators,  $\prod_{i=1}^m n_{l_i} \prod_{i=m+1}^p (1 - n_{l_i}) = M_j^+(m, p) M_j^-(m, p)$ , we are able to relate  $\mathcal{E}$  to the spectral weight/residue ( $Z_j(\kappa, i)$ ) of the composite  $m$  electron- $(p-m)$  hole associated with the cluster excitation operator  $M_j^-(m, p, \mathcal{P})$

$$\mathcal{E}(\kappa, \Phi_{(j)}^i) = 1 - Z_j(\kappa, i). \quad (2.88)$$

This results in the quantum fluctuation scale-dependent renormalization of  $m$  particle- $(p-m)$  hole spectral weight:  $\Delta Z_j(\kappa, i) = -\Delta \mathcal{E}(\kappa, \Phi_{(j)}^i)$ . This relation clearly demonstrates the dynamical nature of the renormalization group: it shows the connection between the phenomenon of UV-IR mixing [417] and dynamical spectral weight transfer (as observed, for instance, between the lower and upper Hubbard bands of a Mott insulator [418]). On the other hand, passage under RG from a fixed point at which  $Z_1 = 1$ ,  $\mathcal{E} = 0$  (Fermi liquid) to one at which  $Z_1 \rightarrow 0$ ,  $\mathcal{E} \rightarrow 1$  (non-Fermi liquid) signals a quantum phase transition in which the ground state fidelity (in terms of one-particle excitations) vanishes. This is a realisation of the Anderson orthogonality catastrophe [419, 420, 416].

For the case of an fluctuation scale  $\omega$  at which all  $n$ -particle off-diagonal vertices are RG irrelevant, i.e.  $\Delta \Gamma_{(l, \mu)_n^1}^{2n, (j)} < 0$ , the RG flow leads to a number-diagonal Hamiltonian  $H_{(j)}^D(\omega)$ . In fermionic systems with translational invariance, such RG flows approach the Fermi surface. By this, we mean that states at a distance  $\Lambda_j$  from the Fermi surface(FS) are successively decoupled leading to a more number-diagonal Hamiltonian, i.e. with a lower magnitude of the off-diagonal coefficients. Further, among the  $n$ -particle self/correlation energies, if only the single-particle self-energy is

relevant:  $\Delta\Sigma_l^{2,(j)} > 0$ ,  $\Delta\Sigma_l^{2n,(j)} < 0 \forall n > 2$ , the Fermi liquid fixed point is reached at the FS with a growth of the one-particle residue

$$\lim_{\Lambda_j \rightarrow 0} Z_j(k_{\Lambda_j \hat{s}}, \omega) = 1 - \mathcal{E}(\mathbf{k}_{\Lambda_j \hat{s}}, \omega) \rightarrow 1 , \quad (2.89)$$

where  $\hat{s}$  denotes the directions normal to the FS. This relations shows the decay of the entanglement measure  $\mathcal{E}$  at the Fermi liquid fixed point, resulting in a separable state (green disk in Fig.(2.5)(b)). Similar arguments can also be formulated for RG flows that approach a fixed point corresponding to a gapless non-Fermi liquid.

Finally, the quasiparticle residue defined precisely on the Fermi surface,  $Z_F = (\langle \hat{n}_{\mathbf{k}_F \hat{s}} \rangle)^2 = 1$ , allows us to recast Volovik's topological invariant  $N_1$  [421] along every normal direction  $\hat{s}$  for every point on FS (see discussion in Sec.3.1) in terms of the entanglement measure

$$N_1 = \sqrt{1 - \mathcal{E}(\mathbf{k}_F \hat{s}, \omega)} . \quad (2.90)$$

Remarkably, this relation links the topological stability of the FS to an entanglement property of the FS.

### 2.5.5 Evolution of the Fubini Study metric under RG flow

The Hilbert space geometry of many-body eigenstates can be quantified via a Fubini-Study metric defined in the space of parameters: polar and azimuthal angles- $(\theta_l, \phi_l)$  for electronic states labelled by  $l$  ranging between 1 and  $N$ . The rotation  $\theta_l, \phi_l$  for electronic state  $l$  is a ray on a unit Bloch sphere constructed in the occupancy basis:  $\{1_l, 0_l\}$ . We will now show that the unitary RG evolution of the eigenbasis eq.(2.50) yields a RG flow of the Fubini-Study metric, thus describing the holographic renormalization of Hilbert space geometry within the bulk of the EHM (see discussion below eq. 2.72). To begin with, the Fubini-Study distance between a separable state  $|\theta, \phi\rangle$  and the many-body eigenstate  $|\Psi\rangle$  is given by

$$d^2(\theta, \phi, \Psi) = 1 - |\langle \theta, \phi | \Psi \rangle|^2 . \quad (2.91)$$

We note that  $|\theta, \phi\rangle$  is a many-particle separable state whose entanglement arises purely from fermionic statistics. Here,  $\theta = \{\theta_1, \dots, \theta_N\}$  and  $\phi = \{\phi_1, \dots, \phi_N\}$  are a collection of polar or azimuthal angles respectively. The state  $|\theta, \phi\rangle$  is constructed by applying a direct product of local unitary rotations in the space of occupied/unoccupied electron states

$$|\theta, \phi\rangle = U(\theta_1, \phi_1) \otimes \dots \otimes U(\theta_N, \phi_N) |0\rangle , \quad (2.92)$$

where

$$U_l = \exp \left( i \frac{\theta}{2} \boldsymbol{\sigma} \hat{n} \right), \hat{n} = \cos \phi \hat{x} + \sin \phi \hat{y} , \quad (2.93)$$

and  $\boldsymbol{\sigma} = 2^{-1}(c_l^\dagger + c_l)$ ,  $2^{-1}i(c_l^\dagger - c_l)$ ,  $n_l - 1/2$ . Upon performing a variation of the distance by infinitesimal variations of  $\theta$  and  $\phi$ , we obtain

$$\begin{aligned} \delta d^2(\theta, \phi, \Psi^i) &= \sum_{i,j=1}^N g_{\theta_i \theta_j} \delta \theta_i \delta \theta_j + g_{\theta_i \phi_j} \sin \theta_j \delta \theta_i \delta \phi_j + g_{\theta_j \phi_i} \sin \theta_j \delta \theta_i \delta \phi_j \\ &\quad + g_{\phi_i \phi_j} \sin \theta_i \sin \theta_j \delta \phi_i \delta \phi_j , \end{aligned} \quad (2.94)$$

where the metric

$$g_{ij} = \langle \partial_{ij}, (\theta, \phi) | \Psi \rangle - \langle \partial_i, (\theta, \phi) | \Psi \rangle \langle \partial_j, (\theta, \phi) | \Psi \rangle . \quad (2.95)$$

In the above equation for the metric  $g_{ij}$ , the labels  $(i, j)$  belong to the four possible pairs of parameters, i.e.,  $(\theta_i, \theta_j)$ ,  $(\theta_i, \phi_j)$ ,  $(\phi_i, \theta_j)$  and  $(\phi_i, \phi_j)$ . The holographic renormalization of the metric is then obtained by incorporating the state space renormalization of eq.(2.72) in the RG relation for the metric

$$\begin{aligned} \Delta g_{ij}^{(l)} &= \langle \partial_{ij}, (\theta, \phi) | U_{(j)} | \Psi_{(j)} \rangle - \langle \partial_i, (\theta, \phi) | U_{(j)} | \Psi_{(j)} \rangle \langle \partial_j, (\theta, \phi) | U_{(j)} | \Psi_{(j)} \rangle \\ &\quad - \langle \partial_{ij}, (\theta, \phi) | \Psi_{(j)} \rangle + \langle \partial_i, (\theta, \phi) | \Psi_{(j)} \rangle \langle \partial_j, (\theta, \phi) | \Psi_{(j)} \rangle , \end{aligned} \quad (2.96)$$

where  $l$  is the RG step number.

Note that the state  $|\theta, \phi\rangle$  can be written down as a superposition of occupation number configurations

$$|\theta, \phi\rangle = \sum_{\beta} C_{\beta}(\theta, \phi) |\beta\rangle . \quad (2.97)$$

The coefficients are constrained such that for any given bipartition of the state, the Schmidt rank is one [422]. This is the criterion for the separability of the state  $|\theta, \phi\rangle$ . With the above representation in place, we can write down the RG flow for the quantum metric in terms of the wavefunction coefficient RG flow eq.(2.72)

$$\begin{aligned} \Delta g_{ij}^{(l)} &= \sum_{\beta} \partial_{ij} C_{\beta}(\theta, \phi) \Delta C_{\beta}^{(l)} \\ &\quad - \sum_{\beta, \beta'} \partial_i C_{\beta}(\theta, \phi) \partial_j C_{\beta'}(\theta, \phi) (\Delta C_{\beta}^{(l)} \Delta C_{\beta'}^{(l)} + C_{\beta}^{(l)} \Delta C_{\beta'}^{(l)} + \Delta C_{\beta}^{(l)} \Delta C_{\beta'}^{(l)}) . \end{aligned} \quad (2.98)$$

Note that since the coefficient RG flow  $\Delta C_{\beta}^{(j)}$  is generated via vertex renormalization  $\Delta \Gamma^{(j)}$  (as seen in eq.(2.72)), the RG flow of the quantum metric is also governed by that of the vertices. This interplay is another important finding of our work, as it provides an explicit demonstration of the holographic principle (or holographic renormalisation) for the case of correlated electrons. Finally, we also note that, upon tracking the geodesic in this metric space, we obtain the RG flow of the geometric measure of entanglement [412, 415] given earlier in eq.(2.85). For the case of the Fermi liquid metal with a gapless Fermi surface discussed earlier in eqs.(2.88)-(2.90), we find that the journey from UV to IR establishes adiabatic continuity with the non-interacting Fermi gas via the disentanglement of all degrees of freedom in momentum-space. This reflects the self-similarity of the state space generated by the RG flow to an integrable, quantum critical IR theory.

### 2.5.6 Change in entanglement entropy generated in disentangling one electronic state per RG step

We end this section by accounting for the change in entanglement entropy generated by the process of disentangling a single electronic state at every step of the RG. We begin by writing

the state  $|\Phi_{(j)}^i\rangle$  as a superposition of two many-body entangled states

$$|\Phi_{(j)}^i\rangle = \sqrt{a_{(j)}^i} |\Phi_{(j)}^{i,1_j}\rangle + \sqrt{b_{(j)}^i} |\Phi_{(j)}^{i,0_j}\rangle, \quad (2.99)$$

where  $|\Phi_{(j)}^{i,1_j}\rangle, |\Phi_{(j)}^{i,0_j}\rangle$  are orthogonal many-body states with electron occupancy and non-occupancy for the state  $j$  defined following eq.(2.61)

$$\begin{aligned} |\Phi_{(j)}^{i,1_j}\rangle &= \frac{1}{\sqrt{a_{(j)}^i}} \sum_{\alpha_1} C_{\alpha_1}^{i,(j)} |\alpha_1\rangle, a_{(j)}^i = \sum_{\alpha_1} |C_{\alpha_1}^{i,(j)}|^2, \\ |\Phi_{(j)}^{i,0_j}\rangle &= \frac{1}{\sqrt{b_{(j)}^i}} \sum_{\alpha_1} C_{\alpha_1}^{i,(j)} |\alpha_1\rangle, b_{(j)}^i = \sum_{\beta_1} |C_{\beta_1}^{i,(j)}|^2. \end{aligned} \quad (2.100)$$

We observe that the criterion for the distentanglement of the state  $j$  involves the vanishing of one of the coefficients of the above linear superposition, say,  $a_{(j-1)}^i = 0$ . By placing eq.(2.99) into the unitary flow eq.(2.56) for the state  $|\Phi_{(j)}^i\rangle$ , and using the constraint equation eq.(2.71), the vanishing of the coefficient  $a_{(j-1)}^i$  then leads to

$$\frac{a_{(j)}^i}{b_{(j)}^i} = \frac{\sum_{\alpha_1} \left| \sum_{k=1}^{a_j^{max}} \sum_{\gamma_1} \{ \Gamma_{\alpha_1' \gamma_1}^{2k} G_{\gamma_1 \gamma_1'}^{4k-2\bar{p}} C_{\gamma_1'}^i \}^{(j)} \right|^2}{\sum_{\beta_1} |C_{\beta_1}^i|^2}. \quad (2.101)$$

The reduced single-electron density matrix prior to the RG step  $j$  can be computed from eq.(2.99) via partial tracing over the states  $\{1, j-1\} = \bar{j}$

$$\begin{aligned} \rho_{(j),j} &= Tr_{\bar{j}}(|\Phi_{(j)}^i\rangle\langle\Phi_{(j)}^i|) \\ &= |a_{(j)}^i|^2 |1_j\rangle\langle 1_j| + |b_{(j)}^i|^2 |0_j\rangle\langle 0_j|, \end{aligned}$$

which is clearly a mixed state. Upon disentanglement via the RG step  $j$  (see also discussion below eq.(2.58)), the single-electron density matrix becomes pure  $\rho_{(j-1),j} = |0_j\rangle\langle 0_j|$ . The change in entanglement entropy of the state  $j$  is  $\Delta SEE_{(j)} = -Tr(\rho_{(j),j} \log \rho_{(j),j})$ . The difference of this entropy gain and the maximum entropy gain possible from the process of disentanglement ( $\ln 2$ ) gives us a measure of probing the quantum entanglement from the perspective of the decoupled states

$$S_1 = \Delta SEE_{(j)} - \ln 2. \quad (2.102)$$

The  $\ln 2$  is a signature of a maximally mixed single-electron density matrix, i.e., denoting states that were maximally entangled prior to the process of disentanglement. Thus, the quantity  $S_1$  is a measure of the quantum entanglement content of the decoupled states.

# Chapter 3

## Perturbing the Fermi surface: insights into fermionic criticality

In this chapter, we turn our sights towards employing the URG framework in reaching some broad insights into the quantum criticality of systems of interacting electrons. We begin by presenting in Sec.3.1.1 a URG study that demonstrates the emergence of the tight-binding band picture for the electrons in a weak periodic potential and without any electronic correlations. Then, in the remainder of Sec.3.1 and in all of Sec.3.2, we use the URG approach for studying effects of electronic correlations leading to breakdown of Landau’s Fermi liquid theory. This is associated with changes in topological numbers that characterize the topological stability of the Fermi surface, e.g., Luttinger’s sum and the Friedel’s sum rule. Further, in Sec.3.1.2, we demonstrate the existence of log-divergences in the one-particle self-energy signalling breakdown of the Landau quasiparticle picture, and emergence of a novel non-Fermi liquid metal. We end this chapter with Sec.3.2, describing the phenomena of bound-state formation resulting from a gapping instability of the Fermi surface. In this case, the Fermi surface is replaced by a Luttinger surface of zeros, and characterised of the change in the topological numbers associated with the Fermi surface. Together, the two sections 3.1 and 3.2 unravel the nature of fermionic criticality for a general model of interacting electrons with translation invariance. We demonstrate that various sum-rules are obeyed by the URG method, and reach very broad conclusions for the emergence of novel states of fermionic quantum matter.

### 3.1 The gapless Fermi surface: Fermi liquid and beyond

In a strongly correlated electronic system, the electronic spectral weight is widely distributed across various inter-electron interaction-induced scattering channels. Indeed, the phenomena of spectral weight transfer has a long history in the context of Mott Hubbard systems [423–426, 418]. These studies indicate the breakdown of Landau’s paradigm of adiabatic continuity (between the non-interacting electron and the electronic quasiparticle for the Fermi liquid [14]) for the normal state of the Mott-Hubbard system, owing to the strong mixing of spectral weight between ultraviolet and infra-red degrees of freedom. Instead, in the Mott insulating state at  $T = 0$ , a (Luttinger) surface of zeros is observed for the single particle Green’s function from both numerical and analytical techniques [427, 428, 276, 429]. Further, a non-Fermi liquid nature has

been proposed for the normal metallic state of such Mott-Hubbard systems, and attributed to the phenomena of UV-IR mixing [430]. This appears to be consistent with findings from cluster variants of the dynamical mean-field theory (e.g., CDA+DMFT [58, 59, 57]) and CDMFT ([67])). As discussed earlier in Sec.2.5, the RG method proposed by us can account for such UV-IR mixing. In this section, we begin by performing a URG study for the electrons in a weak periodic potential and without any electronic correlations, demonstrating the adiabatic continuity towards the tight-binding band picture. This leads to emergence of a preserved Luttinger volume and topological protection of the Fermi surface arising from the band gap. Next, we employ our method in unveiling the physics leading to the breakdown of the Landau quasiparticle in the presence of strong correlations. For this, we depict the usage of the unitary decoupling operation (eq.(2.4)) towards identifying a composite degree of freedom that can replace the quasiparticles of the Fermi liquid in the *normal state* of strongly correlated systems. As long as there are no instabilities of the FS, the propagator associated with the composite degree of freedom will be shown to preserve the Luttinger volume for the Fermi surface (FS) [431, 88]. Further, the geometry of the FS will also be shown to be affected by the presence of such composite objects in its immediate neighbourhood. Finally, we will demonstrate the need for a full-fledged RG treatment in deciding whether or not Landau quasiparticles populate the low-energy neighbourhood of the FS.

### 3.1.1 RG flow from Nearly Free Fermi gas to Tight binding Metal

A system of nearly-free electrons placed in one spatial dimensions (and with periodic boundary conditions) is confined via a weak periodic potential  $V(x)$ , such that its dynamics is described by the Hamiltonian

$$H = \int [-\psi_x^\dagger \partial_x^2 \psi_x + \psi_x^\dagger V(x) \psi_x] . \quad (3.1)$$

The imposition of periodic boundary conditions,  $\psi(x) = \psi(x + L)$ , leads to a non-trivial Hilbert space topology of a circle  $S_1$  associated with winding numbers  $n_x = \pi_1(S_1)$  identified in terms of the momentum labels  $k = \pi n_x / L$ . This system of length  $L$  and with  $N$  potential wells has a discrete translation symmetry group,  $Z_N$ , due to the period  $a = L/N$  of the potential  $V(x) = V(x + a)$ . The real-space creation/annihilation operators are written as a discrete Fourier sum over the  $k$  states

$$\psi_x^\dagger = \sqrt{L^{-1}} \sum_k e^{ikx} c_k^\dagger . \quad (3.2)$$

The potential  $V(x)$  is written in the Fourier basis of the reciprocal lattice vectors  $Q_j$  as  $V(x) = \sum_{j=1}^p e^{iQ_j x} V_{Q_j}$ , such that  $Q_j a = 2j\pi$ . Note that we have also truncated the Fourier components upto  $Q_p$ . Now, by replacing the Fourier decompositions in the Hamiltonian eq.(3.1), we attain the momentum-space representation of the Hamiltonian as

$$H = \sum_{n,j} \epsilon_{k_{nj}} \hat{n}_{k_{nj}} + \sum_{m,n,j} V(Q_{nm}) \left( c_{k_{nj}}^\dagger c_{k_{mj}} + h.c. \right) , \quad (3.3)$$

where  $1 \leq n \leq p$ ,  $0 \leq j \leq N - 1$ . The reciprocal lattice vectors have the following periodicity  $Q_{nm} = Q_n - Q_m$ . The wave vectors for the  $n$ -th Brillouin zone (BZ) are represented as  $k_{nj} =$

$k_j + Q_n$ , where  $\{k_j\} \in \{-\frac{1}{2}Q_1, \dots -\frac{1}{2}Q_1 + \frac{\pi j}{Na}, \dots, \frac{1}{2}Q_1 - \frac{\pi}{Na}\}$  represents the set of wave-vectors in the first BZ.

Further,  $V(Q_{nm})$  represent the Fourier components obtained by summing the modulated potential over a unit cell  $x \in [0, a]$ . This off-diagonal term represents connectivities between Brillouin zones with wave-vector differences  $Q_{nm}$  leading to the following non-trivial commutation relation

$$[H, \hat{n}_{k_{m,j}}] = \sum_n V(Q_{n-m}) [c_{k_{m,j}}^\dagger c_{k_{n,j}} - h.c.] , \quad (3.4)$$

and is the source of quantum fluctuations in the occupation numbers of the single-particle states labelled by  $k$ . The bare dispersion  $\epsilon_{k_{n,j}} = k_{n,j}^2$  is associated with the unrestricted motion of electrons in the 1D system. The presence of the quantum fluctuations (characterised by  $V(Q_{n-m})$ ) indicates that these are not eigen-energies in the low energy sector. In order to determine the effective lowest-band picture, i.e., for  $n = 0$ , we need to take account of the inter-band scattering effects while respecting the discrete translational symmetry of the underlying potential. This can be done by decoupling single-particle fermionic states successively starting from the highest dispersion energy  $\epsilon_{k_{n,j}}$ .

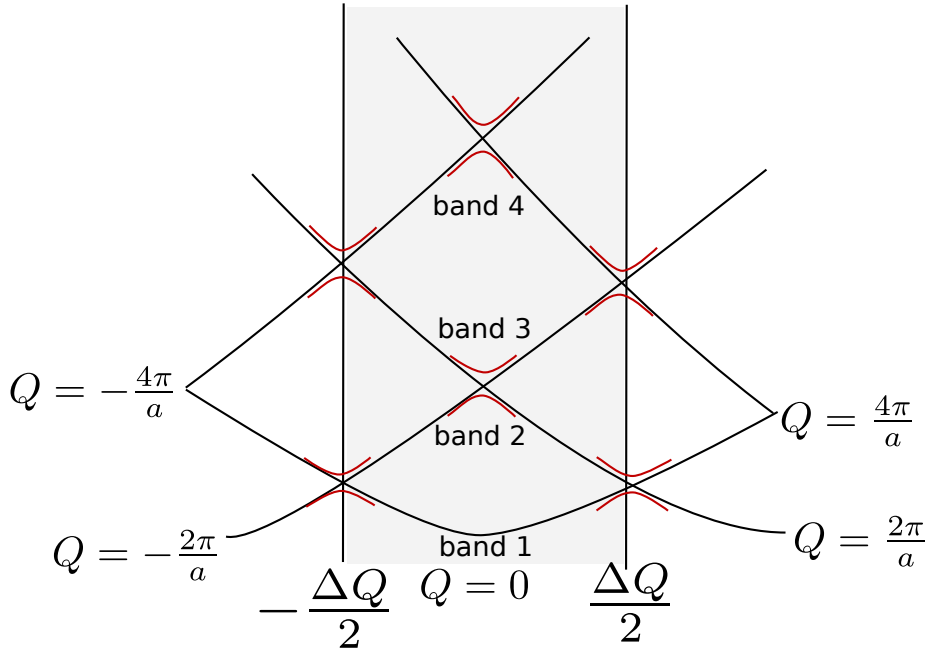


Figure 3.1: Formation of Brillouin zone bands of  $\epsilon_{k_{n,j}}$  separated by band gaps.

The Hamiltonian eq.(3.3) does not involve connectivities between  $k_{n,j}$  and  $k_{m,j'}$ , allowing it to be written as a decoupled sum of Hamiltonians  $H = \sum_j H_{k_j}$  that commute with one another,  $[H_{k_j}, H_{k_{j'}}] = 0$ . Owing to the  $Z_N$  symmetry of  $V(x)$ , an entire band (say  $l$ ) of  $N$  single-particle fermionic states can be simultaneously unitarily decoupled at RG step  $(l)$  using the unitary transformation

$$U_{(l)} = \frac{1}{\sqrt{2}} \sum_{j=0}^{N-1} [1 + \eta_{(l),j} - \eta_{(l),j}^\dagger] , \quad (3.5)$$

and resulting in the flow equation  $H_{(l-1)} = U_{(l)} H_{(l)} U_{(l)}^\dagger$ . Note that, in the above,  $\eta_{(l),j}^\dagger$  is the e-h transition operator (eq.(2.12)) that resolves the quantum fluctuations of the occupation number configurations for the  $j$ -th electronic state  $\mathbf{k}_{l,j}$  in the  $l$ -th band.

The RG flow equation for the dispersion ( $\epsilon_{k_n,j}^{(l)}$ ) and Fourier components of the periodic potential ( $V^{(j)}(Q_n)$ ) are given by

$$\begin{aligned}\Delta\epsilon_{k_n,j}^{(l)} &= \frac{(V^{(l)}(Q_{ln}))^2}{\omega - \epsilon_{k_l,j}^{(l)}(1 - \hat{n}_{k_l,j})}, \quad 0 < n \leq l-1, \\ \Delta V^{(l)}(\omega, Q_{ab}) &= \sum_{j=0}^{N-1} \frac{V^{(l)}(Q_{al})V^{(l)}(Q_{lb})}{\omega - \epsilon_{k_l,j}^{(l)}},\end{aligned}\quad (3.6)$$

where  $0 \leq (a-b) \leq m-1$ . All the bands upto  $l$  have been decoupled, resulting in the off-diagonal terms  $V^{(l)}(\omega, Q_{ab}) = 0$  for  $a-b > l$ . The renormalized potential at the RG step  $l$  is given by

$$V^{(l-1)}(x) = \sqrt{l^{-1}} \sum_{n=0}^{l-1} V^{(m-1)}(Q_n) e^{iQ_n x}, \quad (3.7)$$

which is RG relevant for the quantum fluctuation scale  $\omega > \max(\epsilon_{k_l,j}) = \epsilon_{k_{p,-N}}$ . This indicates the growth of the renormalized band-gap between the  $l$ -th and  $l+1$ -th band given by

$$\Delta E_{l,l+1}^{(l)} = 2 \frac{\sum_{s=0}^{l-1} V^{(l)2}(Q_{l-s})}{\omega - \epsilon_{N-1}^{(l)}}. \quad (3.8)$$

We now place the chemical potential in the bottom-most band (band 1 in Fig.3.1), such the states within this band undergo inter-band scattering with the bands lying above it. The Green's function for the single-particle states  $k_{0,j}$  in band 1 at the RG step  $l$  is given by

$$G_{(l)}(\omega, k_{0,j}) = \frac{1}{\omega - (\epsilon_{k_{0,j}}^{(l)} - \mu) - i\Sigma_{im}^{(l)}(\omega)}, \quad (3.9)$$

where  $\Sigma_{im}^{(l)}(\omega)$  is the Kramers-Kronig partner of the real part of the self-energy

$$\Sigma_{re}^{(l)}(\omega) = \epsilon_{k_{0,j}}^{(l)} - \epsilon_{k_{0,j}}, \quad (3.10)$$

and is also the inverse-lifetime of electronic states induced by the inter-band scattering between band 1 and the rest of the  $l-1$  bands above it.

The final step of the block-diagonalization URG procedure involves decoupling the connectivity between the  $l=1$  and  $l=0$  lowest two bands. In order to get the final renormalized dispersion ( $\epsilon_{k_{0,j}}^{(0)}$ ) of the lowest band ( $l=0$ ), and the final band gap lying above it, an effective Hamiltonian ( $H_{eff}$ ) can be constructed involving the entire lowest band, together with the final off-diagonal coupling remaining between the highest energy state  $k_{0,N-1}$  in the lowest ( $l=0$ ) band along with the lowest energy state  $k_{1,0}$  belonging to the  $l=1$  band, such that the final band gap arises from

the unitary removal of the quantum fluctuation term represented by the off-diagonal entries in the  $2 \times 2$  matrix part of  $H_{eff}$  defined in the state space of  $k_{1,0}$  and  $k_{0,N-1}$

$$H_{eff} = \sum_{j=0}^{N-2} H_{k_{0,j}} + H_{k_{0,N-1} \leftrightarrow k_{1,0}}, \quad H_{k_{0,j}} = \epsilon_{k_{0,j}}^{(0)} \hat{n}_{k_{0,j}}, \quad (3.11)$$

$$H_{k_{0,N-1} \leftrightarrow k_{1,0}} = \epsilon_{k_{1,0}}^{(1)} (\hat{n}_{k_{0,N-1}} + \hat{n}_{k_{1,0}}) + V^{(1)} [c_{k_{0,N-1}}^\dagger c_{k_{1,0}} + h.c.] . \quad (3.12)$$

A final block-diagonalization of  $H_{k_{0,(N-1)} \leftrightarrow k_{1,0}}$  leads to the formation of the bonding and anti-bonding eigenstates  $|\psi_{N,\pm}\rangle = \sqrt{2^{-1}} [ |1_{k_{1,N-1}} 0_{k_{2,0}}\rangle \pm |0_{k_{1,N-1}} 1_{k_{2,0}}\rangle ]$ , residing at the edges of the 0-th and 1st bands, with the renormalized band gap of  $\Delta E_{0,1} = 2V^{(1)}$ .

The effective real-space hopping Hamiltonian represented in Wannier state basis (localized at the lattice sites  $ja$ ) over the first BZ leads to the Wannier/ tight-binding metal

$$H_{eff} = - \sum_{i,j} (t_{ij} c_i^\dagger c_j + h.c.) . \quad (3.13)$$

Here,  $t_{ij} = t_{ji}$ ,  $t_{i+a,j+a} = t_{ij}$  are the off-diagonal hopping matrix elements in Wannier state basis, and the tight-binding dispersion for the lowest band is  $\epsilon_{k_{0,j}}^{(0)} = -2t_{ij} \cos(k_{0,j})$  ( $j \in [0, N-1]$ ). With the final decoupling, the states in the lowest band affected neither by inter-band or intra-band scattering processes. Thus, the Green's function eq.(3.9) for the single-particle states ( $k_{0,j}$ ) has a diverging lifetime (i.e., vanishing  $\Sigma_{im}^{(0)}(\omega)$ ). This leads to the emergence of a preserved Luttinger volume for the Fermi sea of the non-interacting system, together with a topological protection for the Fermi surface (with Fermi momentum  $k_F$  and energy  $\epsilon_{k_F}^{(0)} = \mu = E_F$ ) given by the Volovik invariant [421]

$$N_1 = -\frac{i}{2\pi} \oint dz G_{(0)}^{-1}(z, k_F) \partial_z G_{(0)}(z, k_F) = 1 . \quad (3.14)$$

Having observed the emergence of a well-defined Fermi surface for a nearly-free Fermi gas at the tight-binding metallic fixed point of the RG, we will, in the remainder of this chapter, look into the cases when the Fermi surface either remains stable or is destabilized under RG due to electronic interactions.

### 3.1.2 Fate of single-particle excitations

Let  $|\psi\rangle$  be an eigenstate of a many-particle Hamiltonian,  $\hat{H}|\psi\rangle = E|\psi\rangle$ , such that adding an electronic excitation of momentum  $\mathbf{k}$  and spin  $\sigma$  to it leads to the following many-body state

$$|\psi_{1_{\mathbf{k}\sigma}}\rangle = Z_1^{-1/2} c_{\mathbf{k}\sigma}^\dagger |\psi\rangle , \quad (3.15)$$

where  $Z_1$  is the wavefunction renormalisation known as the quasiparticle residue (and identical to  $Z_F(1,1)$  in the previous chapter). If the single-particle occupation number operator  $\hat{n}_{\mathbf{k}\sigma}$  commutes with the Hamiltonian,  $[H, \hat{n}_{\mathbf{k}\sigma}] = 0$ , the state  $|\psi_{1_{\mathbf{k}\sigma}}\rangle$  is also an eigenstate of  $H$  but with a shifted energy. On the other hand, the case of  $[H, \hat{n}_{\mathbf{k}\sigma}] \neq 0$  denotes the existence of quantum fluctuations (QF) given by

$$(H - E)|\psi_{1_{\mathbf{k}\sigma}}\rangle = [H, c_{\mathbf{k}\sigma}^\dagger] c_{\mathbf{k}\sigma} |\psi_{1_{\mathbf{k}\sigma}}\rangle .$$

The expression on the R.H.S can, very generally, be decomposed into number diagonal (energy shift) and off-diagonal (QF) parts with respect to the state  $|\psi_{1_{\mathbf{k}\sigma}}\rangle$

$$(i) \hat{n}_{\mathbf{k}\sigma}[H, c_{\mathbf{k}\sigma}^\dagger]c_{\mathbf{k}\sigma}\hat{n}_{\mathbf{k}\sigma}|\psi_{1_{\mathbf{k}\sigma}}\rangle = \Delta E_{\mathbf{k}\sigma}|\psi_{1_{\mathbf{k}\sigma}}\rangle , \quad (3.16)$$

$$(ii) (1 - \hat{n}_{\mathbf{k}\sigma})[H, c_{\mathbf{k}\sigma}^\dagger]c_{\mathbf{k}\sigma}\hat{n}_{\mathbf{k}\sigma}|\psi_{1_{\mathbf{k}\sigma}}\rangle = C|\psi_{0_{\mathbf{k}\sigma}}\rangle , \quad (3.17)$$

where  $\langle\psi_{1_{\mathbf{k}\sigma}}|\psi_{0_{\mathbf{k}\sigma}}\rangle = 0$ . We see that the number diagonal term shifts the energy of the many-body configuration, but preserves the spectral weight of the single particle excitation. The off-diagonal term encodes QF in the occupation number space of the state  $|\psi_{1_{\mathbf{k}\sigma}}\rangle$ , preventing the single-particle excitation from being infinitely long-lived. Given the presence of such QF terms, we present below the qualitative outcome of the creation of a single particle excitation on a many-body eigenstate in a very general setting of a system of interacting fermions with lattice translational symmetry.

We begin by defining a single particle excitation Hamiltonian (SEH) using the e-h scattering terms,

$$H_{[\mathbf{k}\sigma]} = \frac{1}{2} \left( [H, c_{\mathbf{k}\sigma}^\dagger]c_{\mathbf{k}\sigma} + h.c. \right) .$$

It is important to note that the Hamiltonian  $H$  of a system of electrons with four-fermi interactions and lattice translation symmetry can be built from the Hamiltonian  $H_{[\mathbf{k}\sigma]}$

$$H = \sum_{\mathbf{k}\sigma} \left[ Tr_{\mathbf{k}\sigma}(H_{[\mathbf{k}\sigma]}\hat{n}_{\mathbf{k}\sigma})\hat{n}_{\mathbf{k}\sigma} + \frac{1}{2} \left( c_{\mathbf{k}\sigma}^\dagger Tr_{\mathbf{k}\sigma}(H_{[\mathbf{k}\sigma]}c_{\mathbf{k}\sigma}) + h.c. \right) \right] , \quad (3.18)$$

where the first and second terms denote the *energy shift* and *QF* terms associated with the state  $|\psi_{1_{\mathbf{k}\sigma}}\rangle$  sum up to give the various scattering terms of the entire Hamiltonian. Thus, for the generic case of a single band of strongly correlated electrons with four-fermionic interactions

$$H_{SFIM} = \sum_{\mathbf{k}} \epsilon_{\mathbf{k}} \hat{n}_{\mathbf{k}\sigma} + \sum_{\mathbf{k}\mathbf{k}'\mathbf{q}} V_{\mathbf{k}\mathbf{k}'\mathbf{q}}^{\sigma\sigma'} c_{\mathbf{k}+\mathbf{q}\sigma}^\dagger c_{\mathbf{k}'-\mathbf{q}\sigma'}^\dagger c_{\mathbf{k}'\sigma'} c_{\mathbf{k}\sigma} , \quad (3.19)$$

the single-particle excitation Hamiltonian  $H_{[\mathbf{k}\sigma]}$  has the form

$$H_{[\mathbf{k}\sigma]} = (\epsilon_{\mathbf{k}} + \sum_{\mathbf{k}'\sigma'} V_{\mathbf{k}\mathbf{k}'0}^{\sigma\sigma'} \hat{n}_{\mathbf{k}'\sigma'})\hat{n}_{\mathbf{k}\sigma} + \sum_{\mathbf{k}'\sigma',\mathbf{q}} V_{\mathbf{k}\mathbf{k}'\hat{\mathbf{q}}}^{\sigma\sigma'} c_{\mathbf{k}\sigma}^\dagger c_{\mathbf{k}'\sigma'}^\dagger c_{\mathbf{k}'-\mathbf{q}\sigma'} c_{\mathbf{k}+\mathbf{q}\sigma} . \quad (3.20)$$

The number diagonal and off-diagonal contributions of the SEH,  $H_{[\mathbf{k}\sigma]}$ , can be written in the occupation number representation of the state  $|\psi_{1_{\mathbf{k}\sigma}}\rangle$  as

$$H_{[\mathbf{k}\sigma]} = \begin{pmatrix} H_{[\mathbf{k}\sigma],e} & c_{\mathbf{k}\sigma}^\dagger T_{[\mathbf{k}\sigma],e-h} \\ T_{[\mathbf{k}\sigma],e-h}^\dagger c_{\mathbf{k}\sigma} & H_{[\mathbf{k}\sigma],h} \end{pmatrix} , \quad (3.21)$$

where the energy shifts are obtained from

$$H_{[\mathbf{k}\sigma],e} = Tr_{\mathbf{k}\sigma}(H_{[\mathbf{k}\sigma]}\hat{n}_{\mathbf{k}\sigma}), H_{[\mathbf{k}\sigma],h} = Tr_{\mathbf{k}\sigma}(H_{[\mathbf{k}\sigma]}(1 - \hat{n}_{\mathbf{k}\sigma})) , \quad (3.22)$$

and the QF are indicated by the term

$$T_{[\mathbf{k}\sigma],e-h} = Tr_{\mathbf{k}\sigma}(H_{[\mathbf{k}\sigma]}c_{\mathbf{k}\sigma}) . \quad (3.23)$$

The off-diagonal (QF) elements in eq.(3.21) are associated with the mixing between UV and IR degrees of freedom via the occupation number fluctuations of the state  $|\psi_{1_{\mathbf{k}\sigma}}\rangle$  (eq.(3.17)). By solving the decoupling equation eq.(2.4), the Hamiltonian eq.(3.21) can be brought into a block diagonal form

$$H_{[\mathbf{k}\sigma]} = U_{[\mathbf{k}\sigma]}^\dagger \begin{pmatrix} \tilde{H}_{[\mathbf{k}\sigma]}^e & 0 \\ 0 & \tilde{H}_{[\mathbf{k}\sigma]}^h \end{pmatrix} U_{[\mathbf{k}\sigma]} , \quad (3.24)$$

and where the form of decoupling unitary operator is given by eq.(2.22). Following the decomposition shown in eq.(2.30), the block diagonal forms  $\tilde{H}_{[\mathbf{k}\sigma]}^{e/h}$  can be resolved into number diagonal piece ( $D$ ) and off-diagonal ( $X$ ) pieces

$$\tilde{H}_{[\mathbf{k}\sigma]}^{e/h} - H_{[\mathbf{k}\sigma]}^{e/h} = \Delta H_{[\mathbf{k}\sigma]}^{e/h,D} + \Delta H_{[\mathbf{k}\sigma]}^{e/h,X} , \quad (3.25)$$

where the number diagonal term  $H_{[\mathbf{k}\sigma]}^{e/h,D}$  contains the renormalised energy shift terms (i.e. shifts in both self and correlation energies). On the other hand, the off-diagonal term  $H_{[\mathbf{k}\sigma]}^{e/h,X}$  contain the renormalised scattering vertices with respect to the remaining coupled single particle states. By putting eq.(3.24) into the Hamiltonian  $H$  eq.(3.19), and using the following unitary transformation relations for the creation ( $c_{\mathbf{k}\sigma}^\dagger$ ) and number ( $\hat{n}_{\mathbf{k}\sigma}$ ) operators

$$U_{[\mathbf{k}\sigma]}\hat{n}_{\mathbf{k}\sigma}U_{[\mathbf{k}\sigma]}^\dagger = \frac{1}{2} \left[ 1 + \eta_{[\mathbf{k}\sigma]} + \eta_{[\mathbf{k}\sigma]}^\dagger \right] , \quad (3.26)$$

$$U_{[\mathbf{k}\sigma]}c_{\mathbf{k}\sigma}^\dagger U_{[\mathbf{k}\sigma]}^\dagger = \frac{1}{2}c_{\mathbf{k}\sigma}^\dagger - \frac{1}{2}[\eta_{[\mathbf{k}\sigma]}, c_{\mathbf{k}\sigma}^\dagger] - \frac{1}{2}\eta_{[\mathbf{k}\sigma]}c_{\mathbf{k}\sigma}^\dagger\eta_{[\mathbf{k}\sigma]} , \quad (3.27)$$

we obtain the renormalized Hamiltonian for the occupied/unoccupied (e/h) block as

$$\tilde{H}^{e/h} = H + \sum_{\mathbf{k}\sigma} (\Delta H_{[\mathbf{k}\sigma]}^{e/h,D} + \Delta H_{[\mathbf{k}\sigma]}^{e/h,X}) . \quad (3.28)$$

Here, the e-h transition operator  $\eta_{[\mathbf{k}\sigma]}$  is defined by putting the block-matrix representation of the excitation Hamiltonian (eq.(3.21))  $H_{[\mathbf{k}\sigma]}$  and has the form

$$\eta_{[\mathbf{k}\sigma]} = G_{[\mathbf{k}\sigma],h} \Gamma_{\mathbf{k}\sigma,\alpha}^{4,(0)} \tilde{c}_\alpha^\dagger c_{\mathbf{k}\sigma} , \quad (3.29)$$

where the Green's function  $G_{[\mathbf{k}\sigma],h}^4$  is associated with the intermediate many-body configurations and is given by

$$G_{[\mathbf{k}\sigma],h} = \frac{1}{\hat{\omega} + \epsilon_{\mathbf{k}}\tau_{\mathbf{k}\sigma} + V_{\mathbf{k}\mathbf{k}_1}^{\sigma\sigma_1}\tau_{\mathbf{k}\sigma}\tau_{\mathbf{k}_1\sigma_1}} . \quad (3.30)$$

Note that we have used the Einstein summation convention on the indexes  $(\mathbf{k}_1, \sigma_1)$ . In the above Green's function operator eq.(3.30),  $\tau_{\mathbf{k}\sigma} = \hat{n}_{\mathbf{k}\sigma} - \frac{1}{2}$  is the occupation number operator

defined about the electron/hole symmetric point. The operator  $\hat{\omega}$  is the *quantum fluctuation operator* defined in eq.(2.9), whose spectral decomposition are the correlation/self energies of the number-diagonal configurations of the coupled states( see cluster expansion of the Green's function eq.(2.48)). The action of the unitary operator on the single-particle creation/annihilation operator leads to the expansion given in eq.(3.27), where the commutator between the e-h transition operator and the creation operator appears as the first higher order term

$$U_{[\mathbf{k}\sigma]} c_{\mathbf{k}\sigma}^\dagger U_{[\mathbf{k}\sigma]}^\dagger \rightarrow \frac{1}{2} [\eta_{[\mathbf{k}\sigma]}, c_{\mathbf{k}\sigma}^\dagger] = \frac{1}{2} \tau_{\mathbf{k}\sigma} G_{[\mathbf{k}\sigma],h} \Gamma_{\mathbf{k}\sigma,\alpha}^{4,(0)} \tilde{c}_\alpha^\dagger , \quad (3.31)$$

where  $\alpha = \{(\mathbf{k}'\sigma', 0), ((\mathbf{k}'-\mathbf{q})\sigma', 1), ((\mathbf{k}+\mathbf{q})\sigma, 1)\}$ . Here  $\tilde{c}_\alpha^\dagger$  represents a 2-electron 1-hole correlated excitation.

We note that a similar expansion was obtained in Ref.[432] in the context of decoupling total doublon-number subspaces in the 2D Hubbard model. Note that we have used the Einstein summation convention on the indexes  $(l, \mu)_3^1$ . In the expression above,  $\Gamma_{\mathbf{k}\sigma,\alpha}^{4,(0)}$  is the bare 2-particle (or 4-point) vertex  $V_{\mathbf{k}\mathbf{k}'\mathbf{q}}$  in Hamiltonian eq.(3.19). The two-particle vertex is connected to the leading correlated excitation  $\tilde{c}_\alpha^\dagger$  (defined in Sec.1.1.2), which corresponds here to a two-electron and one-hole (2e-1h) creation operator with indices  $(l, \mu)_3^1$  given by

$$\alpha = \{(\mathbf{k}'\sigma', 0), ((\mathbf{k}' - \mathbf{q})\sigma', 1), ((\mathbf{k} + \mathbf{q})\sigma, 1)\} . \quad (3.32)$$

The members of the set  $\alpha$  are constrained indexes that manifest the translation symmetry of the Hamiltonian  $H_1$ , and are responsible for pairwise momentum conservation. This 2e-1h excitation configuration is therefore the primary decay channel for the single-electron excitation (Fig.3.2a), as can be seen by the unitary map of the many body state  $|\psi_{1_{\mathbf{k}\sigma}}\rangle$  (eq.(3.15))

$$\begin{aligned} U_{[\mathbf{k}\sigma]} |\psi_{1_{\mathbf{k}\sigma}}\rangle &= Z_1^{-1/2} \left( U_{[\mathbf{k}\sigma]} c_{\mathbf{k}\sigma}^\dagger U_{[\mathbf{k}\sigma]}^\dagger \right) U_{[\mathbf{k}\sigma]} |\psi\rangle \\ &= -\frac{1}{2} Z_1^{-1/2} \tau_{\mathbf{k}\sigma} G_{[\mathbf{k}\sigma],h} \Gamma_{\mathbf{k}\sigma,\alpha}^{4,(0)} \tilde{c}_\alpha^\dagger U_{[\mathbf{k}\sigma]} |\psi\rangle + \frac{1}{2} c_{\mathbf{k}\sigma}^\dagger U_{[\mathbf{k}\sigma]} |\psi\rangle . \end{aligned} \quad (3.33)$$

The rotated state  $U_{[\mathbf{k}\sigma]} |\psi\rangle$  is in the hole-occupation subspace corresponding to the label  $\mathbf{k}\sigma$ , and annihilated by the third term in eq.(3.27). We can, therefore drop the third term. From this demonstration, we conclude that the spectral weight transfer naturally happens from the single particle excitation to the next term in the expansion of the unitary transformed electron creation eq.(3.27): the 2-electron 1-hole composite. As shown in eq.(3.28), these changes are also brought about concomitantly in the effective Hamiltonian blocks at a given *QF* scale. Thus, the dispersion of these composite objects is given by the change in the number-diagonal part of the Hamiltonian  $\Delta H_e^D(\omega)$

$$\Delta H_e^D(\omega) = G_{[\mathbf{k}\sigma],h}(\omega) (V_{\mathbf{k}\mathbf{k}'\mathbf{q}}^{\sigma\sigma'})^2 (1 - \hat{n}_{\mathbf{k}'\sigma'}) \hat{n}_{\mathbf{k}+\mathbf{q}\sigma} \hat{n}_{\mathbf{k}'-\mathbf{q}\sigma'} , \quad (3.34)$$

where the 2e-1h projector is equal to the product of the composite e-h excitation/de-excitation operators

$$(1 - \hat{n}_{\mathbf{k}'\sigma'}) \hat{n}_{\mathbf{k}+\mathbf{q}\sigma} \hat{n}_{\mathbf{k}'-\mathbf{q}\sigma'} = \tilde{c}_\alpha^\dagger \tilde{c}_\alpha . \quad (3.35)$$

We recall that such three-particle terms were studied on phenomenological grounds in Refs.[433] and [434] towards explaining the the linear resistivity of the marginal Fermi liquid. The associated

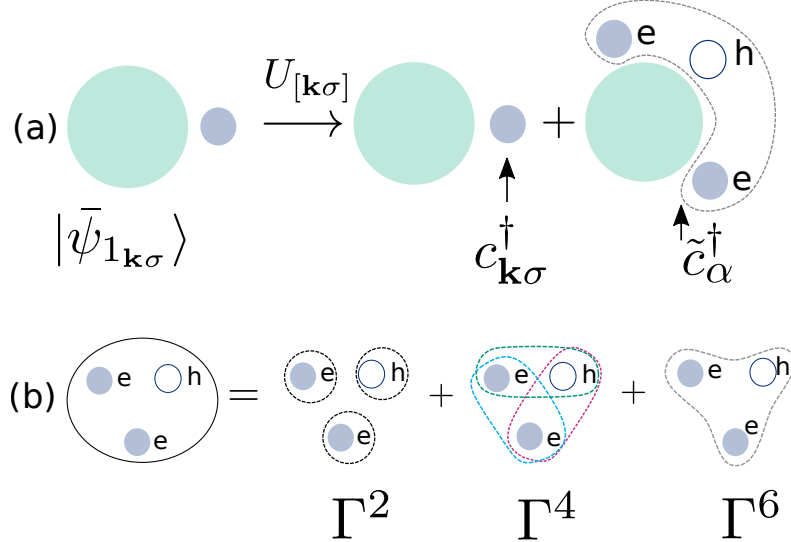


Figure 3.2: (a) Schematic diagram representing decay of the single-electron spectral weight into the one-electron channel and 2 electron-1 hole channel. (b) A pictorial depiction of the composition of a three-particle dispersion, i.e., one particle self-energy ( $\Gamma^2$ ), two-particle correlation energy ( $\Gamma^4$ ) and three-particle correlation energy ( $\Gamma^6$ ).

new three-particle number off-diagonal scattering terms that are generated in  $\Delta H_{[\mathbf{k}\sigma],e}^X$  provide the source of three-particle bound-state formation [434].

From the cluster decomposition of  $\Delta \tilde{H}^D$  (see Sec.(2.4)), we obtain the self/correlation energies as

$$\Delta H^D(\omega) = \sum_{n=1}^3 \Delta \Gamma_{(\mathbf{k}\sigma)_n^1}^{2n} \prod_{l=1}^n \tau_{\mathbf{k}_l \sigma_l}. \quad (3.36)$$

This cluster decomposition reveals the one-, two- and three-particle contributions (Fig. 3.2b) to the 2e-1h composite.

### 3.1.3 One-particle self-energy

From eq.(3.36), the one-particle components in the 2e-1h composite leads to the leading order one-particle self-energy ( $\hat{\Sigma}_{\mathbf{k}'\sigma'}^I = \Gamma_{\mathbf{k}'\sigma'}^2$ ) in the form of an energy shift of the kinetic energy

$$\hat{\Sigma}_{\mathbf{k}'\sigma'}^I = \left[ \sum_{\mathbf{k}\sigma} \text{Tr} (\Delta H_{[\mathbf{k}\sigma],e}^D \tau_{\mathbf{k}'\sigma'}) \right] \tau_{\mathbf{k}'\sigma'}. \quad (3.37)$$

For the Hamiltonian eq.(3.19), the self energy  $\Sigma_{\mathbf{k}'\sigma'}$  for the state  $\mathbf{k}'\sigma'$  is computed by taking the bare Fermi distribution  $\theta(E_F - \epsilon_k)$  at  $T = 0$  and  $E_F$  being the Fermi energy, and by considering the contribution from all  $\mathbf{k}\sigma$  states within the energy range  $\epsilon_{\mathbf{k}'} > \epsilon_{\mathbf{k}} \geq E_F$

$$\hat{\Sigma}_{\mathbf{k}'\sigma'}^I(\omega) = \sum_{\mathbf{k}\sigma, \mathbf{q}} (V_{\mathbf{k}\mathbf{k}'\mathbf{q}}^{\sigma\sigma'})^2 f_{\mathbf{k},\mathbf{k}',\mathbf{q}} G_{[\mathbf{k}\sigma],h}(\omega) \tau_{\mathbf{k}'\sigma'}. \quad (3.38)$$

In the above equation,  $f_{\mathbf{k}, \mathbf{k}', \mathbf{q}}$  is a function that sets the allowed energy ranges of the 2e-1h composite

$$\begin{aligned} f_{\mathbf{k}, \mathbf{k}', \mathbf{q}} &= \theta(\epsilon_{\mathbf{k}+\mathbf{q}} - E_F) \theta(\epsilon_{\mathbf{k}'-\mathbf{q}} - E_F) \\ &\quad \theta(\epsilon_{\mathbf{k}'} - \epsilon_{\mathbf{k}+\mathbf{q}}) \theta(\epsilon_{\mathbf{k}'} - \epsilon_{\mathbf{k}'-\mathbf{q}}) . \end{aligned}$$

The  $QF$  term associated with  $\mathbf{q} \neq 0$  scattering terms leads to a self-energy term  $\hat{\Sigma}_{\mathbf{k}'\sigma'}(\omega)$  that can be decomposed into a zeroth piece of the self-energy shift and another contribution associated with changes in the shape of the Fermi surface

$$\hat{\Sigma}_{\mathbf{k}'\sigma'}^I(\omega) = \hat{\Sigma}_{\mathbf{k}'\sigma'}^{I,(0)}(\omega) + (\hat{\Sigma}_{\mathbf{k}'\sigma'}^I(\omega) - \hat{\Sigma}_{\mathbf{k}'\sigma'}^{I,(0)}(\omega)) , \quad (3.39)$$

where  $\hat{\Sigma}_{\mathbf{k}'\sigma'}^{I,(0)}(\omega)$  defined as (here  $\Delta\epsilon_{\mathbf{k}} = \epsilon_{\mathbf{k}} - E_F$ ),

$$\begin{aligned} \hat{\Sigma}_{\mathbf{k}'\sigma'}^{I,(0)}(\omega) &= \sum_{\mathbf{k}\sigma} \frac{C^{(0)}}{\omega + \frac{1}{2}\Delta\epsilon_{\mathbf{k}} + V^{(0)}} \theta(\epsilon_{\mathbf{k}'} - \epsilon_{\mathbf{k}}) \theta(\epsilon_{\mathbf{k}} - E_F) , \\ C^{(0)} &= \frac{1}{\text{Vol}^2} \sum_{\mathbf{k}'\mathbf{k}\mathbf{q}\sigma\sigma'} (V_{\mathbf{k}\mathbf{k}'\mathbf{q}}^{\sigma\sigma'})^2 f_{\mathbf{k}, \mathbf{k}', \mathbf{q}} , \\ V^{(0)} &= \frac{1}{\text{Vol}^2} \sum_{\mathbf{k}'\mathbf{k}\sigma\sigma'} V_{\mathbf{k}\mathbf{k}'} \theta(E_F - \epsilon_{\mathbf{k}'}) . \end{aligned} \quad (3.40)$$

The Fermi surface (FS) geometry is identified by the family of unit vectors  $\hat{\mathbf{s}} = \mathbf{v}_F / |\mathbf{v}_F|$ , where  $\mathbf{v}_F$  are the Fermi surface velocities  $\mathbf{v}_F = \nabla\epsilon_{\mathbf{k}}|_{\mathbf{k}=\mathbf{k}_F}$  at every point on the FS. The self-energy component  $\Sigma_{\mathbf{k}'\sigma'}^{(0)}(\omega)$  then leads to

$$\begin{aligned} \tilde{\epsilon}_{\mathbf{k}'} &= \epsilon_{\mathbf{k}'} + \Sigma_{\mathbf{k}'\sigma'}^{I,(0)}(\omega) , \\ \nabla_{\mathbf{k}'} \tilde{\epsilon}_{\mathbf{k}'} &= \left[ |\nabla_{\mathbf{k}'} \epsilon_{\mathbf{k}'}| + \frac{C^{(0)}}{\omega + \Delta\epsilon_{\mathbf{k}'} - \frac{V^{(0)}}{4}} |\nabla_{\mathbf{k}'} \epsilon_{\mathbf{k}'}| \right] \hat{\mathbf{s}} , \\ \hat{\mathbf{s}} &= \frac{\nabla_{\mathbf{k}'} \tilde{\epsilon}_{\mathbf{k}'}}{|\nabla_{\mathbf{k}'} \tilde{\epsilon}_{\mathbf{k}'}|}|_{\mathbf{k}'=\mathbf{k}_F} = \hat{\mathbf{s}} . \end{aligned} \quad (3.41)$$

Thus, we find that the zeroth self-energy piece  $\Sigma_{\mathbf{k}'\sigma'}^{(0)}(\omega)$  leaves the Fermi surface normal vectors  $\hat{\mathbf{s}}'$ s invariant preserving the Fermi surface geometry.

### Universal logarithmic contribution to self-energy from the Fermi surface

Within the zeroth piece of the self-energy,  $\Sigma_{\mathbf{k}'\sigma'}^{I,(0)}(\omega)$ , there exists a logarithmic contribution to the *energy shift* arising from the density of states  $D(E) = \sum_{\epsilon_{\mathbf{k}}} \delta(E - \epsilon_{\mathbf{k}})$  at the Fermi surface

$$\begin{aligned} \Sigma_{\mathbf{k}'\sigma'}^{I,(0)}(\omega) &= \sum_{E=E_F}^{E'} \frac{C^{(0)} D(E)}{\omega + (E - E_F) + V^{(0)}} \\ &= \frac{C^{(0)}}{(\epsilon_{\mathbf{k}'} - E_F)} D(E_F) \log \left( 1 + \frac{\epsilon_{\mathbf{k}'} - E_F}{\omega - \frac{V^{(0)}}{4}} \right) \\ &+ \sum_{E=E_F}^{E'} \frac{C^{(0)} (D(E) - D(E_F))}{\omega + (E - E_F) - \frac{V^{(0)}}{4}} . \end{aligned} \quad (3.42)$$

For instance, for the Hubbard model with  $V_{\mathbf{k}\mathbf{k}'\mathbf{q}}^{\sigma\sigma'} = U$ , the self-energy term  $\Sigma_{\mathbf{k}'\sigma'}^{(I)}(\omega)$  is equal to its zeroth piece

$$\Sigma_{\mathbf{k}'\sigma'}^I(\omega) = \Sigma_{\mathbf{k}'\sigma'}^{I,(0)}(\omega), \quad (3.43)$$

leading to the conclusion that, while there is no shape deformation of the Fermi surface caused by the Hubbard repulsion, there is nevertheless a logarithmic contribution to the self-energy coming from the density of states at the Fermi surface eq.(3.42). In this case, the logarithmic singularity of the self-energy shows that the FS is shifted from the non-interacting FS at  $\omega = 0$  and  $\epsilon_{\mathbf{k}} = E_F$  to  $\omega \rightarrow V^{(0)}/4$  and  $\epsilon_{\mathbf{k}} \rightarrow E_F$ , due to the zero momentum transfer  $\mathbf{q} = 0$  mode forward-scattering amplitudes arising from the 2e-1h composites (eq.(3.36)). Such log-divergences provide a reason to turn to a renormalization group procedure that takes account of the *QF* term (eq.(3.17)). The *QF* term can lead to two important possibilities: (a) the destabilization of the Fermi surface through bound-state formation (as seen via generalized Luttinger surfaces of zeros of the one-particle Green's function [88, 276]) and, (b) renormalization of the 2e-1h dispersion . We will provide results obtained for these possibilities from the RG formulation in the next section.

Below, we assume that the self-energy contribution  $\Sigma_{\mathbf{k}\sigma}^I$  of the non-interacting single-particle Green's function respects separate conservation laws for every direction  $\hat{s}$  normal to the Fermi surface in the form of Luttinger-Ward identities. We then demonstrate the topological features of the count of occupied states along the orientation  $\hat{s}$  associated with a given point on the Fermi surface. This enables the definition of a *Luttinger point*, together with the notion of a partial Luttinger sum associated with every Luttinger point.

### 3.1.4 Partial Luttinger sum and Luttinger points

The single-particle Green's function is given by

$$G_{\mathbf{k}\sigma}(\omega) = \frac{1}{\omega - Tr(H_{[\mathbf{k}\sigma]}(\hat{n}_{\mathbf{k}\sigma} - \frac{1}{2})) - \Sigma_{\mathbf{k}\sigma}(\omega)}. \quad (3.44)$$

With the set of reference normal vectors of the Fermi surface  $\{\hat{s}\}$ , we recast the momentum-space wave-vectors as follows

$$\begin{aligned} \mathbf{k} &= \mathbf{k}_{\perp\hat{s}} + \mathbf{k}_{\parallel\hat{s}}, \quad \mathbf{k}_{\perp\hat{s}} \cdot \mathbf{k}_{\parallel\hat{s}} = 0, \\ \mathbf{k}_{\parallel\hat{s}} &= (\mathbf{k} \cdot \hat{s})\hat{s}, \quad \mathbf{k}_{\perp\hat{s}} = \hat{s} \times (\mathbf{k} \times \hat{s}). \end{aligned} \quad (3.45)$$

With respect to the Fermi surface curvilinear frame of reference, we write the single-particle Green's function in the coordinates of  $\hat{s}$  and the distance from FS along  $\hat{s}$ ,  $\Lambda = (\mathbf{k}_{\parallel\hat{s}} - \mathbf{k}_{F\hat{s}}) \cdot \hat{s}$ , as

$$G_{\Lambda\hat{s},\sigma}(\omega) = \frac{1}{\omega - Tr(H_{[\Lambda\hat{s}\sigma]}(\hat{n}_{\Lambda\hat{s}\sigma} - \frac{1}{2})) - \Sigma_{\Lambda\hat{s}\sigma}(\omega)}. \quad (3.46)$$

**Theorem 1** *If the Luttinger-Ward identity*

$$\partial_{\omega}\Sigma_{\Lambda\hat{s}\sigma}(\omega) + \partial_{\omega}G_{\Lambda\hat{s}\sigma}^{-1}(\omega) = 1$$

holds for every  $\hat{s}$  normal to FS, and if

$$I_{2,\Lambda\hat{s}} = \sum_{\omega=-\infty}^{\infty} G_{\Lambda\hat{s},\sigma}(\omega) \frac{\partial \Sigma_{\Lambda\hat{s}\sigma}(\omega)}{\partial \omega} = 0 ,$$

then the partial Luttinger sum defined as

$$N_{\hat{s}} = \sum_{\omega,\Lambda,\sigma} G_{\Lambda\hat{s},\sigma}(\omega)$$

is an integer, and corresponds to a topological winding in the energy-momentum space along  $\hat{s}$ .

**Proof:** The single-particle Green's function  $G$  is defined as  $G^{-1} = G_0^{-1} - \Sigma$ , where  $G_0^{-1} = \omega - \epsilon_{\mathbf{k}}$  is the Green's function of the non-interacting problem and  $\Sigma$  is the self-energy. The Luttinger Ward identity [435] satisfied by the Green's function is:  $\partial_{\omega}G^{-1} + \partial_{\omega}\Sigma = 1$ . Following Dzyaloshinskii [431], the summation of the Green's function over an energy-momentum space contour

$$N = \sum_{\Lambda,\hat{s},\sigma} \left[ \oint dz \frac{\partial}{\partial z} \ln G_{\Lambda,\hat{s},\sigma}(z)^{-1} + \int dz G_{\Lambda,\hat{s},\sigma}(z) \frac{\partial}{\partial z} \Sigma_{\Lambda\hat{s},\sigma}(z) \right] . \quad (3.47)$$

equals the number of electrons  $N$ . Further, if the relation

$$I_{2\hat{s}} = \sum_{\Lambda} \int G_{\Lambda\hat{s},\sigma}(z) \frac{\partial}{\partial z} \Sigma_{\Lambda\hat{s},\sigma}(z) = 0 \quad (3.48)$$

holds,  $N$  corresponds to the total number of occupied states such that the count stops due to a change of sign of Green's function upon reaching the unoccupied states in energy-momentum space.  $N$  can then be written as a sum of integers  $\sum_{\hat{s}} N_{\hat{s}}$ , where the number  $N_{\hat{s}}$  is defined as follows

$$N_{\hat{s}} = \sum_{\Lambda\sigma} \oint dz \frac{\partial}{\partial z} \ln \det G_{\Lambda,\hat{s},\sigma}(z)^{-1} .$$

This proves that  $N_{\hat{s}}$  is the count of occupied states, the partial Luttinger sum, along the direction  $\hat{s}$  normal to the Fermi surface, and corresponds to a topological winding number in energy-momentum space centered around a point on the Fermi surface point  $\mathbf{k} = \mathbf{k}_F(\hat{s})$ ,  $E_F = \epsilon_{\mathbf{k}_F(\hat{s})}$ . For every such point on the Fermi surface, there exists an associated Volovik invariant [421]

$$N_1 = -\frac{i}{2\pi} \sum_{\sigma} \oint dz G_{\Lambda,\hat{s},\sigma}^{-1}(z) \partial_z G_{\Lambda,\hat{s},\sigma}(z)|_{\Lambda=0} , \quad (3.49)$$

such that the partial Luttinger count can be written as a sum of the Volovik invariant at points on the Fermi surface and the partial Luttinger volume leading upto it

$$N_{\hat{s}} = \sum_{\Lambda \neq 0, \sigma} \oint dz \frac{\partial}{\partial z} \ln G_{\Lambda,\hat{s},\sigma}(z)^{-1} + N_1 , \quad (3.50)$$

where  $N_1$  is represented by the Fermi surface point (the center of the blue circle) in Fig.3.3 and the rest of the partial volume leading upto it is represented by the black line. This completes the proof that a partial Luttinger sum is a topological winding number associated with the existence of a pole at the Fermi surface point.

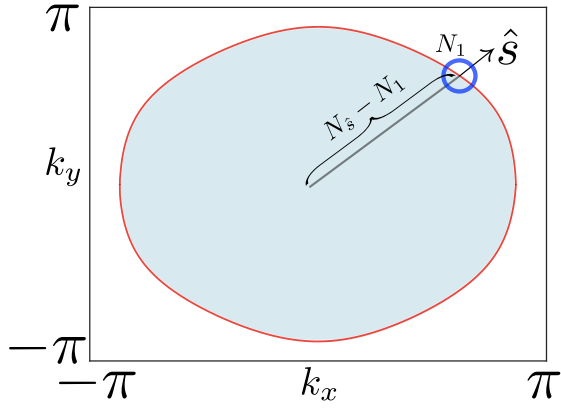


Figure 3.3: Graphical representation of the Fermi volume (light blue region) and Fermi surface (FS, red boundary) for the triangular lattice. The small dark blue circle represents a given point on the FS, and  $N_1$  is the Volovik invariant associated with this Fermi point (see discussion in text). The line extending from the origin of the Brillouin zone to the FS point represents the partial Luttinger volume  $\hat{N}_s - N_1$  for that particular FS point.

Further, following Ref.[436], the existence of separate Luttinger-Ward identities [435] along every direction normal to the FS allows us to visualize the FS as a collection of 1+1D chiral conformal field theories (CFTs).

### 3.1.5 Oshikawa's topological argument

Following Oshikawa [40], we can now connect the topological invariant  $N_s$  with the change in the center of mass momentum arising from changing boundary conditions along the direction normal to the Fermi surface given by  $\hat{s}$ . For this, we need a twist operator that changes precisely the momentum of electronic states along  $\hat{s}$

$$O_{\hat{s}} = \exp \left[ 2\pi i \sum_{x||\hat{s}} \frac{x_{||\hat{s}} \hat{n}_{\mathbf{x}}}{L} \right], \quad (3.51)$$

and the center of mass momentum vector along  $\hat{s}$  is defined as  $P_{cm,\hat{s}} = \sum_{\Lambda} \mathbf{k}_{||\hat{s}} \hat{n}_{\mathbf{k}\sigma}$ . Applying the twist operator on the Hamiltonian changes  $H \rightarrow O_{\hat{s}} H O_{\hat{s}}^{\dagger}$ , and the state space  $|\psi\rangle \rightarrow O_{\hat{s}} |\psi\rangle$ . Defining  $\hat{T}_{\hat{s}} = \exp[iP_{cm,\hat{s}}]$  as the translation operator, we use the identity

$$O_{\hat{s}} \hat{T}_{\hat{s}} O_{\hat{s}}^{-1} = \exp \left[ i2\pi \sum_{x||\hat{s}} \frac{\hat{n}_{\mathbf{x}}}{L} \right] \hat{T}_{\hat{s}},$$

to see that the center of mass momentum along  $\hat{s}$  changes as

$$P'_{cm,\hat{s}} = P_{cm,\hat{s}} + \frac{2\pi}{L} N_s. \quad (3.52)$$

This change arises from the fact that, for  $I_{2\hat{s}} = 0$ , the quantity  $\sum_{x||\hat{s}} \hat{n}_{\mathbf{x}}$  is preserved in the presence of interactions.

### 3.1.6 Preservation of partial Luttinger's count

In Theorem (1), we have shown that when  $I_{2\hat{s}} = 0$ , the total particle number is conserved in the presence of interactions

$$N = \sum_{\omega, \Lambda, \hat{s}, \sigma} G_{\Lambda, \hat{s}}^0(\omega) = \sum_{\omega, \Lambda, \hat{s}, \sigma} G_{\Lambda, \hat{s}}^I(\omega) , \quad (3.53)$$

where  $G_{\Lambda, \hat{s}}^I(\omega)$  and  $G_{\Lambda, \hat{s}}^0(\omega)$  are the interacting and non-interacting single-particle Green's functions respectively. The second of these relations is non-trivial, as a state count over the entire energy-momentum space for the interacting Green's function  $G_{\Lambda, \hat{s}}^I(\omega)$  involves keeping track of both its poles as well as its zeros. The unchanged Luttinger count in the presence of interactions leads to a relation for  $I_{2\hat{s}}$  involving the ratio of  $G_0$  and  $G$  [88]

$$I_{2\hat{s}} = \sum_{\Lambda} \int_{-\infty}^0 dz \frac{\partial}{\partial z} \ln \left( \frac{1 - \Sigma_{\Lambda, \hat{s}}^I(\omega) G_{\Lambda, \hat{s}}^0(\omega)}{1 - \Sigma_{\Lambda, \hat{s}}^{I*}(\omega) G_{\Lambda, \hat{s}}^{0*}(\omega)} \right) .$$

We can see that the integral  $I_{2\hat{s}}$  becomes equal to the difference of phase of  $G_0/G$

$$I_{2\hat{s}} = \sum_{\Lambda} [\phi_{\Lambda, \hat{s}}(-\infty) - \phi_{\Lambda, \hat{s}}(0)] ,$$

where  $\phi_{\Lambda, \hat{s}}(\omega) = \ln \left( \frac{1 - \Sigma_{\Lambda, \hat{s}}^I(\omega) G_{\Lambda, \hat{s}}^0(\omega)}{1 - \Sigma_{\Lambda, \hat{s}}^{I*}(\omega) G_{\Lambda, \hat{s}}^{0*}(\omega)} \right)$ .

We can now reach some conclusions for the single-particle self-energy  $\Sigma_{\mathbf{k}\sigma}^I(\omega)$  (eq.(3.38)) computed earlier for the generic interacting Hamiltonian (eq.(3.19)). As  $\Sigma_{\mathbf{k}\sigma}^I(\omega)$  is analytic at  $\omega = 0$ , the phase difference  $[\phi_{\Lambda, \hat{s}}(-\infty) - \phi_{\Lambda, \hat{s}}(0)] = 0$  and leads to  $I_{2\hat{s}} = 0$ . The partial Luttinger sum  $N_{\hat{s}}$  is then preserved for every  $\hat{s}$ , and we can use the individual Luttinger-Ward identity for every Fermi point in reconstructing the Luttinger sum for the entire connected Fermi surface. This is despite the fact that, upon the inclusion of two-particle interactions, the resulting three-particle effective Hamiltonian  $\Delta H_{[\mathbf{k}\sigma], e}^D(\omega)$  (eq.(3.34)) leads to a damping of the quasiparticle peak in the single-particle Green's function. However, the concomitant appearance of logarithmic non-analyticities at finite frequencies signals the need for a renormalization group treatment in reaching a firmer conclusion. We will turn to this in a later chapter.

## 3.2 RG for bound state condensation: gapping the Fermi surface

In a strongly coupled electronic system, the destabilization of the gapless Fermi surface is signaled by the appearance of surfaces of zeros of the single-electron Green's function in the complex frequency vs. momentum plane [431, 276]. This surface of zeros brings about a change in Luttinger's sum [431, 88], and is accounted for by the Friedel-Levinson phase shift [437, 438] indicating the number of bound charge composites formed out of a collection of single electronic states. The change in the Luttinger sum has, for instance, been investigated in the context of Anderson impurity models [278], and Kondo lattice systems [439] where a larger Fermi surface replaces the

non-interacting Fermi surface in the heavy-electron phase. We recall that, in the context of electronic pairing via a attractive interaction potential, Cooper [440] had demonstrated bound-state formation out of degenerate electron pairs with zero *pair-momentum* placed outside the Fermi surface. A condensation of such bound Cooper pair states leads to the BCS instability [15] for the Fermi surface.

The associated loss of electronic spectral weight in the condensation process is accounted for by the Ferrel-Glover-Tinkham sum rule [441, 365] via an addition of the zero-frequency superfluid spectral weight along with the normal state quasiparticle spectral weight at finite frequency. This addition of partial spectral weights, i.e., the spectral weight from the Fermi surface to a cut-off scale together with that beyond the cut-off scale, is required for the conservation of the f-sum rule and denotes the process of *dynamical spectral weight transfer* between high and low energies [395]. The cut-off scale itself emerges from some underlying microscopic mechanism, e.g., the Debye cutoff scale for phonon-driven BCS superconductivity. In this way, both Luttinger's sum rule and the f-sum rule carry signatures of bound state formation. Other examples of the gapping of the Fermi surface, and a subsequent breakdown of the Luttinger sum rule, include the high- $T_C$  superconductors [442, 443] and doped Mott insulators [276, 444]. Both examples again imply the formation of bound states in these states of matter.

Indeed, the pairing of electronic states (e.g., Cooper pairing of  $\mathbf{k} \uparrow$  with  $-\mathbf{k} \downarrow$ ) happens together with a projection of the microscopic Hamiltonian and its associated eigenbasis onto a sub-configuration space (e.g., the Anderson-pseudospin subspace with the constraint  $\hat{n}_{\mathbf{k}\uparrow} = \hat{n}_{-\mathbf{k}\downarrow}$  [413]), enabling an effective description in terms of bound objects. As we shall see below, by starting from a microscopic theory, a renormalization group treatment is best suited towards generating such an effective description in a controlled manner. By starting from a microscopic Hamiltonians for electrons like eq.(3.19), the renormalization group treatment we have outlined in Sec.(2.4) can be used to reach effective Hamiltonians at stable fixed points in terms of paired electronic states or Anderson-like pseudospins [413]. We note that the problem of BCS superconductivity, as well as in theories of nuclear pairing, models belonging to the Richardson class of Hamiltonians (see Ref.[445] and references therein) are written in terms of paired electronic state operators or generalized *Anderson pseudospins*. This includes the BCS reduced Hamiltonian [15] and the nuclear pairing force models [446, 447].

In order to set the stage for a renormalization group analysis, we will demonstrate the generalized Cooper-pairing problem for strongly correlated systems. By creating a two-electron or electron-hole excitation on the eigenstates of the Hamiltonian  $H$ , and then applying the unitary decoupling operation eq.(2.4) on it, we will observe the phenomenon of dynamical spectral weight distribution across multiple two-electron or electron-hole pair-momenta channels. From the most singular spectral weight transfer process (and its associated correlation energy), we will find signatures of bound-state formation in the form of log-divergent T-matrix elements and an associated Friedel's scattering phase shift. This approach is similar to the calculation presented for the Kondo problem in, e.g., Ref.[395]). These signatures will, very generally, help in identifying the appropriate pairing-force Hamiltonian for strongly correlated electronic systems. We will then verify the connection between the total Friedel's phase shift of the electronic pairs and the change in Luttinger's volume [278, 88] of strongly correlated electrons, thereby revealing the *Luttinger surface of zeros* [427, 428, 276, 429] in the reduced Hilbert space of the associated pairing-force Hamiltonians.

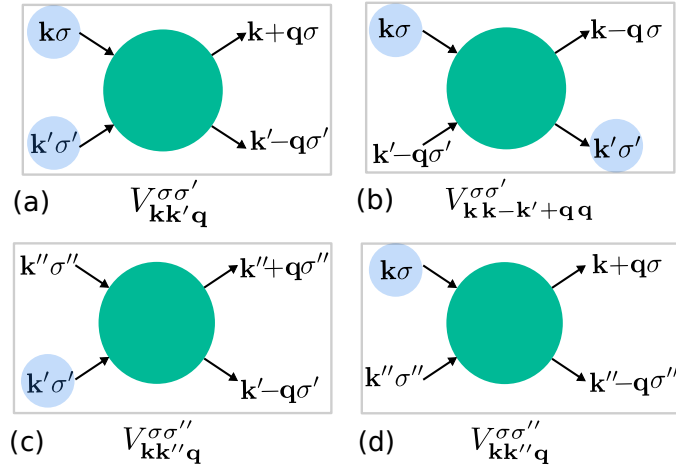


Figure 3.4: Schematic diagram of various 2-particle (i.e., 4-point) vertices representing the quantum fluctuation terms in the two-particle excitation Hamiltonian. (a) represents the ee/hh 2-particle scattering vertex, (b) represents the eh/he 2-particle scattering vertex and (c,d) represent 2-particle scattering vertices involving another state  $\mathbf{k}''\sigma''$ .

### 3.2.1 Outcome of two-particle excitations

We begin by considering a two-electron (ee) or electron-hole (eh) excitation on an eigenstate  $|\psi\rangle$  of a Hamiltonian  $H$  with  $E$  as its eigenvalue

$$|\bar{\psi}_{1_{\mathbf{k}\sigma}1_{\mathbf{k}'\sigma'}}\rangle = Z_{pp,2}^{-1/2} c_{\mathbf{k}\sigma}^\dagger c_{\mathbf{k}'\sigma'}^\dagger |\psi\rangle , \quad (3.54)$$

$$|\bar{\psi}_{1_{\mathbf{k}\sigma}0_{\mathbf{k}'\sigma'}}\rangle = Z_{ph,2}^{-1/2} c_{\mathbf{k}\sigma}^\dagger c_{\mathbf{k}'\sigma'} |\psi\rangle . \quad (3.55)$$

Our considerations are in the same spirit as Cooper's problem [440] of placing two electrons in proximity to the effectively noninteracting Fermi sea, but with one major difference: here,  $|\Psi\rangle$  is the eigenstate of the complete Hamiltonian  $H$ . This being the case, the final outcome of such excitations will have contributions from strong electronic correlations present in the Hamiltonian. The action of  $H$  on the state  $|\bar{\psi}_{1_{\mathbf{k}\sigma}1_{\mathbf{k}'\sigma'}}\rangle$  leads to a number diagonal two-particle energy shift of the bare energy  $E$

$$\begin{aligned} & \hat{n}_{\mathbf{k}\sigma} \hat{n}_{\mathbf{k}'\sigma'} \left[ H, c_{\mathbf{k}\sigma}^\dagger c_{\mathbf{k}'\sigma'}^\dagger \right] c_{\mathbf{k}'\sigma'} c_{\mathbf{k}\sigma} \hat{n}_{\mathbf{k}\sigma} \hat{n}_{\mathbf{k}'\sigma'} |\bar{\psi}_{1_{\mathbf{k}\sigma}1_{\mathbf{k}'\sigma'}}\rangle \\ &= \Delta E |\bar{\psi}_{1_{\mathbf{k}\sigma}1_{\mathbf{k}'\sigma'}}\rangle , \end{aligned} \quad (3.56)$$

as well as an off-diagonal quantum fluctuation(QF) term (similar to that present in eq.(3.17) for a single electron excitation) induced by two particle scattering

$$\begin{aligned} & (1 - \hat{n}_{\mathbf{k}\sigma} \hat{n}_{\mathbf{k}'\sigma'}) \left[ H, c_{\mathbf{k}\sigma}^\dagger c_{\mathbf{k}'\sigma'}^\dagger \right] c_{\mathbf{k}'\sigma'} c_{\mathbf{k}\sigma} \hat{n}_{\mathbf{k}\sigma} \hat{n}_{\mathbf{k}'\sigma'} |\bar{\psi}_{1_{\mathbf{k}\sigma}1_{\mathbf{k}'\sigma'}}\rangle \\ &= C |\bar{\psi}_{\mathbf{k}\sigma,\mathbf{k}'\sigma'}^\perp\rangle . \end{aligned} \quad (3.57)$$

A similar set of matrix elements exist for an eh excitation. Using the ee and eh scattering terms and their conjugate processes, the two-particle excitation Hamiltonian (TEH)  $H_{[\mathbf{k}\sigma,\mathbf{k}'\sigma']}$  can be

written as

$$\begin{aligned} H_{[\mathbf{k}\sigma, \mathbf{k}'\sigma']} &= \frac{1}{2} \left( [H, c_{\mathbf{k}\sigma}^\dagger c_{\mathbf{k}'\sigma'}^\dagger] c_{\mathbf{k}'\sigma'} c_{\mathbf{k}\sigma} \right. \\ &\quad \left. + [H, c_{\mathbf{k}\sigma}^\dagger c_{\mathbf{k}'\sigma'}] c_{\mathbf{k}'\sigma'}^\dagger c_{\mathbf{k}\sigma} \right) + h.c. . \end{aligned} \quad (3.58)$$

The sub-figures in Fig.(3.4) represent the QF terms in TEH for the single-band four-fermion interacting model  $H_1$  (eq.(3.19)) as follows: (a) represents the ee/hh scattering vertices containing the pair of two-electron excitations (eq.(3.54)) while (b) represents the eh/he scattering vertices for electron-hole excitations (eq.(3.55)). Sub-figure (c) represents the correlated scattering of state  $\mathbf{k}\sigma$  with other electronic states not including  $\mathbf{k}'\sigma'$ , and (d) represents the same for the state  $\mathbf{k}'\sigma'$ .

In order to observe the effect of QF terms (e.g., eq.(3.57)) on the self/correlation energies and correlated scattering terms, we proceed as in Sec.(3.1) for the case of single-particle excitations. We begin by bringing the Hamiltonian  $H_{[\mathbf{k}\sigma, \mathbf{k}'\sigma']}$  into block-diagonal form. This is accomplished by first by writing the Hamiltonian  $H_{[\mathbf{k}\sigma, \mathbf{k}'\sigma']}$  in the form of a block matrix

$$H_{[\mathbf{k}\sigma, \mathbf{k}'\sigma']} = \begin{pmatrix} H_{[\mathbf{k}\sigma, \mathbf{k}'\sigma']}^{1_{\mathbf{k}\sigma}} & c_{\mathbf{k}\sigma}^\dagger T_{[\mathbf{k}\sigma, \mathbf{k}'\sigma'], e-h} \\ T_{[\mathbf{k}\sigma, \mathbf{k}'\sigma'], e-h}^\dagger c_{\mathbf{k}\sigma} & H_{[\mathbf{k}\sigma, \mathbf{k}'\sigma']}^{0_{\mathbf{k}\sigma}} \end{pmatrix},$$

and then by decoupling the state  $\mathbf{k}\sigma$  in the TEH

$$H_{[\mathbf{k}\sigma, \mathbf{k}'\sigma']} = U_{[\mathbf{k}\sigma, \mathbf{k}'\sigma']}^\dagger \begin{pmatrix} \tilde{H}_{[\mathbf{k}\sigma, \mathbf{k}'\sigma']}^{1_{\mathbf{k}\sigma}} & 0 \\ 0 & \tilde{H}_{[\mathbf{k}\sigma, \mathbf{k}'\sigma']}^{0_{\mathbf{k}\sigma}} \end{pmatrix} U_{[\mathbf{k}\sigma, \mathbf{k}'\sigma']}.$$

Note that in the block matrix form of the Hamiltonian  $H_{[\mathbf{k}\sigma, \mathbf{k}'\sigma']}$ , the off-diagonal blocks contain the electron creation/annihilation operator in product with  $T_{[\mathbf{k}\sigma, \mathbf{k}'\sigma'], e-h}$ . The definition of  $T_{[\mathbf{k}\sigma, \mathbf{k}'\sigma'], e-h}$  is that given in eq.(3.1.2), and represents the associated electronic states that comprise the various  $n$ -particle vertices of the cluster expansion. As before, the unitary decoupling operator  $U_{[\mathbf{k}\sigma, \mathbf{k}'\sigma']}$  is determined by solving eq.(2.4). The e-h transition operator  $\eta_{\mathbf{k}\sigma}$  constituting the unitary operator,  $U_{[\mathbf{k}\sigma, \mathbf{k}'\sigma']} = \sqrt{2^{-1}}[1 + \eta_{\mathbf{k}\sigma} - \eta_{\mathbf{k}\sigma}^\dagger]$ , is written down in terms of the off-diagonal occupation number fluctuation terms ( $c_{\mathbf{k}\sigma}^\dagger T_{[\mathbf{k}\sigma, \mathbf{k}'\sigma'], e-h}$ ) and the number-diagonal many-body Green's function ( $G_{[\mathbf{k}\sigma, \mathbf{k}'\sigma']}^e = (\hat{\omega} - H_{[\mathbf{k}\sigma, \mathbf{k}'\sigma']}^D)^{-1}$ , using eq.(2.12)):

$$\eta_{\mathbf{k}\sigma} = \frac{1}{\hat{\omega} - H_{[\mathbf{k}\sigma, \mathbf{k}'\sigma']}^D} c_{\mathbf{k}\sigma}^\dagger T_{[\mathbf{k}\sigma, \mathbf{k}'\sigma'], e-h}, \quad (3.59)$$

where  $\hat{\omega}$  represents the QF operator (eq.(2.9)) taking account of the differences between exact energies of the TEH and its diagonal part  $H_{[\mathbf{k}\sigma, \mathbf{k}'\sigma']}$ .

For the four-fermion interacting model ( $H_1$ ), the diagonal piece of TEH is given by

$$H_{[\mathbf{k}\sigma, \mathbf{k}'\sigma']}^D = \epsilon_{\mathbf{k}} \tau_{\mathbf{k}\sigma} + \epsilon_{\mathbf{k}'} \tau_{\mathbf{k}'\sigma'} + V_{\mathbf{k}\mathbf{k}'}^{\sigma\sigma'} \tau_{\mathbf{k}\sigma} \tau_{\mathbf{k}'\sigma'}, \quad (3.60)$$

containing both the individual kinetic energy and correlation energy terms. The operator  $\tau_{\mathbf{k}\sigma}$  is the occupation number operator  $\hat{n}_{\mathbf{k}\sigma}$  defined in a manifestly particle-hole symmetric manner.

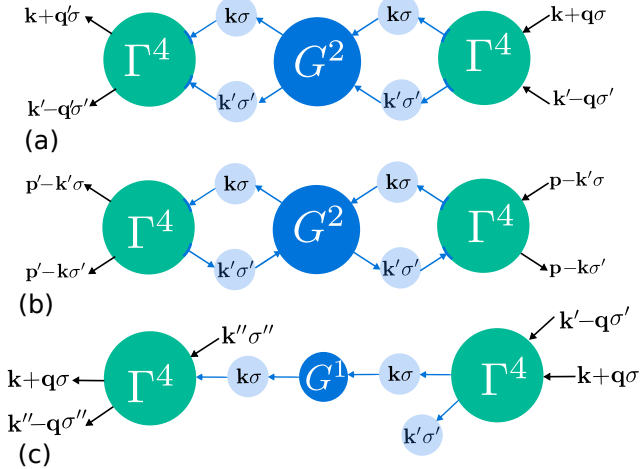


Figure 3.5: The figures represent the 2- and 3-particle vertices that are generated via the unitary decoupling of the state  $\mathbf{k}\sigma$  that block diagonalizes the TEH. (a,b) represent the 2-particle scattering vertices (green circles) generated via the ee/hh and eh/he intermediate configurations respectively of the states  $\mathbf{k}\sigma$  and  $\mathbf{k}'\sigma'$  (light blue circles). These processes involve the intermediate two particle propagator  $G^2$  (dark blue circles) for the  $\mathbf{k}\sigma$  and  $\mathbf{k}'\sigma'$  states. (c) represents the three-particle vertex generated via the sandwiching of the single-particle propagator  $G^1$  in the e/h-configuration of the state  $\mathbf{k}\sigma$  by the ee/hh scattering vertex (for states  $\mathbf{k}\sigma$ ,  $\mathbf{k}'\sigma'$ ) on one side, and the scattering vertex of  $\mathbf{k}\sigma$  with the state  $\mathbf{k}''\sigma''$  on the other side.

The one-step renormalization of the two decoupled blocks in the block-diagonal Hamiltonian can be decomposed generically into number-diagonal and number off-diagonal parts

$$\tilde{H}_{[\mathbf{k}\sigma, \mathbf{k}'\sigma']}^{1_{\mathbf{k}\sigma}} - H_{[\mathbf{k}\sigma, \mathbf{k}'\sigma']}^{1_{\mathbf{k}\sigma}} = \Delta H_{[\mathbf{k}\sigma, \mathbf{k}'\sigma']}^{D, 1_{\mathbf{k}\sigma}} + \Delta H_{[\mathbf{k}\sigma, \mathbf{k}'\sigma']}^{X, 1_{\mathbf{k}\sigma}}, \quad (3.61)$$

containing contributions due to QFs in occupation number of state  $\mathbf{k}\sigma$  that are generated via 2-particle scattering processes given by Fig.(3.4(a,b,d)). The two-particle scattering (off-diagonal) and energy shift terms (diagonal) terms present in  $\Delta H$  (the RHS of eq.(3.61)) possess contributions from three classes of processes. The first two of these are: (i) the ee or hh mediated scattering (Fig.4.2(a)) with occupied/unoccupied configurations of the states  $\mathbf{k}\sigma$  and  $\mathbf{k}'\sigma'$  and involving diagram Fig.3.4(a) and, (ii) the eh or he mediated scattering (Fig.4.2(b)) with only one among the states  $\mathbf{k}\sigma$  and  $\mathbf{k}'\sigma'$  being occupied and involving diagram Fig.3.4(b). This two processes generate one step renormalization of the two particle vertices. The third process mixes ee/hh and eh/he configurations. This process proceeds as follows: first, an ee/hh (or eh/he) pair of  $\mathbf{k}\sigma$  and  $\mathbf{k}'\sigma'$  states are created by the 2-particle vertices Fig.3.4(a) (or (b)) in the intermediate occupation number configuration. Then, that pair is broken due to  $\mathbf{k}\sigma$  scattering with other electronic states like  $\mathbf{k}''\sigma''$ , as shown in Fig.3.4(d). This involves an intermediate single-electron Green's function  $G^1$  (for the state  $\mathbf{k}\sigma$ ), and the result three particle scattering process is shown in Fig.4.2(c).

The processes (i), (ii) and (iii) described above lead to new energy costs and quantum dynamics of various (ee/hh), (eh/he) and higher ( $n$ -particle,  $m$ -hole) composite objects into which the two-electron or electron-hole configurations decay. This can, for instance, be seen from the application

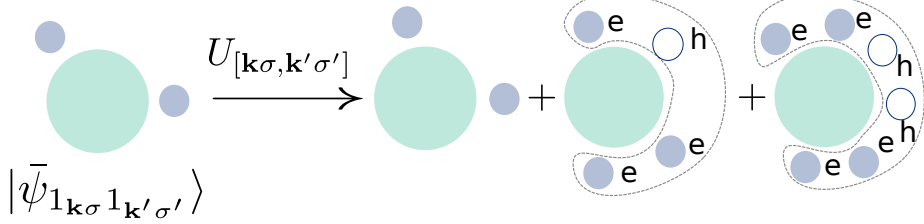


Figure 3.6: The decay channels of the many-body wave function  $|\bar{\psi}_{1_{\mathbf{k}\sigma} 1_{\mathbf{k}'\sigma'}}\rangle$  containing the two-electron excitation configuration.

of the unitary operator on the state space of the ee/hh excitations (eq.(3.54))

$$U_{[\mathbf{k}\sigma, \mathbf{k}'\sigma']} |\bar{\psi}_{1_{\mathbf{k}\sigma} 1_{\mathbf{k}'\sigma'}}\rangle = Z_{pp,2}^{-1} \tilde{c}_{\mathbf{k}\sigma}^\dagger \tilde{c}_{\mathbf{k}'\sigma'}^\dagger U_{[\mathbf{k}\sigma, \mathbf{k}'\sigma']} |\psi\rangle , \quad (3.62)$$

where  $\tilde{c}_{\mathbf{k}\sigma}^\dagger = U_{[\mathbf{k}\sigma, \mathbf{k}'\sigma']} c_{\mathbf{k}\sigma}^\dagger U_{[\mathbf{k}\sigma, \mathbf{k}'\sigma']}^\dagger$  represents the rotated electron creation operators. This rotated operator can be recast in the a cluster expansion as in eq.(3.33) (see Sec.2.4). Then, the cluster expansion of the single creation operator will contain (as before) a 1-electron creation operator and a 2-electron+ 1-hole (a three-fermion) creation operator. Therefore, the cluster expansion of the product of the rotated two e-creation operator will contain a 2-e configuration, a 3-e+1-h configuration and a 4-e+2-h configuration. The 4-e+2-h configuration appears at a next-to-leading order in the bare interaction vertex ( $\Gamma^{4,(N)}$ )<sup>2</sup>, making the 3-e+1-h configuration the leading decay channel for the two-particle excitation (Fig.3.6). This 3-e+1-h excitation is composed of an ee excitation together with an eh excitation, and manifests in the dynamical mixing of the pairs with different net electronic charge. We will now detail this process.

### 3.2.2 Dynamical mixing between ee/hh, eh/he pairs

The feedback of the three-particle scattering process (Fig. 4.2(c)) on ee/hh and eh/he scattering processes (Fig.4.2(a,b)) is an outcome of the non-commutativity between two operators. The first of these is the composite-electron creation operator  $(1 - \hat{n}_{\mathbf{k}\sigma}) c_{\mathbf{k}'\sigma'}^\dagger$ , which is dependent on the occupation of the state  $\mathbf{k}'\sigma'$  (as can be seen from the blue  $\mathbf{k}'\sigma'$  circle adjacent to the green circle in Fig. 4.2(c)), and the second are the ee-hh/eh-he pseudospin operators [413],  $c_{\mathbf{k}\sigma}^\dagger c_{\mathbf{k}'\sigma'}^\dagger$  and  $c_{\mathbf{k}\sigma}^\dagger c_{\mathbf{k}'\sigma'}$ . The leading contributions of the three-particle vertices resulting from Fig. 4.2(c) can then be included into the two- particle vertices (Fig.4.2(a,b)) by performing a rotation in the space of operators described above. This rotation induces a probabilistic superposition between these two kinds of pairs, with  $p$  being the probability coefficient.

The composite-electron operator carries 1 unit each of electronic charge and spin, the ee/hh pair operator has a 2 units of charge and the eh/he pair operator has a 0 unit charge. The *spin-charge hybridized* pseudospin excitations resulting out of the rotation are then given by

$$\begin{aligned} c_{\mathbf{k}\sigma}^\dagger \gamma_{\mathbf{k}'\sigma'}^{p\dagger} &= \sqrt{p} c_{\mathbf{k}\sigma}^\dagger c_{\mathbf{k}'\sigma'}^\dagger + \sqrt{1-p} (c_{\mathbf{k}\sigma}^\dagger c_{\mathbf{k}'\sigma'}) c_{\mathbf{k}'\sigma'}^\dagger , \\ c_{\mathbf{k}\sigma}^\dagger \nu_{\mathbf{k}'\sigma'}^{p\dagger} &= -\sqrt{1-p} c_{\mathbf{k}\sigma}^\dagger c_{\mathbf{k}'\sigma'}^\dagger + \sqrt{p} (c_{\mathbf{k}\sigma}^\dagger c_{\mathbf{k}'\sigma'}) c_{\mathbf{k}'\sigma'}^\dagger , \end{aligned} \quad (3.63)$$

and describe *mixed valence configurations* arising out of electronic correlations. Such mixed valence regimes are known to exist in the heavy fermion systems, where they arise from *quantum fluctuations* between different electron occupation number configurations mixing spin and

charge degrees of freedom [396]. The basis states that are obtained via rotations of the empty configurations of  $\mathbf{k}\sigma$  and  $\mathbf{k}'\sigma'$  are

$$\begin{aligned} |1_{\mathbf{k}\sigma}\psi_{\mathbf{k}'\sigma',p}\rangle &= \sqrt{p}|1_{\mathbf{k}\sigma}1_{\mathbf{k}'\sigma'}\rangle + \sqrt{1-p}|1_{\mathbf{k}\sigma}0_{\mathbf{k}'\sigma'}\rangle \\ |1_{\mathbf{k}\sigma}\psi_{\mathbf{k}'\sigma',p}^\perp\rangle &= \sqrt{1-p}|1_{\mathbf{k}\sigma}1_{\mathbf{k}'\sigma'}\rangle - \sqrt{p}|1_{\mathbf{k}\sigma}0_{\mathbf{k}'\sigma'}\rangle . \end{aligned} \quad (3.64)$$

The spectral decomposition of the spin-charge hybridized pseudospin Green's functions can now be written down in this basis. Here, we present the Green's function corresponding to the configuration  $|1_{\mathbf{k}\sigma}\psi_{\mathbf{k}'\sigma',p}\rangle$

$$G_{[\mathbf{k}\sigma,\mathbf{k}'\sigma'],p}^e(\omega) = \frac{1}{\omega - p\epsilon_{\mathbf{k}\sigma,\mathbf{k}'\sigma'}^{ee} - p'\epsilon_{\mathbf{k}\sigma,\mathbf{k}'\sigma'}^{eh} - \frac{1}{4}V_{\mathbf{k},\mathbf{k}'}^{\sigma\sigma'}}, \quad (3.65)$$

where  $\epsilon_{\mathbf{k}\sigma,\mathbf{k}'\sigma'}^{ee/eh} = 2^{-1}(\tilde{\epsilon}_{\mathbf{k}\sigma} \pm \tilde{\epsilon}_{\mathbf{k}'\sigma'})$  and  $V_{\mathbf{k},\mathbf{k}'}^{\sigma\sigma'}$  represent the ee/hh and eh/he pairwise kinetic energies and pair correlation energy respectively, and the probability  $p' = 1 - p$ . The energy  $\tilde{\epsilon}_{\mathbf{k}\sigma}$  is the electronic dispersion measured from Fermi energy( $E_F$ ), i.e.,  $\tilde{\epsilon}_{\mathbf{k}\sigma} = \epsilon_{\mathbf{k}\sigma} - E_F$ , such that states lying outside/inside Fermi sea has positive/negative energy. The magnitude of the spin-charge hybridization term  $p \equiv p(\omega)$  is determined by maximizing the two-electron Green's function contribution at a given quantum fluctuation scale  $\omega$ (i.e., the eigenvalue of the  $\hat{\omega}$  operator) in the spin-charge hybridized second-quantized basis of the operators  $c_{\mathbf{k}\sigma}^\dagger \gamma_{\mathbf{k}'\sigma'}^{p\dagger}$  and  $c_{\mathbf{k}\sigma}^\dagger \nu_{\mathbf{k}'\sigma'}^{p\dagger}$ . With this set up in place, we will determine the two particle self-energies.

### 3.2.3 Self-energy hybridized by ee-eh pair mixing

The two-electron spin-charge hybridized Green's function  $G_{[\mathbf{k}\sigma,\mathbf{k}'\sigma'],p}^e$  sandwiched between off-diagonal two-particle scattering vertices results in the (ee/hh)/(eh/he) hybridized self-energies. Taking account of the hybridized pseudospin correlation terms present in the renormalized TEH,  $\Delta H_{[\mathbf{k}\sigma,\mathbf{k}'\sigma']}^{D,1_{\mathbf{k}\sigma}}$ , we obtain the two-particle self-energy

$$\hat{\Sigma}_{\mathbf{k}\sigma,\mathbf{k}'\sigma',p}^2(\omega) = \sum_{\mathbf{q} \neq 0} G_{[\mathbf{k}+\mathbf{q}\sigma,\mathbf{k}'-\mathbf{q}\sigma'],p}^e(V_{\mathbf{k}\mathbf{k}'\mathbf{q}}^{\sigma\sigma'})^2 f_{\mathbf{k}\mathbf{k}'\mathbf{q}} \tau_{\mathbf{k}\sigma} \tau_{\mathbf{k}'\sigma'} .$$

Here,  $f_{\mathbf{k}\mathbf{k}'\mathbf{q}}$  (eq.(3.38)) represents the restriction of the scattered states energies as follows:  $\epsilon_{\mathbf{k}'} > \epsilon_{\mathbf{k}+\mathbf{q}}, \epsilon_{\mathbf{k}'-\mathbf{q}} \geq E_F$ . The self-energy  $\hat{\Sigma}_{\mathbf{k}\sigma,\mathbf{k}'\sigma'}(\omega)$  can be decomposed into a two-particle correlation energy shift ( $\hat{\Sigma}_{\mathbf{k}\sigma,\mathbf{k}'\sigma',p}^{2,(0)}$ ) and terms that are dependent on the lattice geometry

$$\hat{\Sigma}_{\mathbf{k}\sigma,\mathbf{k}'\sigma',p}^2 = \hat{\Sigma}_{\mathbf{k}\sigma,\mathbf{k}'\sigma',p}^{2,(0)} + (\hat{\Sigma}_{\mathbf{k}\sigma,\mathbf{k}'\sigma',p}^2 - \hat{\Sigma}_{\mathbf{k}\sigma,\mathbf{k}'\sigma',p}^{2,(0)}) , \quad (3.66)$$

with  $\hat{\Sigma}_{\mathbf{k}\sigma,\mathbf{k}'\sigma',p}^{2,(0)}(\omega)$  given by

$$\Sigma_{\mathbf{k}\sigma,\mathbf{k}'\sigma',p}^{2,(0)}(\omega) = \sum_{\mathbf{q} \neq 0} \frac{C_{\mathbf{k}\sigma,\mathbf{k}'\sigma'}^{(0)}}{\omega - E_{\mathbf{k}\mathbf{k}'\mathbf{q}}^p - \frac{1}{4}V_{\mathbf{k}\mathbf{k}'}^{\sigma\sigma'(0)}} . \quad (3.67)$$

In the above,  $C_{\mathbf{k}\sigma,\mathbf{k}'\sigma'}^{(0)} = N^{-1} \sum_{\mathbf{q}} (V_{\mathbf{k}\mathbf{k}'\mathbf{q}}^{\sigma\sigma'})^2 f_{\mathbf{k}\mathbf{k}'\mathbf{q}}$  and  $V_{\mathbf{k}\mathbf{k}'}^{\sigma\sigma'(0)} = N^{-1} \sum_{\mathbf{q}} V_{\mathbf{k}+\mathbf{q}\mathbf{k}'-\mathbf{q}}^{\sigma\sigma'}$ . The hybridized pairwise-energy is given by  $E_{\mathbf{k}\mathbf{k}'\mathbf{q}}^p = p\tilde{\epsilon}_{\mathbf{k}+\mathbf{q},\mathbf{k}'-\mathbf{q}}^{pp} + p'\tilde{\epsilon}_{\mathbf{k}+\mathbf{q},\mathbf{k}'-\mathbf{q}}^{ph}$ .

We will show below that one part of the zeroth piece of the hybridized pairwise correlation energy  $\Sigma_{\mathbf{k}\sigma,\mathbf{k}'\sigma',p}^{2,(0)}(\omega)$  has a generic logarithmic form in the vicinity of the erstwhile Fermi surface, enabling the observation of a pairing instability of the Fermi surface associated with the formation of two-particle bound condensates.

### 3.2.4 Bound-state formation near the Fermi surface

The  $T = 0$  Fermi distribution functions in  $f_{\mathbf{kk}'\mathbf{q}}$  (eq.(3.38)) cuts off the momentum-space states through a lower cutoff  $\mathbf{q}_{min} = 0$ , and an upper  $\mathbf{q}_{max}$  cutoff given by

$$\text{if } \epsilon_{\mathbf{k}} < \epsilon_{\mathbf{k}'} \rightarrow \mathbf{q}_{max} = \mathbf{k}_F - \mathbf{k} \text{ else } \mathbf{q}_{max} = \mathbf{k}' - \mathbf{k}_F . \quad (3.68)$$

The kinetic energy associated with the wavevectors  $\mathbf{q}_{max}, \mathbf{q}_{min}, \mathbf{k}$  and  $\mathbf{k}'$  measures how close excitations can approach Fermi energy, as seen from the the hybridized kinetic energy  $E_{\mathbf{kk}'\mathbf{q}_{max}}^p$  given by

$$\begin{aligned} E_{\mathbf{kk}'\mathbf{q}_{max}}^p &= p(\epsilon_{\mathbf{k}+\mathbf{k}'-\mathbf{k}_F} - E_F) + (1-p)(E_F - \epsilon_{\mathbf{k}'+\mathbf{k}-\mathbf{k}_F}) , \\ E_{\mathbf{kk}'\mathbf{q}_{min}}^p &= p(\epsilon_{\mathbf{k}} + \epsilon_{\mathbf{k}'} - 2E_F) + (1-p)(\epsilon_{\mathbf{k}} - \epsilon_{\mathbf{k}'}) . \end{aligned} \quad (3.69)$$

Thus, one finds that the constraints on the summation over  $\mathbf{q}'s$  in eq.(3.38) are given by

$$E_F < \epsilon_{\mathbf{k}+\mathbf{q}} < \epsilon_{\mathbf{k}} , \quad E_F < \epsilon_{\mathbf{k}'-\mathbf{q}} < \epsilon_{\mathbf{k}'} . \quad (3.70)$$

Using the definition of  $\mathbf{q}_{max}$ , we then write the summation eq.(3.67) as

$$\Sigma_{\mathbf{k}\sigma,\mathbf{k}'\sigma',p}^{2,(0)}(\omega) = \sum_{\substack{E_{\mathbf{kk}'\mathbf{q}_{min}}^p=0}}^{E_{\mathbf{kk}'\mathbf{q}_{max}}^p} \frac{C_{\mathbf{k}\sigma,\mathbf{k}'\sigma'}^{(0)} g_{\mathbf{kk}'\mathbf{q}}}{\omega - E_{\mathbf{kk}'\mathbf{q}}^p - \frac{1}{4}V_{\mathbf{kk}'}^{\sigma\sigma'(0)}} , \quad (3.71)$$

where  $g_{\mathbf{kk}'\mathbf{q}} = D(\epsilon_{\mathbf{k}+\mathbf{q}})\theta(\epsilon_{\mathbf{k}'} - \epsilon_{\mathbf{k}}) + D(\epsilon_{\mathbf{k}'-\mathbf{q}})\theta(\epsilon_{\mathbf{k}} - \epsilon_{\mathbf{k}'})$ . The density of states (DOS)  $D(E)$  is defined as usual:  $D(E) = \sum_{\mathbf{k}} \delta(E - \epsilon_{\mathbf{k}})$ . Writing the DOS about the Fermi surface as  $D(E) = D(E_F) + D(E) - D(E_F)$ , we have

$$\Sigma_{\mathbf{k}\sigma,\mathbf{k}'\sigma',p}^{2,(0)}(\omega) = \sum_{\substack{E_{\mathbf{kk}'\mathbf{q}_{min}}^p=0}}^{E_{\mathbf{kk}'\mathbf{q}_{max}}^p} \frac{C_{\mathbf{k}\sigma,\mathbf{k}'\sigma'}^{(0)} D(E_F)}{\omega - E_{\mathbf{kk}'\mathbf{q}}^p - \frac{1}{4}V_{\mathbf{kk}'}^{\sigma\sigma'(0)}} + \sum_{\substack{E_{\mathbf{kk}'\mathbf{q}_{min}}^p=0}}^{E_{\mathbf{kk}'\mathbf{q}_{max}}^p} \frac{C_{\mathbf{k}\sigma,\mathbf{k}'\sigma'}^{(0)} (g_{\mathbf{kk}'\mathbf{q}} - D(E_F))}{\omega - E_{\mathbf{kk}'\mathbf{q}}^p - \frac{1}{4}V_{\mathbf{kk}'}^{\sigma\sigma'(0)}} . \quad (3.72)$$

The first summation in eq.(3.72) gives a logarithm contribution to the 2-particle self-energy

$$\begin{aligned} \Sigma_{\mathbf{k}\sigma,\mathbf{k}'\sigma',p}^{2,(0)}(\omega) &\approx \frac{C_{\mathbf{k}\sigma,\mathbf{k}'\sigma'}^{(0)}}{E_{\mathbf{kk}'\mathbf{q}_{min}}^p - E_{\mathbf{kk}'\mathbf{q}_{max}}^p} D(E_F) \\ &\times \log \left( 1 + \frac{E_{\mathbf{kk}'\mathbf{q}_{min}}^p - E_{\mathbf{kk}'\mathbf{q}_{max}}^p}{\omega - \frac{1}{4}V_{\mathbf{kk}'}^{\sigma\sigma'}} \right) . \end{aligned} \quad (3.73)$$

This calculation shows that  $\Sigma_{\mathbf{k}\sigma,\mathbf{k}'\sigma',p}^{2,(0)}(\omega)$  has a logarithmic non-analyticity at  $\omega \rightarrow V_{\mathbf{kk}'}^{\sigma\sigma'}$  and  $E_{\mathbf{kk}'\mathbf{q}_{min}}^p = E_{\mathbf{kk}'\mathbf{q}_{max}}^p$ . The leading contribution to this non analyticity exists for total momenta  $\mathbf{k} + \mathbf{k}'$  pairs whose energy is resonant with the Fermi energy  $E_F$ , satisfying the condition

$$E_{\mathbf{kk}'\mathbf{q}_{max}}^p = 0 \equiv \mathbf{k} + \mathbf{k}' = \mathbf{k}_F + \mathbf{k}'_F , \quad (3.74)$$

where  $\mathbf{k}'_F$  is a general Fermi wave vector not necessarily the same as  $\mathbf{k}_F$ . Such a logarithmic term signals an instability of the Fermi surface via a four-fermion interaction with the above pair-momentum constraint (eq.(3.74)). As mentioned earlier, this is a generalized version of Cooper's pairing instability [440] for attractive interactions on a circular Fermi surface. We remind the reader that the *dynamical spectral weight transfer* along channels such a logarithmic instability is observed in the decay of the two-particle excitation (Fig.3.6) from the action of the unitary operator on the two-particle excitation subspace (eq.(3.62)).

### 3.2.5 Bound-state condensation, Friedel's phase shift and RG flows

We will now show that the formation of pairwise spin-charge hybridized composites is accompanied by a change in Luttinger's volume [431, 276] via the appearance of surfaces of Luttinger zeros. This change in Luttinger volume is quantified by the Freidel-Levinson phase shift [448, 278], and can be seen naturally through a scattering-matrix formulation of the above problem. The emergence of pseudospin pairing will, in general, be restricted to a energy-momentum shell  $\Lambda^*$  around the erstwhile Fermi surface of the non-interacting problem, where  $\Lambda^*$  is the normal displacement from the Fermi sea (described in text below eq.(3.45)). The  $\Lambda^*$  momentum-space scale ought to arise from a stable fixed point theory attained via renormalization group procedure implemented on the microscopic model. The RG procedure we have detailed in the previous chapter can be used to reach a final stable fixed point theory owing to a frequency-dependent self-energy feedback in the RG flow equations (eq.(2.48)), leading to the emergence of the momentum scale  $\Lambda^*$ .

From the cluster- and spectral- decompositions of the Hamiltonian RG relation  $H_{(j-1)} = U_{(j)} H_{(j)} U_{(j)}^\dagger$  and state space renormalization  $|\Psi_{(j-1)}\rangle = U_{(j)} |\Psi_{(j)}\rangle$ , the 4-point vertex flow equation (using eq.(2.47)) and the 2-particle excitation flow equations (using eq.(3.54)) can be obtained. The cluster expansion of the excitations about the momentum-space number-diagonal configurations is given by

$$|\Psi_{(j)}^i\rangle = \sum_{n=1}^{a_{max}^j} c_\alpha^{n,(j)} \tilde{c}_\alpha^\dagger |\Psi_{D,(j)}^i\rangle , \quad (3.75)$$

here  $\alpha$  is a set of electronic state labels which are in occupied configuration, and  $c_\alpha^{n,(j)}$  is the coefficient of the  $n$ -body cluster. Using eq.(3.75) with the cluster expansion of the Hamiltonian eq.(2.31) at every step of the RG, we find the RG flow equations for the 4-point vertex ( $\Gamma_{\alpha\beta}^4$ ) and the coefficient of the 2-body cluster ( $c_\alpha^2$ ) as

$$\begin{aligned} \Delta\Gamma_{\alpha\beta}^{4,(j)}(\omega^i) &= \sum_{p_1,p_3}^{2a_j^{max}} \sum_{\gamma,\gamma'} \{\Gamma_{\alpha\gamma}^{p_1} G_{\gamma\gamma'}^{2p_2} \Gamma_{\gamma'\beta}^{p_3}\}^{(j)}(\omega^i), \\ \Delta c_\alpha^{2,(j)} &= \frac{3}{4} c_\alpha^{2,(j)} + \frac{1}{2} \left[ G_{\beta\beta'}^{4,(j)} \Gamma_{\beta\alpha}^{4,(j)} c_\beta^{2,(j)} + \frac{1}{2} \Delta\Gamma_{\alpha\beta}^{4,(j)} c_\beta^{2,(j)} \right]. \end{aligned} \quad (3.76)$$

At quantum fluctuation energy scales ( $\omega$ ) in the regime

$$\sum_{i=1}^n \epsilon_{l_i} > \epsilon_{\mathbf{k}\sigma,\mathbf{p}'\sigma'}^{ee/eh} > \omega > \epsilon_{\mathbf{k}\sigma,\mathbf{p}\sigma'}^{ee/eh}, (\mathbf{k}\sigma, \mathbf{p} - \mathbf{k}\sigma') , \quad (3.77)$$

the signature of the Green's function  $G_{\beta\beta'}^4$  (eq.(2.48)) is negative, leading to the RG irrelevance of all vertices greater than the 4-point vertex:  $\Gamma^{2n}$ ,  $n > 2$ . The RG flow equations can, therefore, be simplified to contain only the 4-point vertices with pairing-momentum  $\mathbf{p}$ . Subsequently, the two-particle Green's function can be resolved in the spin-charge hybridized mixed valence basis (eq.(3.65)). Concomitantly, the leading contributor to the state-space renormalization (eq.(3.76)) are the two-electron/electron-hole *pseudospins* for  $\mathbf{p}$  net momentum, as  $\Delta\Gamma_{\mathbf{p}}^{4,(j)}$  has relevant contributions only from 4-point vertices. As the denominator in the hybridized ee/eh Green's function (eq.(3.65)) within the flow equations eq.(3.76) vanishes, the quantum fluctuation energy scale  $\omega$  obtains the exact eigenvalue of the paired electronic states, and we attain a stable fixed point pairing force pseudospin Hamiltonian[445] along with its renormalized Hilbert space. This will be seen in more detail in a accompanying work for the effective Hamiltonians reached from the four-fermion interacting model eq.(3.19).

In the vicinity of the Fermi energy, these pseudospin pairs condense independently along every pairwise normal directions  $(\hat{s}, \hat{s}')$ , as seen from the constraint in eq.(3.74). Following this process for every normal direction  $\hat{s}$ , and at the quantum fluctuation scale  $\omega$ , a momentum scale  $\Lambda^*(\omega, \hat{s})$  is generated at the stable fixed point. This corresponds to the low-energy window formed around the Fermi surface (FS) associated with the condensation phenomenon. Using the unitary matrix connection to the scattering matrix[180], we can define the T-matrix at the final fixed point theory. This T-matrix satisfies the generalized optical theorem [449], as shown in the appendix. We resolve this T-matrix within the low-energy window in the ee/eh mixed-valence configuration of pairwise states  $(\mathbf{k}, \mathbf{k}')$  (eq.(3.64)) along pairwise normal directions  $(\hat{s}, \hat{s}')$  at a distance  $\Lambda$  from the FS fulfilling constraint eq.(3.74). The backscattering T-matrix thus obtained has the form

$$\begin{aligned} T_{\hat{s}, \hat{s}' \rightarrow -(\hat{s}, \hat{s}')}^\Lambda(\omega) &= i \frac{V_{\hat{s}, \hat{s}' \rightarrow -(\hat{s}, \hat{s}')}^{\sigma\sigma', \text{eff}}(\omega)}{\omega - E_{\mathbf{kk}'}^p - \Sigma_{ss'}^{2,(0)}(\omega)}, \\ T_{\hat{s}, \hat{s}' \rightarrow -(\hat{s}, \hat{s}')}^\Lambda(\omega) &= -(T_{\hat{s}, \hat{s}' \rightarrow -(\hat{s}, \hat{s}')}^\Lambda(\omega))^*, \quad \Lambda < \Lambda^*(\omega, \hat{s}), \end{aligned}$$

where we have carried out a spectral-decomposition of the unitary operator. The backscattering diagrams are present in  $H$  if  $\mathbf{k}_{F,\hat{s}} + \mathbf{k}_{F,\hat{s}'} = \mathbf{k}_{F,-\hat{s}} + \mathbf{k}_{F,-\hat{s}'}$ , or there is an offset in the pair-momentum equal to a reciprocal-lattice vector. Within a  $2 \times 2$  subspace of four fermionic states (but with two states occupied), i.e.,  $|1_{\hat{s}\sigma} 1_{\hat{s}'\sigma'} 0_{-\hat{s}\sigma} 0_{-\hat{s}'\sigma'}\rangle$ ,  $|0_{\hat{s}\sigma} 0_{\hat{s}'\sigma'} 1_{-\hat{s}\sigma} 1_{-\hat{s}'\sigma'}\rangle$ , the T-matrix can be written as

$$\hat{T}_{\hat{s}, \hat{s}' \rightarrow -(\hat{s}, \hat{s}')}^\Lambda = \begin{pmatrix} 0 & T_{\hat{s}\hat{s}' \rightarrow -\hat{s}-\hat{s}'} \\ T_{\hat{s}\hat{s}' \rightarrow -\hat{s}-\hat{s}'}^* & 0 \end{pmatrix}.$$

In the eigenbasis of bonding (+) and antibonding(-) states, the T matrix elements are given by

$$\hat{T}_{\hat{s}\hat{s}', -\hat{s}-\hat{s}'}^\pm(\omega) = \pm \frac{1}{2} \left| \frac{V_{s,s' \rightarrow -(\hat{s}, \hat{s}')}^{\sigma\sigma', \text{eff}}(\omega)}{\omega - E_{\mathbf{kk}'}^p - \Sigma_{ss'}^{2,(0)}(\omega)} \right|. \quad (3.78)$$

A similar T-matrix calculation for the Kondo problem is presented in Ref.[395]. The change in the Luttinger volume  $\Delta N$  [278, 431] is known to be connected to the Friedel's phase shift. In the same way, the change in the partial Luttinger volume for every normal  $\hat{s}$  defined in Theorem 1

can be connected to the net Friedel's phase shift for states within the low energy window along a normal  $\hat{s}$ [88]

$$N_{\hat{s}} - \bar{N}_{\hat{s}} = -\frac{i}{\pi} \sum_{\Lambda < \Lambda^*(\omega, \hat{s})} \text{Tr} \ln S_{\hat{s}, \hat{s}' \rightarrow -(\hat{s}, \hat{s}')}^\Lambda(\omega) , \quad (3.79)$$

where the scattering matrix for the paired states

$$S_{\hat{s}, \hat{s}' \rightarrow -(\hat{s}, \hat{s}')}^\Lambda = 1 + iT_{\hat{s}, \hat{s}' \rightarrow -(\hat{s}, \hat{s}')}^\Lambda = e^{i\hat{\delta}_{\hat{s}\hat{s}'}^\Lambda} \quad (3.80)$$

is written in terms of the T-matrix. The opposite signatures and equal magnitudes of the T matrix elements in eq.(3.78) leads to a net phase shift  $\delta_{\Lambda, \hat{s}, \hat{s}', +} + \delta_{\Lambda, \hat{s}, \hat{s}', -} = 0$  or  $2\pi$ , where  $2\pi$  originates from summing the phases  $\delta_{\Lambda, \hat{s}, \hat{s}', +} = \theta$  from a given Riemann sheet and  $2\pi - \theta$  from the next Riemann sheet. These phase shifts are the eigenvalues of the phase operator  $\hat{\delta}_{\hat{s}\hat{s}'}^\Lambda$ . The net phase shift leads to a integer change of 2 in the Luttinger volume for every pair of electrons at a given distance  $\Lambda$  (and involving the pair of normal directions  $(\hat{s}, \hat{s}')$ ). The change in partial Luttinger sum is given by

$$\Delta N_{\hat{s}} = N_{\hat{s}} - \bar{N}_{\hat{s}} = \sum_{\Lambda \leq \Lambda^*(\omega, \hat{s})} 2 , \quad (3.81)$$

such that half of  $\Delta N_{\hat{s}}$  counts the number of bound states formed along the normal direction  $\hat{s}$ . This patch of Luttinger zeros along the normal direction  $\hat{s}$  can also be seen through the sensitivity towards boundary conditions by the adiabatic application of a twist operator that affects electronic states along a normal direction (eq.(3.51)) within the fixed point low-energy window. The change in partial Luttinger volume is given by the non-commutativity between twist and translation operator ( $T$ )

$$\Delta N_{\hat{s}} = \frac{i}{\pi} \text{Tr} \ln(T \hat{O}_{\hat{s}, \Lambda^*}^L T^\dagger \hat{O}_{\hat{s}, \Lambda^*}^{\dagger L}) , \quad (3.82)$$

offering an equivalent topological characteristic observed through an argument involving invariance under a large gauge transformation.  $L$  is the total number of states along  $\hat{s}$ . Summing up this partial Friedel's phase shift for all pair of normal directions, we get the change in Luttinger volume [88],  $\Delta N = \sum_{\hat{s}} \Delta N_{\hat{s}}$ . In this way, we find a non-perturbative signature of a connected Luttinger surface of zeros [427] describing a gapped phase in a strongly correlated system of electrons. Further note that in Sec. 2.5 of the previous chapter, we had shown that the pairing of electrons into bound states mitigates the Fermion sign present in the electronic model. Via URG, the Hilbert space morphs from an fermionic Hilbert space to a  $SU(2)$  spin-1/2 Hilbert space. The mechanism outlined here displays how a collection of 1+1D chiral conformal field theories (CFTs) composing a Fermi surface [436] breaks down due to the emergent momentum scale generated via the RG. In chapters following this one, we have performed the RG treatment on various microscopic strongly correlated electronic models [183], with a view towards obtaining simpler effective models from the stable fixed points of the RG flow. In some of these effective models, we will demonstrate the existence of (i) bound state formation with Luttinger zero surfaces, and (ii) two-electron one-hole composite degrees of freedom about a gapless Fermi surface which preserve the Luttinger volume.

# Chapter 4

## Scaling theory for Mott-Hubbard transitions - I : $T = 0$ phase diagram of the 1/2-filled Hubbard model

In this chapter, we employ the URG formalism introduced in chapter 2 to develop a scaling theory for the 2D Hubbard model on a square lattice. The phenomenology and predictions based on this model have been briefly reviewed in Sec1.2.1 of chapter 1. In Sec.4.1, we present the model Hamiltonian and renormalization group scheme. In Section4.2, we present the marginal Fermi liquid as the parent metal of the Mott insulating phase of the 2D Hubbard model at half-filling. We follow this in Section4.3 by detailing the journey through the pseudogap phase at half-filling, and the nature of the Mott-Hubbard MIT. In Section4.4, we present some features of topological order for the insulating Mott liquid phase obtained from the RG, as well as benchmark some of its properties with the numerical results obtained from Refs. [49, 77, 450]. We also demonstrate how a RG relevant symmetry-breaking perturbation leads to the Néel antiferromagnetic Mott state. Finally, we conclude our presentation in Section 5.4 with a detailed discussion of the relevance of our work to Mott insulating systems, and by presenting future perspectives. Further details of the derivations of various RG relations are presented in the appendices.

### 4.1 The model and the RG scheme

We analyze the Hubbard model on the two-dimensional square lattice with nearest neighbour hopping (strength  $t$ ) and on-site repulsion (strength  $U_0$ )

$$\hat{H} = \sum_{\mathbf{k},\sigma} (\epsilon_{0\mathbf{k}} - \mu_{eff}) c_{\mathbf{k}\sigma}^\dagger c_{\mathbf{k}\sigma} + U_0 \sum_{\mathbf{r}} \hat{\tau}_{\mathbf{r}\uparrow} \hat{\tau}_{\mathbf{r}\downarrow}, \quad (4.1)$$

where  $c_{\mathbf{k}\sigma}^\dagger / c_{\mathbf{k}\sigma}$  is the electron creation/annihilation operator with wave-vector  $\mathbf{k}$  and spin  $\sigma$ ,  $\hat{n}_{\mathbf{r}\sigma} = \hat{n}_{\mathbf{r}\sigma} - \frac{1}{2}$ ,  $\hat{n}_{\mathbf{r}\sigma} = c_{\mathbf{r}\sigma}^\dagger c_{\mathbf{r}\sigma}$  is the number operator at lattice site  $\mathbf{r} = j_1\hat{x} + j_2\hat{y}$ , and  $\epsilon_{0\mathbf{k}}$  is the bare dispersion. The effective chemical potential,  $\mu_{eff} = \mu - \frac{U_0}{2}$ , accounts for the energy imbalance between doublons (doubly occupied sites) and holons (empty sites). The hopping

term is clearly diagonal in momentum-space, with a dispersion for the square lattice given by  $\epsilon_{0\mathbf{k}} = -2t(\cos k_x + \cos k_y)$ . On the other hand, the Hubbard repulsion term is diagonal in real-space, i.e., it contains off-diagonal elements in the momentum basis causing fluctuations in the dispersion ( $\Delta(\epsilon_{\mathbf{k}\sigma}\hat{n}_{\mathbf{k}\sigma})$ ). Below, we will reveal the effects of such quantum fluctuations via a Hamiltonian renormalization group (RG) method. Further, we will study the Mott metal-insulator transition (MIT) at 1/2-filling, i.e., by setting the doublon-holon chemical potential  $\mu_{eff}^0 = \mu - \frac{U_0}{2} = 0$  [451, 452].

#### 4.1.1 RG via the decoupling of single-particle occupation states

In this section, we design the RG scheme that implements the algorithm shown in Fig. 1.2 for decoupling single-particle Fock states. We will define shells that are isogeometric to the non-interacting Fermi surface (see Fig. 5.1.1). This involves identifying the Fermi surface of the half-filled tight-binding model on the 2d square lattice at  $E_F = \mu_{eff}^0 = 0$ . The Fermi surface (FS) is then defined as a collection of unit normal wave-vectors  $\hat{s} = \nabla\epsilon_{\mathbf{k}}/|\nabla\epsilon_{\mathbf{k}}||_{\epsilon_{\mathbf{k}}=E_F}$ . The  $C_4$  symmetric square FS also has four van-Hove singularities along the antinodal (AN) directions: two along  $\mathbf{Q}_y = (0, \pi)$  and another two along  $\mathbf{Q}_x = (\pi, 0)$  (Fig. 5.1.1). The nodal (N) directions are given by the bisectors:  $\mathbf{Q} = \mathbf{Q}_x + \mathbf{Q}_y$  and  $\mathbf{Q}_{\perp} \perp \mathbf{Q}$ . The normal vectors are defined as  $\hat{s} = \mathbf{Q}/|\mathbf{Q}|$  on one quadrant of the square Fermi surface, which on crossing the van-Hove to the other arm becomes orthogonally oriented to  $\hat{s}$ :  $\hat{s}_{\perp} = \mathbf{Q}_{\perp}/|\mathbf{Q}_{\perp}|$ ,  $\hat{s}_{\perp} \cdot \hat{s} = 0$ .

The normal translations of the Fermi surface wave-vectors  $\mathbf{k}_{\Lambda, \hat{s}} = \mathbf{k}_F(\hat{s}) + \Lambda\hat{s}$  represent *isogeometric curves* displaced parallel by distance  $\Lambda$  from the FS (i.e., the black lines parallel to the FS shown in Fig. 5.1.1(a)). Importantly, the anisotropy of the dispersion term with  $\hat{s}$  on the Fermi surface ( $k_{Fx} + k_{Fy} = \pi$ ), together with the non-commutativity of the hopping and onsite  $U$  term, leads to a variety of quantum fluctuation scales ranging from the anti-nodes (AN:  $k_{Fx} = 0$ ) to the nodes (N:  $k_{Fx} = \pi/2$ ). Given the redefinition of the electronic wave vectors in terms of  $\Lambda$  and  $\hat{s}$ , we will devote a few lines to describe the labelling scheme. States are ordered in terms of distances  $\Lambda_N > \dots > \Lambda_j > \Lambda_{j-1} > \dots > 0$ , where  $\Lambda_N$  lies near the Brillouin zone (BZ) edge and the smallest  $\Lambda$  is proximate to the Fermi surface. Following this construction, the electronic states are labelled equivalently as  $|j, l\rangle \equiv |\mathbf{k}_{\Lambda_j, \hat{s}}\sigma\rangle (l = \{\hat{s}, (\sigma = \uparrow, \downarrow)\})$ . By employing unitary transformations iteratively, the RG disentangles electronic states in shells, starting from near the BZ edge and scaling towards  $E_F$ . Thus, at step  $j$ , all the states on the curve labelled by  $\Lambda_j$  are disentangled via a unitary rotation  $U_{(j)}$ . The resulting Hamiltonian  $H_{(j-1)} = U_{(j)}H_{(j)}U_{(j)}^\dagger$  is off-diagonal only for states with  $\Lambda < \Lambda_j$ . The momentum-space representation of the Hubbard term contains four-fermionic off-diagonal scattering pieces coupling states between isogeometric curves (longitudinal scattering), and between normal directions  $\hat{s}$  (tangential scattering). Thus, the renormalization group (RG) flow takes place via the decoupling of an isogeometric curve ( $\Lambda_j$ ) farthest from the FS at every step by using a product of unitary operations ( $U_{(j)}$ ), itself a product of unitary operators  $U_{(j,l)}$  that decouple individual states  $(j, l) \equiv (\mathbf{k}_{\Lambda_j, \hat{s}}, \sigma)$  along a given normal  $\hat{s}$

$$U_{(j)} = \prod_{l=(\hat{s},\sigma)} U_{(j,l)}, \quad U_{(j,l)} = \frac{1}{\sqrt{2}}[1 + \eta_{(j,l)}^\dagger - \eta_{(j,l)}] . \quad (4.2)$$

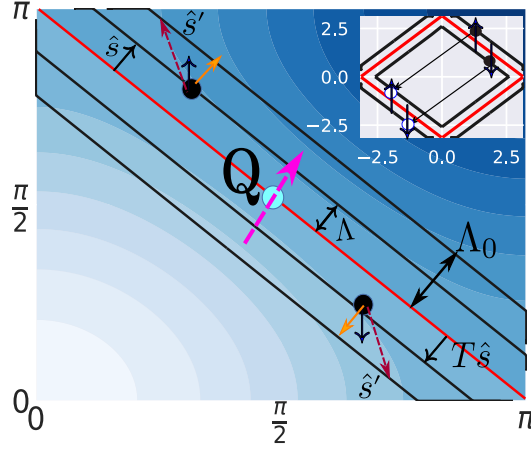


Figure 4.1: (Colour Online)Schematic representation of shells (black lines parallel to and formed around the FS (red line)) of states that are integrated out from first quadrant of Brillouin zone (BZ):  $0 < k_x, k_y < \pi$ . The black dots represents a pair of opposite spin electronic states.  $\hat{s}$  represents the direction normal to F, the orange arrows represent the forward scattering process.  $T\hat{s} = (s_y, s_x)$  represents the orientation vector symmetrically placed about the nodal vector  $\mathbf{Q}$ (pink arrow). The pair of brown dashed lines shows tangential scattering from  $\hat{s}, T\hat{s} \rightarrow \hat{s}', T\hat{s}'$ . Inset (top right): Umklapp scattering of electron pairs.

Here  $\eta_{(j,l)}$  is defined as ( $n = (j, l)$ ,  $m = (j, l + 1)$ ),

$$\eta_{(n)} = \frac{1}{\hat{\omega}_{(m)} - Tr_n(H_{(m)}^D(1 - \hat{n}_n))(1 - \hat{n}_n)} Tr_n(c_n^\dagger H_{(m)})c_n . \quad (4.3)$$

and  $\eta_{(j,l)}^\dagger$  is the hermitian conjugate, and they fulfill the algebra  $\{\eta_{(j,l)}^\dagger, \eta_{(j,l)}\} = 1$ ,  $[\eta_{(j,l)}^\dagger, \eta_{(j,l)}] = 2\hat{n}_{(j,l)} - 1$  presented in eq.(2.22), eq.(2.23).

The flow equation for the Hamiltonian is then given by

$$H_{(j-1)} = U_{(j)} H_{(j)} U_{(j)}^\dagger , \quad (4.4)$$

where the count of RG step  $j$  involves a countdown from  $N$  (the number of isogeometric curves from the BZ boundaries to FS), such that the bare Hamiltonian  $H \equiv H_{(N)}$ . In a later section, we show the method for obtaining the vertex RG flow equations using the form of the rotated Hamiltonian like that obtained in eq.2.21.

### 4.1.2 Fermi surface instabilities

As we will now see, the perfect nesting of the square FS (Fig.5.1.1) indicates a putative instability of the FS via Umklapp back-scattering of a electronic pair . By summing over the elements of the transition matrix ( $T(\Omega)$ ) for the Umklapp back-scattering processes we obtain the second order  $T$ -matrix element connecting electronic states asymmetrically positioned about FS: one at

distance  $\Lambda$  along  $\hat{s}$  outside FS other at distance  $-\Lambda - \delta$  along  $\hat{s}'$  inside FS,

$$\lim_{\Omega \rightarrow 0} T_{\hat{s}, \hat{s}' \rightarrow -\hat{s}, -\hat{s}'}^{(2)}(\Omega) = \frac{1}{vol^2} \lim_{\Omega \rightarrow 0} \sum_{\Delta\epsilon_{\Lambda,\delta}^{pair}(\hat{s})}^W \frac{U_0^2}{\Omega - \Delta\epsilon_{\Lambda,\delta}^{pair}(\hat{s}, \hat{s}')} = \frac{U_0^2}{(vol)^2 W} \ln \frac{W}{\Delta\epsilon_{\Lambda,\delta}^{pair}(\hat{s}, \hat{s}')}. \quad (4.5)$$

Here  $W$  is the bandwidth,  $vol$  is the system volume and  $\Delta\epsilon_{\Lambda,\delta}^{pair}(\hat{s}, \hat{s}')$  is the net pair energy difference between the initial configuration i.e. a pair of electrons one above another below FS in the same quadrant and the scattered configuration i.e. a similar pair in the opposite quadrant. For pairs positioned symmetrically about the nodal vector ( $\mathbf{Q}$ ,  $\hat{s}' = T\hat{s} = (s_y, s_x)$ ) and around the FS ( $\delta = 0$ ) the difference in pair energy  $\Delta\epsilon_{\Lambda,\delta}^{pair} \rightarrow 0$  vanishes due to nesting in a square Fermi surface. Resultingly  $T$ -matrix has a leading order log divergence as  $\lim_{\delta \rightarrow 0} \Delta\epsilon_{\Lambda,\delta}^{pair} \rightarrow 0$ . This indicates that the *resonant pairs* ( $\delta = 0, \hat{s}' = T\hat{s}$ ) are more susceptible to instability compared to their assymetric counterparts, and will therefore dominate the physics of the Mott insulating state at low energies ( $\Omega \rightarrow 0$ ). As in the Kondo problem [301], such a log divergence in the  $T$ -matrix signals the need for a RG treatment of the FS instability.

A similar instability can be shown due to the *spin backscattering* process of opposite spin electron pairs ( $\uparrow$ )-hole ( $\downarrow$ ) across the FS. It is important to note that the  $T$ -matrix elements are sensitive to Fermi surface geometry via dependence of  $\Delta\epsilon_{\Lambda,\delta}^{pair}(\hat{s}, \hat{s}')$  on the normal  $\hat{s}$  to the FS. This results in *electronic differentiation*: a range of quantum fluctuation scales associated with the instabilities across the FS (i.e., from the AN to the N), one for every  $\hat{s}$  normal to Fermi surface. In the next section, we will treat these instabilities via the Hamiltonian Renormalization group procedure eq.4.4, as well as identify the parent interacting metallic state of the Mott problem at 1/2-filling. We will also see that electronic differentiation leads to the nodal-antinodal dichotomy at the heart of the pseudogap phenomenon observed in doped Mott insulators [325, 351, 5].

#### 4.1.3 RG flow equations for Longitudinal and Tangential scattering processes

In keeping with the discussions in the earlier section, we treat the Fermi surface instabilities arising from the two-particle scattering processes via the unitary operator based Hamiltonian RG formalism. Starting from the form of the unitary RG flow equation eq.(4.4) we can obtain the RG flow equation for the two and three particle scattering vertices. Below we describe the steps leading to the RG flow equations.

In the figure Fig.4.2(a,b) we depict the primary renormalization group contributions to the two particle vertices where the intermediate high energy state is a pair of electrons or a electron-hole pair respectively. Fig.4.2(c) depicts mixing between the various electron-electron and electron-hole scattering terms leading to three-particle scattering vertices. This is an outcome of the non-commutativity between the composite electron creation operator  $(1 - \hat{n}_{\mathbf{k}\sigma})c_{\mathbf{k}'\sigma'}^\dagger$  and the ee/eh pseudospin pair operators[413]  $c_{\mathbf{k}\sigma}^\dagger c_{\mathbf{k}'\sigma'}^\dagger$  and  $c_{\mathbf{k}\sigma}^\dagger c_{\mathbf{k}'\sigma'}$ .

In order to incorporate the effect of off-diagonal three particle scattering vertices into the two particle vertices we perform a  $\omega$ -dependent rotation,  $\tan^{-1}(\sqrt{\frac{1-p}{p}})$ , in the space of the electron/hole

configurations of  $(\mathbf{k}', -\sigma) = (j, l')$ , where  $\mathbf{k}' = \mathbf{k}_{-\Lambda_j + \delta, T\hat{s}}$ .

$$\begin{aligned} |\uparrow\rangle &:= |1_{\mathbf{k}\sigma}\psi_{\mathbf{k}'-\sigma}\rangle = \sqrt{p}|1_{\mathbf{k}\sigma}1_{\mathbf{k}'-\sigma}\rangle + \sqrt{1-p}|1_{\mathbf{k}\sigma}0_{\mathbf{k}'-\sigma}\rangle, \\ |\downarrow\rangle &:= |0_{\mathbf{k}\sigma}\psi_{\mathbf{k}'-\sigma}^\perp\rangle = \sqrt{1-p}|1_{\mathbf{k}\sigma}0_{\mathbf{k}'-\sigma}\rangle - \sqrt{p}|0_{\mathbf{k}\sigma}0_{\mathbf{k}'-\sigma}\rangle. \end{aligned} \quad (4.6)$$

The state  $|\mathbf{k}_{-\Lambda_j, T\hat{s}}\rangle$  is the reflected partner of the state  $|\mathbf{k}_{\Lambda_j, \hat{s}}\rangle$  about the nodal direction  $N$  and constitutes a resonant pair. The momentum off-resonance  $\delta$  in wavevector  $\mathbf{k}' = \mathbf{k}_{-\Lambda_j + \delta, T\hat{s}}$  accounts for the asymmetric location of the state about the  $N$  direction. By projecting the operator RG flow equations for the forward and backward scattering vertices's (4.A) in the spin/charge hybridized configurations  $|\uparrow\rangle$  and  $|\downarrow\rangle$  we obtain the coupling RG equations for the charge  $((V_c/K_c)_l^{(j)})$  and spin  $((V_s/K_s)_l^{(j)})$  type scattering vertices's ( $p_+ = p = 1 - p_-$ )

$$\frac{\Delta V_{c/s,l}^{(j)}(\delta)}{\Delta \log \frac{\Lambda_j}{\Lambda_0}} = \pm \frac{p_\pm(V_{c/s,l}^{(j)}(\delta))^2}{e^{i\gamma_l^\pm}|G_{j,l}^{p,\pm}|^{-1} - \frac{V_{p,l}^{(j)}(\delta)}{4}}, \quad \frac{\Delta K_{c/s,l}^{(j)}(\delta)}{\Delta \log \frac{\Lambda_j}{\Lambda_0}} = \pm \frac{p_\pm(K_{c/s,l}^{(j)}(\delta))^2}{e^{i\gamma_l^\pm}|G_{j,l}^{p,\pm}|^{-1} - \frac{K_{p,l}^{(j)}(\delta)}{4}}, \quad (4.7)$$

where  $V_{p,l}^{(j)} = p_+V_{c,l}^{(j)} - p_-V_{s,l}^{(j)}$  and  $K_{p,l}^{(j)} = p_+K_{c,l}^{(j)} - p_-K_{s,l}^{(j)}$ . The Green's function  $[G_{j,l}^{p,\pm}]^{-1}$  is defined as

$$[G_{j,l}^{p,\pm}]^{-1} = [\omega - p_+ \left( \frac{\epsilon_{j,l} + \epsilon_{j,l'}}{2} - \Delta\mu_{eff} \right) - p_- \frac{\epsilon_{j,l} - \epsilon_{j,l'}}{2}]^{-1} \quad (4.8)$$

where a special value for  $p$  is chosen such that  $G_{j,l}^{p,\pm}$  is maximized,

$$p := p' \text{ s.t. } G_{j,l}^{p,\pm} = \max_{0 < p' < 1} G_{j,l}^{p',\pm}. \quad (4.9)$$

And the electronic dispersion  $\epsilon_{j,l'}$  in the definition of  $G_{j,l}^{p,\pm}$  is for the state  $|(j, l')\rangle = |\mathbf{k}_{-\Lambda_j + \delta, \hat{s}'}, -\sigma\rangle$ . The Green's function  $[G_{j,l}^{p,\pm}]^{-1} = -[G_{j,l}^{p,\pm}]^{-1}$  accounts for the poles of the orthogonal state  $\downarrow$ . This special value in turn causes the maximization of the 2-particle vertex RG flows, ensuring their domination over the 3-particle off-diagonal vertex RG flows. Further,  $\gamma_{\hat{s}}^{(\uparrow,\downarrow)}(\omega) = e^{i\pi(N_l^{\uparrow,\downarrow}(\omega)+1)}$  is the topological phase of the Green's function eq.5.5 with the topological invariant [453]  $N_l^{\uparrow,\downarrow}(\omega) = \oint dz[G_{\uparrow/\downarrow}^{(j,l)}]^{-1} \partial_z G_{\uparrow/\downarrow}^{(j,l)}$  where  $[G_{\uparrow/\downarrow}^{(j,l)}]^{-1} = z - [\hat{G}_{p,(\uparrow/\downarrow)}^{(j,l)}]^{-1}$ . These topological invariants are constrained by the relation  $N_l^{\uparrow}(\omega) + N_l^{\downarrow}(\omega) = 1$ , such that a RG relevant forward scattering coupling implies an irrelevant backward scattering coupling. By integrating the RG eqs.5.2, we obtain the RG invariant ( $C$ )

$$C = [pV_{s,l}^{(j)}(\delta)]^{-1} + [(1-p)V_{c,l}^{(j)}(\delta)]^{-1} = [pK_{s,l}^{(j)}(\delta)]^{-1} + [(1-p)K_{c,l}^{(j)}(\delta)]^{-1}. \quad (4.10)$$

In the Hubbard model (eq.5.1), the bare values of various couplings are:  $V_{s,l}^{(N)} = V_{c,l}^{(N)} = K_{s,l}^{(N)} = V_{c,l}^{(N)} = \bar{U}_0$ , therefore  $C^{-1} = p(1-p)\bar{U}_0$ .

For tangential scattering processes(vertices represented by  $L^{(j)}$ ), the intermediate state configuration necessarily involves electronic states on the entire isogeometric curve, i.e., the various many-body configurations obtained for a collective pseudospin angular momentum operator  $L_j^z = 2^{-1} \sum_l (\hat{n}_{j,l} + \hat{n}_{j,l'} - 1)$ . The scattering configuration are generated by collective pairwise

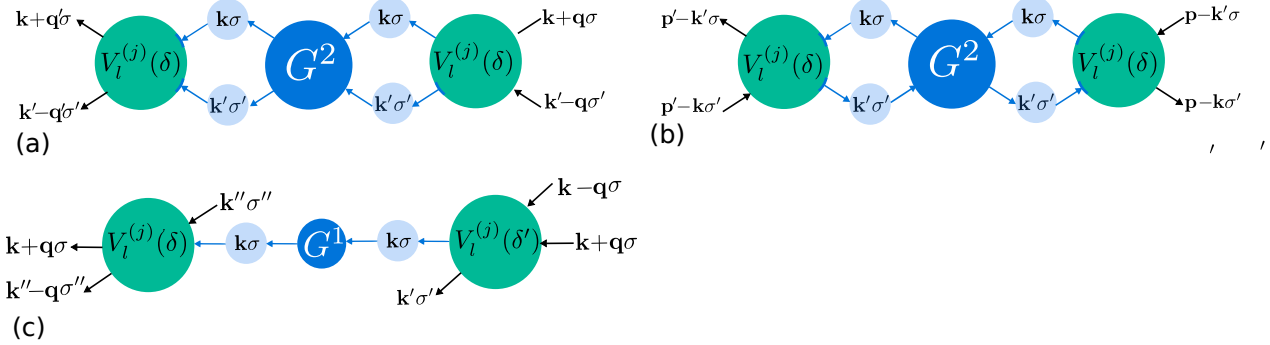


Figure 4.2: (Colour Online) Figures (a) and (b) Renormalization of the two particle scattering processes in the ee/hh, eh/he configurations respectively of the states  $\mathbf{k}\sigma$ ,  $\mathbf{k}'\sigma'$ . Blue circle represents the intermediate ee or eh propagator. (c) Three particle processes generated from two particle scattering pairs  $(\mathbf{k}\sigma, \mathbf{k}'\sigma')$ ,  $(\mathbf{k}\sigma, \mathbf{k}''\sigma'')$  sharing a common state.

electron raising/lowering operators  $L_j^+ = \sum_l c_{j,l}^\dagger c_{j,l'}^\dagger$  and  $L_j^-$  operators. The tangential scattering processes can involve the following class of intermediate state configurations,

$$|L_j = N_j + \frac{1}{2}, L_j^z = m + \frac{1}{2}\rangle = \sum_{m_1=m+1-N_j}^{N_j} C_{m_1}^{j,m} \left| \frac{N_j}{2}, m_1 \right\rangle \otimes \left| \frac{N_j+1}{2}, m - \frac{1}{2} - m_1 \right\rangle \quad (4.11)$$

where the quantum number  $m$  is related to the no. of electrons  $N_j - m$  on the isogeometric curve. The above state has been represented in the tensor product space of two collective pseudospins  $\mathbf{L}_j = \mathbf{L}_{1j} + \mathbf{L}_{2j}$ , where  $\mathbf{L}_{1j}$  is the net pseudospin vector made of  $N_j + 1$  pseudospins and  $\mathbf{L}_{2j}$  is made of  $N_j$  pseudospins. The isogeometric curve constitutes  $2N_j + 1$  pseudospins,  $N_j$  pseudospins in each of the two stretches  $[(\pi, 0), (\frac{\pi}{2}, \frac{\pi}{2})]$ ,  $[(\frac{\pi}{2}, \frac{\pi}{2}), (0, \pi)]$  and 1 pseudospin along the nodal  $N = (\frac{\pi}{2}, \frac{\pi}{2})$  direction. In this Schmidt decomposition the Clebch Gordon coefficients  $C_{m_1}^{j,m}$  are the Schmidt coefficients and the Schmidt rank[422] is  $2N_j - m - 1$ . These states are coupled by tangential scattering, such that the lower the magnitude of  $|m|$ , the higher is Schmidt rank; thus, for  $m = 0$ , the state  $|L_j^z = \frac{1}{2}\rangle$  has the highest entanglement content.

The RG flow equation of the tangential scattering vertices can be found from the operator RG equation in 4.A for the configuration given above in eq.4.11

$$\Delta L^{(j)} = \frac{(N_j + m)(N_j - m + 1)(L^{(j)})^2}{\omega + W sgn(\Delta\mu_{eff}) + \tilde{\epsilon}_{j,avg}^c - \frac{1}{4}L^{(j)}}, \quad (4.12)$$

where  $\tilde{\epsilon}_{j,avg}^c = N_j^{-1} \sum_l (\epsilon_{j,l} + \epsilon_{j,l'} - 2\Delta\mu_{eff})$  is the average kinetic energy of the electrons on the high-energy isogeometric curve. The eigenvalues of  $L_j^2$  and  $L_j^{z2}$  are  $= N_j(N_j + 1)$  and  $m^2$  respectively. We observe that the highly entangled  $m = 0$  configuration maximizes the RG flow rate in eq.5.3. This indicates that due to the rich entanglement structure of the state with  $m = 0$ , the breaking of an electronic configuration with off-resonance pairs is unfavourable under RG. The value of the fluctuation operator scale  $\omega$  is given by  $\omega + W sgn(\Delta\mu_{eff})$ , where  $W = 8t$  is the single-particle bandwidth. This can be argued as follows. For  $\Delta\mu = 0$ , beyond a minimum value of  $\Delta\mu_{eff}^{min} = -W$ , the tight-binding band has only holes with a Fermi surface shifted to the BZ

center  $\mathbf{k} = (0, 0)$ . As the low energy off-diagonal tangential scattering processes ( $L^{(j)}(\delta)$ ) cause fluctuations of the minimum hole energy  $E_{hole}^{min} = -(W/2) \times 2 = -\Delta\mu_{eff}^{min}$ , the correct energy scale for quantum fluctuations is now given by  $\omega + W sgn(\Delta\mu_{eff})$ .

Gapless parts of the FS neighbourhood are characterised by back-scattering being RG irrelevant, but with forward scattering. The low lying excitations on such gapless stretches of the FS are strongly influenced by the RG flow equations of the three-particle scattering vertex operator(eq.4.61) resulting out of forward scattering vertices. In the RG procedure the high energy states are chosen in a spin charge mixed configuration leading to the coupling flow equation for the three-particle scattering vertices as

$$\begin{aligned}\Delta R_{\hat{s},\delta\delta'}^{(j)} &= \frac{V_l^{(j)}(\delta)V_l^{(j)}(\delta')}{\omega - \epsilon_{j,l}} + \frac{K_l^{(j)}(\delta)K_l^{(j)}(\delta')}{\omega - \epsilon_{j,l}} + \frac{R_{l,\delta\delta''}^{(j)}R_{l,\delta''\delta'}^{(j)}}{[G_{j,l,3}]^{-1} + \frac{1}{8}R_{l,\delta''}^{(j)}}, \\ [G_{j,l,3}]^{-1} &= p \left( \frac{\epsilon_{j,l} + \epsilon_{j,l'}}{2} - \Delta\mu_{eff} \right) + (1-p) \frac{\epsilon_{j,l} - \epsilon_{j,l'}}{2} - \omega.\end{aligned}\quad (4.13)$$

It is easily seen that the choice of  $\Lambda' = 0$ , together with the optimal choice of the mixing parameter  $p$ (as made earlier in eq5.2) made in eq.4.61, maximises the 2 electron-1 hole (2e-1h) contribution to the above RG equation.

We now mention some other salient features of this RG formulation. First, the effective Hamiltonian at a given RG step can be formulated, with contributions from longitudinal (forward and backscattering, eq.5.2), tangential (eq.5.3) and three-particle diagonal and off-diagonal scattering vertices (eq5.4). The detailed form of the effective Hamiltonian is shown in 4.B. Next, the configuration energy for an mixed e-h/e-e intermediate pair is minimum for *resonant pairs* ( $\delta = 0$ ) due to nesting geometry of the Fermi surface(see Sec. 4.1.2). This leads to the propagator for  $\delta = 0$  resonant pairs ( $|\hat{G}_{p,\uparrow}^{j,l}|$ ) having the highest magnitude in the RG equations for longitudinal scattering (eq.5.2). In turn, this leads to the smallest denominators in these RG relations, ensuring that the resonant pairs dominate the RG flows for longitudinal scattering vertices.

Further, fixed points of the RG flows equations for longitudinal, tangential and three-particle vertices (eqns.5.2, 5.3 and 5.4 respectively) are associated with the vanishing of their respective denominators: attaining a stable fixed point is related to the vanishing of quantum fluctuations such that no further decoupling of states can be carried out under the RG transformations (see eq.2.25) [409]. Given that the resonant pairs dominate the RG flows, the spectral weight (characterised by the final distance from the FS,  $\Lambda^*(\delta, \hat{s}, \omega)$ ) is also the highest at a RG fixed point for such pairs.

We find the dominant contributions to the RG equation for the 1 electron self energy comes from the backscattering ( $K_l^{(j)}(\delta)$ ) and the three particle scattering ( $R^{(j)}$ ) vertices,

$$\Delta\Sigma_{\Lambda\hat{s}}^{(j)} = \frac{K_l^{(j)}(\delta)K_l^{(j)}(\delta')}{\omega - \epsilon_{j,l} + \frac{1}{2}\epsilon_{j,l'} + \Sigma_{\Lambda_j\hat{s}}^{(j)}} + \sum_{\Lambda < \Lambda_j} \frac{(R_X^{(j)})^2}{\bar{\omega} - \frac{1}{2}\epsilon_{j,l}^c + \frac{1}{8}R_D^{(j)}}. \quad (4.14)$$

where  $R_X^{(j)} = R_{l\delta\delta'}^{(j)}$ ,  $R_D^{(j)} = R_{l\delta}^{(j)}$ . We note that the Green's function of the first term involve a 2e-1h composite [454] of states:  $|\mathbf{k}_{\Lambda_j\hat{s}}\uparrow\rangle$ ,  $|\mathbf{k}_{\Lambda_j\hat{s}}\downarrow\rangle$  and  $|\mathbf{k}_{-\Lambda_jT\hat{s}\downarrow}\rangle$ , where the first two refer to the electron occupied states above the Fermi surface and the last to a hole state located below the Fermi surface. Similarly,  $\epsilon_{j,l}^c = \epsilon_{j,l} + \epsilon_{j,l'}$  appearing in the denominator of the second term is

the dispersion for a three electrons and two hole composite, of which one electron and two holes reside at Fermi energy. We now show that the quantum fluctuation scale  $\omega$  determines the nature of the self energy RG equation. At scales  $4 - \omega > 4 - \omega_{PG}$ , the backscattering vertex ( $K^{(j)}$ ) is RG irrelevant everywhere on the Fermi surface, resulting in the renormalization of  $\Sigma$  solely from the three-particle vertex. The fixed point neighbourhood can then be explored via a diagonal and off-diagonal two electron particle vertex with strengths  $R_D$  and  $R_X$  respectively. This will be discussed in a later section. Upon lowering  $4 - \omega$  below  $4 - \omega_{ins}$ , however, the backscattering vertex is dominant everywhere on the Fermi surface, leading to the self energy being renormalized predominantly by them. Given that the denominator of the first term is always positive, the RG flow of  $\Sigma$  is towards a strong coupling fixed point  $\Sigma \rightarrow \infty$ . This naturally leads to a zero in the 1 electron Green's function, and as we will see below, a gapping of the Fermi surface. In Appendix 4.A, we present a comparison of our results with those obtained from a weak-coupling functional RG approach.

In this way, we have provided a RG-based justification for the backscattering T-matrix argument given earlier (eq.4.5). Finally, the RG equations can be solved numerically in an iterative manner on a two-dimensional momentum-space grid, leading to fixed point values of various couplings, spectral weights and gaps. From these, we can draw a RG phase diagram, as well as compute several physical observables. In the following sections, we adopt this procedure in unveiling the physics of the  $T = 0$  Mott-Hubbard transitions at and away from 1/2-filling.

## 4.2 Mott MIT at 1/2-filling: the normal state

The  $T = 0$  phase diagram obtained by integrating the RG equations set out in the previous section at 1/2-filling ( $\mu_{eff}^0 = 0$ ) is shown in Fig. 4.3. Prior to the detailed discussions that will follow, we outline the key aspects displayed in the RG phase diagram. First, an explanation of the axes: the  $y$ -axis represents the energy scale  $\omega$  for quantum fluctuations where  $0 \leq \frac{W}{2} - \omega \leq 8t$  and the x-axis represents the bare value of the on-site Hubbard coupling ranging from weak to strong coupling ( $0 < U_0 \leq 16 = 2W$ ). A striking observation is that the Mott metal-insulator transition (MIT) involves the passage from a gapless metallic normal state at high  $\omega$  to a gapped insulating Mott liquid (ML) ground state at low  $\omega$ , but through a pseudogapped (PG) state of matter (at intermediate values of  $\omega$ ) arising from a differentiation of electrons based on the monotonic variation of their dispersion from linear in momentum at node (N) to quadratic at antinode (AN) [66, 455].

To obtain the above phase diagram, we have accounted for the RG flow of the forward( $V_l^{(j)}$ ), backward( $K_l^{(j)}$ ) and tangential( $L^{(j)}$ ) scattering vertices in the electron-electron(BCS) and electron-hole(ZS and ZS') channels. In the figures Fig.(4.5) and Fig.(4.6) we present the RG scale dependence of the forward( $V_{c,l}^{(j)}$ ) and backward( $K_{c,l}^{(j)}$ ) scattering vertices for four normal directions(two near N and other two near AN) associated with the Fermi surface wave vectors  $\mathbf{k}_F$ : 1 :  $-(\frac{\pi}{2}, \frac{\pi}{2})$ , 2 :  $-(\frac{\pi}{4}, \frac{3\pi}{4})$ , 3 :  $-(\frac{\pi}{8}, \frac{7\pi}{8})$ , 4 :  $-(\frac{\pi}{16}, \frac{15\pi}{16})$ . Fig.(4.5) panel *a* and panel *b* represents the RG flow of the vertices at  $\omega = -1$ (within NFL phase) and  $\omega = 3$ (within ML phase) respectively. Panel *a* left figure shows the RG irrelevant backscattering vertices  $K_{c,l}^{(j)}$  in the electron-electron channel for the four normal directions, while the right figure of panel *a* shows RG relevant forward scattering vertices  $V_{c,l}^{(j)}$  that stops at a intermediate coupling fixed point. Panel *b* on the other

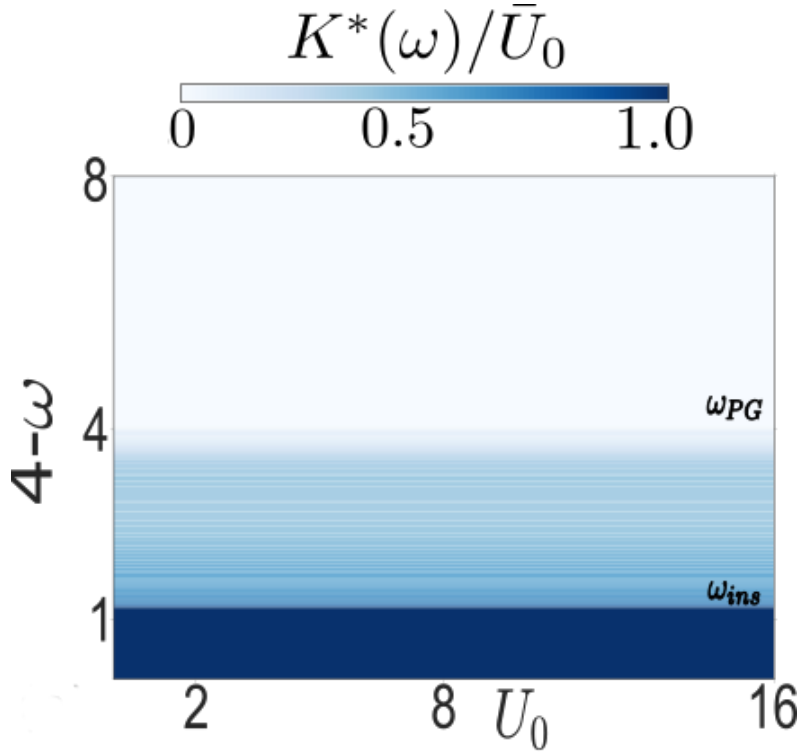


Figure 4.3: (Colour Online)  $T = 0$  Renormalisation group phase diagram at 1/2-filling in the quantum fluctuation energyscale ( $4 - \omega$ )-bare repulsion ( $U_0$ ) plane. Colourbar represents ratio of renormalized coupling to bare coupling  $K^*/\bar{U}_0$ . Transition from non-Fermi liquid (NFL, white) to Mott liquid (ML, dark blue) insulator is through a pseudogap (PG, shaded blue) for all  $U_0 > 0$ .  $\omega_{PG}$  and  $\omega_{ins}$  are energy scales for Lifshitz transitions that initiate and end the PG respectively. This phase diagram was obtain for a  $1024 \times 1024$  sized momentum space grid.

hand shows the opposite behavior i.e. a relevant backscattering vertex that attains a fixed point and a irrelevant forward scattering vertex that vanishes along the RG flow, this leads to the ML phase. Also note that in the left figure in panel(b) of Fig.(4.5), the black curve representing the backscattering vertex  $K_c$  close to antinodes( $\pi/16, 15\pi/16$ ) has the highest magnitude and it falls upon approaching the nodal direction. This peculiar dependence of the vertex RG flows on the different nature of the electronic dispersion across the Fermi surface (from AN to N) is observed in all the figures in Fig.4.5 and Fig.4.6.

Fig. (4.6) panel a represents relevant and irrelevant vertices at the onset of the PG phase  $\omega = 0.05 \sim \omega_{PG}$ . Along the normal directions 1, 2, 3 (starting from AN) the NFL persist, however along the nodal direction 1 the NFL is replaced by the gapped Mott liquid phase. Fig.(4.6) panel b represents the vertices in the vicinity of the final transit from PG into the Mott liquid phase  $\omega = 2.5$ . Evidently the fluctuation scale  $\omega$  play an important role in determining the relevant vertices and there associated fixed points. Altogether  $\omega$  governs the nature of the fixed point theories.

The PG phase is described by partial gap in the neighbourhood of AN, with a gapless stretch centered around N. The gapping process is initiated at the ANs as an FS topology-changing

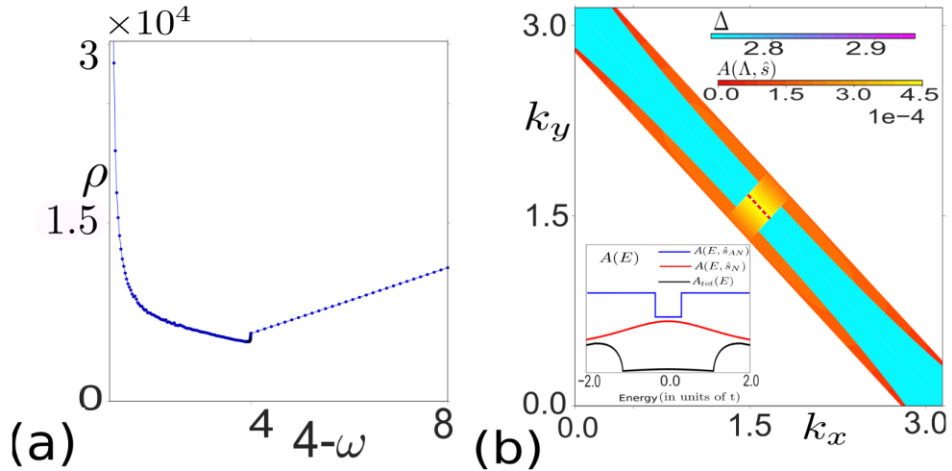


Figure 4.4: (Colour Online)(a) Linear variation of resistivity ( $\rho$ ) with  $\omega < \omega_{PG}$  in NFL crosses over through PG ( $\omega_{PG} < \omega < \omega_{ins}$ ) into the ML (diverging  $\rho$  for  $\omega > \omega_{ins}$ ). (b)  $A(E)$  (colourbar: red to yellow) and  $\Delta$  (magnitude of the backscattering vertex, colourbar: cyan to violet) in first quadrant of BZ with changing  $\omega = 2.5$ . The dashed red line represents the remnant Fermi surface in the gapless stretch. Inset: Quasiparticle (qp) spectral function ( $A(E)$ ) for  $\omega = 2.5$ , showing NFL at N (red curve) and gap at AN (blue curve) and averaged over FS ( $A_{tot}$ , black curve). The resistivity plot in a and contour plot for  $\Delta$  and  $A(\Lambda, \hat{s})$  in b were obtained for a  $1024 \times 1024$  sized momentum space grid.

Lifshitz transition of the normal phase at fluctuation scale  $\omega = \omega_{PG} \equiv 0.034t$ , and proceeds until the Ns are gapped out in a Mott liquid state via a second Lifshitz transition at  $\omega = \omega_{ins}$  (Fig. 4.4(b), Video S1). Figure 4.4(b) represents a snapshot of the gapped and gapless parts of FS at  $\omega = 2.5$ . The cyan region (colorbar represents the fixed point backscattering coupling  $\Delta = K^*(\Lambda, \hat{s})$  obtained from RG equations)  $R_1: [-\Lambda_{\hat{s}}^*, \Lambda_{\hat{s}}^*]$  for  $\hat{s}$  between  $[\hat{s}_{\pi,0}, \hat{s}_1]$  and  $[\hat{s}_1, \hat{s}_{0,\pi}]$  represents the nonuniform window of width  $2\Lambda_{\hat{s}}^*$  along the gapped part of Fermi surface. Region  $R_2$  stretching along FS  $[\hat{s}_N - \delta\hat{s}, \hat{s}_N + \delta\hat{s}]$  represents the gapless arc centered about the nodal direction:  $2\delta\hat{s}$  is the length of the gapless stretch. The spectral function  $A(\Lambda, \hat{s})$  in region  $R_2$  is represented by the red to yellow colorbar. Region  $R_3: [-\Lambda_0, -\Lambda_{\hat{s}}^*]$  and  $[\Lambda_{\hat{s}}^*, \Lambda_0]$  represents the nonuniform quasiparticle spectral function  $A(\Lambda, \hat{s})$  present outside the region  $R_1$ . Here  $\Lambda_0$  is the bare momentum space cut-off scale. The inset shows the spectral function  $A(E, \hat{s})$  along two normal directions, i.e., along the nodal direction  $A(E, \hat{s}_N)$  in red, the antinodal  $A(E, \hat{s}_{AN})$  in blue, while the average spectral function  $A(E)$  is shown in the black curve.

We develop the RG fixed point theory for the normal phase in this section. The next section is devoted to the PG phase and the Lifshitz transition leading to it. We complete our discussion for the Mott MIT at 1/2-filling by focusing on the Mott liquid in detail in a subsequent section. It is also worth noting the flatness of the phase boundaries: this indicates the absence of a critical  $(U/t)_c$  for the metal-Mott insulator transition for the 1/2-filled Hubbard model on the 2d square lattice with only nearest neighbour hopping, and results from the perfectly nested FS [456, 457]. This is consistent with recent DGA and quantum Monte Carlo simulations of the unfrustrated Hubbard model by Schafer et al [288]. We anticipate the presence of a critical

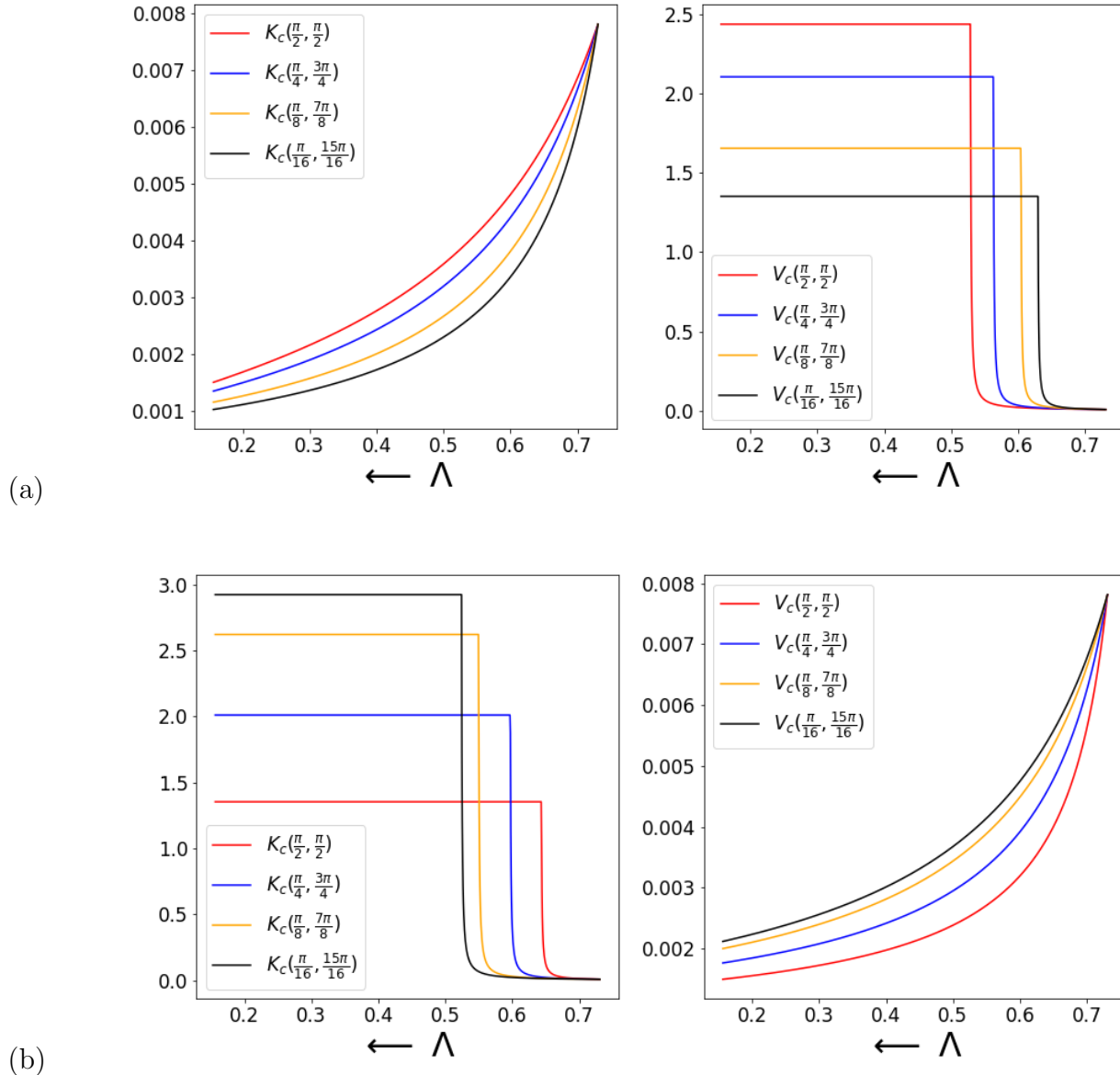


Figure 4.5: Panel *a* represents the RG flow for the forward(right figure) and backward(left figure) scattering vertices describing the NFL phase at  $\omega = -1$ . Panel *b* represents the RG flow of the vertices in the ML phase.  $\Lambda$  represents the RG cutoff scale. Numerical simulations for the RG equations were performed on a  $1024 \times 1024$  momentum space grid.

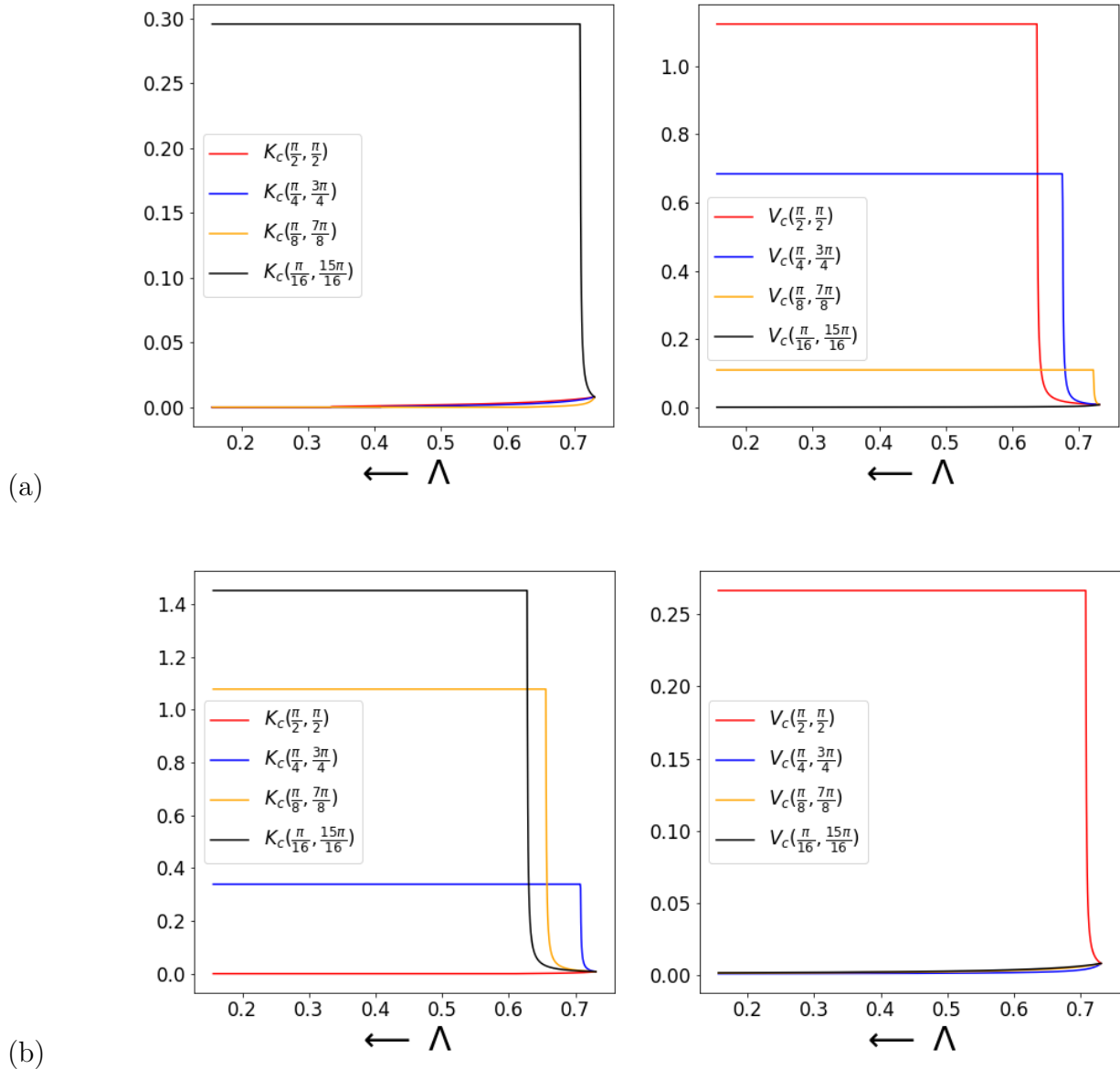


Figure 4.6: Panel *a* represents the RG flow for the forward(right figure) and backward(left figure) scattering vertices describing the onset of the PG phase at  $\omega = 0.05$ . Panel *b* represents the RG flow of the vertices at the vicinity of the transition  $\omega = 2.5$  from the PG to ML phase.  $\Lambda$  represents the RG cutoff scale. The numerical simulations for the RG equations were performed on a  $1024 \times 1024$  momentum space grid.

$(U/t)_c$  in the generalised Hubbard model with an additional (frustrating) next-nearest neighbour hopping, as has been demonstrated in dynamical mean-field theory (DMFT) studies [458, 459]. The  $U_0$  independent gapping of the antinodes can be anticipated from the divergence of the second order T-matrix element eq.4.5 for both resonant ( $\delta = 0$ ) as well as off-resonant ( $\delta \neq 0$ ) pairs. This results from the vanishing of the energy transfer at the antinodes  $k_x, k_y = \pi, 0$  and  $0, \pi$ . at  $\Omega = 0$  and the existence of van Hove singularities of the DOS at the antinodes. Thus, this event marks the onset energy scale of the pseudogap,  $\omega_{PG} = \frac{1}{2}(\epsilon_{\Lambda_0, \hat{s}_{AN}} - \epsilon_{-\Lambda_0, T\hat{s}_{AN}})$  where  $\epsilon_{\Lambda_0, \hat{s}_{AN}}$  is the energy of the electronic state along the antinodal direction residing at the bare cutoff scale  $\Lambda_0$  outside FS. The energy of the partner hole state is  $-\epsilon_{-\Lambda_0, T\hat{s}_{AN}}$ . On the other hand, along the nodal direction  $k_x = k_y = \pi/2$ , the energy transfer is  $\Delta E = 4t \sin \frac{\Lambda}{\sqrt{2}} \left[ \cos \frac{\delta}{\sqrt{2}} - 1 \right] \neq 0$ . This lowers considerably the gapping of the nodal points on the FS, and therefore the onset energy scale for the Mott insulator,  $\omega_{ins} = \frac{1}{2}(\epsilon_{\Lambda_0, \hat{s}_N} - \epsilon_{-\Lambda_0, T\hat{s}_N})$  where  $\epsilon_{\Lambda_0, \hat{s}_N}$  is the energy of the electronic state along the nodal direction residing at the bare cutoff scale  $\Lambda_0$  outside FS. The energy of the partner hole state is  $-\epsilon_{-\Lambda_0, T\hat{s}_N}$ . This is indicated by the fact that only the resonant ( $\delta = 0$ ) scattering events along the nodal direction contribute to the T-matrix element in a divergent manner at  $\Omega \rightarrow 0$  (eq.4.5). Further, this divergence is again  $U_0$  independent. These arguments show that the Fermi surface topology-changing events, i.e., the disconnection of the antinodes at  $\omega_{PG}$  and the vanishing of the nodal arcs at  $\omega_{ins}$ , are both  $U_0$  independent and are only related to the geometry of the underlying lattice.

### 4.2.1 Normal state for the Mott insulator

In charting the physics of the normal state from which the gapped Mott insulator arises, we will carry out the RG analysis using the two particle and three particle vertex scattering RG flow equations eq. (5.2), eq. (5.4). For this, we note that in the quantum fluctuation range  $\frac{W}{2} < \frac{W}{2} - \omega < W$ , from the RG eqns. eq.(5.2) all the backscattering vertices that destabilize the FS(eq.(4.5)) are RG irrelevant while forward scattering vertices are RG relevant. This ensures the existence of metallic state topologically protected by global index  $N_{\hat{s}}^{\downarrow}(\omega) = 1 \forall \hat{s}$ .

Further, the tangential scattering coupling (whose flow equation is shown in eq.(5.3)) is also found to be RG irrelevant, as the denominator is negative  $\omega + \tilde{\epsilon}_{\Lambda_j, avg}^c < 0$ . Thus from the stable fixed points of the RG flow equations we obtain an effective Hamiltonian  $H^* = H_1 + H_2$  in two parts:  $H_1$  describes nature of the normal state near FS,  $H_2$  describes the normal state away from FS. First we describe the physics of  $H_2$ ,

$$H_2 = \sum_{j,l} \epsilon_{\Lambda_j, \hat{s}} \hat{n}_{j,l} + \sum_{j,j',l} R_{l\delta}^{(j)} \hat{n}_{j,l} \hat{n}_{j,l'} (1 - \hat{n}_{j',l}) + \sum_{j,j',l} V_l^{(j)}(\delta) \hat{n}_{j,l} \hat{n}_{j,l'} . \quad (4.15)$$

The states  $|j, l\rangle = |\mathbf{k}_{\Lambda_j, \hat{s}} \sigma\rangle$ ,  $|j, l'\rangle = |\mathbf{k}_{-\Lambda_j + \delta T\hat{s}} \sigma\rangle$ ,  $|j', l\rangle = |\mathbf{k}_{\Lambda_{j'}, \hat{s}} \sigma\rangle$  For the one particle dispersion  $\epsilon_{\Lambda_j, \hat{s}}$  and two particle correlation energy  $V_l^{(j)}$  the summation is restricted to  $\Lambda_j > \Lambda_{\hat{s}}^{**}$ , for every normal  $\hat{s}$ . The 2 particle 1 hole dispersion  $R_{l\delta}^{(j)}$  is restricted to  $\Lambda_{\hat{s}}^* > \Lambda_j > \Lambda_{\hat{s}}^{**}$ . The momentum space scales  $\Lambda_{\hat{s}}^*, \Lambda_{\hat{s}}^{**}$  generated by the RG scheme will be described below. As the RG proceeds by decoupling states far from FS we reach an effective theory described by forward scattering processes only,  $K_{c,l}^{(j*)}(\delta) = K_{s,l}^{(j*)}(\delta) = 0$  and  $V_{c,l}^{(j*)}(\delta) = \frac{1}{2}(\epsilon_{j*,l} + \epsilon_{j*,l'} - \omega)$ . Scattering processes associated with different off-resonant pairs  $\delta$  is restricted to different momentum space widths

$\Lambda_{\delta}^*$  around FS. In this way we obtain the scale  $\Lambda_{\delta}^* = \max_{\delta} \Lambda_{\delta,\hat{s}}^*$  that is the largest among all the momentum space widths. Further the scale  $\Lambda_{\delta}^*$  is anisotropic in momentum space manifested by the  $C_4$  lattice geometry. Beyond the  $\Lambda_{\delta}^*$  window only two particle number diagonal interactions  $V_{c,l}^{(j*)}(\delta)$  persist in momentum space describing a Fermi liquid-like gapless metallic state of matter. This Fermi liquid is positioned farthest away from the non-interacting FS in energy as well as in  $k$ -space.

The non-commutativity between different forward scattering terms within the window  $\Lambda_{\delta}^*$ , leads to an effective three-particle (2e-1h) scattering term following eq.(5.4) (shown in Fig.4.2). By performing a second step RG at fluctuation energy scale  $\bar{\omega} = \max_{\delta,\hat{s}} 2^{-1}(\epsilon_{j^*,l} + \epsilon_{j^*,l'})$  in the vicinity of the momentum space window  $\Lambda_{\delta}^*$  we find that the forward scattering couplings are RG irrelevant and flow towards vanishing coupling,  $V_{c,l}^{(j**)}(\delta) = 0$ . On the other hand, we find that the flow of the 2e-1h off-diagonal scattering terms generated from the forward scattering processes (first term in eq.5.4) are initially RG relevant. Given that backscattering vertices are RG irrelevant so the 2nd term in eq.5.4 vanishes. As the 2e-1h scattering processes becomes bigger in magnitude, the third term in eq.5.4 eventually cuts off their growth to the fixed point,

$$\frac{R_{l\delta}^*}{8} = \bar{\omega} - \frac{1}{2}(\epsilon_{j^{**},l} + \epsilon_{j^{**},l'}) , \quad V_{l\delta}^{**} = 0 , \quad (4.16)$$

where  $(j^{**},l) = (\mathbf{k}_{\Lambda^{**}\hat{s}}\sigma)$ . This leads to the generation of a second momentum space scale  $\Lambda_{\delta}^{**}$  below which the Fermi liquid is absent. Thus, the momentum space region  $\Lambda_{\delta}^* > \Lambda > \Lambda_{\delta}^{**}$  constitutes a admixture of the two particle and three particle number diagonal terms. This gradual crossover leads to a very different gapless metallic state of matter in the immediate neighbourhood of the FS described by

$$H_1 = \sum_{j,l} \epsilon_{j,l} \hat{n}_{j,l} + \sum_{j,j',l} R_{l\delta}^* \hat{n}_{j,l} \hat{n}_{j,l'} (1 - \hat{n}_{j',l}) . \quad (4.17)$$

The first and second terms in the expression have their summations limited to  $j$  and  $j'$ , such that  $\Lambda_j, \Lambda_{j'} < \Lambda_{\delta}^{**}$  for the various normal  $\hat{s}$  to FS. Thus, the intermediate window involves a gradual crossover from a Fermi liquid to another metallic state of matter (see Fig.4.7(a)) which we characterise below.

## 4.2.2 Marginal Fermi liquid in the IR

We will now see that the gapless state of matter lying at lowest energies possesses properties ascribed phenomenologically to the Marginal Fermi liquid [460]. Of primary importance is the renormalisation of the 1-particle self-energy arising from three particle scattering terms in the neighbourhood of the fixed point (eq.4.16). From the discussion following eq.4.14, the dominant contribution to the one particle self energy RG flow in the regime  $4 - \omega > 4 - \omega_{PG}$  is

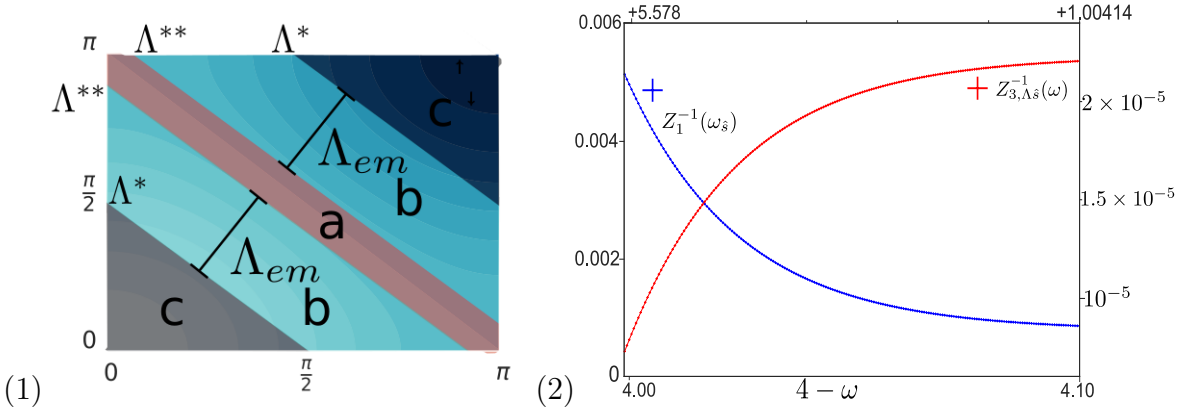


Figure 4.7: (1)(Colour Online) Momentum-space map partitioned into regions with different Hamiltonian structures for the normal state. (a) represents the Marginal Fermi liquid (MFL), (b) represents a correlated Fermi liquid, i.e., containing both MFL and Fermi liquid (FL), (c) represents a FL. (2)(Colour Online) Inverse quasiparticle residue averaged over a gapless connected Fermi surface  $Z_{avg}^{-1}$  at energies above the entry into the pseudogap phase shows a logarithmic growth as  $4 - \omega$  is lowered toward the Fermi energy ( $\omega \rightarrow 4-$ ). Vanishing of the quasiparticle residue (as the Fermi energy is approached) is an important characteristic of the destruction of the Fermi liquid. Instead,  $Z_{3,\Lambda\hat{s}}^{-1}$  gradually rises to unity near the Fermi energy.

$$\begin{aligned}
 \Delta\Sigma_{\Lambda,\hat{s}}^{Re,*}(\bar{\omega}) &= N(\Lambda_j, \hat{s}) \frac{(R_X^{(j)})^2}{R_D^{(j)}} \int_{0,\delta \rightarrow 0}^{\Lambda_j} \frac{d\epsilon_{\Lambda_j}}{\bar{\omega} - \frac{1}{2}\epsilon_{j,l}^c + \frac{1}{8}R_D^{(j)}} \\
 &= N(\Lambda^{**}, \hat{s}) \frac{(R_X^*)^2}{R_D^*} \ln \frac{\bar{\omega}}{\bar{\omega} - \frac{1}{2}\epsilon_{j^{**},l}^c + \frac{1}{4}R_D^{**}} \\
 &= N(\Lambda^{**}, \hat{s}) \left( \bar{\omega} - \frac{1}{2}\epsilon_{j^{**},l} \right) \ln \left| \frac{8\bar{\omega}}{\bar{\omega} - \frac{1}{2}\epsilon_{j^{**},l}} \right| , \tag{4.18}
 \end{aligned}$$

where  $R_X^* = R_{l\delta\delta'}^{(j**)}$ ,  $R_D^* = R_{l\delta}^{(j**)}$  and  $\epsilon_{j,l}^c = \epsilon_{j,l} + \epsilon_{j,l'}$  is the dispersion for a electronic pair. Note that we have replaced the summation on the right hand side of eq.4.14 by an integral. We have introduced the total number of states within window  $\Lambda^{**}$  along a given  $\hat{s}$  as  $N(\Lambda^{**}, \hat{s})$ . In the last step we have used the RG invariant relation  $C = R_X^{(j)} - R_D^{(j)} = 0$  resulting from the RG equation  $\Delta R_X^{(j)} = \Delta R_D^{(j)}$  and used the fixed point value of  $R_{l\delta}^{(j**)}$  eq.(4.16). As the self energy renormalization has a branch-cut log singularity at the FS, we may approximate  $\Sigma_{\mathbf{k}\Lambda\hat{s}}^{Re,(j)}(\omega) \approx \Delta\Sigma_{\mathbf{k}\Lambda\hat{s}}^{Re,(j)}(\omega) + O(\omega)$ . From these relations, we obtain the self energy  $\Sigma$  and the quasiparticle residue  $Z_1$  as

$$\Sigma(\tilde{\omega}_{\hat{s}}) = \tilde{\omega}_{\hat{s}} \ln \left| \frac{N^*(\hat{s}, \omega)\bar{\omega}}{\tilde{\omega}_{\hat{s}}} \right| , \quad Z_1(\tilde{\omega}_s) = \frac{1}{2 - \ln \left| \frac{\tilde{\omega}_{\hat{s}}}{N(\hat{s}, \Lambda^{**})\bar{\omega}} \right|} , \tag{4.19}$$

where  $\tilde{\omega}_{\hat{s}} = N^*(\hat{s}, \omega)(\bar{\omega} - \frac{1}{2}\epsilon_{\Lambda^{**},\hat{s}})$ . The quasiparticle residue  $Z_1(\tilde{\omega}_s)$  vanishes as  $\tilde{\omega}_{\hat{s}} \rightarrow 0$ , indicating breakdown of Landau's quasiparticle picture. These well-known expressions for the Marginal

Fermi liquid have been proposed on phenomenological grounds towards understanding the strange metal phase encountered in the hole-doped cuprates [460]. While  $\Sigma$  has the same structure as proposed in Ref. [460], it is worth noting that the Marginal Fermi liquid we find arises from singular forward scattering normal to the Fermi surface.

The imaginary part of the self energy can be computed from the real part of the self energy using the Kramers-Kronig relations

$$\Sigma_{\Lambda_j, \hat{s}}^{Im,(j)}(\bar{\omega}_{\hat{s}}) = \frac{1}{\pi} \mathcal{P} \int_{-\infty}^{\infty} \frac{\Sigma_{\Lambda_j, \hat{s}}^{Re,(j)}(\omega)}{\omega - \bar{\omega}_{\hat{s}}} = \tilde{\omega}_{\hat{s}} . \quad (4.20)$$

From here, we obtain the quasiparticle lifetime as  $\tau = 2\pi\tilde{\omega}_{\hat{s}}^{-1}$ , in keeping with the proposed relation for the marginal Fermi liquid. Further using the equivalence relation between the quantum fluctuations assisted broadening  $\tilde{\omega}_{\hat{s}}$  and thermal broadening (eq.2.29), we can obtain the largest temperature scale ( $T$ ) upto which the single particle description is well defined

$$k_B T = \hbar \max_{\hat{s}} \tilde{\omega}_{\hat{s}} . \quad (4.21)$$

The inverse lifetime  $\tau^{-1}$  is thus associated with a linear-in- $T$  Drude resistivity,  $\rho \propto T$ , arising from the excitations of the gapless Fermi surface.

As  $\omega \rightarrow 0$  and  $\Lambda^{**} \rightarrow 0$ , the 2e-1h dispersion eq.4.16 vanishes  $R_{l\delta}^* \rightarrow 0$  therefore the two-electron 1 hole residue  $Z_3 \rightarrow 1$ , making the composite degree of freedom well defined. This is exhibited by the fixed point Hamiltonian eq.4.17. The spectral weights/residues for 1e ( $Z_1(\omega_{\hat{s}})$ ) and 2e-1h composite ( $Z_{3,\Lambda\hat{s}}(\omega) \rightarrow 1$ ) are computed numerically from the above Green's functions, and shown in Fig. 4.7(b). The figure shows that as the FS is approached ( $\omega \rightarrow 4$ ), a vanishing  $Z_1(\omega_{\hat{s}})$  is compensated by a  $Z_{3,\Lambda\hat{s}} \rightarrow 1$ . In the following sections, we describe the destabilization of the marginal Fermi liquid metallic state leading to various other exotic phases at lower fluctuation scales.

### 4.3 RG flow through the Pseudogap

In the energy range  $\frac{W}{2} - \omega_{PG} < \frac{W}{2} - \omega > \frac{W}{2} - \omega_{ins}$ , the pseudogap is initiated in the form of a FS topology-changing Lifshitz transition that disconnects the connected FS via a gaping of the antinodes for  $\omega < \omega_{PG} \equiv 0$ , and proceeds until the nodes are gapped via a second Lifshitz transition at  $\omega = \omega_{ins}$  (Fig. 1(d), Video S1). This is an outcome of electronic differentiation arising out of a variation of the electronic dispersion from quadratic to linear along the Fermi surface [66] which influences the ee or eh paring energy. While the resistivity shows a linear behaviour with  $W/2 - \omega$  in the metallic phase (i.e., in the range  $\omega_{PG} \leq W/2 - \omega \leq W$ ), in the PG phase (Fig.4.4(a)), the resistivity shows a crossover into a insulator phase, i.e., an increase with lowering  $\frac{W}{2} - \omega$  beyond  $\omega = \omega_{PG}$ . At a given fluctuation scale within the above given energy range , the fixed point Hamiltonian of the gapped parts of the FS is described by *resonant pairs* as they condensed at lowest energies carrying the highest spectral weight,

$$\hat{H}^*(\omega) = \sum_{\hat{s}} N_{\hat{s}}^{\uparrow}(\omega) \left( K_{c,\hat{s}}^*(\omega) \mathbf{A}_{*,\hat{s}} \cdot \mathbf{A}_{*,-\hat{s}} - K_{s,\hat{s}}^*(\omega) \mathbf{S}_{*,\hat{s}} \cdot \mathbf{S}_{*,-\hat{s}} \right) + \sum_{\hat{s}} N_{\hat{s}}^{\downarrow}(\omega) H^*(\omega, \hat{s}) , \quad (4.22)$$

where the charge (**A**) and spin (**S**) are the net pseudospin operator, defined as

$$\mathbf{A}_{*,\hat{s}} = \sum_{\Lambda < \Lambda_{\hat{s},\omega}^*} \mathbf{A}_{\Lambda,\hat{s}}, \quad \mathbf{S}_{*,\hat{s}} = \sum_{\Lambda < \Lambda_{\hat{s},\omega}^*} \mathbf{S}_{\Lambda,\hat{s}}, \quad \mathbf{A}_{\Lambda,\hat{s}} = f_{\Lambda,\hat{s}}^{c;\dagger} \frac{\sigma}{2} f_{\Lambda,\hat{s}}^c, \quad \mathbf{S}_{\Lambda,\hat{s}} = f_{\Lambda,\hat{s}}^{s;\dagger} \frac{\sigma}{2} f_{\Lambda,\hat{s}}^s \quad (4.23)$$

where  $(\Lambda, \hat{s})$  are as defined earlier and  $\Lambda_{\hat{s}}^*$  is the window width along  $\hat{s}$  at the fixed point.  $f_{\Lambda,\hat{s}}^{c;\dagger} = [c_{\Lambda,\hat{s},\sigma}^\dagger \ c_{-\Lambda,T\hat{s},-\sigma}]$ ,  $f_{\Lambda,\hat{s}}^{s;\dagger} = [c_{\Lambda,\hat{s},\sigma}^\dagger \ c_{\Lambda-2\Lambda_{\hat{s}}^*,T\hat{s},-\sigma}^\dagger]$ , are the spinorial representation for a pair of Fermions. This Hamiltonian is easily seen as a sum of mutually commuting Hamiltonian of one-dimensional systems, each involving a distinct pair of normal directions  $(\hat{s}, T\hat{s})$ .  $H^*$  represents the Hamiltonian for the gapless parts. This results from the fact that tangential scattering between different  $\hat{s}$  directions is RG irrelevant. Further, as each of these 1D Hamiltonians involves scattering across all ranges in momentum-space, the scattering vertices  $K_{c,\hat{s}}^*(\omega)$  and  $K_{s,\hat{s}}^*(\omega)$  are inversely proportional to the number of states along a given  $\hat{s}$ :  $K_{c,\hat{s}}^*(\omega) \sim U_0/\sqrt{Vol}$ ,  $K_{s,\hat{s}}^*(\omega) \sim U_0/\sqrt{Vol}$  where  $Vol$  is the no. of lattice sites.

The charge/spin pseudospin flip scattering terms  $(A_{*,\hat{s}}^+ A_{*,-\hat{s}}^- + h.c.) / (S_{*,\hat{s}}^+ S_{*,-\hat{s}}^- + h.c.)$  present in the fixed point Hamiltonian eq.4.22 comprise the charge/spin backscattering processes for resonant pairs ( $\delta = 0$ ). We had earlier shown in eq.4.5 the appearance of log-divergences in the 2nd order corrections of the T-matrix arising from scattering in the resonant-pair subspaces. Here, through the RG flow, we show the condensation of the pseudospins in these subspaces

$$\hat{n}_{\mathbf{k}_{\Lambda_j\hat{s}\sigma}} = \hat{n}_{\mathbf{k}_{-\Lambda_jT\hat{s}-\sigma}} \rightarrow (\mathbf{A}_{\Lambda\hat{s}})^2 = \frac{3}{4}, \quad \hat{n}_{\mathbf{k}_{\Lambda_j\hat{s}\sigma}} = 1 - \hat{n}_{\mathbf{k}_{\Lambda_j-2\Lambda_{\hat{s},\omega}^*T\hat{s}-\sigma}} \rightarrow (\mathbf{S}_{\Lambda\hat{s}})^2 = \frac{3}{4}. \quad (4.24)$$

The fixed point values of the backscattering couplings are given by

$$[\omega - p \frac{\epsilon_l^* + \epsilon_{l'}^*}{2} - (1-p) \frac{\epsilon_l^* - \epsilon_{l'}^*}{2}] = \frac{K_{p,\hat{s}}^*}{4}. \quad (4.25)$$

The topological indices  $N_{\hat{s}}^\uparrow(\omega)$  and  $N_{\hat{s}}^\downarrow(\omega)$  appearing in eq.4.22 characterise the pseudogap phase as follows

$$\begin{aligned} I : N_{\hat{s}}^\uparrow(\omega) &= 1 - N_{\hat{s}}^\downarrow(\omega) = 1 \quad \forall \hat{s} \in [\hat{s}_{AN}, \hat{s}'], \\ II : N_{\hat{s}}^\downarrow(\omega) &= 1 - N_{\hat{s}}^\uparrow(\omega) = 1 \quad \forall \hat{s} \in [\hat{s}', \hat{s}_N]. \end{aligned} \quad (4.26)$$

In this way, the first term in Hamiltonian  $H^*(\omega)$  describes the gapped parts of the FS (I in eq.4.26), while the second term  $H^{3*}(\omega, \hat{s})$  (of the form eq.(4.17)) describes the gapless terms of the FS (II in eq.(4.26)) in terms of composites of 2e-1h degrees of freedom. At the second Lifshitz transition involving the gapping of the FS at the nodes,  $\hat{s}' = \hat{s}_N$  and the resulting Mott liquid (discussed in more detail in Section 4.4) is described by the global topological invariant  $N_{\hat{s}}^\uparrow(\omega) = 1 \forall \hat{s}$ . The pseudogap phase is thus a coexistence of gapped and gapless parts of the FS, and can also be characterised by a different global topological invariant

$$N_{\hat{s}}^{PG} = N_{R\hat{s}} + N_{T\hat{s}}, \quad (4.27)$$

where  $N_{R/T\hat{s}} = |N_{\hat{s}}^\uparrow(\omega) - N_{\hat{s}+(R/T)\hat{s}}^\uparrow(\omega)|$ , and the parity operation  $R\hat{s} : \hat{s}_x \leftrightarrow \hat{s}_x, : \hat{s}_y \leftrightarrow -\hat{s}_y$  (or vice versa). It is easily seen that  $N_{\hat{s}}^{PG} = 1 \forall \hat{s}$  in the PG phase, and vanishes in the metallic and insulating phases. These non-local order parameters ensure that the two  $T = 0$  Fermi surface topology-changing Lifshitz transitions at the passage into and out of the pseudogap phase do not belong to the Ginzburg-Landau-Wilson paradigm [66].

## 4.4 Properties of the Mott liquid

In the energy range  $\frac{W}{2} > \omega > \omega_{ins}$ , the spin-charge interplay parameter is found to be  $p = 0$  (eq.6.22). In turn, this makes the RG flow for the Umklapp process marginal, such that we obtain the fixed point coupling  $K_c^*(\omega) = \bar{U}_0$ . Then, using the RG invariant relation eq.4.10, we obtain the fixed point value for the spin backscattering coupling as

$$K_s^*(\omega) = \frac{\bar{U}_0(1-p)K_c^*(\omega)}{K_c^*(\omega) - p\bar{U}_0}|_{p=0, K_c^*(\omega)} = \bar{U}_0. \quad (4.28)$$

Thus, we obtain the fixed point Hamiltonian for the Mott liquid state as

$$\hat{H}^*(\omega) = \sum_{\hat{s}} \bar{U}_0 \left[ \mathbf{A}_{*,\hat{s}} \cdot \mathbf{A}_{*,-\hat{s}} - \mathbf{S}_{*,\hat{s}} \cdot \mathbf{S}_{*,-\hat{s}} \right], \quad (4.29)$$

where the psuedospins  $\mathbf{A}_{*,\hat{s}}$  and  $\mathbf{S}_{*,\hat{s}}$  are as defined in earlier sections. As mentioned in an earlier section, this Hamiltonian is again a collection of 1D Hamiltonians, and the renormalised coupling  $\bar{U}_0$  is therefore given by  $\bar{U}_0 = U_0/\sqrt{Vol}$ . The Hamiltonian thus obtained has antiferromagnetic and ferromagnetic exchange interactions in the charge-type pseudospin and spin-type pseudospin sectors respectively. A temperature scale  $T_{ML}$  associated with the formation of the gapped Mott liquid can be obtained by using the connection between a quantum fluctuation scale and a thermal scale (eq.2.29) as follows. From the form of the two electron Hartree self energy contribution  $K_{p,\hat{s}}^*$  and eq. (2.29), we determine  $T_{ML}$  as

$$T_{ML} = \frac{\hbar}{k_B} \max_{\hat{s}} \tilde{\omega}_{\hat{s}} = \frac{\hbar N^*(\hat{s}_1, 0)}{2k_B} (\epsilon_{\Lambda_0, \hat{s}_N} - \epsilon_{\Lambda^{**}(\omega_{ins}), \hat{s}_N}), \quad (4.30)$$

where the normal  $\hat{s}_1 = \left(1 - \frac{\Lambda_0}{\sqrt{2}\pi}\right) \hat{s}_{AN}$  is defined in the immediate vicinity of  $\hat{s}_{AN}$  in order to avoid the discontinuity at the van Hove points. The normal distance  $\Lambda^{**}(\omega_{ins})$  is obtained from the eq.4.16.

### 4.4.1 Low energy eigenstates of the Mott liquid

Some of the many-body eigenstates for  $H$  (eq.7.2) are obtained by entangling every charge pseudospin with a unique pair of occupied electronic states residing outside the window, such that the spin pseudospins have vanishing magnitude ( $(\mathbf{S}_{\Lambda\hat{s}})^2 = 0$ ). We now lay out the construction of such states. The vacuum state along a pair of normal  $\hat{s}$  is given by

$$|0\rangle_d = |[0_1' 0_1 0_{-1} 0_{-1'}]..[0_{j'} 0_j 0_{-j} 0_{-j'}]..[0_n' 0_n 0_{-n} 0_{-n'}]\rangle_d, \quad (4.31)$$

where the labels  $(j, d) := \mathbf{k}_{\Lambda_j, \hat{s}}, \sigma$  and  $(-j, d) := \mathbf{k}_{-\Lambda_j, T\hat{s}}, -\sigma$  represent momentum vectors *within* the emergent window  $\Lambda_j < \Lambda_{\hat{s}}^*$ . On the other hand, the labels  $(j', d) := \mathbf{k}_{\Lambda_{j'} - 2\Lambda_{\hat{s}}^*, \hat{s}}, \sigma$ ,  $(-j', d) = \mathbf{k}_{\Lambda_{j'} - 2\Lambda_{\hat{s}}^*, \hat{s}}, -\sigma$  represent the momentum vectors residing *outside* the emergent window  $\Lambda_{\hat{s}}^* < |\Lambda_j - 2\Lambda_{\hat{s}}^*|$ . The boundary states of the emergent window are represented by  $(n, d) = \mathbf{k}_{\Lambda_{j*}, \hat{s}}, \sigma$  and  $(-n, d) = \mathbf{k}_{-\Lambda_{j*}, T\hat{s}}, -\sigma$ .

We denote the configurations of a single charge pseudospin and its associated pair of electronic states by

$$|\uparrow_j\rangle_d := |1_{\mathbf{k}_{\Lambda_j}\hat{s}\sigma} 1_{\mathbf{k}_{-\Lambda_j,T\hat{s}},-\sigma}\rangle, |\downarrow_j\rangle_d := |0_{\mathbf{k}_{\Lambda_j,\hat{s}},\sigma} 0_{\mathbf{k}_{-\Lambda_j,T\hat{s}},-\sigma}\rangle . \quad (4.32)$$

The vacuum can then be rewritten in the charge pseudospin basis

$$|0\rangle_d = |[0_1' \downarrow_1 0_{-1'}]..[0_{2'} \downarrow_2 0_{-1'}]..[0_{n'} \downarrow_n 0_{-n'}]\rangle_d = |A_{*,\hat{s}} = N_{\hat{s}}^*, A_{*,\hat{s}}^z = -N_{\hat{s}}^* ,\rangle \quad (4.33)$$

where  $2N_{\hat{s}}^*$  is the number of charge pseudospins along  $\hat{s}$ . The application of operator  $M_{k,d}^+ = c_{j,d}^\dagger A_{j',d}^+ c_{-j',d}^\dagger$  flips a charge pseudospin in the  $\uparrow$  configuration along with creating electrons in two associated states:  $M_{j,d}^+|0\rangle = |[1_{j'} \uparrow_j 1_{-j'}]\rangle_d$ . From the above operation, it can be easily seen that for every charge pseudospin-flip operation, a pair of electrons created outside the window get entangled. Further, we find that the spin pseudospin raising and lowering operators annihilate this composite space

$$S^\pm |[1_{j'} \uparrow_j 1_{-j'}]\rangle = 0 , S^\pm |[0_{j'} \downarrow_j 0_{-j'}]\rangle = 0 . \quad (4.34)$$

The  $z$ -component can also be shown to vanish in a similar fashion. With these constraints, we can now determine eigenstates of the total charge pseudospin angular momentum operator along  $\hat{s}$   $\mathbf{A}_{*,\hat{s}} = \sum_{\Lambda=0}^{N_{\hat{s}}^*} \mathbf{A}_{\Lambda\hat{s}}$

$$|A_{*,\hat{s}} = N = A_{*,\hat{s}}^z\rangle = \sum_{j_1, \dots, j_l} \begin{vmatrix} e^{ij_1 q_1} & \dots & e^{ij_1 q_l} \\ \vdots & \ddots & \vdots \\ e^{ij_l q_1} & \dots & e^{ij_l q_l} \end{vmatrix} \prod_i M_{j_i,a}^+ |0\rangle_d \quad (4.35)$$

where the Slater determinant involves states with wavevectors  $q_s = \frac{s\pi}{2N_{\hat{s}}^*} \in [-\pi, \pi]$ ,  $l = N + N_{\hat{s}}^*$ . The eigenvalue of  $\mathbf{A}_{*,\hat{s}}^2$  for the state  $|A_{*,\hat{s}} = N = A_{*,\hat{s}}^z\rangle$  is given by  $A_{*,\hat{s}}^2 = N(N+1)$ . This can be obtained by noting that

$$\mathbf{A}_{*,\hat{s}}^2 = \frac{3}{4}(2N_{\hat{s}}^*) + \sum_{i < j=1}^{2N_{\hat{s}}^*} P_{ij} - \frac{1}{2} \binom{2N_{\hat{s}}^*}{2} \quad (4.36)$$

where  $P_{ij} = (2\mathbf{A}_{\Lambda_i\hat{s}} \cdot \mathbf{A}_{\Lambda_j\hat{s}} + \frac{1}{2})$  is the permutation operator that exchanges the  $i$  and  $j$  charge pseudospin configurations.

One class of eigenstates for the Hamiltonian in eq.(7.2) can now be obtained by entangling states  $|A_{*,\hat{s}} = N, A_{*,\hat{s}}^z = p\rangle$  from one side of Fermi surface with  $|A_{*,-\hat{s}} = N, A_{*,-\hat{s}}^z = p\rangle$  from the diametrically opposite side

$$\begin{aligned} & |A_* = m, A_*^z = p, A_{*,\hat{s}} = N_1, A_{*,-\hat{s}} = N_2\rangle \\ &= \sum C_{N_1,p_1;N_2,p_2}^{m,p} \times |A_{*,\hat{s}} = N_1, A_{*,\hat{s}}^z = p_1; A_{*,-\hat{s}} = N_2, A_{*,-\hat{s}}^z = p_2\rangle \end{aligned} \quad (4.37)$$

where  $p_1 = p - p_2$  and  $C_{N_1,p_1;N_2,p_2}^{m,p}$  are Clebsch-Gordon coefficients [461]. The energy eigenvalues for these states are then obtained as

$$E = \sum_{\hat{s}} \frac{\bar{U}_0}{2} [m(m+1) - N_1(N_1+1) - N_2(N_2+1)] . \quad (4.38)$$

From the expression, we observe that low-lying eigenstates of the spectrum reside in the space of states

$$|\Psi_{\hat{s}}, m\rangle = |A_* = m, A_{*,\hat{s}} = A_{*,-\hat{s}} = N_{\hat{s}}^*, S_{\Lambda\hat{s}} = 0\rangle , \quad (4.39)$$

where the charge pseudospin angular momentum of the two normal directions  $\hat{s}$  and  $-\hat{s}$  have magnitude  $N_{\hat{s}}^*(N_{\hat{s}}^* + 1)$ . The eigenvalue of the Hamiltonian  $H^*(\omega)|\Psi_{\hat{s},m}\rangle = E_m^c|\Psi_{\hat{s},m}\rangle$  associated with the eigenstates eq.(4.39) are

$$E_m^c = \sum_{\hat{s}} \bar{U}_0 \frac{1}{2} (m(m+1) - 2N_{\hat{s}}^*(N_{\hat{s}}^* + 1)) , \quad (4.40)$$

where  $N_{\hat{s}}^*$  is the number of states in the window  $[0, \Lambda_{\hat{s}}^*]$  and  $0 \leq m \leq 2N_{\hat{s}}^*$ . The lowest lying eigenstate  $|\Psi_{\hat{s}}, 0\rangle$  is obtained for  $m = 0$ , i.e., a charge pseudospin singlet with energy  $E_1 = -\bar{U}_0 \sum_{\hat{s}} N_{\hat{s}}^*(N_{\hat{s}}^* + 1)$ .

Another family of eigenstates

$$|\Phi_{\hat{s}}, m\rangle = |S_* = m, S_{*,\hat{s}} = S_{*,-\hat{s}} = N_{\hat{s}}^*, A_{\Lambda\hat{s}} = 0\rangle \quad (4.41)$$

is obtained from the spin pseudospin subspace  $S_{\Lambda\hat{s}}^2 = \frac{3}{4}$ , and where all the individual charge pseudospins  $\mathbf{A}_{\Lambda\hat{s}} = 0$ . The energy spectrum for this class of wave functions,  $H^*(\omega)|\Phi_{\hat{s},m}\rangle = E_m^s|\Phi_{\hat{s},m}\rangle$ , is given by

$$E_m^s = - \sum_{\hat{s}} \bar{U}_0 \frac{1}{2} (m(m+1) - 2N_{\hat{s}}^*(N_{\hat{s}}^* + 1)) , \quad (4.42)$$

where  $m \in (0, 2N_{\hat{s}}^*)$  once again. For the lowest lying eigenstate  $m = 2N_{\hat{s}}^*$  configuration, the energy is given by  $E_2 = -\bar{U}_0 \sum_{\hat{s}} N_{\hat{s}}^{*2}$ .

But have we accounted for all the states within the window  $\Lambda_{\hat{s}}^*$ ? An answer can be found by first computing the size of the Hilbert space for the Hamiltonian  $H^*(\omega)$ . By choosing every pair of two states  $(\Lambda, \hat{s}), (-\Lambda, T\hat{s})$ , where  $\Lambda < \Lambda_{\hat{s}}^*$ , there are two more electronic states that are chosen accordingly, i.e.,  $(\Lambda - 2\Lambda_{\hat{s}}^*, \hat{s}), (-\Lambda - 2\Lambda_{\hat{s}}^*, T\hat{s})$ . Thus, the total size of the Hilbert space within the window  $\Lambda_{\hat{s}}^*$  is given by  $2^{2N_{\hat{s}}^*}$ . On the other hand, the total number of eigenstates of type  $|\Psi_{\hat{s}}, m\rangle$  is  $2^{N_{\hat{s}}^*}$ , as there are 2 choices per composite subspace (eq.4.32) and there are  $N_{\hat{s}}^*$  such subspaces. An identical count of  $2^{N_{\hat{s}}^*}$  is obtained similarly for the Hilbert space of the states  $|\Phi_{\hat{s}}, m\rangle$ . Therefore, these two sets of eigenstates do not exhaust the entire eigenspectrum; there are other exotic combinations of entangled states possible, whose count is  $2^{2N_{\hat{s}}^*} - 2^{N_{\hat{s}}^*+1}$ .

The state spaces eqs.4.39 and 4.41 have been chosen such that they possess either  $\langle(\Delta S_{\Lambda\hat{s}}^{x,y,z})^2\rangle = 0$  or  $\langle(\Delta A_{\Lambda\hat{s}}^{x,y,z})^2\rangle = 0$ . This sets them out as excellent candidate members of the low energy spectrum: any locally spin-charge combination must, on the other hand, involve non-zero uncertainties  $\langle(\Delta S_{\Lambda\hat{s}}^{x,y,z})^2\rangle \neq 0$  as well as  $\langle(\Delta A_{\Lambda\hat{s}}^{x,y,z})^2\rangle \neq 0$ , raising their energy. We can now conclude on the ground states of  $H^*(\omega)$ . Clearly,  $|\Psi_{\hat{s}}, m = 0\rangle$  and  $|\Phi_{\hat{s}}, m = 2N_{\hat{s}}^*\rangle$  are the lowest energy states (with energies  $E_1$  and  $E_2$  respectively). In order for them to be degenerate ground states, we need to take the thermodynamic limit  $N_{\hat{s}}^* \gg 1$ , such that  $N_{\hat{s}}^{*2} > N_{\hat{s}}^*$  leading to  $E_1 = E_2 \equiv E_g$ . Further, in this limit, the sum and difference combinations of the states eqs.4.39 and 4.41

$$|\Gamma_{\pm}, m\rangle = \prod_{\hat{s}} \frac{1}{\sqrt{2}} [|\Psi_{\hat{s}}, m\rangle \pm |\Phi_{\hat{s}}, 2N_{\hat{s}}^* - m\rangle] \quad (4.43)$$

are also eigenstates of  $H^*(\omega)$ .

One of the lowest excitations lying above these ground states can be written by noting that the magnitude of the pseudospins  $A_*^{\hat{s}}$  and  $A_*^{-\hat{s}}$  are lowered from  $N_{\hat{s}}^*$  to  $N_{\hat{s}}^* - 1$ , such that the charge pseudospin singlet formed from these two has the form

$$|A_* = 0, A_{*,\hat{s}} \equiv A_{*,-\hat{s}} = N_{\hat{s}}^* - 1, S_{\Lambda\hat{s}} = 0\rangle . \quad (4.44)$$

Similarly, another lowest lying excitation is given by

$$|A_{\Lambda\hat{s}} = 0, S_* = 2N_{\hat{s}}^* - 2, S_{*,\hat{s}} \equiv S_{*,-\hat{s}} = 2N_{\hat{s}}^* - 2\rangle . \quad (4.45)$$

The energy cost to reach the lowest lying excited state (i.e., the spectral gap) in the thermodynamic limit ( $N_{\hat{s}}^* \gg 1$ ) is also easily obtained as  $\Delta E = \bar{U}_0 \sum_{\hat{s}} N_{\hat{s}}^*$ .

#### 4.4.2 Topological features of the Mott liquid

By putting periodic boundary conditions on the momentum-space window, we can construct a set of nonlocal operators  $W_m$

$$W_m = \exp \left[ i \frac{\pi}{2} (|\Gamma_+, m\rangle\langle\Gamma_+, m| - |\Gamma_-, m\rangle\langle\Gamma_-, m|) - 1 \right] ,$$

such that  $W_m$  commutes with the  $SU(2) \times SU(2)$  pseudospin rotational invariant Hamiltonian in the projected subspace of  $P_c + P_s$

$$[(P_c + P_s)H^*(P_c + P_s), W_m] = 0 \quad \forall m , \quad (4.46)$$

where the projection operators are given by  $P_c = \sum_m |\Psi_{\hat{s}}, m\rangle\langle\Psi_{\hat{s}}, m|$  and  $P_s = \sum_m |\Phi_{\hat{s}}, m\rangle\langle\Phi_{\hat{s}}, m|$ . Further, it is clear that  $W_m|\Gamma_{\pm}, m\rangle = \pm|\Gamma_{\pm}, m\rangle$ . Thus, the simultaneous degenerate ground state eigenfunctions of the Hamiltonian  $H^*$  of the Mott liquid and the operator  $W_{m=0}$  can be written as

$$|\Gamma_{\pm}, 0\rangle = \prod_{\hat{s}} \left[ \frac{1}{\sqrt{2}} (|\Psi_{\hat{s}}, 0\rangle \pm |\Phi_{\hat{s}}, 2N_{\hat{s}}^*\rangle) \right] . \quad (4.47)$$

These two degenerate ground states are connected via a twist operator/ nonlocal gauge transformation  $\hat{O}$

$$\hat{O} = \exp \left[ 4\pi i \sum_{\Lambda\hat{s}} \frac{(S_{\Lambda\hat{s}}^z)^2}{N_{\hat{s}}^*} \right] , \quad \hat{O}|\Gamma_{\pm}, 0\rangle = |\Gamma_{\mp}, 0\rangle . \quad (4.48)$$

As these two states are protected by the many body gap  $\Delta E = \bar{U}_0 \sum_{\hat{s}} N_{\hat{s}}^*$  (where  $\bar{U}_0 = U_0/vol$ ) given above, adiabatic passage between these degenerate ground states via the application of the twist operator  $\hat{O}$  involve the creation of charge-1/2 excitations [462, 42, 22], seen from the anticommutation relation  $\{\hat{O}, W_0\} = 0$ . The above relation, along with  $[\hat{O}^2, W_0] = 0$ , allows us to conclude that the ground state manifold is *topologically* degenerate in the thermodynamic limit.

### 4.4.3 Benchmarking against existing numerical results

In order to benchmark the results obtained from the effective low-energy Hamiltonian and wavefunctions given above against those found from existing numerical methods applied to the 2D Hubbard model on the square lattice [49, 77, 450], we present results for the ground state energy per particle  $E_g$  and the fraction of bound pairs ( $Bp$ ) in the gapped Mott liquid ground state. The analytic forms of  $E_g$  and  $Bp$  are computed from the spin and charge backscattering parts of the effective Hamiltonian given above ( $H^*(\omega)$ ) and are found to be

$$E_g = \frac{E_2}{N_e} = - \sum_{\hat{s}} \frac{\bar{U}_0(N_{\hat{s}}^*)^2}{N_e}, \quad Bp = \frac{\sum_{\hat{s}} N_{\hat{s}}^*}{N_e}, \quad Ubp = 1 - Bp, \quad (4.49)$$

where the fraction of unbound pairs is denoted by  $Ubp$ . The plots for  $E_g$  and  $(Bp, Ubp)$  versus the probe energy scale  $\omega$  are shown in Fig. 4.8(a) and Fig. 4.8(b) respectively. A comparison of the saturation value of the ground state energy for the largest  $k$ -space grid used in our simulations ( $2^{15} \times 2^{15}$ ),  $E_g^* = -0.526t$  (shown in Fig. (4.8)), is well within the range  $-0.51t < E_{gs} < -0.53t$  obtained in the thermodynamic limit from several state-of-the-art numerical methods applied to the half-filled 2D Hubbard model at  $U = 8t$  [49, 77, 450]. Similarly, the average saturation value for the fraction of unbound pairs ( $Ubp^*$ ) in the Mott liquid obtained from a finite-size scaling analysis (inset of Fig. (4.8)),  $Ubp^* \sim 0.051$ , lies slightly below the range  $0.0535 < Ubp < 0.0545$  obtained in Ref.[49]. The code used for the numerical computation of the ground state energy shown here is made available electronically [463]. As an added note, we point the reader to

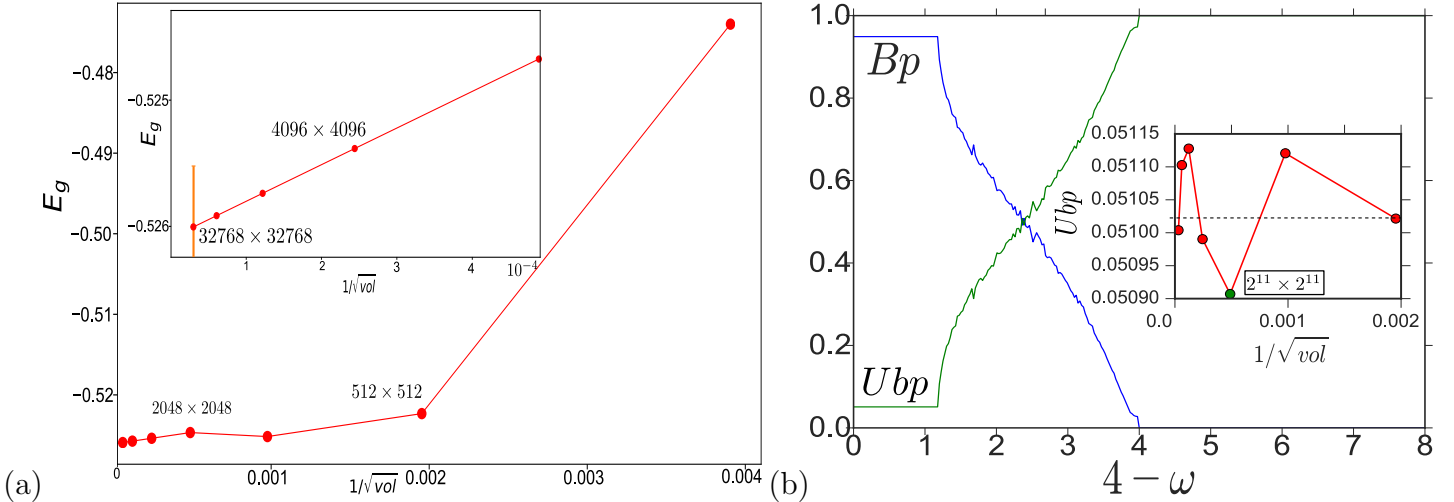


Figure 4.8: (a)(Colour Online) Finite-size scaling of the saturation value for  $E_g \equiv E_{gs}$  with  $1/\sqrt{Vol}$  with increasing  $k$ -space grid size from  $2^8 \times 2^8$  to  $2^{15} \times 2^{15}$ . The saturation  $E_{gs}$  for the largest grid is observed to be  $-0.526$ (for  $t = 1$ ). The error bar for all data points is  $\sim O(10^{-4})$ . Inset: Zoomed view of finite-size scaling plot for lattice sizes  $2^{11} \times 2^{11}$  to  $2^{15} \times 2^{15}$ .(b)(Colour Online) Blue curve: Growth/decay in fraction of bound/unbound pairs ( $Bp, Ubp$ ) across the phase diagram with varying  $\omega$ . Inset: Finite-size scaling of the saturation value for the fraction of unbound pairs ( $Ubp^*$ ) in the Mott liquid with  $1/\sqrt{vol}$ . The saturation fraction display small fluctuations about an average value  $Ubp^* \sim 0.051$ . Error bar for all data points is  $\sim O(10^{-5})$ .

further benchmarking exercises presented in 5.B for the cases of  $U/t = 2, 4, 6, 10$  at half-filling. We continue to find excellent quantitative agreement with exact diagonalization studies from Ref.[450] and other numerical methods reported in Refs.[49, 77]. We stress that this offers confidence in the effective Hamiltonian and ground-state wavefunction we have obtained for the half-filled Mott liquid.

#### 4.4.4 Symmetry breaking of the Mott Liquid: Néel Antiferromagnetism

Our RG analysis can also be extended to show that the topologically ordered Mott liquid ground state is replaced, under renormalisation, by a chosen ordered state with an order parameter corresponding to a defined broken symmetry. As RG transformations are, by definition, meant to preserve the symmetries of the Hamiltonian they act upon, such symmetry-broken states can only be reached from our RG analysis by first explicitly including an order parameter-field term in the Hamiltonian and then proceeding with the RG transformations [464]. In this way, we can reach a  $(\pi, \pi)$  spin density wave (SDW) Néel ground state in the presence of a staggered magnetic field( $h$ ). Using the Hamiltonian renormalization equation given earlier, we find the RG equation for the tangential Umklapp scattering processes: between the neighbourhood of different antinodal patches, is given in terms of the dimensionless coupling  $V'_\Lambda = \frac{V_\Lambda}{h_\Lambda}$  as

$$\Delta V'_{\Lambda_j} = \frac{\Delta V'_{\Lambda_j}}{\Delta \log \frac{\Lambda_j}{\Lambda_0}} = N_\Lambda \frac{V'^2_{\Lambda_j}}{1 - V'_{\Lambda_j} N_\Lambda (N_\Lambda + 1)}. \quad (4.50)$$

Note that  $\Lambda_j = \Lambda_0 \exp(-j)$  and  $\Lambda_{j-1} = \Lambda_0 \exp(-(j-1))$  such that  $\Delta \log \frac{\Lambda_j}{\Lambda_0} = 1$ . Here,  $N_\Lambda$  is the number of states near the AN( $(0, k_y)$ ,  $(k_x, 0)$ ) region at distance  $\Lambda$  from it. Given the flat geometry of the quadratic dispersion  $\epsilon_{k_y, 0} = k_y^2/2$  near the AN the density of states diverges logarithmically  $N_\Lambda = \ln|\Lambda_0/\Lambda|$ . For weak coupling  $V'_\Lambda \ll 1/N_\Lambda(N_\Lambda + 1)$ , we find the continuum form of the RG equation as,

$$\frac{dV'_\Lambda}{d \ln \frac{\Lambda}{\Lambda_0}} = \ln \left| \frac{\Lambda_0}{\Lambda} \right| V'^2_\Lambda \rightarrow V_\Lambda = \frac{U_0}{1 + (\log \frac{\Lambda}{\Lambda_0})^2 \frac{U_0}{2h}} \rightarrow \frac{\Lambda}{\Lambda_0} = \exp \left( -\frac{2h}{\sqrt{U_0}} \right), \quad (4.51)$$

where the RHS of the equation possesses the logarithmic divergence [465–467]. In this way, we find the well-known form for the gap function  $\Lambda$  corresponding to the Néel SDW state obtained from a mean-field analysis [227].

#### 4.4.5 Cooper-pair fluctuations within the Mott liquid

The pseudospin flip interaction  $-\bar{U}_0(S_{*,\hat{s}}^+ S_{*,-\hat{s}}^- + h.c.)$  present within the Mott liquid can be rewritten in terms of interactions between finite-momentum Cooper pairing terms as follows:

$$\sum_{\Lambda\Lambda'} [S_{\Lambda\hat{s}}^+ S_{\Lambda'\hat{s}}^- + h.c.] = \sum_{\mathbf{k}, \mathbf{p}} c_{\mathbf{k}\uparrow}^\dagger c_{\mathbf{p}-\mathbf{k}\downarrow}^\dagger c_{\mathbf{p}-\mathbf{k}'\downarrow} c_{\mathbf{k}'\uparrow}, \quad (4.52)$$

where  $\mathbf{k} = \mathbf{k}_{\Lambda,\hat{s}}$  and  $\mathbf{k}' = \mathbf{k}_{2\Lambda_s^* - \Lambda, \hat{s}}$ . This observation will be shown to coincide with the presence of a decaying off-diagonal long range order (ODLRO). The presence of entanglement between

the charge/spin type pseudospins in eq.4.47, along with mixing between different  $\mathbf{p}$ -momentum pairs, is captured in the off-diagonal long range order ODLRO,

$$\rho(\mathbf{r} - \mathbf{r}') = \langle \Psi_1 | \psi_{\mathbf{r}\uparrow}^\dagger \psi_{\mathbf{r}\downarrow}^\dagger \psi_{\mathbf{r}'\downarrow} \psi_{\mathbf{r}'\uparrow} | \Psi_1 \rangle = \frac{1}{2} \sum_{\hat{s}, \mathbf{p}=0}^{2\Lambda_s^*} \frac{N_{\Lambda_s^*}}{L^2} \cos(\mathbf{p} \cdot (\mathbf{r} - \mathbf{r}')) . \quad (4.53)$$

Here, we have chosen the quantization axis of  $\mathbf{S}_{\Lambda\hat{s}}$  along the x-direction. From this expression, we observe that the ODLRO decays for  $|(\mathbf{r} - \mathbf{r}') \cdot \hat{s}| > (2\Lambda_s^*)^{-1}$ . The prefactor of 1/2 in the expression for the ODLRO arises from the superposition of the two types of many body states (eq.4.47), while its anisotropic form results from the geometry of the Fermi surface in the tight-binding problem. Finally,  $N_{\Lambda_s^*}$  is the number of composite objects along the  $\hat{s}$  direction. We saw earlier the susceptibility of the Mott liquid towards a symmetry-broken Néel antiferromagnet. From the analysis presented for the ODLRO above, we find that the global spin-charge entanglement prevents the condensation of zero-momentum Cooper pairs. This leads us to conclude that antiferromagnetism is clearly favored over a  $U(1)$ -symmetry broken superconducting state as an instability of the Mott liquid, consistent with the finding of subdominant superconducting correlations in the insulating phase at half-filling from VMC studies [468].

## 4.5 Conclusions and perspectives

There are several interesting consequences of our RG analysis of the 2D Hubbard model on the square lattice, and we now discuss each of these in turn. At the very outset, we wish to stress that the simplicity of the Hubbard Hamiltonian (i.e., possessing effectively only a single parameter  $U/t$ ) offers the possibility that several of our results are of likely importance for the broad understanding of the phenomenology of bandwidth-driven Mott transitions in a variety of strongly correlated electronic systems with strong electronic differentiation arising from the tight binding dispersion [2]. Thus, even as our results are immediately relevant to the physics of correlated electrons on bipartite lattices with unfrustrated interactions and hoppings, we expect that they offer insight on systems in which these restrictions have been lifted.

First among our findings is the fact that in the RG phase diagram (Fig.4.3), the low-energy ground state is Mott insulating for any Hubbard repulsion  $U > 0$  at 1/2-filling. The absence of a critical Hubbard coupling  $U^*$  at 1/2-filling is consistent with the results of several recent numerical investigations of the problem (Refs.[317, 318, 288, 287, 288, 84, 319]). Further, our study pinpoints the marginal Fermi liquid as the parent metal of the insulating Mott liquid state. All of this provides evidence for the fact that the Mott metal-insulator transition of the 2D Hubbard model is truly nonperturbative in nature, and inaccessible via a weak-coupling many-body perturbation theory about the Fermi liquid fixed point (adiabatically continuous to the non-interacting electron gas). Instead, our work reveals the nature of the FS topology-changing Mott metal-insulator transition at  $T = 0$ , highlighting the existence of a pseudogap phase as the pathway from the metallic to the insulating phase. This appears to confirm the conjecture of Ref.[455] on the nature of the  $T = 0$  Mott transition.

The marginal Fermi liquid is found to arise from singular forward scattering in directions normal to the nested Fermi surface of the underlying tight-binding problem, causing the destruction of Landau quasiparticles and leading to a linear variation of resistivity with temperature. We

derive analytically an effective Hamiltonian for the marginal Fermi liquid from the RG analysis. Importantly, this meets an outstanding formal challenge by providing a microscopic basis for the rich phenomenology of the marginal Fermi liquid theory. Remarkably, a computation of the quasiparticle residue of the 2e-1h constituents comprising the marginal Fermi liquid reveals that they are effectively non-interacting in the neighbourhood of the Fermi surface. This establishes firmly the marginal Fermi liquid theory as a paradigmatic fixed point theory for a non-Fermi liquid. In keeping with considerable recent activity in the area of holographic dualities, our results offer encouraging support in the search for other novel gapless states of quantum matter.

The pseudogap phase is observed to arise from the electronic differentiation encoded within the nested Fermi surface of the half-filled tight-binding model [455], and involves the gradual gapping of the Fermi surface (from antinodes to nodes [65]) via charge and spin excitations that are mutually entangled. We have clarified the topological quantum numbers (non-local order parameters) that quantify the passage through the pseudogap, as well as qualify as it as a phase of quantum matter distinct from the normal and Mott insulating phases. Our finding of pseudogap and non-Fermi liquid phases at 1/2-filling also offer a natural explanation of experimental observations in the cuprates of such phases being proximate to the Mott insulating phase upon doping lightly with holes (see, e.g., [469]).

By obtaining analytically the many-particle wavefunctions for the Mott liquid phase at low energies, we demonstrate that it possesses signatures of topological order: a two-fold degeneracy of the ground state on the torus, and fractionally-charged topological excitations that interpolate between them. The ground state energy and double-occupancy fraction obtained from these wavefunctions, together with the effective Hamiltonian for the Mott liquid, display remarkable agreement with those obtained from state-of-the art numerical methods [49, 77, 450] for a wide range of the parameter  $2 \leq U/t \leq 12$ . Such microscopic insight into a topologically ordered gapped state of strongly correlated quantum matter has, to the best of our knowledge, seldom been available and constitutes a fundamental advance afforded by the RG method developed in this work. The benchmarking against results from numerical methods reinforces our confidence in the effective theory we have obtained for the Mott liquid phase, and paves the way for a systematic investigation of the many-particle entanglement of such an exotic state of quantum matter.

Importantly, upon including the possibility of symmetry-breaking within the RG formalism, the Mott liquid is found to turn into the familiar Néel spin-ordered charge-insulating Mott insulator. As we demonstrate in an accompanying work [470], this has important consequences for the nature of the hole-doped Mott insulator [327]. For instance, we will show there that the dominant charge gapping of the 1/2-filled Mott liquid is steadily suppressed with hole-doping, leading to a novel quantum critical point. The subdominant Cooper pairing of the Mott liquid state at half-filling becomes dominant at this critical hole-doping, leading to a d-wave superconducting phase that surrounds the quantum critical point. Finally, where do we expect some of our predictions to be tested experimentally? In recent years, cold fermionic gases have emerged as a leading contender for the study of strongly correlated fermionic systems (see, e.g., [471] for a recent review, and [472] for a recent experiment). Another possibility is the recent demonstration of the phenomenology of the high-temperature superconducting bulk cuprate systems in a monolayer crystal of  $\text{Bi}_2\text{Sr}_2\text{CaCu}_2\text{O}_{8+\delta}$  [320]. Both systems offer exciting prospects in probing the 2D Mott-Hubbard transition in a controlled manner and at very low temperatures. Finally, as a

particle-hole transformation on one of the sublattices of the 2D square lattices connects between the repulsive and attractive Hubbard models ([473]), we believe that our results are also significant in understanding the physics of the latter.

# Appendix

## 4.A The Hamiltonian renormalization group flow

Starting from the Hamiltonian RG flow eq.4.4, and using the expressions for the unitary operator eq.4.2, we obtain

$$\Delta H_{(j)} = \sum_l Tr_{j,l}(c_{j,l}^\dagger H_{(j)}) c_{j,l} G_{(j),l} c_{j,l}^\dagger Tr_{j,l}(H_{(j)}) c_{j,l} , \quad (4.54)$$

where  $G_{(j),l} = (\omega - \hat{n}_{j,l} Tr_{j,l}(H_{(j)}^D \hat{n}_{j,l}))^{-1}$  and the diagonal Hamiltonian  $H_{(j)}^D$  is given by

$$\begin{aligned} Tr_{j,l}(H_{(j)}^D \hat{n}_{j,l}) &= \epsilon_{j,l} \hat{n}_{j,l} + \sum_{l'} V_l^{(j)}(\delta) \left( \hat{n}_{j,l} - \frac{1}{2} \right) \left( \hat{n}_{j,l'} - \frac{1}{2} \right) \\ &\quad + \sum_{l''} L^{(j)}(\delta) \hat{n}_{j,l} \hat{n}_{j',l''} + \sum_{l''} R_{\delta\delta}^{(j)} \hat{n}_{j,l} \hat{n}_{j,l'} (1 - \hat{n}_{j,l''}) + \dots \end{aligned} \quad (4.55)$$

The various terms in  $H_{(j)}^D$  are: the first term is the electronic dispersion ( $\epsilon_{j,l}$ ), the term with coupling  $V_l^{(j)}(\delta)$  is the longitudinal density-density interaction in the (ee-hh) and (eh-he) channels, the term with coupling  $L^{(j)}(\delta)$  is the tangential density-density interaction and, finally, the term with coupling  $R_{\delta\delta}^{(j)}$  is the 2e-1h interaction. The renormalization  $\Delta H_{(j)}^F$  for the forward-scattering part of the Hamiltonian in the electron(e)-electron, hole(h)-hole, eh and he channels are obtained from eq.4.54 as

$$\begin{aligned} \Delta H_{(j)}^F &= \sum_{k,k',l'} \left[ c_{k',l}^\dagger c_{k',l'}^\dagger c_{j,l'} c_{j,l} \frac{(V_l^{(j)}(\delta))^2}{[G_{j,l}]^{-1} - V_l^{(j)}(\delta) \tau_{j,l} \tau_{j,l'}} c_{j,l}^\dagger c_{j,l'}^\dagger c_{k,l'} c_{k,l} \right. \\ &\quad + c_{j,l}^\dagger c_{j,l'}^\dagger c_{k',l'} c_{k',l} \frac{(V_l^{(j)}(\delta))^2}{[G_{j,l}]^{-1} - V_l^{(j)}(\delta) \tau_{j,l} \tau_{j,l'}} c_{k,l}^\dagger c_{k,l'}^\dagger c_{j,l'} c_{j,l} \\ &\quad + c_{k',l}^\dagger c_{k,l'} c_{k,l'}^\dagger c_{j,l} \frac{(V_l^{(j)}(\delta))^2}{[G_{j,l}]^{-1} - V_l^{(j)}(\delta) \tau_{j,l} \tau_{j,l'}} c_{j,l}^\dagger c_{j,l'} c_{k',l'}^\dagger c_{k,l} \\ &\quad \left. + c_{j,l}^\dagger c_{j,l'} c_{k',l}^\dagger c_{k,l'} \frac{(V_l^{(j)}(\delta))^2}{[G_{j,l}]^{-1} - V_l^{(j)}(\delta) \tau_{j,l} \tau_{j,l'}} c_{k',l'}^\dagger c_{k,l} c_{j,l'}^\dagger c_{j,l} \right] \\ &= \sum_{k,k',l'} c_{k',l}^\dagger c_{k',l'}^\dagger \frac{4(V_l^{(j)}(\delta))^2 \tau_{j,l} \tau_{j,l'}}{[G_{j,l}]^{-1} - V_l^{(j)}(\delta) \tau_{j,l} \tau_{j,l'}} c_{k,l'} c_{k,l} . \end{aligned} \quad (4.56)$$

Here,  $(G_{j,l})^{-1} = \hat{\omega} - \epsilon_{j,l}\tau_{j,l} - \epsilon_{j,l'}\tau_{j,l'}$  is the inverse Green's function operator. The index  $(j, l)$  refers to the momentum and spin labelled state  $|\mathbf{k}_{\Lambda_j, \hat{s}}, \sigma\rangle$ , index  $(j, l')$  refers to the partner electronic state  $|\mathbf{k}_{-\Lambda_j + \delta, T\hat{s}}, \sigma\rangle$ . The index  $l$  essentially is a collective label that accounts for the normal direction  $\hat{s}$  and spin  $\sigma$ . This labelling scheme was defined just before eq.4.2 and here we are recalling it to bring clarity into the present discussion.

Finally, some remarks are in order on the similarities and differences with the weak coupling functional RG (FRG) for the 2d Hubbard model [474]. The states  $|j, l\rangle, |j, l'\rangle$  located at a distance  $\Lambda_j$  from FS are disentangled at the RG step  $j$ , leading to renormalization of the forward scattering vertices. Similar to FRG, the states  $(j, l), (j, l')$  in the RG equations above are energetically proximate to the renormalized cutoff scale  $\Lambda$ , and are integrated out leading to the vertex flow equation. Additionally, note that in forward scattering RG eq.4.56, the first two lines comprise the nonperturbative renormalization in the ee/hh channel and account for the *BCS* diagrams. On the other hand, the last two lines comprise the renormalization in the eh/he channel and account for the *ZS/ZS'* diagrams.

We can also observe the structural similarity of our RG equations to the one loop weak coupling RG equations obtained from FRG [108] by performing a Taylor expansion of the RG equation about small  $V \ll 1$ ,

$$\Delta H_{(j)}^F = \sum_{k, k', l'} c_{k', l}^\dagger c_{k', l'}^\dagger c_{k, l'} c_{k, l} \left[ \frac{4(V_l^{(j)}(\delta))^2 \tau_{j, l} \tau_{j, l'}}{\omega - \epsilon_{j, l} \tau_{j, l} - \epsilon_{j, l'} \tau_{j, l'}} - \frac{4(V_l^{(j)}(\delta))^3 \tau_{j, l}^2 \tau_{j, l'}^2}{(\omega - \epsilon_{j, l} \tau_{j, l} - \epsilon_{j, l'} \tau_{j, l'})^2} + \dots \right]. \quad (4.57)$$

The leading term in the RG eqn. 4.57 for  $V_l^{(j)} \ll 1$  has denominator similar to that obtained from weak coupling FRG in the ee channel (BCS) [111]:  $(\omega - \epsilon_{j, l} \tau_{j, l} - \epsilon_{j, l'} \tau_{j, l'})|1_{j, l} 1_{j, l'}\rangle = 2^{-1}(\omega - \epsilon_{j, l} - \epsilon_{j, l'})$ . Similarly, in the eh channel, the denominator of the RG equations have resemblance with terms *ZS* and *ZS'* of weak coupling FRG [111]. The additional contribution of  $\omega$  reflects the intrinsic quantum fluctuation energy scale (Sec.2.3), reflecting the retardation effects intrinsic to our RG procedure. As shown in eq.4.14, the RG of backscattering and three-particle vertices affect those of the 1 particle self energy  $\Sigma$ . The present discussion clarifies that the  $\Sigma$  obtained from our approach is consistent with that obtained from FRG.

Similarly, the renormalization  $\Delta H_{(j)}^B$  for backscattering terms is given by

$$\Delta H_{(j)}^B = \sum_{k, k', l'} c_{k', p}^\dagger c_{k', p'}^\dagger \frac{4V_l^{(j)}(\delta) K_l^{(j)}(\delta) \tau_{j, l} \tau_{j, l'}}{[G_{j, l}]^{-1} - V_l^{(j)}(\delta) \tau_{j, l} \tau_{j, l'}} c_{k, l'} c_{k, l}, \quad (4.58)$$

where the same Green's function operator has been used. The renormalization of the tangential scattering terms in the Hamiltonian can be similarly obtained by decoupling a collective configuration of states on the  $j$ th isogeometric curve

$$\Delta H_{(j)}^T = \sum_{kk'} c_{k, m}^\dagger c_{k, m'}^\dagger \frac{(L^{(j)})^2 L_j^+ L_j^-}{\hat{\omega} - \tilde{\epsilon}_{j, avg}^c L_j^z - L^{(j)} L_j^{z2}} c_{k', n'} c_{k', n}. \quad (4.59)$$

Here,  $L_j^+ = \sum_m c_{j, m}^\dagger c_{j, m'}^\dagger$ ,  $L_j^z = 2^{-1} \sum_m (\hat{n}_{j, m} + \hat{n}_{j, m'} - 1)$  and  $L_j^-$  is the hermitian conjugate to  $L_j^+$ . The intermediate configurations of the states involved in the tangential scattering processes are labeled by

$$(j, m) = \mathbf{k}_{\Lambda_j, \hat{s}}, \sigma), (j, m') = \mathbf{k}_{-\Lambda_j, T\hat{s}}, -\sigma),$$

$$(j, n) = \mathbf{k}_{\Lambda_j, \hat{s}'}, \sigma), (j, n') = \mathbf{k}_{-\Lambda_j, T\hat{s}'}, -\sigma).$$

Using the angular momentum algebra  $L_j^+ L_j^- = L_j^2 - L_j^{z2} - L_z$ , we obtain

$$\Delta H_{(j)}^T = \sum_{kk',m,n} c_{k,m}^\dagger c_{k,m'}^\dagger \frac{(L^{(j)})^2(L_j^2 - L_j^{z2} - L_j^z)}{\omega - \tilde{\epsilon}_{j,avg}^c L_j^z - L^{(j)} L_j^{z2}} c_{k',n'} c_{k',n}. \quad (4.60)$$

The Hamiltonian RG for the 3-particle scattering vertices terms are obtained as

$$\begin{aligned} \Delta H_{(j)}^3 &= \sum_{k'',k',l',l''} c_{k',l}^\dagger c_{k',l'}^\dagger c_{j,l'} V_l^{(j)}(\delta) V_l^{(j)}(\delta') \tau_{j,l} c_{j,l''}^\dagger c_{k'',l} c_{k'',l'} \\ &+ \sum_{k'',p',l',l''} c_{p',l}^\dagger c_{p',l'}^\dagger c_{j,l'} K_l^{(j)}(\delta) K_l^{(j)}(\delta') \tau_{j,l} c_{j,l''}^\dagger c_{k'',l} c_{k'',l'} \\ &+ \sum_{\Lambda' < \Lambda_j, p', k''} c_{p',l}^\dagger c_{p',l'}^\dagger c_{j',l'} \frac{8R_{l,\delta\delta''}^{(j)} R_{l,\delta'\delta''}^{(j)} \prod_{i=1}^3 \tau_i}{[G_{j,l,3}]^{-1} - R_{l,\delta'',\delta''}^{(j)} \prod_{i=1}^3 \tau_i} c_{j',l''}^\dagger c_{k'',l} c_{k'',l'}, \end{aligned} \quad (4.61)$$

where the states are labeled by  $i = 1 : (\mathbf{k}_{\Lambda_j, \hat{s}}, \sigma)$ ,  $2 : (\mathbf{k}_{-\Lambda_j + \delta'', T\hat{s}}, -\sigma)$ ,  $3 : (\mathbf{k}_{\Lambda' \hat{s}}, \sigma)$ .

## 4.B The renormalized Hamiltonian at RG step $j$

The Hamiltonian at RG step  $j$  using flow equations eq.5.2, eq.5.3 and eq.5.4 is given by

$$\begin{aligned} H_{(j)}(\omega) &= \sum_{\Lambda < \Lambda_j} (\epsilon_{\Lambda \hat{s}} - \Delta \mu_{eff}) \left( \hat{n}_{\Lambda, \hat{s}, \sigma} - \frac{1}{2} \right) + \sum_{\delta, \hat{s} \neq \pm s'} L^{(j)(\omega)} c_{\Lambda, \hat{s}, \sigma}^\dagger c_{-\Lambda, T\hat{s}, -\sigma}^\dagger c_{-\Lambda', T\hat{s}', -\sigma} c_{\Lambda', \hat{s}', \sigma} \\ &+ \sum_{\delta, \hat{s}, \Lambda < \Lambda_j} (V_{c,l}^{(j)}(\omega) c_{\Lambda, \hat{s}, \sigma}^\dagger c_{-\Lambda + \delta, T\hat{s}, -\sigma}^\dagger c_{-\Lambda' + \delta, T\hat{s}, -\sigma} c_{\Lambda', \hat{s}, \sigma} + K_{c,l}^{(j)}(\omega) c_{\Lambda, \hat{s}, \sigma}^\dagger c_{-\Lambda + \delta, T\hat{s}, -\sigma}^\dagger c_{-\Lambda' - \delta, -T\hat{s}, -\sigma} c_{\Lambda', -\hat{s}, \sigma}) \\ &- \sum_{\delta, \hat{s}, \Lambda < \Lambda_j} (V_{s,l}^{(j)}(\omega) c_{\Lambda, \hat{s}, \sigma}^\dagger c_{-\Lambda + \delta, T\hat{s}, -\sigma}^\dagger c_{\Lambda', T\hat{s}, -\sigma}^\dagger c_{2\Lambda + \Lambda' - \delta, \hat{s}, \sigma} + K_{s,l}^{(j)}(\omega) c_{\Lambda, \hat{s}, \sigma}^\dagger c_{-\Lambda + \delta, T\hat{s}, -\sigma}^\dagger c_{\Lambda', -\hat{s}, -\sigma}^\dagger c_{\Lambda' + \delta - 2\Lambda, -T\hat{s}, \sigma}) \\ &+ \sum_{\delta, \hat{s}, \Lambda, \Lambda', \Lambda'' < \Lambda_j} R_{l,\delta\delta'}^{(j)}(\omega) c_{\Lambda, \hat{s}, \sigma}^\dagger c_{-\Lambda + \delta, T\hat{s}, -\sigma}^\dagger c_{-\Lambda' + \delta, \hat{s}, \sigma}^\dagger c_{-\Lambda'' + \delta', \hat{s}, \sigma} c_{-\Lambda'' + \delta', T\hat{s}, -\sigma} c_{\Lambda'', \hat{s}, \sigma} \end{aligned} \quad (4.62)$$

## 4.C Benchmarking results for $2 \leq U/t \leq 12$

Here we present results for the ground state energy per site  $E_g$  obtained from the RG fixed point theories for various values of  $U/t$  at hole-fraction  $f_h = 0$ . The values in the third and fifth columns for  $U/t = 2, 4, 6, 8, 12$  are obtained from several different numerical methods [49, 77]. The ground state energy values for  $U/t = 10$  are obtained from exact diagonalization studies of a  $4 \times 4$  Hubbard-cluster [450].

Table 4.C.1: Ground state energy per site values obtained from the RG fixed points for  $U/t = 2, 4, 6, 8, 10, 12$ . The error bar for all data obtained from the RG is  $O(10^{-4}t)$ . Third column for  $U/t = 2, 4, 6, 8$  and 12 represent the range of values obtained for the ground state per site for several different numerical methods [49, 77, 450]

$U_0/t$	$E_g$ from RG at hole-fraction $f_h = 0$	Range of $E_g$ from various numerical methods at $f_h = 0$ collated from [49, 450]
2	-1.199	(-1.176)–(-1.16)
4	-0.854	(-0.864)–(-0.85)
6	-0.652	(-0.658)–(-0.651)
8	-0.526	(-0.53)–(-0.51)
10	-0.439	-0.439
12	-0.367	(-0.369)–(-0.362)

# Chapter 5

## Scaling theory for Mott-Hubbard transitions - II : Quantum Criticality of the doped Mott insulator

In this chapter, we extend the unitary RG formalism to the treatment of the hole-doped 2D Hubbard model on the square lattice. In Section 5.1, we introduce the Hubbard model with the chemical potential term and review some major results from Chapter 4. We then present the RG equations for the doped 2D Hubbard model. In Section 5.2, we unveil the presence of a quantum critical point (QCP) reached at a critical doping. We then present results for the numerical benchmarking of the doped Mott liquid against results obtained from Refs. [49, 77, 450]. This is followed by the presentation of a body of analytical results that explain a large body of experimental phenomenology observed in the hole-doped cuprates. The latter includes, for instance, a detailed analysis of the origin of Homes law [44] and Planckian dissipation [323]. We then present results in Section 5.3 for the presence of symmetry-broken states of matter (including superconductivity) in the RG analysis, and compare once more the results obtained with the well-known phenomenology of the cuprates. Finally, we conclude our presentation in Section 5.4 by a detailed discussion of the relevance of our work to the cuprates, and by presenting future perspectives. Further details of the derivations of various RG relations are presented in several appendices.

### 5.1 Hubbard model with finite chemical potential

In this section we briefly discuss the RG scheme, the RG equations for various scattering vertices's obtained from applying URG to the doped 2D Hubbard model , and end by presenting the effective Hamiltonian obtained earlier in chapter 4 for the parent metal phase of the Mott insulating phase. Later sections will be devoted to adapting the technique for studying the 2D Hubbard model on the square lattice with a chemical potential away from 1/2-filling. To begin

with, we present the Hamiltonian of the 2D Hubbard model

$$\hat{H} = \sum_{\mathbf{k},\sigma} (\epsilon_{0\mathbf{k}} - \mu_{eff}) c_{\mathbf{k}\sigma}^\dagger c_{\mathbf{k}\sigma} + U_0 \sum_{\mathbf{r}} \hat{\tau}_{\mathbf{r}\uparrow} \hat{\tau}_{\mathbf{r}\downarrow}, \quad (5.1)$$

where  $c_{\mathbf{k}\sigma}^\dagger/c_{\mathbf{k}\sigma}$  is the electron creation/annihilation operator with wave-vector  $\mathbf{k}$  and spin  $\sigma$ ,  $\hat{\tau}_{\mathbf{r}\sigma} = \hat{n}_{\mathbf{r}\sigma} - \frac{1}{2}$ ,  $\hat{n}_{\mathbf{r}\sigma} = c_{\mathbf{r}\sigma}^\dagger c_{\mathbf{r}\sigma}$  is the number operator at lattice site  $\mathbf{r} = j_1\hat{x} + j_2\hat{y}$ , and  $\epsilon_{0\mathbf{k}}$  is the bare dispersion. The effective chemical potential,  $\mu_{eff} = \mu - \frac{U_0}{2}$ . The dispersion for the square lattice is  $\epsilon_{0\mathbf{k}} = -2t(\cos k_x + \cos k_y)$ . In this work, we will study doping-driven quantum phase transitions seen by tuning the effective field  $\Delta\mu_{eff} = \mu_{eff}^0 - \frac{\Delta U_0}{2}$  ( $\mu_{eff}^0 = 0$ ), in the subspace of doublons and holons.

Initial steps involve setting up the labelling scheme for the states in energy-momentum space with reference to the non-interacting Fermi surface (F) wave-vectors  $\mathbf{k}_F$ . We mark the states in terms of unit vectors normal to F ( $\hat{s} = \frac{\nabla\epsilon_{\mathbf{k}}}{|\nabla\epsilon_{\mathbf{k}}|}|_{\epsilon_{\mathbf{k}}=E_F}$ ) and lying at a distance  $\Lambda$  from F:  $\mathbf{k}_{\Lambda\hat{s}} = \mathbf{k}_F\hat{s} + \Lambda\hat{s}$  (see Fig. 5.1.1). States are thus ordered in terms of distances  $\Lambda_N > \dots > \Lambda_j > \Lambda_{j-1} > \dots > 0$ , where  $\Lambda_N$  lies near the Brillouin zone (BZ) edge and the smallest  $\Lambda$  is proximate to the Fermi surface. Following this construction, the electronic states are labelled equivalently as  $|j, l\rangle \equiv |\mathbf{k}_{\Lambda_j\hat{s}}\sigma\rangle (l = \{\hat{s}, (\sigma = \uparrow, \downarrow)\})$ . By employing unitary transformations iteratively, the RG disentangles electronic states in shells, starting from near the BZ edge and scaling towards  $E_F$ . Thus, at step  $j$ , all the states on the curve labelled by  $\Lambda_j$  are disentangled via a unitary rotation  $U_{(j)}$ . The resulting Hamiltonian  $H_{(j-1)} = U_{(j)} H_{(j)} U_{(j)}^\dagger$  is off-diagonal only for states with  $\Lambda < \Lambda_j$ .

The disentanglement of an entire curve at distance  $\Lambda_j$  is represented via a product of unitary rotations  $U_{(j)} = \prod_{l \in \{\hat{s}, \sigma=\uparrow/\downarrow\}} U_{(j,l)}$ , where  $U_{(j,l)}$  eq.(4.2) disentangles one state  $\mathbf{k}_{\Lambda_j\hat{s}}\sigma$  on the curve  $\Lambda_j$ . Thus, at step  $j$ , all the states on the curve labelled by  $\Lambda_j$  are disentangled via a unitary rotation  $U_{(j)}$ . The resulting Hamiltonian  $H_{(j-1)} = U_{(j)} H_{(j)} U_{(j)}^\dagger$  is off-diagonal only for states with  $\Lambda < \Lambda_j$ . From the Hamiltonian flow equation we obtain a hierarchy of RG flow-equations for various  $n$ -particle interaction vertices. In this work, we have studied only the 1-particle self-energy, as well as 2- and 3-particle scattering vertices. From the stable fixed-point solutions of these vertex-RG flow-equations, we obtain effective Hamiltonians. Further, from the unitary RG evolution of the Hamiltonian  $H_{(j-1)} = U_{(j)} H_{(j)} U_{(j)}^\dagger$ , we can extract the spin- / charge-type forward scattering ( $V_{s/c,l}^{(j)}$ ), backscattering ( $K_{s/c,l}^{(j)}$ ), tangential scattering ( $L^{(j)}$ ) and the three-particle vertex ( $R_{s,\delta}^{(j)}$ ) RG equations as follows (chapter 4)

$$\Delta V_{c/s,l}^{(j)} = \pm \frac{p_\pm (V_{c/s,l}^{(j)})^2}{-[G_{j,l}^{p,\uparrow}]^{-1} - \frac{V_{p,l}^{(j)}}{4}}, \quad \Delta K_{c/s,l}^{(j)} = \pm \frac{p_\pm (K_{c/s,l}^{(j)})^2}{[G_{j,l}^{p,\uparrow}]^{-1} - \frac{K_{p,l}^{(j)}}{4}}, \quad (5.2)$$

$$\Delta L^{(j)} = \frac{N_j^2 (L^{(j)})^2}{\bar{\omega} + \tilde{\epsilon}_{j,avg}^c - \frac{1}{4} L^{(j)}}, \quad (5.3)$$

$$\Delta R_{s,\delta}^{(j)} = \frac{V_l^{(j)}(\delta) V_l^{(j)}(\delta')}{\omega - \epsilon^{(j)}}_{j,l} + \frac{K_l^{(j)}(\delta) K_l^{(j)}(\delta')}{\omega - \epsilon^{(j)}}_{j,l} + \frac{R_{l,\delta\delta''}^{(j)} R_{l,\delta''\delta'}^{(j)}}{-[G_{j,l}^{p,\uparrow}]^{-1} + \frac{1}{8} R_{l,\delta''}^{(j)}}. \quad (5.4)$$

Here  $\delta$  represents a shift in one of the momentum vectors describing an asymmetric pair about the nodal direction (black dashed arrow in Fig. 5.1.1)  $|\mathbf{k}_{\Lambda,\hat{s}}\rangle, |\mathbf{k}_{-\Lambda+\delta,T\hat{s}}\rangle$  (symmetric pair is made of

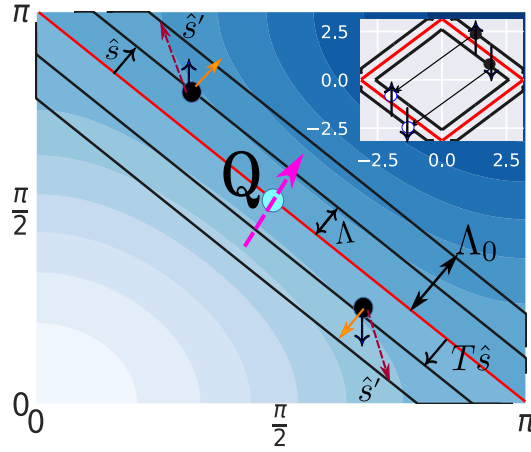


Figure 5.1.1: (Colour Online) Schematic representation of shells (black lines parallel to and formed around the FS (red line)) of states that are integrated out from first quadrant of Brillouin zone (BZ).  $\hat{s}$  represents the direction normal to F,  $T\hat{s} = (s_y, s_x)$  represents the orientation vector symmetrically placed about the nodal vector  $\mathbf{Q}$ . Black dots represent the states symmetrically placed about FS.

the black dots in Fig.5.1.1).  $\bar{\omega} = \omega + \text{sgn}(\Delta\mu_{eff})W$  is the effective fluctuation scale for tangential scattering renormalized by the bandwidth  $W = 8t$ .  $V_{p,l}^{(j)}(\delta) = p_+ V_{c,l}^{(j)}(\delta) - p_- V_{s,l}^{(j)}(\delta)$  is the spin charge hybridized interaction strength, and  $p_{\pm}$  are the coefficients for the hybridisation of spin and charge fluctuations with  $p_+ = p = 1 - p_-$ . The Green's function  $[G_{j,l}^{p,\uparrow}]^{-1}$  is defined as

$$[G_{j,l}^{p,\uparrow}]^{-1} = [\omega - p_+ \left( \frac{\epsilon_{j,l} + \epsilon_{j,l'}}{2} - \Delta\mu_{eff} \right) - p_- \frac{\epsilon_{j,l} - \epsilon_{j,l'}}{2}]^{-1}, \quad (5.5)$$

where  $p$  is chosen so as to maximise  $G_{j,l}^{p,\uparrow}$ . Additionally, from the RG eq.(5.2), we obtain an RG invariant  $C = [pK_{s,l}^{(j)}]^{-1} + [(1-p)K_{c,l}^{(j)}]^{-1}$ .

We can now review the effective theory for the parent metallic phase of the Mott insulating phase in the 2D Hubbard model at half filling chapter4. At large fluctuation scales  $\frac{W}{2} - \omega > \frac{W}{2}$ , the effective Hamiltonian for the parent metallic state is found to be eq.(4.17)

$$H_1 = \sum_{j,l} \epsilon_{j,l} \hat{n}_{j,l} + \sum_{j,j',l} R_{l\delta}^* \hat{n}_{j,l} \hat{n}_{j,l'} (1 - \hat{n}_{j',l}), \quad (5.6)$$

where  $\frac{R_{l\delta}^*}{8} = \bar{\omega} - 2^{-1}(\epsilon_{\Lambda^{**},\hat{s}} + \epsilon_{-\Lambda^{**},\hat{s}})$ . Here  $\Lambda_s^{**}$  is the momentum scale below which the Fermi liquid is absent, and  $\bar{\omega} = \max_{\delta,\hat{s}} 2^{-1}(\epsilon_{j^*,l} + \epsilon_{j^*,l'})$  is the renormalized fluctuation scale determined from the fixed point of the RG for forward scattering. The ground state for the metallic phase is given by

$$|\Psi_{gapless}\rangle = \prod_{\hat{s}_N}^{\hat{s}_{AN}} \prod_{\Lambda\Lambda'\delta} |1_{\Lambda\hat{s}} 1_{-\Lambda+\delta T\hat{s}} 0_{-\Lambda'\hat{s}}\rangle. \quad (5.7)$$

By incorporating the three-particle vertices in the one-particle self-energy, we obtain the renormalised self-energy and quasiparticle residue ( $Z$ ) as

$$\Sigma(\tilde{\omega}_{\hat{s}}) = \tilde{\omega}_{\hat{s}} \ln \left| \frac{N(\hat{s}, \Lambda^{**})\bar{\omega}}{\tilde{\omega}_{\hat{s}}} \right|, \quad Z(\tilde{\omega}_s) = \left( 2 - \ln \left| \frac{\tilde{\omega}_{\hat{s}}}{N(\hat{s}, \Lambda^{**})\bar{\omega}} \right| \right)^{-1}, \quad (5.8)$$

where  $\tilde{\omega}_{\hat{s}} = N(\hat{s}, \Lambda^{**})(\bar{\omega} - \frac{1}{2}\epsilon_{\Lambda^{**}, \hat{s}})$ , and  $N(\Lambda^{**}, \hat{s})$  is the total number of states within the window  $\Lambda^{**}$  along the direction  $\hat{s}$  normal to the FS. Thus, the imaginary part of the self-energy (and therefore the inverse lifetime) has the form  $\Sigma^{Im} = \tau^{-1} = \tilde{\omega}_{\hat{s}}$ . Altogether, this reproduces the Marginal Fermi liquid phenomenology proposed for the strange metal phase of the cuprates [460].

## 5.2 Mottness Collapse and quantum criticality with hole-doping

We present the RG phase diagram for the 2D Hubbard model with doping away from 1/2-filling in Fig. 5.2.1. This phase diagram results from longitudinal and tangential scattering RG equations (eq.5.2, eq.5.3) upon including effects of doping  $\Delta\mu_{eff} \neq 0$  and Cooper pair scattering processes across the Fermi surface. Upon doping the Mott insulator via an effective chemical potential, we observe a marginal Fermi liquid metal (whitish-blue region in Fig. 5.2.1) in the energy scale  $\frac{W}{2} < \frac{W}{2} - \omega < W$ . This phase is analytically continued from that observed at 1/2-filling case ( $\Delta\mu_{eff} = 0$ ) with a 2e-1h dispersion contained in the Hamiltonian eq.4.17. On lowering the energy scale, the marginal Fermi liquid undergoes once again a Lifshitz transition into the pseudogap phase (misty blue region in Fig. 5.2.1) with spin gapping at the antinodes (AN). The onset energy scale for spin fluctuations that gap the AN is  $\omega > \omega_{PG} \equiv \omega_{PG}^s$ .

Further lowering the energy scale gaps the charge fluctuations at the AN, i.e., creates a charge pseudogap at AN. The energy scale for the gapping of charge fluctuations at the AN (dotted red line in Fig. 5.2.1) is delayed, falling linearly with increasing doping:  $\omega > \omega_{PG}^c = -\Delta\mu_{eff}$ . Upon yet lowering the energy scale for fluctuations causes the exit from the pseudogap via a second Lifshitz transition into a Mott liquid state (solid blue region). The Mott liquid insulator comprises the following region in the phase diagram (Fig.5.2.1, Video S4):  $(\frac{W}{2} - \omega < 1.2t)$  with  $\Delta\mu_{eff} > -2.8t$ , and  $(\frac{W}{2} - \omega < -2\Delta\mu_{eff})$  with  $\Delta\mu_{eff}^* < \Delta\mu_{eff} < -2.8t$  and  $\Delta\mu_{eff}^* = -\frac{W}{2}$ .

The variation of spin charge hybridization parameter  $p$  (see Sec.4.1) with doping  $\Delta\mu_{eff}$  leads to a separation of the charge gap-dominated and spin gap-dominated parts of the pseudogap within the phase diagram Fig.5.2.1, such that the boundary of the charge gap-dominated pseudogap (dotted red line in Fig.5.2.1) is observed to fall with increasing doping straight into a quantum critical point (QCP) at  $\omega_{PG}^{c,*} = W/2 = -\Delta\mu_{eff}^*$ . This is called the collapse of Mottness [475, 476]. The QCP is associated with point-like Fermi surfaces at the four nodal points, and spin-gapping that increases monotonically from near the nodes to the antinodes (Fig.5.2.2(b), Videos S2, S3). The resulting nodal metal supports a 2e-1h dispersion that is analytically continued from  $\frac{W}{2} - \omega = W$  at  $\Delta\mu_{eff} = 0$  down to  $\frac{W}{2} - \omega = 0$ , and given by  $\epsilon_{\mathbf{k}_{\Lambda^{**}, N}} = -\sqrt{2t}\Lambda$ . This linear dispersion signals the Lorentz invariance emergent precisely at the QCP. Thus, the  $U(1)$  symmetry of the charge fluctuations is promoted to  $SU(2)$  at the QCP due to the emergent particle-hole symmetry of the gapless nodal Dirac electrons. Indeed, these findings for the QCP are in striking agreement with the works of Phillips and co-workers [477].

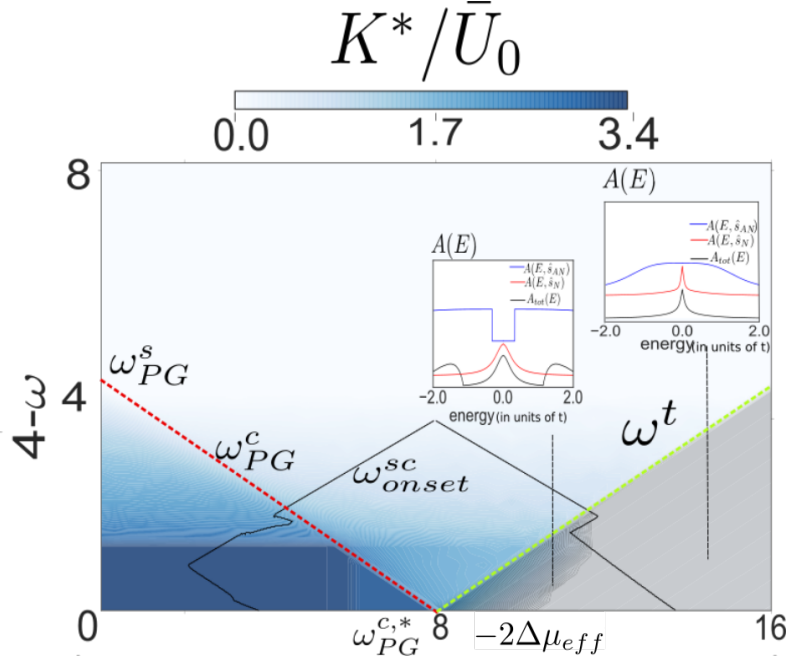


Figure 5.2.1: (Colour Online) RG phase diagram with hole doping showing quantum critical point (QCP) at  $-\Delta\mu_{eff} = 4 = \omega$  and its wedge extending to higher energies. All phases (NFL, PG, ML, correlated Fermi liquid (CFL), PG-CFL and QCP-wedge) and related energy scales are shown in the colour bars, and discussed in detail in the text. Dashed line shows highest energy scale for superconducting fluctuations. Insets: N, AN and FS-averaged spectral function ( $A(E)$ ) for the QCP and gapless CFL (grey region:  $\omega = 3.2, \Delta\mu_{eff} = -7.5$ ).

For  $\omega > \omega_{PG}^{c,*}$ , to the left of the QCP, lies the Mott liquid discussed earlier. For  $\omega > \omega^t = \Delta\mu_{eff} - 2\Delta\mu_{eff}^*$ , to the right of the QCP, lies a correlated Fermi liquid (CFL) arising from RG relevant tangential scattering (Fig. 2(a) inset). The CFL is associated with well-defined electronic quasiparticles coexisting with the 2e-1h composites of the marginal Fermi liquid on different parts of the gapless FS. For  $-\Delta\mu_{eff}^* < -\Delta\mu_{eff} < 5$ , the FS forms four gapless stretches centred around the nodes, and with spin-gapped regions at the antinodes. Here, the FL quasiparticles are present in regions around the nodes, while the MFL 2e-1h composites are positioned at the ends of the gapless stretches. For  $\Delta\mu_{eff} > \Delta\mu_{eff}^S$ , the FS reconnects, and the MFL is confined to the antinodes.

### 5.2.1 Low energy eigenstates of the doped Mott liquid and the QCP

From the RG eqs.5.2 at finite  $\Delta\mu_{eff}$ , we obtain the relation between the fixed point spin and charge backscattering coupling

$$K_s^*(\omega, \Delta\mu_{eff}) = \frac{\bar{U}_0(1-p)K_c^*(\omega, \Delta\mu_{eff})}{K_c^*(\omega, \Delta\mu_{eff}) - \bar{U}_0p}, \quad (5.9)$$

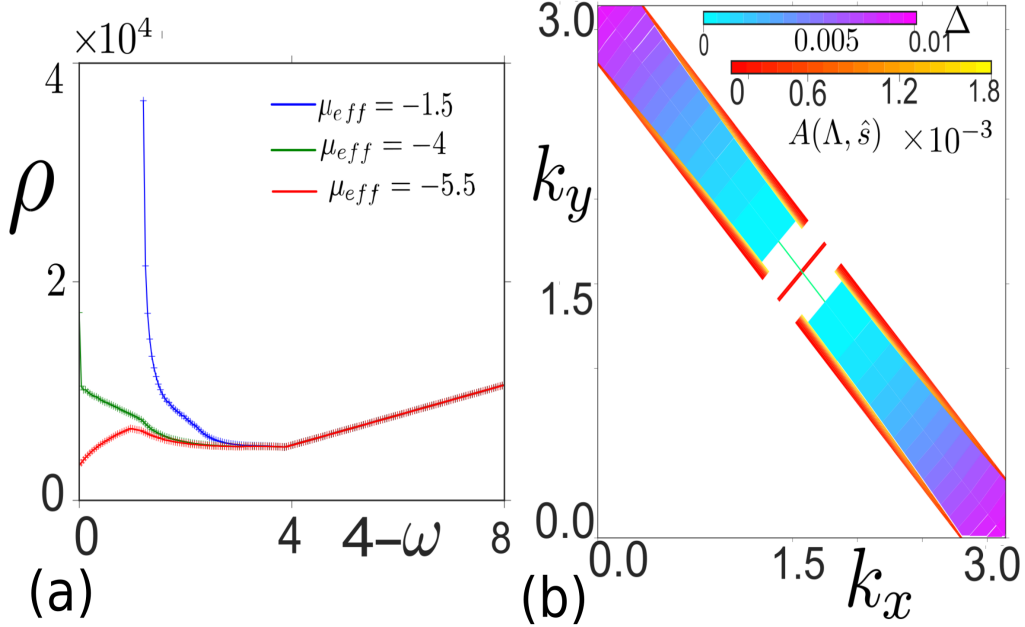


Figure 5.2.2: (Colour Online) (a) Resistivity ( $\rho$ ) vs.  $4 - \omega$  for various  $\Delta\mu_{eff}$ , showing passage from NFL into (blue) ML, (green) the QCP and (red) PG-CFL. (b) Map of  $A(E)$  at the QCP.

where the parameter  $p$  is determined upon maximizing the green function eq. 5.5. For instance within the Mott liquid phase on  $W/2 - \omega = 0$  axis  $p = 0$  for  $2.9 > -\Delta\mu_{eff} > 0$ ,  $p = 1$  for  $W/2 > -\Delta\mu_{eff} > 2.9$ . For these two cases,  $K_s^*(\omega, \Delta\mu_{eff}) = K_c^*(\omega, \Delta\mu_{eff}) = \bar{U}_0$ , such that the fixed point Hamiltonian is given by,

$$H^*(\Delta\mu_{eff}) = \sum_{\hat{s}} \bar{U}_0 (\mathbf{A}_{*,\hat{s}} \cdot \mathbf{A}_{*,-\hat{s}} - \mathbf{S}_{*,\hat{s}} \cdot \mathbf{S}_{*,-\hat{s}}) + \Delta\mu_{eff} \sum_{\hat{s}} A_{\hat{s}}^z. \quad (5.10)$$

The pseudospins are defined as,

$$\mathbf{A}_{*,\hat{s}} = \sum_{\Lambda < \Lambda_{\hat{s}}^*} \mathbf{A}_{\Lambda,\hat{s}}, \mathbf{S}_{*,\hat{s}} = \sum_{\Lambda < \Lambda_{\hat{s}}^*} \mathbf{S}_{\Lambda,\hat{s}}, \mathbf{A}_{\Lambda,\hat{s}} = f_{\Lambda,\hat{s}}^{c;\dagger} \frac{\boldsymbol{\sigma}}{2} f_{\Lambda,\hat{s}}^c, \mathbf{S}_{\Lambda,\hat{s}} = f_{\Lambda,\hat{s}}^{s;\dagger} \frac{\boldsymbol{\sigma}}{2} f_{\Lambda,\hat{s}}^s \quad (5.11)$$

Here  $f_{\Lambda,\hat{s}}^{c;\dagger} = [c_{\Lambda,\hat{s},\sigma}^\dagger \ c_{-\Lambda,T\hat{s},-\sigma}]$ ,  $f_{\Lambda,\hat{s}}^{s;\dagger} = [c_{\Lambda,\hat{s},\sigma}^\dagger \ c_{\Lambda-2\Lambda_{\hat{s}}^*,T\hat{s},-\sigma}^\dagger]$ , are the spinorial representation for a pair of Fermions. The low-lying eigenstates and eigenenergies of the doped Mott liquid is given by,

$$|\Psi\rangle = \prod_{\hat{s}} |A_{*,\hat{s}} = A_{*,-\hat{s}} = N_{\hat{s}}^*, A = n, A^z = n, S_{\Lambda\hat{s}} = 0\rangle, \quad (5.12)$$

$$E(n) = \sum_{\hat{s}} \frac{\bar{U}_0}{2} [n(n+1) - 2N_{\hat{s}}^*(N_{\hat{s}}^* + 1)] + \Delta\mu_{eff}n. \quad (5.13)$$

This many body wavefunction can be seen as resulting out of the doping the ground state wavefunction for the Mott liquid at half filling ( $\Delta\mu_{eff} = 0$ ) with  $n$  holes, where  $n$  is bounded

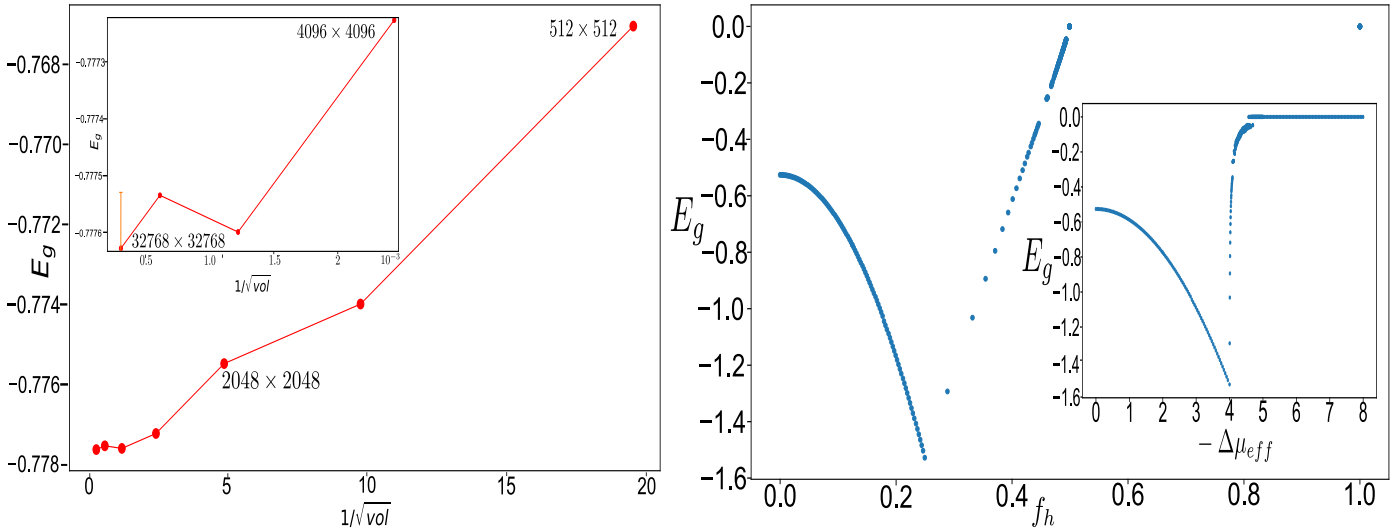


Figure 5.2.3: (a)(Colour Online) Variation of ground state energy per particle  $E_g$  of the doped Mott liquid (for  $U_0 = 8t$  and hole doping  $f_h = 0.125$ ) with inverse square root of system size ( $1/\sqrt{vol}$ , ranging from  $512 \times 512$ - to  $32768 \times 32768$ -sized  $k$ -space grids) and showing saturation at  $-0.776t$ . (b) Variation of ground state energy  $E_g$  with hole doping  $f_h$  for lattice size  $1024 \times 1024$  and  $U_0 = 8t$ . Inset: Variation of ground state energy  $E_g$  with  $-\Delta\mu_{eff}$ .

$0 \leq n \leq 2N_s^*$  from angular momentum algebra. These low lying states have been obtained by respecting the attractive nature of the spin pseudospin interactions and the repulsive nature of the charge pseudospin interactions. The ground state energy  $E_g(\Delta\mu_{eff}) = E(n^*)$ , and hence  $n^*$ , can then be obtained from a numerical search of the lowest eigenvalue of the energy function  $E(n)$  eq5.13. From this, we can obtain the hole-doping fraction  $f_h = \frac{n^*}{2N}$ . We conducted a test of these results by comparing the ground state energy obtained for  $U = 8t$  and at a hole-doping fraction of  $f_h = 0.125$  (i.e., 12.5% hole doping) against that obtained from various other numerical methods as given in Ref.[49]. Fig.5.2.3(a) shows a finite-size scaling plot of  $E_g(\Delta\mu_{eff})$  per particle at 12.5% hole doping and system sizes (i.e., number of sites) varying between  $32 \times 32$  to  $32768 \times 32768$ . The value of  $E_g(\Delta\mu_{eff})$  per particle in the thermodynamic limit from this analysis appears to be converging towards  $-0.776$  (in units of the hopping amplitude  $t$ ), and compares well with the range of  $-0.74 > (E_g/\text{per particle}) > -0.77$  obtained from Ref.[49, 77]. We also point the reader to further benchmarking exercises presented in Appendix-5.B with  $U/t = 2, 4, 6, 10$  at 12.5% doping. Once more, we find excellent agreement with the results obtained from the numerical methods employed in Refs.[450] and [49, 77], offering confidence on the effective Hamiltonian and ground state wavefunction derived for the doped Mott liquid.

A plot of  $E_g$  as a function of  $f_h$  (Fig.5.2.3(b)) clearly shows cusp-like behaviour at  $f_h = 0.25$ , signalling a quantum critical point (QCP). The discontinuity in the first derivative is also seen in a plot of  $E_g$  vs.  $-\Delta\mu_{eff}$  (inset of Fig.5.2.3(b)), as well as a plot of  $f_h$  vs.  $-\Delta\mu_{eff}$  (Fig.5.2.4(a)). The step-like discontinuity observed in  $f_h$  at  $-\Delta\mu_{eff} \simeq 7.2$  indicates the topological reconstruction of a fully connected Fermi surface as the spin pseudogapped parts of the FS vanish at this value of the chemical potential. This is reinforced by a plot of the number compressibility  $\kappa$  with the chemical potential  $\Delta\mu_{eff}$  in the inset of Fig.5.2.4(a)): the first spike indicates the appearance

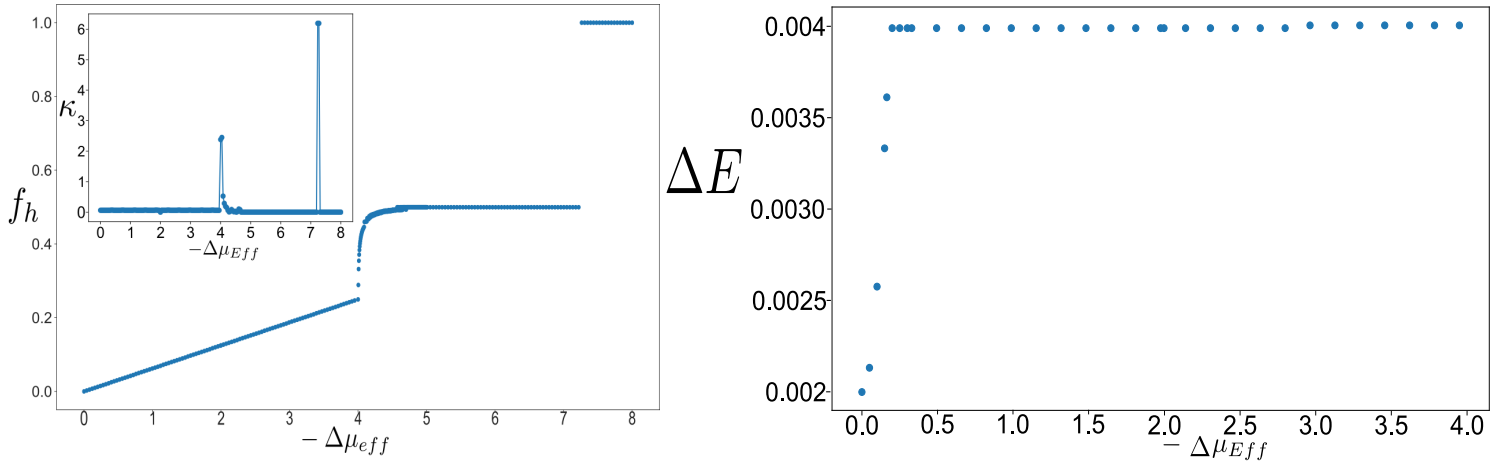


Figure 5.2.4: (a) Variation of hole doping  $f_h$  with chemical potential  $\Delta\mu_{eff}$  for lattice size  $1024 \times 1024$ . Inset: Number compressibility  $\kappa$  as a function of chemical potential  $\Delta\mu_{eff}$ . Spikes in  $\kappa$  are visible at  $-\Delta\mu_{eff} = 4$  and at  $-\Delta\mu_{eff} \sim 7.2t$ . (b) Variation of the energy gap  $\Delta E$  per particle of the doped Mott Liquid along the nodal direction with the chemical potential  $\Delta\mu_{eff}$ .

of point-like nodal FS at the QCP, while the second denotes the reconstruction of a fully connected FS. Note that in Ref.[478] the authors find a peculiar feature in the doping dependence of the chemical potential, resulting from a fermi surface shift due to doping. This feature is not present in our approach as we treat  $\Delta\mu_{eff}$  as an effective field in the space of doublons and holons. A future investigation of this feature is necessary where we treat a Fermi surface shift in our approach. In order to understand better the nature of the QCP, we present a plot of the energy gap  $\Delta E$  per particle along the nodal direction in the doped Mott liquid with varying  $-\Delta\mu_{eff}$  in Fig.5.2.4(b). The plot shows that  $\Delta E$  per particle rises steadily from a value of  $0.002t$  and saturates at  $0.004t$  well before the QCP is approached from the underdoped side. This saturated value of  $\Delta E$  appears to be robust very close to the QCP, and collapses abruptly to 0 at the QCP. This signals the nucleation of gapless nodal Fermi points precisely at the QCP, and corresponds to a topology change in the Luttinger surface of zeros for the gapped Mott liquid. The QCP is an example of a Lifshitz transition driven by electronic correlations [66]. We can also compute the doublon occupancy from the hole-doping fraction  $f_h, D = D_0(1 - f_h)$ , where  $D_0$  is the doublon fraction at half-filling. This is shown in Fig.5.2.5, and shows a steady decline in the doublon occupancy of the doped Mott liquid from half-filling till the QCP. We also note that the value of 0.045 is obtained for the doublon occupancy  $D$  at a hole doping of 12.5%, and compares well with the range  $0.04 < D < 0.045$  obtained from various numerics in Ref.[49].

The eigenenergies for the gapped parts of the FS at and across the QCP  $-W \leq \Delta\mu_{eff} \leq -\frac{W}{2}$  can be similarly obtained from the fixed point Hamiltonians at  $\omega = \frac{W}{2}$  (eq.5.18). For the gapless regions, the lowest excitations appear near zero energy. Taken together, this allows for a determination of the ground state energy ( $E_g$ ) and hole-doping fraction ( $f_h$ ) as a function of chemical potential  $\Delta\mu_{eff}$  for a range of chemical potential that crosses the QCP. The results are shown in Fig.5.2.3(b) and 5.2.4(a). Specifically, we find that  $E_g$  rises steadily with  $\Delta\mu_{eff}$  from its value at the QCP to zero as the chemical potential leads to the reconstruction of a fully connected FS (inset of Fig.5.2.3(b)). Interestingly,  $f_h$  is seen to attain a plateau upon increasing

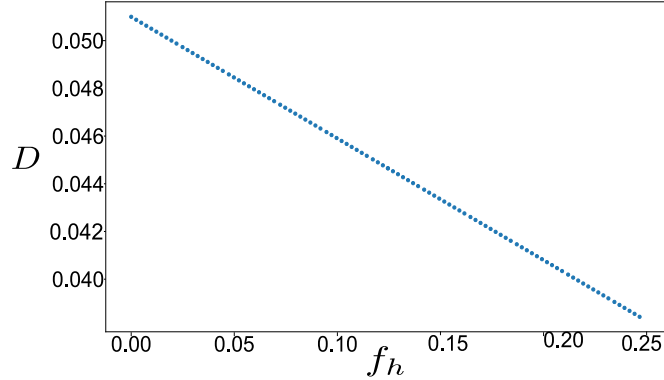


Figure 5.2.5: (Colour Online) Variation of the Double occupancy  $D$  of the doped Mott liquid with the hole fraction  $f_h$ . The plot shows a steady decline of  $D$  as  $f_h$  is increased towards the QCP.

$\Delta\mu_{eff}$  away from the QCP, transitioning abruptly at the FS reconstruction. These findings are consistent with results obtained from the dynamical cluster quantum Monte Carlo method applied to the 2D Hubbard model with doping away from 1/2-filling [58, 479], and unveil the mechanism responsible for the experimentally observed topological reconstruction of the Fermi surface near critical doping [480–482]. We will further discuss these results below, as we study the interplay of spin, charge, Cooper and tangential scattering processes in the vicinity of the QCP. The codes used for the numerical computations of the ground state energy and hole fraction shown here are made available electronically [463].

### 5.2.2 Signature of QCP in ground state fidelity susceptibility with doping

The fidelity of many-body ground state wavefunctions, computed as an overlap between wavefunctions obtained by tuning a parameter, has emerged recently as a candidate for tracking quantum phase transitions (QPT) [483, 484]. In this section, we will use fidelity to observe signatures of the QCP seen above. Fidelity is computed here from the overlap between ground states at  $\frac{W}{2} - \omega = 0$  obtained for infinitesimal variation ( $\epsilon > 0$ ) of the effective chemical potential  $\Delta\mu_{eff}$

$$F(\Delta\mu_{eff}, \epsilon) = |\langle \Psi_g(\Delta\mu_{eff}) | \Psi_g(\Delta\mu_{eff} - \epsilon) \rangle| . \quad (5.14)$$

The ground state wavefunctions for  $\Delta\mu_{eff} > -\frac{W}{2}$  can be represented purely in terms of pseudospins (eq.5.12), in which the quantum number  $n(\Delta\mu_{eff})$  is determined by minimizing the energy density eq.(5.13). For  $-\Delta\mu_{eff} < \frac{W}{2}$ , the fidelity is obtained as  $F(\Delta\mu_{eff}, \epsilon) = \delta_{n(\Delta\mu_{eff}), n(\Delta\mu_{eff} - \epsilon)} .$  However, for  $-\Delta\mu_{eff} > W/2$ , a gapless node formed at  $N = (\pi/2, \pi/2)$  stretches subsequently into an arc in momentum space. The gapped states in the AN regions can still be described in terms of the pseudospin wavefunctions eq.(5.12), whereas the gapless regions are described by separable eigenstates of the Hamiltonian eq.(4.17) in the occupation number basis of  $|\mathbf{k}\sigma\rangle$ . Thus, the ground states describing the journey across the QCP can, using eqs.(5.7) and (5.12),

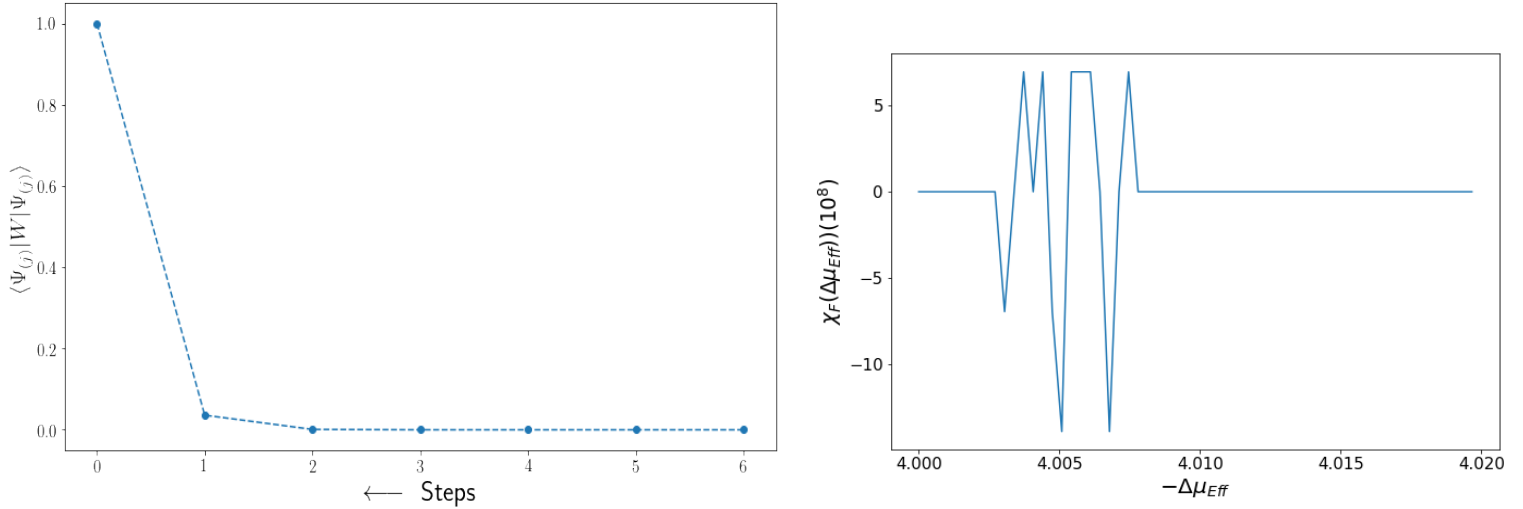


Figure 5.2.6: (a)  $\log(F(\Delta\mu_{eff}))$  Logarithm of fidelity, (b)  $\chi_F(\Delta\mu_{eff})$  fidelity susceptibility plotted against effective chemical potential( $\Delta\mu_{eff}$ ). The sudden changes in  $\log F$  and  $\chi_F$  at  $-\Delta\mu_{eff} \sim 4$  indicates the QCP. See detailed discussions in text.

be written as  $|\Psi_g(\Delta\mu_{eff})\rangle = |\Psi_{gapped}\rangle |\Psi_{gapless}\rangle$ . From here, the overlap between neighboring ground states for  $-\Delta\mu_{eff} > W/2$  axis is obtained as

$$\langle \Psi_g(\Delta\mu_{eff}) | \Psi_g(\Delta\mu_{eff} - \epsilon) \rangle = \binom{2N^*}{n(\Delta\mu_{eff} - \epsilon) + N^*}^{-l(\Delta\mu_{eff}, \epsilon)}, \quad (5.15)$$

where  $l(\Delta\mu_{eff}, \epsilon)$  is the increment of the gapless stretch and  $2N^*$  is the number of electronic states transformed into  $N^*$  bound pairs in the momentum-space window.

Plots Fig.5.2.6(a) and (b) show the variations of  $\log(F(\Delta\mu_{eff}))$  and fidelity susceptibility ( $\chi_F(\Delta\mu_{eff}) = d^2 \log(F(\Delta\mu_{eff}))/d\Delta\mu_{eff}^2$ ) with  $-\Delta\mu_{eff}$  respectively in the neighbourhood of the QCP at  $-\Delta\mu_{eff} \simeq 4$ . Note that, in order to avoid the log singularities in the numerical evaluation of  $F(\Delta\mu_{eff}) = 0$ , we have added a lower cutoff of  $10^{-323}$ .

Precisely at the QCP ( $-\Delta\mu_{eff} \simeq 4$ ),  $\log F$  falls suddenly to zero as the nodal points become gapless, and  $\chi_F$  shows a large sudden variation. This indicates that an increase in the gapless region from nodal point to arc forces the many-body wavefunction through a cascade of orthogonality catastrophies. The fidelity then rises  $F \rightarrow 1$  with increasing  $\Delta\mu_{eff}$ , indicating the recreation of a connected Fermi surface.

### 5.2.3 Theory for the vicinity of the QCP

Doping via an effective chemical potential  $\Delta\mu_{eff} = -\frac{\Delta U_0}{2}$  generates a doublon-holon imbalance via a field-like term for the charge pseudospins  $-\Delta\mu_{eff}(A_{*,\hat{s}}^z + A_{*,-\hat{s}}^z)$ . This lowers the global  $SU(2)$  charge symmetry to  $U(1)$ . Doublon-holon imbalance at lower values competes with the umklapp scattering term ( $A_{*,\hat{s}}^+ A_{*,-\hat{s}}^- + h.c.$ ) and finally dominates over it at larger values. On the other hand, this uniform field favours spin-backscattering of different finite  $\mathbf{p}$  pair momentum Anderson pseudospins ( $c_{\mathbf{k}_{\Lambda\hat{s}}\uparrow}^\dagger c_{\mathbf{p}-\mathbf{k}_{\Lambda\hat{s}}\downarrow}^\dagger$ ). Indeed, there exists a direct equivalence between  $\mathbf{p}$  pair

momentum (centered about  $\mathbf{p} = 0$ ) spin-backscattering terms and the electron hole pseudospin scattering terms,

$$\sum_{\mathbf{p}, \mathbf{k}, \mathbf{l}} K_{s,\alpha} c_{\mathbf{k},\uparrow}^\dagger c_{\mathbf{p}-\mathbf{k},\downarrow}^\dagger c_{\mathbf{k}',\downarrow} c_{\mathbf{p}-\mathbf{k}',\uparrow} = - \sum_{a,b} K_{s,\alpha} (S_a^+ S_b^- + h.c.) . \quad (5.16)$$

Here  $\alpha = \{\mathbf{p}, \hat{s}, \delta\}$  is a set comprising of pair momentum ( $\mathbf{p}$ ),  $\hat{s}$  normal to FS and  $\delta$  i.e. is the momentum shift from a pair of states  $|\mathbf{k}_{\Lambda\hat{s}}\rangle, |\mathbf{k}_{-\Lambda,T\hat{s}}\rangle$  chosen symmetrically about the nodal points.  $\mathbf{k} = \mathbf{k}_{\Lambda,\hat{s}}, \mathbf{k}' = \mathbf{k}_{\Lambda',T\hat{s}}$  are momentum state involved in the scattering where  $\Lambda' = \Lambda - 2\Lambda^* + \delta$ .  $\Lambda^*$  is the momentum space width around FS obtained from the fixed point of the spin backscattering RG equation eq. 5.2. In the equivalent pseudospin description  $\mathbf{S}_a = f_a^{s;\dagger} \frac{\sigma}{2} f_a^s$  where  $f_a^{s;\dagger} = (c_{\mathbf{k}\uparrow}^\dagger, c_{\mathbf{k}'\downarrow}^\dagger)$  and  $a = (\mathbf{k}, \mathbf{k}')$ ,  $b = (\mathbf{p} - \mathbf{k}, \mathbf{p} - \mathbf{k}')$ .

In accounting for all possible pair-scattering processes in the vicinity of the QCP, we include the contribution of Cooper and tangential scattering channels eq.5.3 in the spin-backscattering RG equation ( $\Delta K_{s,\alpha}^{(j)}$ ) eqs.5.2

$$\Delta K_{s,\alpha}^{(j)} = \frac{-(1-p)(K_{s,\alpha}^{(j)})^2}{e^{i\gamma_l^\uparrow} |G_{j,l}^{p,\uparrow}|^{-1} - \frac{K_{p,\alpha}^{(j)}}{4}} + \frac{(K_{s,\alpha}^{(j)})^2}{\omega - \frac{1}{2}\epsilon_j - |\Delta\bar{\mu}_{eff}| - \frac{K_{p,\alpha}^{(j)}}{4}} - \frac{N_j^2 (L_\delta^{(j)})^2}{\bar{\omega} + \epsilon_{j,avg}^s - \frac{L^{(j)}(\delta)}{4}} , \quad (5.17)$$

where  $\epsilon_j = \epsilon_{\mathbf{k}_{\Lambda_j\hat{s}}} + \epsilon_{\mathbf{p}-\mathbf{k}_{\Lambda_j\hat{s}}}$  is the pair kinetic energy,  $\Delta\bar{\mu}_{eff} = \Delta\mu_{eff} - \Delta\mu_{eff}^*$  is the effective chemical potential for the marginal Fermi liquid centered around the node, and renormalized by the fluctuation scale  $\omega_{PG}^{c,*} = \Delta\mu_{eff}^*$ .  $\epsilon_{j,avg}^s = N_j^{-1} \sum_{\hat{s}} (\epsilon_{\mathbf{k}_{\Lambda_j\hat{s}}} - \epsilon_{\mathbf{k}_{\Lambda_1,j,T\hat{s}}})$  and  $\Lambda_{1,j} = \Lambda_j - 2\Lambda^* + \delta$  is the longitudinal momentum of the electronic state comprising the electron hole pair. In the above RG equation, the spin-charge hybridized backscattering strength (with Cooper channel contribution) is given by  $K_\alpha^{(j)} = pK_{c,\alpha}^{(j)} + (1-p)K_{s,\alpha}^{(j)}$ ,  $K_{c,\alpha}^{(j)}$  being the vertex strength for finite momentum Umklapp scattering pairs. The negative sign of the first and third terms in the above RG equation originates from the interchanging of electron and hole creation operators. The second term contains contributions to spin-backscattering from the Cooper channel due to Cooper pairs with zero and non-zero pair-momentum. The third term accounts for the influence of tangential scattering on the spin-backscattering.

On either side of the QCP, spin-backscattering with  $\mathbf{p} = 0$  pair-momentum is suppressed by tangential scattering ( $\omega > \omega_t$ ) and  $\pi$ -momentum e-h pair-backscattering ( $\omega > \omega_{PG}^c$ ) processes, leading to the establishing of the CFL and Mott liquid phases respectively. Remarkably, right above the QCP (i.e.,  $\omega_{PG}^c < \omega < \omega_t$ ), we observe that the antinodal spin gap (composed of  $\mathbf{p} = 0$  pair-momentum Cooper pairs) carries the highest spectral weight. This can be seen from the smallest magnitude of the inverse Green function for  $\mathbf{p} = 0$  pair-momentum:  $G_{\Lambda\hat{s}}^{-1}(\omega, \mathbf{p}) = (\omega - (\epsilon_{\mathbf{k}_{\Lambda\hat{s}}} + \epsilon_{\mathbf{p}-\mathbf{k}_{\Lambda\hat{s}}})/2)$ . We also note that for  $\Delta\mu_{eff} = 0$ , only the first term has leading contribution in the above RG equation, thus analytically continuing to the  $\Delta\mu_{eff} = 0$  (i.e., 1/2-filled) case (eq.5.2).

The fixed point Hamiltonian obtained by investigating the RG relation eq.(5.17) for the gapped

parts and the 2e-1hole RG relation for the gapless parts of the FS (eq.5.4)

$$\begin{aligned}
 H^* = & \sum_{\Lambda, \hat{s}=\hat{s}_N, \delta}^{\hat{s}'} R_\rho^* \hat{n}_{\mathbf{k}, \uparrow} \hat{n}_{\mathbf{k}', \downarrow} (1 - \hat{n}_{\mathbf{l}, \uparrow}) + \sum_{\hat{s}=\hat{s}'}^{\hat{s}_{AN}} K_{c, \hat{s}}^* \mathbf{A}_{*, \hat{s}} \cdot \mathbf{A}_{*, -\hat{s}} + \sum_{\hat{s}=\hat{s}_{AN}, c, d}^{\hat{s}'} \frac{K_{s, \alpha}^*}{2} (B_c^+ B_d^- + h.c.) \\
 & - \sum_{\hat{s}=\hat{s}_{AN}, a, b}^{\hat{s}'} K_{s, \alpha}^{*, l} S_a^z S_b^z + \sum_{\delta, \hat{s}, \hat{s}'', \Lambda} L_\delta^* \hat{n}_{\mathbf{k}, \uparrow} \hat{n}_{\mathbf{k}'', \downarrow} + \sum_{\Lambda, \hat{s}=\hat{s}_N} \tilde{\epsilon}_{\mathbf{k}} \hat{n}_{\mathbf{k}} + \sum_{\hat{s}=\hat{s}'} (\Delta \bar{\mu}_{eff} B_c^z + \Delta \mu_{eff}^* A_{\Lambda, \hat{s}}^z) \quad (5.18)
 \end{aligned}$$

where the charge ( $\mathbf{A}$ ) fluctuation pseudospins has been defined earlier, and the generalized Cooper pairs/Anderson pseudospins are given by  $\mathbf{B}_c = f_c^{cp\dagger} \frac{\sigma}{2} f_c^{cp}$ ,  $f_c^{cp} = (c_{\mathbf{k}\uparrow}^\dagger c_{\mathbf{p}-\mathbf{k}\downarrow})$  and indices  $c = (\mathbf{k}, \mathbf{p} - \mathbf{k})$ ,  $d = (\mathbf{k}', \mathbf{p} - \mathbf{k}')$  label these pseudospins. The momentum vectors in terms of  $\Lambda$ ,  $\hat{s}$  are  $\mathbf{k} = \mathbf{k}_{\Lambda, \hat{s}}$ ,  $\mathbf{k}' = \mathbf{k}_{\Lambda'', T\hat{s}}$ ,  $\mathbf{l} = \mathbf{k}_{\Lambda', \hat{s}}$ ,  $\mathbf{k}'' = \mathbf{k}_{\Lambda'', T\hat{s}''}$  and  $\hat{s}' = \hat{s}(\omega, \Delta \mu_{eff})$  is the normal vector upto which gapless part stretches.  $\Lambda'' = -\Lambda + \delta$  is the normal distance at which the partner electronic state of 2-electron 1-hole composite is placed.  $\rho = \{\delta, \hat{s}\}$  is a set comprising of offset momentum  $\delta$  and normal  $\hat{s}$ . The set  $\alpha$  and indices  $a$  and  $b$  are as defined earlier. The  $\mathbf{p} = 0$  pair-momentum Cooper pair pseudospin scattering terms can, as discussed earlier, be recast in terms of the electron-hole pseudospins  $-(S_a^+ S_b^- + h.c.) = (B_c^+ B_d^- + h.c.)$ . This confirms that even as we study a model of repulsive electronic correlations, the effective attractive nature of spin pseudospin backscattering is responsible for the formation of preformed Cooper pairs in the gapped antinodal regions of the FS [485, 486]. Thus, the first term in eq.5.18 corresponds to the 2e-1h nodal Marginal Fermi liquid metal. The second and third terms govern the gapping mechanisms of the Fermi surface by charge and Anderson pseudospins respectively. The fourth term is associated with tangential scattering in the gapless stretches of the FS, while the fifth term (proportional to  $B_{\Lambda, \hat{s}}^z$ ) reflects the doublon-holon disparity with hole doping.

The Hamiltonian  $H^*(\omega, \Delta \mu_{eff})$  naturally encompasses the doped Mott liquid Hamiltonian with insulating ground states in the region  $0 > -\Delta \mu_{eff} > -\Delta \mu_{eff}^*$  and  $\omega = \frac{W}{2}$ . This can be seen as follows:  $R_{\hat{s}, \delta}^* = 0$  for all  $\hat{s}$ ,  $L_\delta^* = 0$  from eq5.2, eq5.3. Then the resonant pairs with  $\delta = 0$  interacting via scattering vertex dominates over all others eq5.17. Further, the z-component of the total Cooper-pair pseudospin is equal to the z-component of the total charge pseudospin:  $\sum_{\Lambda, \hat{s}} B_{\Lambda, \hat{s}}^z = \sum_{\Lambda, \hat{s}} A_{\Lambda, \hat{s}}^z$ . This leads to the Hamiltonian for the insulating Mott liquid eq5.10 centered about the QCP( $B_*^z = \sum_{\Lambda, \hat{s}} B_{\Lambda, \hat{s}}^z$ )

$$H^*(\omega, \Delta \mu_{eff}) = \sum_{\hat{s}} \bar{U}_0 (\mathbf{A}_{*, \hat{s}} \cdot \mathbf{A}_{*, -\hat{s}} - \mathbf{S}_{*, \hat{s}} \cdot \mathbf{S}_{*, -\hat{s}}) + \sum_{\hat{s}} \Delta \mu_{eff}^* A_{*, \hat{s}}^z + \Delta \bar{\mu}_{eff} B_*^z. \quad (5.19)$$

The existence of competing gapping instabilities of some parts of the FS, as well as tangential scattering of Landau quasiparticles and preformed Cooper pairs between the gapless nodal regions and the gapped antinodes signals a drastic change in the nature of many-particle entanglement across the QCP [476]. This can be seen simply from the nature of the state of the nodal points on the FS. The QCP at optimal doping is associated with a sudden appearance of the nodal Marginal Fermi liquid's excitations which can be written in terms of a separable state, while on either side the state at the node is strongly entangled through longitudinal and tangential scattering in the Mott liquid (underdoped) and CFL (overdoped) phases respectively. Thus, the nodal state is an eigenstate of the Mott liquid Hamiltonian (involving the charge pseudospins  $\mathbf{A}$ ) upon underdoping away from the QCP as discussed above, and possesses Landau quasiparticles

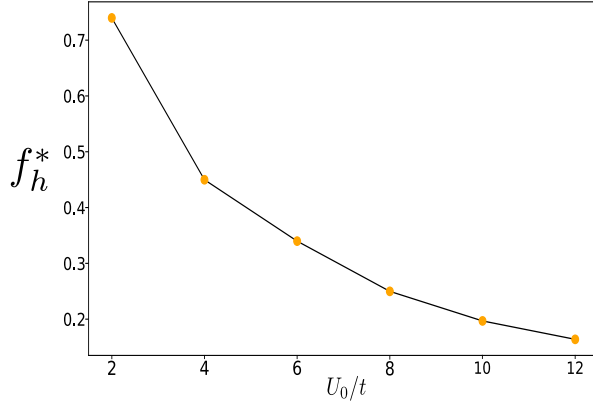


Figure 5.2.7: Figure shows variation of the critical doping( $F_h^*$ ) value against the value of bare Hubbard coupling( $U_0$ ). Numerically plotted for  $U = 12t, 10t, 8t, 6t, 4t, 2t$  with  $t = 1$ , we find the critical doping  $f_h^*$  varying from 16.4% – 74%. This has been done for lattice size  $2048 \times 2048$

with  $0 < Z_1 < 1$  upon overdoping away from the QCP. Finally, the nodal excitations precisely at the QCP show  $Z_1 \rightarrow 0$  and  $Z_3 \rightarrow 1$ . The phase precisely above the QCP contains preformed Cooper pairs in spin-gapped antinodal regions coupling with the MFL's excitations in the gapless nodal stretches, extending into the entire conical region lying above the QCP in the phase diagram shown in Fig.5.2.1. This feature of the phase diagram is reminiscent of the *quantum critical cone* typically observed at finite temperatures above a QCP, but with temperature (i.e., the energy scale for thermal fluctuations) here replaced by  $\omega$  (the scale for the quantum fluctuations). We will turn to a discussion of this in the next subsection. We end this subsection with an interesting observation on the variation of critical doping for the QCP ( $f_h^*$ ) against the Hubbard repulsion  $U$  (shown in Fig.5.2.7). The plot shows that the value of critical doping lowers with increasing  $U_0$ :  $f_h^* = 74\%$  for  $U_0 = 2t$ , while  $f_h^* = 16.4\%$  for  $U = 12t$ . We stress that we have computed  $f_h^*$  only for those values of  $U_0/t$  at which we have benchmarked our ground state energy against other numerical methods (see 5.B). We have also checked that the qualitative feature of the phase diagram presented in Fig. 5.2.1 for  $U_0/t = 8$  remains unchanged for  $2 \leq U_0/t \leq 12$ . We also note that for this entire range, the QCP always appears at a fixed chemical potential independent of  $U_0$ :  $\Delta\mu_{eff} = -\frac{W}{2}$ . The variation of  $f_h^*$  with  $U/t$  certainly deserves further investigation.

#### 5.2.4 $T = 0$ origin of Homes Law: Planckian dissipation and pre-formed Cooper pairs

The V-shaped region bounded by the lines  $\omega_{PG}^c < \omega < \omega^t$  in the phase diagram Fig. 5.2.1 has a simpler fixed point Hamiltonian compared to eq.5.18 owing to the RG irrelevance of charge backscattering and tangential scattering terms

$$H_1^* = \sum_{\Lambda, \rho} R_\rho^* \hat{n}_{\mathbf{k}, \uparrow} \hat{n}_{\mathbf{k}', \downarrow} (1 - \hat{n}_{\mathbf{l}, \uparrow}) + \sum_{\alpha} \frac{K_{s,\alpha}^*}{2} (B_{*,s}^+ B_{*,s}^- + h.c.) + \sum_{\mathbf{k}, s=\hat{s}_N} \tilde{\epsilon}_{\mathbf{k}} \hat{n}_{\mathbf{k}} + \Delta\bar{\mu}_{eff} B_*^z . \quad (5.20)$$

The set  $\rho, \alpha$  has been defined earlier, here  $\alpha$  is restricted to the sets  $\alpha = \{\mathbf{p} = 0, \hat{s}, \delta\}$ . The second term then describes the zero momentum cooper pair scattering processes. We will now focus our attention on the physics of the AN and N points on the FS. The nodal points are important as the QCP is realized with four nodal gapless MFL metals. On the other hand, the antinodes possess the largest spin gap (Fig. 5.2.2(b)): the highest single-particle spectral weight (due to the van Hove singularities of the electronic dispersion) are converted to that of Cooper pairs at the antinodes.

The spin-backscattering RG equations for the N and AN points at fluctuation scales ( $\tilde{\omega}_c, \Delta\mu_{eff}$ ) and ( $\tilde{\omega} = 0, \Delta\mu_{eff} = \Delta\mu_{eff}^*$ ) within the ‘V’ shaped region in the vicinity of the QCP are given by

$$\begin{aligned}\Delta K_{s,\alpha_1}^{(j)} &= \frac{-p_s(K_{s,\alpha_1}^{(j)})^2}{\omega_c - p_s\epsilon_{\Lambda_j \hat{s}_{AN}}^s - (1-p_s)\epsilon_{\Lambda_j \hat{s}_{AN}}^c - \frac{K_{\alpha_1}^{(j)}}{4}} + \frac{(K_{s,0,\hat{s}_{AN}}^{(j)})^2}{\omega_c - \epsilon_{j,\hat{s}_{AN}} - |\Delta\bar{\mu}_{eff}| - \frac{K_{\alpha_1}^{(j)}}{4}} \\ \Delta K_{\alpha_2}^{(j)} &= \left( \frac{-(K_{\alpha_2}^{(j)})^2}{\frac{W}{2} - \frac{1}{2}(\epsilon_{\mathbf{k}_{\Lambda\hat{s}_N}} - \epsilon_{\mathbf{k}_{-\Lambda\hat{s}_N}}) - \frac{K_{\alpha_2}^{(j)}}{4}} + \frac{(K_{s,0,\hat{s}_N}^{(j)})^2}{\frac{W}{2} - \frac{1}{2}(\epsilon_{\mathbf{k}_{\Lambda\hat{s}_N}} + \epsilon_{-\mathbf{k}_{\Lambda\hat{s}_N}}) - \frac{K_{\alpha_1}^{(j)}}{4}} \right) = 0 \quad (5.21)\end{aligned}$$

where  $\alpha_1 = \{\mathbf{p} = 0, \hat{s}_{AN}\}$  and  $\alpha_2 = \{\mathbf{p} = 0, \hat{s}_N\}$ . From the second of these RG relations, we find that the Cooper instability is marginal along the nodal directions. This results from the fact that the Cooper pair and e-h pair along  $\hat{s} \equiv N$  has the same dispersion energy:  $(\epsilon_{\mathbf{k}_{\Lambda\hat{s}_N}} + \epsilon_{-\mathbf{k}_{\Lambda\hat{s}_N}}) = (\epsilon_{\mathbf{k}_{\Lambda\hat{s}_N}} - \epsilon_{-\mathbf{k}_{\Lambda\hat{s}_N}}) \approx v_{F\hat{s}_N} \Lambda \hat{s}_N$ . This then leads to the exact cancellation of the two terms in the RG relation for  $\Delta K_{s,0,\hat{s}_N}^{(j)}$ . This leads to protection of the gapless nodal points from gapping via a Cooper instability. Therefore, the nodal Hamiltonian precisely at the QCP is composed of 2e-1h degrees of freedom described by the above Hamiltonian (eq.5.20), but with  $K_{s,0}^{*,l}(\omega, \Delta\mu_{eff}, \delta) = 0$  and  $B_{\Lambda\hat{s}}^z = 0$

$$H_{QCP}^*(\omega, \Delta\mu_{eff}^*) = \sum_{\hat{s}=\hat{s}_N, \delta}^{\hat{s}(\omega, \Delta\mu_{eff}^*)} R_{\hat{s}, \delta}^* \hat{n}_{\mathbf{k}_{\Lambda, \hat{s}}, \uparrow} \hat{n}_{\mathbf{k}_{-\Lambda+\delta, T\hat{s}}, \downarrow} (1 - \hat{n}_{\mathbf{k}_{\Lambda', \hat{s}}, \uparrow}) + \sum_{\mathbf{k}} (\epsilon_{\mathbf{k}} - \Delta\mu_{eff}^*) \hat{n}_{\mathbf{k}_{\Lambda\hat{s}}} . \quad (5.22)$$

The nodal liquid state described here possesses 2e-1h composite excitations of the MFL with a gapless Dirac dispersion, i.e., the dynamical exponent of the excitations is  $z = 1$ . Signatures of a nodal liquid state appear to have been observed in ARPES measurements carried out within the PG phase of the slightly underdoped cuprate Bi2212 above the superconducting dome [487], as well as in transport measurements [323]. The direct experimental evidence for the 2e-1h composite excitations is, however, desirable.

At the AN points, however, the Cooper-channel scattering RG relation is relevant, with a final fixed point window ( $\Lambda_{\hat{s}_{AN}}^*$ ) determined from the criterion

$$\omega_{onset}^{sc} - |\Delta\mu_{eff} - \Delta\mu_{eff}^*| - \frac{1}{2}(\epsilon_{\Lambda^*\hat{s}_{AN}} + \epsilon_{-\Lambda^*\hat{s}_{AN}}) = \frac{K_{s,0,\hat{s}}^{(j*)}}{4} . \quad (5.23)$$

The frequency scale ( $\omega_{onset}^{sc}$ ) lying above the QCP in the phase diagram Fig. 5.2.1 at which superconducting fluctuations are able to condense into preformed pairs is a function of  $\Delta\mu_{eff}$ . A non-zero spectral weight for Cooper pairs along the AN direction at optimal doping  $\rho =$

$\Lambda_{\hat{s}_{AN}}^*(\omega_{onset}^{sc}, \Delta\mu_{eff} = \Delta\mu_{eff}^*)$  is then obtained from eq.5.23 for  $\omega_{onset}^{sc} \rightarrow 0+$ . Therefore, the fluctuation scale  $\frac{W}{2} - \omega_{onset}^{sc}$  is largest at optimal doping  $\Delta\mu_{eff} = \Delta\mu_{eff}^*$ , and falls away from optimality. This explains the dashed line in Fig. 5.2.1 displaying the onset of a gapped state at the AN regions involving the formation of Cooper pairs. We stress that this state comprises of a fixed number of Cooper pairs, and therefore lacks the off-diagonal long-ranged order (ODLRO) associated with phase stiffness characteristic of superconductivity. Thus, such a state should display large superconducting phase fluctuations. Indeed, signatures of large superconducting phase fluctuations at temperatures much higher than the superconducting  $T_c$  have been observed in careful Nernst effect measurements on the cuprates [488]. Remarkably, the experiments reveal a “dome” associated with the onset of phase fluctuations enveloping the dome of true d-wave superconductivity, similar to that observed in the RG phase diagram Fig.5.2.1.

We have just established that the net spectral weight of the spin gapped regions around the AN is converted into that for preformed Cooper pairs within the low energy subspace (eq.5.11) in the vicinity of the QCP. Further, the nodal marginal Fermi liquid at the QCP can be shown to adiabatically continue to the region lying outside the gapped parts of the FS, and described by Hamiltonian eq.4.17. This marginal Fermi liquid metal has earlier been shown to follow the Planckian dissipation law (Sec. 4.1). Indeed, Planckian dissipation has received experimental confirmation as the origin of the linear-in- $T$  resistivity in several members of the cuprate family of materials recently [323]. Thus, the coexistence of preformed pairs at the AN alongwith a Planckian dissipator at the N calls for an investigation of the experimentally observed Homes law [44]. This is an empirical relation between the normal state Drude conductivity  $\sigma(T_c)$ , the superconducting critical temperature  $T_c$  and the superfluid weight  $\rho_s$  observed for the d-wave superconductivity in the cuprates:  $A\sigma_{DC}(T_c)T_c = \rho_s$ , where  $A$  is a universal constant. We search for the  $T = 0$  origin of this relation in the theory of the state residing within the conical-shaped part of the phase diagram lying above the QCP. Thus, we first compute the antinodal (AN) superfluid weight from the Ferrel-Glover-Tinkham (FGT) sum rule

$$\int_0^\infty d\tilde{\omega} \operatorname{Re}[\sigma_{n,\hat{s}_{AN}}(\tilde{\omega}) - \sigma_{s,\hat{s}_{AN}}(\tilde{\omega})] = \frac{\pi}{2}\rho_s , \quad (5.24)$$

where  $\sigma_{n,\hat{s}_{AN}}(\tilde{\omega})$  is the normal state conductivity for the marginal Fermi liquid metal present initially at the AN before the instability. On the other hand,  $\sigma_{s,\hat{s}_{AN}}(\tilde{\omega})$  is the conductivity of the many-body state that contains preformed Cooper pairs, and we have labelled  $\tilde{\omega} = \frac{W}{2} - \omega$ . We then decompose the integral over  $\tilde{\omega}$  into one over  $0 < \tilde{\omega} < \tilde{\omega}_{onset}^{sc}$  and another over  $\tilde{\omega}_{onset}^{sc} < \tilde{\omega} < \infty$

$$\begin{aligned} \int_0^\infty d\tilde{\omega} \operatorname{Re}[\sigma_{n,\hat{s}_{AN}}(\tilde{\omega}) - \sigma_{s,\hat{s}_{AN}}(\tilde{\omega})] &= \int_0^{\tilde{\omega}_{onset}^{sc}} d\tilde{\omega} \operatorname{Re}[\sigma_{n,\hat{s}_{AN}}(\tilde{\omega}) - \sigma_{s,\hat{s}_{AN}}(\tilde{\omega})] \\ &+ \int_{\tilde{\omega}_{onset}^{sc}}^\infty d\tilde{\omega} \operatorname{Re}[\sigma_{n,\hat{s}_{AN}}(\tilde{\omega}) - \sigma_{s,\hat{s}_{AN}}(\tilde{\omega})] . \end{aligned} \quad (5.25)$$

The second integral vanishes because the integrated spectral weight of the 2e-1h continuum in the normal and gapped state of preformed Cooper pairs is equal. Further, in the first integral, there is no contribution from  $\sigma_{s,\hat{s}_{AN}}(\tilde{\omega})$  as the 2e-1h degrees of freedom are not present within the momentum space window along  $\hat{s}_{AN}$  ( $[-\Lambda_{\hat{s}_{AN}}^*, \Lambda_{\hat{s}_{AN}}^*]$ ). For  $\tilde{\omega} < \tilde{\omega}_{onset}^{sc}$ , denoting the antinodal conductivity as  $\sigma_{n,\hat{s}_{AN}}(\tilde{\omega}_{onset}^{sc}) = \sigma_{n,\hat{s}_{AN}}(\tilde{\omega})$ , the FGT sum rule amounts to

$$\int_0^{\tilde{\omega}_{onset}^{sc}} d\tilde{\omega} \operatorname{Re}[\sigma_{n,\hat{s}_{AN}}(\tilde{\omega}_{onset}^{sc})] = \tilde{\omega}_{onset}^{sc} \sigma_{n,\hat{s}_{AN}}(\tilde{\omega}_{onset}^{sc}) = \frac{e^2 \Lambda_{\hat{s}_{AN}}^*(\Delta\mu_{eff})}{m} = \frac{\pi}{2}\rho_s , \quad (5.26)$$

where we have used the relation  $n = \Lambda_{\hat{s}_{AN}}^*(\Delta\mu_{eff})/2\pi$  for the state number density  $n$  in the Drude relation for the conductivity. Using the Planckian dissipation law Sec. 4.1, along with the FGT relation for the superfluid weight given above, we obtain a relation analogous to Homes law for the onset scale for superconducting fluctuations at the antinodes ( $T_{ons} = \hbar\tilde{\omega}_{onset}^{sc}/k_B$ )

$$\rho_s(\Delta\mu_{eff}, 0) = \frac{4k_B}{h}\sigma_{n,\hat{s}_{AN}}(T_{ons}) T_{ons}(\Delta\mu_{eff}) . \quad (5.27)$$

The frequency scale  $\tilde{\omega}_{onset}^{sc}$  is itself obtained from 5.8, and by picking up the normal  $\hat{s}_1 = \left(1 - \frac{\Lambda_0}{\sqrt{2}\pi}\right)\hat{s}_{AN}$  in the vicinity of  $\hat{s}_{AN}$  to avoid the discontinuity at the antinodal van Hove singularities

$$\begin{aligned} \tilde{\omega}_{onset}^{sc} &= N(\hat{s}_1, 0)\left(\frac{1}{2} \max_{\delta, \hat{s}}(\epsilon_{\Lambda^*, \hat{s}} + \epsilon_{-\Lambda^* + \delta, \hat{s}}) - \frac{1}{2} \max_{\delta}(\epsilon_{\Lambda^{**}, \hat{s}_1} + \epsilon_{-\Lambda^{**} + \delta, \hat{s}_1})\right) \\ &= \frac{N(\hat{s}_1, 0)}{2} (\epsilon_{\Lambda_0, \hat{s}_N} - \epsilon_{\Lambda^{**}, \hat{s}_1}) . \end{aligned} \quad (5.28)$$

From the geometry of the square Fermi surface the number of states within the gapped window along normal  $\hat{s}$  is determined to be  $N^*(\hat{s}_1, 0) = \frac{\Lambda^{**}}{\Lambda_0} N\left(\frac{1}{2\sqrt{2}} - \frac{\Lambda_0}{4\pi}\right)$ . In the above equation  $\Lambda^*$ ,  $\Lambda^{**}$  are determined from eq.5.4 respectively and  $N^*(\hat{s}_1, 0)$  is the total number of gapped states at  $\omega = 0$ . In keeping with our earlier discussion,  $T_{ons}$  is largest at optimality ( $\Delta\mu_{eff}^*$ ) and falls off with doping away from optimality on either side. In the next section, these fluctuations will be seen to interplay with the spin-gap in leading to d-wave superconductivity [479]. Further, we have shown in eq.5.45 (see Appendix 5.A for a detailed derivation) that the superconducting critical temperature  $T_C$  is linearly related to  $T_{ons}$ , with a proportionality constant related to the extent of the pseudogap (seen in terms of the difference between the electronic dispersion at the antinodes and the nodes). In this way, we offer insight into the  $T = 0$  origin of Homes law [44].

### 5.2.5 Mixed optical conductivity of the Correlated Fermi liquid

The fluctuation scale  $\omega_t : \omega - \frac{\Delta\mu_{eff}}{2} + W sgn(\Delta\mu_{eff}) > 0$  marks the boundary across which the tangential scattering processes become RG relevant (eq.5.3). Starting from the QCP ( $\frac{W}{2} - \omega = 0, \Delta\mu_{eff} = \Delta\mu_{eff}^*$ ), and proceeding into the region  $\omega > \omega_t$ , the gapless stretch of the FS increases steadily. This enhances the spectral weight of states taking part in the tangential scattering process,  $N_j(\omega, \Delta\mu_{eff}) = \sum_{\hat{s}=\hat{s}_N}^{\hat{s}_\omega} 1$ . As can be seen from the numerator of eq5.3, a growing spectral weight gradually enhances the RG flow rate for tangential scattering processes. It is also important to note that on these gapless stretches, the effect of forward scattering is still RG relevant (eq.5.4) leading to 2e-1h composite excitations of the marginal Fermi liquid. The tangential scattering processes, on the other hand, enhance the quasi-particle excitations of the Fermi liquid. The outcome of these competing tendencies is captured by the effective 1-particle self energy

$$\Sigma_{\Lambda\hat{s}}(\omega) = L^*(\delta, \omega)\theta(\Lambda_1^*(\omega) - \Lambda) + R_{\hat{s}, \delta}^*\theta(\Lambda_2^*(\omega) - \Lambda) \ln \left| \frac{\bar{\omega} + \Delta\mu - \epsilon_{\Lambda\hat{s}}}{\bar{\omega}} \right| , \quad (5.29)$$

where  $\bar{\omega} = \max_{\delta, \hat{s}} \frac{\epsilon_{j^*, l} + \epsilon_{j^*, l'}}{2}$ , and  $j^*$  is obtained from the fixed point condition eq.5.4. The fixed point values of the couplings are given by

$$L^* = \omega + W sgn(\Delta\mu_{eff}) + \epsilon_{\Lambda_1^*, avg}^c - \Delta\mu_{eff}, \frac{R_{l\delta}^*}{8} = \bar{\omega} - \frac{1}{2}(\epsilon_{\Lambda_2^*, l} + \epsilon_{\Lambda_2^*, l'}) + \Delta\mu_{eff} . \quad (5.30)$$

The above equations for  $L^*$  and  $R_{l\delta}^*$  are satisfied within the windows  $\Lambda_1^*$  and  $\Lambda_2^*$  respectively. Near the QCP,  $\Lambda_1^* < \Lambda_2^*$ , such that the MFL dominates over the FL within the gapless regions of the FS. Upon gradually increasing the doping away from the QCP leads to  $\Lambda_1^* > \Lambda_2^*$ , such that the enhanced tangential scattering on the enlarged gapless stretches leads to the Fermi liquid quasiparticles dominating over the composite excitations of the MFL. The imaginary part of the single particle self-energy Sec. 4.1 then allow us to obtain the inverse quasiparticle lifetime as a mixture of MFL and FL forms

$$(\tau(\Delta\mu_{eff}))^{-1} = \alpha(\Delta\mu_{eff})\omega + \beta(\Delta\mu_{eff})\omega^2 , \quad (5.31)$$

where the coefficients  $\alpha$  and  $\beta$  are functions of the chemical potential  $\Delta\mu_{eff}$ , and undergo a gradual evolution from QCP to the overdoped regions of the phase diagram. This gives rise to a mixed nature of the optical conductivity as a function of  $\Delta\mu_{eff}$ . This appears to be consistent with the observations of van der Marel et al. [489], where a form of the optical conductivity that departs from the expected MFL form was attributed to quantum critical scaling in the neighbourhood of a QCP at optimal doping.

## 5.3 Symmetry breaking Orders and superconductivity

In this section, we perform analysis of symmetry-broken phases for the Hubbard model upon doping away from 1/2-filling. As before, this involves a renormalization group analysis in the background of symmetry breaking fields: staggered chemical potential  $\sum_{i,j}(-1)^{i+j}\hat{n}_r$  (for the  $\pi, \pi$  charge density wave), staggered magnetic field  $\sum_{i,j}(-1)^{i+j}S_r^z$  (for the  $\pi, \pi$  spin density wave), the spin-nematic order field  $Q_{\alpha\beta}^0 f(\mathbf{r}_1 - \mathbf{r}_2) S_{\mathbf{r}_1}^\alpha S_{\mathbf{r}_2}^\beta$ , and finally a  $U(1)$  symmetry-breaking field  $\sum_{\mathbf{k}\sigma} c_{\mathbf{k}\sigma}^\dagger c_{-\mathbf{k}-\sigma}^\dagger$  for superconductivity. The corresponding RG equations are given in Appendix 5.A. The full RG phase diagram away from 1/2-filling, and with  $(\pi, \pi)$  CDW,  $(\pi, \pi)$  SDW, spin-nematic and d-wave superconducting broken symmetry orders, is shown in Fig.5.3.1. The effective Hamiltonians and gap functions familiar for these symmetry broken states of matter are easily obtained from the dominant symmetry breaking coupling at the RG fixed point. Results for symmetry-broken orders at finite-temperature can then be obtained via standard mean-field methods. Below, we confine ourselves to a discussion of the findings shown in the phase diagram Fig.5.3.1.

We find the  $(\pi, \pi)$  SDW Neel antiferromagnet for energies  $4 - \omega \geq 4 - \omega_{ins} = 1.2$  and doping  $0 > \Delta\mu_{eff} \geq -1.75$  (deep underdoping), and the  $(\pi, \pi)$  CDW for energies  $4 - \omega \geq 0.8$  and doping  $-3.05 \geq \Delta\mu_{eff} \geq -4$  (moderately underdoped). A d-wave superconducting dome is found to extend between a doping range of  $-1.5 \geq \Delta\mu_{eff} \geq -6$  and has an optimal gap scale ( $\Delta_{SC}$ ) at the critical doping  $\Delta\mu_{eff} = -4$  corresponding to the QCP. We have already presented earlier our finding for the variation of the superfluid density  $\rho_s$  with chemical potential, with a discussion on why  $\rho_s$  is maximal at optimal doping. In keeping with this, the highest  $\Delta_{SC}$  arises from a maximal density of bound Cooper pairs in the gapped regions of the Fermi surface interplaying with the critical fluctuations of the gapless regions for a chemical potential tuned to the QCP [490] (see green curve in Fig.5.3.6(b)). The optimal quantum fluctuation energy scale for the onset of superconductivity is the kinetic energy of a pair of electrons from diametrically opposite nodal points on the FS:  $W/2 - \omega_{SC} = W/2 - 2\epsilon_{\Lambda^* s_{node}}$ , where  $\Lambda^*/\Lambda_0$  is the dimensionless

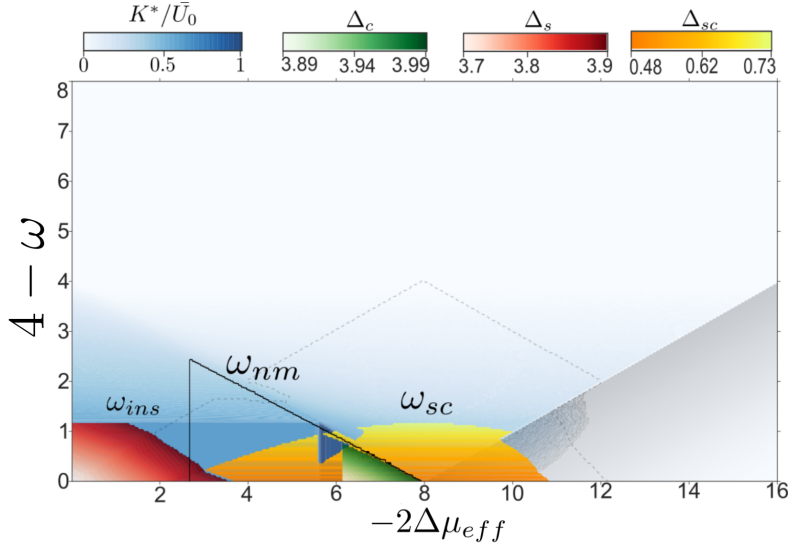


Figure 5.3.1: (Colour Online) RG phase diagram for 2D Hubbard model with doping and  $(\pi, \pi)$  CDW (green),  $(\pi, \pi)$  SDW (red) and d-wave superconducting (SC) orders (yellow) included.  $K^*/\bar{U}_0$  in the white-deep blue colourbar represents the ratio of renormalized coupling to bare coupling symmetry unbroken PG and ML states. Gap scales for various symmetry broken phases are shown in the colour bars. Origin of superconductivity from spin-PG nodal NFL with superconducting fluctuations is described in text. The SC “dome” is centered about the QCP (optimality) and falls away on either side due to competition with insulating orders (underdoped) and gapless CFL (overdoped). The solid black line indicates the chemical potential dependent energy scale for the onset of nematic fluctuations, while the thin dashed line denotes the onset of superconducting fluctuations.

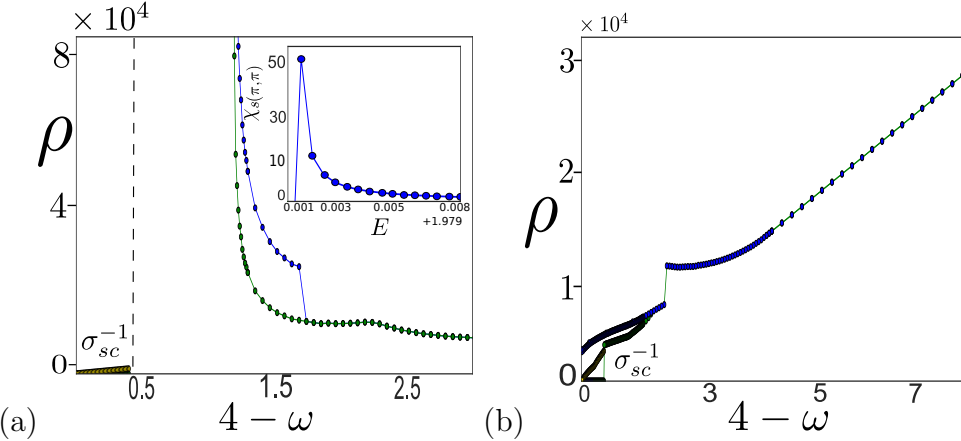


Figure 5.3.2: (Colour Online) Figures (a) and (b) represents resistivity with (green) and without any form of symmetry breaking (blue), and inverse superfluid stiffness ( $\sigma_{sc}^{-1}$ , yellow) at various dopings. (a)  $\Delta\mu_{eff} = -1.75$ : passage from PG to ML (blue), from PG to SC through spin-gap dominated ML. Inset: Peak in spin susceptibility within SC region  $\Delta\mu_{eff} = -1.75$ . (b)  $\Delta\mu_{eff} = -5.5$ : passage from NFL to PG-CFL (blue), from NFL to SC through PG-CFL (green).

spectral weight for the marginal nodal electronic quasiparticles obtained from the RG. Deep in the underdoped regime ( $-1.5 \geq \Delta\mu_{eff} \geq -1.75$ ), a coexistence of  $(\pi, \pi)$  SDW and d-wave superconducting orders appears likely [491] (see inset of Fig. 5.3.2(a)). Similarly, within the lightly underdoped region, a coexistence of  $(\pi, \pi)$  CDW and d-wave SC orders appears likely (see inset of Fig. 5.3.3(b)).

As a clear demonstration of the d-wave nature of the superconducting order parameter, we show in Fig.5.3.5 the variation of the superconducting(SC) gap from maximum at one antinode(AN1=(0,  $\pi$ )) to a node at the nodal point  $k_x, k_y = (\pm\pi/2, \pm\pi/2)$  and finally maximizing again at (AN2=( $\pi$ , 0)). The three curves are made at the brink of entry into SC dome from underdoping (blue), optimal (green) doping, and overdoping (red) sides. At optimality, the connected Fermi surface becomes an arc with lowering quantum fluctuation scale  $4 - \omega$  and collapses to a point on entering the superconducting dome. The journey from above the superconducting dome to the final entry into superconducting dome at optimal doping can be seen from the variation of the gap from antinodes to the nodes in Fig.5.3.6(a).

The experiments in Ref.([490]) appear to show that optimal superconductivity is associated with the largest Fermi surface volume at the brink of entering SC dome as optimality is approached from the underdoped side. We find evidence for this, as shown in Fig.5.3.6(b). The graph for the mildly underdoped regime ( $-2\Delta\mu_{eff} < W$ ) shows that a smaller Fermi pocket with high concentrations of holons and low concentration of bound spinon pairs undergoes a superconducting d-wave transition where the Fermi volume shrinks to a point. In the optimally doped regime ( $-2\Delta\mu_{eff} \sim W$ ) on the brink of transiting into the superconducting dome, we observe a larger gapless Fermi pocket with a peak in the concentration of Cooper pairs (in the gapped parts of the Fermi surface) and an intermediate concentration of holons. On the brink of entering the dome at overdoping ( $-2\Delta\mu_{eff} > W$ ), we find a reduction in the Cooper pair density at the neighborhood of the antinodes coinciding with a lowering hole concentration on a fully connected

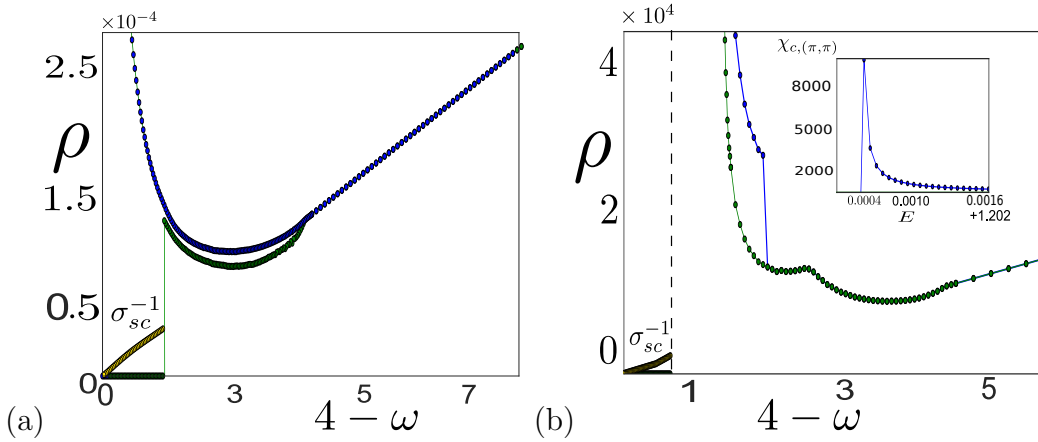


Figure 5.3.3: (Colour Online) Figures (a) and (b) show resistivity ( $\rho$ ) with (green) and without any form of symmetry-breaking (blue), and inverse superfluid stiffness ( $\sigma_{sc}^{-1}$ , yellow) at various dopings. (a)  $\Delta\mu_{eff} = -4$ : passage from PG to ML (blue), from PG to SC through charge-gap dominated ML. Inset: Peak in charge susceptibility within SC region. (b)  $\Delta\mu_{eff} = -3.25$ : passage from NFL with connected FS to spin-PG nodal NFL at QCP (blue), from NFL to SC through spin-PG nodal NFL (green).

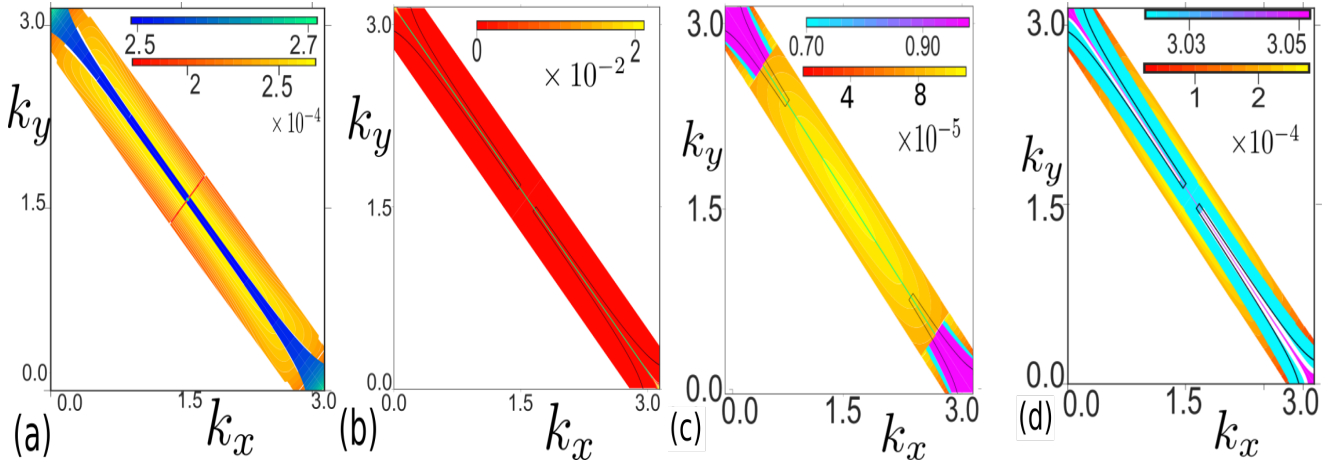


Figure 5.3.4: (Colour Online) Figures (a) - (d) show the full momentum space resolved spectral function  $A(\mathbf{k}_{A\hat{s}})$ , where the black curves show extent of SC fluctuations around Fermi surface. (a): to the right of SC dome (CFL). (b): within d-wave SC dome, with nodal NFL. (c): to the left of SC dome (ML). (d): vertically above SC dome at optimal doping.

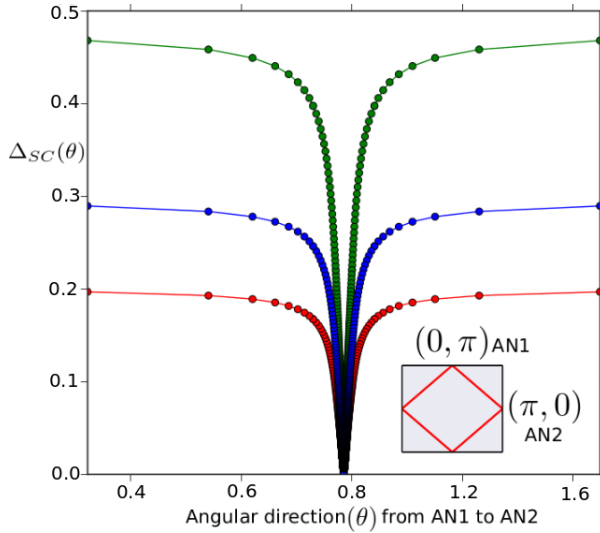


Figure 5.3.5: (Colour Online) Gap  $\Delta_{SC}(\theta)$  vs the angular coordinate  $\theta$  for chemical potential and  $4-\omega$  values given by  $\mu_{eff} = -2.5, 4-\omega_{c1} = 0.8$  (red curve) in the underdoped regime. At optimal doping  $\Delta\mu_{eff} = -4.0, 4-\omega_{c2} = 1.2$  (green curve). At overdoping  $\Delta\mu_{eff} = -5.5, 4-\omega_{c3} = 0.5$  (blue curve).

Fermi surface. This shows that optimality arises from an interplay of a peak in the density of Cooper pairs in the gapped parts of the Fermi surface (as well as the superfluid density  $\rho_s$ ) and the critical fluctuations associated with a quantum critical Fermi surface (arising from the QCP). The dome-like structure of  $T_C$  is observed to be inherited from the similar structure of  $T_{ons}$  (as discussed earlier; also see Appendix 5.A), and offers an explanation for the quadratic dependence of  $T_C$  on the hole-doping concentration commonly observed in the cuprates [492].

We now establish the origin of the nodal structure of d-wave superconducting order as the QCP at  $\mu_{eff}^* = -4$ . We have shown above that the nodal points support a gapless NFL metal, as the irrelevance of all gapping mechanisms at the nodes arise from the topological signature of the doublon propagator. Thus, the onset of superconductivity at critical doping takes place in the backdrop of this protection for the nodal gapless states. We have also seen that the spin-gap at optimal doping has d-wave structure, but without a sign change across the nodes. The  $U(1)$  phase rotation symmetry breaking RG calculation presented in Appendix 5.A further reveals that the nodal points act as domain walls for the growth of the superconducting order upon scaling down to low energies: the RG-integrated superconducting order parameter  $\langle c_{\Lambda-T\hat{s}\downarrow}^\dagger c_{\Lambda\hat{s}\uparrow}^\dagger \rangle = -\langle c_{\Lambda-\hat{s}\downarrow}^\dagger c_{\Lambda T\hat{s}\uparrow}^\dagger \rangle \propto e^{i\gamma_{\hat{s},\hat{s}_{node}}}$ , where the relative phase  $\gamma_{\hat{s},\hat{s}_{node}} = -i \ln(sgn[2(\epsilon_{\Lambda\hat{s}} - \epsilon_{\Lambda\hat{s}_{node}})])$  and  $2(\epsilon_{\Lambda\hat{s}} - \epsilon_{\Lambda\hat{s}_{node}})$  is the energy scale for a Cooper pair (with respect to the nodes). The alternation of sign in this energy scale is, thus, the alternation in sign of the pairing order parameter.

The suppression of d-wave superconductivity is clearly observed in the presence of the CDW order (Fig.5.3(a)), while the charge-gap dominated Mott liquid (dark blue region in Fig.5.3(a)) leads to further suppression of superconductivity. These results obtained are in consonance with the finding of two distinct antinodal energy-gap scales in recent ARPES and STM experiments carried out on the PG phase of the cuprate La-Bi2201 [493], one of which appears to be linked with the onset of superconductivity and the other with charge ordering. The black curve in

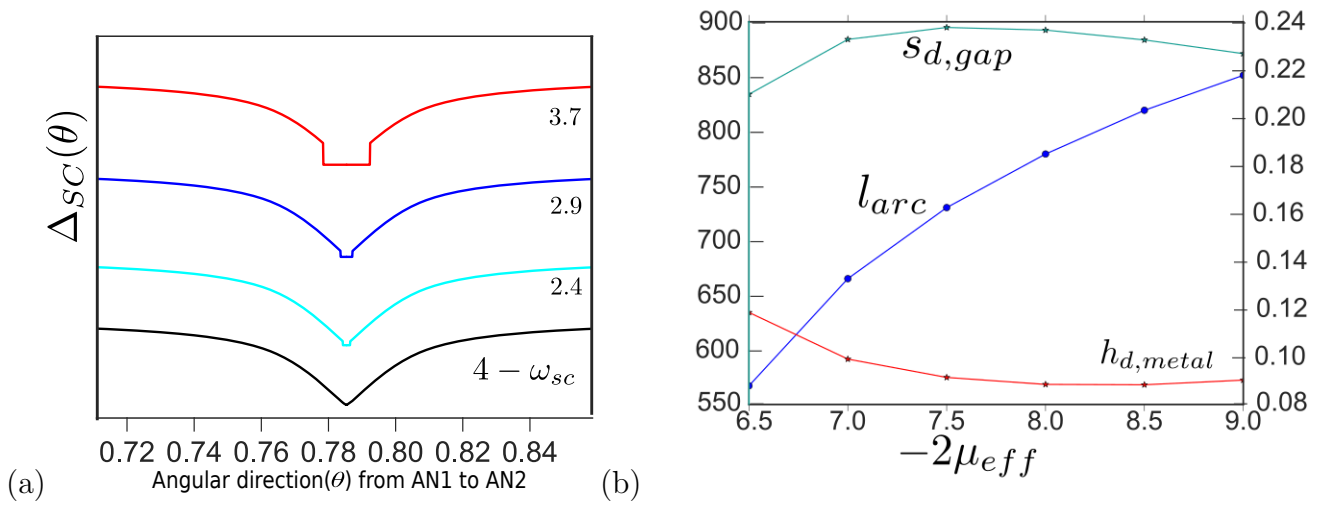


Figure 5.3.6: (a) (Colour Online) Gap  $\Delta(\theta)$  vs. the angular coordinate  $\theta$  along the  $\Delta\mu_{eff} = -4.0$  optimal doping axis for different values of  $4 - \omega_{sc}$  lying above the dome. The different curves have been staggered for purposes of clarity. The gap  $\Delta(\theta)$  vs. the angular coordinate upon just entering the superconducting dome is given by the black curve. (b) Left vertical axis: Blue curve represents the gapless arc length of the Fermi surface at the brink of the superconducting transition for six different  $\omega_{sc}^{critic}$  and  $-2\Delta\mu_{eff}$  values i.e.,  $(2.922, 6.5), (2.869, 7.0), (2.837, 7.5), (2.827, 8.0), (2.839, 8.5)$ , and  $(2.87, 9.0)$ . Right vertical axis: At those same values, the green curve represents the Cooper pair density in the gapped regions in the neighbourhood of the antinodes, and the red curve represents the holon densities in the gapless parts neighboring the nodes.

the RG phase diagram corresponds to the onset of spin-nematic fluctuations, and appears to be confined within a range of chemical potential  $-1.4 \geq \Delta\mu_{eff} \geq -4$  associated with moderate to light underdoping. The highest scale (in  $4 - \omega$ ) for the onset of spin-nematic fluctuations lies well within the pseudogapped part of the phase diagram, in broad agreement with recent experimental findings in the cuprates [494–498]. For  $-4 \geq \Delta\mu_{eff} \geq -6$ , the competition between the nodal NFL metal, the spin-pseudogapped parts of the FS and the tangential scattering leads to the reconstruction of the FS. This is apparent in the suppression of superconducting fluctuations (dashed line in Fig.5.3) beyond critical doping and shows how competition with the CFL suppresses d-wave superconductivity. Variations of the resistivity ( $\rho$ ) and inverse superfluid stiffness ( $\sigma_{SC}^{-1}$ ) upon tuning  $\omega$  towards the QCP is shown in Figs. 5.3.3(a,b) (see also Videos S5, S6). Maps of the single-particle spectral function  $A(E)$  within and in the neighbourhood of the d-wave SC phase are also presented in Figs. 5.3.4(a,b) and 5.3.4(c,d). These results are in excellent agreement with several transport and spectroscopy measurements made in various parts of the cuprates phase diagram [5, 324, 325, 480–482, 487, 488, 493–498].

Finally, we close this section by computing numerical values for some of the temperature scales, e.g.,  $T_{ons}$  (the onset of the formation of pre-formed Cooper pairs at the gapped antinodal regions) and  $T_{ML}$  (the scale at which the entire FS is gapped during the formation of the Mott liquid), for the materials  $HgBa_2CuO_4$  and  $La_2CuO_4$  by using the values for the parameters of the effective one-band Hubbard model found in Ref.[499]. First, in the limit of large system size  $N \rightarrow \infty$ , using the formula for  $\tilde{\omega}_{onset}^{sc}$  (eqs.(5.28) and (5.4)), we obtain

$$\tilde{\omega}_{onset}^{sc} \leq \omega_{PG} = t \frac{\Lambda^{**} N^2}{8\pi\sqrt{2}} \frac{16\pi^2}{N^2} = \sqrt{2}t\pi\Lambda^{**} = \sqrt{2}t\pi \arcsin\left(\frac{\bar{\omega}}{2t}\right) = 0.067t , \quad (5.32)$$

where  $\bar{\omega} \approx \omega_{PG} = 0.034t$  as given earlier. Then, using the values of the hopping parameter  $t$  for  $HgBa_2CuO_4$  and  $La_2CuO_4$  with  $t = -0.461, -0.482eV$  [499], we find the onset temperature scale of pair formation  $T_{ons}$  is bounded (on the upper side) by the pseudogap temperature  $T_{PG}$  are given by  $T_{PG} = 0.067t \times 11605K = 358K$  and  $374K$  for HBCO and LCO respectively. This is in fair agreement with experimental estimates of  $T_{PG} \sim 200K - 300K$  for most of the cuprates [500]. That the onset temperature scale for pairing  $T_{ons}$  is less than  $T_{PG}$  is consistent with the findings from Nernst measurements of Ref.[488]. Further, we find  $T_{ML} \approx \frac{\frac{W}{2} - \omega_{ML}}{\frac{W}{2} - \omega_{PG}} T_{ons} = 119K$  and  $124K$  for HBCO and LCO respectively. Recalling the relation between  $T_{ML}$  and the superconducting transition temperature  $T_C$  obtained in eq.5.46, we see that the upper bound for  $T_C$  is provided by  $T_{ML}$ . An upper bound of around  $120K$  for the  $T_C$  is reasonable for the experimentally known  $T_C$  of  $40K$  for LCO and  $90K$  for HBCO. Importantly, as  $T_C$  is also found to be bounded (on the upper side) by  $T_{ons}$  (see eq.5.45), it appears plausible to search for mechanisms that can raise  $T_C$  further towards  $T_{ons}$ . We will further discuss this point briefly in the concluding section.

## 5.4 Conclusions and perspectives

There are several interesting consequences of our RG analysis of the hole-doped 2D Hubbard model on the square lattice, and we now discuss each of these in turn. First, we wish to stress that the simplicity of the Hubbard Hamiltonian (i.e., possessing effectively only two parameters,  $U/t$  and  $\mu/t$ ) offers the possibility that several of our results are of likely importance for the broad

understanding of the phenomenology of filling-driven Mott transitions in a variety of strongly correlated electronic systems with strong electronic differentiation arising from the tight binding dispersion [2]. Equally importantly, given the recent experimental demonstration in Ref.[320] of the encapsulation the entire cuprate phase diagram from experiments on a monolayer crystal of  $\text{Bi}_2\text{Sr}_2\text{CaCu}_2\text{O}_{8+\delta}$  containing only two Cu-O planes, we believe that our study is of importance in learning the physical mechanisms responsible for the complexity of the phase diagram. Indeed, the striking similarities between the RG phase diagram presented in Fig.5.3 with the well-known experimental phase diagram of the cuprates [5] (with the quantum fluctuation axis  $\omega$  in the former replaced by temperature in the latter) suggest that we have taken strides in meeting our goal.

In the RG phase diagram Fig.5.2.1, the collapse of the pseudogap for charge excitations (Mottness) upon hole doping is seen to lead to a QCP lying between Mott liquid and correlated Fermi liquid phases. The QCP involves a drastic change in the nature of the ground state as well as the many-body spectrum: the underdoped side of the QCP is a gapped and hole-doped Mott liquid, while the overdoped side involves the appearance of electronic quasiparticles that gradually lead to the topological reconstruction of a fully connected Fermi surface. Precisely at the QCP, we find the existence of nodal marginal Fermi liquid with gapless 2e-1h composite excitations. We believe that the search for unambiguous experimental evidence on the existence of such 2e-1h composite excitations is important. The pseudogapped state at underdoping is formed from a dominant charge gapping of the antinodes, as well as possesses strong spin-nematic fluctuations and sub-dominant superconducting phase fluctuations. The underdoped Mott liquid leads, upon including the effects of symmetry breaking, to Neel SDW and chequerboard CDW orders.

In the v-shaped quantum critical region within the RG phase diagram of Fig.5.2.1, we find spin-gapped antinodal regions of the Fermi surface containing pre-formed Cooper pairs co-existing with gapless stretches of marginal Fermi liquid on arcs centered about the nodes. This appears to confirm dominant spin excitations emerging from the collapse of Mottness as the mechanism for the formation of hole pairs. Upon including the possibility of phase stiffness within the RG, we find the existence of a dome of d-wave superconductivity that surrounds the QCP. Remarkably, even as the superconducting phase shields the QCP, it possesses properties of that criticality (e.g., gapless nodes, gap with d-wave symmetry). In this way, we find that the pseudogap is both friend and foe to the emergent superconductivity: the underdoped Mottness-related pseudogap contains fluctuations that can nucleate various orders (SDW, CDW and spin-nematicity) inimical to superconducting order, its collapse unveils the spin-pseudogapped state of matter that finally leads to a state with pre-formed Cooper pairs (and eventually phase stiffness and the ODLRO pertaining to superconductivity).

We can now address the striking qualitative agreement of RG phase diagram Fig.5.3 with the experimentally obtained temperature versus doping phase diagram for the cuprates [5]. We believe that this arises from the fact that the RG unveils an entire hierarchy of energy scales on the quantum fluctuation axis  $\omega$  related to the metallic, pseudogap, Mott liquid and symmetry broken phases. Further, at various points in this work, we have shown analytic relations between these  $T = 0$  energy scales and equivalent temperature scales at which these phases can be observed. Importantly, we have also established that the heirarchy of temperature scales for the pseudogap ( $T_{PG}$ ), onset temperature for pairing ( $T_{ons}$ ), formation of the Mott liquid ( $T_{ML}$ ) and superconductivity ( $T_C$ ) obtained from our analysis is quantitatively consistent with that observed

experimentally for some members of the cuprates.

The effective Hamiltonians and low-energy wavefunctions obtained for the fixed points of the RG formalism has afforded considerable insight into the nature of the Mott liquid at half-filling, as well as with hole doping. This is evidenced by the remarkable consistency between the numbers obtained for the ground state energy per site and double occupancy fraction with those obtained from various numerical methods in Ref.[49, 77, 450]. This benchmarking gives us confidence in the nature of the Mott liquid state as well as in the quantum phase transition that it undergoes upon doping. The effective Hamiltonians have also enabled an understanding of the essence of various universal features of the large body of experimental results obtained for the cuprates, e.g., Homes law, Planckian dissipation and the T-linear resistivity of the normal state, the mixed nature of the optical conductivity at overdoping, optimality with doping and the dome-like structure of the superconducting phase etc. In seeking further comparisons with the extensive body of experimental data available for the cuprates, it appears plausible to carry out a numerical simulation of these effective Hamiltonians at finite temperature. We leave this for a future work.

Even as these results offer considerable evidence that the strong correlation physics of the one-band Hubbard model at, and away from, 1/2-filling is pertinent to the physics of high-temperature superconductivity [501], they also open several new directions for further investigation. Foremost among these lies the search for answers to questions on what makes certain members of the cuprate family special in the search for higher superconducting  $T_C$ , as well as what could enable a raise in  $T_C$ . In reaching some conclusions on the former, the results obtained from recent DFT+downfolding study of Hirayama et al. [499] on  $\text{La}_2\text{CuO}_4$  and  $\text{HgBa}_2\text{CuO}_4$  offer some insight. This study appears to conclude that the latter member of the cuprate family has a higher  $T_C$  than the former as it is better described by an effective one-band Hubbard model in two dimensions, whereas the former is likely to have a larger hybridisation with a second dispersive band (arising from the Cu  $3d_{3z^2-r^2}$  orbital) near the putative Fermi surface. It appears quite plausible that such hybridisation will be harmful to the physics of the Mott liquid and resulting emergent superconductivity we find from our studies, and can be studied in future. This suggests that materials that afford the isolation of Cu-O planes described by an effective 2D one-band Hubbard model are more likely to offer a higher superconducting  $T_C$ , and is consistent with the recent findings of high-temperature superconductivity from a monolayer crystal of  $\text{Bi}_2\text{Sr}_2\text{CaCu}_2\text{O}_{8+\delta}$  [320].

In seeking answers to the question on how to further raise the superconducting  $T_C$ , it is important to make an increasingly realistic model pertinent to the cuprates. Thus, one should first investigate the role played by next-nearest neighbour hopping within the Cu-O plane. Our results predict, for instance, that shortening the extent of the pseudogap will likely enhance the optimal quantum fluctuation energy scale for the onset of d-wave superconducting order. This can be achieved, for instance, by tuning the curvature of the Fermi surface via next-nearest neighbour hopping [502]. Similarly, a study of the effects of an inter-plane electron hopping element appears relevant, as the presence of other Cu-O planes is observed in some members of the cuprates (e.g.,  $\text{Bi}_2\text{Sr}_2\text{Ca}_2\text{Cu}_3\text{O}_{10}$  (Bi2223) [503],  $\text{HgBa}_2\text{Ca}_2\text{Cu}_3\text{O}_9$  (Hg1223) [504] and  $\text{YBa}_2\text{Cu}_3\text{O}_7$  (Y123) [505] as being important in leading to higher  $T_C$  upon the application of pressure. Our findings are also likely to be pertinent to the ubiquitous presence of superconductivity in several other forms of strongly correlated quantum matter, e.g., the heavy-fermion systems, where there exist proposals for how the collapse of Mottness can lead to superconductivity [506]. For instance, as a

particle-hole transformation on one of the sublattices of the 2D square lattices connects between the repulsive and attractive Hubbard models ([473]), we believe that our results are also significant in understanding the physics of the latter. Finally, given that we now have wavefunctions available for the ground and low-lying excited states of the doped Mott liquid, a direction worth pursuing is to understand the nature of many-body entanglement in this system. Given the effort presently invested in such investigations, any progress in this direction will likely help usher new ways in which to think about the many-particle physics of strongly correlated electronic systems.

# Appendix

## 5.A RG equation of the symmetry breaking orders

In the doped Mott liquid Hamiltonian (eq.5.19, we include  $(\pi, \pi)$  charge density wave,  $(\pi, \pi)$  spin density wave symmetry-breaking fields together with the Hamiltonian for the 1-e and 2e-1h composites (eq.4.17)

$$\begin{aligned} \hat{H} = & \sum_{\hat{s}, \Lambda} \Delta A_{\Lambda, \hat{s}}^x + \sum_{\hat{s}, \Lambda} \Delta S_{\Lambda, \hat{s}}^x + \sum_{\hat{s}, \Lambda} (\epsilon_{\Lambda, \hat{s}} - \Delta \mu_{eff}) \left( \hat{n}_{\Lambda, \hat{s}, \sigma} - \frac{1}{2} \right) + \sum_{\hat{s}, \Lambda, \delta} R_{l\delta}^{(j)} \hat{n}_{k, l} \hat{n}_{-k, l'} (1 - \hat{n}_{k', l'}) \\ & + \sum_{\hat{s}} \bar{U}_0 [\mathbf{A}_{*, \hat{s}} \cdot \mathbf{A}_{*, -\hat{s}} - \mathbf{S}_{*, \hat{s}} \cdot \mathbf{S}_{*, -\hat{s}}] + \Delta \mu_{eff}^* \sum_{\hat{s}} B_{*, \hat{s}}^z + (\Delta \mu_{eff} - \Delta \mu_{eff}^*) \sum_{\hat{s}} A_{*, \hat{s}}^z , \end{aligned} \quad (5.33)$$

where  $A_{\Lambda, \hat{s}}^x$  and  $S_{\Lambda, \hat{s}}^x$  are the  $x$ -components of the charge and spin pseudospins respectively given by eq.5.11. We now perform a second level of the RG calculation for the symmetry-breaking instabilities by block-diagonalizing in the eigenbasis of the single-particle piece of the Hamiltonian eq.5.33

$$\begin{aligned} \hat{H}_1 = & \sum_{\hat{s}, \Lambda} (\epsilon_{\Lambda, \hat{s}} - \Delta \mu_{eff} + \Delta \mu_{eff}^* + \Sigma(\hat{s})) \left( \hat{n}_{\Lambda, \hat{s}, \sigma} - \frac{1}{2} \right) + \Delta_{c, \Lambda} A_*^x + \Delta_s S_*^x \\ \hat{H}_1 = & \sum_{\hat{s}, \Lambda} \tilde{\epsilon}_{c, \Lambda \hat{s}} \tilde{A}_{\Lambda, \hat{s}}^z + \tilde{\epsilon}_{s, \Lambda \hat{s}} \tilde{S}_{\Lambda, \hat{s}}^z . \end{aligned} \quad (5.34)$$

Here, the self energy  $\Sigma(\hat{s})$  incorporates the effects of the 2e-1h dispersion (eq.5.8). With this, the renormalized charge/spin pseudospin dispersion is given by  $\tilde{\epsilon}_{c/s, \Lambda, \hat{s}} = \sqrt{(\epsilon_{\Lambda, \hat{s}} \pm \epsilon_{-\Lambda, T\hat{s}} + \Delta \mu_{eff} - \Delta \mu_{eff}^* + \Sigma(\hat{s}))}$ . The RG equations for the CDW and SDW instabilities are given by

$$\frac{\Delta K_{c/s, \hat{s}}}{\Delta \log \Lambda} = \frac{K_{c/s, \hat{s}}^2}{\omega - \tilde{\epsilon}_{c/s, \Lambda, \hat{s}} - \frac{1}{4} K_{c/s, \hat{s}}} . \quad (5.35)$$

The fixed point values of the SDW and CDW gaps can be obtained from the fixed points reached by solving the RG equations

$$\omega - \tilde{\epsilon}_{c/s, \Lambda^*, \hat{s}} - \frac{1}{4} K_{c/s, \hat{s}}^* = 0 \rightarrow \Delta_c^* = \frac{1}{\sum_{\hat{s}} 1} \sum_{\hat{s}} K_{c, \hat{s}}^* \langle A_{*, \hat{s}}^x \rangle, \Delta_s^* = \frac{1}{\sum_{\hat{s}} 1} \sum_{\hat{s}} K_{s, \hat{s}}^* \langle S_{*, \hat{s}}^x \rangle . \quad (5.36)$$

Finally, in order to achieve the phase stiffness and ODLRO associated with superconductivity, we add a  $U(1)$  symmetry-breaking field to the Hamiltonian eq.5.18  $H_{SB} = \sum_{\Lambda, \hat{s}} \Delta_{sc} B_{\Lambda, \hat{s}}^x$ , where

$B_{\Lambda,\hat{s}}^+ = c_{\mathbf{k}_{\Lambda\hat{s}},\sigma}^\dagger c_{-\mathbf{k}_{\Lambda\hat{s}},-\sigma}^\dagger$  is defined in eq5.11. By performing the block-diagonalization in the rotated single-particle basis (i.e., similar to eq.5.34) leads to a modified RG equation (eq.5.17) for the superconducting fluctuation terms in eq.5.18

$$\begin{aligned} \Delta K_{s,0,\hat{s}}^{(j)}(\delta) = & \frac{-(1-p)(K_{s,0,\hat{s}}^{(j)}(\delta))^2}{\omega - \frac{p}{2}\sqrt{\Delta_{sc}^2 + (\epsilon_{\Lambda,\hat{s}} + \epsilon_{-\Lambda,T\hat{s}} + |\Delta\mu_{eff} - \Delta\mu_{eff}^*| + 2\Sigma(\hat{s}))^2} - \frac{(1-p)}{2}(\epsilon_{\Lambda\hat{s}} - \epsilon_{-\Lambda T\hat{s}}) - \frac{K_{p,0,\hat{s}}^{(j)}(\delta)}{4}} \\ & + \frac{(K_{s,0,\hat{s}}^{(j)}(\delta))^2}{\omega - \frac{1}{2}\sqrt{\Delta_{sc}^2 + (\epsilon_{\mathbf{k}_{\Lambda\hat{s}}} + \epsilon_{-\mathbf{k}_{\Lambda\hat{s}}} + |\Delta\mu_{eff} - \Delta\mu_{eff}^*| + 2\Sigma(\hat{s}))^2} - \frac{K_{p,0,\hat{s}}^{(j)}(\delta)}{4}} \\ & - \frac{N_j^2(L_\delta^{(j)})^2}{\omega + sgn(\Delta\mu_{eff})W + (\epsilon_{j,avg}^s - \Delta\mu_{eff}) - L^{(j)}(\delta)}. \end{aligned} \quad (5.37)$$

The RG equation at critical doping  $\Delta\mu_{eff} = \Delta\mu_{eff}^*$  is given by

$$\begin{aligned} \Delta K_{s,0,\hat{s}}^{(j)}(\delta) = & \frac{(K_{s,0,\hat{s}}^{(j)}(\delta))^2}{\omega - \frac{1}{2}\sqrt{\Delta_{sc}^2 + (\epsilon_{\mathbf{k}_{\Lambda\hat{s}}} + \epsilon_{-\mathbf{k}_{\Lambda\hat{s}}} + 2\Sigma(\hat{s}))^2} - \frac{(1-p)K_{p,0,\hat{s}}^{(j)}(\delta)}{4}} \\ & - \frac{(K_{s,0,\hat{s}}^{(j)}(\delta))^2}{\omega - \frac{1-p}{2}(\epsilon_{\Lambda\hat{s}} - \epsilon_{-\Lambda T\hat{s}}) - \frac{p}{2}(\epsilon_{\Lambda\hat{s}} + \epsilon_{-\Lambda T\hat{s}}) - \frac{K_{p,0,\hat{s}}^{(j)}(\delta)}{4}}. \end{aligned} \quad (5.38)$$

In what follows, we show how this RG equation unveils the d-wave symmetry of the SC order. For  $\omega < \omega^* = 2^{-1} \max_{\hat{s}} (\epsilon_{\Lambda,\hat{s}} + \epsilon_{\Lambda,-T\hat{s}}) = 2^{-1}(\epsilon_{\Lambda,\hat{s}_N} + \epsilon_{\Lambda,-T\hat{s}_N}) = 4 \sin(\Lambda_0/\sqrt{2})$  (the highest kinetic energy of pairwise states present along the nodes at a distance  $\Lambda_0$ ) in an momentum-space arc centered about the nodes, we find that the RG equation for superconducting fluctuations is RG irrelevant:  $\Delta K_{s,0,\hat{s}_N}^{(j)} < 0$ , as  $\omega - \frac{1}{2}\sqrt{\Delta_{sc}^2 + (\epsilon_{\mathbf{k}_{\Lambda\hat{s}_N}} + \epsilon_{-\mathbf{k}_{\Lambda\hat{s}_N}} + \Sigma(\hat{s}))^2} < 0$ . On the other hand, the RG equation for superconducting fluctuations for all the other normal directions to the FS are RG relevant.

Beyond  $\omega \geq \omega^*$ , a gapless nodal stretch extends on both sides of the FS from  $\hat{s}_N$  to  $\hat{s}^* \rightarrow \min_{\hat{s}^*} (\omega - \frac{1}{2}\sqrt{\Delta_{sc}^2 + (\epsilon_{\mathbf{k}_{\Lambda\hat{s}^*}} + \epsilon_{-\mathbf{k}_{\Lambda\hat{s}^*}} + \Sigma(\hat{s}))^2}) > 0$ . The fixed point Hamiltonian for  $\Delta\mu_{eff} = \Delta\mu_{eff}^*$  and for  $2^{-1}W > \omega \geq \omega^*$  (with the initial  $\Delta_{sc} \rightarrow 0$ ) is given by

$$\begin{aligned} H_{sc}^* = & \sum_{\Lambda,\hat{s}=\hat{s}_N}^{\hat{s}^*} \epsilon_{\Lambda,\hat{s}} B^z + \sum_{\hat{s}_N,\Lambda,\delta}^{\hat{s}^*} R_{l\delta}^{(j)} \hat{n}_{k,l} \hat{n}_{-k,l'} (1 - \hat{n}_{k',l'}) + \sum_{\Lambda>\Lambda^*(\hat{s}),\hat{s}=\hat{s}_{AN}}^{\Lambda_0,\hat{s}^*} \sqrt{(\epsilon_{\Lambda,\hat{s}} + \Sigma(\hat{s}))^2 + (\Delta_{\hat{s}}^*(\omega))^2} \tilde{B}_{\Lambda,\hat{s}}^z \\ & + \sum_{\Lambda=0,\hat{s}=\hat{s}_{AN}}^{\Lambda^*(\hat{s}),\hat{s}^*} \epsilon_{\Lambda,\hat{s}} \tilde{B}_{\Lambda,\hat{s}}^z + \frac{1}{2} \sum_{\Lambda,\hat{s}=\hat{s}_{AN}}^{\hat{s}^*} \left( \sum_{\delta} [K_{s,0,\hat{s}}^*(\delta) \langle B_{-2\Lambda^*+\Lambda+\delta,T\hat{s}}^- \rangle] B_{\Lambda,\hat{s}}^+ + h.c. \right) \\ & + \sum_{\Lambda,\hat{s}=\hat{s}_{AN},\delta}^{\hat{s}^*} K_{s,0,\hat{s}}^*(\delta) (B_{-2\Lambda^*+\Lambda+\delta,T\hat{s}}^- - \langle B_{-2\Lambda^*+\Lambda+\delta,T\hat{s}}^- \rangle) (B_{\Lambda,T\hat{s}}^+ - \langle B_{\Lambda,T\hat{s}}^+ \rangle), \end{aligned} \quad (5.39)$$

where  $\Delta_{\hat{s}}^*(\omega) = (\sum_{\delta} K_{s,0,\hat{s}}^*(\delta) \langle B_{-2\Lambda^*+\Lambda+\delta,T\hat{s}}^- \rangle)$  and  $K_{s,0,\hat{s}}^*(\delta) = 4(\omega - \frac{1}{2}(\epsilon_{\mathbf{k}_{\Lambda\hat{s}}} + \epsilon_{-\mathbf{k}_{\Lambda\hat{s}}} + \Sigma_{\Lambda,\hat{s}}))$ . Here ,the first and second terms are the 1e and 2e-1h dispersions of the gapless nodal stretches respectively. The third and fourth terms denote the dispersion of the antinodal stretch residing

outside and inside the emergent window respectively. The single-particle states residing outside the emergent window, i.e.,  $\Lambda > \Lambda_{\hat{s}}^*$ , corresponds to gapped marginal Fermi liquid quasiparticles with self energy given by eq.5.8. Finally, the fifth and sixth terms describe the effective  $U(1)$  symmetry-breaking mean-field and the (emergent Nambu-Goldstone) superconducting fluctuations respectively.

In this way, we obtain the self consistency equations for the superconducting order parameter (with d-wave symmetry) from the eigenstates of the symmetry-broken Hamiltonian lying within the emergent window

$$\langle c_{\Lambda-\hat{s}\downarrow}^\dagger c_{\Lambda\hat{s}\uparrow}^\dagger \rangle = \frac{\Delta_{\hat{s}}^*(\omega)}{\sqrt{\Delta_{\hat{s}}^{*2}(\omega) + (\epsilon_{\Lambda,\hat{s}} + \Sigma_{\Lambda,\hat{s}})^2}}, \quad \langle c_{\Lambda,-T\hat{s}\downarrow}^\dagger c_{\Lambda,T\hat{s}\uparrow}^\dagger \rangle = \frac{\Delta_{T\hat{s}}^*(\omega)}{\sqrt{\Delta_{\hat{s}}^{*2}(\omega) + (\epsilon_{\Lambda,\hat{s}} + \Sigma_{\Lambda,\hat{s}})^2}} \quad (5.40)$$

and  $\langle c_{\Lambda-\hat{s}_N\downarrow}^\dagger c_{\Lambda T\hat{s}_N\uparrow}^\dagger \rangle = 0$ . For minimizing the energy, we require  $\langle c_{\Lambda-\hat{s}\downarrow}^\dagger c_{\Lambda\hat{s}\uparrow}^\dagger \rangle = -\langle c_{\Lambda-T\hat{s}\downarrow}^\dagger c_{\Lambda T\hat{s}\uparrow}^\dagger \rangle$ , such that  $K_{s,0,\hat{s}}^*(\delta)(\langle c_{\Lambda-\hat{s}\downarrow}^\dagger c_{\Lambda\hat{s}\uparrow}^\dagger \rangle \langle c_{\Lambda-T\hat{s}\downarrow}^\dagger c_{\Lambda T\hat{s}\uparrow}^\dagger \rangle) < 0$ . The vanishing of the nodal order parameter  $\langle c_{\Lambda-\hat{s}_N\downarrow}^\dagger c_{\Lambda T\hat{s}_N\uparrow}^\dagger \rangle$ , along with the above displayed change of sign in the order parameter upon crossing the nodes, manifests in the d-wave nature of the superconductivity.

From the above analysis, we can now extract a temperature scale for the symmetry-broken d-wave superconductor using the relation between the quantum fluctuation scale  $\omega$  and temperature([180]) and the effective 1e self-energy of the states residing outside the emergent window. For this, we first expand the gapped dispersion energy about the one-particle gap  $\Delta_{\hat{s}}^*$

$$\sqrt{(\epsilon_{\Lambda^*,\hat{s}} + \Sigma(\hat{s}))^2 + \Delta_{\hat{s}}^{*2}} = \Delta_{\hat{s}}^* \sqrt{1 + \frac{(\epsilon_{\Lambda^*,\hat{s}} + \Sigma_{\Lambda^*,\hat{s}})^2}{\Delta_{\hat{s}}^{*2}}} \approx \Delta_{\hat{s}}^* + \frac{(\epsilon_{\Lambda^*,\hat{s}} + \Sigma(\hat{s}))^2}{2\Delta_{\hat{s}}^*} \approx \Delta_{\hat{s}}^* + \frac{\epsilon_{\Lambda^*,\hat{s}} \Sigma(\hat{s})}{\Delta_{\hat{s}}^*}. \quad (5.41)$$

We thus obtain the renormalized self-energy along the nodal direction by choosing  $\omega = \omega^*$  and using eq.5.8

$$\Sigma^{ren}(\hat{s}) = \Delta_{\hat{s}}^* = 4(\omega^* - \epsilon_{\Lambda^*,\hat{s}} - \Sigma(\hat{s}))f(\hat{s}, \omega^*) = 2\tilde{\omega}_{\hat{s}}^* \frac{f(\hat{s}, \omega^*)}{N^*(\hat{s}, \omega^*)} \ln \left| \frac{N^*(\hat{s}, \omega^*))\bar{\omega}}{\tilde{\omega}_{\hat{s}}^*} \right|, \quad (5.42)$$

where  $f(\hat{s}, \omega) = \sum_{\delta} \langle B_{-\Lambda^*+\delta, T\hat{s}}^- \rangle$  is the net spectral weight of the Cooper pairs along the normal  $\hat{s}$  obtained from the self-consistency equations eq.5.40. In the above expression, we can determine  $\tilde{\omega}_{\hat{s}}^*$  by following the steps leading to the derivation of eq.5.28

$$\tilde{\omega}_{\hat{s}}^* = \frac{N^*(\hat{s}_1, \omega^*)}{2} (\epsilon_{\Lambda_0, \hat{s}_N} - \epsilon_{\Lambda^{**}, \hat{s}}). \quad (5.43)$$

Here,  $\Lambda^{**}$  is fixed point for eq. 5.4. Using the relation between the quantum fluctuation scale  $\omega$  and an equivalent temperature scale, we obtain the  $T_C$  for the d-wave superconductivity as follows

$$T_c = \frac{2\hbar}{k_B} \max_{\hat{s}} \tilde{\omega}_{\hat{s}}^* f(\hat{s}, \omega^*) = \frac{2\hbar}{k_B} (\epsilon_{\Lambda_0, \hat{s}_N} - \epsilon_{\Lambda^{**}, \hat{s}_1}) f(\hat{s}_1, \omega^*), \quad (5.44)$$

where  $\hat{s}_1 = \hat{s}_{AN} \left( 1 - \frac{\Lambda_0}{\sqrt{2\pi}} \right)$ . The ratio of  $T_C$  with onset scale of superconductivity  $T_{ons}$  is then obtained as

$$\frac{T_c}{T_{ons}} = 2 \frac{\epsilon_{\Lambda_0, \hat{s}_N} - \epsilon_{\Lambda^{**}(\omega^*), \hat{s}_1}}{\epsilon_{\Lambda_0, \hat{s}_N} - \epsilon_{\Lambda^{**}(0), \hat{s}_1}} \frac{f(\hat{s}_1, \omega^*)}{N^*(\hat{s}_1, 0)}. \quad (5.45)$$

For the Mott liquid, the temperature scale  $T_{ML} = \frac{\hbar N^*(\hat{s}_1, 0)}{2k_B} (\epsilon_{\Lambda_0, \hat{s}_N} - \epsilon_{\Lambda^{**}(\omega_{ins}), \hat{s}_N})$  ([180]). As  $\epsilon_{\Lambda_0, \hat{s}} + \epsilon_{\Lambda_0, -\hat{s}} \simeq \epsilon_{\Lambda_0, \hat{s}} - \epsilon_{-\Lambda_0, T\hat{s}}$ , we find  $\omega_{ins} \simeq \omega^*$ , and we can write the ratio of  $T_c$  and  $T_{ML}$  as

$$\frac{T_c}{T_{ML}} = 2 \frac{f(\hat{s}_1, \omega^*)}{N^*(\hat{s}_1, 0)}. \quad (5.46)$$

Finally, the Hamiltonian that describes the inclusion of spin-nematic ordering for the spins is given by

$$H_{nm} = Q(S_{tot}^x)^2 + Q(S_{tot}^y)^2 - 2Q(S_{tot}^z)^2, \quad (5.47)$$

where  $S_{tot}^i = \sum_{\mathbf{r}} S_{\mathbf{r}}^i$ ,  $i = (x, y, z)$  are the net spin angular-momentum operators along the  $x$ ,  $y$  and  $z$  directions. The RG equation for spin-nematic ordering has the form

$$\Delta Q_{(j)} = \frac{Q_{(j)}^2}{\omega - \frac{Q_{(j)}}{4}} - \frac{p_s(K_{s,0}^{(j)})^2}{\omega - \epsilon_{p,\Lambda_j} - K_{p,0}^{(j)} - \frac{Q_{(j)}}{4}}, \quad (5.48)$$

where the first term denotes the contribution from spin-nematic fluctuations, while the second term denotes the contributions from superconducting fluctuations that suppress nematicity.

## 5.B Benchmarking results for $2 \leq U/t \leq 12$

Here we present results for the ground state energy per site  $E_g$  obtained from the RG fixed point theories for various values of  $U/t$  at  $f_h = 0$  and  $f_h = 0.125$  hole doping (see main text for details of the method). The values in the third and fifth columns for  $U/t = 2, 4, 6, 8, 12$  are obtained from several different numerical methods, as presented in LeBlanc et. al. [49] and Ehlers et al. [77]. The ground state energy values for  $U/t = 10$  are obtained from exact diagonalization studies [450] of a  $4 \times 4$  Hubbard-cluster. The value in the fifth column for  $U/t = 12$  and  $f_h = 0.125$  is absent, as no values are available in the literature to compare against. Further, in Fig.5.B, we present a plot of the ground state energy per site ( $E_g$ ) obtained for  $U/t = 8$  from the RG method for a  $k$ -space grid of size  $1024 \times 1024$  (blue circles) and exact diagonalisation (ED) on a  $4 \times 4$  cluster (from data in Ref.[450]). The two approaches are in close agreement for small hole-doping ( $f_h \leq 12.5\%$ ). However, while the RG unveils a QCP upon increasing doping, the ED calculations show a rounded-out minima. We have checked that the precisely the same QCP is attained at  $U/t = 8$  from the RG for  $k$ -space grid sizes down to  $256 \times 256$ . This reveals the fact that while ED calculations show the crossover behaviour expected for a small system, the RG captures well the physics arising from divergent fluctuations of the doped Mott liquid near critical hole-doping  $f_h^*$ .

Table 5.B.1: Ground state energy per site values obtained from the RG fixed points for  $U/t = 2, 4, 6, 8, 10, 12$ . The error bar for all data obtained from the RG is  $O(10^{-4}t)$ . Third and fifth columns for  $U/t = 2, 4, 6, 8$  and  $12$  represent the range of values obtained for the ground state per site from several different numerical methods (presented in Refs. [49], [77] and [450]) for the half-filled ( $f_h = 0$ ) and the doped ( $f_h = 1/8$ ) Hubbard model respectively.

$U_0/t$	$E_g$ from RG $f_h = 0$	$E_g$ from various numerical methods( $f_h = 0$ ) collated from [49, 450]	$E_g$ from RG at $f_h = \frac{1}{8}$	$E_g$ from other numerical methods( $f_h = \frac{1}{8}$ ) collated from [49, 450]
2	-1.199	(-1.176)–(-1.16)	-1.28	(-1.285)–(-1.267)
4	-0.854	(-0.864)–(-0.85)	-0.996	(-1.026)–(-1.0)
6	-0.652	(-0.658)–(-0.651)	-0.857	(-0.863)–(-0.829)
8	-0.526	(-0.53)–(-0.51)	-0.777	(-0.766)–(-0.709)
10	-0.439	-0.439	-0.753	-0.675
12	-0.367	(-0.369)–(-0.362)	-0.744	–

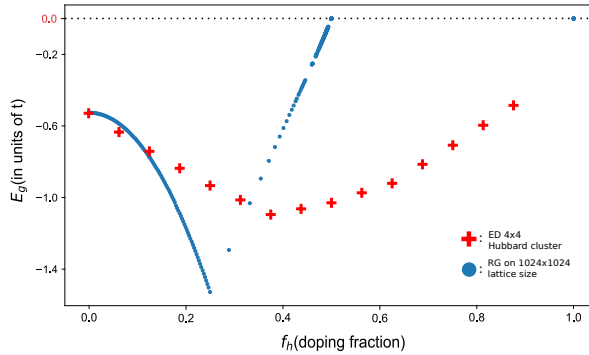


Figure 5.B.1: (Colour Online) Plot of the ground state energy per site ( $E_g$ ) obtained for  $U/t = 8$  from the RG method for a  $k$ -space grid of size  $1024 \times 1024$  (blue circles) and exact diagonalisation (ED) on a  $4 \times 4$  cluster (from data in Ref.[450]). The two approaches are in close agreement for small hole-doping ( $f_h \leq 12.5\%$ ). However, while the RG unveils a QCP upon increasing doping, the ED calculations show a crossover behaviour expected for a small system.



# Chapter 6

## Tensor RG theory for four-fermi interacting models

In this chapter, we apply the URG method introduced in chapter 2 for studying two paradigmatic models of strongly correlated electrons. One of these is a model of a single band of translationally invariant electrons with a very general form of four-fermionic interactions. We consider the interplay of inter-particle interactions and disorder in the second: the generalized Sachdev-Ye model [283], comprised of hopping, on-site and four-fermionic interactions, all of whose amplitudes are drawn randomly from separate Gaussian distributions. We have motivated the study of these two models in the Sec.1.2.2 of Chapter 1. The goal in the present chapter is to obtain effective low-energy descriptions of the various phases of electronic quantum matter that are emergent within these models. Towards this, we will demonstrate the primary advantage of the URG method: the RG flows of this method help obtain effective Hamiltonians, as well as insights into the many-particle entanglement content of its eigenstates at stable IR fixed points.

We now offer some further justification for our choice of the two models we study in the present work. Most importantly, both the translationally invariant four-fermi interacting model and the Sachdev-Ye model are very general in their scope, i.e., they have a wide parameter space, such that several well known phenomenological models (e.g., Fermi liquids and non-Fermi liquids, the reduced BCS Hamiltonian, Anderson’s model for disordered non-interacting electrons etc.) can well lie within the sub-parameter regimes of these two models. Indeed, we will demonstrate that this is the case, and that the URG approach is an efficient method for the discovery of these phases. It is important to recall that problems of interacting electrons with translational invariance and an extended Fermi surface is known to be challenging, and have been studied using FRG methods over the last three decades [507, 100, 364, 508–510, 101, 511, 512, 108, 513]. FRG approaches have reported signatures of several novel states of electronic matter, including the Mott insulator, non-Fermi liquid, pseudogap, d-wave superconductivity etc. phases within the realms of the four-fermi interacting model [124, 125, 120, 514, 126]. We have earlier studied the effects of an extended and nested Fermi surface in the case of the 2D Hubbard model on the square lattice at 1/2-filling in Refs.[180, 181], as well as the case of a (Dirac) point-like spinon Fermi surface of a XXZ Kagome antiferromagnet in a finite magnetic field in Ref.[185]. Here, we will present here a detailed study of the effects of electronic correlations for extended Fermi surfaces that are both nested as well as non-nested in spatial dimensions  $D \geq 2$ . Further, as mentioned above, the electronic Sachdev Ye (SY<sub>4</sub>) [283] model described above, upon being embedded on a

lattice, allows an investigation of the interplay between disorder and strong correlation. Studies on this model shows the fascinating phenomena of many-body localization and thermalization, with a novel transition between these two phases [515, 23]. However, an ab-initio derivation of the effective Hamiltonians of these phases is a challenge that we aim to meet in this chapter.

The chapter is organized as follows. In Section 6.1, we present the scaling relation of the single-electron entanglement entropy and its holographic upper bound. This will be useful for the study of the many-particle entanglement in various gapped and gapless phases of effective Hamiltonians reached via URG. In Section 6, we perform a URG treatment of the single band four-fermi interacting model, revealing the various IR fixed points as well as obtaining the tensor network representation of the various gapped/gapless phases. Section 6.3 describes the gauge theoretic description for the gapped theories reached under RG. In Section 6.4, we perform the URG analysis of a generalized  $SY_4$  model for electrons, revealing various translation invariant and non-invariant fixed points. We conclude in Section 7.6. Finally, the details of certain calculations are presented in appendices.

## 6.1 URG scaling of the Ryu-Takayanagi entanglement entropy bound

As any nonlocal unitary rotation can be decomposed as a tensor product of 2-local and local qubit rotations, the unitary operators of the URG framework form a entanglement holographic mapping network [177, 232]. As a consequence, the renormalized states in the bulk of the EHM network respect the Ryu-Takayanagi entanglement entropy bound formula [147]: the entanglement entropy of a region  $R$  is bounded from above by the number of linkages between it and its complement. We have given an explicit demonstration of this entropy bound for the parent metallic state and the insulating ground state of the 2D Hubbard model at half-fillingin Ref.[184]. This shows that the entanglement renormalization obtained via URG generates a holographic dual space-time along the RG direction. We aim here to reveal the URG scaling features of the Ryu-Takayanagi entanglement entropy bound for various metallic and insulating states obtained in the IR starting from generic strongly correlated models. In this section, we will obtain the expression for one-electron entanglement entropy in terms of the coefficient tensors. This is important as the maximum one-electron entanglement entropy among the electrons in a region  $R$ , when multiplied by the number of entangled links at a given RG step  $j$ , leads to the scaling of the holographic entropy bound.

The many-body eigenstate  $|\Psi_{(j)}\rangle$  at an RG step  $j$  can be written in a Schmidt-decomposed form with respect to 1-electron state  $k$  and the rest of the system

$$|\Psi_{(j)}\rangle = a_0 |\phi_{0,l}\rangle |\Psi_{0,(j)}\rangle + a_1 |\phi_{1,l}\rangle |\Psi_{1,(j)}\rangle . \quad (6.1)$$

Here  $\langle \phi_{1,l} | \phi_{0,l} \rangle = 0 = \langle \Psi_{1,(j)} | \Psi_{0,(j)} \rangle$ . Note that for  $l < j$ , the electronic state is a part of the entangled subspace, ensuring that the Schmidt coefficients  $a_1$  and  $a_0$  take values between 0 and 1. The states  $|\Psi_{0,(j)}\rangle$  and  $|\Psi_{1,(j)}\rangle$  can be written in terms of the coefficient tensors as follows

$$|\Psi_{1,(j)}\rangle = \frac{1}{\sqrt{\sum_{\beta_1} |C_{\beta_1}^{1,(j)}|^2}} \sum_{\beta_1} C_{\beta_1}^{1,(j)} |\beta'_1\rangle , \quad |\Psi_0\rangle = \frac{1}{\sqrt{\sum_{\alpha_1} |C_{\alpha_1}^{0,(j)}|^2}} \sum_{\alpha_1} C_{\alpha_1}^{0,(j)} |\alpha'_1\rangle . \quad (6.2)$$

Here the labels  $\alpha'_1$  and  $\beta'_1$  represent the collection of electronic states that are occupied. Given the orthogonality condition  $\langle \Psi_{0,(j)} | \Psi_{1,(j)} \rangle = 0$ , the Schmidt coefficients have the following expression

$$a_{1,(j)} = \sqrt{\sum_{\beta_1} |C_{\beta_1}^1|^2}, a_{0,(j)} = \sqrt{\sum_{\alpha_1} |C_{\alpha_1}^0|^2}, \quad (6.3)$$

with the constraint  $a_{1,(j)}^2 + a_{0,(j)}^2 = 1$ . The one-electron entanglement entropy is obtained in terms of Schmidt coefficients

$$S_{(j)}(k) = \log 2 - \frac{1}{2}(1+x)\log(1+x) - \frac{1}{2}(1-x)\log(1-x), \quad (6.4)$$

$$\text{where } x = \sqrt{1 - 4a_{1,(j)}^2 a_{0,(j)}^2}.$$

We now obtain the leading terms in  $S_{(j)}$  for two extreme cases: (i) when the URG flow leads to IR fixed points where the ground state is completely separable, and (ii) when the URG flow generates a highly entangled subspace in the IR. For case (i), and with  $x = 1 - \epsilon$  ( $\epsilon \rightarrow 0$ ), we have

$$S_{(j)}^1(k) = -(1 - \frac{\epsilon}{2})\log\left(1 - \frac{\epsilon}{2}\right) - \frac{\epsilon}{2}\log\frac{\epsilon}{2} \approx \epsilon/2 = \sum_{\beta_1, \alpha_1} |C_{\beta_1}^{1,(j)} C_{\alpha_1}^{0,(j)}|^2. \quad (6.5)$$

For case (ii0, with  $x \rightarrow 0$ , we find

$$S_{(j)}^2(k) \approx \log 2 - \frac{x^2}{2} = \log 2 - \frac{1}{2} + 2 \sum_{\beta_1, \alpha_1} |C_{\beta_1}^{1,(j)} C_{\alpha_1}^{0,(j)}|^2. \quad (6.6)$$

Next, we will obtain the renormalization of entanglement entropy  $S_{(j)}^1$  for case (i) in the lowest order of  $\Delta C_\rho^{(j)}$

$$\begin{aligned} \Delta S_{(j)}^1(k) &= \sum_{\beta_1, \alpha_1} |(C_{\beta_1}^{1,(j)} + \Delta C_{\beta_1}^{1,(j)})(C_{\alpha_1}^{0,(j)} + \Delta C_{\alpha_1}^{0,(j)})|^2 - \sum_{\beta_1, \alpha_1} |C_{\beta_1}^{1,(j)} C_{\alpha_1}^{0,(j)}|^2 \\ &\approx \sum_{\beta_1} 2\text{Re}(C_{\beta_1}^{1,(j)} \Delta C_{\beta_1}^{1,(j)}) a_{0,(j)}^2 + \sum_{\alpha_1} 2\text{Re}(C_{\alpha_1}^{0,(j)} \Delta C_{\alpha_1}^{0,(j)}) a_{1,(j)}^2. \end{aligned} \quad (6.7)$$

Note that for a separable state, either  $a_{1,(j)} \rightarrow 1$  or  $a_{0,(j)} \rightarrow 1$ , resulting in

$$\Delta S_{(j)}^1(k) = \sum_{\beta_1} 2\text{Re}(C_{\beta_1}^{1,(j)} \Delta C_{\beta_1}^{1,(j)}). \quad (6.8)$$

Similarly, for highly entangled states in case (ii),  $\Delta S_{(j)}^2(k) = \sum_{\beta_1} 4\text{Re}(C_{\beta_1}^{1,(j)} \Delta C_{\beta_1}^{1,(j)})$ . Finally, note that, following the Ryu-Takayanagi formula [147], the entanglement entropy of a region  $R$  is bounded as follows

$$\Delta S_{(j)}(R) \leq N_{(j)}(R) \Delta \max_{k \in R} S_{(j)}^i(k), \quad (6.9)$$

where  $N_{(j)}(R)$  is the number of electrons in the region  $R$  that belong to the entangled subspace at RG step  $j$ . In a later section, we will obtain the entropy bound scaling relation for various gapless and gapped IR fixed points obtained from a generic strongly correlated model.

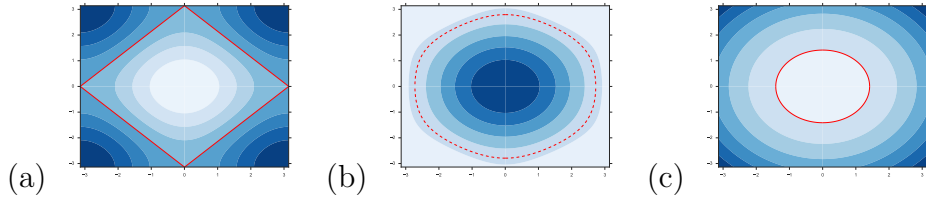


Figure 6.2.1: Figure represents iso-geometric curves that are displaced parallelly from the Fermi surface (red curve), and cover the Brillouin zone in the limit of  $(L_x, L_y) \rightarrow \infty$  limit for (a) the square lattice at chemical potential  $\mu = 0$ , (b) the triangular lattice at  $\mu = -7.0t$  and (c) the continuum circular dispersion at  $\mu = 0$ .

## 6.2 Four Fermi interacting model with translational invariance

We begin the analysis by representing the single-band translational invariant four- fermion interacting model (SFIM) as follows

$$\hat{H}_{SFIM} = \sum_{\mathbf{k}} (\epsilon_{\mathbf{k}} - \mu) \hat{n}_{\mathbf{k}\sigma} + \sum_{\mathbf{k}\mathbf{k}'\mathbf{p}} V_{\alpha\beta} c_{\mathbf{k}\sigma}^{\dagger} c_{\mathbf{p}-\mathbf{k}\sigma'}^{\dagger} c_{\mathbf{p}-\mathbf{k}'\sigma'} c_{\mathbf{k}'\sigma} , \quad (6.10)$$

where  $\mathbf{p}$  is the net pair-momentum and  $\mathbf{k} - \mathbf{k}'$  is the momentum transfer. The four-fermion interaction vertex can be compactly represented as  $V_{\alpha\beta} = V_{\mathbf{k}\mathbf{k}'\mathbf{p}}^{\sigma\sigma'}$ , where  $\alpha := \{(\mathbf{k}, \sigma, 1); (\mathbf{p} - \mathbf{k}, \sigma', 1)\}$ ,  $\beta := \{(\mathbf{p} - \mathbf{k}', \sigma', 0); (\mathbf{k}', \sigma, 0)\}$ , and the indices 1 and 0 represent the  $c^{\dagger}$  and  $c$  operators respectively. The zero momentum transfer vertices are denoted as  $V_{\alpha\alpha'}$  (where  $\alpha' = \{(\mathbf{k}, \sigma, 0); (\mathbf{p} - \mathbf{k}, \sigma', 0)\}$ ). For an overall understanding of the various zero temperature phases, we develop below the Hamiltonian renormalization group scheme for  $H_{SFIM}$ . We will, thereby, display the tensor network representation of the Hamiltonian RG flows towards various fixed point theories.

The scheme adopted for the RG involves decoupling initially states whose energy is highest with respect to Fermi energy  $E_F = \mu$ , followed by ones closer to the Fermi surface. This is ensured by defining parallel curves *isogeometric* to the Fermi surface (see Fig.6.2.1). The wave-vectors  $\mathbf{k}_{\Lambda\hat{s}} = \mathbf{k}_F(\hat{s}) + \Lambda\hat{s}$  are relabelled by the distance  $\Lambda$  from the Fermi surface and the unit normal vector to it,  $\hat{s} = \nabla\epsilon_{\mathbf{k}}/|\nabla\epsilon_{\mathbf{k}}|_{\epsilon_{\mathbf{k}}=E_F}$ . The renormalization group flow of the Hamiltonian,  $H_{(j-1)} = U_{(j)} H_{(j)} U_{(j)}^{\dagger}$ , takes place via disentangling an entire isogeometric curve by a unitary operation  $U_{(j)} = \prod_l U_{(j,l)}$ , where the collective coordinates  $l = (\hat{s}, \sigma)$ ,  $(j, l) \equiv \mathbf{k}_{\Lambda_j\hat{s}}\sigma$  represent the state labelled by the quantum numbers  $\mathbf{k}_{\Lambda_j\hat{s}}\sigma$ .  $U_{(j,l)}$  represents an individual unitary operation that decouples a single electronic state  $(j, l) \equiv \mathbf{k}_{\Lambda_j\hat{s}}\sigma$  and has the form

$$U_{(j,l)} = \frac{1}{\sqrt{2}} [1 + \eta_{(j,l)}^{\dagger} - \eta_{(j,l)}] , \quad (6.11)$$

where the form of the e-h transition operators  $\eta_{(j,l)}$  are shown in eq.(4.3) of Chapter 4. Following the RG flow equations chapter2 eq.(2.47) obtained from the Hamiltonian renormalization, we will investigate various parameter regimes for the microscopic  $H_{SFIM}$  theory, culminating in the RG phase diagram for the model. In keeping with our discussion of the influence of 3-particle vertices on the 1-particle self-energy and 2-particle correlation energy, we truncate the RG flow equation heirarchy in eq.(2.47) to six-point vertices.

### 6.2.1 Derivation of the RG equation for 1 particle self energy $\Sigma_{\mathbf{k}\sigma}(\omega)$

Translational invariance of  $H_{SFIM}$  ensures that the two-point vertices are purely number diagonal in momentum space:  $\Gamma_{\alpha\alpha'}^{2,(j)}(\omega_{(j)}) = \epsilon_{\Lambda,\hat{s}} + \Sigma_{\Lambda,\hat{s}}^{(j)}(\omega_{(j)})$ . Further, from eq.(2.47), the RG flow of  $\Gamma_{\alpha\alpha'}^2$  can be attributed to the contribution from 4- and 6-point vertices to the RG flow of the single-particle self-energy

$$\Delta\Sigma_{\Lambda,\hat{s},\sigma}^{(j)}(\omega_{(j)}) = \sum_{\gamma} \Gamma_{\alpha\gamma}^{4,(j)}(\omega_{(j)}) G_{\gamma\gamma'}^{6,(j)}(\omega_{(j)}) \Gamma_{\gamma'\alpha'}^{4,(j)}(\omega_{(j)}) + \sum_{\gamma_1} \Gamma_{\alpha_1\gamma_1}^{6,(j)}(\omega_{(j)}) G_{\gamma_1\gamma'_1}^{10,(j)}(\omega_{(j)}) \Gamma_{\gamma'_1\alpha'_1}^{6,(j)}(\omega_{(j)}) . \quad (6.12)$$

Here,  $G_{\gamma\gamma'}^{6,(j)}(\omega_{(j)})$  and  $G_{\gamma\gamma'}^{10,(j)}(\omega_{(j)})$  are Green's function operators that contain the kinetic and interaction energies of three particles and five particles respectively, with explicit forms given by

$$\begin{aligned} G_{\gamma\gamma'}^{6,(j)}(\omega_{(j)}) &= \frac{8\tau_{\mathbf{k}_{\Lambda_j\hat{s}_1}\sigma',\mathbf{p}-\mathbf{k}_{\Lambda_j\hat{s}_1}\sigma',\mathbf{p}-\mathbf{k}_{\Lambda\hat{s}}\sigma}}{\omega_{(j)} - h_{(j)}^1 - h_{(j)}^2 - h_{(j)}^3} , \\ h_{(j)}^1 &= (\epsilon_{\mathbf{k}_{\Lambda_j\hat{s}_1}} + \Sigma_{\mathbf{k}_{\Lambda_j\hat{s}_1}}^{(j)}(\omega_{(j)}))\tau_{\mathbf{k}_{\Lambda_j\hat{s}_1}\sigma'} - (\epsilon_{\mathbf{p}-\mathbf{k}_{\Lambda_j\hat{s}_1}} + \Sigma_{\mathbf{p}-\mathbf{k}_{\Lambda_j\hat{s}_1}}^{(j)}(\omega_{(j)}))\sigma_{\mathbf{p}-\mathbf{k}_{\Lambda_j\hat{s}_1}\sigma'} \\ &\quad - (\epsilon_{\mathbf{p}-\mathbf{k}_{\Lambda\hat{s}}} + \Sigma_{\mathbf{p}-\mathbf{k}_{\Lambda\hat{s}}}^{(j)}(\omega_{(j)}))\sigma_{\mathbf{p}-\mathbf{k}_{\Lambda\hat{s}}\sigma} \\ h_{(j)}^2 &= \Gamma_{(\mathbf{k}_{\Lambda\hat{s}},\sigma'),(\mathbf{p}-\mathbf{k}_{\Lambda\hat{s}},\sigma)}^{4,(j)}\sigma_{\mathbf{p}-\mathbf{k}_{\Lambda_j\hat{s}_1},\sigma'}\sigma_{\mathbf{p}-\mathbf{k}_{\Lambda\hat{s}},\sigma} + \Gamma_{(\mathbf{k}_{\Lambda_j\hat{s}_1},\sigma'),(\mathbf{p}-\mathbf{k}_{\Lambda\hat{s}},\sigma)}^{4,(j)}\tau_{\mathbf{k}_{\Lambda_j\hat{s}_1},\sigma'}\sigma_{\mathbf{p}-\mathbf{k}_{\Lambda\hat{s}},\sigma} \\ &\quad + \Gamma_{(\mathbf{k}_{\Lambda_j\hat{s}_1},\sigma'),(\mathbf{p}-\mathbf{k}_{\Lambda_j\hat{s}_1},\sigma)}^{4,(j)}\tau_{\mathbf{k}_{\Lambda_j\hat{s}_1},\sigma'}\sigma_{\mathbf{p}-\mathbf{k}_{\Lambda_j\hat{s}},\sigma} \\ h_{(j)}^3 &= \Gamma_{(\mathbf{k}_{\Lambda_j\hat{s}_1},\sigma'),(\mathbf{p}-\mathbf{k}_{\Lambda\hat{s}},\sigma),(\mathbf{p}-\mathbf{k}_{\Lambda_j\hat{s}_1},\sigma')}^{6,(j)}\sigma_{\mathbf{p}-\mathbf{k}_{\Lambda_j\hat{s}_1},\sigma'}\sigma_{\mathbf{p}-\mathbf{k}_{\Lambda\hat{s}},\sigma}\tau_{\mathbf{k}_{\Lambda_j\hat{s}_1},\sigma'} . \end{aligned} \quad (6.13)$$

and

$$\begin{aligned} G_{\gamma\gamma'}^{10,(j)}(\omega_{(j)}) &= \frac{32 \prod_{i=1}^4 \sigma_{\mathbf{k}_i,\sigma_i} \tau_{\mathbf{k}_{\Lambda_j\hat{s}_1},\sigma'}}{\omega - h_{(j)}} , \\ h_{(j)} &= \sum_{(\mathbf{k}_i,\sigma) \in \rho \subset \gamma} \Gamma_{\rho\rho'}^{2,(j)} \sigma_{\mathbf{k}_i,\sigma} + \sum_{\substack{((\mathbf{k}_i,\sigma), \\ (\mathbf{k}_j,\sigma')) \in \rho \subset \gamma}} \Gamma_{\rho\rho'}^{4,(j)} \sigma_{\mathbf{k}_i,\sigma} \sigma_{\mathbf{k}_j,\sigma'} \\ &\quad + \sum_{\substack{((\mathbf{k}_i,\sigma), \\ (\mathbf{k}_j,\sigma'), \\ (\mathbf{k}_l,\sigma'')) \in \rho \subset \gamma}} \Gamma_{\rho\rho'}^{6,(j)} \sigma_{\mathbf{k}_i,\sigma} \sigma_{\mathbf{k}_j,\sigma'} \tau_{\mathbf{k}_{\Lambda_j\hat{s}_1},\sigma'} , \end{aligned} \quad (6.14)$$

respectively. The labels  $\alpha$ ,  $\gamma$  and  $\alpha'$  are defined similar to that discussed below eq.(2.31), as the collection of pairwise labels  $\{(\mathbf{k}, \sigma, \mu)\}$ , such that  $l$  represents the electronic state labels and  $\mu = 0/1$  represent the electron annihilation/creation operator. The labels  $\alpha = \{((\mathbf{k}_{\Lambda\hat{s}}, \sigma), \mu_1), ((\mathbf{p} - \mathbf{k}_{\Lambda\hat{s}}, \sigma'), \mu_2)\}$ ,  $\gamma = \{((\mathbf{k}_{\Lambda_j\hat{s}}, \sigma), \mu_1), ((\mathbf{p} - \mathbf{k}_{\Lambda_j\hat{s}}, \sigma'), \mu_2)\}$ .  $\alpha'$  and  $\gamma'$  involve the same electronic states with  $\mu_1, \mu_2$  replaced by the complement  $\bar{\mu}_{1,2} = 1 - \mu_{1,2}$ . Similar definitions exist for  $\alpha_1, \gamma_1$  and  $\alpha'_1, \gamma'_1$ . In the above equation, the operators  $\tau_{\mathbf{k}\sigma} = n_{\mathbf{k}\sigma} - \frac{1}{2}$  represents decoupled degrees of freedom that commute with the Hamiltonian, while the operators  $\sigma_{\mathbf{k}\sigma} = n_{\mathbf{k}\sigma} - \frac{1}{2}$  belong to the coupled space and do not commute with the Hamiltonian. We now derive the four-point and six-point vertex RG flow equations.

## 6.2.2 Derivation of RG flow equations for $\Gamma_{\alpha\beta}^4$ and $\Gamma_{\alpha\beta}^6$

Using the RG flow equation hierarchy of eq.(2.47), the RG flow equation for the four-point vertex at the  $l$ -th step and along a given isogeometric curve  $j$  is given by

$$\begin{aligned}\Delta\Gamma_{\alpha\beta}^{4,(j,l)}(\omega_{(j,l)}) &= \Gamma_{\alpha\beta}^{4,(j,l)}(\omega_{(j,l)}) - \Gamma_{\alpha\beta}^{4,(j,l-1)}(\omega_{(j,l-1)}) \\ &= \sum_{\gamma} \Gamma_{\alpha\gamma}^{4,(j,l)} G_{\gamma\gamma'}^{4,(j,l)}(\omega_{(j,l)}) \Gamma_{\gamma'\beta}^{4,(j,l)} + \sum_{\gamma} \Gamma_{\alpha\gamma}^{6,(j,l)} G_{\gamma\gamma'}^{8,(j,l)}(\omega_{(j,l)}) \Gamma_{\gamma'\beta}^{6,(j,l)}.\end{aligned}\quad (6.15)$$

Here,  $G_{\gamma\gamma'}^{4,(j,l)}(\omega_{(j,l)})$ ,  $G_{\gamma\gamma'}^{6,(j,l)}(\omega_{(j,l)})$ ,  $G_{\gamma\gamma'}^{8,(j,l)}(\omega_{(j,l)})$  are four-, six- and eight-point Green's functions respectively. We also note that the four-point off-diagonal vertex scattering between normals  $\hat{s}$  and  $\hat{s}'$  takes places either directly ( $\hat{s} \rightarrow \hat{s}'$ ) or via correlated (i.e., higher order) tangential scattering processes (e.g.,  $\hat{s} \rightarrow \hat{s}_1 \rightarrow \hat{s}'$ ,  $\hat{s} \rightarrow \hat{s}_1 \rightarrow \hat{s}_2 \rightarrow \hat{s}'$ ). Taken together, the first term in eq.(6.15)) involves the contribution to the four-point vertex RG flow  $\Delta\Gamma^{4,(j)}$  in eq(6.15) due to other four-point vertices (including the effects of correlated scattering between states residing on the same isogeometric curve ( $j$ ))

$$\begin{aligned}\Delta\Gamma_{\alpha\beta}^{4,(j)}(\omega_{(j)}) &\rightarrow \sum_{\gamma} \Gamma_{\alpha\gamma}^{4,(j)} G_{\gamma\gamma'}^{4,(j)} \Gamma_{\gamma'\beta}^{4,(j)} + \sum_{\gamma_1} \Gamma_{\alpha\gamma}^{4,(j)} G_{\gamma\gamma'}^{4,(j)} \Gamma_{\gamma'\gamma_1}^{4,(j)} G_{\gamma_1\gamma'_1}^{4,(j)} \Gamma_{\gamma'_1\beta}^{4,(j)} + \dots \\ &= \sum_{\gamma_i} \prod_{i=1}^{n-1} \Gamma_{\alpha\gamma_i}^{4,(j)} G_{\gamma_i\gamma'_i}^{4,(j)} \Gamma_{\gamma'_i\gamma'_{i+1}}^{4,(j)} G_{\gamma_n\gamma'_n}^{4,(j)} \Gamma_{\gamma'_n\beta}^{4,(j)}.\end{aligned}\quad (6.16)$$

In the above expression, the renormalization contribution from the  $k$ -correlated 4-point off-diagonal scattering vertex (i.e.,  $\Gamma^4(G^4\Gamma^4)\dots_{(k-2)-\text{times}}\dots(G^4\Gamma^4)$  for a  $D$ -dimensional system scales with volume as  $L^{(k-1)(D-1)}L^{-kD} = L^{-D-k+1}$ . This scaling can be understood as follows. The unit  $G^4\Gamma^4$  is repeated  $k$  times, each of which gives a factor  $L^{D-1}/L^D$  and where the  $L^{D-1}$  factor arises from the area of the shell of single-particle states that are decoupled and the  $L^{-D}$  factor comes from the  $\Gamma^4$  vertex. Finally, note that the string begins with a factor  $\Gamma^4$ , contributing a final  $L^{-D}$ . Thus, in the thermodynamic limit (TL,  $L \rightarrow \infty$ ), the contributions from all strings starting from  $\Gamma^4G^4\Gamma^4G^4\Gamma^4$  and longer are sub-dominant compared to the leading contribution arising from the  $\Gamma^4G^4\Gamma^4$  term. The same holds true for the  $\Gamma^6G^8\Gamma^6$  and  $\Gamma^6G^6\Gamma^4$  renormalization contributions to  $\Gamma^{4,(j)}$  in eq.(6.15), with volume dependence  $L^{-(k+1)D-k+1}$  and  $L^{-3kD}$  respectively.

Accounting for the leading contributions in the thermodynamic limit, a compact form of the flow equations for 4-point vertices and 6 point off-diagonal vertices is given by

$$\begin{aligned}\Delta\Gamma_{\alpha\beta}^{4,(j)}(\omega_{(j)}) &= \sum_{\gamma} \Gamma_{\alpha\gamma}^{4,(j)} G_{\gamma\gamma'}^{4,(j)}(\omega_{(j)}) \Gamma_{\gamma'\beta}^{4,(j)} + \sum_{\gamma} \Gamma_{\alpha\gamma}^{6,(j)} G_{\gamma\gamma'}^{8,(j)}(\omega_{(j)}) \Gamma_{\gamma'\beta}^{6,(j)}, \\ \Delta\Gamma_{\alpha\beta}^{6,(j)}(\omega_{(j)}) &= \sum_{\gamma} \Gamma_{\alpha\gamma}^{4,(j)} G_{\gamma\gamma'}^{2,(j)}(\omega_{(j)}) \Gamma_{\gamma'\beta}^{4,(j)} + \sum_{\gamma} \Gamma_{\alpha\gamma}^{6,(j)} G_{\gamma\gamma'}^{6,(j)}(\omega_{(j)}) \Gamma_{\gamma'\beta}^{6,(j)} \\ &\quad + \sum_{\gamma} \Gamma_{\alpha\gamma}^{6,(j)} G_{\gamma\gamma'}^{4,(j)}(\omega_{(j)}) \Gamma_{\gamma'\beta}^{4,(j)}.\end{aligned}\quad (6.17)$$

Finally, the RG flow equations for the 6-point diagonal vertices are given by

$$\Delta\Gamma_{\alpha\alpha'}^{6,(j)}(\omega_{(j)}) = \sum_{\gamma} \Gamma_{\alpha\gamma}^{4,(j)} G_{\gamma\gamma'}^{2,(j)}(\omega_{(j)}) \Gamma_{\gamma'\beta}^{4,(j)} + \sum_{\gamma} \Gamma_{\alpha\gamma}^{6,(j)} G_{\gamma\gamma'}^{6,(j)}(\omega_{(j)}) \Gamma_{\gamma'\beta}^{6,(j)}.\quad (6.18)$$

In the above flow equations, the Green's functions  $G_{\gamma\gamma'}^{2,(j)}(\omega_{(j)})$ ,  $G_{\gamma\gamma'}^{4,(j)}(\omega_{(j)})$ ,  $G_{\gamma\gamma'}^{6,(j)}(\omega_{(j)})$  and  $G_{\gamma\gamma'}^{8,(j)}(\omega_{(j)})$  contain the energy contributions from one-particle self energies, as well as two- and three-particle correlation energies. The form of the two-particle Green's function  $G_{\gamma\gamma'}^{4,(j)}(\omega_{(j)})$  is given by

$$G_{\gamma\gamma'}^{4,(j)}(\omega_{(j)}) = \frac{4\tau_{\mathbf{k}_{\Lambda_j\hat{s}_1},\sigma',\sigma} - \tau_{\mathbf{k}_{\Lambda_j\hat{s}_1},\sigma,\sigma'}}{\omega_{(j)} - h_{(j)}^1 - h_{(j)}^2} \\ h_{(j)}^1 = \epsilon_{\mathbf{k}_{\Lambda_j\hat{s}_1}}\tau_{\mathbf{k}_{\Lambda_j\hat{s}_1},\sigma'} + \epsilon_{\mathbf{p}-\mathbf{k}_{\Lambda_j\hat{s}_1}}\sigma_{\mathbf{p}-\mathbf{k}_{\Lambda_j\hat{s}_1},\sigma}, h_{(j)}^2 = \Gamma_{(\mathbf{k}_{\Lambda_j\hat{s}_1},\sigma'),(\mathbf{p}-\mathbf{k}_{\Lambda_j\hat{s}_1},\sigma)}^{4,(j)}\tau_{\mathbf{k}_{\Lambda_j\hat{s}_1},\sigma'}\tau_{\mathbf{p}-\mathbf{k}_{\Lambda_j\hat{s}_1},\sigma}. \quad (6.19)$$

The four-particle Green's function  $G_{\gamma\gamma'}^{8,(j)}(\omega_{(j)})$  can be obtained similarly, while the three-particle Green's function  $G_{\gamma\gamma'}^{6,(j)}(\omega_{(j)})$  has already been given earlier.

An important point can now be made. When relevant under RG flow, the contribution of six-point scattering vertices  $\Gamma_{\alpha\beta}^{6,(j)}$  is responsible for the dynamical mixing of opposite spin electron-electron and electron-hole configurations. This feature results from the non-commutativity between the composite electron creation operator  $(1 - \hat{n}_{\mathbf{k}\sigma})c_{\mathbf{k}'\sigma'}^\dagger$  and the ee/eh pseudospin pair operators [413],  $c_{\mathbf{k}\sigma}^\dagger c_{\mathbf{k}'\sigma'}$  and  $c_{\mathbf{k}\sigma}^\dagger c_{\mathbf{k}'\sigma'}$ . In order to incorporate this effect within the four-point vertex RG equations, we follow Refs.[180, 182] and perform an  $\omega$ -dependent rotation,  $\tan^{-1}(\sqrt{\frac{1-p}{p}})$ , in the space of the electron/hole configurations of the pair of electronic states:  $|1_{\mathbf{k}_{\Lambda\hat{s}}} 1_{\mathbf{p}-\mathbf{k}_{\Lambda\hat{s}}}\rangle$  and  $|1_{\mathbf{k}_{\Lambda\hat{s}}} 0_{\mathbf{p}-\mathbf{k}_{\Lambda\hat{s}}}\rangle$ . This is manifested in the RG equations of  $\Gamma^{4,(j)}$ , obtained in a rotated basis of occupied and unoccupied electronic states

$$\Delta\Gamma_{\alpha\beta}^{4,(j)}(\omega_{(j)}) = \sum_{\gamma} \left[ \frac{p\Gamma_{\alpha\gamma}^{4,(j)}\Gamma_{\gamma\beta}^{4,(j)}}{\omega_{(j)} - \epsilon_{p,\mathbf{k}_{\Lambda_j\hat{s}'},\mathbf{p}}^{(j)} - \frac{2p-1}{4}\Gamma_{\gamma\gamma'}^{4,(j)}} - \frac{(1-p)\Gamma_{\alpha_1\gamma_1}^{4,(j)}\Gamma_{\gamma_1\beta_1}^{4,(j)}}{\omega_{(j)} - \epsilon_{p,\mathbf{k}_{\Lambda_j\hat{s}'},\mathbf{p}'}^{(j)} - \frac{2p-1}{4}\Gamma_{\gamma_1\gamma_1'}^{4,(j)}} \right] \\ + \sum_{\gamma} \Gamma_{\alpha\gamma}^{6,(j)} G_{\gamma\gamma'}^{8,(j)}(\omega_{(j)}) \Gamma_{\gamma'\beta}^{6,(j)}, \quad (6.20)$$

where the ee/eh hybridized pair-dispersion is given by

$$\epsilon_{p,\mathbf{k}_{\Lambda_j\hat{s}'},\mathbf{p}}^{(j)} = \frac{p}{2}(\epsilon_{\mathbf{k}_{\Lambda_j\hat{s}'}}^{(j)} + \epsilon_{\mathbf{p}-\mathbf{k}_{\Lambda_j\hat{s}'}}^{(j)}) + \frac{1-p}{2}(\epsilon_{\mathbf{k}_{\Lambda_j\hat{s}'}}^{(j)} - \epsilon_{\mathbf{p}-\mathbf{k}_{\Lambda_j\hat{s}'}}^{(j)}). \quad (6.21)$$

In the above RG equation, the indices  $\alpha, \beta, \gamma, \alpha', \beta', \gamma_1$  are related as follows: for  $\alpha = \{(\mathbf{k}, \sigma, 1), (\mathbf{p}-\mathbf{k}, \sigma', 1)\}$ ,  $\beta = \{(\mathbf{k}', \sigma, 0), (\mathbf{p}-\mathbf{k}', \sigma', 0)\}$  and  $\gamma = \{(\mathbf{k}_{\Lambda_j\hat{s}_1}, \sigma, 0), (\mathbf{p}-\mathbf{k}_{\Lambda_j\hat{s}_1}, \sigma', 0)\}$ , the indices  $\alpha_1 = \{(\mathbf{k}, \sigma, 1), (\mathbf{p}-\mathbf{k}, \sigma', 0)\}$ ,  $\beta_1 = \{(\mathbf{k}', \sigma, 0), (\mathbf{p}-\mathbf{k}, \sigma', 1)\}$  and  $\gamma_1 = \{(\mathbf{k}_{\Lambda_j\hat{s}}, \sigma, 0), (\mathbf{p}+\mathbf{k}_{\Lambda_j\hat{s}}-\mathbf{k}', \sigma', 1)\}$ . In order to manifest the dominant effect of the six-point off-diagonal vertices, the hybridisation parameter  $p(\omega)$  is chosen so as to maximize the spin-charge hybridized Green's function  $G^{p,j}(\omega_{(j)}) = (\omega_{(j)} - \epsilon_{p,\mathbf{k}_{\Lambda_j\hat{s}'},\mathbf{p}}^{(j)})^{-1}$ ,

$$p := p' \text{ s.t. } G^{p,j}(\omega_{(j)}) = \max_{0 < p' < 1} G^{p',j}(\omega_{(j)}). \quad (6.22)$$

With these RG equations in place, we have laid the platform for investigating the low energy fixed point Hamiltonians of various quantum fluctuation energy scales and parameter regimes.

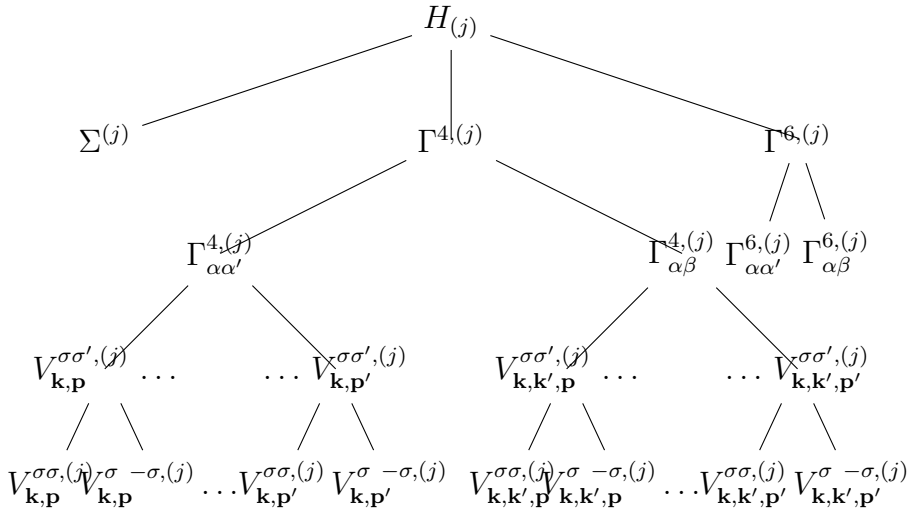


Figure 6.2.2: Tree tensor network representation of the 2-point, 4-point and 6-point vertices, where the 4-point and 6-point vertex tensor are comprised of diagonal and off-diagonal parts. The 4-point vertex tensor is further decomposed in various total pair-momentum  $\mathbf{p}$  and spin-pair  $\sigma\sigma'$  channels. Note that  $\alpha := \{(l, \mu)\}$  and  $\alpha' := \{(l, \bar{\mu})\}$  and  $\beta := \{(l', \bar{\mu})\}$ , where the index  $l$  represents a collection of labels marking states in the coupled space and  $\mu = 1/0$  refers to a particular state being either occupied or unoccupied (converse for  $\bar{\mu}$ ).

### 6.2.3 RG flows towards Fermi liquid and BCS fixed points

We begin with an illustration in Fig.6.2.2 of various 2-, 4- and 6-point vertices obtained from a tree-like decomposition of the heirarchical Hamiltonian RG flow. This will be seen to assist us in describing the RG flows towards various stable phases of fermionic quantum matter obtained across several parameter regimes. The first level of branching involves the separation into the 2-point (self-energy  $\Sigma$ ), 4-point ( $\Gamma^4$ ) and 6-point ( $\Gamma^6$ ) vertices. A second level of branching involves that of the 4- and 6-point vertices ( $\Gamma^{4,(j)}, \Gamma^{6,(j)}$ ) into diagonal ( $\Gamma_{\alpha\alpha'}^{4,(j)}, \Gamma_{\alpha\alpha'}^{6,(j)}$ ) and off-diagonal ( $\Gamma_{\alpha\beta}^{4,(j)}, \Gamma_{\alpha\beta}^{6,(j)}$ ) elements. In order to make the tensorial dependence on momenta and spin indices explicit, the diagonal and off-diagonal 4-point vertex elements ( $\Gamma_{\alpha\alpha'}^{4,(j)}, \Gamma_{\alpha\beta}^{4,(j)}$ ) are further decomposed into different pair-momenta  $\mathbf{p}$  and spin-pair channels  $\sigma, \sigma' = \sigma, \sigma$  and  $\sigma, \sigma' = \sigma, -\sigma$  as  $\Gamma_{\alpha\alpha'}^{4,(j)} \equiv V_{\mathbf{k}\mathbf{p}}^{\sigma\sigma',(j)}$ ,  $\Gamma_{\alpha\beta}^{4,(j)} \equiv V_{\mathbf{k}\mathbf{k}'\mathbf{p}}^{\sigma\sigma',(j)}$  respectively. The notation  $\alpha\beta$  and  $\alpha\alpha'$  employed for the 4-point vertices are 4-element sets chosen as follows:

$$\begin{aligned} \alpha\beta &= \{(\mathbf{k}, \sigma, 1), (\mathbf{p} - \mathbf{k}, \sigma', 1), (\mathbf{p} - \mathbf{k}', \sigma', 0), (\mathbf{k}', \sigma', 0)\} , \\ \alpha\alpha' &= \{(\mathbf{k}, \sigma, \mu_1), (\mathbf{p} - \mathbf{k}, \sigma', \mu_2), (\mathbf{p} - \mathbf{k}, \sigma', \bar{\mu}_2), (\mathbf{k}, \sigma, \bar{\mu}_1)\} , \end{aligned} \quad (6.23)$$

where the first two indices label the state and  $\mu = 1, 0$  represents creation or annihilation operation on that state and  $\bar{\mu}$  is its compliment.

Similarly, the 6-point vertices are decomposed into diagonal  $\Gamma_{\alpha\alpha'}^{6,(j)} \equiv R_{\mathbf{k}\mathbf{k}'\mathbf{k}''}^{\sigma\sigma'\sigma,(j)}$  and off-diagonal vertices  $\Gamma_{\alpha\beta}^{6,(j)} \equiv R_{\mathbf{k}\mathbf{k}_1\mathbf{k}_2\mathbf{k}_3\mathbf{k}_4}^{\sigma\sigma'\sigma,(j)}$ . Again, the notation  $\alpha\beta$  and  $\alpha\alpha'$  for the six point vertices are 6-

element sets chosen as follows:

$$\begin{aligned}\alpha\beta &= \left\{(\mathbf{k}, \sigma, 1), (\mathbf{p} - \mathbf{k}, \sigma', 1), (\mathbf{p}' - \mathbf{k}', \sigma', 1), (\mathbf{p} - \mathbf{k}', \sigma', 0), (\mathbf{k}'', \sigma', 0), (\mathbf{p}' - \mathbf{k}'', \sigma, 0)\right\} \\ \alpha\alpha' &= \left\{(\mathbf{k}, \sigma, \mu_1), (\mathbf{p} - \mathbf{k}, \sigma', \mu_2), (\mathbf{p} - \mathbf{k}', \sigma', \mu_3), (\mathbf{p} - \mathbf{k}', \sigma', \bar{\mu}_3), (\mathbf{k}, \sigma, \bar{\mu}_1), (\mathbf{p} - \mathbf{k}, \sigma', \bar{\mu}_2)\right\}\end{aligned}\quad (6.24)$$

Given the complex tensorial structure of the vertices, a simplified representation is needed by which families of RG flow equations can be characterized into different phases. Thus, we define the quantities

$$\begin{aligned}r_{\mathbf{p}}^{\sigma\sigma',(j)} &= \frac{\operatorname{sgn}(V_{\mathbf{k}\mathbf{k}'\mathbf{p}}^{\sigma\sigma',(j)}) \sqrt{\sum_{\mathbf{k}\mathbf{k}'} |V_{\mathbf{k}\mathbf{k}'\mathbf{p}}^{\sigma\sigma',(j)}|^2}}{\sqrt{\sum_{\mathbf{k} \neq \mathbf{k}'} |V_{\mathbf{k}\mathbf{k}'\mathbf{p}}^{\sigma\sigma',(j)}|^2 + \sum_{\mathbf{k}} |V_{\mathbf{k}\mathbf{p}}^{\sigma\sigma',(j)}|^2}}, \\ s^{\sigma\sigma'\sigma,(j)} &= \frac{\sqrt{\sum_{\mathbf{k}\mathbf{k}'\mathbf{k}''} |R_{\mathbf{k},\mathbf{k}'\mathbf{k}''}^{\sigma\sigma'\sigma,(j)}|^2}}{\sqrt{\sum_{\mathbf{k}\mathbf{k}'\mathbf{k}''} |R_{\mathbf{k}\mathbf{k}'\mathbf{k}''}^{\sigma\sigma'\sigma,(j)}|^2 + \sum_{\substack{\mathbf{k}\mathbf{k}_1\mathbf{k}_2 \\ \mathbf{k}_3\mathbf{k}_4}} |R_{\mathbf{k}\mathbf{k}_1\mathbf{k}_2\mathbf{k}_3\mathbf{k}_4}^{\sigma\sigma'\sigma,(j)}|^2}}.\end{aligned}\quad (6.25)$$

Importantly, we add that our analysis is confined to models with off-diagonal 4-point vertices that are either  $V_{\mathbf{k}\mathbf{k}'\mathbf{p}}^{\sigma\sigma'} < 0$  or  $V_{\mathbf{k}\mathbf{k}'\mathbf{p}}^{\sigma\sigma'} > 0$  for all  $\mathbf{k}, \mathbf{k}', \mathbf{p}$ . It is clear from this assumption that  $-1 < r_{\mathbf{p}}^{\sigma\sigma',(j)} < 1$ ,  $0 < s^{\sigma\sigma'\sigma,(j)} < 1$ . As shown in Tables 6.2.1 and 6.2.2, we can now tabulate the stable fixed point theories corresponding to various low-energy regimes by using the relevance, irrelevance and dominance criteria of various  $\Gamma^{2,(j)}$ ,  $\Gamma^{4,(j)}$  and  $\Gamma^{6,(j)}$  vertex RG flows. Further, the RG flows for regimes (I-III) in Table 6.2.1 and regimes (IV and V) in Table 6.2.2 are represented via tree diagrams in Figs.6.2.3-6.2.8. Below, we discuss various low energy fixed point theories arising from these RG flow equations.

### I. The Fermi Liquid

Fermi liquid theory [14] arises in the low-energy regime I in Table 6.2.1 due to vanishing of all the non-zero momentum  $\mathbf{k} - \mathbf{k}'$  scattering vertices  $V_{\mathbf{k},\mathbf{k}',\mathbf{p}}^{\sigma\sigma'}$ . We discuss the details of this RG flow here. The condition 1 in regime I provides the ranges for fluctuation scale  $\omega_{(j)}$  and number diagonal vertex  $V_{\mathbf{k},\mathbf{p}}^{\sigma\sigma',(j)}$  for which the Green's function  $G_{\gamma\gamma'}^{4,(j)}$  appearing in eq.(6.17) picks up a negative signature

$$G_{\gamma\gamma'}^{4,(j)} = \left( \omega_{(j)} - \frac{1}{2}(\epsilon_{\mathbf{k}_{\Lambda_j\hat{s}}}^{(j)} + \epsilon_{\mathbf{p}-\mathbf{k}_{\Lambda_j\hat{s}}}^{(j)}) - \frac{V_{\mathbf{k},\mathbf{p}}^{\sigma\sigma',(j)}}{4} \right)^{-1} < 0, \quad (6.26)$$

leading to the RG irrelevance for both the off-diagonal and diagonal vertices, i.e.,  $(\Delta V_{\mathbf{k},\mathbf{k}',\mathbf{p}}^{\sigma\sigma',(j)}, \Delta V_{\mathbf{k},\mathbf{p}}^{\sigma\sigma',(j)}) \rightarrow 0$ . Further, condition 2 in regime I ensures that in the limit of large system sizes ( $L \rightarrow \infty$ ), the off-diagonal vertices vanishes  $V_{\mathbf{k},\mathbf{k}',\mathbf{p}}^{\sigma\sigma',(j)} \rightarrow 0$ , whereas the diagonal vertices reach a intermediate value given by the fixed point condition (corresponding to a vanishing of the denominator in

	Cases	$r_{\mathbf{p}}^{\sigma\sigma',(j)}, s^{\sigma\sigma'\sigma,(j)}$
I	<ol style="list-style-type: none"> <li>1. <math>\frac{V_{\mathbf{k}_{\Lambda_j \hat{s}}, \mathbf{p}}^{\sigma\sigma',(j)}}{4} &gt; \omega_{(j)} - \frac{1}{2}(\epsilon_{\mathbf{k}_{\Lambda_j \hat{s}}}^{(j)} + \epsilon_{\mathbf{p}-\mathbf{k}_{\Lambda_j \hat{s}}}^{(j)}) &gt; 0</math></li> <li>2. <math>V_{\mathbf{k}_{\Lambda_j \hat{s}}, \mathbf{p}}^{\sigma\sigma',(j)} &gt; V_{\mathbf{k}_{\Lambda_j \hat{s}}, \mathbf{k}, \mathbf{p}}^{\sigma\sigma',(j)}</math></li> </ol>	<ol style="list-style-type: none"> <li>1. <math>r_{\mathbf{p}}^{\sigma\sigma',(j)} \rightarrow 0+</math> for all <math>\mathbf{p}</math></li> <li>2. <math>s^{\sigma\sigma'\sigma,(j)} \rightarrow 0+</math></li> </ol>
II	<ol style="list-style-type: none"> <li>1. <math>\omega_{(j)} - \frac{1}{2}(\epsilon_{\mathbf{k}_{\Lambda_j \hat{s}}}^{(j)} + \epsilon_{-\mathbf{k}_{\Lambda_j \hat{s}}}^{(j)}) &lt; 0</math></li> <li>2. <math>\epsilon_{\mathbf{k}_{\Lambda_j \hat{s}}}^{(j)} &gt; E_F</math></li> <li>3. <math>V_{\mathbf{k}, \mathbf{p}}^{\sigma, \sigma',(j)} &gt; 0</math></li> <li>4. <math>V_{\mathbf{k}_{\Lambda_j \hat{s}}, \mathbf{k}, \mathbf{p}}^{\sigma, -\sigma, (j)} &lt; 0</math></li> <li>5. <math>V_{\mathbf{k}_{\Lambda_j \hat{s}}, \mathbf{k}, \mathbf{p}}^{\sigma, \sigma, (j)} &gt; 0</math></li> <li>6. <math> V_{\mathbf{k}_{\Lambda_j \hat{s}}, \mathbf{p}}^{\sigma, -\sigma, (j)}  &lt;  V_{\mathbf{k}_{\Lambda_j \hat{s}}, \mathbf{k}, \mathbf{p}}^{\sigma, -\sigma, (j)} </math></li> </ol>	<ol style="list-style-type: none"> <li>1. <math>r_{\mathbf{p}=0}^{\sigma, -\sigma, (j)} \rightarrow -1</math></li> <li>2. <math>\left. \frac{V_{\mathbf{k}\mathbf{k}'\mathbf{p}'}^{\sigma, -\sigma}}{V_{\mathbf{k}\mathbf{k}'\mathbf{p}=0}^{\sigma, -\sigma}} \right _{L \rightarrow \infty} \rightarrow 0+</math> for <math>\epsilon_{\mathbf{p}'-\mathbf{k}} &gt; E_F</math></li> <li>3. <math>r_{\mathbf{p}'}^{\sigma, -\sigma, (j)} \rightarrow 0+</math> for <math>\epsilon_{\mathbf{p}'-\mathbf{k}} &lt; E_F</math></li> <li>4. <math>r_{\mathbf{p}}^{\sigma, \sigma, (j)} \rightarrow 0</math> for all <math>\mathbf{p}</math></li> <li>5. <math>\left. \frac{s^{\sigma\sigma'\sigma, (j)}}{r_{\mathbf{p}=0}^{\sigma, -\sigma, (j)}} \right _{L \rightarrow \infty} \rightarrow 0+</math></li> </ol>
III	<ol style="list-style-type: none"> <li>1. <math>\omega_{(j)} - \frac{1}{2}(\epsilon_{\mathbf{k}_{\Lambda_j \hat{s}}}^{(j)} + \epsilon_{-\mathbf{k}_{\Lambda_j \hat{s}}}^{(j)}) &lt; 0</math></li> <li>2. <math>\epsilon_{\mathbf{k}_{\Lambda_j \hat{s}}}^{(j)} &gt; E_F</math></li> <li>3. <math>V_{\mathbf{k}, \mathbf{p}}^{\sigma, \sigma',(j)} &gt; 0</math></li> <li>4. <math>V_{\mathbf{k}_{\Lambda_j \hat{s}}, \mathbf{k}, \mathbf{p}}^{\sigma, -\sigma, (j)} &lt; 0</math></li> <li>5. <math>V_{\mathbf{k}_{\Lambda_j \hat{s}}, \mathbf{k}, \mathbf{p}}^{\sigma, \sigma, (j)} &gt; 0</math></li> <li>6. <math> V_{\mathbf{k}_{\Lambda_j \hat{s}}, \mathbf{p}}^{\sigma, -\sigma, (j)}  &gt;  V_{\mathbf{k}_{\Lambda_j \hat{s}}, \mathbf{k}, \mathbf{p}}^{\sigma, -\sigma, (j)} </math></li> </ol>	<ol style="list-style-type: none"> <li>1. <math>r_{\mathbf{p}=0}^{\sigma, -\sigma, (j)} \rightarrow -r, r &lt; 1</math></li> <li>2. <math>\left. \frac{V_{\mathbf{k}\mathbf{k}'\mathbf{p}'}^{\sigma, -\sigma}}{V_{\mathbf{k}\mathbf{k}'\mathbf{p}=0}^{\sigma, -\sigma}} \right _{L \rightarrow \infty} \rightarrow 0+</math> for <math>\epsilon_{\mathbf{p}'-\mathbf{k}} &gt; E_F</math></li> <li>3. <math>r_{\mathbf{p}'}^{\sigma, -\sigma, (j)} \rightarrow 0+</math> for <math>\epsilon_{\mathbf{p}'-\mathbf{k}} &lt; E_F</math></li> <li>4. <math>r_{\mathbf{p}}^{\sigma, \sigma, (j)} \rightarrow 0</math> for all <math>\mathbf{p}</math></li> <li>5. <math>\left. \frac{s^{\sigma\sigma'\sigma, (j)}}{r_{\mathbf{p}=0}^{\sigma, -\sigma, (j)}} \right _{L \rightarrow \infty} \rightarrow 0+</math></li> </ol>

Table 6.2.1: Table representing various parameter space regimes (Column II) and the associated flow of quantities describing nature of fixed point theory (Column III). Regimes I, II, III leads to fixed point Hamiltonians  $H_{FL}^*$ ,  $H_{RBCS}^{*,XY}$ ,  $H_{RBCS}^{*,XXZ}$  respectively in the main text.

	Cases	$r_{\mathbf{p}}^{\sigma\sigma',(j)}, s^{\sigma\sigma'\sigma,(j)}$
IV	1. $\omega_{(j)} - \frac{1}{2}(\epsilon_{\mathbf{k}_{\Lambda_j\hat{s}}}^{(j)} + \epsilon_{-\mathbf{k}_{\Lambda_j\hat{s}}}^{(j)}) < 0$	1. $r_{\mathbf{p}}^{\sigma,-\sigma,(j)} \rightarrow -1$
	2. $\epsilon_{\mathbf{k}_{\Lambda_j\hat{s}}}^{(j)} > E_F$	2. $\left. \frac{V_{\mathbf{k}\mathbf{k}'\mathbf{p}'}^{\sigma,-\sigma}}{V_{\mathbf{k}\mathbf{k}'\mathbf{p}}^{\sigma,-\sigma}} \right _{L \rightarrow \infty} \rightarrow 0+$ for $\epsilon_{\mathbf{p}'-\mathbf{k}} > E_F$
	3. $V_{\mathbf{k},\mathbf{p}}^{\sigma,\sigma',(j)} > 0$	3. $r_{\mathbf{p}'}^{\sigma,-\sigma,(j)} \rightarrow 0+$ for $\epsilon_{\mathbf{p}'-\mathbf{k}} < E_F$
	4. $V_{\mathbf{k}_{\Lambda_j\hat{s}},\mathbf{k},\mathbf{p}}^{\sigma,-\sigma,(j)} < 0$	4. $r_{\mathbf{p}}^{\sigma,\sigma,(j)} \rightarrow 0$ for all $\mathbf{p}$
	5. $V_{\mathbf{k}_{\Lambda_j\hat{s}},\mathbf{k},\mathbf{p}}^{\sigma,\sigma,(j)} > 0$	5. $\left. \frac{s^{\sigma\sigma'\sigma,(j)}}{r_{\mathbf{p}}^{\sigma,-\sigma,(j)}} \right _{L \rightarrow \infty} \rightarrow 0+$
	6. $ V_{\mathbf{k}_{\Lambda_j\hat{s}},\mathbf{p}}^{\sigma,-\sigma,(j)}  <  V_{\mathbf{k}_{\Lambda_j\hat{s}},\mathbf{k},\mathbf{p}}^{\sigma,-\sigma,(j)} $	
V	1. $\omega_{(j)} - \frac{1}{2}(\epsilon_{\mathbf{k}_{\Lambda_j\hat{s}}}^{(j)} + \epsilon_{-\mathbf{k}_{\Lambda_j\hat{s}}}^{(j)}) < 0$	1. $r_{\mathbf{p}}^{\sigma,-\sigma,(j)} \rightarrow -r, r < 1$
	2. $\epsilon_{\mathbf{k}_{\Lambda_j\hat{s}}}^{(j)} > E_F$	2. $\left. \frac{V_{\mathbf{k}\mathbf{k}'\mathbf{p}'}^{\sigma,-\sigma}}{V_{\mathbf{k}\mathbf{k}'\mathbf{p}}^{\sigma,-\sigma}} \right _{L \rightarrow \infty} \rightarrow 0+$ for $\epsilon_{\mathbf{p}'-\mathbf{k}} > E_F$
	3. $V_{\mathbf{k},\mathbf{p}}^{\sigma,\sigma',(j)} > 0$	3. $r_{\mathbf{p}'}^{\sigma,-\sigma,(j)} \rightarrow 0+$ for $\epsilon_{\mathbf{p}'-\mathbf{k}} < E_F$
	4. $V_{\mathbf{k}_{\Lambda_j\hat{s}},\mathbf{k},\mathbf{p}}^{\sigma,-\sigma,(j)} < 0$	4. $r_{\mathbf{p}}^{\sigma,\sigma,(j)} \rightarrow 0$ for all $\mathbf{p}$
	5. $V_{\mathbf{k}_{\Lambda_j\hat{s}},\mathbf{k},\mathbf{p}}^{\sigma,\sigma,(j)} > 0$	5. $\left. \frac{s^{\sigma\sigma'\sigma,(j)}}{r_{\mathbf{p}}^{\sigma,-\sigma,(j)}} \right _{L \rightarrow \infty} \rightarrow 0+$
	6. $ V_{\mathbf{k}_{\Lambda_j\hat{s}},\mathbf{p}}^{\sigma,-\sigma,(j)}  >  V_{\mathbf{k}_{\Lambda_j\hat{s}},\mathbf{k},\mathbf{p}}^{\sigma,-\sigma,(j)} $	
VI	1. $\frac{1}{2}\epsilon_{\mathbf{k}_{\Lambda_j\hat{s}}}^{(j)} < \omega_{(j)} < \frac{1}{2}(\epsilon_{\mathbf{k}_{\Lambda_j\hat{s}}}^{(j)} + \epsilon_{-\mathbf{k}_{\Lambda_j\hat{s}}}^{(j)})$	1. $s^{\sigma,-\sigma,\sigma,(j)} \rightarrow 1$
	2. $\epsilon_{\mathbf{k}_{\Lambda_j\hat{s}}}^{(j)} > E_F$	2. $s^{\sigma,\sigma,\sigma,(j)} = 0$
	3. $V_{\mathbf{k}_{\Lambda_j\hat{s}},\mathbf{k},\mathbf{p}}^{\sigma,\sigma',(j)} > 0$	3. $r_{\mathbf{p}}^{\sigma\sigma',(j)} \rightarrow 0$

Table 6.2.2: Table representing various parameter space regimes (Column II) and the associated flow of quantities describing nature of fixed point theory (Column III). Regimes IV, V, VI leads to fixed point Hamiltonians  $H_{SPDW}^{*,XY}$ ,  $H_{SPDW}^{*,XXZ}$ ,  $H_{MFL}^*$  respectively in main text.

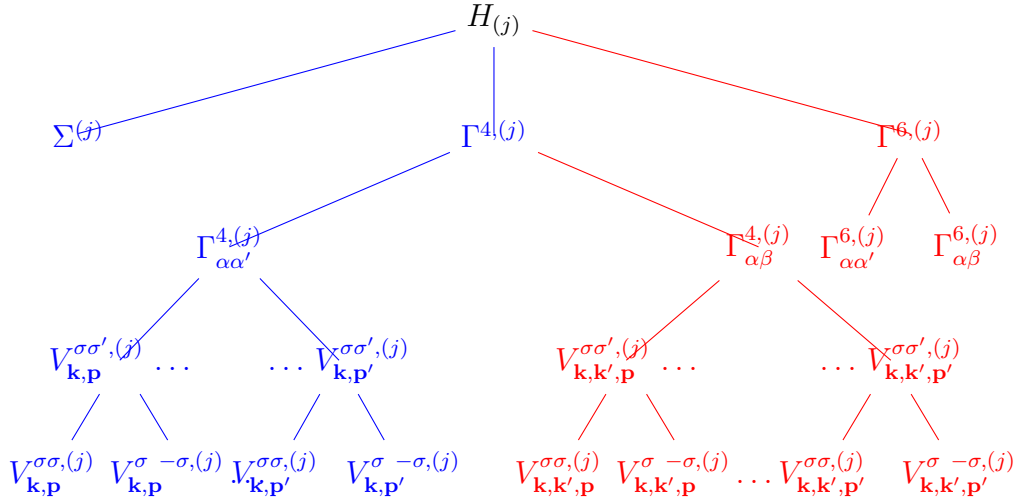


Figure 6.2.3: Tree tensor diagram representing the Fermi liquid (regime-I in Table 6.2.1). The off-diagonal 4-point vertices are RG irrelevant (i.e., flow towards zero) and are represented in red. Further, diagonal and off-diagonal 6-point vertices are irrelevant and are represented in red colour. The 1-particle self-energy and the 2-particle Hartree contribution is RG relevant, approaches fixed point values, and are reprented in blue.

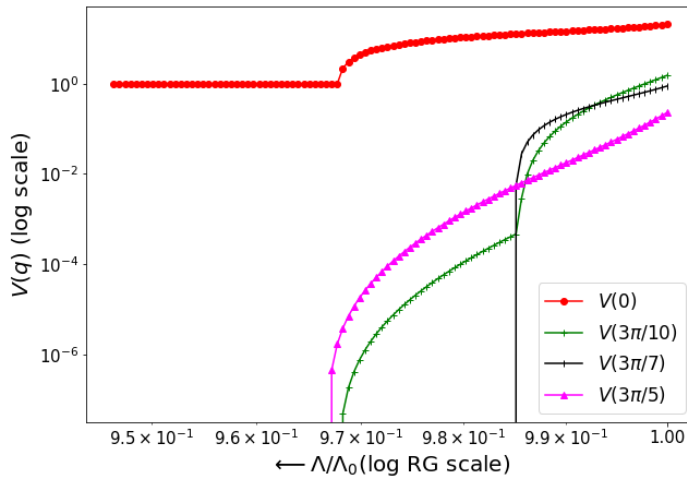


Figure 6.2.4: Log-log plot for renormalization of two-particle vertices  $V(q)$  with momentum transfer  $|\mathbf{q}| = 0, 3\pi/10, 3\pi/7$  and  $3\pi/5$ . The  $x$ -axis is the RG scale  $\Lambda/\Lambda_0$  and the  $y$ -axis is the magnitude of the scattering vertex  $V(q)$ . For the numerical evaluation, we have solved RG eq.(6.17) by taking a system volume of  $1024 \times 1024$  lattice sites,  $\omega = \epsilon_{\Lambda_0} + 0.1$  ( $\Lambda_0 = \pi/20$ ) and  $V(q) = \eta^2 V(0)/(q^2 + \eta^2)$  with  $\eta = 0.2$ ,  $V(0) = 20.5$ .

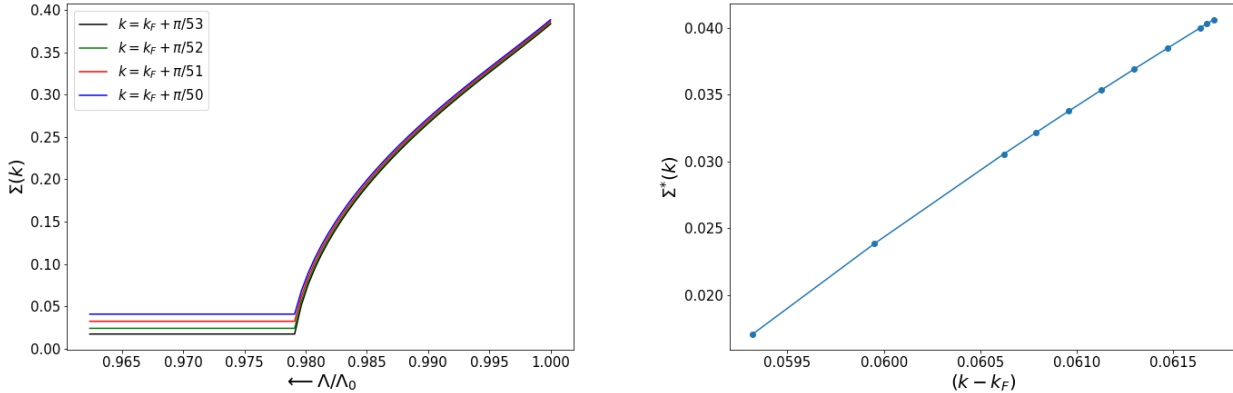


Figure 6.2.5: Left Panel: RG flow (eq.(6.12)) of the single-particle self-energy for four different wave-vectors  $\mathbf{k}$  close to  $\mathbf{k}_F$ . Right Panel: Variation of renormalized single-particle self-energy at the IR fixed point upon approaching the Fermi surface with lowering  $|\mathbf{k} - \mathbf{k}_F|$ .

eq.(6.17))

$$\omega_{(j^*)} - \frac{1}{2} \left( \epsilon_{\mathbf{k}_{\Lambda_{j^*}, \hat{s}}}^{(j^*)} + \epsilon_{\mathbf{p}-\mathbf{k}_{\Lambda_{j^*}, \hat{s}}}^{(j^*)} \right) = \frac{1}{4} V_{\mathbf{k}_{\Lambda_{j^*}, \hat{s}}, \mathbf{p}}^{\sigma\sigma', (j^*)}. \quad (6.27)$$

The tree diagram Fig. 6.2.3 represents the vertex tensor RG flow, where the blue branches and nodes represent vertices whose magnitudes flow towards a finite value at the stable fixed point. On the other hand, the magnitudes of the red branches flow towards zero. As  $V_{\mathbf{k}, \mathbf{k}', \mathbf{p}}^{\sigma\sigma'}$  is RG irrelevant, the 6-point vertices  $R^{\sigma\sigma'\sigma''}$  also do not contribute in the limit of  $L \rightarrow \infty$ . This results in the quantities  $r_{\mathbf{p}}^{\sigma\sigma', (j)} \rightarrow 0$  and  $s^{\sigma\sigma'\sigma, (j)} \rightarrow 0$ . Thus, the theory at the Fermi liquid fixed point is free of all 2-particle as well as higher order off-diagonal vertices, leading to Landau's Fermi liquid Hamiltonian [14]

$$H_{FL}^*(\omega) = \sum_{\Lambda < \Lambda_{j^*}, \hat{s}} \epsilon_{\mathbf{k}_{\Lambda, \hat{s}}} \hat{n}_{\mathbf{k}_{\Lambda, \hat{s}}} + \sum_{\Lambda < \Lambda_{j^*}, \hat{s}, \mathbf{p}} V_{\mathbf{k}_{\Lambda, \hat{s}}, \mathbf{p}}^{\sigma\sigma', (j^*)} (\omega_{(j^*)}) \hat{n}_{\mathbf{k}_{\Lambda, \hat{s}}} \hat{n}_{\mathbf{p} - \mathbf{k}_{\Lambda, \hat{s}}}^{\sigma'}. \quad (6.28)$$

For a quantitative demonstration of the Fermi liquid fixed point theory from our URG analysis, we numerically analyse below the URG equations for various 2- and 3-particle vertices, the 1-particle self-energy ( $\Sigma$ ) and the quasiparticle residue ( $Z$ ). For this, we consider a screened interaction potential  $V(|\mathbf{q}|) = \eta^2 V(0)/(q^2 + \eta^2)$ , with  $V(0) = 20.5$ ,  $\eta = 0.2$ , a two-dimensional circular Fermi surface with  $|k_F| = \pi/20$  and  $\omega = \epsilon_{\Lambda_0} + 0.1$  (Regime-I of Table 6.2.1) and a system volume represented by a  $k$ -space grid of 1024 lattice sites  $\times$  1024 lattice sites. In Fig. 6.2.4, the 2-particle scattering vertices  $V(|\mathbf{q}|)$  with non-zero ( $\mathbf{q} \neq 0$ ) momentum transfer (red, green and orange curves) are found to be irrelevant under RG flow. On the other hand, the  $|\mathbf{q}| = 0$  vertices  $V(0)$  (red curve, corresponding to the couplings associated with terms like  $\hat{n}_{\mathbf{k}\sigma} \hat{n}_{\mathbf{k}'\sigma'}$ ) attain a finite value at the IR fixed point. In this way, we numerically confirm the RG flow towards the effective Fermi liquid Hamiltonian  $H_{FL}^*(\omega)$  given in eq.(6.28). In Fig. 6.2.5 (left panel), we see that the 1-particle self-energy  $\Sigma_k^{(j)}$  renormalizes to a finite value  $\Sigma_k^*$  at the RG fixed point, and that the  $|k\rangle$  states closer to the Fermi surface ( $k_F$ ) have a lower  $\Sigma_k^*$  (Fig.6.2.5 (right panel)). Fig.6.2.6

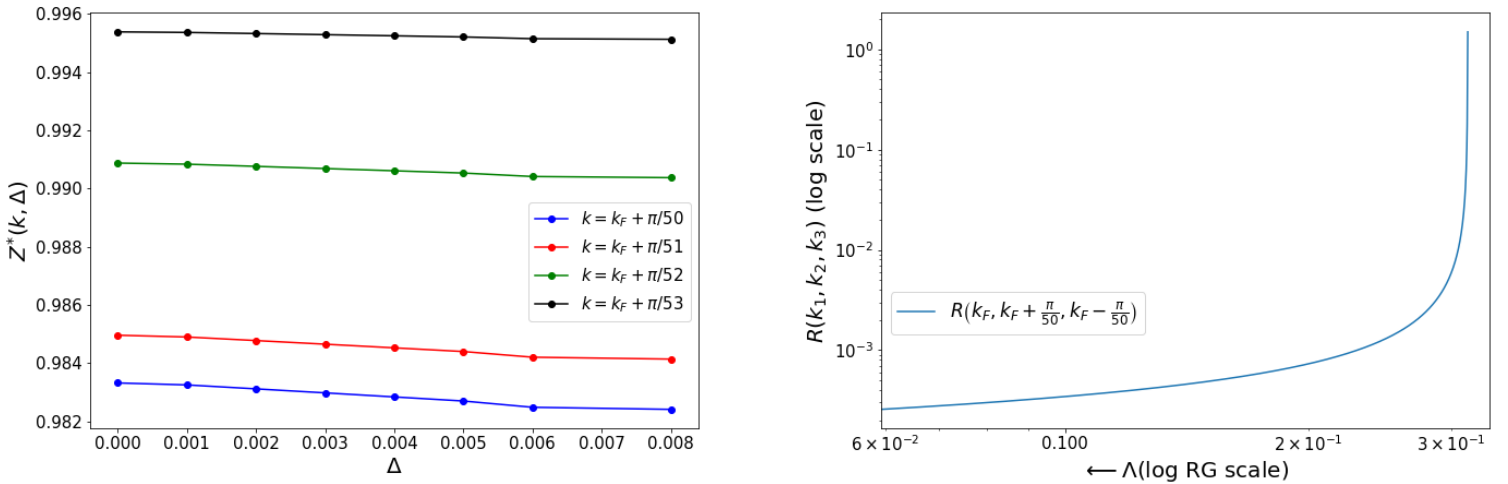


Figure 6.2.6: Left Panel: Variation of the quasiparticle residue for electronic states  $\mathbf{k}$  with lowering excitation energy scale  $\Delta$  about  $E_F$ . Right Panel: RG flow (eq.(6.18)) of the number diagonal three-particle vertex with wave-vectors  $k_F$ ,  $k_F + \frac{\pi}{50}$ ,  $k_F - \frac{\pi}{50}$ .

(left panel) shows that the quasiparticle residue  $Z(k, \Delta) \rightarrow 1$  upon approaching the Fermi energy  $\Delta \rightarrow 0$ , demonstrating the existence of well-defined Landau quasiparticles in the neighbourhood of the Fermi surface. Fig. 6.2.6 (right panel) shows the RG irrelevance of 2-electron 1-hole scattering vertices (which constitute the primary decay channel for the Landau quasiparticles). Taken together, these results verify numerically the phenomenology of the Landau Fermi liquid theory (eq.(6.28)) as derived from the URG analysis of the  $H_{SFIM}$  model (eq.(6.10)).

In a companion manuscript [182], we derive the form of the renormalized Friedel's scattering phase shift starting from the exponential representation of the unitary operator  $\Delta N = Tr(\log(U_{(j)})) = i\frac{\pi}{4}Tr(\eta_{(j)} - \eta_{(j)}^\dagger)$ . Further, we note that this is similar to Langer and Ambegaokar's definition of scattering phase shift [448]. As all off-diagonal terms are RG irrelevant in the Fermi liquid,  $\eta^\dagger$  and  $\eta$  both vanish at the RG fixed point. As a consequence, the Friedel's phase shift for the Fermi liquid is given by  $\Delta N = 0$ , i.e., upon placing a test charge near the Fermi surface, no electrons are permanently displaced from within it and the Luttinger volume is preserved [88, 278]. The incompressibility displays the topological protection for the Fermi surface ( $FS$ ) associated with the Volovik invariant [421], as shown in Ref.[182]. Further, we obtain a vanishing thermal scale in eq.(2.29),  $T = 0K$ , corresponding to  $\omega_{(j^*)} = 0$  and  $\Lambda_{(j^*)} = 0$  for the Fermi liquid.

## II. Reduced BCS theory-XY interaction

The reduced BCS theory [15] constitutes attractive interactions between opposite-spin pairs of electrons with zero net-momentum  $\mathbf{p} = 0$ . This theory is an outcome of (i) RG irrelevance for the 2-particle number-diagonal vertices, (ii) dominant RG flow for zero-momentum  $\mathbf{p} = 0$  electronic pairs and (iii) the sub-dominance (or RG irrelevance) of the  $\mathbf{p} \neq 0$  pair-scattering vertices. The above features of the RG flows is an outcome of the conditions listed as 1-6 in

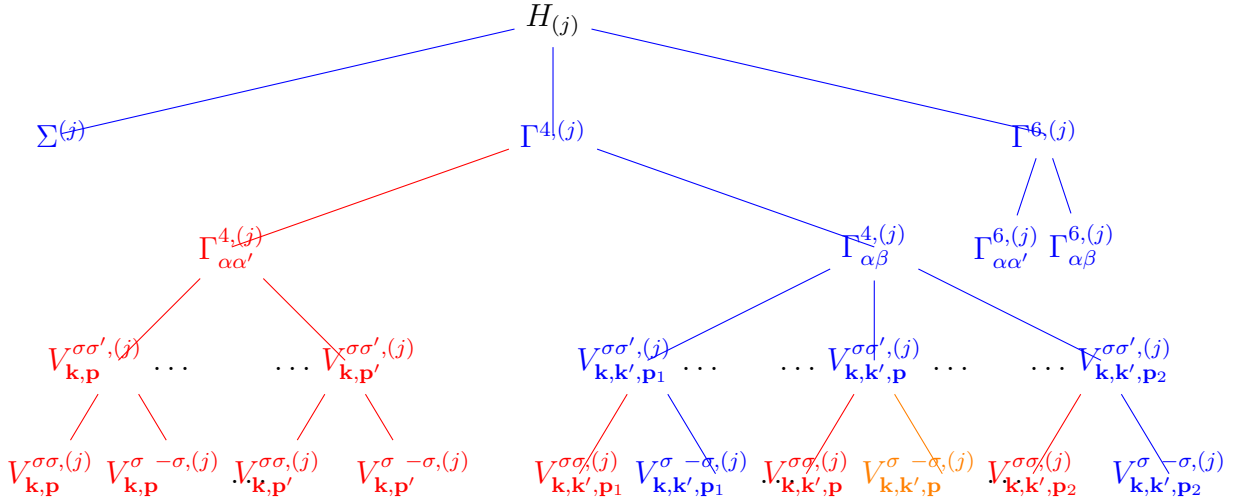


Figure 6.2.7: Tree tensor diagram representing the zero-momentum ( $\mathbf{p} = 0$ ) pairing reduced BCS model (regime-II in Table 6.2.1), and the SPDW state composed of finite-momentum ( $\mathbf{p}$ ) pseudospin-pairs interacting via XY interaction (regime-IV in Table 6.2.1). The blue branches and the nodes of the vertex tensors represent the relevant scattering vertices, while orange branches and nodes represent the dominant RG relevant scattering vertices. The red branches and nodes represent RG irrelevant scattering vertices.

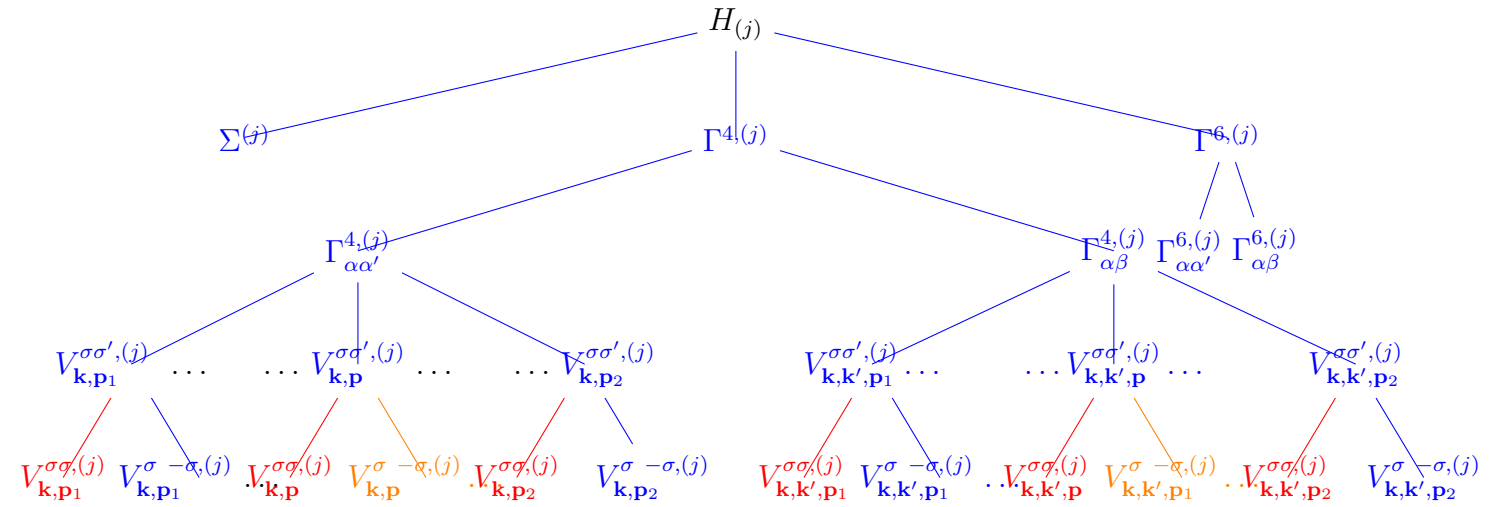


Figure 6.2.8: Tree tensor diagram representing the zero-momentum ( $\mathbf{p} = 0$ ) pairing reduced BCS model (regime-III in Table 6.2.1) and the SPDW state made of finite-momentum ( $\mathbf{p}$ ) pseudospin-pairs interacting via XXZ interaction (regime-V in Table 6.2.1). The blue branches and the nodes of the vertex tensors represent the relevant scattering vertices, while orange branches and nodes represent the dominant RG relevant scattering vertices. The red branches and nodes represent RG irrelevant scattering vertices.

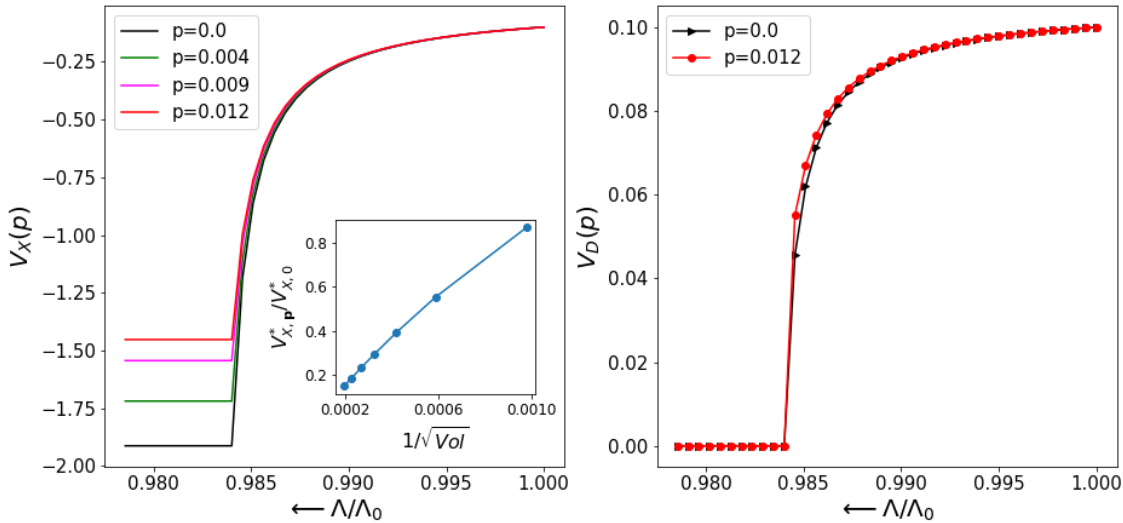


Figure 6.2.9: Left/right panel represents the RG flow of two-particle number off-diagonal/diagonal (eqs.(6.17)) scattering vertices for  $p = 0$  ( $V_{X,p=0}^{(j)}$ ) and  $p \neq 0$  finite-momentum pairs ( $(V_{X,p'}^{(j)})$ ). Numerical evaluations are for system size =  $1024 \times 1024$  and bare  $V_{D,p} = -0.1$ ,  $V_{X,p} = -0.25$  (in units of  $t$ ),  $\omega = \epsilon_{\Lambda_0} - 0.5$ . Left panel inset: Finite size scaling plot of the ratio  $V_{X,p=0.004}^*/V_{X,p=0}^*$  with  $1/\sqrt{Vol}$ .

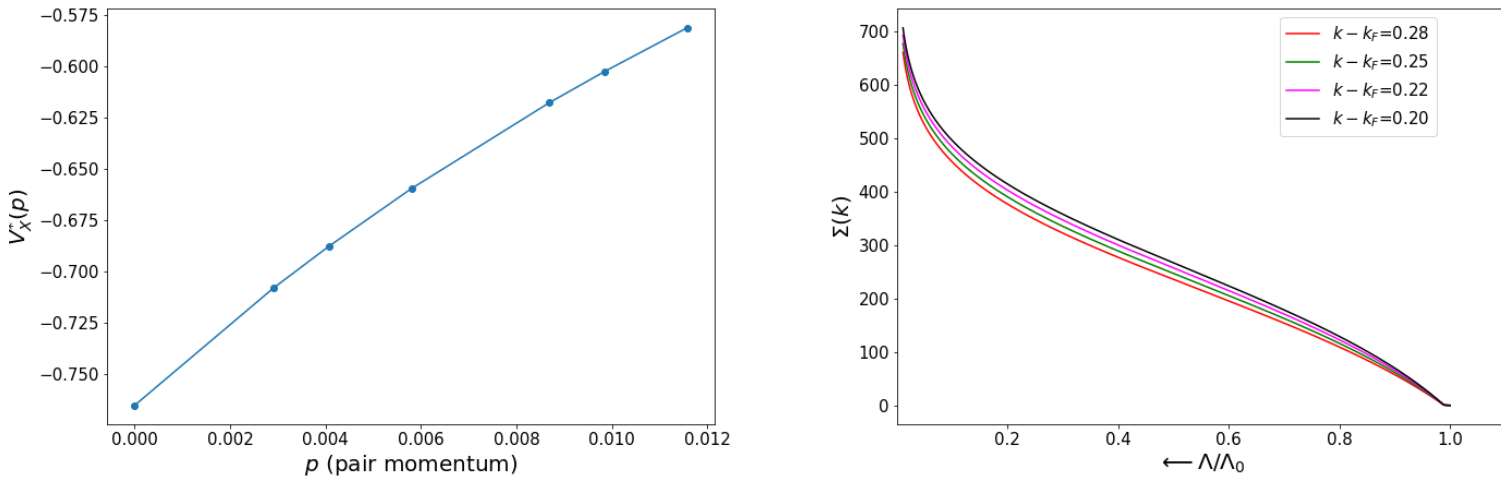


Figure 6.2.10: Left panel shows the variation of electronic pair-scattering vertex magnitude attained at RG fixed point  $V_X^*(p)$  as a function of pair-momentum  $p$ . Right panel shows the RG flow (eq.(6.32)) of the single-particle self-energy for four different  $|k\rangle$  states close to Fermi momentum  $k_F$ .

regime II of Table 6.2.1. Conditions 1-3 imply that the Green's function

$$G_{\gamma\gamma'}^{4,(j)} \equiv G_{\mathbf{k}_{\Lambda_j\hat{s}},\mathbf{p}}^{4,(j)} = \left( \omega_{(j)} - \frac{1}{2}(\epsilon_{\mathbf{k}_{\Lambda_j\hat{s}}} + \epsilon_{\mathbf{p}-\mathbf{k}_{\Lambda_j\hat{s}}}) \right)^{-1}, \quad (6.29)$$

has a negative signature:  $G_{\mathbf{k}_{\Lambda_j\hat{s}},\mathbf{p}}^{4,(j)} = -|G_{\mathbf{k}_{\Lambda_j\hat{s}},\mathbf{p}}^{4,(j)}|$ . As  $G_{\mathbf{k}_{\Lambda_j\hat{s}},\mathbf{p}}^{4,(j)}$  appears in the RG flow eq.(6.20) (for  $\mathbf{p} = 0$ ), scattering between opposite-spin pairs due to attractive couplings ( $V_{\mathbf{k},\mathbf{k}',\mathbf{p}}^{\sigma,-\sigma,(j)}$ ) become RG relevant, while repulsive Hartree interactions ( $V_{\mathbf{k},\mathbf{p}}^{\sigma,\sigma',(j)}$ ) are RG irrelevant. Further, condition 4 ensures that all scattering vertices with identical spin ( $V_{\mathbf{k},\mathbf{k}',\mathbf{p}}^{\sigma,\sigma,(j)}$ ) are RG irrelevant. Given the range of the fluctuation scale  $\omega_{(j)}$  in condition 1, and for  $\epsilon_{\mathbf{p}'-\mathbf{k}}^{(j)} > E_F$ , the 2-particle Green's function for  $\mathbf{p} > 0$  momentum pairs  $G_{\gamma\gamma'}^{4,(j)} = G_{\mathbf{k}_{\Lambda_j\hat{s}},\mathbf{p}}^{4,(j)}$  is smaller in magnitude compared to the zero-momentum pair ( $\mathbf{p} = 0$ )

$$|G_{\mathbf{k}_{\Lambda_j\hat{s}},\mathbf{p}}^{4,(j)}| < |G_{\mathbf{k}_{\Lambda_j\hat{s}},\mathbf{p}=0}^{4,(j)}|. \quad (6.30)$$

This Green's function appears in the RG flow equation eq.(6.20) for the vertices  $V_{\mathbf{k},\mathbf{k}',\mathbf{p}}^{\sigma,-\sigma,(j)}$ , rendering it sub-dominant compared to the vertex  $V_{\mathbf{k},\mathbf{k}',\mathbf{p}=0}^{\sigma,-\sigma,(j)}$ . As a result,  $r_{\mathbf{p}}^{\sigma,-\sigma,(j)}/r_{\mathbf{p}=0}^{\sigma,-\sigma,(j)} \rightarrow 0$ , as shown in regime-II Table 6.2.1. Condition 6 ensures that the number-diagonal interaction  $V_{\mathbf{k},\mathbf{p}}^{\sigma,-\sigma,(j)} \rightarrow 0$ . Finally, as the RG flow leads to dominance of only a given pair-momentum vertices compared to all others, the renormalization of the 6-point vertices  $\Gamma^{6,(j)}$  that arise out of the interplay between different pair-momentum vertices in eq.(6.17) is sub-dominant compared to the  $\mathbf{p} = 0$  vertices. Thus, they are represented by the ratio  $s^{\sigma\sigma'\sigma,(j)}/r_{\mathbf{p}=0}^{\sigma,-\sigma,(j)}|_{L \rightarrow \infty} \rightarrow 0+$  in regime II. All of these features finally lead to the fixed point condition

$$\omega_{(j*)} = \frac{1}{2}(\epsilon_{\mathbf{k}_{\Lambda_{j*}\hat{s}}}^{(j*)} + \epsilon_{-\mathbf{k}_{\Lambda_{j*}\hat{s}}}^{(j*)}) = \epsilon_{\mathbf{k}_{\Lambda_{j*}\hat{s}}}^{(j*)}, \quad (6.31)$$

where we have used the band symmetry  $\epsilon_{\mathbf{k}} = \epsilon_{-\mathbf{k}}$ .

Further, at this RG fixed point, the 1-particle self-energy  $\Sigma_{\mathbf{k}}^{(j)} = \epsilon_{\mathbf{k}}^{(j)} - \epsilon_{\mathbf{k}}$  diverges. This can be seen as follows. The RG flow equation for  $\Sigma_{\mathbf{k}}^{(j)}$  (eq.(6.12)) now has a dominant contribution from the zero pair-momentum scattering vertices

$$\Delta\Sigma_{\mathbf{k}}^{(j)} = \left( V_{\mathbf{k}_{\Lambda_j\hat{s}},\mathbf{k},\mathbf{p}=0}^{\sigma,-\sigma,(j)} \right)^2 (\omega_{(j)} - \epsilon_{\mathbf{k}_{\Lambda_j\hat{s}}}^{(j)} + \frac{1}{2}\epsilon_{\mathbf{k}} + \frac{1}{2}\Sigma_{\mathbf{k}}^{(j)})^{-1}. \quad (6.32)$$

From this relation, we see that the self-energy is RG relevant. For the electronic states labelled  $\mathbf{k}$  (i.e., residing within the emergent window), the self-energy RG flow equation has a fixed point at  $\Sigma_{\mathbf{k}}^{(j*)} \rightarrow \infty$  as  $\omega_{(j*)} = \frac{1}{2}\epsilon_{\mathbf{k}_{\Lambda_{j*}\hat{s}}}^{(j*)}$ , indicating the breakdown of the Landau quasiparticles of the Fermi liquid. As discussed in an earlier section, the diverging self-energy corresponds to zeros in the single-particle Green's function

$$G(\mathbf{k}, \omega) = \frac{1}{\omega - \epsilon_{\mathbf{k}} - \Sigma_{\mathbf{k}}} \rightarrow 0. \quad (6.33)$$

This indicates the breakdown of the Luttinger volume sum-rule, i.e.,  $N_e \neq \sum_{\mathbf{k}\sigma} G(\mathbf{k}, \omega)$ . Instead, we find that the total number of Cooper pairs  $N_{CP}$  within the low-energy window equals the

net Friedel's phase shift,  $\Delta N = \text{Tr}(\log(U_{(j)})) = N_{CP} \in 2\mathbb{Z}$ , i.e., two electronic states are lost for each bound pair. This provides a way for taking accounts for the Luttinger surface of zeros [442]: the Friedel phase shift compensates precisely the mismatch observed via the accumulation of topological phases arising from the non-commutativity of the twist and translation operators [40, 516] (as shown in a companion work [182]).

The effective Hamiltonian,  $H_{RBCS}^{*,XY}(\omega)$ , at the stable fixed point of the flow has the form

$$H_{RBCS}^{*,XY}(\omega) = \sum_{\mathbf{k}} \epsilon_{\mathbf{k}_{\Lambda\hat{s}}}^{(j^*)} A_{\mathbf{k}_{\Lambda\hat{s}}}^z - \sum_{\mathbf{k}_{\Lambda\hat{s}}} V_{\mathbf{k}_{\Lambda\hat{s}}, \mathbf{k}_{\Lambda'\hat{s}'}, 0}^{\sigma, -\sigma, (j^*)} A_{\mathbf{k}_{\Lambda\hat{s}}}^+ A_{\mathbf{k}_{\Lambda'\hat{s}'}}^- , \quad (6.34)$$

where the set  $\alpha' = \{(\mathbf{k}_{\Lambda'\hat{s}'}, \sigma); (-\mathbf{k}_{\Lambda'\hat{s}'}, -\sigma)\}$ . This is the generalized reduced BCS Hamiltonian/pairing-force model [15, 445], where the pseudospin  $\mathbf{A}_{\mathbf{k}_{\Lambda\hat{s}}}$  components are defined as [413]

$$A_{\mathbf{k}_{\Lambda\hat{s}}}^z = \frac{1}{2}(\hat{n}_{\mathbf{k}_{\Lambda\hat{s}}\sigma} + \hat{n}_{-\mathbf{k}_{\Lambda\hat{s}}-\sigma} - 1), A_{\mathbf{k}_{\Lambda\hat{s}}}^+ = c_{\mathbf{k}\sigma}^\dagger c_{-\mathbf{k}-\sigma}^\dagger, A_{\mathbf{k}_{\Lambda\hat{s}}}^- = c_{-\mathbf{k}-\sigma} c_{\mathbf{k}\sigma} . \quad (6.35)$$

In order to verify quantitatively the effective theory given in eq.6.34, we numerically simulated the RG equations for the bare couplings  $V_{X,p} = -0.25$ ,  $V_{D,p} = 0.1$  and the fluctuation energy scale  $\omega = \epsilon_{\Lambda_0} - 0.5$  (Regime-II in Table 6.2.1) and an identical  $k$ -space grid as mentioned earlier. Fig.6.2.9 (left panel) represents the RG flow for the two-particle off-diagonal scattering vertices involving electronic pairs with net-momentum  $p = 0, 0.004, 0.009$  and  $0.012$  respectively. The inset in the left panel of Fig.6.2.9 shows that the ratio  $V_{X,p'}/V_{X,p=0}^*$  diminishes with increasing system volume (which we have taken to range from  $1024 \times 1024$  lattice to a  $5000 \times 5000$  lattice), indicating the dominance of  $p = 0$  momentum scattering vertices at low-energies and describing the condensation of Cooper pair degrees of freedom. Fig.6.2.9 (right panel) shows that all the number-diagonal scattering vertices are RG irrelevant, and vanish along the RG flow. As seen in Fig.6.2.10 (left panel), we find that the  $p = 0$  momentum electronic pair scattering vertices have the highest magnitude  $|V_{X,p=0}^*| > |V_{X,p'}^*|$  ( $V_{X,0}^* = V_{k,k',0}^{\sigma,-\sigma}$ ,  $V_{X,p'}^* = V_{k,k',p'}^{\sigma,-\sigma}$ ) at low-energies, and the magnitude of  $V_{X,p'}^*$  monotonically decreases with increasing pair-momentum ( $p$ ). The relevance of off-diagonal  $p = 0$  momentum scattering vertices, together with the RG irrelevance of number-diagonal scattering vertices, describes the effective Hamiltonian  $H_{RBCS}^{*,XY}$  (eq.(6.34)) at the RG fixed point. Finally, Fig.6.2.10 (right panel) shows a divergent renormalized self-energy  $\Sigma_k$  (eq.(6.32)) for the  $|k\rangle$  states, where  $|k - k_F| < \Lambda^*$  and  $\Lambda^*$  is width of the momentum-space shell around the erstwhile Fermi surface.

The condensation of the pseudospins (i.e., Cooper pairs [440] with the electronic spins locked into singlets) in this subspace is described by the fixation of the pseudospin angular momentum value to  $\frac{3}{4}$

$$\mathbf{A}_{\mathbf{k}_{\Lambda\hat{s}}}^2 = \frac{3}{4}(\hat{n}_{\mathbf{k}_{\Lambda\hat{s}}\sigma} + \hat{n}_{-\mathbf{k}_{\Lambda\hat{s}}-\sigma} - 1)^2 = \frac{3}{4}, \quad \Lambda < \Lambda_{j^*} . \quad (6.36)$$

Thus, the emergence of the constraint  $\hat{n}_{\mathbf{k}_{\Lambda\hat{s}}\sigma} = \hat{n}_{-\mathbf{k}_{\Lambda\hat{s}}-\sigma}$  describes the phenomenon of condensation of Cooper pairs within the low-energy window of the BCS fixed point theory. For the case of a spherical Fermi surface, i.e.,  $\epsilon_{\Lambda\hat{s}} = \epsilon_\Lambda$ , the phase described by the BCS reduced model (eq.(6.34)) will persist upto the thermal scale (from eq(2.29))

$$T^* = \frac{1}{\pi k_B} \left[ 2\epsilon_{\Lambda_{j^*}}^0 + (\epsilon_{\Lambda_{j^*}}^0 - \omega) \log \left| \frac{\omega - \epsilon_{\Lambda_{j^*}}^0}{\omega + \epsilon_{\Lambda_{j^*}}^0} \right| \right] . \quad (6.37)$$

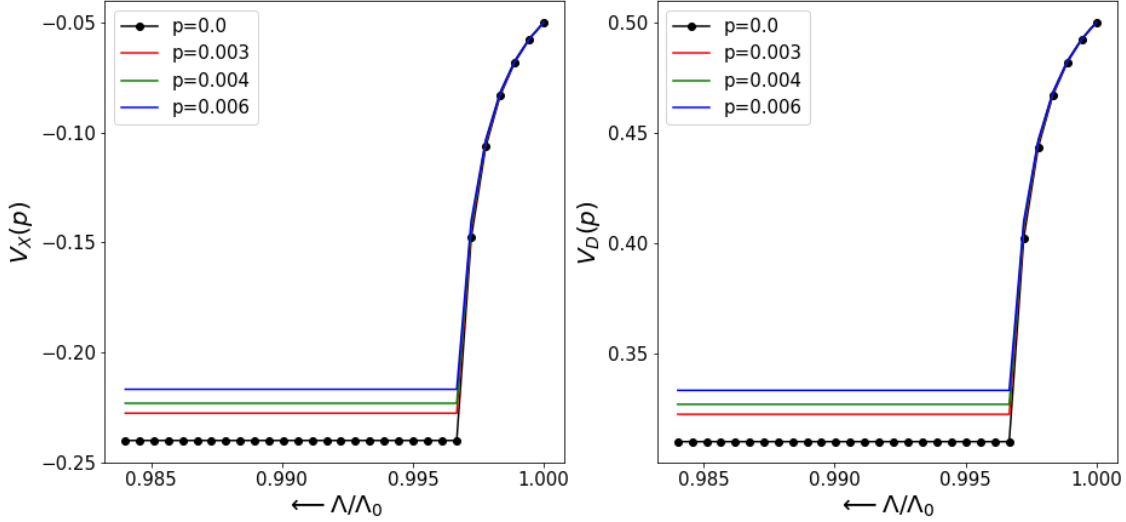


Figure 6.2.11: Left/right panel represents the RG flow (eqs.(6.17)) of two-particle number off-diagonal/diagonal scattering vertices for  $p = 0$  ( $V_{X,p=0}^{(j)}$ ) and  $p \neq 0$  finite-momentum pairs ( $(V_{X,p'}^{(j)})$ ). Numerical evaluations are for system volume  $1024 \times 1024$  and with bare  $V_{D,p} = 0.5$ ,  $V_{X,p} = -0.05$  (in units of  $t$ ),  $\omega = \epsilon_{\Lambda_0} - 0.5$ .

The above equation is obtained from the self-energy of the electronic state at the momentum-space boundary of the emergent phase in eq.(2.29):  $\Sigma_{\Lambda_j^*}^{(j^*)} = \omega - \epsilon_{\Lambda_j^*}^0$ , where  $\epsilon_{\Lambda_j^*}^0$  is the bare dispersion magnitude. The temperature scale  $T^*$  is greater than the critical temperature  $T_c$  obtained from the BCS mean-field solution [15], and indicates the presence of pairing in the ground state of the reduced BCS Hamiltonian but without the off-diagonal long-ranged order (ODLRO) that characterises the phase-stiff BCS ground state. We will present further insights on the ground state properties of this quantum liquid in Sec.6.93. Finally, the tree decomposition of the vertices representing this phase is shown in Fig. 6.2.7.

### III. Reduced BCS theory-XXZ interaction

For the case when  $V_{\mathbf{k},\mathbf{p}}^{\sigma\sigma'} > V_{\mathbf{k},\mathbf{k}',\mathbf{p}}^{\sigma\sigma'}$  (regime-IV in Table 6.2.2), the diagonal vertices do not vanish under RG. Here, the fixed point condition becomes

$$\frac{1}{2} \left( \epsilon_{\mathbf{k}_{\Lambda^* s}}^{(j^*)} + \epsilon_{-\mathbf{k}_{\Lambda^* s}}^{(j^*)} \right) - \omega = \frac{1}{4} V_{\mathbf{k}_{\Lambda^* s},0}^{\sigma,-\sigma,(j^*)}. \quad (6.38)$$

As an outcome, the fixed point is described by a modified XXZ pseudospin Hamiltonian

$$H_{RBCS}^{*,XXZ}(\omega) = \sum_{\mathbf{k}} \epsilon_{\mathbf{k}_{\Lambda s}}^{(j^*)} A_{\mathbf{k}_{\Lambda s}}^z - \sum_{\Lambda, \Lambda' < \Lambda^*} V_{\mathbf{k}_{\Lambda s}, \mathbf{k}_{\Lambda' s}, 0}^{\sigma, -\sigma, (j^*)} A_{\mathbf{k}_{\Lambda s}}^+ A_{\mathbf{k}_{\Lambda' s}}^- + \sum_{\mathbf{k}_{\Lambda s}, \mathbf{p}} V_{\mathbf{k}_{\Lambda s}, \mathbf{p}}^{\sigma, -\sigma, (j^*)} A_{\mathbf{k}_{\Lambda s}}^z A_{\mathbf{p} - \mathbf{k}_{\Lambda s}}^z \quad (6.39)$$

where  $V_{\mathbf{k}_{\Lambda s}, \mathbf{p}}^{\sigma, -\sigma, (j^*)}$  is the value of the Ising coupling at the fixed point. The RG flow features for this phase is represented via the tree diagram Fig.6.2.8. In this phase, finite magnitudes for both

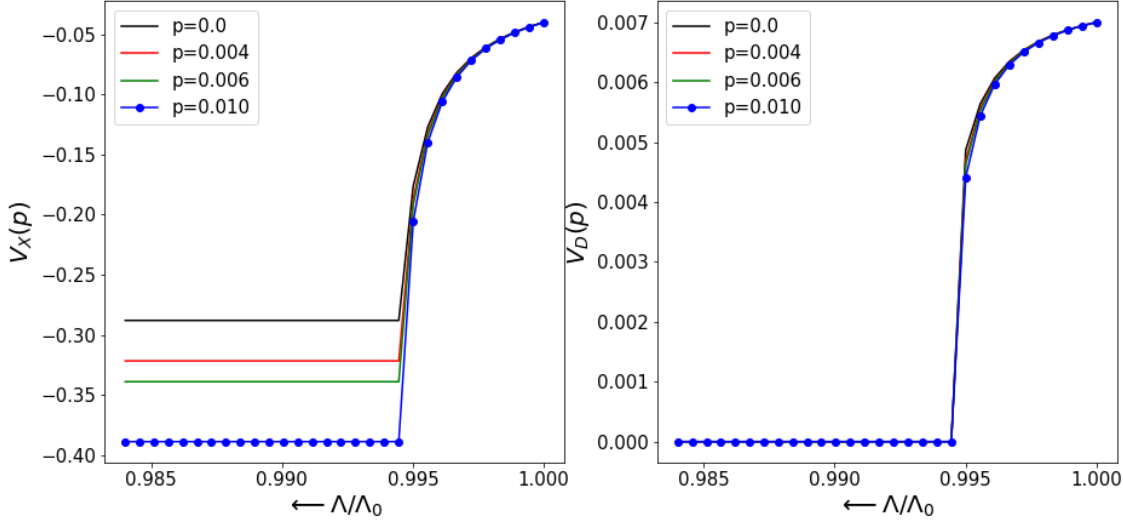


Figure 6.2.12: Left/right panel represents the RG flow (eqs.(6.17)) of two-particle number off-diagonal/diagonal scattering vertices respectively for  $p = 0$  ( $V_{X,p=0}^{(j)}$ ) and  $p \neq 0$  finite-momentum pairs ( $(V_{X,p'}^{(j)})$ ). Numerical evaluations are for system volume  $1024 \times 1024$  and with bare  $V_{D,\mathbf{p}} = 0.007$ ,  $V_{X,\mathbf{p}} = -0.05$  (in units of  $t$ ),  $\omega = \frac{1}{2}(\epsilon_{k_{\Lambda_0}} + \epsilon_{0.01-\mathbf{k}_{\Lambda_0}}) - 0.5$ .

the number-diagonal as well as off-diagonal interactions lead to the quantities  $r_{\mathbf{p}=0}^{\sigma,-\sigma,(j*)} = -r$  (where  $r < 1$ ). The left and right panels of Fig.6.2.11 represent the RG flows for the 2 particle off-diagonal and diagonal scattering vertices respectively, involving electronic pairs with net-momentum  $p = 0.0, 0.003, 0.004$  and  $0.006$ . The bare couplings  $V_{X,p} = -0.05$ ,  $V_{D,p} = 0.5$  ( $|V_{X,p}| < |V_{D,p}|$ ) and fluctuation scale  $\omega = \epsilon_{\Lambda_0} - 0.5$  (Regime-III in Table 6.2.1), and a system volume as mentioned earlier. As the low-energy fixed point in this regime is dominated by  $p = 0$  momentum electronic pair scattering vertices:  $|V_{X,p=0}^*| > |V_{X,p'}^*|$ ,  $|V_{D,p=0}^*| > |V_{D,p'}^*|$ , the resulting theory is described by the presence of both Ising and XY interactions between pseudospins (eq.(6.39)).

#### IV. Reduced BCS theory for finite momentum pairs-XY regime

In regime IV of Table 6.2.2, for the fluctuation energy scale lying in the range

$$\frac{1}{2}(\epsilon_{\mathbf{k}_{\Lambda_j\hat{s}}}^{(j)} + \epsilon_{\mathbf{p}-\mathbf{k}_{\Lambda_j\hat{s}}}^{(j)}) > \omega > \frac{1}{2}(\epsilon_{\mathbf{k}_{\Lambda_j\hat{s}}}^{(j)} + \epsilon_{-\mathbf{k}_{\Lambda_j\hat{s}}}^{(j)}) , \quad (6.40)$$

finite  $\mathbf{p}$  pair-momentum pseudospins attain a reduced BCS theory like fixed-point Hamiltonian. The fixed point is given by the condition

$$\frac{1}{2} \left( \epsilon_{\mathbf{k}_{\Lambda^*\hat{s}}}^{(j*)} + \epsilon_{\mathbf{p}-\mathbf{k}_{\Lambda^*\hat{s}}}^{(j*)} \right) - \omega = 0 , \quad (6.41)$$

and with an effective fixed point Hamiltonian described by

$$H_{SPDW}^{*,XY}(\omega) = \sum_{\mathbf{k}} \epsilon_{\mathbf{k}_{\Lambda\hat{s}},\mathbf{p}}^{(j^*)} A_{\mathbf{k}_{\Lambda\hat{s}},\mathbf{p}}^z - \sum_{\mathbf{k}_{\Lambda\hat{s}},\Lambda < \Lambda^*} V_{\mathbf{k}_{\Lambda\hat{s}},\mathbf{k}_{\Lambda'\hat{s}'},\mathbf{p}}^{\sigma,-\sigma} A_{\mathbf{k}_{\Lambda\hat{s}},\mathbf{p}}^+ A_{\mathbf{k}_{\Lambda'\hat{s}'},\mathbf{p}}^-, \quad (6.42)$$

where the set  $\nu = \{(\mathbf{k}_{\Lambda\hat{s}}, \sigma); (\mathbf{p} - \mathbf{k}_{\Lambda\hat{s}}, -\sigma)\}$  corresponds to a pair of electronic states with net momentum  $\mathbf{p}$ . The ground state of  $H_{SPDW}^{*,XY}$  is composed of symmetry-unbroken pair-density waves (SPDWs) [517, 518]. The pseudospin vector components for such finite-momentum pair of electrons are defined as

$$A_{\mathbf{k}_{\Lambda\hat{s}},\mathbf{p}}^+ = c_{\mathbf{k}_{\Lambda\hat{s}}\sigma}^\dagger c_{\mathbf{p}-\mathbf{k}_{\Lambda\hat{s}}-\sigma}^\dagger, A_{\mathbf{k}_{\Lambda\hat{s}},\mathbf{p}}^- = A_{\mathbf{k}_{\Lambda\hat{s}},\mathbf{p}}^{+\dagger}, A_{\mathbf{k}_{\Lambda\hat{s}},\mathbf{p}}^z = \frac{1}{2}[A_{\mathbf{k}_{\Lambda\hat{s}},\mathbf{p}}^+, A_{\mathbf{k}_{\Lambda\hat{s}},\mathbf{p}}^-]. \quad (6.43)$$

Given that Ising terms are absent from the effective Hamiltonian, we obtain the quantity  $r_{\mathbf{p}}^{\sigma,-\sigma,(j^*)} = -1$  for the fixed point theory. The RG flow features for this phase is represented via the tree diagram in Fig.6.2.7. A numerical evaluation of the RG flow is shown in Fig.6.2.12 left and right panels for 2-particle off-diagonal and number-diagonal scattering vertices respectively, and involving electronic pairs with net momentum  $p = 0.0, 0.004, 0.006, 0.01$ . The bare couplings  $V_{X,p} = -0.05$ ,  $V_{D,p} = 0.5$  ( $|V_{X,p}| < |V_{D,p}|$ ) and fluctuation scale  $\omega = \frac{1}{2}(\epsilon_{k_{\Lambda_0}} + \epsilon_{p-k_{\Lambda_0}}) - 0.5$  (Regime-IV in Table 6.2.2), and system volume as mentioned earlier. In this regime, we find that the off-diagonal scattering vertices  $V_{X,p}^* = V_{k,k',p}^{\sigma,-\sigma}$  with the largest non-zero pair-momentum (here, the curve for  $p = 0.01$  in Fig.6.2.12 (left panel)) dominate the low energy physics. However, we find the Ising interactions to be RG irrelevant for all pair momenta (Fig.6.2.12 (right panel)), and the phase is described in terms of  $p = 0.01$  momentum pseudospin pairs interacting via XY interactions (eq.(6.39)).

## V. Reduced BCS theory for finite momentum pairs-XXZ regime

Similarly, in regime V in Table 6.2.2, we obtain a phase composed of finite-momentum pseudospins interacting via XXZ interaction. The effective Hamiltonian describing this phase is

$$H_{SPDW}^{*,XXZ}(\omega) = \sum_{\mathbf{k}} \epsilon_{\mathbf{k}_{\Lambda\hat{s}}}^{(j^*)} A_{\mathbf{k}_{\Lambda\hat{s}}}^z - \sum_{\Lambda,\Lambda' < \Lambda^*} V_{\mathbf{k}_{\Lambda\hat{s}},\mathbf{k}_{\Lambda'\hat{s}'},0}^{\sigma,-\sigma,(j^*)} A_{\mathbf{k}_{\Lambda\hat{s}},\mathbf{p}}^+ A_{\mathbf{k}_{\Lambda'\hat{s}'},\mathbf{p}}^- + \sum_{\mathbf{k}_{\Lambda\hat{s}},\mathbf{p}} V_{\mathbf{k}_{\Lambda\hat{s}},\mathbf{p}'}^{\sigma,-\sigma,(j^*)} A_{\mathbf{k}_{\Lambda\hat{s}},\mathbf{p}}^z A_{\mathbf{p}'-\mathbf{k}_{\Lambda\hat{s}},\mathbf{p}}^z. \quad (6.44)$$

Finite magnitudes for both the number-diagonal and off-diagonal interactions leads to the quantity  $r_{\mathbf{p}=0}^{\sigma,-\sigma,(j^*)} = -r$ , where  $r < 1$ . The tree diagram Fig.6.2.8 represents the corresponding vertex tensor RG flow. As shown in Fig.6.2.13 (left and right panels), a numerical evaluation of the RG flow for bare coupling  $V_{X,p} = -0.04$ ,  $V_{D,p} = 0.64$  and  $\omega = \frac{1}{2}(\epsilon_{\Lambda_0} + \epsilon_{0.01-k_{\Lambda_0}}) - 0.5$  (Regime-V in Table6.2.2) reveals that at the IR fixed point, both off-diagonal and number-diagonal renormalized couplings attain a finite magnitude. The low-energy fixed point theory is, therefore, dominated by finite-momentum pseudospin pairs interacting by a XXZ interaction (eq.(6.44)).

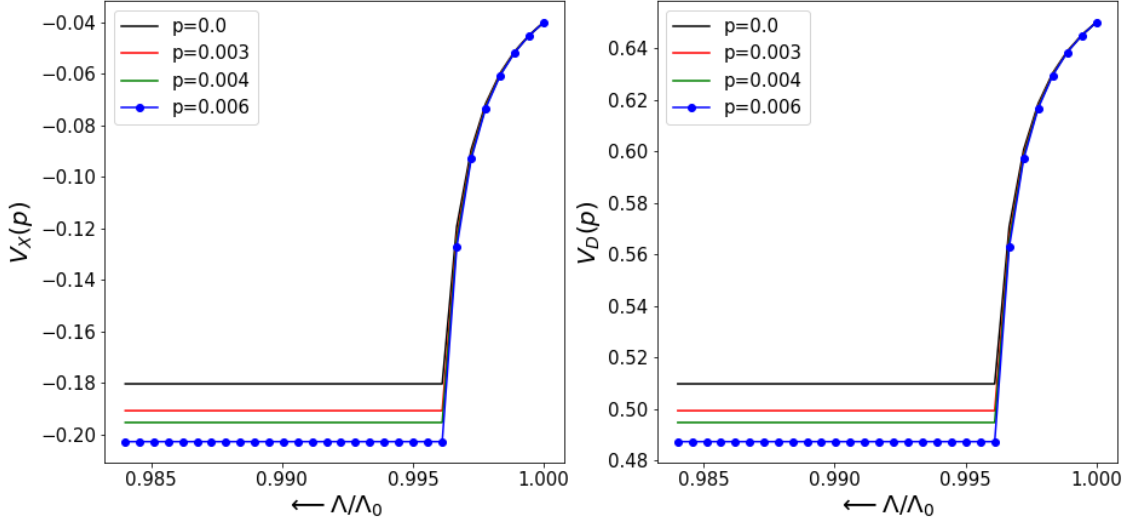


Figure 6.2.13: Left/right panel represents the RG flow of two-particle number off-diagonal/diagonal scattering vertices (eqs.(6.17)) respectively for  $p = 0$  ( $V_{X,p=0}^{(j)}$ ) and  $p \neq 0$  finite-momentum pairs ( $(V_{X,p'}^{(j)})$ ). Numerical evaluations are for system volume  $1024 \times 1024$  and with bare  $V_{D,p} = 0.64$ ,  $V_{X,p} = -0.04$  (in units of  $t$ ),  $\omega = \frac{1}{2}(\epsilon_{k\Lambda_0} + \epsilon_{0.01-\mathbf{k}\Lambda_0}) - 0.5$ .

## VI. Tensor network representation of the reduced BCS model and Fermi liquid theory

The above fixed point Hamiltonians for regimes I-V Table 6.2.1 and 6.2.2 can be broadly classified into gapless and gapped phases. The Fermi liquid corresponds to the gapless phase containing purely number-diagonal interactions, such that  $H_{FL}^*$  eq(6.28) is purely number-diagonal in Fock space and various terms in it commute. Therefore, all the number operators  $\hat{n}_{\mathbf{k}\sigma}$  corresponding to states  $|\mathbf{k}\sigma\rangle$  (lying within the window whose boundaries are given by the states  $\mathbf{k}_{\Lambda^*s}$ , eq.(6.27)) commute with  $H_{FL}$ , such that their eigenvalues correspond to integrals of motion. Following our demonstration of a tensor network representation for the unitary RG flow in [182], the RG flow towards Fermi liquid fixed point is displayed as a tensor network in Fig.6.2.14 below; the features of the emergent Fermi liquid theory discussed above are clearly visible at the final layer of the network.

The reduced BCS theory  $H_{(j^*)XY}^{RBCS}$  (eq.(6.34)) and its variants  $H_{(j^*)XXZ}^{RBCS}$ ,  $H_{(j^*)XY}^{SPDW}$ ,  $H_{(j^*)XY}^{SPDW}$  all correspond to gapped condensates. In contrast to that shown for the Fermi liquid, the tensor network representation of the RG flow towards such gapped ground states displays an emergent pairing of the legs in the final layer. The pairing of legs  $\mathbf{k}\sigma$  and  $-\mathbf{k}-\sigma$  can be seen in the grey boxes in Fig.6.2.15, while the emergent condensate as a whole is encircled in the black dashed line. The dashed oval in Fig. 6.2.15 represents the XY and Ising interaction between this pseudospins. Having achieved the Fermi liquid and BCS regimes, we will turn below towards looking for more exotic states of matter, such as the marginal Fermi liquid and gapped condensate ground states that involve hybridised spin- and charge-pseudospin pairing.

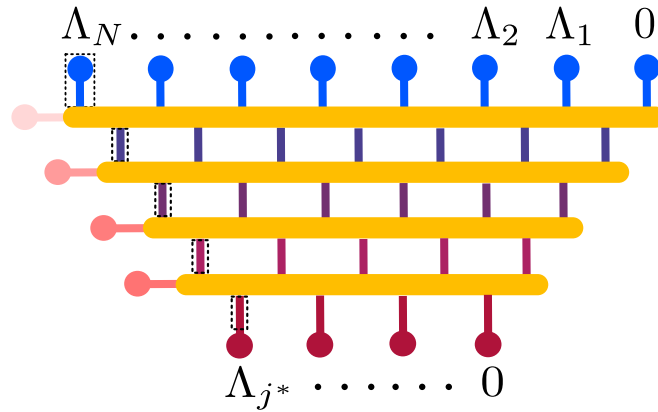


Figure 6.2.14: Vertex tensor network representation of the RG flow towards the Fermi liquid. The blue legs labelled  $0, \dots, \Lambda_n$  represent the holographic boundary composed of electronic states, the yellow blocks represent nonlocal unitary disentanglers that map the boundary states to the bulk with lowering energies (UV to IR, varying from light to deeper shade of red). The variation in the colour of the input legs into the subsequent unitary operators (yellow blocks) depicts the change of the entanglement content within the remnant coupled electronic states as the RG flows from UV to IR. The final unitary transformation layer leads to a theory comprised of decoupled legs labelled  $0, \dots, \Lambda_{j^*}$ . These are represented in brown, and each leg has an integral of motion associated with it.

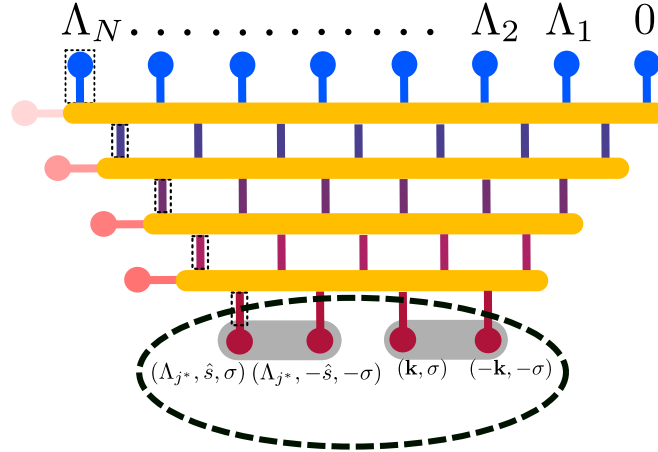


Figure 6.2.15: Entanglement holographic mapping network representation of the RG flow towards the reduced BCS theory. Pairs of brown legs (in grey boxes) represents pairs of electronic states with zero net-momentum and zero net-spin. The dashed oval represents the interaction between the pseudospins.

#### 6.2.4 The Marginal Fermi liquid

In this subsection, we explore the possibility of a metallic phase different from the Fermi liquid being found within the parameter space of the  $H_{SFIM}$  model. For this, one possible distinguishing feature could be the nature of long-lived excitations in the proximity of the Fermi surface that replace the Landau quasiparticles of the Fermi liquid. Thus, we investigate the physics of

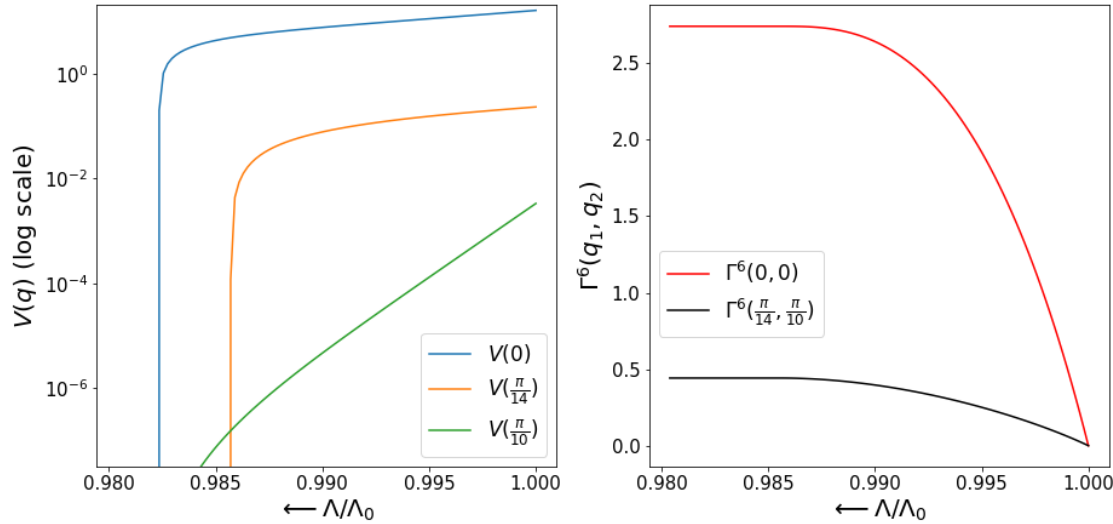


Figure 6.2.16: Left panel: RG flows for finite-momentum transfer  $q \neq 0$  off-diagonal two-particle forward scattering vertices ( $V(q)$ , orange and green curves) and number-diagonal ( $q = 0$ , blue curve) scattering vertices (eqs.(6.17)), both represented in log-scale on the  $y$ -axis. Right panel: RG flows for the number off-diagonal  $\Gamma^6(q_1, q_2)$  (eqs.(6.46)) three-particle scattering vertex (black curve), and two-particle one-hole number-diagonal ( $\Gamma^6(0)$ ) scattering vertex(eq.(6.47)) (red curve).

the lowest-order decay channel of 1-particle (Landau quasiparticle) excitations, i.e., 2-electron 1-hole composites with a net charge  $e$  and net spin  $1/2$ . Although 6-point (or 3-particle) scattering vertices are absent in the bare Hamiltonian  $H_{SFIM}$  (eq.(6)), they are generated under RG [182]. Such 6-point diagonal/off-diagonal scattering terms describe the interaction between the 2-electron 1-hole composites. These interactions bring about a log-divergence in the 1-particle self-energy [182], and require therefore a controlled RG treatment to study the nature of the resulting metallic phase.

We will now see that the conditions 1-3 listed under regime VI in Table 6.2.2 correspond to the formation of the non-Fermi liquid gapless phase best described as a marginal Fermi liquid. We begin by exploring the implications of these conditions using 4- and 6-point vertex flow equations in eq.(6.17). To proceed, we first note the form of the six point diagonal and off diagonal vertices

$$\begin{aligned}
 H_{(j)}^6 &= \sum_{\substack{\mathbf{k}, \mathbf{k}' \mathbf{k}'' \\ \mathbf{p}, \mathbf{p}'}} R_{\mathbf{k}\mathbf{k}'\mathbf{k}''\mathbf{p}\mathbf{p}'}^{\sigma\sigma'\sigma} \left( c_{\mathbf{k},\sigma}^\dagger c_{\mathbf{p}-\mathbf{k},\sigma'}^\dagger c_{\mathbf{p}'-\mathbf{k}',\sigma'}^\dagger c_{\mathbf{p}-\mathbf{k}',\sigma'} c_{\mathbf{k}'',\sigma'} c_{\mathbf{p}'-\mathbf{k}'',\sigma} \right) \\
 &+ \sum_{\mathbf{k}, \mathbf{k}', \mathbf{p}} R_{\mathbf{k}\mathbf{k}'\mathbf{p}}^{\sigma\sigma'\sigma} \tau_{\mathbf{k}\sigma} \tau_{\mathbf{p}-\mathbf{k}\sigma'} \tau_{\mathbf{p}-\mathbf{k}'\sigma'} .
 \end{aligned} \tag{6.45}$$

Then, the RG flow equations for the 6-point diagonal (eq.(6.18)) and off-diagonal vertices (eq.(6.25))

are given by

$$\begin{aligned}\Delta\Gamma_{\alpha\beta}^{6,(j)} &= \Gamma_{\alpha\gamma}^{4,(j)}G_{\gamma\gamma'}^{2,(j)}\Gamma_{\gamma'\beta}^{4,(j)} - \Gamma_{\alpha\gamma}^{6,(j)}G_{\gamma\gamma'}^{6,(j)}\Gamma_{\gamma'\beta}^{6,(j)} \\ &+ \Gamma_{\alpha\gamma}^{6,(j)}G_{\gamma\gamma'}^{4,(j)}\Gamma_{\alpha\gamma}^{4,(j)},\end{aligned}\quad (6.46)$$

$$\Delta\Gamma_{\alpha\alpha'}^{6,(j)} = \Gamma_{\alpha\gamma}^{4,(j)}G_{\gamma\gamma'}^{2,(j)}\Gamma_{\gamma'\alpha'}^{4,(j)} - \Gamma_{\alpha\gamma}^{6,(j)}G_{\gamma\gamma'}^{6,(j)}\Gamma_{\gamma'\alpha'}^{6,(j)}. \quad (6.47)$$

In the above expressions,  $G_{\gamma\gamma'}^{6,(j)}$  is obtained from eq.(6.13) in the 2-electron 1-hole eigenconfiguration of the three-fermion string  $\tau_{\mathbf{k}_{\Lambda_j\hat{s}_1}\sigma'\sigma_{\mathbf{p}-\mathbf{k}_{\Lambda_j\hat{s}_1}}\sigma'\sigma_{\mathbf{p}-\mathbf{k}_{\Lambda\hat{s}}\sigma}} = -\frac{1}{8}$ , leading to a negative sign in the RG equations given above in eqs.(6.46) and (6.47). Now, for the fluctuation energy in the range (regime VI condition 1)

$$\frac{1}{2}\epsilon_{\mathbf{k}_{\Lambda\hat{s}}} < \omega < \frac{1}{2}(\epsilon_{\mathbf{k}_{\Lambda\hat{s}}} + \epsilon_{\mathbf{p}-\mathbf{k}_{\Lambda\hat{s}}}), \text{ for } \epsilon_{\mathbf{p}-\mathbf{k}_{\Lambda\hat{s}}}^{(j)} > 0, \quad (6.48)$$

we have  $G_{\gamma\gamma'}^{4,(j)} < 0$  (eq(6.19)). Following eq.(6.20), this results in the 4-point vertex RG flow being irrelevant:  $\Delta\Gamma_{\alpha\beta}^{4,(j)} < 0$ .

Importantly, note that  $G_{\gamma\gamma'}^{4,(j)} < 0$  leads to an additional negative contribution in the RG equation (eq.(6.46)) for the off-diagonal 6-point vertices  $\Gamma_{\alpha\beta}^{6,(j)}$ , while such a term is absent in the RG equation for the diagonal 6-point vertices  $\Gamma_{\alpha\alpha'}^{6,(j)}$  (eq.(6.47)). This extra negative contribution leads to  $\Delta\Gamma_{\alpha\alpha'}^{6,(j)} < \Delta\Gamma_{\alpha\beta}^{6,(j)}$ . We now argue that the above inequality implies  $\Gamma_{\alpha\alpha'}^{6,(j)} < \Gamma_{\alpha\beta}^{6,(j)}$ . For this, we first note that the 6-point vertices are generated only at the first RG step from the 4-point vertices (eq.(6.25)) as follows

$$\begin{aligned}\Gamma_{\alpha\beta}^{6,(N-1)} &= \Delta\Gamma_{\alpha\beta}^{6,(N)} = \Gamma_{\alpha\gamma}^{4,(N)}G_{\gamma\gamma'}^{4,(N)}\Gamma_{\gamma'\beta}^{4,(N)}, \\ \Gamma_{\alpha\alpha'}^{6,(N-1)} &= \Delta\Gamma_{\alpha\alpha'}^{6,(N)} = \Gamma_{\alpha\gamma}^{4,(N)}G_{\gamma\gamma'}^{4,(N)}\Gamma_{\gamma'\alpha'}^{4,(N)}.\end{aligned}\quad (6.49)$$

As the 2-point Green's function  $G_{\gamma\gamma'}^{2,\sigma,(j)} = (\omega_{(j)} - \frac{1}{2}\epsilon_{(j)}) > 0$  carries positive signature in the energy range of eq.(6.48), the 3-particle interactions are repulsive in nature. It is then simple to observe from the above expression that the diagonal and the off-diagonal 6-point vertices have similar magnitude  $\Gamma_{\alpha\beta}^{6,(N-1)} \sim \Gamma_{\alpha\alpha'}^{6,(N-1)}$ . Then, from the discussion above, we conclude that under RG, the renormalised 6-point vertices satisfy

$$\Gamma_{\alpha\beta}^{6,(j)} < \Gamma_{\alpha\alpha'}^{6,(j)}. \quad (6.50)$$

In order to numerically evaluate the renormalized six-point vertices generated under RG and their precise ordering (eq.(6.50)), we assume a simplified bare form of the vertices.  $\Gamma^{6,(j)}(0,0)$  represents the strength of the number diagonal vertices (i.e., the second term in eq.(6.45)), and  $\Gamma^6(q_1, q_2) = \Gamma_{\alpha\beta}^{6,(j)}(\mathbf{q}_1 = \mathbf{k} - \mathbf{p}' + \mathbf{k}'', \mathbf{q}_2 = \mathbf{p} - \mathbf{p}')$  the strength of the six-point off-diagonal vertex (i.e., the first term in eq.(6.45)). As shown in the right panel of Fig.6.2.16, both  $\Gamma^6(0,0)$  and  $\Gamma^6(q_1, q_2)$  grow under RG and saturate at fixed points  $\Gamma^{6,*}(0,0) < \Gamma^{6,*}(q_1, q_2)$  with  $\Lambda^* = 0.98\Lambda_0$ . Given that in the vicinity of the fixed point, both number-diagonal and off-diagonal four-point vertices vanish under RG (Fig.6.2.16 (left panel)),  $\Gamma_{\alpha\beta}^{4,(j)} \rightarrow 0$ , we find that the RG equations for the six-point diagonal and off-diagonal vertices attain a simplified form

$$\begin{aligned}\Delta\Gamma_{\alpha\beta}^{6,(j)} &= -\Gamma_{\alpha\gamma}^{6,(j)}G_{\gamma\gamma'}^{6,(j)}\Gamma_{\gamma'\beta}^{6,(j)}, \\ \Delta\Gamma_{\alpha\alpha'}^{6,(j)} &= -\Gamma_{\alpha\gamma}^{6,(j)}G_{\gamma\gamma'}^{6,(j)}\Gamma_{\gamma'\alpha'}^{6,(j)},\end{aligned}\quad (6.51)$$

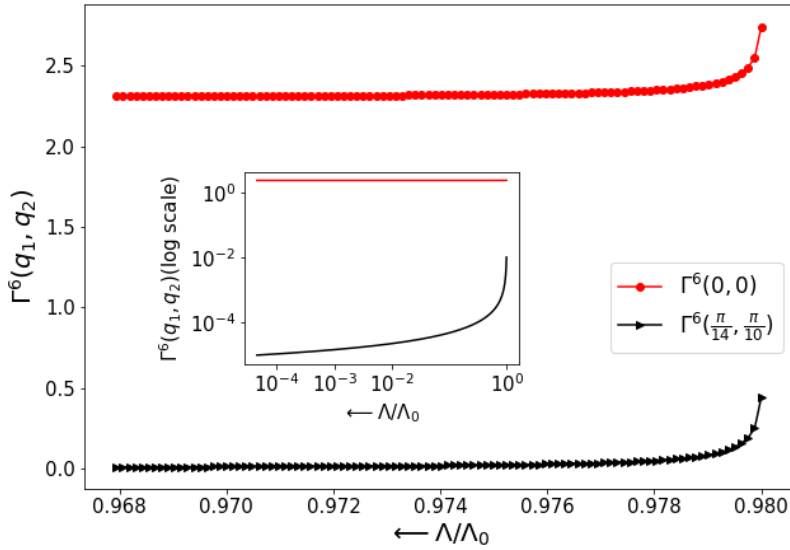


Figure 6.2.17: RG flow of the six-point off-diagonal ( $\Gamma^6(q_1, q_2)$ , black curve) / diagonal ( $\Gamma^6(0, 0)$ , red curve) scattering vertices (eqs.(6.51)) for  $\Lambda < 0.98\Lambda_0$ . The inset plot shows the same curves in log-scale for both  $x$ - and  $y$ -axes.

where, by using eq.(6.13),  $G_{\mathbf{k}_{\Lambda_j \hat{s}}, \mathbf{p}, \mathbf{p}'}^{6, \sigma\sigma'\sigma, (j)} (\omega_{(j)} = \omega)$  is given by

$$\begin{aligned} G_{\gamma\gamma'}^{6,(j)} = & \left( \omega - \epsilon_{\mathbf{k}_{\Lambda_j \hat{s}}}^{(j)} \tau_{\mathbf{k}_{\Lambda_j \hat{s}}\sigma} - \epsilon_{\mathbf{p}'-\mathbf{k}_{\Lambda_j \hat{s}}}^{(j)} \tau_{\mathbf{p}'-\mathbf{k}_{\Lambda_j \hat{s}}, \sigma'} - \epsilon_{\mathbf{p}-\mathbf{k}_{\Lambda_j \hat{s}}}^{(j)} \tau_{\mathbf{p}-\mathbf{k}_{\Lambda_j \hat{s}}, \sigma} \right. \\ & \left. - \Gamma_{\gamma\gamma'}^{6,(j)} \tau_{\mathbf{k}_{\Lambda_j \hat{s}}\sigma} \tau_{\mathbf{p}-\mathbf{k}_{\Lambda_j \hat{s}}, \sigma'} \tau_{\mathbf{p}'-\mathbf{k}_{\Lambda_j \hat{s}}, \sigma} \right)^{-1}. \end{aligned} \quad (6.52)$$

In order to obtain the stable fixed point theory, we choose an intermediate configuration ( $\hat{n}_{\mathbf{k}_{\Lambda_j \hat{s}}\sigma} = 1$ ,  $\hat{n}_{\mathbf{p}-\mathbf{k}_{\Lambda_j \hat{s}}\sigma} = 1$ ,  $\hat{n}_{\mathbf{p}'-\mathbf{k}_{\Lambda_j \hat{s}}\sigma} = 0$ ) for the 6-point Green's function. The net configurational energy for such a composite 3-particle is given by a combination of their individual 1-particle energies and the net 3-particle energy

$$E^{(j)} = E_1^{(j)} - \frac{1}{8} R_{\mathbf{k}'', \mathbf{p}, \mathbf{p}'}^{\sigma\sigma'\sigma, (j)}, \quad E_1^{(j)} = \frac{1}{2} (\epsilon_{\mathbf{k}_{\Lambda_j \hat{s}}}^{(j)} + \epsilon_{\mathbf{p}-\mathbf{k}_{\Lambda_j \hat{s}}}^{(j)} - \epsilon_{\mathbf{p}'-\mathbf{k}_{\Lambda_j \hat{s}}}^{(j)}). \quad (6.53)$$

Thus, the 6-point Green's function eq.(6.13) is given by

$$G_{\gamma\gamma'}^{6,(j)}(\omega) = (\omega - E^{(j)})^{-1}. \quad (6.54)$$

The set  $\gamma = \{(\mathbf{k}_{\Lambda \hat{s}}, \sigma, 1), (\mathbf{k}', \sigma', 1), (\mathbf{k}'', -\sigma', 0)\}$ , while the set  $\gamma'$  involves the same momentum and spin labels, but with the 1s and 0s interchanged. In this basis, the RG flows for the off-diagonal 3-particle vertex and the diagonal 2-electron 1-hole dispersion are given by

$$\Delta\Gamma_{\alpha\beta}^{6,(j)} = -\frac{\Gamma_{\alpha\gamma}^{6,(j)}\Gamma_{\gamma\beta}^{6,(j)}}{\omega - E_1^{(j)} + \frac{1}{8}\Gamma_{\gamma\gamma'}^{6,(j)}}, \quad \Delta\Gamma_{\alpha\alpha'}^{6,(j)} = -\frac{\Gamma_{\rho\gamma}^{6,(j)}\Gamma_{\gamma\rho'}^{6,(j)}}{\omega - E_1^{(j)} + \frac{1}{8}\Gamma_{\gamma\gamma'}^{6,(j)}}. \quad (6.55)$$

Finally, from the RG flow of the couplings eq.(6.55), the parameter range eq.(6.50) for the 6-point off-diagonal/diagonal vertices and for fluctuation energies  $\omega < E_1^{(j)}$ , we obtain the fixed point condition for a gapless phase with the 3-particle composite excitations proximate to the Fermi surface

$$\frac{1}{8}\Gamma_{\gamma\gamma'}^{6,(j*)} = E_1^{(j*)} - \omega, \quad \Gamma_{\alpha\beta}^{6,(j*)} = 0. \quad (6.56)$$

Additionally, we note that given  $\frac{1}{2}(\epsilon_{\mathbf{k}}^{(j)} + \epsilon_{\mathbf{p}-\mathbf{k}}^{(j)}) > \omega_{(j)} > \frac{1}{2}\epsilon_{\mathbf{k}}^{(j)}$  (for  $\epsilon_{\mathbf{p}-\mathbf{k}}^{(j)} > E_F$ ), the energy  $E_1^{(j)} > \frac{1}{2}\epsilon_{\Lambda_j^*}^{(j)}$  and the inequality  $\omega < E_1^{(j)}$  is immediately satisfied for the energy of the electron-occupied states lying above  $E_F$  and the energy of the hole configuration lying below  $E_F$ .

At the fixed point theory, the dynamics of the states within the window  $0 < \Lambda < \Lambda_{j*}$  is governed by the effective Hamiltonian

$$H_{MFL}^*(\omega) = \sum_{\Lambda < \Lambda_{j*}, \hat{s}} \epsilon_{\mathbf{k}_{\Lambda\hat{s}}}^* \hat{n}_{\mathbf{k}_{\Lambda\hat{s}}\sigma} + \sum_{\rho, \Lambda < \Lambda_{l*}, \mathbf{p}} \Gamma_{\rho\rho'}^{6,(j*)} \hat{n}_{\mathbf{k}'',-\sigma} \hat{n}_{\mathbf{p}-\mathbf{k}_{\Lambda\hat{s}},\sigma} (1 - \hat{n}_{\mathbf{k}_{\Lambda\hat{s}},\sigma}). \quad (6.57)$$

For  $\Lambda < 0.98\Lambda_0$ , the RG flows of six-point vertices have no contribution from two-particle vertices (as already observed in Fig.6.2.16), and is generated purely by the six-point vertices (eq.(6.55)). The nature of the RG flow for the six-point vertices  $\Gamma^6(q_1, q_2)$  and  $\Gamma^6(0)$  below the RG scale  $\Lambda < 0.98\Lambda_0$  is thus obtained in Fig.6.2.17 from a numerical computation of eqs.(6.55). The plots indicate vanishing of the six-point off-diagonal vertices  $\Gamma^6(\pi/14, \pi/10)$  under RG, while the two-particle one-hole vertices  $\Gamma^6(0, 0)$  reach an RG fixed point with a finite (and large) value. The inset in Fig.6.2.17 shows that  $\Gamma^6(\pi/14, \pi/10)$  reduces in magnitude from  $O(1)$  to  $O(10^{-4})$  (black curve), while  $\Gamma^6(0, 0)$  saturates at  $O(1)$ . In this way, we demonstrate numerically the MFL effective Hamiltonian (eq.(6.57)). We note that the MFL fixed point Hamiltonian is purely number-diagonal (similar to the Fermi liquid), translational invariant and has a gapless continuum spectrum that is a function of the wave-vector. All of this indicates the metallic nature of the ground state obtained at this new fixed point.

Next, we proceed to find the effect of such three-particle vertices on the 1-electron excitations in the neighborhood of the fixed point theory. For that, we note that the primary decay channel for the one-electron degrees of freedom due to three-particle off-diagonal scattering terms are three-electron two-hole excitations. Therefore, the electronic self-energy renormalizes via six-point vertices (eq.(6.12))

$$\Delta\Sigma_{\mathbf{k}_{\Lambda\hat{s}}}^{(j)}(\omega) = \sum_{\mathbf{k}'\mathbf{k}''\mathbf{p}} \frac{(\Gamma_{\alpha\beta}^{6,(j)})^2}{\omega - E_{5,1}^{(j)} - E_{5,3}^{(j)}} , \quad (6.58)$$

where

$$E_{5,1}^{(j)} = E_1^{(j)} + \frac{1}{2}(\epsilon_{\mathbf{k}_{\Lambda_1\hat{s}}}^{(j)} + \epsilon_{\mathbf{p}-\mathbf{k}_{\Lambda_1\hat{s}}}^{(j)}) , \quad (6.59)$$

is the collective energy due to 4-p 1-h intermediate configuration of electronic states. Here,  $E_{5,3}^{(j)}$  contains the 2-electron 1-hole correlation energy term  $-\frac{1}{8}\Gamma_{\gamma\gamma'}^{6,(j)}$ , and  $E_1^{(j)}$  is the net energy due to 3-electron 2-hole composite given by eq.(6.53). Now, using the 1-p self-energy RG flow equation

eq.(6.58), and following Appendix 6.A, we arrive at the form for the renormalized self-energy at fixed point  $(j^*)$

$$\Sigma_{\mathbf{k}_{\Lambda_{l^*}} \hat{s}}^{(j^*)}(\omega) = N(0) \frac{(\Gamma_{X, \mathbf{k}_{\Lambda_{l^*}} \hat{s}}^{6, (l^*)}(\omega))^2}{\Gamma_{D, \mathbf{k}_{\Lambda_{l^*}} \hat{s}}^{6, (l^*)}(\omega)} \ln \left| \frac{\omega_c}{\omega} \right|, \quad (6.60)$$

where  $\omega_c = \epsilon_{\mathbf{k}_{\Lambda_{l^*}}}^{(l^*)}$  is the characteristic energy scale that is emergent from the RG fixed point eq.(6.56) and  $N(0)$  is a dimensionless number equal to the total electronic state count at the FS. The ratio of the final fixed point 6-point off-diagonal/diagonal vertex strength for the states at  $\Lambda_{l^*}$  distance from FS (eq.(6.60)) can be computed by investigating their RG equations in its neighborhood. Near the fixed point (and near the FS), the 6-point vertex flow equations (eq.(6.56) ) are simplified by using eq.(6.114) and given by

$$\frac{\Delta \Gamma_{X, \mathbf{k}_{\Lambda_j} \hat{s}}^{6, (j)}}{\Delta \log_b \frac{\Lambda_j}{\Lambda_0}} = \frac{\Delta \Gamma_{D, \mathbf{k}_{\Lambda_j} \hat{s}}^{6, (j)}}{\Delta \log_b \frac{\Lambda_j}{\Lambda_0}} = \frac{(\Gamma_{X, \mathbf{k}_{\Lambda_j} \hat{s}}^{6, (j)})^2}{\omega - \frac{1}{2}\epsilon_{\mathbf{k}_{\Lambda_j} \hat{s}}^{(j)} - \frac{1}{8}\Gamma_{D, \mathbf{k}_{\Lambda_j} \hat{s}}^{6, (j)}(\omega)}, \quad (6.61)$$

where  $\Delta \log_b \frac{\Lambda_j}{\Lambda_0} = 1$  for  $\Lambda_j = \Lambda_0 b^j$ . Here,  $\Gamma_{X, \mathbf{k}_{\Lambda_j} \hat{s}}^{6, (j)} / \Gamma_{D, \mathbf{k}_{\Lambda_j} \hat{s}}^{6, (j)}$  represent the uniform pieces of the off-diagonal/diagonal parts of the three-particle vertex. From eq.(6.61), we obtain the RG invariant relation:  $\Gamma_{X, \mathbf{k}_{\Lambda} \hat{s}}^{6, (j)} = \Gamma_{D, \mathbf{k}_{\Lambda} \hat{s}}^{6, (j)} + C$ , where  $C$  is the RG invariant. At the fixed point eq.(6.56),  $C = 0$  and  $\epsilon_{\Lambda \hat{s}}^{(j)} \rightarrow 0$  as  $\Lambda \rightarrow 0$  (FS), leading to  $\Gamma_{D, \mathbf{k}_{\Lambda} \hat{s}}^{6, (l^*)} = -\omega (\Lambda = \Lambda_{l^*})$ .

Thus, the self energy for states near the FS has the universal  $\mathbf{k}$ -independent form

$$\Sigma^{(l^*)}(\omega) = N(0)\omega \ln \left| \frac{\omega}{\omega_c} \right|. \quad (6.62)$$

The real part of the self-energy in eq.(6.62) has the same structure as the well known form of the self-energy for the *marginal Fermi liquid metal* [519]. Further, this result is a generic outcome for any single band dispersion, and emergent purely from repulsive 4-point and 6-point vertex RG flows. Using eq.(6.62), we obtain the imaginary part of the complex self energy, i.e., the scattering rate ( $\tau$ ) as a function of the fluctuation scale  $\omega$ ; using Kramers-Kronig relations eq.(2.29), we can connect  $\tau$  to the temperature  $T$

$$k_B T = \frac{1}{N(0)} \Sigma^{im, (l^*)}(\omega) = \hbar |\omega| = \hbar 2\pi \tau^{-1}. \quad (6.63)$$

The finite  $T$  resistivity per unit length  $\rho(T)/L$  for layered 2d systems can be obtained from eq.(6.63) by replacing  $N(0) = (2mE_F)^{-1}\hbar^2(\Delta k)^2N_e(E_F)$ , particle density  $n = N_e(E_F)/L^3$  ( $L^3$  is the volume in 3D) and the Fermi energy  $E_F$  in terms of the Fermi Temperature ( $T_F$ )  $E_F = k_B T_F$

$$\frac{\rho}{L} = \frac{m}{ne^2 L \tau} = \frac{\hbar}{2e^2} \frac{T}{T_F}. \quad (6.64)$$

Here,  $\Delta k = 2\pi L^{-1}$  is the momentum space lattice spacing,  $L$  is the system length,  $N_e(E_F)$  number of electrons around FS that comprise the transport. This obtains a universal Planckian

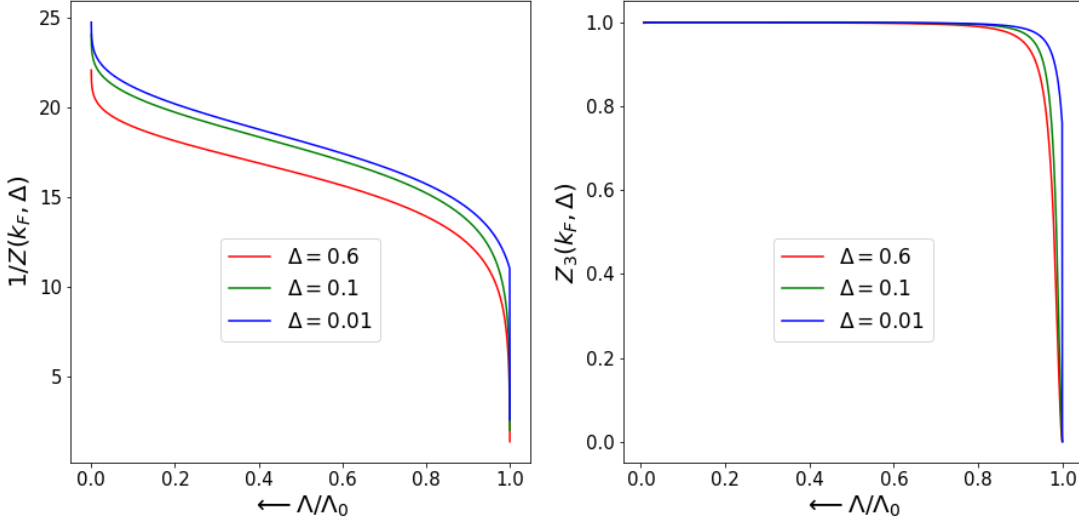


Figure 6.2.18: Left panel: RG flow of the quasiparticle residue  $Z_1(k_F, \Delta)$  obtained from self energy RG flow eqn.(6.58) . Right panel: RG flow of the 2-electron 1-hole residue  $Z_3(k_F, \Delta)$ .  $\Delta$  represents the probe energyscale about  $E_F$ .

$T$ -linear resistivity form starting from a very general microscopic single band model  $H_{SFIM}$ , and supports various experimental observations and theoretical proposals [520, 521, 43]. Following eq.(6.62) and eq.(6.63), the quasiparticle residue has the following form at finite temperatures

$$Z_1(T) = \frac{1}{1 - N(0)(1 + \ln|\frac{k_B T}{\hbar\omega_c}|)} . \quad (6.65)$$

The left and right panels of Fig.6.2.18 represent the renormalization of the quasi-particle residue  $Z_1(k_F, \Delta)$  and 2-particle 1-hole residue  $Z_3(k_F, \Delta)$ . We find that, for  $\Delta = 0.6, 0.1, 0.001$ ,  $Z_1(k_F, \Delta)$  reduces under RG (left panel of Fig.6.2.18), indicating the breakdown of the Landau quasiparticle picture. On the other hand,  $Z_3(k_F, \Delta)$  (right panel of Fig.6.2.18) is seen to increase towards 1, indicating well-formed 2-electron 1-hole composites in the neighbourhood of the Fermi surface. Finally, Fig.6.2.19 is a numerical verification of the logarithmic dependence of  $Z_1(k_F, \Delta)$  on the energy scale  $\Delta (= k_B T)$  given in eq.(6.65).

As the quasi-particle residue  $0 < Z < 1$ , the relation eq.(6.65) holds for  $\omega < \omega_c/e$ , corresponding to a temperature  $T < \hbar\omega_c/(e k_B)$ . The vanishing of the quasiparticle residue,  $Z \rightarrow 0$ , leads to a integer Friedel's phase shift  $\Delta N \in \mathbb{Z}$ : a test electron binds together with a electron-hole pair, forming a three-particle composite. As the Hamiltonian eq.(6.57) is diagonal, the residue of this 2-electron 1-hole composite approaches 1 at the  $FS$ . We note that this was also shown for the parent MFL of the Mott insulating state in the 2D Hubbard model on the square lattice at 1/2-filling in Ref.[180]. We also present the tensor network representation of the RG flow towards the marginal Fermi liquid fixed point in Fig.6.2.20.

In this subsection, we found the parameter and fluctuation regime where three-particle off-diagonal vertices are RG irrelevant, while the 2-electron 1-hole dispersion achieves a finite value

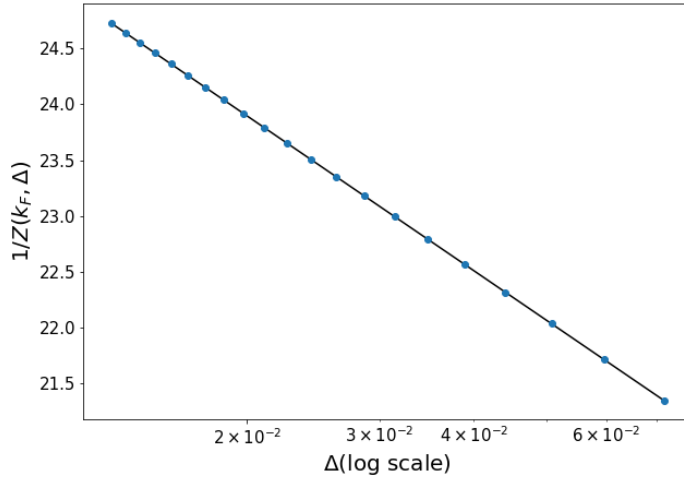


Figure 6.2.19: Variation of the quasiparticle residue  $Z_1(k_F, \Delta)$  with energy scale  $\Delta$  about the Fermi energy ( $E_F$ ).

at the fixed point. This observation provides a perfect setting for the question: what are the primary instabilities of the marginal Fermi liquid metal? We present the answer to this question next.

### 6.2.5 RG flow into the spin/charge hybridized pseudospin-pairing force models

We have seen earlier that the off-diagonal three particle vertices causes dynamical mixing between electron-electron and electron-hole pairs (eq.(6.22)) [182]. The spin/charge backscattering processes in the mixed configuration leads to a two-particle self-energy containing log-divergences as leading corrections[182]. In order to observe the condensation of various spin-charge mixed

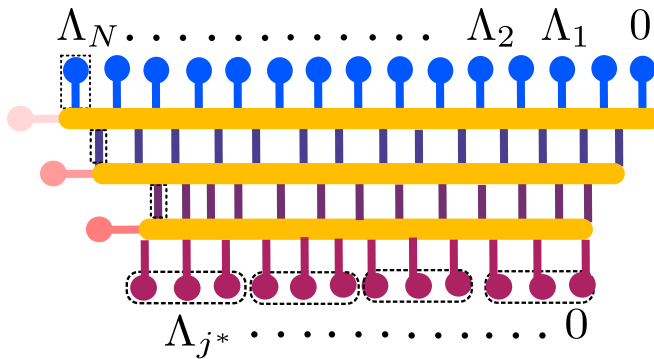


Figure 6.2.20: EHM tensor network representation of the Marginal Fermi liquid. Each dotted circle (comprising three electronic legs) represents a long-lived composite 2 electron-1 hole excitation of the MFL proximate to the Fermi surface.

configurations, we now apply the Hamiltonian RG formalism on the  $H_{SFIM}$ .

If the Fermi surface is nested, there are Umklapp scattering vertices generically present in the Hamiltonian  $H_{SFIM}$ . They are denoted by  $\Gamma_{c,\alpha\beta}^{4,(N)}$  where  $\alpha$  and  $\beta$  represent electronic pairs with pair momentum differing by  $\mathbf{Q}$ . Further, the index  $\alpha = \{\mathbf{k}_{\Lambda_j\hat{s}}\sigma, \mathbf{p} - \mathbf{k}_{\Lambda_j\hat{s}} - \sigma\}$  and  $\beta = \{\mathbf{k}_{\Lambda_j\hat{s}}\sigma, \mathbf{Q} + \mathbf{p} - \mathbf{k}_{\Lambda_j\hat{s}} - \sigma\}$ . The spin backscattering vertices in  $H_{SFIM}$  involve pairs of electronic states that exchange their spin orientations while scattering. These vertices are denoted by  $\Gamma_{s,\alpha\beta}^{4,(N)}$  where  $\alpha = \{\mathbf{k}_{\Lambda_j\hat{s}}\sigma, \mathbf{p} - \mathbf{k}_{\Lambda_j\hat{s}} - \sigma\}$ ,  $\beta = \{\mathbf{k}_{\Lambda_j\hat{s}} - \sigma, \mathbf{p} - \mathbf{k}_{\Lambda_j\hat{s}}\sigma\}$ . For the Umklapp and spin backscattering processes, the RG flow hierarchy yields

$$\begin{aligned}\Delta H_c^{(j)} &= \sum_{\mathbf{k}, \mathbf{k}', \mathbf{p}} \frac{\Gamma_{c,\alpha\gamma}^{4,(j)} \Gamma_{c,\gamma\beta}^{4,(j)} \hat{n}_{\mathbf{k}_{\Lambda_j\hat{s}}\sigma} \hat{n}_{\mathbf{p}-\mathbf{k}_{\Lambda_j\hat{s}}-\sigma}}{\omega - \epsilon_{p,\mathbf{k}_{\Lambda_j\hat{s}'},\mathbf{p}}^{(j)} - \Gamma_{\gamma\gamma}^{4,(j)} \tau_{\mathbf{k}_{\Lambda_j\hat{s}}\sigma} \tau_{\mathbf{p}-\mathbf{k}_{\Lambda_j\hat{s}}\sigma'}} \\ &\quad \times c_{\mathbf{k}\sigma}^\dagger c_{\mathbf{p}-\mathbf{k}-\sigma}^\dagger c_{\mathbf{Q}+\mathbf{p}-\mathbf{k}'-\sigma} c_{\mathbf{k}'\sigma}, \\ \Delta H_s^{(j)} &= - \sum_{\mathbf{k}, \mathbf{k}', \mathbf{p}} \frac{\Gamma_{s,\alpha\gamma}^{4,(j)} \Gamma_{s,\gamma\beta}^{4,(j)} \hat{n}_{\mathbf{k}_{\Lambda_j\hat{s}}\sigma} (1 - \hat{n}_{\mathbf{p}-\mathbf{k}_{\Lambda_j\hat{s}}-\sigma})}{\omega - \epsilon_{p,\mathbf{k}_{\Lambda_j\hat{s}'},\mathbf{p}}^{(j)} - \Gamma_{\gamma\gamma}^{4,(j)} \tau_{\mathbf{k}_{\Lambda_j\hat{s}}\sigma} \tau_{\mathbf{p}-\mathbf{k}_{\Lambda_j\hat{s}}\sigma'}} \\ &\quad \times c_{\mathbf{k}_1\sigma}^\dagger c_{\mathbf{k}_1-\mathbf{p}+2\mathbf{k}_{\Lambda_j\hat{s}}-\sigma}^\dagger c_{\mathbf{k}_2-\sigma}^\dagger c_{\mathbf{k}_2-\mathbf{p}+2\mathbf{k}_{\Lambda_j\hat{s}}\sigma}. \end{aligned} \quad (6.66)$$

The spin-type configuration 1e-1h/1h-1e for the set  $\alpha$  is constrained by the relation

$$n_{\mathbf{k}_{\Lambda_j\hat{s}}\sigma} + n_{\mathbf{p}-\mathbf{k}_{\Lambda_j\hat{s}}-\sigma} = 1 \quad \text{for } \epsilon_{\mathbf{k}_{\Lambda_j\hat{s}}} > E_F, \quad (6.67)$$

and has an associated kinetic energy lying within the range  $\epsilon_{\mathbf{k}_{\Lambda_j\hat{s}}} > \epsilon_{\mathbf{p}-\mathbf{k}_{\Lambda_j\hat{s}}}$ ,  $\omega > \frac{1}{2}(\epsilon_{\mathbf{k}_{\Lambda_j\hat{s}}} - \epsilon_{\mathbf{p}-\mathbf{k}_{\Lambda_j\hat{s}}})$ . The intermediate configuration of eq.(6.67) leads to a spin-type pseudospin configuration  $S_{\mathbf{k},\mathbf{p}}^- = c_{\mathbf{k}\sigma}^\dagger c_{\mathbf{p}-\mathbf{k}-\sigma}$ ,  $S_{\mathbf{k},\mathbf{p}}^+ = (S_{\mathbf{k},\mathbf{p}}^-)^\dagger$  and  $S^z = \frac{1}{2}[S^+, S^-]$ , in which the 4-point vertexes are RG irrelevant. On the other hand, certain 6-point vertexes are RG relevant in this regime, and can be represented in terms of charge- and spin-type pseudospins as follows

$$\begin{aligned} &c_{\mathbf{p}-\mathbf{p}''\sigma}^\dagger c_{\mathbf{p}''-\mathbf{k}_{\Lambda_j\hat{s}'}-\sigma}^\dagger c_{\mathbf{k}_{\Lambda_j\hat{s}'}\sigma}^\dagger c_{\mathbf{k}_{\Lambda_j\hat{s}}\sigma} c_{\mathbf{p}'-\mathbf{k}_{\Lambda_j\hat{s}}-\sigma} c_{\mathbf{p}-\mathbf{p}'-\sigma} \\ &= A_{\mathbf{k}_{\Lambda_j\hat{s}'}, \mathbf{p}''}^+ A_{\mathbf{k}_{\Lambda_j\hat{s}}, \mathbf{p}'}^- S_{\mathbf{p}-\mathbf{p}'', 2\mathbf{p}-\mathbf{p}'-\mathbf{p}''}^-. \end{aligned} \quad (6.68)$$

The operators  $A_{\mathbf{k},\mathbf{p}}^{+/-}$  corresponds to finite momentum pseudospin raising and lowering operators given in eq.(6.43). This spin-charge mixed representation of 6-point vertexes is manifested in the dynamical mixing between the pseudospin state configuration (see discussion below eq.(6.20)), and leads to a hybridized pair-kinetic energy eq. (6.21) entering the 4-point Green's function. In turn, this 4-point Green's function enters the 4-point vertex flow equations given in eq.(6.20). For the  $\mathbf{p}$ -momentum opposite-spin pairs, the 2-particle backscattering processes (with  $\Delta\mathbf{p} = 0$  (spin exchange) and  $\Delta\mathbf{p} = 2\pi$  (Umklapp)) given by

$$\mathbf{k}_{\Lambda\hat{s}}, \mathbf{p} - \mathbf{k}_{\Lambda\hat{s}} \leftrightarrow -\mathbf{k}_{\Lambda_j\hat{s}}, \mathbf{Q}_1 + \mathbf{p} + \mathbf{k}_{\Lambda_j\hat{s}}, \quad \mathbf{Q}_1 = 0, \mathbf{Q} \quad (6.69)$$

produce a log-divergence in the composite self-energy (shown in a companion manuscript [182]), requiring a RG treatment once more. Using eq.(6.20), the charge backscattering vertex flow equation is given by

$$\Delta\Gamma_{c,\alpha\beta}^{4,(j)}(\omega) = \frac{p\Gamma_{c,\alpha\gamma}^{2,(j)}\Gamma_{c,\gamma\beta}^{2,(j)}}{\omega - p\epsilon_{\mathbf{k}_{\Lambda_j\hat{s}},\mathbf{p}}^{ee,(j)} - p'\epsilon_{\mathbf{k}_{\Lambda_j\hat{s}},\mathbf{p}}^{eh,(j)} - \frac{p}{4}\Gamma_{c,\gamma\gamma}^{2,(j)} + \frac{p'}{4}\Gamma_{s,\gamma\gamma}^{2,(j)}}, \quad (6.70)$$

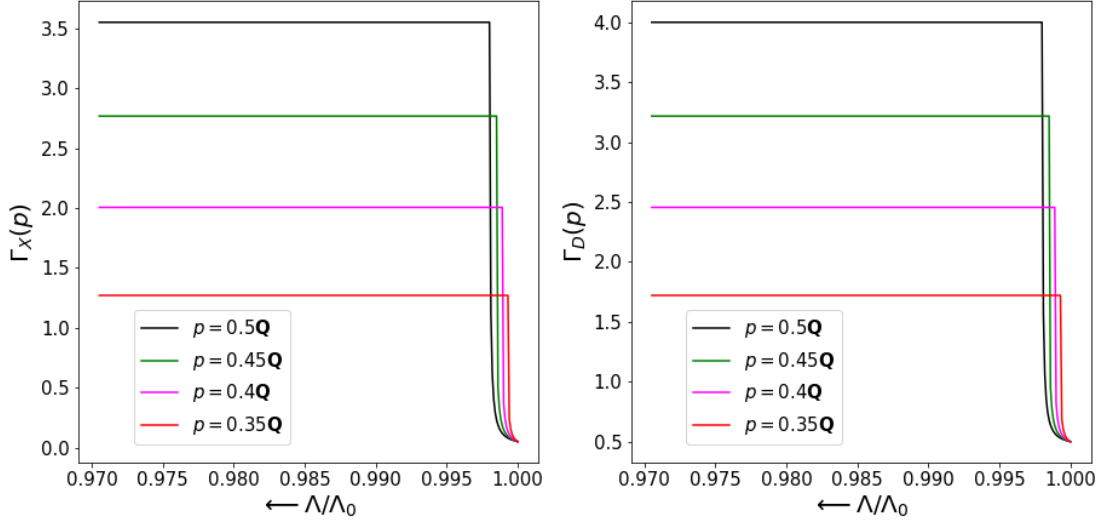


Figure 6.2.21: Left/right panels show the RG flow for the off-diagonal/diagonal  $\Gamma_X/\Gamma_D$  scattering vertices (eqs.(6.20)) respectively for various finite momenta ( $\mathbf{p}$ ) pairs.  $\Gamma_X^0 = 0.1$  is the bare magnitude of the umklapp scattering vertex,  $\Gamma_D^0 = 0.5$ . The  $k$ -space grid (system volume) used is  $1024 \times 1024$ .

where  $p' = 1 - p$ ,  $\epsilon_{\mathbf{k}_{\Lambda_j \hat{s}}, \mathbf{p}}^{ee, (j)} = \epsilon_{\mathbf{k}_{\Lambda_j \hat{s}}, \mathbf{p} - \mathbf{k}_{\Lambda_j \hat{s}}}^{ee, (j)}$  and  $\epsilon_{\mathbf{k}_{\Lambda_j \hat{s}}, \mathbf{p}}^{eh, (j)} = \epsilon_{\mathbf{k}_{\Lambda_j \hat{s}}, \mathbf{p} - \mathbf{k}_{\Lambda_j \hat{s}}}^{eh, (j)}$ . Similarly, the spin backscattering RG flow equation is given by  $\Delta \Gamma_{s, \alpha \beta}^{4, (j)} = (\frac{p-1}{p}) \Gamma_{c, \alpha \beta}^{4, (j)}$ . The stable fixed point is obtained from the condition

$$\omega - p \epsilon_{\mathbf{k}_{\Lambda_j \hat{s}}, \mathbf{p}}^{ee, (j*)} - p' \epsilon_{\mathbf{k}_{\Lambda_j^* \hat{s}}, \mathbf{p}}^{eh, (j*)} = \frac{p}{4} \Gamma_{c, \gamma \gamma'}^{2, (j)} + \frac{p'}{4} \Gamma_{s, \gamma \gamma'}^{2, (j)}, \quad (6.71)$$

leading to the effective pseudospin XXZ Hamiltonian given by

$$\begin{aligned} H_{ML}^{*, XXZ}(\omega) &= \sum_{\mathbf{k}} \epsilon_{\mathbf{k}_{\Lambda \hat{s}}, \mathbf{p}}^{ee, (j*)} A_{\mathbf{k}_{\Lambda \hat{s}}, \mathbf{p}}^z + \epsilon_{\mathbf{k}_{\Lambda \hat{s}}, \mathbf{p}}^{eh, (j*)} S_{\mathbf{k}_{\Lambda \hat{s}}, \mathbf{p}}^z + \sum_{\mathbf{k}_{\Lambda \hat{s}}, \mathbf{k}} \Gamma_{s, \alpha \beta}^{4, (j*)} [S_{\alpha}^+ S_{\beta}^- + h.c.] + \Gamma_{s, \alpha \beta}^{4, (j*)}, \parallel S_{\alpha}^z S_{\beta}^z \\ &+ \sum_{\mathbf{k}_{\Lambda \hat{s}}, \mathbf{k}} \Gamma_{c, \alpha \beta}^{4, (j*)} [A_{\alpha}^+ A_{\beta}^- + h.c.] + \Gamma_{\alpha \beta}^{4, (j*)}, \parallel A_{\alpha}^z A_{\beta}^z, \end{aligned} \quad (6.72)$$

where  $\Gamma_{\mathbf{k}_{\Lambda \hat{s}}, \mathbf{p}, \mathbf{k}, \mathbf{Q}}^{4, (j*)}$  and  $\Gamma_{\mathbf{k}_{\Lambda \hat{s}}, \mathbf{p}, \mathbf{k}, \mathbf{Q}}^{4, (j*)}, \parallel$  are the XY and Ising pseudospin couplings respectively.

Fig.6.2.21 shows the RG flow of the Umklapp scattering vertices connecting opposite sides of a nested Fermi surface for a tight-binding square lattice model at half-filling in two spatial dimensions for electronic pairs with net momentum  $\mathbf{p} = \mathbf{Q}/2, 0.45\mathbf{Q}, 0.4\mathbf{Q}$  and  $0.35\mathbf{Q}$  (where  $(\mathbf{Q} = \pi, \pi)$ ). The left and right panels show the renormalization of the off-diagonal ( $\Gamma_{c,X} = \Gamma_{c,\alpha\gamma}$ ) and diagonal ( $\Gamma_{c,D} = \Gamma_{c,\gamma\gamma}$ ) vertices respectively. The bare couplings are taken to be  $\Gamma_{c,X}^0 = 0.1$ ,  $\Gamma_{c,D}^0 = 0.5$ , and we consider a momentum-space grid of size  $1024 \times 1024$ . As observed in Fig.6.2.21, both off-diagonal and diagonal couplings renormalize to higher magnitudes at the low-energy RG fixed point, such that the resulting theory is described by eq.(6.72). The

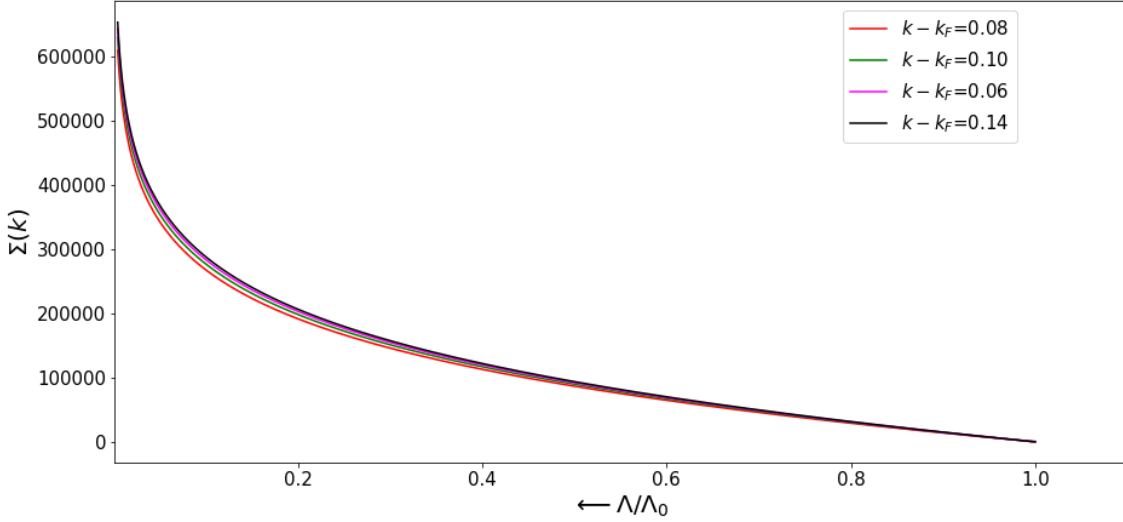


Figure 6.2.22: RG flow of the self-energy  $\Sigma(k)$  for  $k$  (eqs.(6.12)) wave-vectors close to Fermi surface.

associated hybridized pseudospin state space also involves fermion states pairing up in the mixed configuration regime (discussion above in eq.(6.21)), such that the fermionic states transmute into the mixed pseudospin states. The condensation of pseudospins due to the nesting instability leads to a zero of the Greens function,  $G(k, \Delta) = (\Delta - \epsilon_k - \Sigma_k)^{-1}$  (note the similarity with the zero of  $G(k, \Delta)$  for the BCS instability in eq.(6.33)), as can be seen from the divergent self-energy in Fig.6.2.22 as the Fermi surface is approached. The net Friedel phase-shift accounts for the number of mixed pseudospins, as well as the number of bound states formed via the RG. This can be computed through the Luttinger surface of zeros (see discussion below eq.(6.33)). This pseudospin Hilbert space will persist upto a temperature scale  $T^*$  (eq.(2.29)) computed using the renormalized 1-particle self-energy at the fixed point. Finally, we note that the tensor network representation of the RG flows towards the Mott liquid fixed point is similar to that presented in Fig.(6.2.15) for the BCS reduced Hamiltonian displaying pair formation.

### 6.2.6 RG Phase diagram for $H_{SFIM}$

Having numerically verified the RG flows to various IR fixed point theories, we can now gather all our results into the form of a RG phase diagram. In order to characterize efficiently various phases obtained from the RG flows for  $H_{SFIM}$ , we define the following two quantities  $r_2$  and  $r_3$

$$\begin{aligned} r_2 &= sgn(V_{\mathbf{k}, \mathbf{k}', \mathbf{p}}^{\sigma \sigma'}) \sqrt{\frac{\sum_{\alpha \neq \beta} \Gamma_{\alpha \beta}^{4,(N)} \Gamma_{\alpha \beta}^{4,(N)}}{\sum_{\alpha \neq \beta} \Gamma_{\alpha \beta}^{4,(N)} \Gamma_{\alpha \beta}^{4,(N)} + \sum_{\alpha} \Gamma_{\alpha \alpha}^{4,(N)} \Gamma_{\alpha \alpha}^{4,(N)}}}, \\ r_3 &= \sqrt{\frac{\sum_{\gamma \gamma'} \Gamma_{\gamma \gamma'}^{6,(N-1)} \Gamma_{\gamma \gamma'}^{6,(N-1)}}{\sum_{\gamma} \Gamma_{\gamma \gamma'}^{6,(N-1)} \Gamma_{\gamma \gamma'}^{6,(N-1)} + \sum_{\alpha \beta} \Gamma_{\alpha \beta}^{6,(N-1)} \Gamma_{\alpha \beta}^{6,(N-1)}}}. \end{aligned} \quad (6.73)$$

The quantity  $-1 < r_2 < 1$  represent the ratio of (i) the root mean square magnitude (RMS) for bare 4-point off-diagonal (OD) vertices, and (ii) the sum of the mean squares of 4-point diagonal (D) and OD vertices. Thus,  $r_2$  carries the  $(+/-)$  sign for OD terms representing attractive/repulsive interactions respectively. Similarly, the quantity  $0 \leq r_3 \leq 1$  is the ratio of (i) the RMS for 6-point D vertices, and (ii) the square root sum of the mean squares of 6-point D and OD vertices. Recall that the index  $\alpha$  represents a set of two (momentum, spin) indices for 2-particle vertices ( $\Gamma^2$ ) and a set of three (momentum, spin) indices for 3-particle vertices ( $\Gamma^3$ ). We show below that the parameters  $r_2$  and  $r_3$  allow for an efficient encoding of the numerically evaluated RG flows shown earlier at various points.

Fig.(6.2.23) presents the RG phase diagram for  $H_{SFIM}$  using  $\omega$  (quantum fluctuations, y-axis) and  $(r_2, r_3)$  (x-axis). For attractive couplings ( $r_2 < 0$ ) and for  $(\omega < \frac{W}{2})/(\omega > \frac{W}{2})$ , the unfilled circles and squares represent crossover RG flows involving a XXZ symmetry-unbroken reduced BCS (eq.(6.39)) theory for  $\mathbf{p} = 0$  (Fig.6.2.11) and  $\mathbf{p} \neq 0$  pairs (Fig.6.2.13) respectively. The RG flows stop at stable fixed points (red stars/orange hexagons) given by symmetry unbroken XY BCS (eq.(6.34), Figs.6.2.9 and 6.2.10) and PDW (eq.(6.42), Fig.6.2.12) theories respectively. The red squares ( $r_2 = r_3 = 0$ ) are unstable fixed points representing a tight-binding metal. In the repulsive regime  $r_2 \rightarrow 0, r_3 > 0$  and  $\omega < \frac{W}{2}$ , the unfilled diamond are crossover RG flows to three-particle theories with diagonal and off-diagonal terms. The blue circles are stable points representing the marginal Fermi liquid metal (eq.(6.57), Figs.6.2.16 - 6.2.19).

On the other hand, the Mott metal-insulator transition shown in the repulsive regime  $r_2 + r_3 > 0$  and  $\omega > \frac{W}{2}$  is more complicated, due to the appearance of unstable fixed points (red circles) lying at intermediate coupling. These unstable fixed points separate RG flows (unfilled pentagons) to Fermi liquid theories (green triangles, eq.(6.28), Figs.6.2.4 - 6.2.6) with  $r_2 \rightarrow 0, r_3 \rightarrow 0$  from those (yellow pentagons) towards XXZ pseudospin Mott liquids theories with finite values of  $r_2$  and  $r_3$  (magenta pentagons, eq.(6.72), Figs.6.2.21 and 6.2.22). As described in the previous subsection, the physics of nesting is responsible for the stabilisation of such Mott liquids. We recall that a recent RG analysis the half-filled 2D Hubbard model on the square lattice (whose underlying tight-binding Fermi surface is strongly nested) in Ref.[180] identified the marginal Fermi liquid as being the parent metallic phase of the Mott liquid found therein. This leads us to conjecture that the unstable fixed point (red circles) gapless quantum critical theories lying at intermediate coupling correspond to a marginal Fermi liquid theory described by eq.(6.57).

### 6.2.7 Scaling features of holographic entanglement entropy bound for gapless and gapped quantum liquids

In this section, we analyze the RG scaling relations for the holographic entanglement entropy bound for the various phases of the  $H_{SFIM}$  model obtained by isolating a given region  $R$ . Among the IR fixed points, the gapless theories reached via URG comprise the number-diagonal Hamiltonians for the Fermi liquid (eq.(6.28)) and Marginal Fermi liquid phases (eq.(6.57)). For these cases, the ground state wavefunction obtained from the above low-energy Hamiltonians are separable in momentum-space. On the other hand, the gapped IR fixed point theories involve effective Hamiltonians that are number off-diagonal in momentum-space, e.g., the reduced BCS theory (eq.(6.34)) and the Mott liquid (eq.(6.72)). Clearly, the ground states obtained from the latter low-energy effective Hamiltonians are highly entangled. As the scattering vertex and

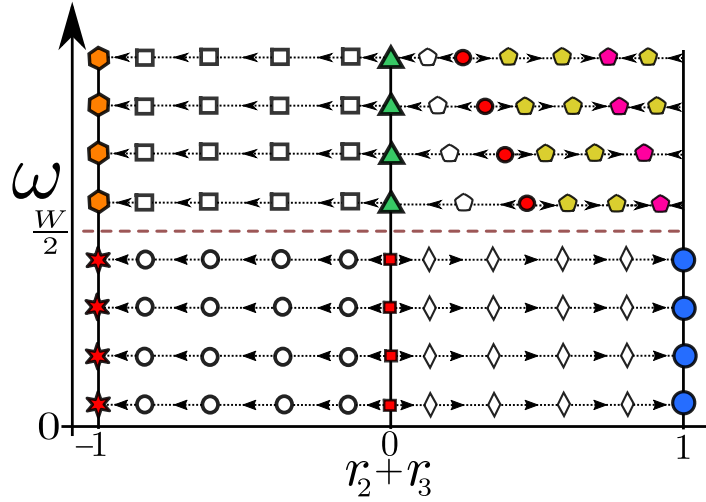


Figure 6.2.23: RG phase diagram for the single-band model of interacting electrons with translational invariance,  $H_{SFIM}$ . The y-axis represents the magnitude for quantum fluctuations ( $\omega$ ),  $W$  represents the bandwidth. The x-axis represents interaction due to two-particle ( $r_2$ ) and three-particle ( $r_3$ ) number diagonal/off-diagonal scattering processes.  $-1 < r_2 < 1$  with (+/-) sign representing nature of interaction, while  $0 < r_3 < 1$  (see text for detailed definitions). The magnitudes of  $r_2$  and  $r_3$  represent the relative magnitude of off-diagonal scattering in 2-particle and 3-particle scattering processes respectively. The red squares on line  $r_2 = r_3 = 0$  correspond to tight-binding metals. The unfilled squares and circles represent crossover RG flows involving symmetry unbroken  $\mathbf{p} \neq 0$  (SPDW)/ $\mathbf{p} = 0$  (RBCS) gapped XXZ pseudospin theories respectively. These flows end at orange hexagon/red stars labelling corresponding stable fixed points with  $XY$  pseudospin interaction. Unstable fixed points (red circles) lie between Ising- (unfilled pentagons) and  $XY$ - (yellow pentagons) dominated XXZ pseudospin Mott liquid theories arising out of charge and spin backscattering. The unfilled pentagons are crossover RG flows to the stable fixed point Fermi liquid (green triangles), while the yellow pentagons are crossovers to XXZ pseudospin gapped stable theories (magenta pentagons). Blue circles represent the marginal Fermi liquid theories residing at the end point of crossover RG flows involving dominant three-particle scattering (unfilled diamonds).

wavefunction RG flows are distinct for various phases, we expect that the same will hold true for their holographic entanglement entropy scaling relations (eq.(6.9)). Investigating this point is the content of this subsection.

The entanglement entropy scaling in the regime (eq.(6.26)) leading to the Fermi liquid (eq.(6.28)) has the form (using eq.(8.5.4))

$$\Delta S_{(j)}^1 = 2 \sum_{\alpha_1, \mu, \nu, \nu'} sgn(\mu, \nu, \nu') \Delta \Gamma_{\mu\nu}^{4,(j)} G_{\nu\nu'}^{4,(j)} C_{\nu'}^{(j)} C_{\alpha_1}^{0,(j)}. \quad (6.74)$$

Note that in arriving at this RG equation, we have restricted ourselves to the contributions from only 4-point ( $\Delta \Gamma_{\mu\nu}^{4,(j)}$ ) vertex RG flows (eq.(6.17)). Further, we assume a uniform magnitude for the diagonal and off-diagonal couplings:  $\Gamma_{\mu\nu}^{4,(j)} G_{0,(j)} = V$ ,  $\Gamma_{\mu\nu}^{4,(j)} + c = \Gamma_{\mu\mu}^{4,(j)}$  ( $c$  is a constant) and

$G_{0,(j)}^{-1} = \omega - \epsilon_{(j)}$ . This leads to the continuum RG equation for the scattering vertex

$$\frac{dV}{d \log \frac{\Lambda}{\Lambda_0}} = V(\omega G_{0,\Lambda} - 1) + \frac{V^2}{1 - cG_{0,\Lambda} - V}, \quad (6.75)$$

where  $G_{0,\Lambda}^{-1} = \omega - \hbar v_F \Lambda$ , we have assumed a spherical Fermi surface  $\epsilon_{\Lambda,j} = \hbar v_F \Lambda$ , and we have replaced the finite difference  $\Delta(\log \frac{\Lambda}{\Lambda_0})$  by the differential quantity  $d \log \frac{\Lambda}{\Lambda_0}$ . For  $cG_{0,\Lambda} > 1$ , the off-diagonal vertices are RG irrelevant ( $dV < 0$ ) as  $\Lambda \rightarrow 0$

$$\frac{dV}{d \log \Lambda / \Lambda_0} = -\frac{\omega V^2}{c - \omega} \Rightarrow V(\Lambda) = \frac{V_0}{1 + \frac{\omega}{c-\omega} V_0 \log \frac{\Lambda_0}{\Lambda}} \approx \frac{c - \omega}{\omega} \frac{1}{\log \frac{\Lambda_0}{\Lambda}}. \quad (6.76)$$

In reaching eq.(6.76) from eq.(6.75), we have dropped the first term of eq.(6.75), as  $(\omega G_{0,\Lambda} - 1) \rightarrow 0$  as  $\Lambda \rightarrow 0$ . We have also dropped  $V$  in the denominator of the second term of eq.(6.75), as  $V \rightarrow 0$  and  $G_{0,\Lambda} \rightarrow \frac{1}{\omega}$ . The RG relation for the entanglement entropy bound of the FL then has the form

$$\frac{dS^1(\Lambda)}{d \log \frac{\Lambda}{\Lambda_0}} = 2 \left( \frac{c - \omega}{\omega} \right)^2 \sum_{\alpha_1, \mu, \nu, \nu'} \frac{\text{sgn}(\mu, \nu, \nu')}{\left( \log \frac{\Lambda_0}{\Lambda} \right)^2} C_{\nu'}^{(j)} C_{\alpha_1}^{0,(j)}. \quad (6.77)$$

As we approach the Fermi surface, the coefficient tensor  $C_{\alpha_1}^{0,(j)}$  (corresponding to the ground state configuration  $|\alpha\rangle$ ) scale towards 1, while all other coefficients scale towards 0. As a result, the fermion signatures for the RG scaling towards the ground state vanish. Taking these points into account, we find that the entropy scaling relation is given by

$$S^1(\Lambda) = \left( \frac{c - \omega}{\omega} \right)^2 \frac{1}{\log \frac{\Lambda_0}{\Lambda}}. \quad (6.78)$$

Finally, we obtain the holographic entanglement entropy bound obtained by *isolating the Fermi surface (in two dimensions)* from the rest of the system is given by

$$S_H(\Lambda) = 2\pi k_F \left( \frac{c - \omega}{\omega} \right)^2 \frac{1}{\log \frac{\Lambda_0}{\Lambda}}. \quad (6.79)$$

For the MFL and reduced BCS theories, the entanglement entropy RG equations are given respectively by

$$\Delta S^{MFL} = 2 \sum_{\alpha_1, \mu, \nu, \nu'} \text{sgn}(\mu, \nu, \nu') \Delta \Gamma_{\mu\nu}^{6,(j)} G_{\nu\nu'}^{6,(j)} C_{\nu'}^{(j)} C_{\alpha_1}^{0,(j)}, \quad (6.80)$$

$$\Delta S^{RBCS} = 2 \sum_{\alpha_1, \mu, \nu, \nu'} \Delta \Gamma_{\mu\nu}^{4,(j)} G_{\nu\nu'}^{4,(j)} C_{\nu'}^{(j)} C_{\alpha_1}^{0,(j)}. \quad (6.81)$$

In the MFL, the renormalization is carried out primarily by six-point vertices as the quasiparticle degrees of freedom are ill-defined (eq. (6.62)). On the other hand, for the reduced BCS theory, the dominant two particle vertex RG flow is present in the zero pair-momentum subspace

(eq.(6.36)). This leads to condensation of the pairs, and the fermion exchange phases are mitigated in the coefficient RG equations [182]. As a result, the fermion exchange phases are also absent in the entanglement scaling relation of the RBCS phase (eq.(6.81)). These deviations in the entanglement RG equations for the MFL (eq.(6.80)) and the RBCS (eq.(6.81)) phases from that obtained for the FL (eq.(6.79)) will likely to lead to a deviation of entropy bound scaling relations of these phases as well. Finally, the Mott liquid phase is described by pseudospins (eq.(6.72)) analogous to the RBCS phase, implying similar conclusions for the Mott liquid. We leave a detailed study of this aspect to a future work.

### 6.3 Gauge theories and Topological order for emergent gapped quantum liquids

In Ref.[258], Hansson et al. show that a  $U(1)$  symmetry broken superconductor possesses signatures of topological order upon coupling to a dynamical electromagnetic field, i.e., it supports ground state degeneracy on the torus, edge states, charge fractionalization, together with a many-body gap that protects these properties. Importantly, the quantum fluctuations of the combined system restores the broken  $U(1)$  phase rotation symmetry of the Cooper pair condensate. In this section, we adopt a different route in unveiling the universal features of topological order for a wide variety of gapped symmetry-preserved quantum liquid ground states arising from electronic correlations. For this, we start with the effective Hamiltonians obtained from RG fixed points which are written in terms of pseudospins. Indeed, we recall that such effective Hamiltonians describe pseudospin dynamics constitute a network of four point vertex tensors  $\Gamma_{\alpha\beta}^{4,*}$ , i.e., a Hamiltonian tensor network. The idea is to rewrite such a network of pseudospins in terms of dual nonlocal objects, i.e. Wilson lines, leading to the formulation of a gauge theory. We will show that, for a simple case, such a gauge theory shows well-known signatures of topological order. The condensates we are concerned with arise from parent metallic systems with a connected Fermi surface (FS). The destabilization of the FS and its neighbourhood due to pseudospin-flip scattering processes (eq.(6.36)) leading to a many-body gap in the 1-particle spectrum, signaling the condensation phenomenon within a momentum-space shell  $\Lambda_{\hat{s}}^*$  around the erstwhile FS. The pseudospin condensate is now part of an emergent  $SU(2)^{\otimes N}$  Hilbert space that originated from the electronic Fock space  $\mathcal{F}^N$ . Below, we consider the XXZ reduced BCS Hamiltonian  $H_{RBCS}^{*,XXZ}$  (eq.(6.39)) as an example in order to demonstrate the origin and signatures of topological order. As shown in Fig.(6.3.1), we notice that the geometry of the 2D momentum-space shell in the pseudospin basis for the zero-pair momentum ( $\mathbf{p} = 0$ ) states with periodic boundary condition (PBC) is topologically equivalent to a torus. Now, the inter-pseudospin interaction terms in the reduced BCS Hamiltonian  $H_{RBCS}^{*,XXZ}$  (eq.(6.39)) can be represented as a Wilson line (dark black line in Fig. (6.3.1)) as follows

$$4A_{\Lambda,\hat{s}}^o A_{\Lambda',\hat{s}'}^o = \exp(i\pi(A_{\Lambda,\hat{s}}^o - A_{\Lambda',\hat{s}'}^o)), \quad (6.82)$$

where we have rewritten the pseudospin operator  $A_{\mathbf{k}_{\Lambda},\hat{s}}^o$  as  $A_{\Lambda,\hat{s}}^o$  for  $o = (x, y, z)$ ,  $\Lambda' = \Lambda + n'\delta\Lambda$ ,  $\delta\Lambda = 2\pi L^{-1}$  and  $\hat{s}' = R^{m'}\hat{s}$ . This Wilson line can in turn be represented as a composition of local Wilson lines (green lines with arrows in Fig.(6.3.1)) along the  $\hat{s}_\perp$  axes (i.e.,  $\hat{s}_\perp$  is perpendicular to  $\hat{s}$ , and along the direction of the hatched blue line in Fig.(6.3.1)) and the  $\hat{s}$  axes (along the

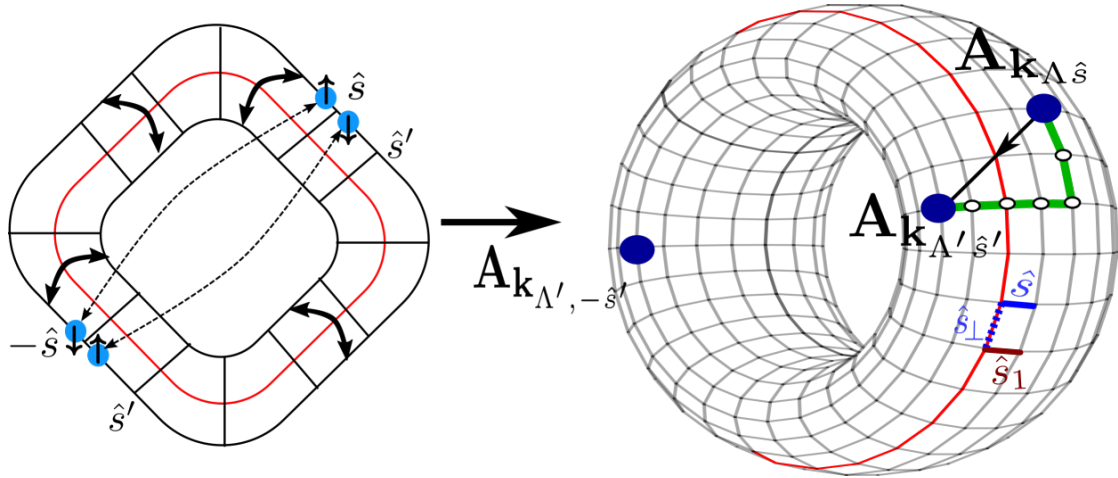


Figure 6.3.1: (Left) Emergent momentum-space window where pairs of electronic states with opposite-spin and net-momentum  $\mathbf{p} = 0$  form bound pairs (dashed double-headed arrows). Thick double-headed arrows indicate the imposition of periodic boundary conditions, and the red curve represents the Fermi surface. (Right) Anderson pseudospins  $\mathbf{A}_{\mathbf{k}_{\Lambda}\hat{s}}$  living on a torus. A composition of local green lines (a Wilson line) represents the inter-pseudospin interaction. Blue dashed/solid line represents the reference pair of orthonormal Wilson lines located on Fermi surface (and along  $\hat{s}_{\perp}$ )/normal to the Fermi surface (and along  $\hat{s} = \hat{x}$ ). The brown line represents the rotated normal direction  $\hat{s}_1$ .

direction of the solid blue line in Fig.(6.3.1))

$$4A_{\Lambda,\hat{s}}^o A_{\Lambda',\hat{s}'}^o = W_{\Lambda,\hat{s} \rightarrow R\hat{s}}^o W_{\Lambda,R\hat{s} \rightarrow R^2\hat{s}}^o \dots W_{\Lambda,R^{m'-1}\hat{s} \rightarrow \hat{s}'}^o \\ \times W_{\Lambda \rightarrow \Lambda + \delta\Lambda,\hat{s}'}^o \dots W_{\Lambda + (n'-1)\delta\Lambda \rightarrow \Lambda'\hat{s}'}^o, \quad (6.83)$$

where  $W_{\Lambda,\hat{s} \rightarrow \hat{s}_1}^o = \exp(i\pi(A_{\Lambda,\hat{s}}^o - A_{\Lambda,\hat{s}_1}^o))$  ( $\hat{s}_1$  is the rotated normal Fig.6.3.1) is the local Wilson line along  $\hat{s}_{\perp}$ , and  $W_{\Lambda \rightarrow \Lambda + \delta\Lambda,\hat{s}}^o = \exp(i\pi(A_{\Lambda + \delta\Lambda,\hat{s}}^o - A_{\Lambda,\hat{s}}^o))$  represents the Wilson line for translation by  $\delta\Lambda$  along  $\hat{s}$ . Here,  $R\hat{x} = -\sin\theta\hat{x} + \cos\theta\hat{y}$  is the smallest  $\delta$  rotation of the  $\hat{x}$  vector normal to the FS. We adopt the gauge choice of first multiplying all Wilson lines along one direction, and then multiply the result obtained with the Wilson lines along the perpendicular direction. All other paths with the end points fixed are equivalent gauge choices, such that the net Wilson line is path independent.

We will now define two sets of generalized translation and twist operators for the  $\hat{s}$  and  $\hat{s}_{\perp}$  directions [40, 41] in the center of mass position and momentum spaces in representing the above Wilson lines

$$\mathcal{T}_{\hat{s}_{\perp}} : A_{\Lambda,\hat{s}}^o \rightarrow A_{\Lambda,R\hat{s}}^o, \quad (6.84)$$

$$\mathcal{T}_{\hat{s}} : A_{\Lambda,\hat{s}}^o \rightarrow A_{\Lambda + \delta\Lambda,\hat{s}}^o, \quad (6.85)$$

$$\hat{O}_{\Lambda}^o = \exp \left[ \frac{\pi}{2} i \sum_{n=0}^{N-1} n A_{\Lambda,R^n\hat{s}}^o \right], \quad (6.86)$$

$$\hat{O}_{\hat{s}'}^o = \exp \left[ \frac{\pi}{2} i \sum_{n=0}^{N-1} n A_{n\delta\Lambda,\hat{s}'}^o \right]. \quad (6.87)$$

The local Wilson lines along a reference pair of directions  $\hat{s}, \hat{s}_\perp = \hat{x}, -\hat{y}$  (blue hatched/solid line in Fig.6.3.1) can then be translated to any orthogonal pairs of Wilson lines as follows

$$\begin{aligned} & \text{Wilson line along } \hat{s}_\perp : \\ & \mathcal{T}_{\hat{s}_\perp}^m \mathcal{T}_{\hat{x}}^n (A_{\mathbf{k}_F, \hat{x}}^o - A_{\mathbf{k}_F, R\hat{x}}^o) \mathcal{T}_{\hat{x}}^{\dagger n} \mathcal{T}_{\hat{s}_\perp}^{\dagger m} = A_{\Lambda, \hat{s}}^o - A_{\Lambda, R\hat{s}}^o, \\ & \mathcal{T}_{\hat{s}_\perp}^m \mathcal{T}_{\hat{x}}^n W_{F, \hat{x} \rightarrow R\hat{x}}^o \mathcal{T}_{\hat{x}}^{\dagger n} \mathcal{T}_{\hat{s}_\perp}^{\dagger m} = W_{\Lambda, \hat{s} \rightarrow R\hat{s}}^o, \end{aligned} \quad (6.88)$$

*Wilson line along  $\hat{s}$  :*

$$\begin{aligned} & \mathcal{T}_{\hat{s}_\perp}^m \mathcal{T}_{\hat{x}}^n (A_{\mathbf{k}_F, \hat{x}}^o - A_{\mathbf{k}_{F+\delta k_F}, \hat{x}}^o) \mathcal{T}_{\hat{x}}^{\dagger n} \mathcal{T}_{\hat{s}_\perp}^{\dagger m} = A_{\Lambda, \hat{s}}^o - A_{\Lambda+\delta\Lambda, \hat{s}}^o, \\ & \mathcal{T}_{\hat{s}_\perp, \hat{s}}^m \mathcal{T}_{\hat{x}, \Lambda}^n W_{0 \rightarrow \delta\Lambda, \hat{x}}^o \mathcal{T}_{\hat{x}, \Lambda}^{\dagger n} \mathcal{T}_{\hat{s}_\perp, \hat{s}}^{\dagger m} = W_{\Lambda \rightarrow \Lambda+\delta\Lambda, \hat{s}}^o, \end{aligned} \quad (6.89)$$

where the number of pseudospins is taken to be  $N = 2(2k+1)$ . The Wilson lines ( $W_{F, \hat{x} \rightarrow R\hat{x}}^o, W_{0 \rightarrow \delta\Lambda, \hat{x}}^o$ ) in eq.(6.88),eq(6.89) are the momentum-space projections of the Wilson loop defined in the center of mass position-momentum space for the major axis (along  $\hat{s}_\perp$ ) and minor axis (along  $\hat{s}$ ) of the torus

$$\mathcal{T}_{\hat{s}_\perp}^2 \hat{O}_{\Lambda=0}^o \mathcal{T}_{\hat{s}_\perp}^{2\dagger} \hat{O}_{\Lambda=0}^{o\dagger} = 2^{4k+2} W_{F, \hat{x} \rightarrow R\hat{x}}^o W_F, \quad (6.90)$$

$$\mathcal{T}_{\hat{s}}^2 \hat{O}_{\hat{s}}^o \mathcal{T}_{\hat{s}}^{2\dagger} \hat{O}_{\hat{s}}^{o\dagger} = 2^{4k+2} W_{0 \rightarrow \delta\Lambda, \hat{x}}^o W_{\hat{x}}, \quad (6.91)$$

and where  $W_F = \prod_{m=0}^{N-1} A_{\mathbf{k}_F, R^m \hat{x}}^o$  and  $W_{\hat{x}} = \prod_{n=0}^{N-1} A_{n\delta\Lambda, \hat{x}}^o$  are Wilson loops for the minor and major axis of the torus along the reference directions (solid blue/hatched lines). The interaction terms  $A_{\Lambda, \hat{s}}^o A_{\Lambda', \hat{s}'}^o$  can now be represented as the momentum-space projections of the product of translated Wilson loops as follows

$$\begin{aligned} 4A_{\Lambda, \hat{s}}^o A_{\Lambda', \hat{s}'}^o &= \prod_{j_1=m, j_2=n}^{m', n'} (\mathcal{T}_{\hat{x}})^{j_1} (\mathcal{T}_{\hat{s}_\perp})^{j_2} W_{F, \hat{x} \rightarrow R\hat{x}}^o W_{0 \rightarrow \delta\Lambda, \hat{x}}^o \\ &\times [(\mathcal{T}_{\hat{x}})^{j_1} (\mathcal{T}_{\hat{s}_\perp})^{j_2}]^\dagger. \end{aligned} \quad (6.92)$$

The reduced BCS Hamiltonian can in turn be written as a  $U(1)$  gauge theory in terms of non-local Wilson loops

$$\begin{aligned} H_{RBCS}^{*, XXZ}(\omega) &= \sum_{\mathbf{k}} \epsilon_{\mathbf{k}\Lambda\hat{s}}^{(j^*)} \ln(W \mathcal{T}_{\hat{s}_\perp, \hat{s}} \mathcal{T}_{\hat{x}, \Lambda} \mathcal{T}_{\hat{s}_\perp} \hat{O}_{\hat{s}_\perp, 0}^z \mathcal{T}_{\hat{s}_\perp}^\dagger \hat{O}_{\hat{s}_\perp, 0}^{z\dagger} [\mathcal{T}_{\hat{s}_\perp, \hat{s}} \mathcal{T}_{\hat{x}, \Lambda}]^\dagger) \\ &- \frac{1}{4} \sum_{\mathbf{k}\Lambda\hat{s}} \Gamma_{\alpha\beta}^{4, (j^*)} \left[ \sum_{o=x, y} \prod_{j_1=m, j_2=n}^{m', n'} (\mathcal{T}_{\hat{x}})^{j_1} (\mathcal{T}_{\hat{s}_\perp})^{j_2} W_{F, \hat{x} \rightarrow R\hat{x}}^o W_{0 \rightarrow \delta\Lambda, \hat{x}}^o [(\mathcal{T}_{\hat{x}})^{j_1} (\mathcal{T}_{\hat{s}_\perp})^{j_2}]^\dagger \right] \\ &+ \frac{1}{4} \Gamma_{\alpha\alpha'}^{4, (j^*), ||} \left[ \prod_{j_1=m, j_2=n}^{m', n'} (\mathcal{T}_{\hat{x}})^{j_1} (\mathcal{T}_{\hat{s}_\perp})^{j_2} W_{F, \hat{x} \rightarrow R\hat{x}}^z W_{0 \rightarrow \delta\Lambda, \hat{x}}^z [(\mathcal{T}_{\hat{x}})^{j_1} (\mathcal{T}_{\hat{s}_\perp})^{j_2}]^\dagger \right]. \end{aligned} \quad (6.93)$$

The above Hamiltonian commutes with the global Wilson loop given by

$$W = \prod_{n=0}^{N-1} W_{n\delta\Lambda}^z, \quad [H_{(j^*), XXZ}^{RBCS}(\omega), W] = 0, \quad (6.94)$$

where  $W_{n\delta\Lambda} = \mathcal{T}_{\hat{x}}^n W_F \mathcal{T}_{\hat{x}}^{\dagger n}$  is a Wilson loop obtained by translating  $W_F$  by  $n$  units. Remarkably, the Wilson loop  $W$  (eq.(6.94)) is an emergent topological invariant for the *Luttinger zero patch* at the RG fixed point, seen from the Friedel's phase shift that takes accounts of the total number of bound states in the emergent window

$$\Delta N = -\frac{i}{\pi} \ln W . \quad (6.95)$$

We will now present a simpler version of the above gauge theory for the case of the effective Hamiltonian  $H_{RBCS}^{*,XXZ}$  with the couplings  $\Gamma_{\alpha\beta}^{4,(j*)} = J_{\perp}$  and  $\Gamma_{\alpha\alpha'}^{4,(j*),||} = J_{||}$ . Our goal is to write once more the effective Hamiltonian in terms of nonlocal Wilson loop operators. For this, we first we write  $H_{RBCS}^{*,XXZ}$  in terms of collective pseudospin operators

$$H_{RBCS}^{*,XXZ} = -J_{\perp}(A_x^2 + A_y^2) + J_{||}A_z^2 , \quad (6.96)$$

where  $A_o = \sum_{n,m} A_{m\delta\Lambda,R^n\hat{s}}^o$  represent the various components of the collective pseudospin vector. We now define nonlocal versions of the twist operators in the space of pseudospins

$$\hat{O}_{\hat{s}}^o = \prod_{n=0}^{N-1} (\hat{O}_{R^n\hat{s}}^o)^{\frac{4}{N}} = \exp \left[ \frac{2\pi i}{N} \sum_{n=0}^{N-1} m A_{m\delta\Lambda,R^n\hat{s}}^o \right] . \quad (6.97)$$

The collective pseudospin vectors can be written in terms of nonlocal twist ( $\hat{O}_{\hat{s}}^o$ ) and translation ( $T_{\hat{s}}$ ) operators. To show this, we obtain the following identity for the nonlocal Wilson loop composed of twist and translation operators

$$\mathcal{T}_{\hat{s}} \hat{O}_{\hat{s}}^o \mathcal{T}_{\hat{s}}^\dagger \hat{O}_{\hat{s}}^{o\dagger} = \exp \left[ \frac{2\pi i}{N} \sum_{\substack{n=0 \\ m=0}}^{N-1} A_{m\Lambda,R^n\hat{s}}^o \right] \exp \left[ 2\pi i \sum_{n=0}^{N-1} A_{\Lambda=0,R^n\hat{s}}^o \right] . \quad (6.98)$$

For every normal vector  $\hat{s}$ , there exists a opposite normal vector  $-\hat{s}$ , such that the total number of pseudospins ( $N$ ) is even. Therefore, the overall phase collected from the strip along one of the minor circles of the torus is trivial:

$$\exp \left[ 2\pi i \sum_{n=0}^{N-1} A_{\Lambda=0,R^n\hat{s}}^o \right] = 1 . \quad (6.99)$$

Thus, the collective pseudospin components  $A_o$  can be represented by a nonlocal Wilson loop

$$A_o = \frac{N}{2\pi i} \log \left[ \mathcal{T}_{\hat{s}} \hat{O}_{\hat{s}}^o \mathcal{T}_{\hat{s}}^\dagger \hat{O}_{\hat{s}}^{o\dagger} \right] . \quad (6.100)$$

This enables us to write the Hamiltonian eq.(6.96) as

$$\begin{aligned} H_{RBCS}^{*,XXZ} &= J_{\perp} \frac{N^2}{4\pi^2} \left( \log \left[ \mathcal{T}_{\hat{s}} \hat{O}_{\hat{s}}^x \mathcal{T}_{\hat{s}}^\dagger \hat{O}_{\hat{s}}^{x\dagger} \right] \right)^2 + J_{\perp} \frac{N^2}{4\pi^2} \left( \log \left[ \mathcal{T}_{\hat{s}} \hat{O}_{\hat{s}}^y \mathcal{T}_{\hat{s}}^\dagger \hat{O}_{\hat{s}}^{y\dagger} \right] \right)^2 \\ &- J_{||} \frac{N^2}{4\pi^2} \left( \log \left[ \mathcal{T}_{\hat{s}} \hat{O}_{\hat{s}}^z \mathcal{T}_{\hat{s}}^\dagger \hat{O}_{\hat{s}}^{z\dagger} \right] \right)^2 . \end{aligned} \quad (6.101)$$

We will now display certain features of topological order for this emergent gauge theory, e.g., ground state degeneracy and charge fractionalisation. Note that the transformations carried out by  $T_{\hat{s}}$  eq(6.85) impart equal and opposite momentum to opposite spin electrons,  $\mathbf{k}_{\Lambda,\hat{s}}, \uparrow \rightarrow \mathbf{k}_{\Lambda+\delta\Lambda,\hat{s}}, \uparrow$  and  $\mathbf{k}_{\Lambda,-\hat{s}}, \downarrow \rightarrow \mathbf{k}_{\Lambda+\delta\Lambda,-\hat{s}}, \downarrow$ , such that there is no net pair momentum  $\mathbf{p} = 0$ . This observation supports the following representation of  $T_{\hat{s}}$  in the position basis

$$\mathcal{T}_{\hat{s}} = \exp \left[ \frac{2\pi i}{2N} \sum_{\mathbf{r}} \mathbf{r} \cdot \hat{s} (\hat{n}_{\mathbf{r}\uparrow} - \hat{n}_{\mathbf{r}\downarrow}) \right], \quad (6.102)$$

where the spacing in the momentum along  $\hat{s}$  is  $\delta\Lambda = \frac{2\pi}{N}$ . A degeneracy of the ground state manifold can show up in its nontrivial topology. Below we probe this using spectral flow arguments that originated with the work of Lieb, Schultz and Mattis [86], and more recently extended to higher dimensions [522, 516, 523, 40, 41, 524, 525, 185]. Initially, we compute the action of the twist operator  $\mathcal{T}_{\hat{s}}$  on an eigenstate of  $H_{RBCS}^{*,XXZ}$  ( $|\Psi\rangle$ )

$$\begin{aligned} \langle \Psi | T_{\hat{x}}^\dagger \mathcal{T}_{\hat{s}} T_{\hat{x}} | \Psi \rangle &= \exp \left[ \frac{2\pi i}{N} \sum_{\mathbf{r}} S_{\mathbf{r}}^z \right] \exp \left[ 2\pi i \sum_{\mathbf{r} \cdot \hat{s}_\perp} S_{\mathbf{r} \cdot \hat{s}_\perp, \mathbf{r} \cdot \hat{x}}^z \right] \\ &\times \langle \Psi | \mathcal{T}_{\hat{s}} | \Psi \rangle. \end{aligned} \quad (6.103)$$

The Hamiltonian  $H_{RBCS}^{*,XXZ}$  commutes with  $S^z = \sum_{\mathbf{r}} S_{\mathbf{r}}^z$ , and its low-energy manifold is comprised of states  $|S = 2k+1, S^z = 0\rangle$  with net  $S^z = 0$ . Using the fact that the total number of pseudospins  $N = 2(2k+1) = L_x L_y$  (i.e.,  $L_x, L_y$  corresponds to the number of pseudospins along the  $x$  and  $y$  directions of the torus), the second exponential term in the above expression is simple:

$$e^{[2\pi i \sum_{\mathbf{r} \cdot \hat{s}_\perp} S_{\mathbf{r} \cdot \hat{s}_\perp, \mathbf{r} \cdot \hat{x}}^z]} = e^{2\pi(2k+1)\frac{1}{2}} = e^{i\pi}. \quad (6.104)$$

In this way, we obtain an equivalent of the LSM relation [86] for higher dimensions [516]. For this case,  $\langle \Psi | T_{\hat{x}}^\dagger \mathcal{T}_{\hat{s}} T_{\hat{x}} | \Psi \rangle = -\langle \Psi | \mathcal{T}_{\hat{s}} | \Psi \rangle$ , implying that the two states  $|\Psi\rangle$  and  $T_{\hat{x}}|\Psi\rangle$  are orthogonal. Finally the important relation

$$[H_{RBCS}^{*,XXZ}, \mathcal{T}_{\hat{s}}] = 0 \quad (6.105)$$

implies that the eigenstates of the twist operator  $\mathcal{T}_{\hat{s}}$  (corresponding to eigenstates of the center of mass momentum  $\mathbf{P}_{cm} = 0, \pi\hat{s}$ ) are simultaneously eigenstates of the Hamiltonian. Therefore, the two groundstates  $|\mathbf{P}_{cm} = 0, S = 2k+1, S^z = 0\rangle$  and  $|\mathbf{P}_{cm} = \pi\hat{s}, S = 2k+1, S^z = 0\rangle$ , both possessing ground state energy  $E_g = -J_\perp(2k+1)(2k+2)$ , are degenerate and protected from excitations via a many-body gap  $2J_\perp(2k+1)$ . The adiabatic passage between these degenerate ground states, achieved via the application of the twist operator  $\mathcal{T}_{\hat{s}}$ , involves the creation of a charge-1/2 excitation [462, 42, 22]. Additionally, we note that given the microscopic Hamiltonian  $[H_{SFIM}, \mathcal{T}_{\hat{s}}] \neq 0$ , the the commutation relation eq(6.105) for the low energy effective Hamiltonian  $H_{RBCS}^{*,XXZ}$  is emergent under RG flow.

Similar gauge theoretic constructions can be attained for the other gapped phases of  $H_{SFIM}$  in terms of the appropriate non-local Wilson loop operators (defined in terms of the respective pseudospin Hilbert spaces). On the other hand, for the gapless Fermi liquid (eq.(6.28)) of  $H_{SFIM}$ , only the first and last terms in eq.(6.93) appear. In this case, the equivalent of eq.(6.95) yields the Luttinger zeroes [88].

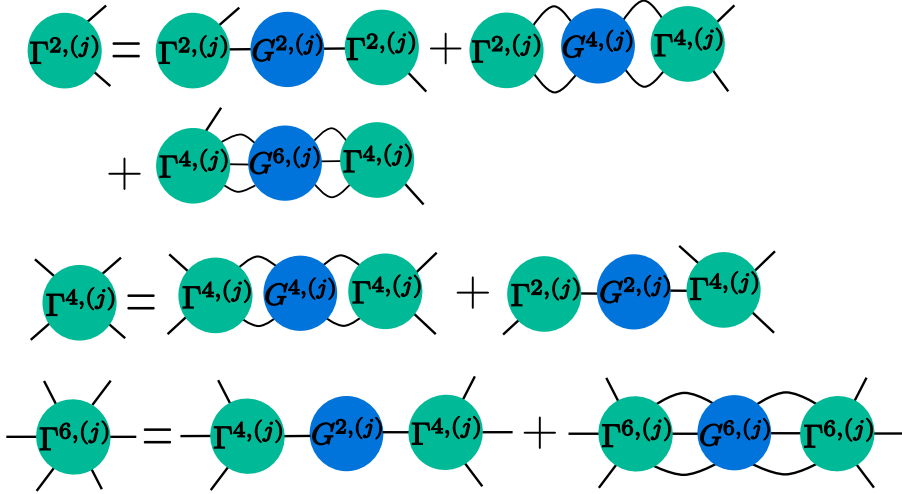


Figure 6.4.1: Schematic representation of RG flow equations for 2-point, 4-point and 6-point vertices. See text for discussion.

## 6.4 RG analysis of the generalized Sachdev-Ye<sub>4</sub> model

In order to understand the interplay between disorder and interactions in a model of correlated electrons [104], we consider a generalized electronic Sachdev-Ye(SY<sub>4</sub>) [283] model with random spin-independent hopping ( $t_{ij}$ ), random on-site potential ( $\epsilon_i$ ) and a random four-Fermi interaction ( $V_{ijkl}^{\sigma\sigma'}$ )

$$H_{SY_4} = \sum_{i \neq j, \sigma\sigma'} t_{ij} c_{i\sigma}^\dagger c_{j\sigma'} + \sum_{i\sigma} \epsilon_i \hat{n}_{i\sigma} + \sum_{ijkl, \sigma\sigma'} V_{ijkl}^{\sigma\sigma'} c_{i\sigma}^\dagger c_{j\sigma'}^\dagger c_{k\sigma'} c_{l\sigma}, \quad (6.106)$$

and place it on a  $D$  spatial-dimensional volume containing  $2N$  points and with a specified geometry. Here, the indices ranging  $i \in [1, 2N]$  ( $2N$  being number of points) correspond to the real-space position vectors  $\mathbf{r}_i$ . The terms  $V_{ijkl}^{\sigma\sigma'} = V_{klji}^{\sigma\sigma'*}$ ,  $t_{ji} = t_{ij}$  and  $\epsilon_{i\sigma}$  are random tensors drawn from separate Gaussian distributions, each with a well-defined mean and standard deviation. The single particle energies  $\epsilon_{i\sigma}$  can be sorted as follows

$$\epsilon_1 \leq \dots \leq \epsilon_N, \quad (6.107)$$

and employed for implementing the iterative steps of the unitary RG, (here *disorder bandwidth* is defined as  $W = \epsilon_N - \epsilon_1$ ).

The Hamiltonian RG flow equation is given by  $H_{(j-1)} = U_{(j)} H_{(j)} U_{(j)}^\dagger$ , where the unitary transformation  $U_{(j)}^\dagger = U_{(j\uparrow)}^\dagger U_{(j\downarrow)}^\dagger$ . From here, we can extract the hierarchy of 2-, 4- and 6-particle vertex flow equations given in eq.(2.47) and shown in Fig.(6.4.1). From the flow equations, we obtain the various parameter regimes belonging to the generalised SY<sub>4</sub> that lead, under RG, to models with emergent translational invariance (TI, e.g.,  $H_{SFIM}$  eq.(6)) as well as non-translationally invariant (NTI) models associated with the physics of *localization*. Having already presented a quantitative verification of the RG flows for various TI phases in the previous section, we will present only those for the NTI phases here.

For this, we first write the microscopic parameters as a sum of translational invariant (TI) and non-invariant (NTI) parts

$$t_{ik} = t(\mathbf{r}_i - \mathbf{r}_k) + t'_{ik}, \quad \epsilon_i = \epsilon + \epsilon'_i, \quad (6.108)$$

$$V_{ijkl}^{\sigma\sigma'} = V^{\sigma\sigma'}(\mathbf{r}_i - \mathbf{r}_j, \mathbf{r}_j - \mathbf{r}_k, \mathbf{r}_k - \mathbf{r}_l) + V'_{ijkl}^{\sigma\sigma'}, \quad (6.109)$$

$$V_{ik}^{\sigma\sigma'} = V^{\sigma\sigma'}(\mathbf{r}_i - \mathbf{r}_k) + V'_{ik}^{\sigma\sigma'}. \quad (6.110)$$

We note that a similar decomposition for the 2-point Green's function was carried out by Ishikawa and Matsuyama [526] for showing the preservation of the momentum-space Ward-Takahashi identity in the integer quantum Hall problem. By analyzing a class of fixed points of the RG flow equations presented in eq.(6.126) – eq.(6.133) (in Appendix 6.B) for the parameter regimes I-VI shown in Tables 6.4.1 and 6.4.2, we obtain fixed point Hamiltonians displayed in Table 6.4.3. We now discuss the physics of each of the 6 regimes in turn.

Regime I (green oval in Fig.6.4.13, Table 6.4.1) leads to a general TI Hamiltonian  $H_I$  (see Table 6.4.3) which, in the single band limit, is equivalent to the Hamiltonian  $H_{SFIM}$  (eq.(6)) considered in the previous section. To see this, we replace the real-space creation/annihilation operators in the fixed point theory by their Fourier transforms  $c_{\mathbf{k}\sigma}^\dagger = \sqrt{\text{Vol}^{-1}} \sum_{\mathbf{r}} e^{i\mathbf{k}\cdot\mathbf{r}} c_{\mathbf{r}\sigma}^\dagger$ . This generic TI model of interacting electrons is obtained in the regime of low randomness, i.e., the magnitude of the NTI parameters (with opposite signs for the hopping, and 4-fermi interactions) compared to their TI counterparts. Following our detailed RG analysis of  $H_{SFIM}$  in the previous section, we know that a non-Fermi liquid phase (blue circle in Fig.6.4.13) is obtained via a second level of the RG on  $H_{SFIM}$ , i.e.,  $H_{SY_4} \xrightarrow{RG} H_{SFIM} \xrightarrow{RG} \dots$  (eq.(6.57)). This non-Fermi liquid is characterized by a logarithmically dependent self-energy (eq.(6.62)), a  $T$ -linear resistivity (eq.(6.64)), a vanishing quasiparticle residue  $Z$ , a finite temperature geometric entanglement content (eq.(6.65)) etc. We recall that non-Fermi liquid phases were also obtained from large  $N$  analyses of the spin- $S$  Heisenberg Sachdev-Ye model [283], and as well as in electronic Sachdev-Ye-Kitaev (SYK) model [527]. We also recall that the  $H_{SFIM}$  possesses an emergent gapless FL phases, as well as several gapped phases that emerge from instabilities of the non-Fermi and Fermi liquids – reduced BCS, symmetry unbroken PDW's, Mott liquid etc. (shown within the green oval in Fig.6.4.13). Similar pairing instabilities of the non-Fermi liquid phase in the SYK model have also been reported recently [528]. Regime II in Table 6.4.1 is one where attractive extended interactions are RG irrelevant, whereas on-site repulsion is RG relevant. This leads under RG flow to the Hubbard model with long-range hopping (shown as a red circle within green oval in Fig.6.4.13, see Table 6.4.3).

In regime-III of Table 6.4.1, we obtain a model displaying the phenomenon of Anderson localisation (AL): disordered noninteracting electrons with long range hopping ( $H_{III}$  in Table 6.4.3). This is obtained from a relevant RG flow for random on-site potential, together with an irrelevant RG flow for all random hopping processes as well as all four-fermionic interactions. The left panel of Fig.6.4.2 represents the numerical evaluation of the RG flow of the disordered interaction strengths  $V(i,j)\hat{n}_i\hat{n}_j$  ( $V(i,j) = V_{i,j,i,j}$ ) and  $V(i,j,k,l)c_i^\dagger c_j^\dagger c_k c_l$  ( $V(i,j,k,l) = V_{i,j,k,l}$ ). We find that both  $V(i,j)$  and  $V(i,j,k,l)$  are RG irrelevant. The inset plot in the right panel of Fig.6.4.2 shows the vanishing of the standard deviation  $\sigma_{V_d}^{(j)}$  of the disordered  $V(i,j,k,l)$  coupling under

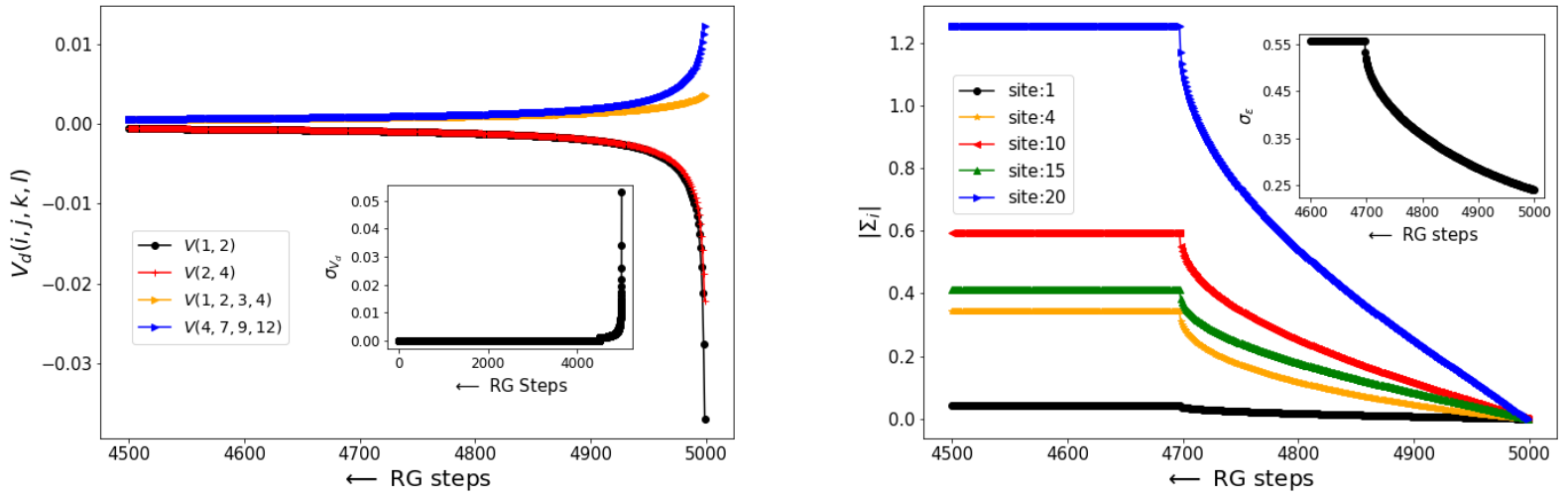


Figure 6.4.2: (Left Panel) Figure represents RG flows for number diagonal/off-diagonal interaction couplings  $V(i, j)/V(i, j, k, l)$  (eq.(6.131))/ $V(i, j, k, l)$  (eq.(6.133)) that are sampled from a gaussian with mean ( $V(i, j, k, l) = 0.1$ ) and standard deviation ( $\sigma_{V_d} = 0.05$ ),  $\omega = 0.5\epsilon'_N$ , system size  $N = 5000$ , disorder bandwidth ( $W = 2$ ),  $\epsilon'_N = -2W$ . Inset plot in left panel tracks the renormalization of standard deviation  $\sigma_{V_d}$ . (Right Panel) Figure represents RG flows for self energy  $\Sigma_i$  (eq.(6.129)) of the onsite disordered energies  $\epsilon'_i$  sampled from a gaussian distribution with  $\bar{\epsilon}'_i = -W$  and  $\sigma_{\epsilon'_i} = 0.25$ . Inset plot in right panel tracks the RG flow for  $\sigma_{\epsilon'}$  of the renormalized onsite energies  $\epsilon'$ .

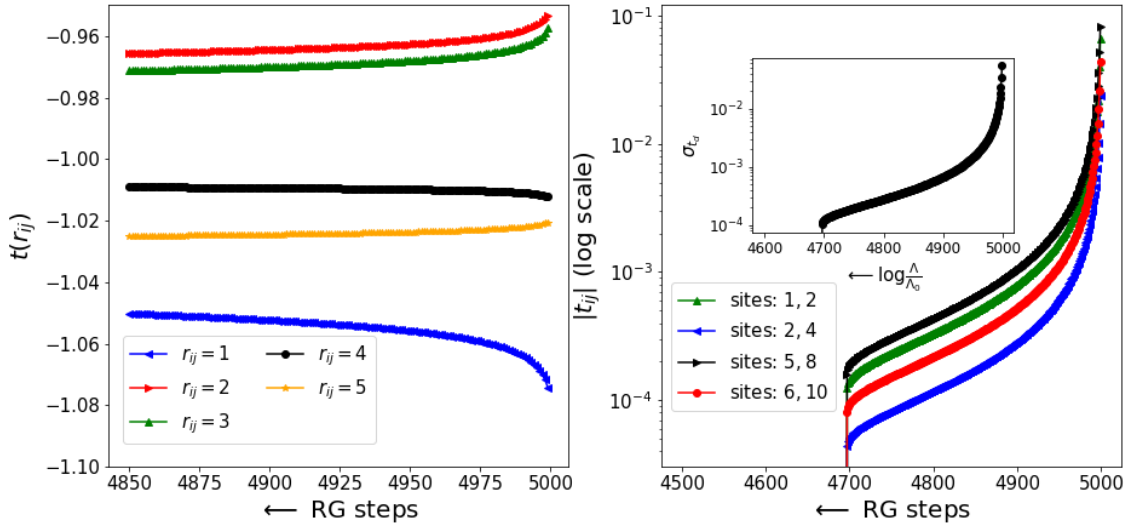


Figure 6.4.3: Left panel: RG flows for translationally invariant hopping strengths  $t(r_{ij})$ (eq.(6.126)) for various distances  $r_{ij}$ . Right panel: RG flows of the disordered hopping strengths  $t'_{ab}$  (eq.(6.127))sampled from a gaussian with mean ( $\bar{t}'_{ab} = 0.2$ ) and standard deviation ( $\sigma_{t_d} = 0.05$ ). Inset plot in right panel displays the RG flow for the standard deviation ( $\sigma_{t_d}$ ) of disordered hopping strengths.

RG flow

$$\sigma_{V_d}^{(j)} = \sqrt{\frac{\sum_{(a,b,c,d) < j} (V(a,b,c,d)^{(j)})^2}{N^4} - \left( \frac{\sum_{(a,b,c,d) < j} V(a,b,c,d)}{N^4} \right)^2}. \quad (6.111)$$

On the other hand, the RG flows for the single-particle self-energy  $\Sigma_i^{(j)} \epsilon_i'^{(j)} = \epsilon_i + \Sigma_i^{(j)}$  are observed to grow in Fig.6.4.2 (right panel), finally saturating at an IR fixed point. The inset plot in the right panel of Fig.6.4.2 shows the growth and saturation of the standard deviation  $\sigma_\epsilon^{(j)}$  of the renormalised onsite energies  $\epsilon_i'^{(j)}$  under the RG flow

$$\sigma_\epsilon^{(j)} = \sqrt{\frac{1}{N} \sum_i (\epsilon_i'^{(j)})^2 - \left( \frac{1}{N} \sum_i \epsilon_i'^{(j)} \right)^2}. \quad (6.112)$$

Finally, the left panel of Fig.6.4.3 shows the saturation under RG flow of translationally invariant variable-range hopping strengths  $t(r_{ij})$  at the IR fixed point. On the other hand, in the right panel of Fig.6.4.3, we find that the disordered hopping  $t'_{ik}$  are found to be RG irrelevant and vanish at an IR fixed point. Similarly, the inset plot in the right panel tracks the reduction under RG flow of the standard deviation  $\sigma_{t_d}$  in the random hopping

$$\sigma_{t_d} = \sqrt{\frac{1}{N^2} \sum_{a,b} t_{a,b}^{(j),2} - \left( \frac{\sum_{i,j} t_{i,j}}{N^2} \right)^2}. \quad (6.113)$$

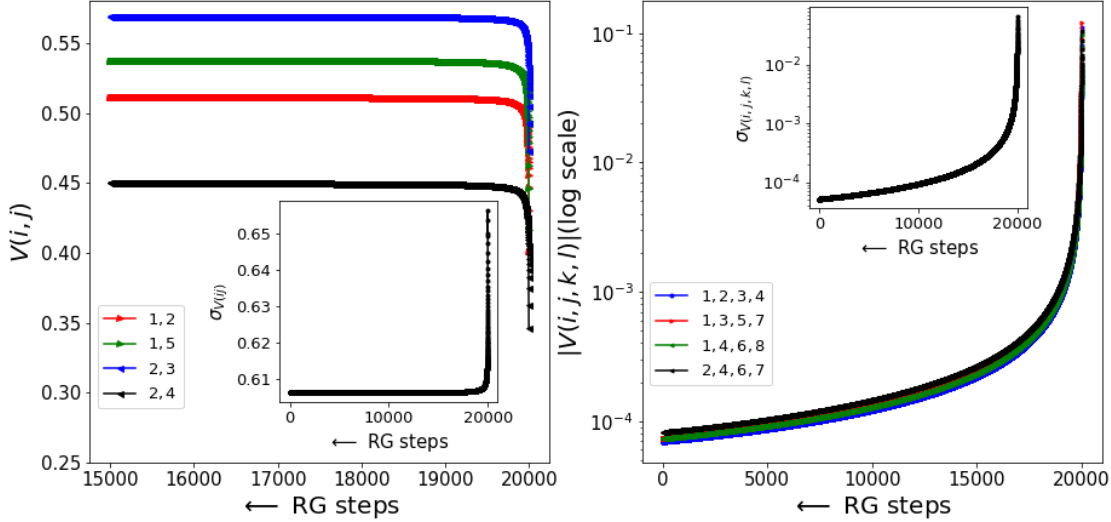


Figure 6.4.4: Left panel: RG flow for the number-diagonal interactions  $V(i,j)$  (eq.(6.130)) for  $\omega = \epsilon_N + 0.1$ . The  $V(i,j)$  are initially sampled from a gaussian distribution with mean  $\bar{V}(a,b) = 0.5$  and  $\sigma_{V(a,b)} = 0.1$ . Inset in left panel tracks the RG flow for  $\sigma_{V(a,b)}$ . Right panel: RG flow for the number off-diagonal interactions  $V(i,j,k,l)$  (eq.(6.133)), whose bare values are sampled from a gaussian distribution with mean  $\bar{V}(i,j,k,l) = -0.1$  and  $\sigma_{V(i,j,k,l)} = 0.01$ . Inset in right panel tracks the RG flow for  $\sigma_{V(i,j,k,l)}$ .

Taken together, Figs.6.4.2 and 6.4.3 establish that in Regime III, the IR fixed point effective Hamiltonian is that for disordered noninteracting electrons with long range hopping ( $H_{III}$  in Table 6.4.3).

Regime IV of Table 6.4.2, with an effective IR fixed point Hamiltonian  $H_{IV}$  (see Table 6.4.3), corresponds to a phase that is a glassy variant of the Fermi liquid (known as the interacting Fermi insulator), and involves the phenomenon of many-body localization (MBL) in Fock space [192, 297, 298]. Fig.6.4.4 (left panel) represents the growth under RG flow and saturation of the number-diagonal interactions at the low-energy fixed point. The inset shows that the standard deviation  $\sigma_{V(a,b)}$  of the renormalized couplings  $V_{ij}$  reduces in magnitude under RG and saturates to a finite value at the fixed point. On the other hand, in right panel of Fig.6.4.4, the off-diagonal interaction couplings  $V_{i,j,k,l}$  are found to be RG irrelevant. In the inset, we observe that the standard deviation of the off-diagonal scattering vertices  $\sigma_{V_{i,j,k,l}}$  diminishes under RG flow, eventually vanishing at the low-energy fixed point. Fig.6.4.5 (left panel) represents the RG irrelevant flows for the hopping strength  $t_{ij}$ . The inset in the left panel shows the reduction in  $\sigma_{t_d}$  under RG flow, eventually vanishing at the IR fixed point. On the other hand, the right panel of Fig.6.4.5 represents the relevant RG flow for the onsite self-energies  $\Sigma_i$ , displaying a growth and saturation at the low-energy fixed point. The inset plot in right panel of Fig.6.4.5 shows that the standard deviation of the renormalized energies  $\sigma_{\epsilon'_i}$  also grows under RG and saturates at low energies. Together, Fig.6.4.4 and 6.4.5 indicate the onset of many-body localization with a Hamiltonian  $H_{IV}$  Table 6.4.3 describing the effective low energy theory.

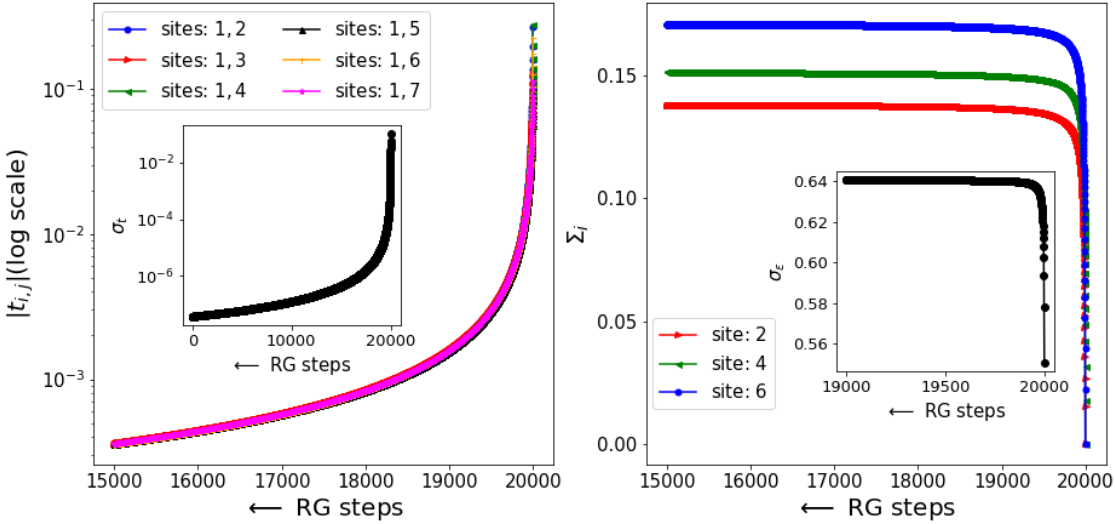


Figure 6.4.5: (Left Panel) Figure represents RG flow for the hopping strengths  $t'_{i,j}$  (eq.(6.127)). Bare values are sampled from a gaussian distribution with mean  $\overline{t'_{i,j}} = -0.2$  and  $\sigma_{t_d} = 0.05$ . Inset in left panel tracks the RG flow for  $\sigma_{t_d}$ . (Right Panel) Figure represents RG flow for the disordered onsite potentials  $\epsilon_i$ 's(eq.(6.129)), the initial values are sampled from a gaussian distribution with mean  $\overline{\epsilon'_i} = 1.0$  and  $\sigma_{\epsilon'_i} = 0.56$ . Inset in right panel tracks the RG flow for  $\sigma_{\epsilon'_i}$ .

Similarly, regime V in Table 6.4.1 corresponds to a many-body localised (MBL) phase that is the glassy variant of a non-Fermi liquid Hamiltonian ( $H_V$  in Table 6.4.3) [192, 298] and we call it the marginal Fermi insulator. The left and right panels of Fig.6.4.6 represent the RG flows for the number diagonal and off-diagonal interactions respectively. Both are found to be RG irrelevant in this regime. The inset plot in the left and right panels show that both  $\sigma_{V_{i,j,k,l}}$  and  $\sigma_{V_{i,j}}$  vanish at low-energies. Nevertheless, even as the two-particle interactions are found to be RG irrelevant, they lead to the generation of RG relevant three-particle off-diagonal scattering terms  $R(i, j, k, l, m, n)c_i^\dagger c_j^\dagger c_k^\dagger c_l c_m c_n$  (right panel of Fig.6.4.7) and two electron-one hole number diagonal interactions  $R(i, j, k)\hat{n}_i\hat{n}_j(1 - \hat{n}_k)$  (left panel of Fig.6.4.7) that are observed to reach finite values at low-energies. The inset plots in both left/right panels of Fig.6.4.7 show that the standard deviation of both the three-particle off-diagonal interaction ( $\sigma_{R_{i,j,k,l,m,n}}$ ) and two electron-one hole diagonal interaction ( $\sigma_{R_{i,j,k}}$ ) grow under RG, and finally saturate to a finite value at the RG fixed point.

Importantly, the hopping strengths  $t_{i,j}$ 's (left panel in Fig.6.4.8 are also found to be RG irrelevant, such that they reduce in magnitude and vanish at the IR fixed point. On the other hand, the onsite self-energies  $\Sigma_i$  are RG relevant (right panel in Fig.6.4.8), as they grow and saturate at a IR fixed point. The inset of the right panel of Fig.6.4.8 shows the growth of the renormalized onsite disordered potential  $\sigma_{\epsilon'_d}$  under RG flow, and its saturation at an IR fixed point. In order to study the effect of three-particle number off-diagonal terms  $R_{i,j,k,l,m,n}$  at low-energies, we perform a second level of the URG analysis. The left and right panels of Fig.6.4.9 represent the RG flows of the two-electron 1-hole  $R(i, j, k)$  and three particle off-diagonal couplings  $R(i, j, k, l, m, n)$

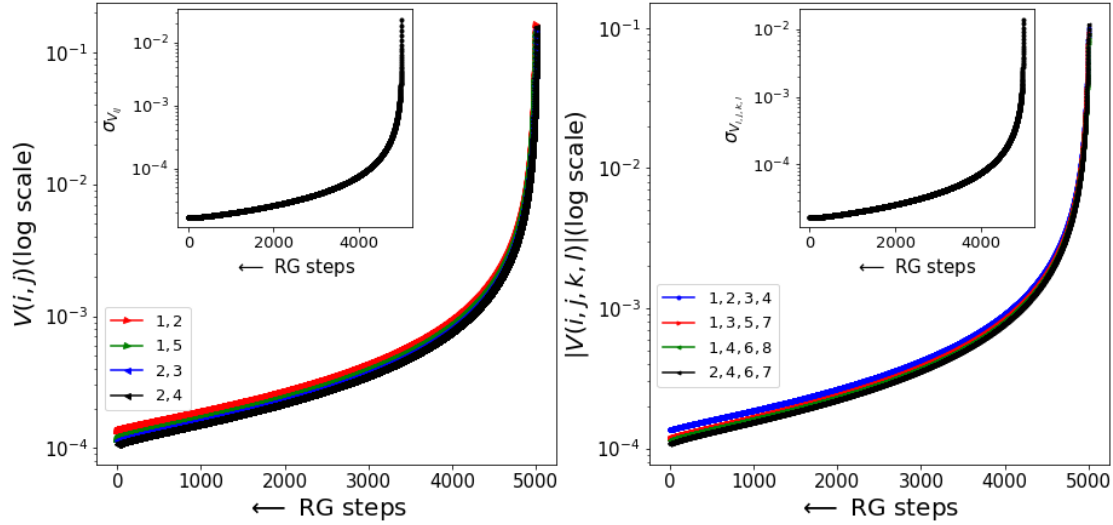


Figure 6.4.6: Left panel: RG flow for the number diagonal interactions  $V(i,j)$  (eq.(6.131) ) for  $\omega = 0.5\epsilon_N + 0.1$ . The bare  $V(i,j)$  are sampled from a gaussian distribution with mean  $\overline{V(i,j)} = 0.15$  and  $\sigma_{V(i,j)} = 0.03$ . Inset in left panel displays the RG flow for  $\sigma_{V(i,j)}$ . Right panel: RG flow for the number off-diagonal interactions  $V(i,j,k,l)$  (eq.(6.133)), whose bare values are sampled from a gaussian distribution with mean  $\overline{V(i,j,k,l)} = -0.1$  and  $\sigma_{V(i,j,k,l)} = 0.01$ . Inset in right panel shows the RG flow for  $\sigma_{V(i,j,k,l)}$ .

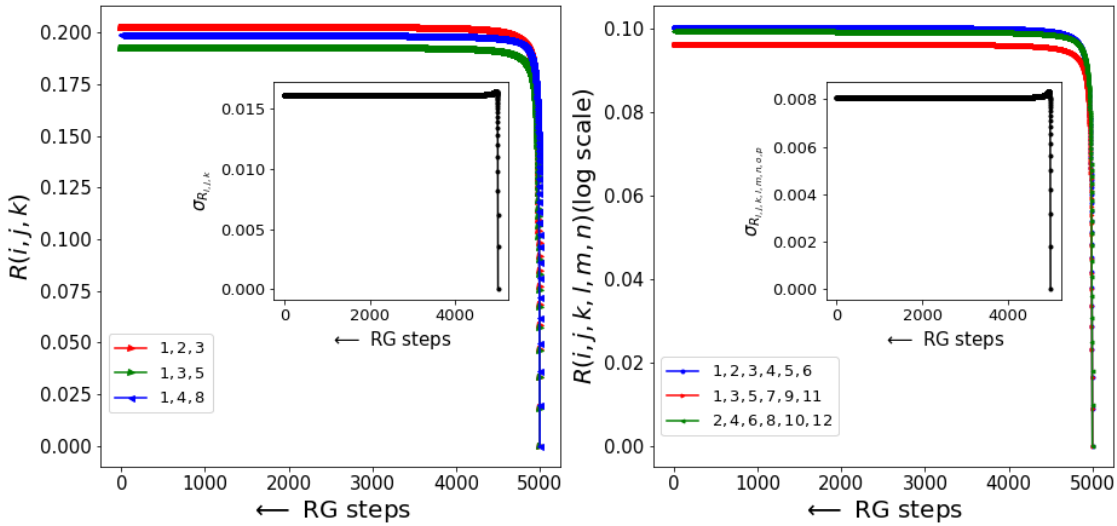


Figure 6.4.7: Left panel: RG flow for the emergent three-particle number diagonal interactions  $R(i,j,k)$  (eq.(6.47)). Inset in left panel diplays the RG flow for  $\sigma_{R(i,j,k)}$ . Right panel: RG flow for the number off-diagonal interactions  $R(i,j,k,l,m,n)$  (eq.(6.17)). Inset in right panel shows the RG flow for  $\sigma_{R(i,j,k,l,m,n)}$ .

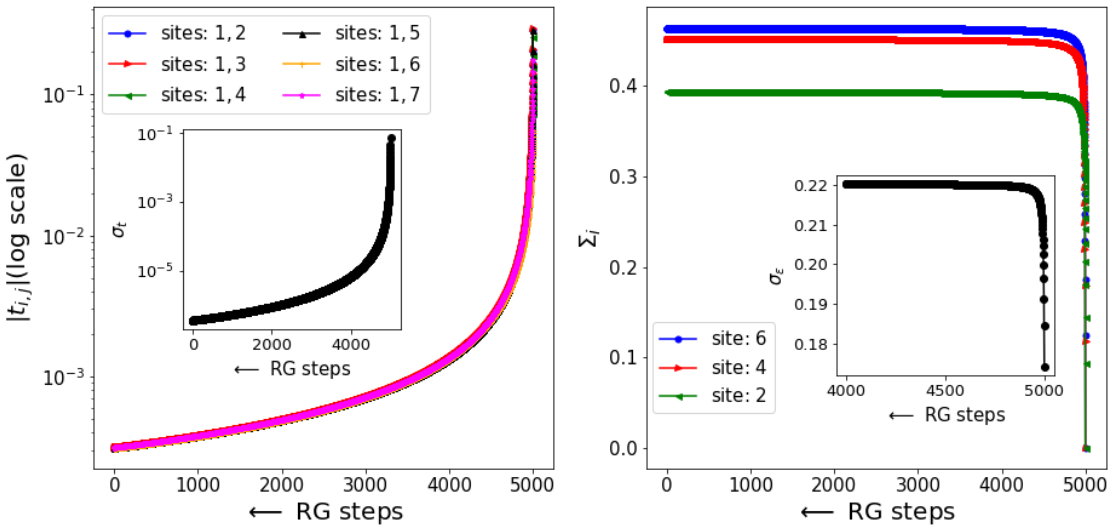


Figure 6.4.8: Left panel: RG flow for the hopping parameters  $t'_{ij}$  eq.(6.126), whose bare values are sampled from a gaussian distribution with mean  $\bar{t}'_{ij} = -0.2$  and  $\sigma_{t'_{ij}} = -0.1$ . Inset in right panel displays the RG flow for  $\sigma_{t'_{ij}}$ . Right panel: RG flow for the onsite energies  $\epsilon_i$  eq.(6.129), whose bare values are sampled from a gaussian distribution with mean  $\bar{\epsilon}_i = 1$  and  $\sigma_{\epsilon_d} = 0.15$ . Inset in left panel shows the RG flow for  $\sigma_{\epsilon_i}$ .

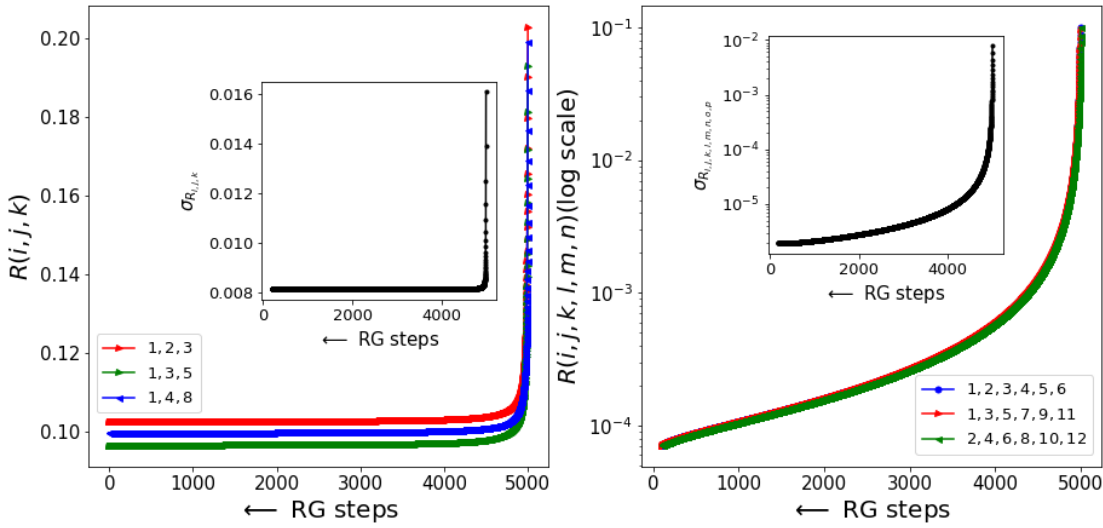


Figure 6.4.9: Left panel: RG flow for the three-particle off-diagonal interactions  $R(i,j,k,l,m,n)$  eq.(6.46). Inset in left panel displays the RG flow for the standard deviation of these couplings ( $\sigma_{R(i,j,k,l,m,n)}$ ). Right panel: RG flow for the two electron-one hole number diagonal interactions  $R(i,j,k)$  eq.(6.47). Inset in right panel shows the RG flow for  $\sigma_{R(i,j,k)}$ .

respectively. The number off-diagonal couplings in the right panel are found to be RG irrelevant. The inset in right panel of Fig.6.4.9 shows that the  $\sigma_{R_{i,j,k,l,m,n}}$  is also RG irrelevant, and diminishes at low-energies. The number diagonal interactions in the left panel of Fig.6.4.9 are RG relevant, and saturate to a finite value. The inset of left panel in Fig.6.4.9 also shows a similar saturation to a finite value at low-energies. Altogether, the plots Fig.6.4.6-6.4.9 provide a numerical verification of the effective Hamiltonian  $H_V$  in Table 6.4.3. As is expected for many-body localised phases of matter, the effective fixed point Hamiltonians obtained for phases IV and V are obtained at higher values of the quantum fluctuation energyscale  $\omega > 0$  than those for all other phases (where  $\omega < 0$ , see Tables 6.4.1 and 6.4.2). The RG flows to these phases also confirm that an extensive number of single-particle occupation numbers ( $n_i$ ) are transformed into integrals of motion under the RG flow [297]. We note that effective Hamiltonians describing many-body localization similar to  $H_{IV}$  and  $H_V$  have been proposed recently in Refs.[297, 201, 229].

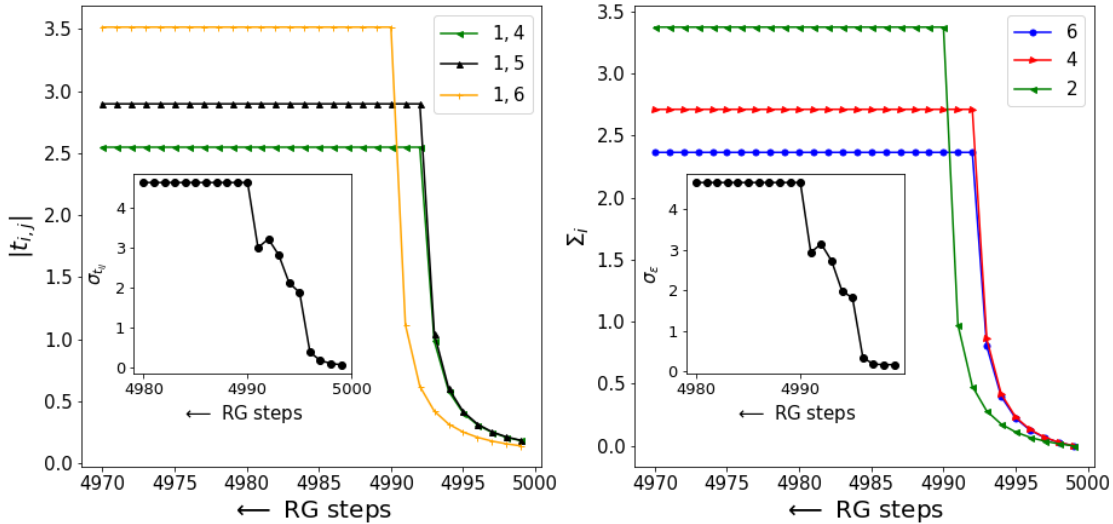


Figure 6.4.10: Left panel: RG flow eq.(6.126) for the hopping strengths ( $t_{i,j}$ ), whose initial values are sampled from a gaussian distribution with mean  $\bar{t}_{i,j} = -0.2$  and  $\sigma_{t_{i,j}} = 0.07$  and  $\omega = -0.15$ . Inset in left panel displays the RG flow for  $\sigma_{t_d}$ . Right panel: RG flow eq.(6.129) for the onsite self-energies, whose bare values are sampled from a gaussian distribution with mean  $\bar{\epsilon}_i = 1$  and  $\sigma_{\epsilon_d} = 0.1$ . Inset in right panel shows the RG flow for  $\sigma_{\epsilon_d}$ .

Last but not least, in regime VI, a numerical evaluation of the RG equations for all the couplings  $t_{i,j}, \epsilon'_i, V'_{i,j}, V'_{i,j,k,l}$  is shown in Fig.6.4.10 and Fig.6.4.11. Importantly, we find that *all* the couplings are found to be RG relevant, with a growth and eventual saturation at an IR fixed point. Further, the standard deviation of all of these couplings is also found to grow under RG and saturate at the IR fixed point. Thus, in this phase, it is safe to say that *none* of the disordered couplings vanish under RG, thereby preserving the form of the bare Hamiltonian given in (eq.(6.106)) but with renormalized couplings. The IR fixed point effective Hamiltonian is shown as  $H_{VI}$  (Table 6.4.3) in Table 6.4.2, and corresponds to the generalized Sachdev-Ye model itself as the stable fixed point theory. Indeed,  $H_{VI}$  possesses the greatest parameter space, and corresponds to

a thermalized regime: the many-particle entanglement content of the eigenstates of this phase possess the greatest complexity. This is reflected in the marginality of all off-diagonal scattering vertices in  $H_{SY_4}$ , as well as in the fact that very few (i.e., of  $\mathcal{O}(10)$  out of 5000 in the numerical simulations) occupation numbers ( $n_i$ ) are transformed into integrals of motion under the RG flow in Regime VI (as can be seen in Figs.6.4.10 and 6.4.11). Finally, Regimes IV and V possess tensor network representations similar to the Fermi liquid (Fig.6.2.14) and marginal Fermi liquid (Fig.6.2.20) respectively. The tensor network representation of regime VI is shown in Fig.6.4.12.

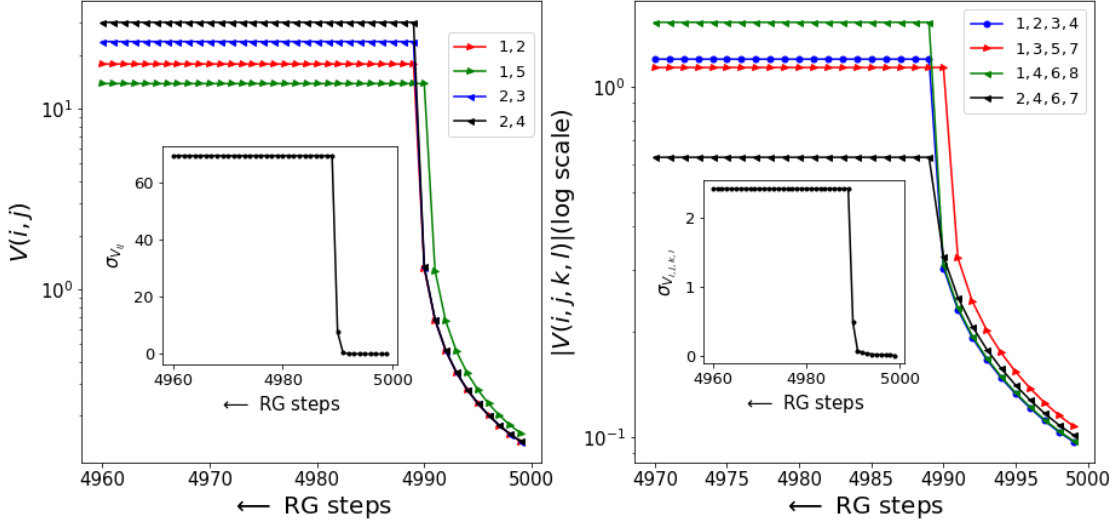


Figure 6.4.11: Left panel: RG flow eq.(6.131) for the number diagonal interactions  $V(i,j)$ , whose initial values are sampled from a gaussian distribution with mean  $\overline{V(a,b)} = 0.15$  and  $\sigma_{V(a,b)} = 0.01$ . Inset in left panel displays the RG flow for  $\sigma_{V(a,b)}$ . Right panel: RG flow eq.(6.133) for the number off-diagonal interactions  $V(i,j,k,l)$ , whose bare values are sampled from a gaussian distribution with mean  $\overline{V(i,j,k,l)} = -0.1$  and  $\sigma_{V(i,j,k,l)} = 0.01$ . Inset in right panel shows the RG flow for  $\sigma_{V(i,j,k,l)}$ .

## 6.5 Conclusions

In this work, we have applied the URG formalism [180–182] to certain prototypical models of strongly correlated electrons. The model of a single band of tight binding electrons with momentum-dependent interactions ( $H_{SFIM}$ ) leads to a diverse family of IR fixed point Hamiltonians including gapless phases in the Fermi and non-Fermi liquids, as well as various insulating liquid phases arising from large momentum transfer/back-scattering across the Fermi surface. In a companion work [182], we have shown how the  $2n$ -point vertex RG flow equations can be interpreted as a tensor network. The nodes of this vertex tensor network is composed of the  $2n$ -point vertices, while the edges represent the electronic states. At each RG step, the vertex tensor net-

Parameters	Regime-I	Regime-II	Regime-III
$\omega$	$\omega < \frac{1}{2}(\epsilon'_l - \epsilon'_j)$ , $\epsilon'_l < \epsilon'_j$	same as I	same as I
$t(\mathbf{r}_{jl})$	$t(\mathbf{r}_{jl}) < 0$	same as I	same as I
$V^{\sigma\sigma'}(\mathbf{r}_{jl})$	$V^{\sigma\sigma'}(\mathbf{r}_{jl}) > 0$	$< \frac{1}{2}(\epsilon'_l - \epsilon'_j) - \omega$	$V^{\sigma-\sigma}(\mathbf{r}_{jl}) < 0$
$V'_{jl}^{\sigma\sigma'}$	$V'_{jl}^{\sigma\sigma'} < 0$	same as I	same as I
$t'_{il}$	$0 < t'_{il} <  t(\mathbf{r}_{jl}) $	same as I	same as I
$\epsilon$	$\epsilon > 2 \omega $	same as I	same as I
$\epsilon'_j$	$0 < \epsilon'_j < \epsilon$	same as I	$\epsilon'_j < 0$
$V'_{ijkl}^{\sigma\sigma'}$	$V'_{ijkl}^{\sigma\sigma'} > 0$	same as I	same as I
$V^{\sigma\sigma'}(\mathbf{r}_{ij}, \mathbf{r}_{ik}, \mathbf{r}_{il})$	$V^{\sigma\sigma'}(\mathbf{r}_{ij}, \mathbf{r}_{ik}, \mathbf{r}_{il}) >  V'_{ijkl}^{\sigma\sigma'} $	$ V'_{ijkl}^{\sigma\sigma'}  < V^{\sigma\sigma'}(\mathbf{r}_{ij}, \mathbf{r}_{ik}, \mathbf{r}_{il}) < -2\omega$	same as I

Table 6.4.1: Parameter space regimes for RG flows of  $H_{SY_4}$ . Regime-I corresponds to a general 4-fermion translational invariant fixed point theory on a  $D$ -dimensional lattice. Regime-II corresponds to the Hubbard model with long-ranged hopping under RG flow. Regime-III leads to the Anderson disorder model with long-ranged hoppings.

Parameters	Regime-IV	Regime-V	Regime-VI
$\omega$	$\omega > \frac{1}{2}(\epsilon_l + \epsilon_j)$ , $\epsilon_l > 0$	$\frac{1}{2}(\epsilon_j + \epsilon_l) > \omega > \frac{1}{2}\epsilon_j$	$\omega < 0$
$t(\mathbf{r}_{jl})$	same as I	same as I	no condition
$V^{\sigma\sigma'}(\mathbf{r}_{jl})$	$V^{\sigma\sigma'}(\mathbf{r}_{jl}) < 0$	$V^{\sigma\sigma'}(\mathbf{r}_{jl}) > \omega - \frac{1}{2}(\epsilon_j + \epsilon_l)$	$V^{\sigma\sigma'}(\mathbf{r}_{jl}) > 0$
$V'_{jl}^{\sigma\sigma'}$	$V'_{jl}^{\sigma\sigma'} >  V'_{ijkl}^{\sigma\sigma'} $	same as IV	$V'_{jl}^{\sigma\sigma'} > 0$
$t'_{il}$	$t'_{il} < 0$	same as IV	$sgn(t(\mathbf{r}_{jl}))$
$\epsilon$	same as I	same as I	$\epsilon > 0$
$\epsilon'_j$	no condition	same as I	$\epsilon'_j > 0$
$V'_{ijkl}^{\sigma\sigma'}$	$V'_{ijkl}^{\sigma\sigma'} < 0$	same as IV	no condition
$V^{\sigma\sigma'}(\mathbf{r}_{ij}, \mathbf{r}_{ik}, \mathbf{r}_{il})$	$0 < V^{\sigma\sigma'}(\mathbf{r}_{ij}, \mathbf{r}_{ik}, \mathbf{r}_{il}) < V^{\sigma\sigma'}(\mathbf{r}_{jl})$	$V^{\sigma\sigma'}(\mathbf{r}_{ij}, \mathbf{r}_{ik}, \mathbf{r}_{il}) > 0$	$sgn(V'_{ijkl}^{\sigma\sigma'})$

Table 6.4.2: Parameter space regimes for RG flows of  $H_{SY_4}$ . Regimes-IV and V corresponds to many-body localized phases. Parameter regime VI leads to the thermalised phase, corresponding to a generalized  $SY_4$  model.

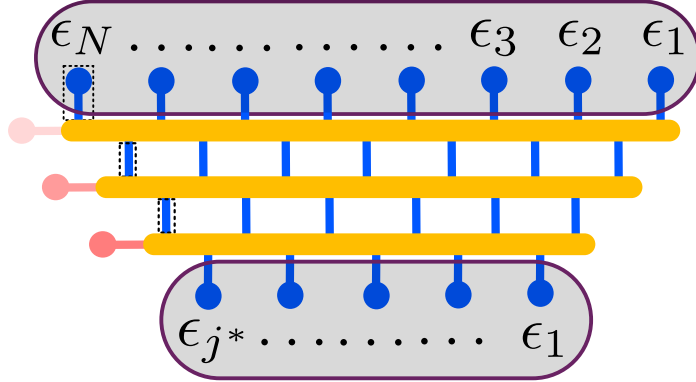


Figure 6.4.12: EHM tensor network representation of RG flow towards the thermalised phase (regime VI of Tables 6.4.2 and 6.4.3) of the generalized  $SY_4$  model. The color of the blue legs do not change, indicating a similarity in the nature of the intermediate theories leading upto a fixed point  $SY_4$  model. The rounded square boxes indicate the interaction comprising all the degrees of freedom in the initial and final points of the RG flow.

Regime	Fixed point Hamiltonian
I	$H_I = \sum_{ij} t^*(\mathbf{r}_{ij}) c_{i\sigma}^\dagger c_{j\sigma} + \epsilon^* \sum_i \hat{n}_{i\sigma}$ $+ \sum_{ij} V^{\sigma\sigma',*}(\mathbf{r}_{ij}) \hat{n}_{i\sigma} n_{j\sigma'}$ $+ \sum_{ijkl} V^{\sigma\sigma',*}(\mathbf{r}_{ij}, \mathbf{r}_{ik}, \mathbf{r}_{il}) c_{i\sigma}^\dagger c_{j\sigma'}^\dagger c_{k\sigma'} c_{l\sigma}$
II	$H_{II} = \sum_{ij} t^*(\mathbf{r}_{ij}) c_{i\sigma}^\dagger c_{j\sigma} + \sum_i V^* \hat{n}_{i\sigma} n_{i-\sigma}$
III	$H_{III} = \sum_{ij} t^*(\mathbf{r}_{ij}) c_{i\sigma}^\dagger c_{j\sigma} + \sum_i \epsilon_i^* \hat{n}_{i\sigma}$
IV	$H_{IV} = \sum_i \epsilon_i^* \hat{n}_{i\sigma} + \sum_i V_{ij}^{\sigma\sigma'} \hat{n}_{i\sigma} \hat{n}_{j\sigma'}$
V	$H_V = \sum_i \epsilon_i^* \hat{n}_{i\sigma} + \sum_{ijk} V_{ijk}^{\sigma\sigma'} \hat{n}_{i\sigma} \hat{n}_{j\sigma'} (1 - \hat{n}_{k\sigma})$
VI	$H_{VI} = H_{SY_4}^*$

Table 6.4.3: Fixed point Hamiltonians obtained via RG from  $H_{SY_4}$  in regimes I-VI.

work transforms via disentanglement of electronic states, and the simultaneous renormalization of the vertex tensors.

Here, we have restricted our attention to the study of the RG flows of two-, four- and six-point vertex tensors. We represent the diagonal and off-diagonal vertex tensors in a tree diagram (see Fig.6.2.2). Each node of the tree represents a subclass of scattering processes. The parameter subspaces are classified in terms of the relative magnitude of the off-diagonal and diagonal vertex tensors. This assists in identifying different IR fixed points reached under RG flow. A numerical evaluation of various RG equations shows that certain vertex scattering processes vanish at these stable fixed points, while certain others become dominant. As a result, the different emergent phases are classified in terms of their distinct tree representations and vertex tensor network diagrams. For the Fermi and non-Fermi liquid phases, the four-point and six-point off-diagonal vertices vanish. This results in their vertex tensor networks being completely disentangled. The

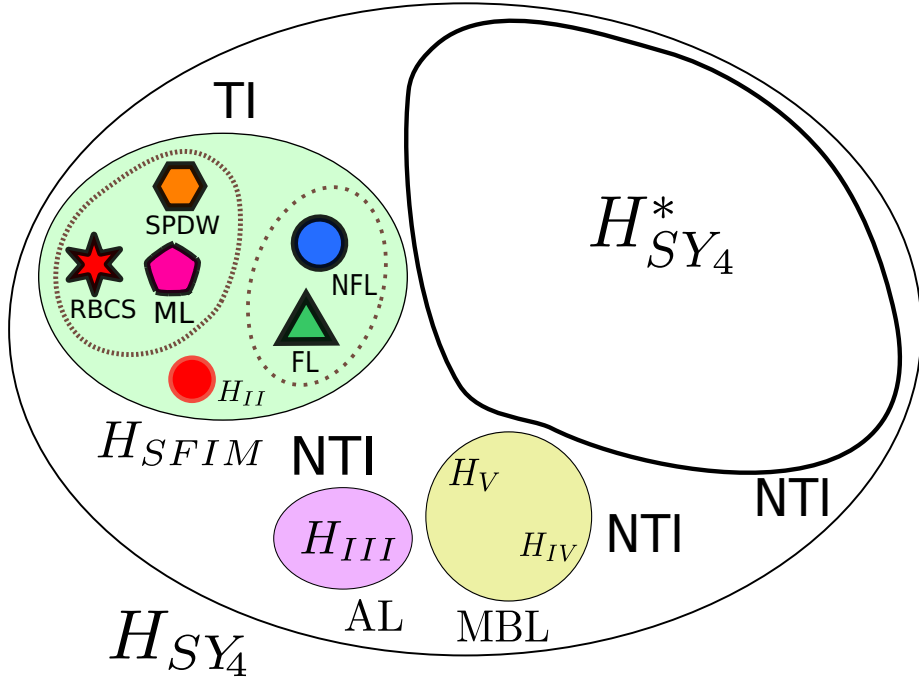


Figure 6.4.13: Schematic description of various parameter-space regimes of the  $SY_4$  model leading to various translationally invariant (TI) and non-translationally invariant (NTI) fixed point Hamiltonians under RG flow. The light green circle comprises various TI phases (arising from an emergent effective Hamiltonian  $H_I = H_{SFIM}$  of Table 6.4.3): (i) Gapped phases: reds star, orange hexagon, magenta pentagon within the dashed boundary represent the reduced BCS model (RBCS), symmetry unbroken PDW (SPDW) and the Mott liquid Hamiltonians (ML) respectively; (ii) Gapless phases: blue circle and green triangle within the dotted boundary represent the Fermi liquid (FL) and Non Fermi liquid (NFL) respectively; (iii) the red circle represents the Hubbard models with long ranged hopping ( $H_{II}$  of Table 6.4.3). The light yellow oval represents many-body localized (MBL) phases, with effective Hamiltonians  $H_{IV}$  and  $H_V$  are 2-electron and 3-electron interacting number-diagonal NTI models respectively (see Table 6.4.3). The pink oval is the Anderson disorder localization regime, with the NTI model  $H_{III}$  of Table 6.4.3. The large white region with black border represents the themalised phase, and corresponds to a generalized  $SY_4$  model reproduced under RG ( $H_{VI}$  of Table 6.4.3).

fixed point theories differ nevertheless: in the Fermi liquid, each output leg describes a electronic degree of freedom, while in the non-Fermi liquid, each composite degree of freedom is described as a composition of three output legs (two in electron-like and one in hole-like configuration). On the other hand, the vertex tensor networks for gapped phases such as the reduced BCS and Mott liquid Hamiltonians display greater complexity: pairs of electronic legs (indicating bound states that have condensed in the IR) are coupled to each other via four-point scattering vertices. Further, the IR fixed point theories describing such gapped phases can be rewritten in terms of nonlocal Wilson loops, leading to a Hamiltonian gauge theory construction. The zero mode of the Hamiltonian gauge theory reveals interesting topological features, e.g., ground state degeneracy, charge fractionalization etc.

In the generalised Sachdev-Ye ( $SY_4$ ) model, the non-translationally invariant (NTI) phases can be separated into two subclasses: one with remnant electronic interactions and the other without. The first NTI subclass contains many-body localised (MBL) and thermalized phases. Our study reveals the MBL phases to be glassy variants of the Fermi and non-Fermi liquid phases. On the other hand, we find that the thermalized phase is described by a theory that involves only a marginal deformation of the parent Hamiltonian ( $H_{SY_4}$ ), and involves a strong interplay between fermion exchange signatures and electronic correlation. The second NTI subclass contains a phase corresponding to the Anderson model of disordered electrons. Further, there is also a finite parameter-space window obtained from the  $SY_4$  for translationally invariant (TI) models such as  $H_{SFIM}$ , which upon further renormalization lead to the various metallic and insulating phases described earlier for  $H_{SFIM}$ .

We have also shown that the entanglement renormalization towards gapless and gapped IR phases is distinct: while gapless phases are characterised by the presence of fermion exchange phases along the RG flow, the passage to gapped phases displays the mitigation of the effects arising from fermion signs. This is due to the fact that dominant RG flow in the latter case occurs in a reduced pseudospin subspace where the elementary degrees of freedoms are pairwise electronic states. Furthermore, we obtained the RG scaling form for the holographic entropy bound of the Fermi liquid phase, and argued with regards to its distinction from that for the marginal Fermi liquid and reduced BCS phases. We also showed separately that the effective IR theories for gapped models support a gauge-theoretic description. In this way, the URG offers an ab-initio formulation of the gauge-gravity duality: the passage from UV to IR involves the holographic generation of spacetime via entanglement renormalization [184, 182] as well as an effective gauge theory from vertex renormalization. Among several exciting future directions, this paves the way for further investigations on the nature the many-particle entanglement of strongly interacting quantum liquids.



# Appendix

## 6.A 1-particle self-energy RG for three-particle MFL Hamiltonian

The net correlation energy for the five electronic states  $E_{5,1}^j$  close to the Fermi surface in eqs.(6.53) and (6.59) attains a simplified expression via the following approximation

$$\epsilon_{\mathbf{k}_{\Lambda_j \hat{s}}}^{(j)} = \epsilon_{\mathbf{p}-\mathbf{k}_{\Lambda_j \hat{s}}}^{(j)} = \epsilon_{\mathbf{p}'-\mathbf{k}_{\Lambda_j \hat{s}}}^{(j)} \Rightarrow E_1^{(j)} = \frac{1}{2} \epsilon_{\mathbf{k}_{\Lambda_j \hat{s}}}^{(j)} \text{ and } \epsilon_{\mathbf{k}_{\Lambda_j \hat{s}}}^{(j)} = \epsilon_{\mathbf{k}_{\Lambda_1 \hat{s}}}^{(j)}, \quad (6.114)$$

such that

$$E_{5,1}^{(j)} = E_1^{(j)} + \epsilon_{\mathbf{k}_{\Lambda_j \hat{s}}}^{(j)} = \frac{3}{2} \epsilon_{\mathbf{k}_{\Lambda_j \hat{s}}}. \quad (6.115)$$

Similarly, we also approximate the net 3-particle correlation energy coming from six-particle terms:  $E_{5,3}^{(j)} = -\frac{3}{4} \Gamma_{(k\sigma,\mu)}^{3,(j)}$ . Putting these two correlation energies into the 1-particle self-energy RG (eq.(6.58)) near the fixed point eq.(6.56), we find that close to the Fermi surface

$$\begin{aligned} \Delta \Sigma_{\mathbf{k}_{\Lambda_l \hat{s}}}^{(l^*)}(\omega) &= \sum_{\epsilon_{\mathbf{k}_{\Lambda_j \hat{s}}}^{(l^*)} < \epsilon_{\mathbf{k}_{\Lambda_l \hat{s}}}^{(l^*)}, \hat{s}'} \frac{(\Gamma_{\alpha\gamma}^{6,(l^*)}(\omega))^2}{\omega - \frac{1}{2} \epsilon_{\mathbf{k}_{\Lambda_j \hat{s}}}^{(j)} + \frac{3}{4} \Gamma_{\gamma\gamma'}^{6,(l^*)}(\omega)}, \\ &= \frac{N(0)}{\Gamma_{\gamma\gamma'}^{6,(l^*)}(\omega)} \int_{\Lambda_j \rightarrow 0,F}^{\Lambda_{l^*}} d\Lambda \frac{(\Gamma_{\alpha\gamma}^{6,(l^*)}(\omega))^2}{\omega - \frac{1}{2} \epsilon_{\mathbf{k}_{\Lambda_l \hat{s}}}^{(j)} + \frac{3}{4} \Gamma_{\gamma\gamma'}^{6,(l^*)}(\omega)}. \end{aligned} \quad (6.116)$$

In the above expression, the set  $\alpha$

$$\alpha = \left\{ (\mathbf{k}_{\Lambda_j \hat{s}} \sigma, 1), (\mathbf{k}' \sigma', 1), (\mathbf{k}_{\Lambda_1 \hat{s}} \sigma'', 1), (\mathbf{p} - \mathbf{k}_{\Lambda_1 \hat{s}} \sigma''', 1), (\mathbf{k}'' \sigma', 0) \right\} \quad (6.117)$$

comprises the 4-electron 1-hole intermediate configuration whose energy appears in the 5-particle Green's function. The index  $\nu = (\mathbf{k}_{\Lambda_j \hat{s}} \sigma, 1)$  labels the electronic state whose self-energy is being renormalized. Integrating the RG equation results in the expression

$$\Delta \Sigma_{\mathbf{k}_{\Lambda_l \hat{s}}}^{(l^*)}(\omega) = N(0) \frac{(\Gamma_{X,\mathbf{k}_{\Lambda_l \hat{s}}}^{6,(l^*)}(\omega))^2}{\Gamma_{D,\mathbf{k}_{\Lambda_l \hat{s}}}^{6,(l^*)}(\omega)} \ln \left| \frac{\omega - \frac{3}{2} \epsilon_{\mathbf{k}_{\Lambda_l \hat{s}}}^{(l^*)} + \frac{1}{8} \Gamma_{D,\mathbf{k}_{\Lambda_l \hat{s}}}^{6,(l^*)}(\omega)}{\omega} \right|, \quad (6.118)$$

where  $N(0)$  is the density of states on the Fermi surface and

$$\Gamma_{\mathbf{k}_{\Lambda_{l^*}} \hat{s} \sigma, \alpha \nu}^{6, (l^*)}(\omega) = \Gamma_{X, \mathbf{k}_{\Lambda_{l^*}} \hat{s}}^{6, (l^*)}(\omega), \quad \Gamma_{\gamma \gamma'}^{6, (l^*)}(\omega) = \Gamma_{D, \mathbf{k}_{\Lambda_{l^*}} \hat{s}}^{6, (l^*)}(\omega). \quad (6.119)$$

Using the fixed point relation eq.(6.56), the self-energy flow relation (eq.(6.118)) can be further simplified to

$$\Delta \Sigma_{\mathbf{k}_{\Lambda_{l^*}} \hat{s}}^{(l^*)}(\omega) = N(0) \frac{(\Gamma_{X, \mathbf{k}_{\Lambda_{l^*}} \hat{s}}^{6, (l^*)}(\omega))^2}{\Gamma_{D, \mathbf{k}_{\Lambda_{l^*}} \hat{s}}^{6, (l^*)}(\omega)} \ln \left| \frac{\epsilon_{\mathbf{k}_{\Lambda_{l^*}} \hat{s}}}{\omega} \right|. \quad (6.120)$$

As the Fermi energy is reached by taking the limits of  $\omega \rightarrow 0$  and  $\Lambda_j \rightarrow 0$ , the change in self-energy  $\Delta \Sigma_{\mathbf{k}_{\Lambda_{l^*}} \hat{s}}^{(j)}(\omega)$  has a branch-cut log singularity. Thus, the self-energy attains the familiar logarithmic form that was proposed on phenomenological grounds for the Marginal Fermi liquid [460]

$$\begin{aligned} \Sigma_{\mathbf{k}_{\Lambda_{l^*}} \hat{s}}^{(l^*)}(\omega) &\approx \Delta \Sigma_{\mathbf{k}_{\Lambda_{l^*}} \hat{s}}^{(j)}(\omega) + O(\omega) \\ &\approx N(0) \frac{(\Gamma_{X, \mathbf{k}_{\Lambda_{l^*}} \hat{s}}^{6, (l^*)}(\omega))^2}{\Gamma_{D, \mathbf{k}_{\Lambda_{l^*}} \hat{s}}^{6, (l^*)}(\omega)} \ln \left| \frac{\epsilon_{\mathbf{k}_{\Lambda_{l^*}} \hat{s}}}{\omega} \right|. \end{aligned} \quad (6.121)$$

## 6.B RG equations for SY<sub>4</sub> model

Using the diagrammatic contributions of the RG flow hierarchy eq.(2.47) (see also Fig.6.4.1), the RG equations for random hopping amplitudes  $t_{ik}$ , on-site potentials  $\epsilon_i$  and random four-fermion interaction amplitudes  $V_{ijkl}^{\sigma\sigma'}$  for the generalized Sachdev-Ye model (eq.(6.106)) is given by

$$\Delta t_{ik}^{(j)} = t_{ij}^{(j)} G_j^{2, (j)} t_{jk}^{(j)} + \sum_{m < j} t_{lj}^{(j)} G_{jl}^{4, \sigma\sigma, (j)} V_{ijlk}^{\sigma\sigma} + \sum_{i, l, m < j} V_{ijlm}^{\sigma\sigma', (j)} G_{jlm}^{6, (j)} V_{jlmk}^{\sigma\sigma', (j)}, \quad (6.122)$$

$$\Delta \epsilon_i^{(j)} = t_{ij}^{(j)} G_j^{2, (j)} t_{ji}^{(j)} + \sum_{l, k < j} V_{ijlk}^{\sigma\sigma', (j)} G_{jlk}^{6, (j)} V_{klji}^{\sigma\sigma', (j)}, \quad (6.123)$$

$$\Delta V_{ik}^{\sigma\sigma', (j)} = - \sum_l V_{ijkl}^{\sigma\sigma', (j)} G_{jl}^{4, \sigma\sigma', (j)} V_{lkji}^{\sigma\sigma', (j)}, \quad (6.124)$$

$$\Delta V_{iklm}^{(j)} = \sum_s V_{ijsm}^{\sigma\sigma', (j)} G_{js}^{4, (j)} V_{ksjl}^{\sigma\sigma', (j)} + t_{jm}^{(j)} G_j^{2, (j)} V_{iklj}^{\sigma\sigma', (j)}. \quad (6.125)$$

By decomposing the 2-point vertex parameters into translational invariant ( $\epsilon^{(j)}$ ,  $t^{(j)}(\mathbf{r})$ ) and non-translation invariant ( $\epsilon_i^{(j)}$ ,  $t_{ij}^{(j)}$ ) parts (eq.(6.108)), and denoting  $\mathbf{r}_{ik} = \mathbf{r}$ ,  $\mathbf{r}_{ij} = \mathbf{r}'$ ,  $\mathbf{r}_{il} = \mathbf{r}''$ ,  $N_j = \sum_{\mathbf{r}' < \max_{i < j}(|\mathbf{r}_{ij}|)} 1$ , we can use eqs.(6.123) and (6.124) to write their separate RG flow equations in the e-h configuration  $\hat{n}_{j\sigma} = 0$ ,  $\hat{n}_{i\sigma'} = 1$  as follows:

1. *Translational invariant hopping term* —

$$\begin{aligned} \Delta t^{(j)}(\mathbf{r}) &= \frac{1}{N_j} \sum_{\mathbf{r}_{ij} < \max_{i < j}(|\mathbf{r}_{ij}|)} \frac{t^{(j)}(\mathbf{r}_{jk}) t^{(j)}(\mathbf{r}_{ij})}{\omega + \frac{1}{2}\epsilon^{(j)} + \frac{1}{2}\epsilon_j'^{(j)}} \\ &+ \sum_{\mathbf{r}_{ij}, \mathbf{r}_{il}} \frac{\frac{1}{N_j} t^{(j)}(\mathbf{r}_{jl}) V^{\sigma\sigma, (j)}(\mathbf{r}, \mathbf{r}_{ij}, \mathbf{r}_{il})}{\omega + \frac{1}{2}\epsilon_j'^{(j)} - \frac{1}{2}\epsilon_l'^{(j)} + \frac{1}{4}V^{\sigma\sigma, (j)}(\mathbf{r}_{jl}) + \frac{1}{4}V_{jl}^{\sigma\sigma, (j)}} , \end{aligned} \quad (6.126)$$

2. *Translational non-invariant hopping term* —

$$\begin{aligned} \Delta t'_{ik}^{(j)} &= \frac{t^{(j)}(\mathbf{r}_{ij})t'_{jk}^{(j)} + t^{(j)}(\mathbf{r}_{jk})t'_{ij}^{(j)} + t'_{ij}^{(j)}t'_{jk}^{(j)}}{\omega + \frac{1}{2}\epsilon_j^{(j)} + \frac{1}{2}\epsilon^{(j)}} \\ &+ \sum_{\mathbf{r}''} \frac{t^{(j)}(\mathbf{r}'')V'^{\sigma\sigma,(j)}_{ijkl} + t'_{jl}^{(j)}V^{\sigma\sigma,(j)}(\mathbf{r}, \mathbf{r}', \mathbf{r}'')}{\omega + \frac{1}{2}\epsilon_j^{(j)} - \frac{1}{2}\epsilon_l^{(j)} + \frac{1}{4}V^{\sigma\sigma,(j)}(\mathbf{r}_{jl}) + \frac{1}{4}V'^{\sigma\sigma,(j)}_{jl}} , \end{aligned} \quad (6.127)$$

3. *Translational invariant chemical potential term* —

$$\begin{aligned} \Delta\epsilon^{(j)} &= \frac{1}{N_j} \sum_{\mathbf{r} < \max_{i < j}(|\mathbf{r}_{ij}|)} \frac{(t^{(j)}(\mathbf{r}))^2}{\omega + \frac{1}{2}\epsilon_j^{(j)} + \frac{1}{2}\epsilon^{(j)}} \\ &+ \frac{1}{N_j} \sum_{l,k < j, \mathbf{r}'} (V^{\sigma\sigma,(j)}(\mathbf{r}, \mathbf{r}_{ij}, \mathbf{r}_{il}))^2 G_{jlk}^{6,\sigma\sigma',(j)} , \end{aligned} \quad (6.128)$$

4. *Translational non-invariant on-site potential term* —

$$\begin{aligned} \Delta\epsilon'_i^{(j)} &= \frac{1}{N_j} \sum_{\mathbf{r} < \max_{i < j}(|\mathbf{r}_{ij}|)} \frac{t^{(j)}(\mathbf{r}')t'_{ji}^{(j)} + t'_{ij}^{(j)}t'_{ji}^{(j)}}{\omega + \frac{1}{2}\epsilon_j^{(j)} + \frac{1}{2}\epsilon^{(j)}} \\ &+ \frac{1}{N_j} \sum_{l,k < j, \mathbf{r}'} (V^{\sigma\sigma,(j)}(\mathbf{r}, \mathbf{r}', \mathbf{r}''))^2 G_{jlk}^{6,\sigma\sigma',(j)} . \end{aligned} \quad (6.129)$$

Similarly, by decomposing the 4-point vertexes  $V'^{\sigma\sigma'}_{ijkl}$  diagonal and off-diagonal parts into translational invariant (eq.(6.109)) and non-invariant parts (eq.(6.110)), their RG equations are obtained from eqs.(6.124) and (6.125) as follows:

5. *Translational invariant density-density interaction term* —

$$\Delta V^{\sigma\sigma',(j)}(\mathbf{r}) = - \sum_{\mathbf{r}_{ij}, \mathbf{r}_{il}} \frac{\frac{1}{N_j}(V^{\sigma\sigma',(j)}(\mathbf{r}, \mathbf{r}_{ij}, \mathbf{r}_{il}))^2}{\omega + \frac{1}{2}\epsilon_j^{(j)} - \frac{1}{2}\epsilon_l^{(j)} + \frac{1}{4}V^{\sigma\sigma',(j)}(\mathbf{r}_{jl}) + \frac{1}{4}V'^{\sigma\sigma',(j)}_{jl}} , \quad (6.130)$$

6. *Translational non-invariant density-density interaction term* —

$$\Delta V'^{\sigma\sigma',(j)}_{ik} = - \sum_{\mathbf{r}_{ij}, \mathbf{r}_{il}} \frac{\frac{1}{N_j}V^{\sigma\sigma',(j)}(\mathbf{r}_{ik}, \mathbf{r}_{ij}, \mathbf{r}_{il})V'^{\sigma\sigma',(j)}_{ijkl} + V'^{\sigma\sigma',(j)}_{ijkl}V'^{\sigma\sigma',(j)}_{ijkl}}{\omega + \frac{1}{2}\epsilon_j^{(j)} - \frac{1}{2}\epsilon_l^{(j)} + \frac{1}{4}V^{(j)}(\mathbf{r}_{jl}) + \frac{1}{4}V'^{\sigma\sigma',(j)}_{jl}} , \quad (6.131)$$

7. *Translational invariant current-current interaction term* —

$$\Delta V^{\sigma\sigma',(j)}(\mathbf{r}_{is}, \mathbf{r}, \mathbf{r}_{im}) = \sum_{\mathbf{r}_{ij}, \mathbf{r}_{il}} \frac{\frac{1}{N_j}V^{\sigma\sigma',(j)}(\mathbf{r}_{ji}, \mathbf{r}_{js}, \mathbf{r}_{jl})V^{\sigma\sigma',(j)}(\mathbf{r}_{lk}, \mathbf{r}_{lm}, \mathbf{r}_{lj})}{\omega + \frac{1}{2}\epsilon_j^{(j)} - \frac{1}{2}\epsilon_l^{(j)} + \frac{1}{4}V^{(j)}(\mathbf{r}_{jl}) + \frac{1}{4}V'^{\sigma\sigma',(j)}_{jl}} , \quad (6.132)$$

8. *Translational non-invariant current-current interaction term* —

$$\Delta V'^{\sigma\sigma',(j)}_{iskm} = \sum_{\mathbf{r}_{ij}, \mathbf{r}_{il}} \frac{\frac{1}{N_j}V^{\sigma\sigma',(j)}(\mathbf{r}_{ji}, \mathbf{r}_{js}, \mathbf{r}_{jl})V'^{\sigma\sigma',(j)}_{lkmj} + V'^{\sigma\sigma',(j)}_{jisl}V'^{\sigma\sigma',(j)}_{lkmj}}{\omega + \frac{1}{2}\epsilon_j^{(j)} - \frac{1}{2}\epsilon_l^{(j)} + \frac{1}{4}V^{\sigma\sigma',(j)}(\mathbf{r}_{jl}) + \frac{1}{4}V'^{\sigma\sigma',(j)}_{jl}} . \quad (6.133)$$



# Chapter 7

## Holographic entanglement renormalisation of topological order in a quantum liquid

In the present chapter, we formalise the momentum-space entanglement renormalization group (MERG) scheme that is implemented as a *reverse* unitary RG (see Fig.9.7.2), and based on the coefficient RG flow studied in Sec.2.5.1 of Chapter 2. Similar reverse RG approaches that involve the re-entangling of hitherto disentangled degrees of freedom has been discussed for some tensor network RG approaches [241, 242]. For this, we start from the many-body state at the *IR* fixed point, and approach the *UV* (i.e., towards the eigenstate of the parent model) by iterative applications of the inverse of the unitary transformations of the URG. The reconstruction method is validated by showing a reduction in the uncertainty of the energy eigenvalue of the reconstructed state with respect to that of the parent model. By representing the many-body states at each RG step as quantum circuits/tensor network [244], and by representing each unitary transformation step as a product of two-local universal gates [243], we obtain an equivalent EHM [232] description for the MERG. We further study the RG evolution of entanglement features such as mutual information [239], entanglement entropy [227] and purity [529] across the MERG tensor network.

The rest of the chapter is organised as follows. In Section4.1, we present the 2D Hubbard model briefly, as well recapitulate details of the unitary RG formalism from Chapter 4 that are pertinent to the present work. We then formulate the MERG scheme for the topologically ordered insulating ground state of the 2D Hubbard model in Section7.2. This is followed by developing quantum circuit representation of the many-particle state as well as the renormalisation procedure, leading to a numerical validation of the MERG. We then present the entanglement holographic mapping (EHM) for the MERG, allowing for a study of the emergence of the topologically ordered ground state from the entanglement RG ,and its visualisation as a quantum error-correcting code. In Section7.3, we compute the ERG flow using several measures of entanglement (e.g., mutual information), developing insight on the distinction between the entanglement signatures of a gapped insulating Mott liquid ground state, a gapless normal metallic state and a Neél antiferromagnetic state. Further, in Section7.4, we analyse the evolution of the many-particle entanglement features of the Mott liquid at half-filling and at the QCP arrived through hole-doping. This will shed light on how d-wave superconductivity arises from the collapse of Mottness at the QCP. Finally,

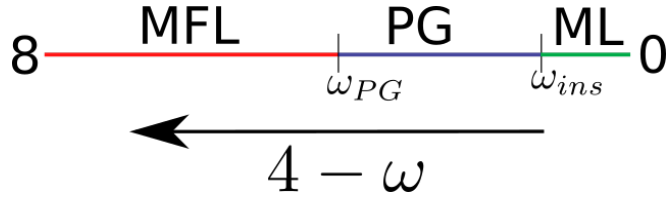


Figure 7.1.1: Schematic representation of the  $T = 0$  RG phase diagram of the 2D Hubbard model at 1/2-filling as a function of quantum fluctuation energyscale ( $8 < 4 - \omega < 0$ , for a tight-binding bandwidth of  $8t$ ,  $t = 1$ ). Red, blue and green regions represent the marginal Fermi liquid metal (MFL), pseudogap (PG) and the Mott insulating liquid (ML) phases respectively.  $\omega_{PG}$  and  $\omega_{ins}$  are energy scales for transitions that initiate and end the PG phase.

in Section 7.5, we use the EHM to develop a deep neural network that can classify the insulating and metallic phases based on their entanglement features. We conclude in Section 7.6. Finally, various details of the URG method, properties of the normal metallic, Neél antiferromagnetic and d-wave superconducting phases, and the theory at the quantum critical point are presented in the appendices.

## 7.1 Normal and topologically ordered (T.O.) insulating phases of the 2D Hubbard model at 1/2-filling

As shown schematically in Fig.7.1.1, the renormalization procedure reveals a  $T = 0K$  phase diagram with the  $x$ -axis given by the one-particle quantum fluctuation energyscale  $\omega$  within  $\hat{\omega}_{(n)}$ . This tracks the single-particle spectral function, i.e., for high energies  $4 - \omega > \omega_{PG}$  (where the tight-binding bandwidth is  $8t$  with  $t = 1$ ), the spectrum is gapless and corresponds to the marginal Fermi liquid phase [180, 181] (red region in Fig.7.1.1). For  $\omega_{ins} < 4 - \omega < \omega_{PG}$ , the spectrum is pseudogapped, while the spectrum is completely gapped for  $4 - \omega < \omega_{ins}$ . It is in this final regime that the insulating Mott liquid state resides, with both spin and charge excitations being gapped [180, 181]. The Hamiltonian for the MFL is found to be

$$H_1^* = \sum_{j,l} \epsilon_{j,l} \hat{n}_{j,l} + \frac{1}{8} \sum_{j,j',l} R_{ll'}^* \hat{n}_{j,l} \hat{n}_{j,l'} (1 - \hat{n}_{j',l}) , \quad (7.1)$$

where  $j, l = \Lambda_j, \hat{s}, \sigma$  and  $j, l' = -\Lambda + \delta, T\hat{s}$ . The first and second terms in Hamiltonian eq.7.1 describes the 1 particle and 2 particle-1 hole dispersions respectively. The 2 particle-1 hole dispersion  $R_{ll'}^* = \omega - 1/2(\epsilon_{j*,l} + \epsilon_{j*,l'})$  arises from the interplay between forward scattering processes involving electronic pairs with different net momentum. About the fluctuation scale  $\frac{W}{2} - \omega_{ins}$ , the system undergoes a transition into a Mott insulating phase (green region in the phase diagram Fig.7.1.1) described by the fixed point Hamiltonian

$$\hat{H}_2^* = \sum_{\hat{s}} K_{\hat{s}}^* \left[ \mathbf{A}_{*,\hat{s}} \cdot \mathbf{A}_{*,-\hat{s}} - \mathbf{S}_{*,\hat{s}} \cdot \mathbf{S}_{*,-\hat{s}} \right] , \quad (7.2)$$

## 7.2. MERG construction for the topologically ordered insulating ground state of the 2D Hubbard model

---

where the charge and spin type pseudospins within the emergent fixed point window  $\Lambda_{\hat{s},\omega}^*$ ,  $\mathbf{A}_{*,\hat{s}}$  and  $\mathbf{S}_{*,\hat{s}}$  respectively, are defined as

$$\mathbf{A}_{*,\hat{s}} = \sum_{\Lambda < \Lambda_{\hat{s},\omega}^*} \mathbf{A}_{\Lambda,\hat{s}}, \mathbf{S}_{*,\hat{s}} = \sum_{\Lambda < \Lambda_{\hat{s},\omega}^*} \mathbf{S}_{\Lambda,\hat{s}}, \mathbf{A}_{\Lambda,\hat{s}} = f_{\Lambda,\hat{s}}^{c;\dagger} \frac{\boldsymbol{\sigma}}{2} f_{\Lambda,\hat{s}}^c, \mathbf{S}_{\Lambda,\hat{s}} = f_{\Lambda,\hat{s}}^{s;\dagger} \frac{\boldsymbol{\sigma}}{2} f_{\Lambda,\hat{s}}^s, \quad (7.3)$$

where  $f_{\Lambda,\hat{s}}^{c;\dagger} = [c_{\Lambda,\hat{s},\sigma}^\dagger \ c_{-\Lambda,T\hat{s},-\sigma}]$  and  $f_{\Lambda,\hat{s}}^{s;\dagger} = [c_{\Lambda,\hat{s},\sigma}^\dagger \ c_{\Lambda-2\Lambda_{\hat{s}}^*,T\hat{s},-\sigma}^\dagger]$  are the spinorial representation for a pair of electrons. Note that the pairing is between two electronic states with net momentum  $\mathbf{Q}$ ; these pairs carry the highest spectral weight among all finite-momentum pairs, and condense into pseudospins at low-energies [180].

$K_{\hat{s}}^*$  is the final magnitude of the backscattering coupling. The degenerate ground state configurations of the Mott insulating phase are labelled by *either* the eigenvalues of the three operators  $\mathbf{A}_* = \mathbf{A}_{*\hat{s}} + \mathbf{A}_{*-\hat{s}}$ ,  $\mathbf{A}_{*\hat{s}}$  and  $\mathbf{A}_{*-\hat{s}}$ , *or* their  $\mathbf{S}$  counterparts

$$\begin{aligned} |\Gamma_+\rangle &= |A_* = 0, A_{\hat{s}}^* = A_{-\hat{s}}^* = N_{\hat{s}}^*, S_{\Lambda\hat{s}} = 0\rangle, \\ |\Gamma_-\rangle &= |S_* = 2N_{\hat{s}}^*, S_*^z = 0, S_{\hat{s}}^* = S_{-\hat{s}}^* = N_{\hat{s}}^*, A_{\Lambda\hat{s}} = 0\rangle. \end{aligned} \quad (7.4)$$

The two configurations  $|\Gamma_+\rangle$  and  $|\Gamma_-\rangle$  are constructed such that  $|\Gamma_+\rangle$  is an eigenstate of the first term in  $H_2^*$  (and has null contribution from the second term), while  $|\Gamma_-\rangle$  is the eigenstate of the second part (and has no contribution from the first). Importantly, we note that the true degeneracy between these ground states is only achieved in the thermodynamic limit. Further, the RG procedure has been quantitatively validated in Refs.[180, 181] by benchmarking the ground state energy per site of the Hubbard model at various dopings against other numerical methods across values of the Hubbard repulsion ( $U$ ) with magnitudes ranging from weak to strong [49].

To characterize the topological features of the gapped two degenerate subspaces, we construct a nonlocal operators  $W$

$$W = \exp \left[ i \frac{\pi}{2} (|\Gamma_+\rangle\langle\Gamma_+| - |\Gamma_-\rangle\langle\Gamma_-| - 1) \right]. \quad (7.5)$$

$W$  commutes with the  $SU(2) \times SU(2)$  pseudospin rotational invariant Hamiltonian  $H_2^*$  in the projected subspace of the states  $|\Gamma_+\rangle$  and  $|\Gamma_-\rangle$ . The two degenerate ground states are adiabatically connected via a twist operator/ nonlocal gauge transformation  $\hat{O}|\Gamma_\pm\rangle = |\Gamma_\mp\rangle$ . As these two states are protected by a many body gap, adiabatic passage between these degenerate ground states involve the creation of charge-1/2 excitations [462, 42, 22]; this is seen from the anticommutation relation  $\{O, W\} = 1$ . Similar twist-translation relation operator relations have also been found recently by some of us for quantum liquid ground states in frustrated quantum antiferromagnets [525, 524]. In the next section, we introduce the entanglement renormalization scheme using the unitary transformations eq.4.2. This will reveal nontrivial entanglement features of gapped topological order, as well as distinguishing it from a gapless state of matter.

## 7.2 MERG construction for the topologically ordered insulating ground state of the 2D Hubbard model

The ground state wavefunction of a parent model such as the 2D Hubbard model is in general difficult to obtain. However, once available, it allows for the computation of various correlation

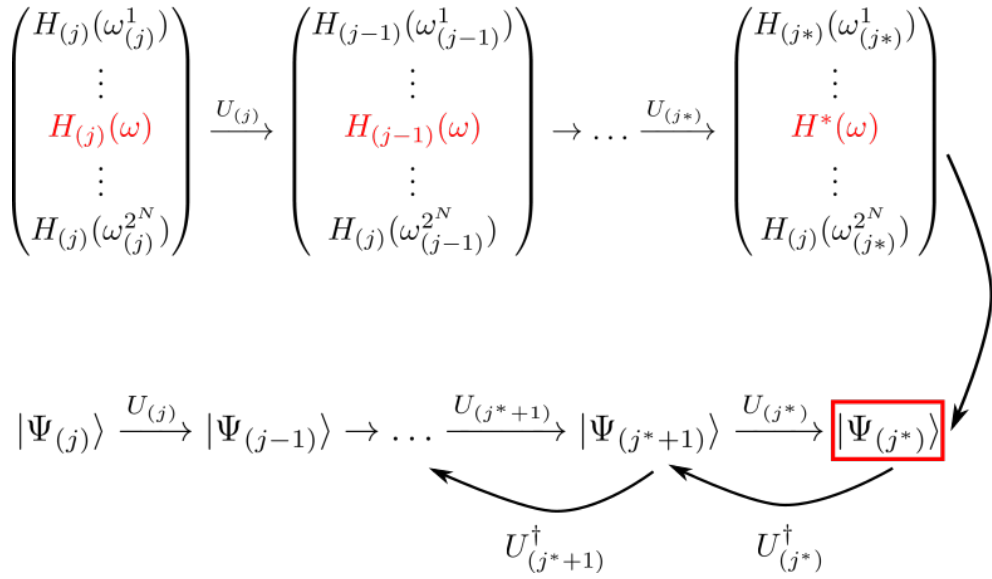


Figure 7.2.1: Upper row: URG flow scheme for Hamiltonians, terminating at fixed point Hamiltonians, e.g.  $H^*(\omega)$ , characterised by fluctuation energy scale  $\omega$ . Lower line: entanglement renormalization RG flow constructed via the inverse unitary transformations  $U_{(j^*+n)}^\dagger$ s on the eigenstate  $|\Psi^*\rangle$  (red bordered box) of  $H^*(\omega)$ .

functions for, e.g., characterizing the low energy features of the system as being either gapless or gapped. We will now demonstrate how this task can be carried out for the 2D Hubbard model using the unitary renormalization group (URG) method. We have already seen above that the URG approach can be carried out in a non-perturbative manner, helping obtain stable fixed point theories at which the RG flows terminate. Further, the stable fixed point Hamiltonians (eq.7.2) are comparatively easier to solve either analytically or numerically than their parent model counterparts [181].

As shown in Fig.9.7.2, the precise program we follow is as follows. We begin by implementing the URG [180] by applying a sequence of unitary transformations to the parent Hamiltonian  $H$ . As demonstrated above, successive unitary transformations lead to a fixed point Hamiltonian  $H^*(\omega)$  and its ground eigenstate  $|\Psi^*\rangle$  at a given quantum fluctuation scale  $\omega$ . Now, by reversing the unitary transformation, we can reconstruct the (a priori unknown) ground eigenstate  $|\Psi\rangle$  of the parent model.

In this way, we realize URG as a momentum space entanglement renormalization group (MERG) procedure carried out for the 2D Hubbard model in Refs.[180, 181]. In those works, we computed various vertex RG equations for the 2D Hubbard model from a URG analysis. By numerically solving the URG flow equations on a momentum-space grid of dimension  $2048 \times 2048$ , we obtained the effective Hamiltonian and the ground state at the Mott liquid stable fixed point. In order to perform a quantitative benchmarking of the URG method, we also carried out a finite size scaling of the ground state energies computed for momentum-space grid sizes ranging from  $1024 \times 1024$  to  $32768 \times 32768$  and achieved excellent agreement with the answers obtained from various numerical methods [49]. URG computations involving eigenfunctions (rather than Hamiltonians) face, however, a considerable challenge: the number of configurations of a many-

## 7.2. MERG construction for the topologically ordered insulating ground state of the 2D Hubbard model

---

body system of interacting qubits grows exponentially with an increase in system size (i.e., the number of qubits). Therefore, in the present work, we consider a simplified construction of the effective theory obtained in Ref.[180, 181].

We begin by solving the Hamiltonian RG equations numerically on a  $2048 \times 2048$  momentum-space grid. As shown in Fig.7.2.2, we then consider an effective problem with a simplified  $k$ -space of only four outward directions normal to the FS,  $\hat{s}_1 = (\pi/4, 3\pi/4)$ ,  $\hat{s}_2 = (\pi/2, \pi/2)$ ,  $\hat{s}_3 = (-\pi/4, -3\pi/4)$ ,  $\hat{s}_4 = (-\pi/2, -\pi/2)$ . 14 electrons reside at low-energies along each normal  $\hat{s}$ , and are paired up to form 7 pseudospins ( $\mathbf{A}$  in eq.7.3). Altogether, this leads to a system of 28 pseudospins (i.e., 56 electrons). The pseudospin states are labelled as follows (see Fig.7.2.2): the states labelled 0, ..., 6 are along  $\hat{s}_1$ , 7, ..., 13 are along  $\hat{s}_2$ , 14, ..., 20 are along  $\hat{s}_3$  and 21, ..., 28 are along  $\hat{s}_4$ . Next, we prepare the system in the eigenstate  $|\Gamma_+\rangle$  of the Hamiltonian  $H_2^*$ . We consider here a simple construction of  $|\Gamma_+\rangle$  (see Fig.7.2.2): two pair of singlets formed out of pair of backscattering pseudospins (6, 20) (involving  $\hat{s}_1$  and  $\hat{s}_3$ ) and (13, 27) (involving  $\hat{s}_2$  and  $\hat{s}_4$ ). The black/white circles in Fig.7.2.2 represent up/down configurations of the disentangled pseudospins. Altogether,  $|\Gamma_+\rangle$  is represented as  $(A_i^z|1_i\rangle = 1/2|1_i\rangle, A_i^z|0_i\rangle = -1/2|0_i\rangle)$ ,

$$|\Gamma_+\rangle = \frac{1}{2} \prod_{n=[0,3]} \prod_{i=[7n,7n+2],j=[7n+3,7n+5]} |0_i 1_j\rangle (|1_6 0_{20}\rangle - |0_6 1_{20}\rangle) (|1_{13} 0_{27}\rangle - |0_{13} 1_{27}\rangle), \quad (7.6)$$

and where we have  $N = 6$  pseudospins along each of the four  $\hat{s}_i$  directions normal to the FS. The two singlets that comprise the initially entangled subspace can be seen from the second and third terms above, while the product of  $|0_i 1_j\rangle$  states correspond to the disentangled pseudospin states. Similarly in terms of the 28 spin type pseudospin qubits  $\mathbf{S}_{\Lambda,\hat{s}}$  the ground state is given by  $(S_i^z|\uparrow_i\rangle = 1/2|\uparrow_i\rangle, S_i^z|\downarrow_i\rangle = -1/2|\downarrow_i\rangle)$ ,

$$|\Gamma_-\rangle = \frac{1}{2} \prod_{n=[0,3]} \prod_{i=[7n,7n+2],j=[7n+3,7n+5]} |\downarrow_i \uparrow_j\rangle (|\uparrow_6 \downarrow_{20}\rangle + |\downarrow_6 \uparrow_{20}\rangle) (|\uparrow_{13} \downarrow_{27}\rangle + |\downarrow_{13} \uparrow_{27}\rangle), \quad (7.7)$$

Note that  $\mathbf{A}$  pseudospin operators annihilate the eigenstates of  $\mathbf{S}$ , and vice versa [180].

We now reintroduce the dominant quantum fluctuations in the state  $|\Gamma_+\rangle$  in the form of tangential scattering, forward scattering and backscattering processes via the successive application of the reverse unitary maps  $U_{(j*)+n}^\dagger$  (see Fig.9.7.2). Importantly, we note that the fluctuations are being added only within the projected subspace of charge pseudospins. We note that for this specific case, the unitary operation  $U_{(j)}$  disentangles four pseudospins labelled  $n(N+1) + N - j$  (where  $n = 0, 1, 2, 3$  is index for the four normal directions, and there are  $N = 6$  pseudospins along each normal direction)

$$U_{(j)} = U_{4N-j+3} U_{3N-j+2} U_{2N-j+1} U_{N-j}. \quad (7.8)$$

In the above,  $U_{n(N+1)+N-j}$  disentangles the pseudospin along the normal  $\hat{s}_{n+1}$  at distance  $\Lambda_{n(N+1)+N-j}$  from the reference non interacting FS, and is defined as follows

$$U_{n(N+1)+N-j} = \frac{1}{\sqrt{2}} \left[ 1 + A_{n(N+1)+N-j}^- \frac{1}{\hat{\omega} - H_{1(j)}^D} C_j B_j^+ - A_{n(N+1)+N-j}^+ \frac{1}{\hat{\omega} - H_{0(j)}^D} C_j B_j^- \right], \quad (7.9)$$

where  $\mathbf{B}_j = [\mathbf{A}_{0j} \ \mathbf{A}_{1j} \ \mathbf{A}_{2j} \ \mathbf{A}_{3j}]^T$ ,  $\mathbf{A}_{nj} = \sum_{l=1}^{N+1} \mathbf{A}_{nl+N-j}$  and the coupling matrix

$$C_j = \begin{pmatrix} V_1^{(j)} & L^{(j)} & K_1^{(j)} & 0 \\ L^{(j)} & V_2^{(j)} & 0 & K_2^{(j)} \\ K_1^{(j)} & 0 & V_1^{(j)} & L^{(j)} \\ 0 & K_2^{(j)} & L^{(j)} & V_2^{(j)} \end{pmatrix}. \quad (7.10)$$

$H_{1(j)}^D$  and  $H_{0(j)}^D$  are the diagonal parts of the Hamiltonian in the projected subspaces of  $\uparrow/\downarrow$  configurations of pseudospin  $j$ , e.g.,

$$H_{1(j)}^D = \sum_{l=1, i=[1,4]}^j \epsilon_{\Lambda_l \hat{s}_i} A_{\Lambda_l \hat{s}_i}^z + B_j^z C B_j^z \quad (7.11)$$

In the coupling matrix,  $V_{(j)}$ ,  $L_{(j)}$  and  $K_{(j)}$  are forward (purple line), backward (orange line) and tangential (green line) scattering couplings respectively displayed in Fig.7.2.2. Finally, the MERG flow equation is given by

$$H_{(j)} = U_{(j)}^\dagger H_{(j-1)} U_{(j)}, \quad (7.12)$$

where the renormalized Hamiltonian

$$H_{(j)} = \mathbf{B}_j C_j \mathbf{B}_j^T. \quad (7.13)$$

From the MERG equation (eq.7.12) and  $U_{(j)}$  (eq.7.9)(l=1,2), we obtain the coupling RG equations accounting for the quantum fluctuations arising from the scattering of a pseudospin pair

$$\begin{aligned} V_l^{(j-1)} &= V_l^{(j)} + \frac{(V_l^{(j)})^2}{\frac{1}{2}(\epsilon_{\Lambda_j \hat{s}} + \epsilon_{\Lambda_j - \hat{s}}) - \omega - \frac{1}{4}V_l^{(j)}}, \\ K_l^{(j-1)} &= K_l^{(j)} + \frac{(K_l^{(j)})^2}{\omega - \frac{1}{2}(\epsilon_{\Lambda_j \hat{s}} + \epsilon_{\Lambda_j - \hat{s}}) - \frac{1}{4}K_l^{(j)}}, \\ L^{(j-1)} &= L^{(j)} + \frac{N_F^2(L^{(j)})^2}{\frac{1}{2N'} \sum_s (\epsilon_{\Lambda_{j-1} \hat{s}} + \epsilon_{\Lambda_{j-1} - \hat{s}}) - \omega - \frac{1}{4}L^{(j)}}. \end{aligned} \quad (7.14)$$

In the above,  $l = 1, 2$  represents the two normal directions  $\hat{s}_1$  and  $\hat{s}_2$ . Additionally, note that we choose  $W/2 - \omega = 0$  in implementing the MERG procedure, corresponding to the lowest quantum fluctuation (QF) scale lying well within the Mott insulating phase shown in the phase diagram Fig.7.1.1. For the QF energy  $W/2 - \omega = 0$ , the  $V$  and  $L$  vertices are RG irrelevant (eq.7.14), while the  $K$  backscattering vertices are RG relevant leading to the effective Hamiltonian  $H_2^*$  (eq.7.2).

In the next subsection, we will represent the fixed point ground state  $\Gamma_+$ , as well as the sequence of states  $|\Psi_{(j)}\rangle$ 's connected to it via  $U_{(j)}^\dagger$ 's, as many-body quantum circuits. As quantum circuits are very generally known to be examples of tensor networks [244, 530], this will help us realize a momentum space tensor network renormalization scheme for the MERG procedure.

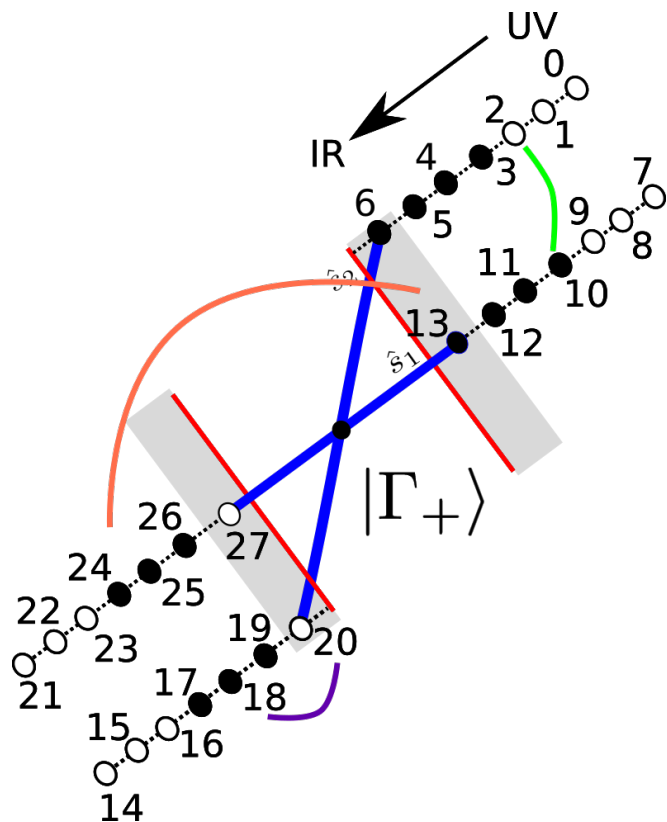


Figure 7.2.2: Representation of the ground state in the MERG construction. The blue lines indicate the singlets formed out of pairs of pseudospins (6, 20) and (13, 27). Dark/white circles represent up/down pseudospins. The arrow labelled UV to IR depicts the high to low variation of the pseudospin dispersion. The orange, green and purple arrows represents the backscattering, tangential scattering, forward scattering processes respectively.

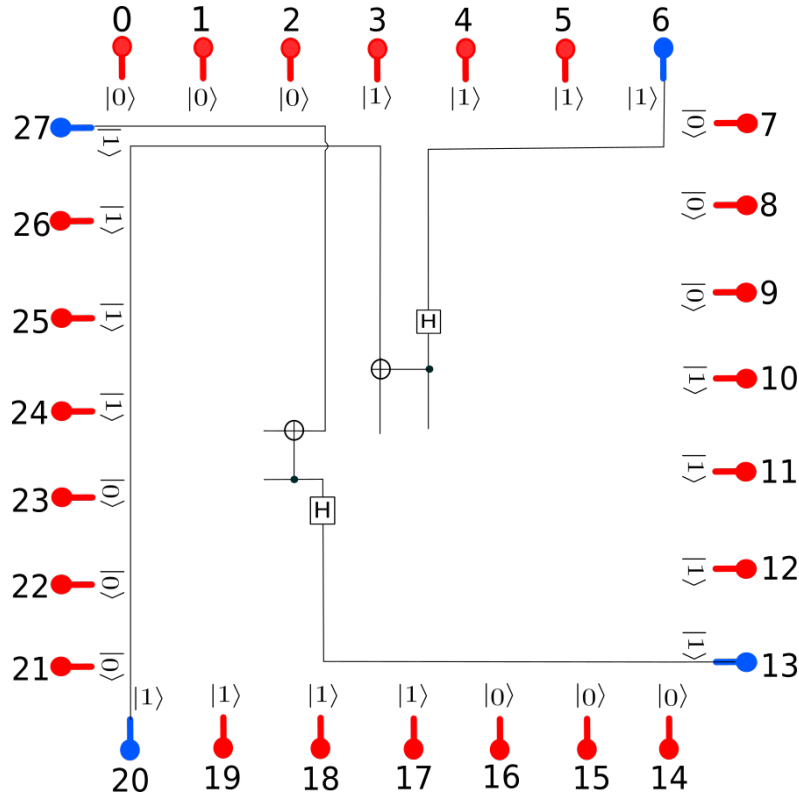


Figure 7.2.3: Quantum circuit representation of  $|\Gamma_+\rangle$  in terms of one- and two-pseudospin gates.

### 7.2.1 Quantum circuit network representation of the T.O. ground state and its renormalization

As seen above, the many body ground state  $|\Gamma_+\rangle$  at the RG fixed point has a simple entanglement structure involving only two maximally entangled pairs (Fig.9.7.2). As can be seen in Fig.7.2.3, this allows a easily computable quantum circuit description involving two controlled not (C-NOT) gates acting between pseudospins (6,20) and (13,27), such that the first pseudospin in each bracket (6 and 13) is a target bit and the second (20 and 27) a control bit. The Hadamard gate  $H$  acts on the control bit, rotating its state  $|1\rangle$  to  $\sqrt{2^{-1}}(|0\rangle - |1\rangle)$ . This is followed by a C-NOT gate acting on 20 and 27, leading to the singlet states (blue qubits in Fig.9.7.2) in eq.7.6. The disentangled states (red qubits in Fig.9.7.2) have either up or down spin configurations, as represented in eq.7.6.

The quantum circuit description for the states generated via reverse RG is (Fig.9.7.2)

$$U_{(j)}^\dagger |\Psi_{(j-1)}\rangle = |\Psi_{(j)}\rangle , \quad (7.15)$$

and can be obtained via a decomposition of  $U_{(j)}$  eq.7.8 as a product of one/two qubit gates[243]

$$\begin{aligned} U_{(j)} &= U_{4N-j+3} U_{3N-j+2} U_{2N-j+1} U_{N-j} \\ U_\alpha &= U_{\alpha,N} \otimes U_{\alpha,N-1} \otimes \dots \otimes U_{\alpha,N-j-1} \otimes U_{\alpha,2N+1} \otimes U_{\alpha,2N} \otimes \dots \otimes U_{\alpha,2N-j} \otimes U_{\alpha,3N+2} \otimes \\ &\quad \otimes U_{\alpha,3N+1} \otimes \dots \otimes U_{\alpha,3N-j+1} \otimes U_{\alpha,4N+3} \otimes U_{\alpha,4N+2} \otimes \dots \otimes U_{\alpha,4N+2-j} H_\alpha , \end{aligned} \quad (7.16)$$

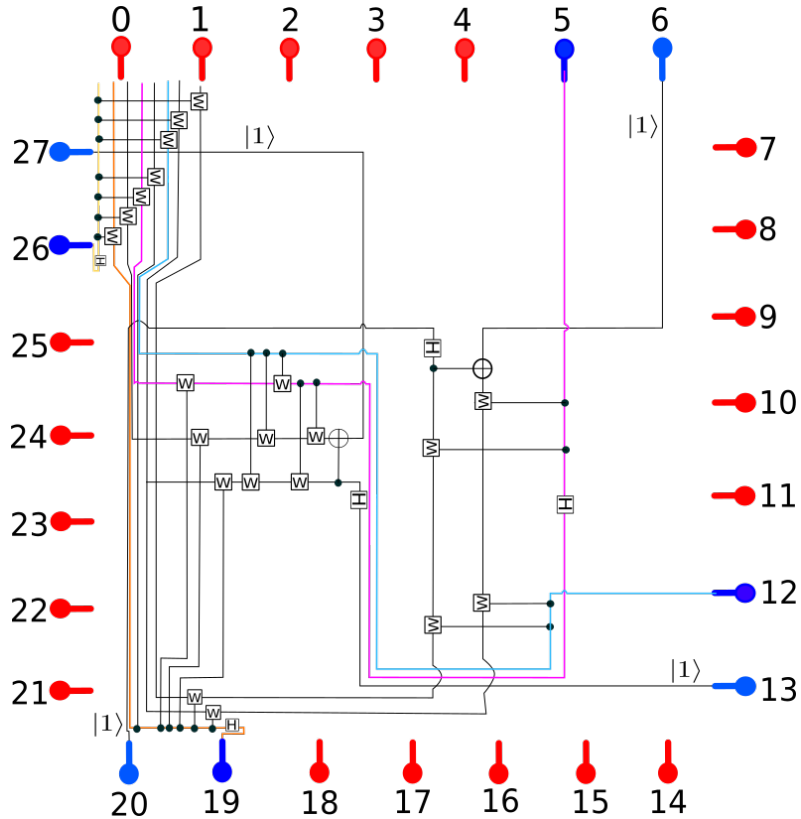


Figure 7.2.4: Quantum circuit representation of the many-body state after 1 reverse RG step in terms of one- and two-pseudospin gates. The purple, cyan, orange and yellow lines represent the entangling pathways of the qubits/pseudospins indexed 5, 12, 19 and 26.

where  $\alpha = n(N+1) + N - j$ ,  $n=0, 1, 2, 3$  and  $N = 6$ . The above decomposition of the unitary circuit into two local CNOT gates, Hadamard gates and phase gates implies that URG is a version of a Clifford stabiliser code [233] that obeys the Gottesman-Knill theorem, i.e., such a quantum circuit can be simulated on a classical computer in polynomial time.

The unitary transformation  $U_{N-j}$  disentangles qubit labelled  $N-j$  (see Fig.7.2.2 for the state labels), with similar definitions for the other unitary transformations.  $H_\alpha$  represents the Hadamard gate. The individual two qubit gates  $U_{n(N+1)+N-j, m(N+1)+N-l}$  can be represented via a controlled- $U$  rotation with  $\alpha = n(N+1) + N - j$  as the control bit and  $\beta = m(N+1) + N - l$  as the target bit

$$U_{\alpha,\beta} = \frac{1}{\sqrt{2}} [|1_\alpha\rangle\langle 1_\alpha| \otimes W_\beta + |0_\alpha\rangle\langle 0_\alpha| \otimes I_2] . \quad (7.17)$$

The form of the single qubit rotation operations,  $W_\beta = \exp\left(\frac{i}{2}\boldsymbol{\sigma}_\beta \cdot \hat{\mathbf{n}}\right)$ , can be obtained by solving the reverse RG eq.7.15 using the decomposition of the unitary operator eq.7.16 and the following representation of the  $|\Psi_{(j)}\rangle$

$$|\Psi_{(j)}\rangle = a|1_{n(N+1)+N-j}\rangle|\Phi\rangle + b|0_{n(N+1)+N-j}\rangle|\chi\rangle , \quad (7.18)$$

where 1 and 0 represent the configurations of the pseudospin labelled  $n(N+1) + N - j$ . The states  $|\Phi\rangle$  and  $|\chi\rangle$  represent the configurations of the rest of the pseudospins. The quantum circuit representation for the state  $|\Psi_{(j^*+1)}\rangle$  is shown in Fig.7.2.4. The number of one/two-local unitary gates needed to obtain the quantum circuit description of the state  $|\Psi_{(j^*+n)}\rangle$  quantifies the circuit complexity (CC) [248]. The CC for the circuit designs of  $|\Psi_{(j)}\rangle$  at every RG step is found to be

$$CC(j) = 8j^2 - 2j - 4 . \quad (7.19)$$

In Figures 7.2.3 and 7.2.4, the quantum circuit description for the states  $|\Psi_{(1)}\rangle$  and  $|\Psi_{(2)}\rangle$  are thus found to possess the circuit complexity  $CC(1) = 2$  and  $CC(2) = 22$  respectively. By using the many body states generated via the reverse RG steps discussed earlier, the variation of the circuit complexity along the RG flow is numerically verified by the blue curve in Fig.7.2.5. The orange curve in Fig.7.2.5 represents the decrement in complexity of the unitary disentangling operation at every RG step. With this construction, we have established MERG as a quantum circuit/tensor network renormalization group scheme. In the next subsection, we validate the RG formalism by displaying its capability in reconstructing the ground state of the parent model from the effective model.

## 7.2.2 Eigenstate reconstruction within the MERG scheme

MERG, being a unitary map involving inverse unitary transformations on the eigenstates of the effective model, allows us to reconstruct the eigenstates of the parent Hubbard model. In this work, we account for only the dominant fluctuations in the charge pseudospin subspace of the operators. Deviation of the various pseudospin scattering couplings  $K, V$ , and  $L$  from a uniform magnitude of  $U_0$  of the parent model can be clearly seen in eq.7.13. Upon reversing the RG steps, this deviation should decrease. We quantify this decrease through the reduction in the pseudospin interaction energy fluctuations in the entangled subspace  $\Delta E_{(j)} = \langle\Psi_{(j)}|(\Delta H_j)^2|\Psi_{(j)}\rangle$

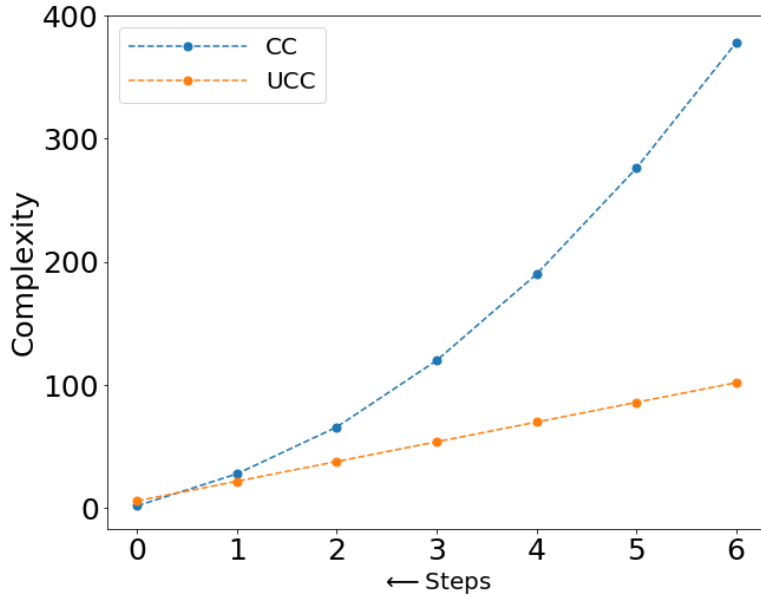


Figure 7.2.5: Orange curve  $CC$  represents circuit complexity of the many-body state, blue curve  $UCC$  represents complexity of the unitary transformation  $U$  (or equivalently  $D$  depth of  $U$ ) along the RG flow trajectory.

(see Fig.7.2.6). After six reverse RG steps, the fluctuations have reduced to 10% of its initial value (see Fig.7.2.6), and we expect a further fall in the value of the fluctuations with increasing system size. This validates the eigenstate reconstruction within the MERG scheme.

### 7.2.3 Entanglement holographic mapping (EHM) representation for the topologically ordered phase

In the earlier section, we have established the URG procedure as a tensor network RG by providing quantum circuit description of many-body states [244]. In Fig.7.2.7, we describe the architecture of the tensor network RG through an equivalent entanglement holographic mapping (EHM) representation [232, 177]. Similar to the case of spectrum bifurcation renormalization group (SBRG) [229], unitary maps preserves the canonical fermion anticommutation relations. At each RG step shown in Fig.7.2.7, the nonlocal unitary operator (yellow block in Fig.7.2.7) disentangles four pseudospins in the *holographic boundary* at high energies (UV), mapping them onto the red *emergent bulk physical qubits* at lower energies (i.e., towards IR). The first layer of unitary transformation disentangles the pseudospins located farthest from the FS (labelled 0, 7, 14, 21), the next step pseudospins distentangled the pseudospins 1, 8, 15, 22 and so on, eventually scaling towards the FS. Alongside these disentanglement RG steps, the pseudospins belonging to the entangled space undergo entanglement resharing. Deep in the IR regime, the system enters into an Mott liquid phase characterized by pseudospins pairing up as singlets (the dotted ovals pairing pseudospins (6,20) and (13,27) in Fig.7.2.7).

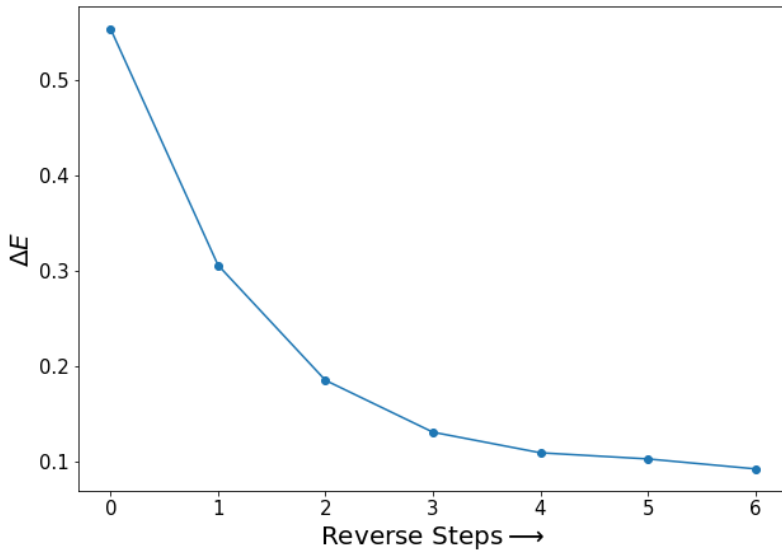


Figure 7.2.6: Plot displaying the reduction in energy uncertainty  $\Delta E$  (with onsite repulsion  $U_0 = 8$ ) upon reversing the RG steps.

Similar to our earlier discussions, an important feature of the nonlocal unitary operation  $U_{(j)}$  (yellow block in Fig. 7.2.7) is that it can be decomposed as a product of local 2-qubit disentanglers. Below we present the decomposition for the operator  $U_{N-j}$

$$\begin{aligned} U_{(j)} &= U_{4N-j+3}U_{3N-j+2}U_{2N-j+1}U_{N-j} \\ U_{N-j} &= U_{N-j,N} \dots U_{N-j,N-j+1}U_{N-j,2N+1} \dots U_{N-j,2N-j+1}U_{N-j,3N+2} \dots U_{N-j,3N-j+2} \\ &\times U_{N-j,4N+3} \dots U_{N-j,4N-j+3} . \end{aligned} \quad (7.20)$$

As an outcome of the complete transformation  $U_{(j)}$ , the four pseudospins labelled  $N - j, 2N - j + 1, 3N - j + 2, 4N - j + 3$  are disentangled, and the *circuit complexity* of the unitary transformation is given by  $UCC_j = 16j - 10$ . It is interesting to note that the circuit complexity for the tensor network representation of the MERG quantum circuit ( $UCC_j \sim O(j)$ ) is substantially less than that of the tensor network representation of the quantum state itself ( $CC \sim O(j^2)$ ).

We now present an algorithm for obtaining the form of the individual disentangler  $U_{\alpha,\beta}$  (where  $\alpha = N - j, \beta = N$ ). For the RG step  $j$ ,  $|\Psi_{(j)}\rangle$  is the input state and  $U_{(j)}|\Psi_{(j)}\rangle = |\Psi_{(j-1)}\rangle$  is the rotated output state. We first perform a decomposition of both the input and output states in terms of the up (1)/down (0) spin basis states labelled  $\alpha, \beta$  and the subsystem configuration of the rest of the pseudospins

$$\begin{aligned} |\Psi_{(j)}\rangle &= \sum_{m,n=[1,n_{max}]} D_{\alpha,\beta}^{m,n,(j)} |m\rangle_{\alpha,\beta} |\Phi_{(j)}^n\rangle , \\ |\Psi_{(j-1)}\rangle &= \sum_{m',n'=[1,n'_{max}]} D_{\alpha,\beta}^{m',n',(j-1)} |m'\rangle_{\alpha,\beta} |\Phi_{(j-1)}^{n'}\rangle . \end{aligned} \quad (7.21)$$

Here, the states  $|\Phi_n\rangle$  and  $|m\rangle$  are orthonormalized, with  $m$  belonging to the configuration set

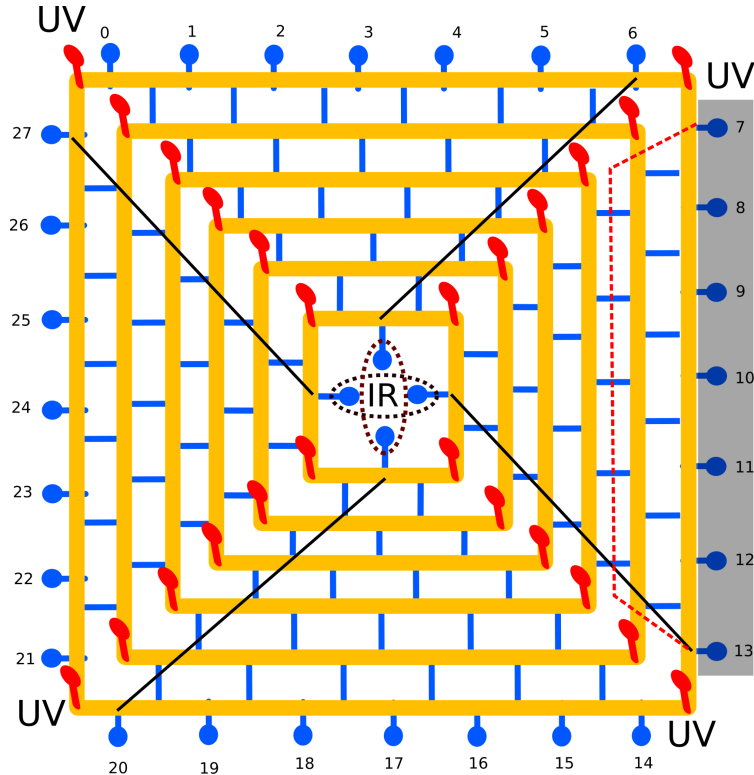


Figure 7.2.7: Entanglement holographic mapping (EHM) representation of MERG. The blue legs represent the holographic boundary made of the physical pseudospin qubits. The yellow block represents a nonlocal unitary disentangler which iteratively maps the boundary (blue) qubits to the bulk (red) qubits. The black lines represent the passage of the qubits 6, 13, 20, 27 from UV to IR. The grey box represents the boundary region 7 – 13 in the UV that is isolated within the bulk of the EHM by the minimal surface/causal cone (dashed red line) after the second RG step.

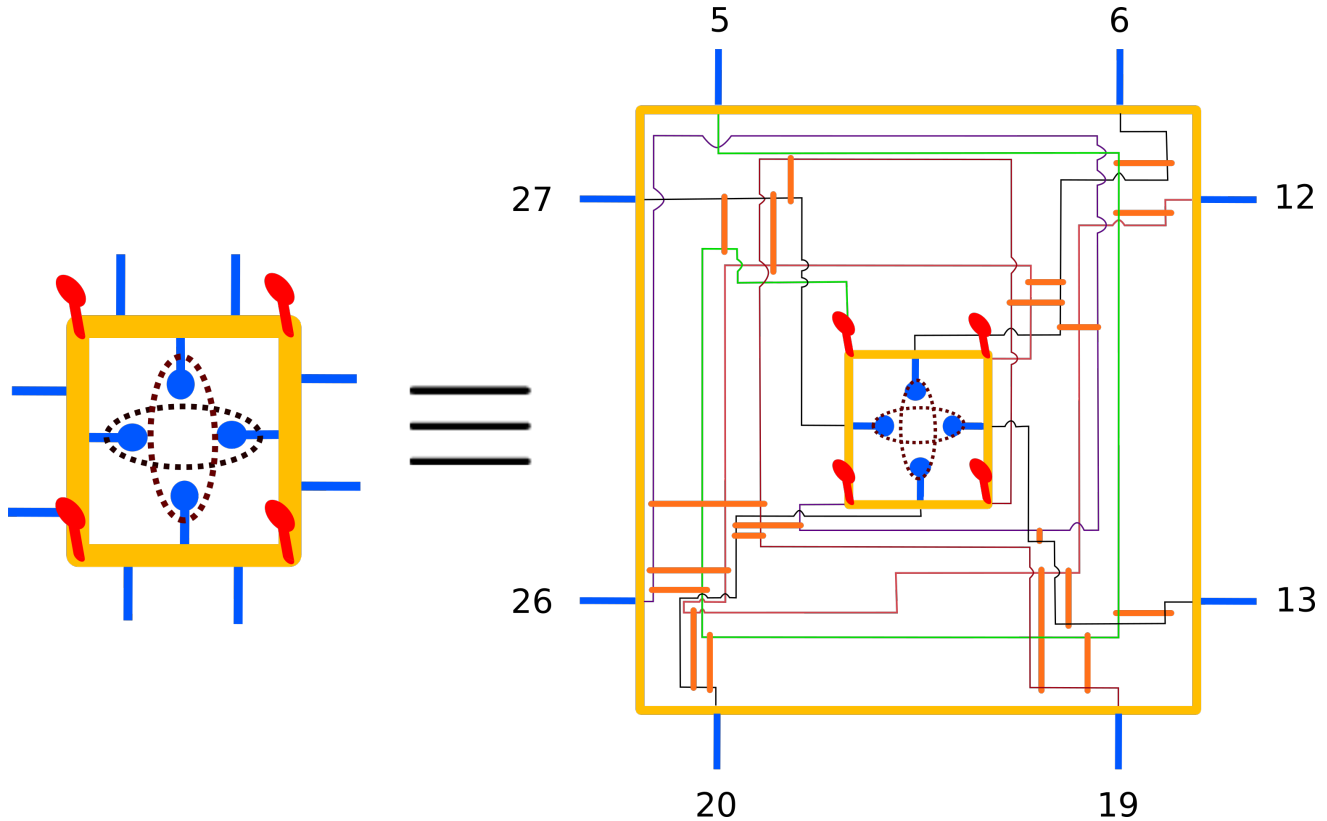


Figure 7.2.8: Decomposition of nonlocal unitary disentangler (yellow block) into arrangement of local two-qubit/pseudospin disentanglers (orange blocks). The green, pink, brown and violet lines represents the Hilbert space for pseudospins labelled 5, 12, 19 and 26 respectively. The orange block operates on the lines crossing its edges.

## 7.2. MERG construction for the topologically ordered insulating ground state of the 2D Hubbard model

---

of two pseudospins  $m \in \{00, 01, 10, 11\}$ . Additionally, we note that in the state  $|\Psi_{(j-1)}\rangle$ , the configuration of pseudospin  $\alpha$  is restricted to 0 or 1; this restricts  $m'$  to one of the two subsets  $m' \in \{00, 01\}$  and  $m' \in \{10, 11\}$ .

We now construct an auxillary state  $|\rho\rangle$  by extracting the two pseudospin configuration of  $\alpha, \beta$  and the state  $|\Psi_{(j-1)}\rangle$ , and embedding it into a higher dimensional Hilbert space that constitutes all the subsystem states  $|\Phi_{(j)}^n\rangle$ . If  $n'_{max} > n_{max}$ , then the states  $|\Phi_{(j)}^n\rangle$  are augmented by the states  $|\chi_{n_{max}+1}\rangle, \dots, |\chi_{n'_{max}}\rangle$  orthogonal to them. This leads to the following  $|\rho\rangle$  for  $n'_{max} \leq n_{max}$

$$|\rho\rangle = \sum_{m',n'} D_{\alpha,\beta}^{m',n',(j-1)} |m'\rangle_{\alpha,\beta} |\Phi_{(j)}^{n'}\rangle . \quad (7.22)$$

On the other hand, if  $n'_{max} \geq n_{max}$ ,

$$|\rho\rangle = \sum_{m',n'=[1,n_{max}]} D_{\alpha,\beta}^{m',n',(j-1)} |m'\rangle_{\alpha,\beta} |\Phi_{(j)}^{n'}\rangle + \sum_{m',p=[n_{max}+1,n'_{max}]} D_{\alpha,\beta}^{m',p,(j-1)} |m'\rangle_{\alpha,\beta} |\chi_p\rangle . \quad (7.23)$$

We now need to find an unitary transformation  $U_{\alpha,\beta}$  that maps  $|\Psi_{(j)}\rangle$  to  $|\rho\rangle$ . This can be constructed by first performing Gram-Schmidt orthonormalization to find a state  $|\rho_\perp\rangle$  that is orthogonal to  $|\Psi_{(j)}\rangle$

$$|\rho^\perp\rangle = \mathcal{N}(|\rho\rangle - |\Psi_{(j)}\rangle\langle\Psi_{(j)}|\rho\rangle) , \quad (7.24)$$

where  $\mathcal{N}$  is the normalisation factor. The inner product  $\langle\Psi_{(j)}|\rho\rangle$  can then be determined from eq.7.22 and eq.7.23, allowing us to determine the state  $|\rho^\perp\rangle$  exactly. From here, we can construct the unitary operation

$$U_{\alpha,\beta} = \exp(\tau(|\rho_\perp\rangle\langle\Psi_{(j)}| - |\Psi_{(j)}\rangle\langle\rho_\perp|)) , \quad (7.25)$$

where the many-body rotation angle is  $\tau = \cos^{-1}(\langle\Psi_{(j)}|\rho\rangle)$ .

In order to find the next unitary operator in the decomposition, we recast  $|\rho\rangle$  in the pseudospin basis of another set of states  $\alpha', \beta'$  (as in eq.7.21). A similar representation for  $|\Psi_{(j-1)}\rangle$  is found in the pseudospin basis of  $\alpha', \beta'$ , following which the steps outlined above are followed once again to obtain the disentangler  $U_{\alpha',\beta'}$ . In this way, the entire decomposition given by eq.7.20 is obtained. A quantum circuit description for a particular nonlocal unitary operator  $U_{(j)}$  (yellow block in Fig.7.2.7) is given in Fig.7.2.8. The orange blocks on the right panel of Fig.7.2.8 disentangles a pair of pseudospins. The existence of a quantum circuit design of the nonlocal disentangler  $U_{(j)}$  as a combination of two local disentanglers justifies a holographic description for MERG [177]. We close this section by providing a comparison between the MERG architecture Figs.7.2.7 and 7.2.8 and other tensor network methods, e.g., multiscale entanglement renormalization group ansatz (MERA) [161] and deep MERA [269]. The first important difference worth noting is that while each transformation layer in MERG is composed only of unitaries, in MERA and DMERA, every transformation layer is composed of a layer of two-local unitaries and a layer of isometries. Next, both MERA and DMERA involve variational parameters in the transformation layers. On the other hand, MERG does not have variational parameters: the unitary transformations are solely determined via the form of the Hamiltonian that is block diagonalized and the choice of quantum fluctuation energy scale  $\omega$  (eq.2.15). Finally, in MERG and DMERA, each unitary

transformation layer is composed of many sublayers of two local unitary disentanglers gates; this is defined as the depth of the unitary gate  $D$ . For instance, in DMERA, the depth  $D$  is equal to the number of variational parameters employed in the transformation layer. However, in MERG, the depth at each unitary RG step ( $D_j$ ) is equal to the circuit complexity, i.e.,  $D_j = UCC_j = 16j - 10$  (Fig.7.2.5).

### 7.2.4 Emergence of T.O. ground state and quantum error correcting code

We will now demonstrate that the topologically ordered ground state manifold of the Mott liquid states  $\{|\Gamma_+\rangle, |\Gamma_-\rangle\}$  (eq.7.6, eq.7.7) can be associated with a stabilizer group  $G$  in the space of the four qubits  $|6\rangle, |13\rangle, |20\rangle, |27\rangle$  that belong to the emergent space shown in Fig.7.2.2. That is, every element  $g \in G$  will satisfy the property  $g|\Gamma_\pm\rangle = |\Gamma_\pm\rangle$  [262, 529]. In the ground state  $|\Gamma_+\rangle$ , the qubit pairs  $(|6\rangle, |20\rangle)$  and  $(|13\rangle, |27\rangle)$  form a pair of **A** pseudospin singlets (eq.7.3), and at the IR fixed point of the URG, these are in tensor product with the rest of the disentangled qubits. Similarly, in  $|\Gamma_-\rangle$ , the qubit pairs  $(|6\rangle, |20\rangle)$  and  $(|13\rangle, |27\rangle)$  form a pair of **S** pseudospin triplets at the IR fixed point (which the decoupled qubits are in tensor product with). The elements of the stabilizer group  $G$  can then be constructed out of the stabilizer groups  $G_1$  and  $G_2$  in the subspace of qubits  $(|6\rangle, |20\rangle)$  and  $(|13\rangle, |27\rangle)$  respectively

$$\begin{aligned} G_1 &= \{-4A_6^z A_{20}^z - 4S_6^z S_{20}^z, -4A_6^x A_{20}^x + 4S_6^x S_{20}^x\}, \\ G_2 &= \{-4A_{13}^z A_{27}^z - 4S_{13}^z S_{27}^z, -4A_{13}^x A_{27}^x + 4S_{13}^x S_{27}^x\}, \\ G &= \{g_1 \otimes g_2, g_1 \in G_1, g_2 \in G_2\} . \end{aligned} \quad (7.26)$$

It can be easily seen that the eigenstates  $|\Gamma_\pm\rangle$  (eqs.7.6 and 7.7) are left invariant by the action of group elements of  $G$ . Furthermore, the elements  $g \in G$  commute with the Wilson loop operator  $W$  (eq.7.5):  $[W, g] = 0$ . Thus, the eigenvalues of  $W$  ( $\pm 1$ ) are good quantum numbers that label the eigenstates  $|\Gamma_\pm\rangle$ :  $W|\Gamma_\pm\rangle = \pm|\Gamma_\pm\rangle$ . In this way, we observe that the MERG program yields the topological Wilson loop operator  $W$  as well as the stabilizer group  $G$  (eqs.7.26) associated with the topologically ordered manifold. Below, this will allow us to construct strategies for topological quantum error correction.

Fig.7.2.9 shows that the Wilson loop expectation value  $\langle\Psi_{(j)}|W|\Psi_{(j)}\rangle$  has minimal growth in the first few RG steps, followed by a sharp rise between the second last and final RG steps, ending at  $\langle\Psi_{(j^*)}|W|\Psi_{(j^*)}\rangle = 1$ . This shows that in the state  $|\Gamma_+\rangle$ , the pseudospins form a pair of maximally entangled singlets that are distilled out from a (bare) state where the entanglement is initially spread among many members. For example, in the second last RG step, there are  $CC(2) = 22$  entangled bonds compared to just the two singlet bonds in  $|\Gamma_+\rangle$ . This explains the sharp distillation of topological order via the URG procedure.

In the language of topological quantum error correcting codes, the the topologically ordered states form the *codewords*, and the unitaries  $U_j$  of the URG *decode* them. On the other hand, the reverse unitaries  $U_j^\dagger$ 's of the MERG sequentially *encode* the codeword  $|\Gamma_+\rangle$  in a higher dimensional Hilbert space by re-entangling them with the decoupled degrees of freedom (Fig. 9.7.2). The identity  $U_j U_j^\dagger = 1$  describes the encoding-decoding program. An example state obtained by the encoding step:  $U_{j^*+1}^\dagger |\Psi_{j^*}\rangle = |\Psi_{j^*+1}\rangle$  is represented in Fig.7.2.4. The decoding strategy  $U_{(j)}|\Psi_{(j)}\rangle = |\Psi_{(j-1)}\rangle$

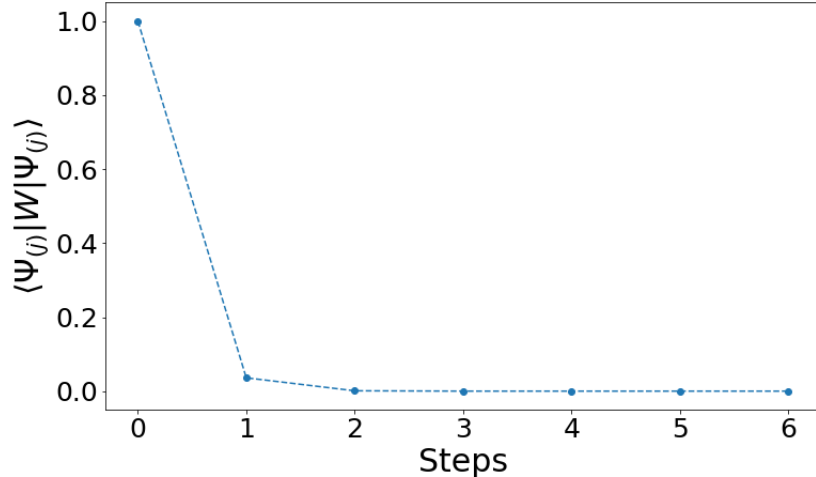


Figure 7.2.9: Evolution of the expectation value of the Wilson loop along the RG trajectory.

(forward RG) leads to the *stabilizer* qubits (disentangled pseudospins) which can maintain a non-trivial error syndrome in the presence of external noise in the encoded state  $|\Psi_{(j)}\rangle$ . In this way, MERG can generate an encoding-decoding program using the form for  $U$  (eq.2.15) for the case of a parametric noise that can be modelled into a Hamiltonian  $H_1$  different from  $H$  (eq.5.1). Thus, MERG is realized as a quantum error correction code that resolves the internal quantum fluctuations, leading to a topological codeword manifold [266]. Further, this platform paves the way for optimal error correction strategies in cases of more general environmental noise. In the next section, we will track the many-body entanglement features along the RG flow that leads to the topological ordered state.

### 7.3 Entanglement RG flow towards the topologically ordered ground state

The entanglement features [531] of a many-body state are formed by a collection of various quantifiers, e.g., mutual information, entanglement entropy, Renyi entropy, purity etc. for the Schmidt (entanglement) spectra obtained for all possible different bipartitions. In the present context, the topologically ordered state [532] is characterized by emergence of (real space) short ranged strongly entangled singlet pairs (similar to the short ranged resonating valence bonds (RVB) [533]) in the low energy subspace. For example, in the Mott liquid ground state wavefunction eq.7.6, the members of the pairs (6,20) and (13,27) (Fig.7.2.2) are maximally entangled and belong to different sides of the  $E_F = 0$  energy boundary (FS); the large  $k$ -space separation ensures that these are short ranged pairs in real space. In this section, we investigate the RG crossover into a system of strongly entangled pairs  $|\Gamma_+\rangle$  amidst scattering between all pseudospin pairs by tracking a subset of their *entanglement features*.

### 7.3.1 Definitions and Computation method

We first define the entanglement features that has been used for the analysis.

1. *Mutual information*( $MI$ ) between a pair of pseudospins characterizes the *strength of entanglement* [240, 177] among the members  $i$  and  $j$

$$I(i:j) = -Tr(\rho_i \ln \rho_i) - Tr(\rho_j \ln \rho_j) + Tr(\rho_{ij} \ln \rho_{ij}) , \quad (7.27)$$

where  $\rho_i, \rho_j$  are the 1-pseudospin reduced density matrices (RDM) and  $\rho_{ij}$  is the 2-pseudospin RDM. More precisely, if pseudospins  $(i, j)$  are individually strongly entangled with the rest of the pseudospins, then  $\rho_{ij}$  has a huge spread in its probability eigenvalues. This lowers the MI content among  $(i, j)$  and characterizes a weakly entangled pair. On the other hand, if the pseudospins are strongly entangled as a pair, then  $\rho_{ij}$  has a smaller spread and characterizes a strongly entangled pair. For example, the singlet pair  $(i, j) = (6, 20)$  in eq.7.6 has maximum possible mutual information  $I(i:j) = 2 \ln 2$ , and clearly  $\rho_{ij} = 1$  is a pure state with zero spread.

2. *Information distance* is a distance measure between pseudospins computed as the negative logarithm of the *MI*

$$d(i,j) = -\ln \frac{I(i:j)}{2 \ln 2} . \quad (7.28)$$

$d(i,j)$  is defined such that strongly entangled pairs have smaller information distance. The maximally entangled pairs  $(6, 20)$  in  $|\Gamma_+\rangle$  has zero information distance  $d(6, 20) = 0$ , while the pair of disentangled pseudospins  $(1, 2)$  has  $d(1, 2) \rightarrow \infty$ . In a many-body state,  $|\Psi\rangle$  is the collection of all possible information distances  $d(i, j)$ , and describes an effective *spacetime geometry* [177]. This provides a link between the quantum circuit network descriptions of state  $|\Psi_{(j)}\rangle$  and the entanglement spacetime geometries  $d(i, j)$ 's obtained at each RG step. In this way, the strongest entangled members in the state  $|\Psi_{(j)}\rangle$  characterizes the *geodesic-*  $d_g = \min_{i,j} d(i, j)$  of the spacetime geometry.

3. *Purity* is defined as  $Tr(\rho^2)$ , and characterizes the spread in the probability eigenvalues of the RDM. Purity is useful for classifying the amount of entanglement information lost in obtaining the RDM, i.e., the partial tracing over the rest of the entangled degrees of freedom.

4. The *Schmidt spectrum*/entanglement spectrum [151] is a set of numbers  $\{\lambda_i\}$  obtained from a Schmidt decomposition of  $|\Psi\rangle$  across a bipartition, e.g., between 2 and  $N - 2$  pseudospins

$$|\Psi\rangle = \sum_{i=1}^k \lambda_i |\phi_i\rangle_2 |\Phi_i\rangle_{N-2} , \quad (7.29)$$

where  $|\phi_i\rangle$  are the mutually orthogonal two-pseudospin states and  $|\Phi_i\rangle$  are the orthogonal many-body configurations of the  $N - 2$  pseudospins. For such a bipartition of 2 and  $N - 2$  pseudospins, the quantity  $k$  is given by  $k < \min(d_A, d_B) = 4$ , where  $d_A, d_B$  are the subsystem Hilbert space dimensions.

5. The *Physical distance*  $d_p(i, j)$  between pseudospin pairs in momentum space is obtained by first computing the  $k$ -space distance using the Euclidean metric

$$d(\mathbf{k}_i, \mathbf{k}_j) = \sqrt{(k_{ix} - k_{jx})^2 + (k_{iy} - k_{jy})^2} , \quad (7.30)$$

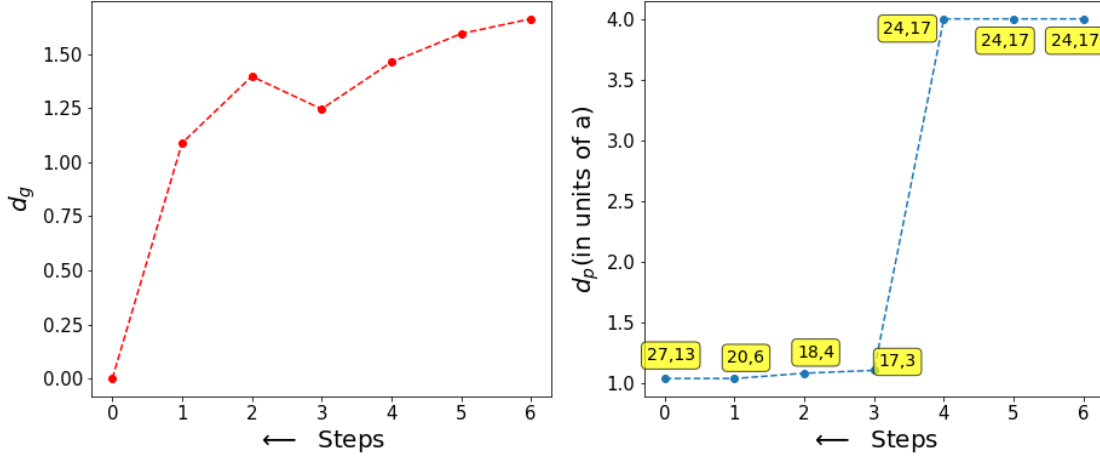


Figure 7.3.1: Left Panel: Scaling of the information geodesic  $d_g$ . Right Panel: Scaling of the corresponding physical distance  $d_p$  between the strongest entangled pseudospin pairs.

and then inverting  $d(\mathbf{k}_i, \mathbf{k}_j)$  to obtain the relation  $d(i, j) = 1/d(\mathbf{k}_i, \mathbf{k}_j)$ .

The computation method we apply is as follows. We first apply the MERG technique on the state  $|\Psi^*\rangle$  to obtain all the states  $|\Psi_{(j)}\rangle$  in the steps outlined in Fig.9.7.2. This is followed by a computation of the one-particle and two-particle Schmidt spectra (as in eq.7.29) for all possible pairs of pseudospins. The various entanglement features listed above can then be computed numerically from the Schmidt spectra.

### 7.3.2 Results on emergence of strongly entangled short-distance pairs

In Fig.7.3.1 (left panel), we present the decrement of the geodesic distance  $d_g$  ( $d_g \rightarrow 0$ ) under RG flow across the EHM network (Fig.7.2.7). This signals the emergence of strongly entangled pairs with high MI content  $I_{max}(i : j) = 2 \ln 2$  and  $d_g = 0$ ) at the low energy stable fixed point of the RG. Complementary insight is obtained in the right-hand panel of Fig.7.3.1, which shows the concomitant reduction in real-space physical distance  $d_p$  between the strongest entangled pseudospins. We have also labelled the pairs carrying the highest MI at each RG step. Initially, the pseudospin pair (24, 17) lying to one side of the FS (see Fig.7.2.2) and connected by tangential scattering vertex  $L$ , carry the highest MI and comprise the geodesic  $d_g = 1.66$ , while the  $d_p$  between them is 4 lattice spacings. However, beyond the second RG step, the system undergoes a crossover into a phase comprised of high MI pseudospin pairs (17, 3), (18, 4) etc. connected via backscattering vertex ( $K$  vertex). The pair (17, 3) is formed by states belonging to opposite side of the FS: the physical distance between these pairs has thus shrunk to  $d_p = 1$  lattice spacing. In this way, we observe the emergence of  $d_p = 1, d_g = 0$  (short distance) strongly entangled pairs (6, 20), (13, 27) amidst competition among various entangled pairs connected via forward scattering ( $V$  vertex), backscattering and tangential scattering. Additionally, we note that the emergence of such pairs is correlated with the quantization of the Wilson loop expectation value signalling the onset of T.O. (Fig.7.2.9).

Fig.7.3.2 shows the MERG analysis of the MI content of the following pairs: (13, 27)-connected

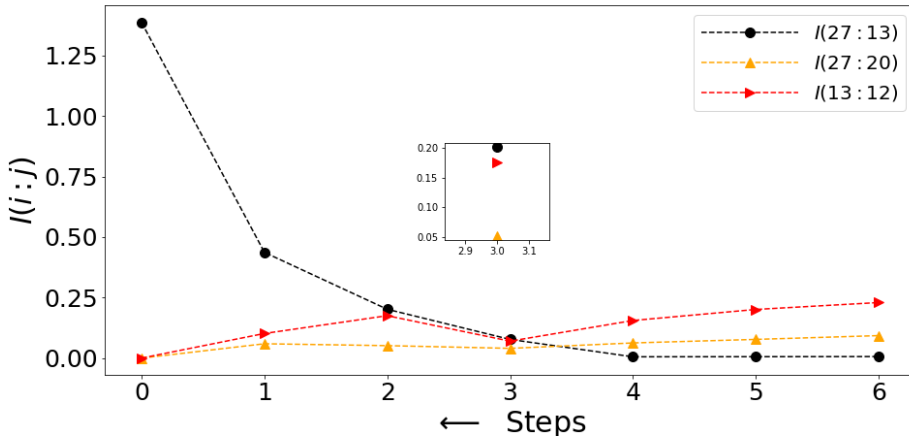


Figure 7.3.2: Variation of Mutual information (MI)  $I(i:j)$  for pseudospin pairs connected via tangential scattering (pair (27, 20)), forward scattering (pair (13, 12)) and backward scattering (pair (27 : 13)) processes. Inset shows the MI values at the third RG step.

via backscattering ( $K$ ), (20, 27)-connected via tangential scattering ( $L$ ) and (13, 12)-connected via forward scattering ( $V$ ). The analysis reveals that, starting from the third RG step,  $I(13 : 27)$  dominates over that of the other two. This again substantiates the emergence of strongly entangled pairs (13, 27) and (6, 20) in the bulk of EHM, and is a direct outcome of the RG relevant backscattering vertex ( $K$ ) together with irrelevant forward ( $V$ ) and tangential ( $L$ ) scattering vertices (see eq. 7.14 and discussion below). Finally, we track the RG contribution of the 1-pseudospin and 2-pseudospin Schmidt spectra in quantifying the growth of MI for the pair (13, 27). The left panel of Figure 7.3.3 represents the RG flow for the Schmidt spectra  $\{\lambda_{13}\}$ ,  $\{\lambda_{27}\}$  of pseudospins 13 and 27. The plot clearly shows that both pseudospins follow an (almost) identical pattern: the distance between the two eigenvalues of, say,  $\{\lambda_{13}\}$  initially grows under the RG till the third step, then showing a dramatic collapse towards a degeneracy at the fixed point. The orange and green curve in the right panel represents the purity of the respective RDMs ( $Tr(\rho_{13}^2)$  and  $Tr(\rho_{27}^2)$ ). Both purities display the crossover of the spread in probability eigenvalues from low to high, leading to increase in their individual entropies. Further, the purity of the pair of the pseudospins  $Tr(\rho_{27,13}^2)$  increases eventually to 1, corresponding to a decrease in the joint entropy for these two pairs of pseudospins:  $-Tr(\rho_{27,13} \ln \rho_{27,13})$ . Taken together, the increase in individual entropies and the decrease in joint entropy signals the increase in the MI of the individual pseudospins. This is another way in which we witness the isolation of strongly entangled pseudospin pairs from the rest in the bulk of the EHM.

Thus, the nature of RG flow equations at a given quantum fluctuation energy scale  $\omega$  can be seen to dictate the *entanglement geometry* content of the EHM network leading to the T.O. ground state. In the next subsection, we discuss the RG evolution of the entanglement geometry, information entropy content and the distinct nature between the gapless and gapped states it give rise to.

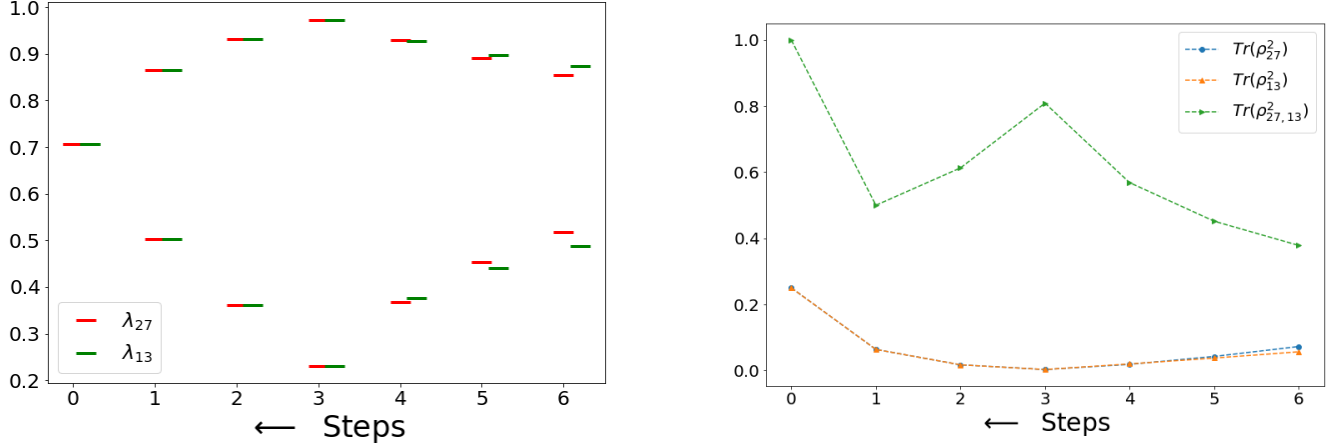


Figure 7.3.3: Left Panel: Schmidt spectrum renormalization for the pseudospin pair (27, 13). Right Panel: Purity for the one- and two- pseudospin reduced density matrix.

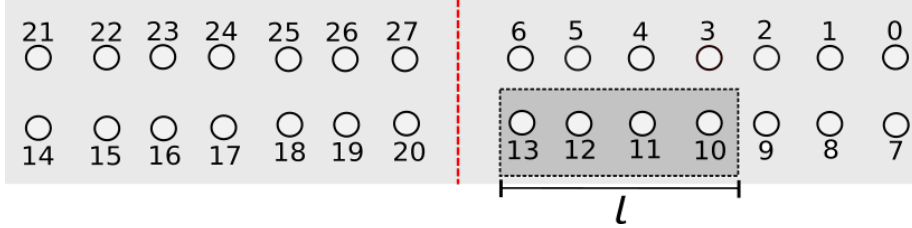


Figure 7.3.4: Momentum space partitioning (red dotted line) across blocks belonging to opposite sides of the Fermi surface.  $l$  is the block size.

### 7.3.3 Entanglement scaling features for the Mott liquid, normal metal and Neel antiferromagnetic insulating phases

We compute here the entanglement entropy across a partition in momentum-space. As shown in Fig.7.3.4), we construct momentum-space blocks of increasing lengths ( $l$ ) on one side of the FS, with the dark/light grey regions being the two members of the partition. For the Mott liquid state, the RG flow of the entanglement entropy (EE, in units of  $\log 2$ ) in shown in the left panel of Fig.7.3.5. The figure shows an initial decrease of EE with different block sizes (ranging from  $l = 7$  to 1), followed by an increase from the third step to the final value of  $EE^* = \log 2$  at the fixed point. As presented earlier, this gradual crossover of EE is manifested by the proliferation of strongly entangled (short distance) pairs formed via pseudospin backscattering across the FS. Importantly, we note that at the fixed point, the entanglement entropy  $EE^* = \log 2$  is independent of subsystem sizes greater than the momentum space shell width, characterizing the perfect disentanglement of the states outside the emergent space. This clearly suggests a *topological* origin of this entanglement entropy. We also carry out a reverse MERG construction (Fig.9.7.2) for the many-body states in the normal metallic phase for  $W > W/2 - \omega > W/2$  of the phase diagram Fig.7.1.1. For this, we start from the ground state eq.7.55 shown in Appendix 7.B. In this case, the EE in right panel of Fig.7.3.5 is seen to decrease for various block sizes along the

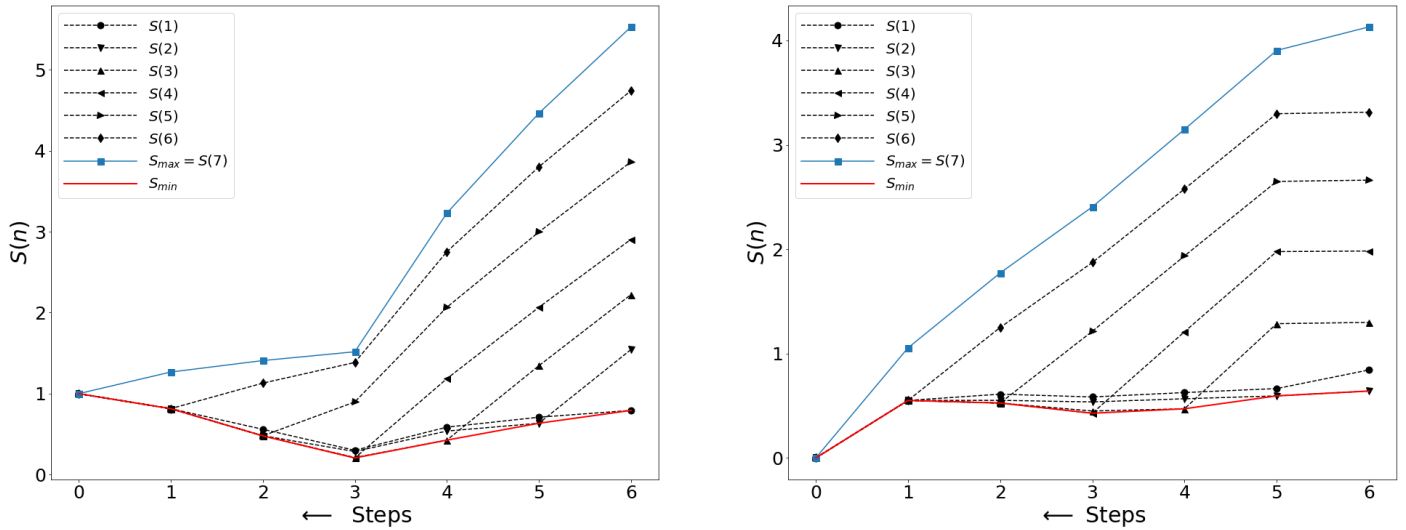


Figure 7.3.5: Entanglement entropy (EE) renormalization across the EHM for momentum space partition block sizes 1-7 on one side of FS for Mott liquid (left panel) and for normal phase (right panel).

RG flow such that at the RG fixed point,  $EE = 0$ . This is consistent with the fact that the state eq.7.55 is separable in terms of momentum space pseudospins. The distinct nature of EE RG flows across the EHM for the gapped T.O and gapless metallic states describes a entanglement phase transition in going from the normal metal phase at  $\omega = -W/2$  to Mott insulating phase at  $\omega = W/2$ .

In order to investigate further the holographic features of the EHMs constructed for the insulating and metallic ground states, we identify at every RG step the causal cone (dashed red line in Fig.7.2.7) that extends across the bulk of the EHM for a given block of the EHM boundary (grey shaded area in Fig.7.2.7). For the block of boundary pseudospins 7 – 13 in Fig.7.2.7, we first compute the maximum single-pseudospin entanglement entropy ( $S_{1,max}$ ). We recall that the Ryu-Takayanagi formula [148] was shown to hold for MERA [161, 241] and EHM [177] respectively, such that at any given RG step we expect

$$S(7) \leq n S_{1,max}, \quad (7.31)$$

where  $n$  corresponds to the perimeter of the causal cone/minimal surface at that RG step, i.e., the number of links that must be cut in order to isolate the boundary block of length 7. Indeed, we find in Fig.7.3.6 that the above relation is satisfied by both the Mott insulating and normal metallic ground states. Importantly, we find that the quantity  $S_{1,max}$  arises from the entanglement of the pseudospin 13 with all the other pseudospins (7 – 12). Pseudospin 13 resides deep in the IR, i.e., proximate to the Fermi surface of the normal phase, and a member of the singlet pair (13, 27) that is part of the topologically ordered insulating ground state. This shows that the last link that is cut by the causal cone deep within the IR corresponds to the degrees of freedom proximate to the nodal Fermi surface (of the 2D tight-binding problem on the

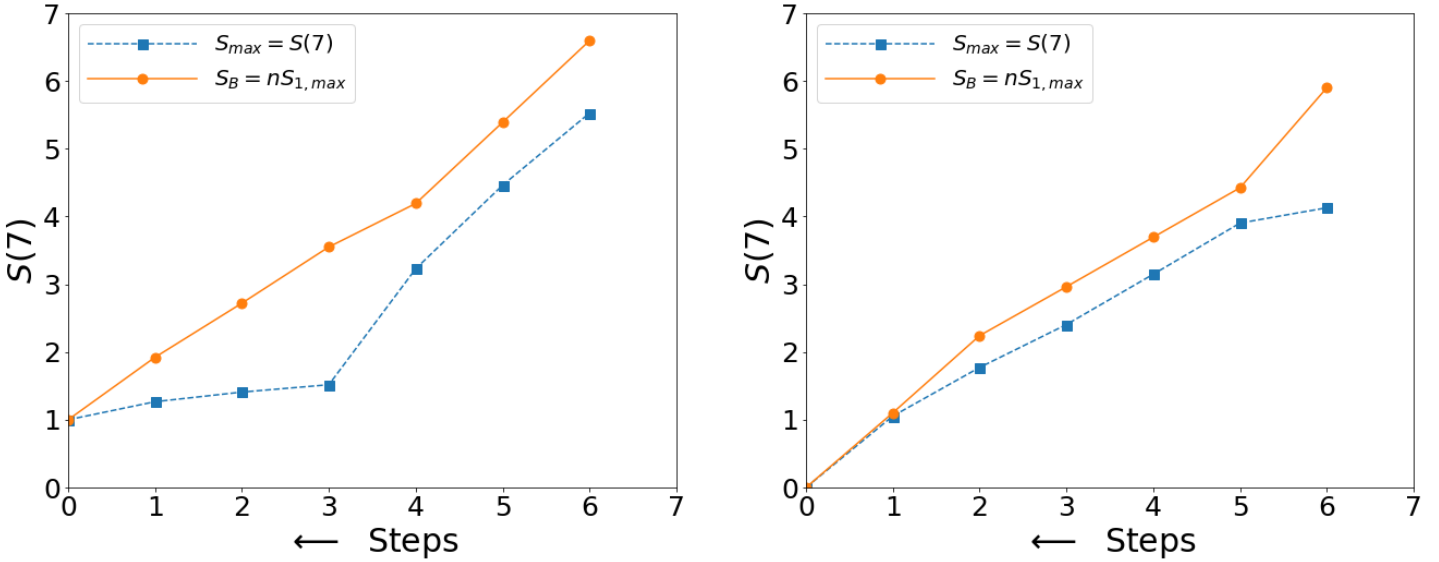


Figure 7.3.6: Blue curve: Entanglement entropy (EE) renormalization across the EHM for momentum space partition block size 7 on one side of FS for Mott liquid (left panel) and for normal phase (right panel). Orange curve: Renormalisation of the entanglement entropy bound obtained from the causal cone/minimal surface of block size 7 for Mott liquid (left panel) and for normal phase (right panel).

square lattice). For the metallic ground state, this reflects the holography arising from the Fermi surface [152]. On the other hand, for the insulator ground state, the causal cone is a holographic witness to the emergence of the nonlocal Wilson loop (eq.7.5, see also Fig.7.2.9)) at the IR fixed point.

The entanglement phase transition between the two phases can also be seen from the contrasting entanglement geometry evolution across the EHM for the two ground states. The left panel of Fig.7.3.7 shows the RG evolution of information distances  $d_{ij}$  in the Mott insulating regime, while the right panel of Fig.7.3.7 shows the evolution of inverse information distances  $1/d_{ij}$  in the marginal Fermi liquid metal. The blue curve ( $D$  and  $1/D$  in the two figures) tracks the RG evolution of the largest information distance (minimal MI pair) in the emergent space geometry. The red curve ( $d_g$  and  $1/d_g$  in the two figures) tracks the geodesic, while the black dots represent the information distances between various  $(i, j)$  pairs. The increase of MI in the emergent window of the Mott liquid is described by a shrinking space, i.e.,  $D - d_g$  reduces under RG flow towards the stable fixed point where all distances collapse to zero. On the other hand, the decrease of MI in the normal metal is described by an expanding space as both  $d_g, D \rightarrow \infty$  under the RG flow. It is important to note that the information distance  $d(a, b)$  in the IR limit is related to the negative logarithm of the two pseudospin (i.e., two electron-two hole) Green's function in momentum space [177]

$$d(a, b) \sim -\log G(a, b) = -\log(\langle \Psi_{(j)} | A_a^+ A_b^- | \Psi_{(j)} \rangle), \quad (7.32)$$

where  $A_a^+$  and  $A_b^-$  are pseudospin raising/lowering operators. Recall that in the Mott insulating

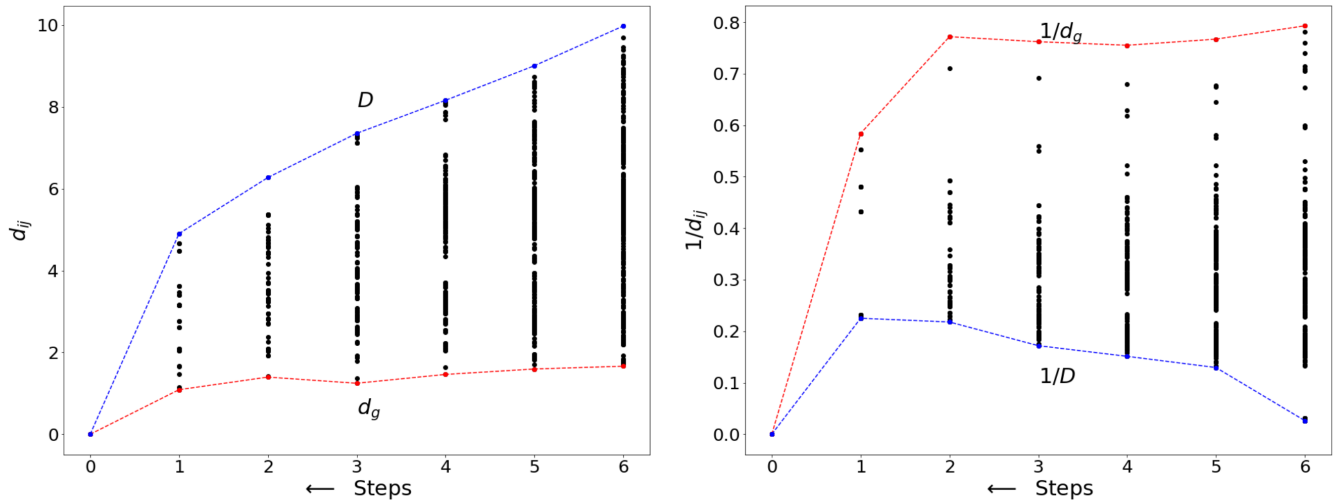


Figure 7.3.7: Evolution of the information distances between various pseudospin pairs across the EHM for the normal state (right panel) and Mott insulating state (left panel).  $D$  and  $d_g$  are the largest and smallest (i.e., geodesic) information distances respectively.

phase Fig.7.3.1 (also the lower boundary in Fig.7.3.7 left panel), the information geodesic  $d_g(a, b)$  is related to the nodal pair (13, 27) that forms the singlet at the IR fixed point in the bulk of the EHM. Following Lee and Qi [177], we note that in our case the information geodesic at the IR fixed point is given by

$$d_g(13, 27) = -\log \exp(-\xi|2k_F|) = \xi|2k_F| , \quad (7.33)$$

where  $\xi$  is the real-space correlation length between the constituents of the Mott pseudospin singlets eq.7.6. This indicates the equivalence between the correlator deep in the EHM and the the 4-particle Green's function proximate to the Fermi surface. Similarly, in the EHM constructed for the metallic ground state, the divergence of  $d_g = -\lim_{k \rightarrow k_F} \ln(|k - k_F|)$  is tied to the RG scaling of the entanglement towards the gapless Fermi surface [152].

We now turn to the study of a third, and related, state of matter. In Ref.[180], a study of the influence of symmetry-breaking perturbations under URG revealed that the Mott liquid insulating phase of the half-filled 2D Hubbard model is unstable towards the formation of Ne  l antiferromagnetic ordering. Thus, in order to study the effects of  $(\pi, \pi)$  checkerboard spin-density waves on the Mott liquid, we first apply the URG method to treat the competition between the staggered magnetic field  $\sum_{\mathbf{r}} (-1)^{i+j} h S_{\mathbf{r}}^z$  and Umklapp scattering processes (strength  $V$ ). This is shown in detail in Appendix 7.C. The nonperturbative RG flow equation eq.7.60 at weak coupling  $V/h < (\log \frac{\Lambda_0}{\Lambda})^{-2}$  yields a exponential square root dependence on the coupling strength that is characteristic of the Ne  l SDW phase [227]. Further, the RG flow equation ends at a IR fixed point with the coupling strength  $V^* = h(\log \frac{\Lambda_0}{\Lambda})^{-2}$ . Next, we carry out the MERG construction (see Fig.9.7.2) starting from the Ne  l antiferromagnet (AFM) symmetry-broken state (eq.7.64 of the effective Hamiltonian in eq.7.62). The block entanglement entropy computed for the Ne  l SDW from the MERG is shown in the left panel of Fig.7.3.8: it is seen to decrease for various

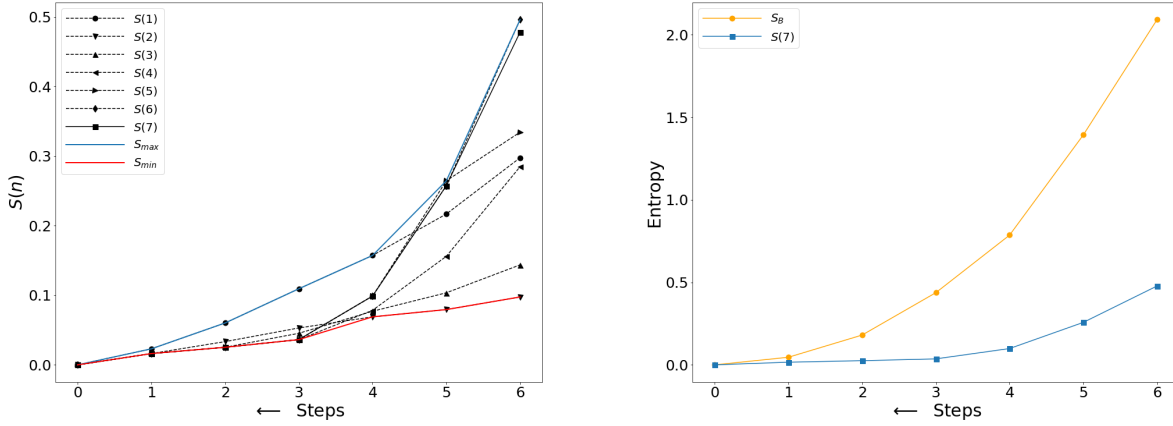


Figure 7.3.8: Block EE renormalisation for the passage towards the symmetry-broken Neél SDW phase. Left panel: EE for momentum-space block sizes ranging from 1 to 7. Right panel: holographic EE bound (orange curve) and the momentum-space partition block of size 7 (blue curve).

block sizes along the RG flow such that at the RG fixed point,  $EE \rightarrow 10^{-5} \log 2$ . This is consistent with the fact that, in the Neél SDW phase, the entanglement is considerably lower compared to the Mott liquid phase (which we found earlier to have  $EE^* = \log 2$ ). A similar flow towards a vanishing value is also observed for the holographic EE bound (right panel of Fig.7.3.8). In this way, the MERG flows of both the block entanglement entropy and the holographic EE bound of the Neél SDW show features that are distinct compared to those observed for the Mott liquid and the non-Fermi liquid phases (Figs.7.3.6). This distinction marks the entanglement phase transition between the Mott liquid and Neél SDW phases.

We summarise by noting that the entanglement features and geometry of the EHM for the topologically ordered insulating, metallic and symmetry-broken phases we have studied here are markedly different: the T.O. phase is marked by a nontrivial  $EE = \log 2$  and vanishing  $d_g$ , the normal phase is characterised by  $EE = 0$  and a diverging  $d_g$  and the symmetry-broken SDW state is characterised by a vanishing  $EE$ . This confirms that our EHM network carries important information with regards to the topological nature of a many-body state, and can sense a transition between the two phases through their entanglement features. In a later section, we will quantify this information flow across the EHM network using measures from information theory and deep learning (DL). We will thus show the equivalence between our MERG based EHM and a deep neural network (DNN) architecture.

## 7.4 Probing the entanglement of the QCP in a hole-doped Mott liquid

In Ref.[181], we observed that the emergence of d-wave superconducting off-diagonal long-ranged order (ODLRO) at  $T = 0$  in the 2D Hubbard model involved the divergent quantum fluctuations

at a novel quantum critical point (QCP) associated with the collapse of Mottness upon doping holes into the system. This raises the question: *how does the many-particle entanglement of the Mott liquid evolve with doping towards the QCP, such that its instability towards a Neél AFM ground state at half-filling [180] is replaced instead with that towards superconducting ODLRO at the QCP [181]?* In this section, we aim to provide an answer to this question through a coherent understanding of entanglement based features and two-point correlation functions for the Mott quantum liquid and Neél SDW ground states at half-filling (hole-doping fraction  $f_h = 0$ ), as well as the Mott quantum liquid and superconducting ground states at quantum critical doping ( $f_h = 0.25$  for  $U_0 = 8t$ ).

At half-filling, we study the URG evolution of the longitudinal spin structure factor defined as

$$S(\mathbf{Q}) = \langle s_{\mathbf{Q}}^z s_{-\mathbf{Q}}^z \rangle, s_{\mathbf{Q}}^z = \sum_{\mathbf{r}} (-1)^{i+j} s_{\mathbf{r}}^z \quad (7.34)$$

for the wavevector  $\mathbf{Q} = (\pi, \pi)$  within the two-fold degenerate symmetry-preserved ground states  $|\Gamma_+\rangle$  (eq.7.6) and  $|\Gamma_-\rangle$  (eq.7.7), as well as the Neél AFM ground state (eq.7.64 in Appendix 7.C). As shown in the right panel of Fig.7.4.1, the UV to IR evolution of  $S(\pi, \pi)$  within the ground states  $|\Gamma_+\rangle$  (red curve) and  $|\Gamma_-\rangle$  (green curve) is towards a much smaller value compared to that observed in the Neél antiferromagnet (black curve). Importantly, the strongly suppressed values of  $S(\pi, \pi)$  for the  $|\Gamma_{\pm}\rangle$  quantum liquid ground states are manifestations of their high entanglement content. In the left panel of Fig.7.4.1, the many-particle entanglement is quantified by the maximum mutual information (MMI)  $\max_{i,j} I(i:j)$  (eq.9.60) between charge pseudospins in  $|\Gamma_+\rangle$  (eq.7.6, red curve) and spin pseudospins in  $|\Gamma_-\rangle$  (eq.7.7, green curve). As the RG progress from UV to IR, the entanglement content is distilled into strongly entangled pseudospin pairs for the two quantum liquid ground states  $|\Gamma_{\pm}\rangle$ . On the other hand, the MMI for the Neél AFM state (eq.7.64, black curve in left panel of Fig.7.4.1) between pseudospin pairs (eq.7.63) decreases monotonically and eventually vanishes upon scaling towards the IR.

From the spin Mott liquid phase (eq.7.7), we also derive an effective low-energy theory for Cooper pair pseudospins (see Appendix 7.D). From this, we compute the MMI between Cooper pair pseudospins (blue curve in left panel of Fig.7.4.1), observing that it grows mildly in passage from UV to IR. On the other hand, the value of the real-space averaged ODLRO  $\langle \rho^2(\mathbf{r} - \mathbf{r}_1) \rangle$

$$\rho^2(\mathbf{r} - \mathbf{r}_1) = -\frac{1}{vol} \sum_{\mathbf{k}, \mathbf{p}} e^{i\mathbf{p} \cdot (\mathbf{r} - \mathbf{r}_1)} \langle c_{\mathbf{k}_{\Lambda, \hat{s}}, \uparrow}^\dagger c_{\mathbf{k}_{-\Lambda, T\hat{s}}, \downarrow} c_{\mathbf{p} - \mathbf{k}_{\Lambda \hat{s}}, \downarrow}^\dagger c_{\mathbf{p} - \mathbf{k}_{-\Lambda, T\hat{s}}, \uparrow} \rangle \quad (7.35)$$

is observed to reduce in magnitude under RG evolution from UV towards IR (blue curve in right panel of Fig.7.4.1). At the UV end, the large ODLRO  $\langle \rho^2(\mathbf{r} - \mathbf{r}_1) \rangle = 0.125$  arises from the presence of  $p \neq 0$  Cooper pairs present in the spin Mott liquid that scatter via tangential, forward and back scattering processes [181]. As can be seen from the blue and green curves in the left panel, these scattering processes reduce the inter-Cooper pseudospin and inter-spin pseudospin entanglements in the UV. Similarly, the enhanced inter-spin pseudospins and inter-Cooper pseudospins entanglement at the IR scale (as quantum fluctuations related to various scattering processes is resolved under RG) coincides with a reduction in the ODLRO.

We now turn to a similar investigation of entanglement and many-body correlations at the QCP. As shown in Appendix 7.E, at the QCP, excitations normal to the Fermi surface in the nodal direction (i.e., along the  $(\pi/2, \pi/2)$  Fermi point) are gapless, and described by a marginal Fermi

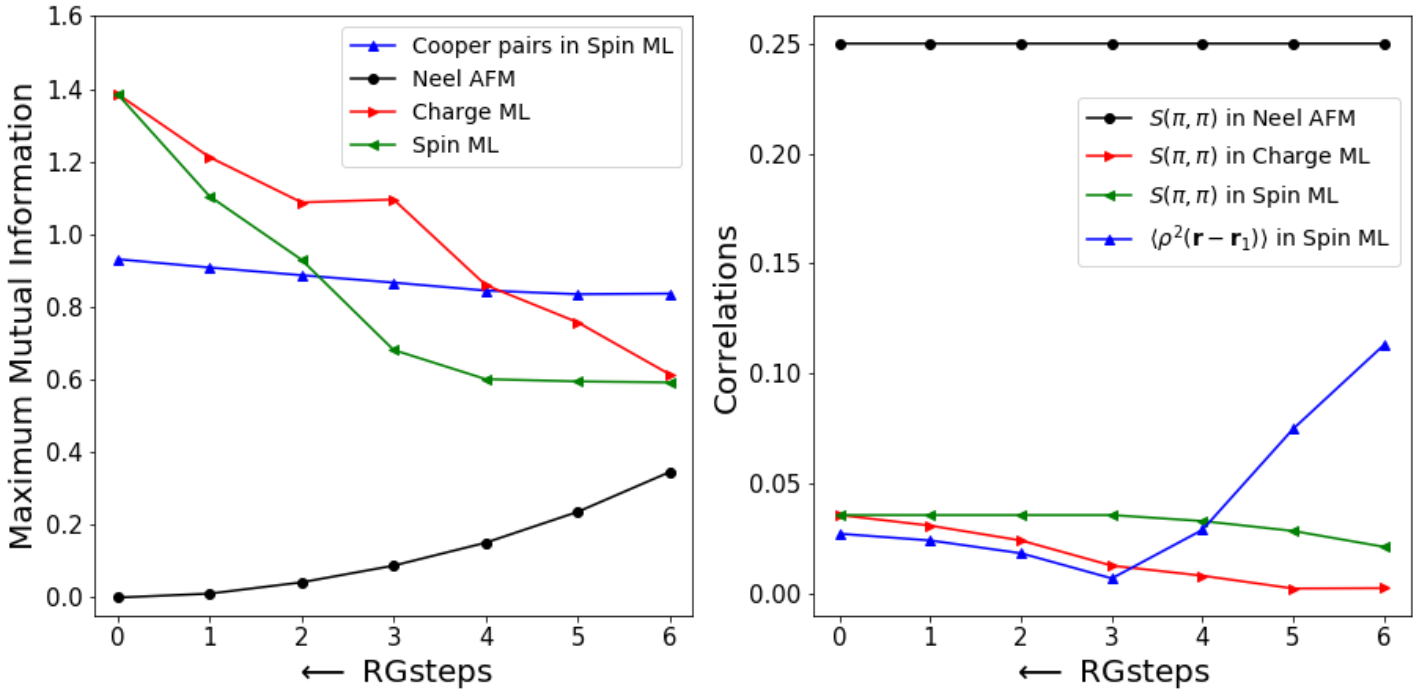


Figure 7.4.1: Left panel: RG flow for the maximum MI between different pairs in the ground state of the half-filled Hubbard Model. The red/green curve represents the MMI between electron-hole pairs of opposite spin constituting the charge/spin-type Mott liquid ground states respectively. The blue curve represents the MMI between different  $\mathbf{p} = 0$  Cooper pairs present within the spin-type Mott liquid. The black curve represents the MMI between different electron-hole pairs of the Neel AFM, where each pair has electronic states in same up/down configuration. Right panel: RG flow of correlation functions in the ground state of the half-filled Hubbard model. The red/green curve represents the longitudinal spin structure factor  $S(\pi, \pi)$  of the  $\mathbf{Q} = \pi, \pi$  checkerboard Neél AFM order within the symmetry-unbroken charge/spin type Mott liquids respectively. The blue curve represent the superconducting off-diagonal long-range order parameter  $\langle \rho^2(\mathbf{r} - \mathbf{r}') \rangle$  (averaged over all sites) in the spin-type Mott liquid.

liquid state. Instead, the antinodal direction (along the  $(3\pi/4, \pi/4)$  Fermi point) is gapped via strong Cooper pair backscattering. Starting from the ground states at the fixed point eq.7.74 and employing the MERG program Fig.9.7.2, we include the backscattering, forward scattering and tangential scattering processes for constructing the eigenstates in passage towards the UV. As before, we compute from these eigenstates the RG evolution of entanglement and many-body correlations. In the left panel of Fig.7.4.2, the MMI value between  $(\pi, \pi)$  net-momentum electronic pairs is seen to decrease under RG along both the antinodal (red curve) and nodal directions (green curve), vanishing altogether at the IR fixed point. This was referred to as the *collapse of Mottness* in Ref.[181]. On the other hand, the MMI between  $(0, 0)$  net-momentum Cooper pairs (red curve) in Fig.7.4.2 (right panel) is seen to increase along the antinodal direction, stopping at the maximum value  $2 \log 2$ ; this corresponds to the singlet pairing between pseudospins 6 and

20. Along the nodal direction, the Cooper pseudospins 13 and 27 within the gapless marginal Fermi liquid comprise a separable state. Therefore, as seen in the green curve in Fig.7.4.2 (right panel), the small MMI between Cooper pairs along the nodal direction in the UV reduces further under RG flow, and vanishes in the IR.

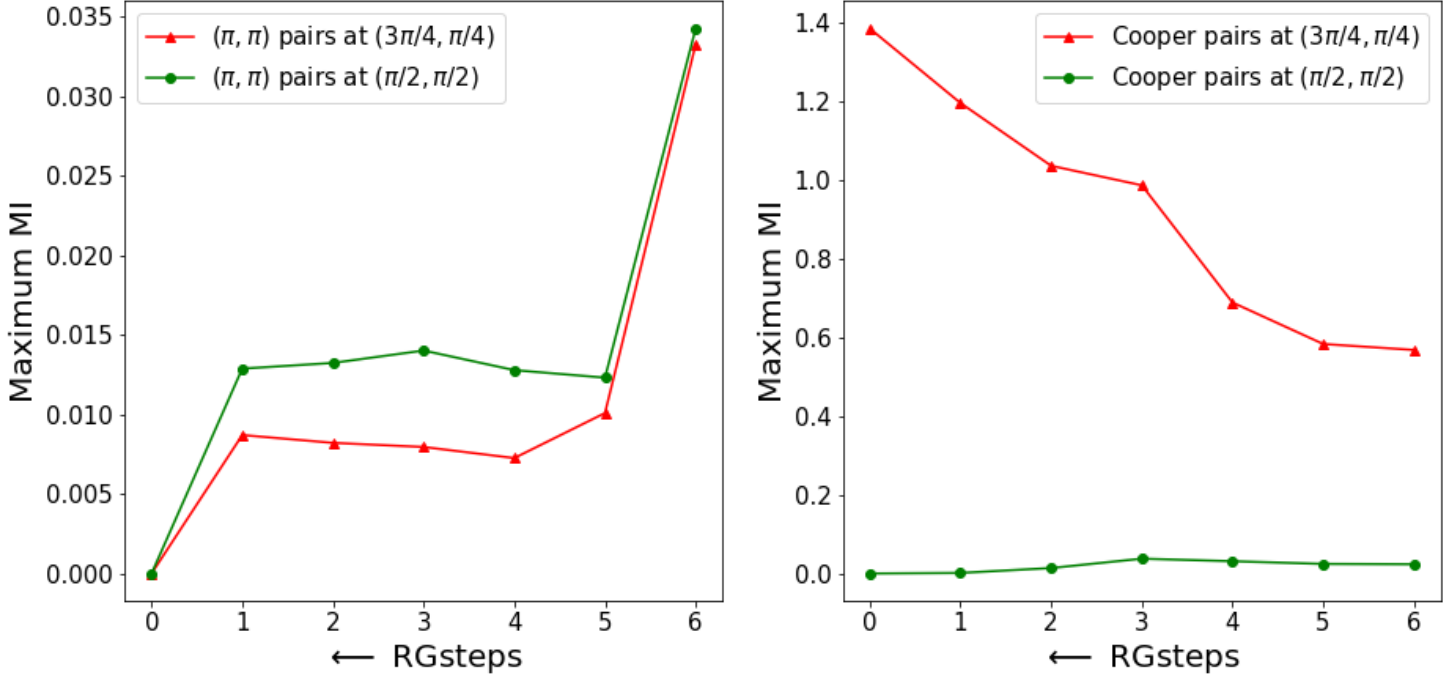


Figure 7.4.2: Left panel: RG flow of MI between charge-pseudospin pairs (with  $\pi, \pi$  net pair momentum) along the nodal ( $\pi/2, \pi/2$ ) direction (green curve) and antinodal ( $3\pi/4, \pi/4$ ) (red curve) directions. Right panel: RG flow of MI between Cooper pairs (with 0 net-momentum) within the symmetry-preserved spin Mott liquid along the antinodal (red curve) and nodal (green curve) directions.

By following Ref.[181], we include a  $U(1)$  phase-rotation symmetry-breaking field  $\Delta(c_{\mathbf{k}_{\Lambda\hat{s}},\uparrow}^\dagger c_{-\mathbf{k}_{\Lambda\hat{s}},\downarrow}^\dagger + h.c.)$  and perform the URG once again, obtaining the d-wave symmetry broken superconductivity phase. As shown in the right panel Fig.7.4.3, the Cooper pairs do not condense along the nodal direction both in the presence (black curve) as well as absence (green curve) of symmetry breaking. This ensures that ODLRO is absent in the IR in both ground states, displaying that the nodal marginal Fermi liquid is protected against symmetry-breaking. However, along the antinodal direction in the  $U(1)$  symmetry-broken state, the ODLRO increases under RG flow from UV to IR (purple curve in the right panel of Fig.7.4.3) even as the MMI of Cooper pairs reduces and eventually vanishes at the IR fixed point (purple curve in left panel of Fig.7.4.3). As a consistency check, we note that within the  $U(1)$  phase-rotation symmetry-preserved Cooper pair quantum liquid ground state (eq.7.74), the ODLRO reduces substantially from UV to IR (red curve in right panel of Fig.7.4.3), and finally terminates at a small value of  $\langle \rho^2(\mathbf{r} - \mathbf{r}_1) \rangle = 0.05$ .

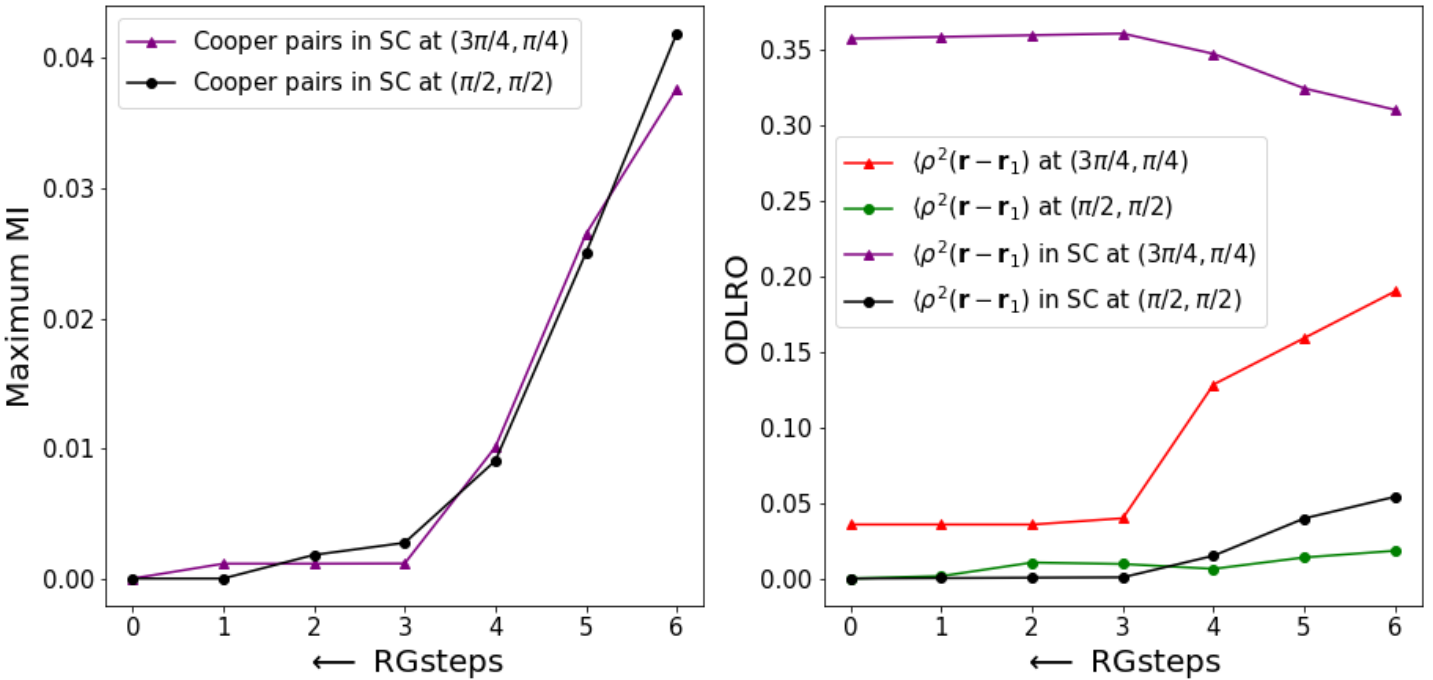


Figure 7.4.3: Left panel: RG flow of MI between Cooper pairs within the symmetry-broken d-wave superconductor at the QCP along the nodal (black curve) and antinodal (purple curve) directions. Right panel: RG flow of the ODLRO within the symmetry-preserved spin Mott liquid at the QCP along the antinodal (red) and nodal (green) directions. The black and purple curves represent the ODLRO along the nodal and antinodal directions within the symmetry-broken d-wave superconductor respectively.

We summarise by noting that our investigations reveal a clear anticorrelation between the RG evolution of the MMI and many-body correlations (such as the spin structure factor and the ODLRO) for the various symmetry-preserved as well as symmetry-broken ground states we have encountered in the 2D Hubbard model at half-filling and the QCP. These results display how the mutual-information based entanglement of the quantum liquid ground states evolves with hole-doping: the spin and charge pseudospins that condensed from the dominant backscattering processes at half-filling to form the Mott liquid ground states are replaced by their Cooper-pairing pseudospin counterparts at the QCP via a collapse of Mottness. Concomitantly, the associated dominant symmetry-broken ground states changes hands from the Neél AFM to d-wave superconductivity (whose nodes are gapless marginal Fermi liquids).

## 7.5 A Deep Neural Network based on EHM

Motivated by the equivalences between tensor network RG and deep learning [534–536], we propose a deep neural network based on the EHM tensor network for classifying the correlated

quantum liquid ground states of the 2D Hubbard model [180, 181]. We begin, however, with a brief discussion of the concepts of the deep neural network (DNN) [537] pertinent to our presentation. A DNN is a sequence of layers of mathematical operations that transform an input feature vector  $X$  into  $\hat{X}$  while keeping only the essential parts relevant to the target output vector  $Y$ . An optimal  $\hat{X}$  can be obtained via Lagrangian minimization [538]

$$\mathcal{L}[p(\hat{x}|x)] = \mathcal{I}(X : \hat{X}) - \beta \mathcal{I}(\hat{X} : Y), \quad (7.36)$$

where the *mutual information like quantity*  $R = \mathcal{I}(\hat{X} : X)$  quantifies the complexity of the representation, and  $\mathcal{I}_Y = \mathcal{I}(\hat{X} : Y)$  is the amount of information relevant to  $Y$  preserved in  $\hat{X}$ . The quantity  $\beta$  is the tradeoff parameter, while the function  $p(\hat{x}|x)$  is the conditional probability. An optimal representation  $\hat{X}$  is one for which the MI ( $R$ ) is reduced and  $\mathcal{I}_Y$  is preserved. This is known as the information bottleneck (IB) principle [538]. A DNN following the IB principle can be considered optimal. In the section below, we will demonstrate that EHM based MERG fulfills the IB principle, and is therefore on par with a optimally functioning supervised DNN.

### 7.5.1 Demonstrating the IB principle for EHM based on MERG

We have seen earlier that the MERG is a family of unitary disentanglement transformations with an input many-body eigenstate (Fig.7.2), leading to simpler representations with a lower number of entangled qubits. It was also demonstrated that the EHM of Fig.7.2.7 is a tensor network representation of MERG. An important question to ask in this regard is: *does the EHM network architecture naturally follow the IB principle?*

In order to perform the information bottleneck analysis, we first prepare the entanglement RG results as a data model. Every pair of qubits in the many-body state can be labelled as  $(a, b)$ . With every pair  $(a, b)$  is associated one *feature*:  $F(a, b) = I(a : b)$  (the MI defined in eq.9.60). The larger the MI, the stronger is the entanglement within the pair. Next, we perform a classification of all pairs into two classes, strongly and weakly entangled, by using a *classifier*  $C(a, b)$

$$C(a, b) = \begin{cases} 0 & 0 \leq F(a, b) < \log 2 \\ 1 & \log 2 \leq F(a, b) \leq 2 \log 2 \end{cases}. \quad (7.37)$$

In order to compute the set  $(R, \mathcal{I}_y)$  at each step of the RG, we first prepare the input vector  $(X)$ , RG transformed vectors  $\hat{X}$  and target vector  $Y$ . The input feature vector  $X = \{F(a, b)\}$  is built from the state  $|\Psi_{(6)}\rangle$ , constituted of MI values for  $\binom{4}{2} = 6$  pairs  $(a, b)$  made of 4 pseudospin qubits (6, 13, 20, 27).  $S$  is a list of these pairs, where  $S_i$  is the  $i$ th element in the list

$$S = \{(13, 6), (20, 6), (27, 6), (20, 13), (27, 13), (27, 20)\} \quad (7.38)$$

Note that the above four qubits (Fig.7.2.2) have been chosen so as to eventually compose the emergent subspace at the RG fixed point, and therefore constitute the entanglement features of the T.O. ground state. We similarly construct the transformed feature vector  $\hat{X}_j$  from  $|\Psi_{(j)}\rangle$  at each RG step. The target vector  $Y = \{C(a, b)\}$  is constructed for pairs eq.7.38 in  $S$  using the state  $|\Gamma_+\rangle$  at the fixed point eq.7.6. From these datasets, we compute the information plane coordinates [538, 539]  $R = \mathcal{I}(\hat{X}_j : X)$  and  $\mathcal{I}_Y = \mathcal{I}(Y : \hat{X}_j)$ .

The representational complexity  $R$  (orange curve) displayed in Fig.7.5.1 is seen to decrease across the EHM, while the mutual information  $I_Y$  (eq.9.60, black curve) is constant throughout at a

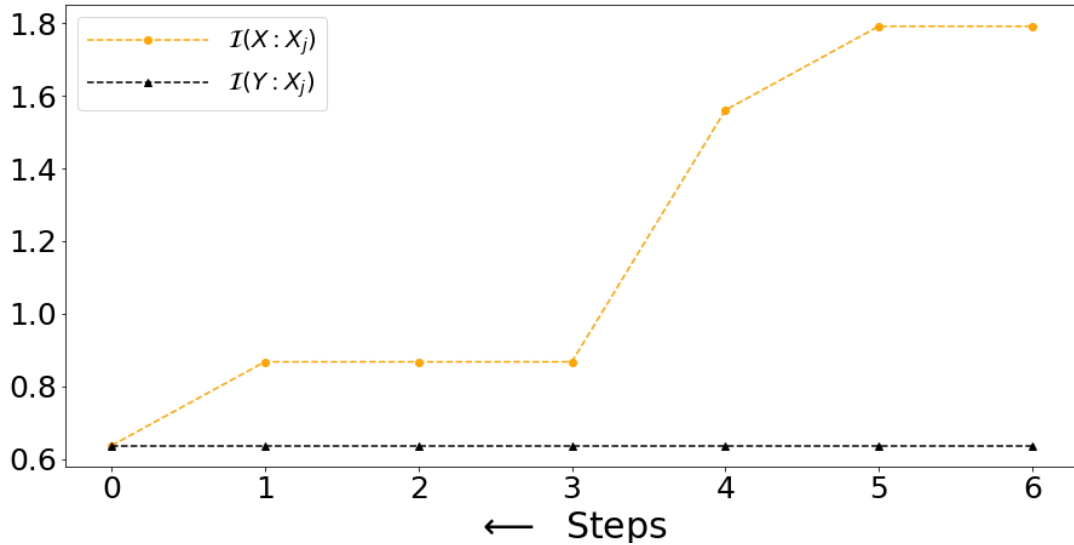


Figure 7.5.1: Testing the information bottleneck principle for EHM network. Orange curve represents the representation complexity  $R = I(\hat{X}_j : X)$ , while black curve represents  $I_Y = I(Y : \hat{X}_j)$ , the information about class  $Y$  present in the representation.

value of 0.636. This demonstrates clearly that the IB principle is met by the MERG based EHM. This allows us to make the following mapping between the MERG based EHM and a DNN: the disentanglement transformations (yellow blocks in Fig.7.2.7) are equivalent to the *hidden layers* of a DNN that outputs simpler representations. A constant value of  $I_Y$  across the EHM suggests a strong dependence between  $Y$  and representation  $\hat{X}_j$  obtained at various RG transformation steps. Fig.7.5.2 verifies the strong dependence between the representation of MI values  $\hat{X}_j$  (Figs. 7.5.2 (a-e)) at each RG step and the class  $Y$  (Fig.7.5.2(f)). We observe that the MI values for the pairs (6, 13) and (20, 27) either belong simultaneously to the strongly entangled class  $C(6, 20) = C(13, 27) = 1$ , or to the weakly entangled class  $C(6, 20) = C(13, 27) = 0$ . This results in the preservation of mutual information  $I(Y : \hat{X}_j)$  at every RG step (black line in Fig.7.5.1).

## 7.5.2 Constructing a DNN model for classifying *entangledness* of a pair

Given the demonstration of the IB principle for the EHM based on MERG, we construct a conditional probability DNN model for predicting the eventual fate of a given pair  $(a, b)$  to be either strongly ( $C(a, b) = 1$ ) or weakly entangled ( $C(a, b) = 0$ ). This is done in the following way: given any pair  $(a, b)$  and its feature  $F(a, b)$  at each RG step  $j$ , we compute the conditional probability  $P(C = 1|F(a, b))$  by performing a statistical analysis of the MI dataset. Below we list the specifics of the MERG based DNN model:

1. The bare representation  $X_6$  is constructed from initial state  $|\Psi_{(6)}\rangle$  by collecting the MI values of all  $\binom{28}{2} = 378$   $(a, b)$  pairs.

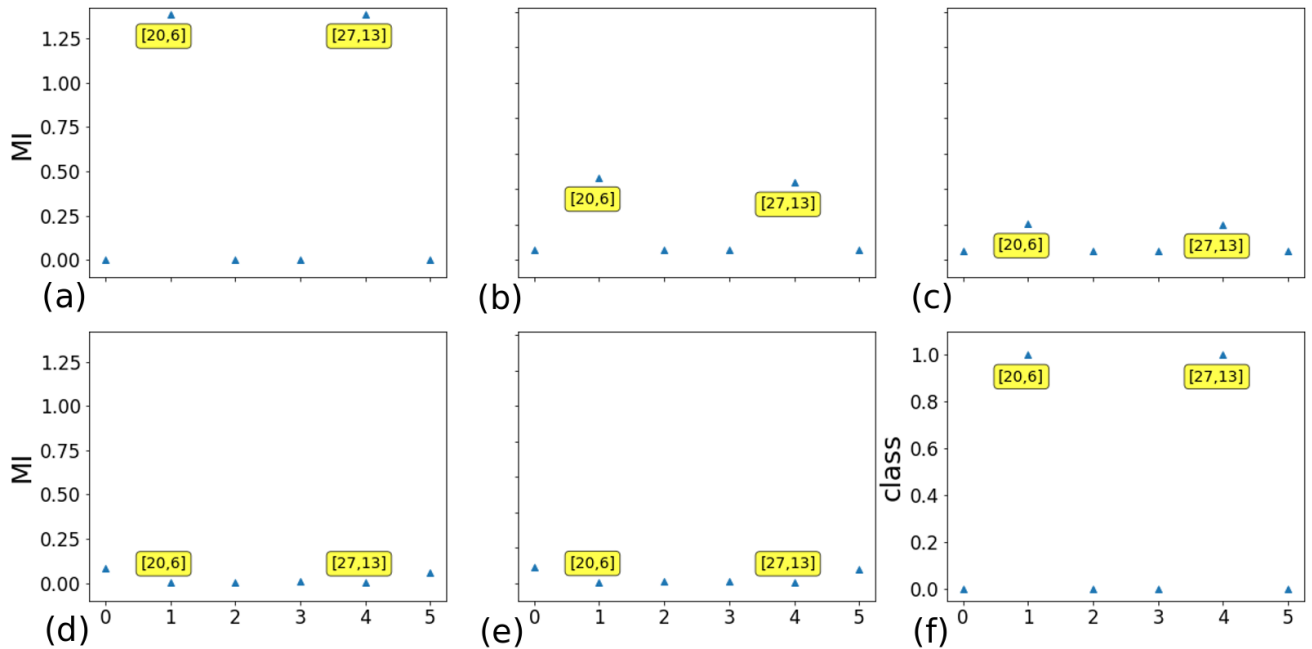


Figure 7.5.2: (a-e) MI values  $\hat{X}_j$  of the list of pairs  $S$  for states  $|\Gamma_+\rangle$ ,  $|\Psi_1\rangle$ ,  $|\Psi_3\rangle$ ,  $|\Psi_4\rangle$ ,  $|\Psi_6\rangle$ . (f) Class  $Y$  for the pairs in  $|\Gamma_+\rangle$ .

2. Unitary transformations equivalent to *hidden layers* are linear maps that act on the state  $|\Psi_{(6)}\rangle$ , followed by state  $|\Psi_{(5)}\rangle = U_6|\Psi_{(6)}\rangle$  and so on. This is in contrast with standard deep learning, where nonlinear filters and weight matrices are chosen variationally in constructing the transformation layers [540]. In our formalism, the unitary operators are constructed exactly (see Sec.2). Furthermore, because of the exact nature of the construction, there is no requirement of a training dataset for the construction of the DNN.
3. From each of the many-body states, we compute the MI values (eq.9.60) using one- and two-pseudospin Schmidt spectra (eq.7.29). The collection of 378 MI values at each RG step  $j$  is referred to as the bottlenecked representation ( $X_j$ ) of  $X_6$ .
4. At each RG step  $j$ , we compute the joint probability  $P(F(a, b), C(a, b))$  between the bottlenecked representation  $X_j$  and the target classifier  $\hat{Y}$ . From this, we compute the conditional probability for the eventual fate at  $j^* = 0$  of the *entangledness* of a pair given its MI value at RG step  $j$ .

We now set the criterion for a DNN model ideal from our perspective: such a DNN should predict that in the bulk of the EHM, the pairs (13, 27) and (6, 20) are strongly entangled ( $C = 1$ ) while all others are weakly entangled ( $C = 0$ ), as observed from the state  $|\Gamma_+\rangle$  (eq.7.6). Note that we have already shown via entanglement RG that the formation of strongly entangled short distance pairs demonstrates the onset of T.O. (Sec.7.3.2). Therefore, if the DNN model correctly predicts the eventual fate of the pairs, it is then equivalent to predicting the onset of T.O.

Fig.7.5.3 shows that the conditional probability  $P(C = 1|F(a, b))$  for the pairs (6, 20) and (13, 27) to be strong ( $C = 1$ ) are small to start with during the RG flow; however, after the third unitary RG step, it rises to value 1. On the other hand, the conditional probability vanishes for two other pairs (20, 4) and (24, 17). In this way, we demonstrate that layers near the UV scale of the EHM network are *holographic witnesses* to the emergence of T.O. at the IR scale. The existence of such holographic witnesses is further demonstrated in Fig.7.5.4 by the prediction of the eventual histogram distribution of MI from the initial layers of the EHM. Specifically, Fig.7.5.4(a-c) is the MI histogram distribution among pairs in  $S$  (formed from the pseudospins 6,13,20,27) and predicted from the zeroth, second and third unitary transformation layers of the EHM network. We find that the MI distribution predicted after only 3 layers already matches with that obtained after 6 layers Fig.7.5.4(d). This prediction process is further validated via a null hypothesis test: can the MI distribution of a random tensor network simulate the predicted MI distribution of the target? The statistical distance histogram displayed in Fig.7.5.5 shows that there is only 4% probability for the predicted MI distribution to be obtained from a random tensor network. This proves the uniqueness of the target tensor network obtained from the DNN.

Finally, we demonstrate two example cases to check the DNN's ability to distinguishing a metal from a insulator. For this, we compute the mutual information content  $\mathcal{I}(X_j, X_{j,U=2})$  between the target vector  $Y$ , obtained from the final RG step for the case of strong repulsion  $U_0 = 8$ , and feature vectors  $X_{j,U=2}$  obtained at each step for a case of weak repulsion  $U_0 = 2$ . The red curve in Fig.7.5.6 represents  $\mathcal{I}(Y : X_{j,U=2})$ , showing saturation at a finite value  $\mathcal{I}(X_j : X_{j,U=2}) = 0.636$ . We note that this is equal to the saturation value between the mutual information of the representation and class  $\mathcal{I}(X_j : Y)$  obtained for the case of strong repulsion  $U_0 = 8$  (seen as the value of the MI (black curve) in Fig.7.5.1). This precise match of results implies that the constructed DNN is able to predict that, even at weak repulsion ( $U_0 = 2$ ) and low quantum

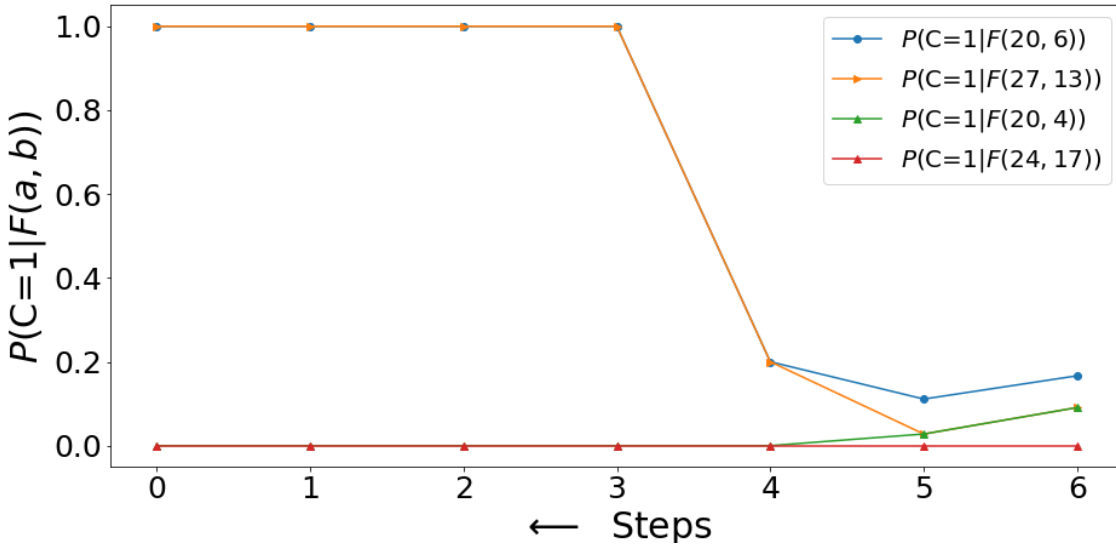


Figure 7.5.3: Predicting the eventual entanglement strength (either strong or weak) of a subset of pairs after each RG step using conditional probability.

fluctuation scales ( $4 - \omega = 0$ ), the phase is a Mott insulator. On the other hand, the green curve in Fig.7.5.6 is obtained from the mutual information between the MI distribution of a metal ( $U_0 = 8, \omega = 8$ ) and the target distribution of a insulator. It shows a final sharp dip to the value  $\mathcal{I}(X_{j,\text{metal}} : Y) = 0$ , implying that the gapless phase is not an insulator. This allows us to conclude that the DNN (constructed from the MERG based EHM) can successfully distinguish between RG flows that lead to a gapless metal and a gapped topological insulator. Such a DNN can, therefore, be employed for characterising the metal-insulator transition between the two phases.

## 7.6 Conclusions and discussions

In summary, we have demonstrated that MERG flow can be used to track the emergence of a topologically ordered (T.O.), gapped insulating state at low energies in the 2D Hubbard model [180]. Upon obtaining the T.O. ground state wavefunction at the Mott insulator fixed point of Ref.[180], we perform the inverse unitary transformations to re-entangle the emergent T.O. state with the decoupled degrees of freedom. The fixed point ground state, and the intermediate states reconstructed therefrom, are shown to have quantum circuit representations. In this way, we obtain the tensor network RG equivalent to MERG, called the entanglement holographic mapping (EHM). Each layer of the EHM is shown to be composed of two-local unitary disentanglers, and has a finite depth quantified by the circuit complexity. We show that MERG functions as a topological quantum error correcting code, leading to quantization of a nonlocal Wilson loop characterising the T.O. Mott insulating fixed point deep in the bulk of the EHM. It does so by resolving exactly the quantum fluctuations intrinsic to the system. The robustness of MERG quantum error correcting code against external quantum fluctuations is left for future study.

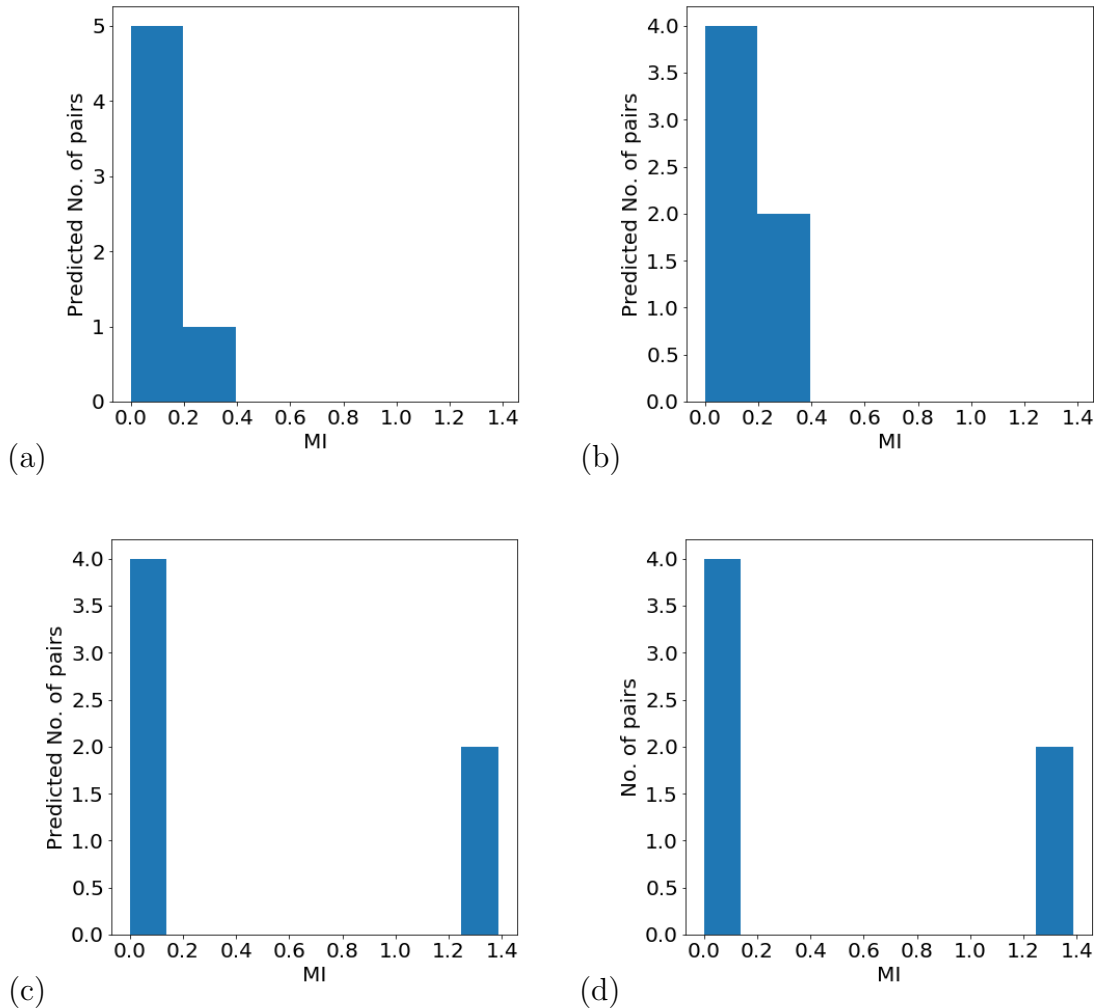


Figure 7.5.4: (a-c) Prediction of MI histogram distribution among pairs in list  $S$  from conditional probability model after (a) 0, (b) 2 and (c) 3 layers of MERG transformation. (d) MI histogram obtained after 6 layers of MERG transformation.

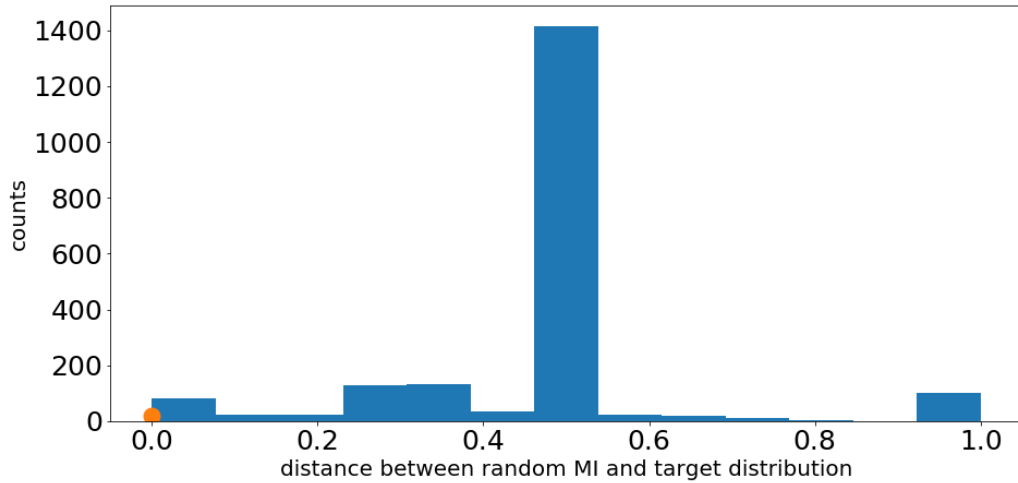


Figure 7.5.5: Histogram plot for the statistical distance between MI distribution of a random tensor network and the DNN's predicted MI distribution at the RG fixed point.

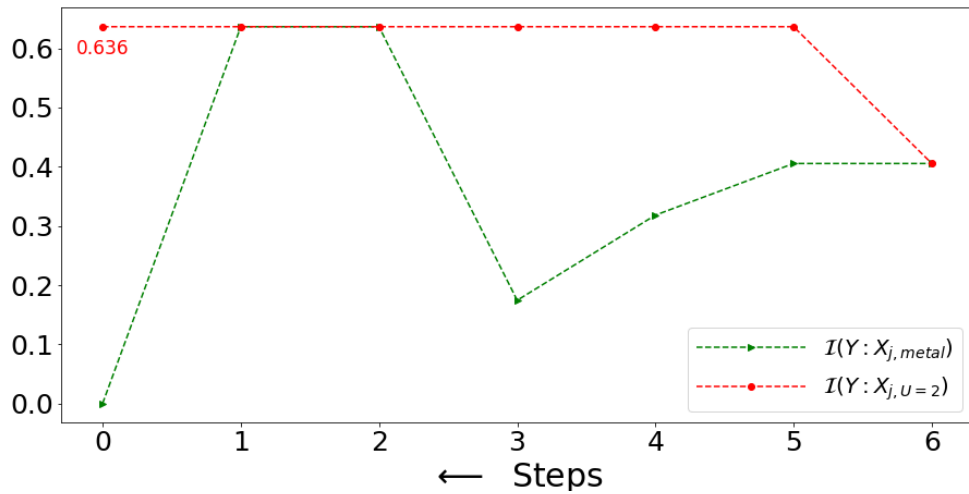


Figure 7.5.6: The red curve shows the mutual information content between the MI feature vector of a Mott insulator  $X_{j,U=2}$  for  $U_0 = 2$ ,  $\omega = 4$  and target vector  $Y$  (Mott insulator at  $U_0 = 8$ ,  $\omega = 4$ ). The green curve show the mutual information content between  $Y$  and the feature vector of a metal at  $U_0 = 8$ ,  $\omega = -4$ .

We have also computed the mutual information for all pseudospin pairs at each RG step, thereby extracting the entanglement geometry content from the EHM. Both the geodesic of the emergent geometry and the physical distance between strongest entangled pairs are shown to shrink along the RG direction, finally vanishing at the IR fixed point. In this way, we show that the emergence of short ranged strongly entangled pairs is concurrent with the emergence of topological order. On the other hand, for the normal metal phase of the 2D Hubbard model, the entanglement geometry is seen to expand and finally approach a separable state in the IR, demonstrating thereby the entanglement content of the EHM in this case is markedly different from that of the T.O. Mott insulating state. We also observe the scaling of momentum space block entanglement entropy (EE) for the metal and T.O. phases. In the T.O. phase the EE displays a nonmonotonic RG flow, i.e., an initial decreases followed by a gradual upsurge to a finite value. Additionally, at the fixed point, the EE is found to be constant for all block sizes. This is in contrast with the monotonic decay of EE in the normal metal phase. Thus, we have realized a concrete example of an EHM network that is witness to T.O. Further, the entanglement content and the  $(\pi, \pi)$  structure factor of the Neél antiferromagnet at half-filling are observed to vanish and grow respectively under RG. A similar study of the entanglement features and d-wave superconducting ODLRO of the Cooper pair liquid at the critical hole-doping related to the QCP reveal that the collapse of Mottness is tied to the growth of ODLRO. Importantly, we observe a clear anticorrelation between the total quantum correlation content (i.e., the maximum quantum mutual information) in a correlated state of quantum matter, and the tendency for symmetry-broken orders to arise from it. In a recent cold-atom experimental realisation of the fermionic 2D Hubbard model [541], it was observed that electrons are delocalised over neighbouring lattice sites even in the strongly correlated half-filled Mott insulating state at very low temperatures. This is consistent with our finding of short-distance strongly entangled pairs in the Mott liquid (see Fig.7.3.1 (right panel)). It would be interesting to test some of our other findings in a similar experiment.

Finally, we show that the EHM network functions as an optimal deep neural network (DNN) satisfying the information bottleneck (IB) principle. The unitary transformations lead to successive disentanglement of qubits, naturally reducing the entanglement spread and leading eventually to simpler representations of the many-body state. However, the essential topological content of the IR fixed point is retained across the EHM. The predictive power of the DNN is tested via formulation of the conditional probability model that can classify a given pair to be either strongly or weakly entangled. The model is found to predict the entanglement features in the bulk of the EHM from the layers near its boundary. This is realised by a successful prediction of the onset of T.O. during the RG flow well before the stable fixed point is reached. Further, the DNN is successfully able to distinguish the gapless normal metal ground state from the T.O. gapped insulating state, as well as classify insulating ground states reached at two different values of the Hubbard coupling as belonging to the same class. In this way, the DNN is able to classify different phases of the 2D Hubbard model, as well as distinguish between the RG flows that lead to them. Our work sets the stage for yet deeper investigations of the many-particle entanglement of novel gapped as well as gapless quantum liquids that arise from systems of strongly interacting electrons. It also heralds the development of applications of the MERG formalism for the creation of novel quantum error correcting codes and deep neural network architectures based on the quantum entanglement of many-particle wavefunctions.



# Appendix

## 7.A Derivation of the unitary operator

We present briefly the formalism developed in Ref.[180].  $H$  is a Hamiltonian belonging to the space  $\mathcal{A}(\mathcal{H}_2^{\otimes N})$ , where  $\mathcal{H}_2$  is a SU(2) Hilbert space spanned by the generators

$$c_N^\dagger, c_N, \hat{n}_N - 1/2 = c_N^\dagger c_N - 1/2 , \quad (7.39)$$

and  $\mathcal{A}$  is the antisymmetrizer. We want to find a unitary operation  $U_N$  that block diagonalizes the Hamiltonian  $H$  in the occupation number space of  $N : \{|1_N\rangle, |0_N\rangle\}$

$$(1 - \hat{n}_N)U_N H U_N^\dagger \hat{n}_N = 0 \Rightarrow P_N H (1 - P_N) = 0 , \quad (7.40)$$

where  $P_N = U_N^\dagger \hat{n}_N U_N$ . Using the definition of  $P_N$ , we construct the Hamiltonian  $H' = P_N H P_N$ , leading to the block equation

$$\begin{aligned} P_N H P_N = H' &\Rightarrow (P_N H P_N + (1 - P_N) H P_N) P_N = H' P_N \\ &\Rightarrow H P_N = H' P_N . \end{aligned} \quad (7.41)$$

It is important to note that

$$P_N H' (1 - P_N) = 0, [H', P_N] = 0 , \quad (7.42)$$

implying that the Hamiltonian  $H'$  is block diagonal in the rotated basis. A state  $|\Psi\rangle$ , belonging to the projected space generated by  $P_N$ , can be written in the occupation number basis of  $N$

$$|\Psi\rangle = a_1(1 + \eta_N)|1_N\Psi_{1_N}\rangle = a_1|1_N\Psi_{1_N}\rangle + a_0|0_N\Psi_{0_N}\rangle , \quad (7.43)$$

where  $\eta_N$  is an (as of now) undetermined operator that connects a many-body state  $|1_N\Psi_{1_N}\rangle$  (with  $N$  occupied,  $|1_N\rangle$ ) to another state  $|0_N\Psi_{0_N}\rangle$  (where state  $N$  is unoccupied,  $|0_N\rangle$ ), and the subsystem configuration of the remaining  $(1, \dots, N-1)$  electrons ( $|\Psi_{1_N}\rangle$ ) is rotated into the configuration  $|\Psi_{0_N}\rangle$ . Taking cue from this decomposition, we can define the projection operator  $P_N$  using the  $\eta_N$  operator and its Hermitian conjugate

$$P_N = \mathcal{N}(1 + \eta_N + \eta_N^\dagger) . \quad (7.44)$$

Next, we solve for  $\eta_N$  by putting  $P_N$  (eq.7.44) into eq.7.41, and projecting onto the state  $|1_N, \Psi_{1_N}\rangle$

$$\hat{n}_N H \hat{n}_N |1_N, \Psi_{1_N}\rangle + \hat{n}_N H (1 - \hat{n}_N) \eta_N |1_N, \Psi_{1_N}\rangle = H' |1_N, \Psi_{1_N}\rangle , \quad (7.45)$$

$$(1 - \hat{n}_N) H (1 - \hat{n}_N) \eta_N |1_N, \Psi_{1_N}\rangle + (1 - \hat{n}_N) H \hat{n}_N |1_N, \Psi_{1_N}\rangle = H' \eta_N |1_N, \Psi_{1_N}\rangle , \quad (7.46)$$

$$\Rightarrow \eta_N = \frac{1}{H' - (1 - \hat{n}_N) H (1 - \hat{n}_N)} (1 - \hat{n}_N) H \hat{n}_N . \quad (7.47)$$

Given the symmetry properties of  $H'$  (eq.7.42), it supports the decomposition into a diagonal piece  $H'^D$ , and an off-diagonal piece  $H'^X_N$  constituting all electronic states apart from  $N$

$$H' = H'^X_N + H'^D . \quad (7.48)$$

Using eq.7.48, we can obtain a simple description of  $\eta_N$

$$\eta_N = \frac{1}{\hat{\omega} - Tr_N(H^D(1 - \hat{n}_N))(1 - \hat{n}_N)} Tr_N(c_N^\dagger H) c_N , \quad (7.49)$$

where  $\hat{\omega} = H'^D + H'^X_N - H_N^X$ , and  $H_N^X$  has a definition similar to  $H'^X_N$ .  $Tr_N(c_N^\dagger H) c_N$  is the collection of selected off-diagonal pieces of  $H$  involving the state  $N$ . Additionally, we note that a form for  $\eta_N^\dagger$  can similarly be obtained by projecting onto state  $|0_N, \Psi_{0_N}\rangle$

$$\eta_N^\dagger = \frac{1}{\hat{\omega} - Tr_N(H^D \hat{n}_N) \hat{n}_N} c_N^\dagger Tr_N(H c_N) . \quad (7.50)$$

In the above equation  $Tr_N(.)$  represents the partial tracing of the electronic state  $N$ , which is carried out in the electronic fock space. Putting  $\eta_N$  eq.7.47 into eq.7.45, and using the form for  $\eta_N^\dagger$ , we obtain the algebra for these operators

$$\{\eta_N^\dagger, \eta_N\} = 1 , \quad [\eta_N^\dagger, \eta_N] = 2\hat{n}_N - 1 . \quad (7.51)$$

An additional set of relations for  $\eta_N$  and  $\eta_N^\dagger$  are:  $\eta_N^2 = \eta_N^{\dagger 2} = 0$ . The state  $|\Psi\rangle$  can now be connected via a similarity transformation to the state  $|1_N \Psi_{1_N}\rangle$

$$|\Psi\rangle = a_1 \exp(\eta_N) |1_N \Psi_{1_N}\rangle . \quad (7.52)$$

Note that in  $|1_N \Psi_{1_N}\rangle$ , the state  $N$  is now disentangled. Finally, we can construct the form for the unitary transformation  $U_N$  from the similarity transformation [139, 137]

$$U_N = \frac{1}{\sqrt{2}} (1 + \eta_N - \eta_N^\dagger) \quad (7.53)$$

Using the algebra eq.7.51 one can verify the identity  $UU^\dagger = U^\dagger U = 1$ .

## 7.B Derivation of the normal phase Hamiltonian in pseudospin subspace

A projection of the gapless marginal Fermi liquid normal phase Hamiltonian (eq.7.1) of the 2D Hubbard model at 1/2-filling [180] in the charge pseudospin subspace gives

$$H^* = \sum_{l=1, i=(1,2)}^{j^*} \epsilon_{\Lambda_l \hat{s}_i} A_{\Lambda_l \hat{s}_i}^z - \sum_{i,j,k=1,2} R_k^* A_{\Lambda_i, \hat{s}_k}^z A_{\Lambda_j, \hat{s}_k}^z . \quad (7.54)$$

The ground state of the gapless normal phase with 14 electrons in 28 states can then be written as

$$|\Psi\rangle_{NP} = \prod_{i=0,n=(0,1)}^6 |\downarrow_{i+21n}\rangle \prod_{i=7,n=(0,1)}^{13} |\uparrow_{i+7n}\rangle . \quad (7.55)$$

Upon projecting the Hamiltonian in the basis of Cooper pair pseudospins  $B_{\Lambda,\hat{s}}^+ = c_{\mathbf{k}_{\Lambda,-\hat{s}},-\sigma}^\dagger c_{\mathbf{k}_{\Lambda,\hat{s}},\sigma}^\dagger$ ,  $B_{\Lambda,\hat{s}}^z = \frac{1}{2}(\hat{n}_{\mathbf{k}_{\Lambda,-\hat{s}},-\sigma} + \hat{n}_{\mathbf{k}_{\Lambda,\hat{s}},\sigma} - 1)$ , we attain the form

$$H^* = \sum_{\Lambda < \Lambda^*, i=1,2} \epsilon_{\Lambda\hat{s}_i} B_{\Lambda\hat{s}_i}^z + \sum_{\Lambda,\hat{s}} R_{\hat{s}}^* \left( B_{\Lambda,\hat{s}}^z + \frac{1}{2} \right) \left( B_{-\Lambda,T\hat{s}}^z + \frac{1}{2} \right) \left( B_{\Lambda',\hat{s}}^z + \frac{1}{2} \right) . \quad (7.56)$$

## 7.C URG study for the symmetry broken Neel SDW state

In an earlier work [180], we showed that upon introducing a staggered magnetic field ( $h$ ) (by adding a term  $h \sum_{i,j} e^{i\pi(i+j)} S_r^z$  to the Hamiltonian) in the Mott liquid (ML) leads to the symmetry-broken Néel antiferromagnetic phase. In order to study the competition between the tendency towards symmetry-breaking and the effects of nested Umklapp scattering, we apply the unitary RG formalism (eq.4.2) to a simplified model Hamiltonian  $H$  which includes only the Umklapp scattering processes (with coupling  $V$ , whose bare value is the Hubbard  $U_0$ ) between electrons in the neighbourhood of the antinodes of the underlying tight-binding Fermi surface, and checkerboard spin density waves (SDW) involving momentum transfer  $\mathbf{Q} = (\pi, \pi)$

$$\begin{aligned} H &= h \sum_{\Lambda,\hat{s},\sigma=\pm 1} \sigma(c_{\Lambda,\hat{s},\sigma}^\dagger c_{\mathbf{k}_{\Lambda,\hat{s}}-\mathbf{Q},\sigma} + h.c.) + V \sum_{\Lambda,\Lambda',\hat{s}} c_{\mathbf{k}_{\Lambda,\hat{s}},\sigma}^\dagger c_{\mathbf{k}_{-\Lambda,T\hat{s}},-\sigma}^\dagger c_{\mathbf{k}_{\Lambda,-\hat{s}},-\sigma} c_{\mathbf{k}_{-\Lambda,-T\hat{s}},\sigma} \\ &= h \sum_{\Lambda,\hat{s},\sigma=\pm 1} \sigma(c_{\Lambda,\hat{s},\sigma}^\dagger c_{\mathbf{k}_{-\Lambda,-T\hat{s}},\sigma} + h.c.) + V \sum_{\Lambda,\Lambda',\hat{s}} c_{\mathbf{k}_{\Lambda,\hat{s}},\sigma}^\dagger c_{\mathbf{k}_{-\Lambda,-T\hat{s}},\sigma}^\dagger c_{\mathbf{k}_{-\Lambda,T\hat{s}},-\sigma} c_{\mathbf{k}_{\Lambda,-\hat{s}},-\sigma} , \end{aligned} \quad (7.57)$$

where the Umklapp scattering processes are restricted to the  $\mathbf{Q} = (\pi, \pi)$  net-momentum pairs, as they carry the dominant spectral weight and lead to the condensation of pseudospins in the IR (eq.7.3) [180]. The symmetry-breaking field  $h$  breaks explicitly the  $SU(2)$  spin-rotation symmetry of the  $H$ , and fixes the quantization axis along the eigen-direction of  $\sigma(c_{\Lambda,\hat{s},\sigma}^\dagger c_{\mathbf{k}_{-\Lambda,-T\hat{s}},\sigma} + h.c.)$

$$|\psi_{\Lambda,\hat{s}}^{\sigma,\pm}\rangle = \frac{1}{\sqrt{2}} [ |1_{\mathbf{k}_{\Lambda,\hat{s}},\sigma} 0_{\mathbf{k}_{-\Lambda,-T\hat{s}},\sigma}\rangle \pm |0_{\mathbf{k}_{\Lambda,\hat{s}},\sigma} 1_{\mathbf{k}_{-\Lambda,-T\hat{s}},\sigma}\rangle ] . \quad (7.58)$$

The unitary disentanglement RG operation block-diagonalizes the Hamiltonian iteratively, and the disentangled electronic states are oriented along the eigen-directions (eq.7.58) governed by the projection operators  $\rho_{j,\hat{s},\sigma} = |\psi_{\Lambda,\hat{s}}^{\sigma,\pm}\rangle \langle \psi_{\Lambda,\hat{s}}^{\sigma,\pm}|$ . This leads to the Hamiltonian RG equation

$$U_{(j)} H_{(j)} U_{(j)}^\dagger - H_{(j)} = \Delta H_{(j)} = \frac{2l_j V_{(j)}^2}{h - l_j^2 V_{(j)}} \sum_{\Lambda < \Lambda_j} c_{\mathbf{k}_{\Lambda,\hat{s}},\sigma}^\dagger c_{\mathbf{k}_{-\Lambda,T\hat{s}},-\sigma}^\dagger c_{\mathbf{k}_{\Lambda,-\hat{s}},-\sigma} c_{\mathbf{k}_{-\Lambda,-T\hat{s}},\sigma} , \quad (7.59)$$

here  $l_j$  is the number-density of electronic states on the momentum-shell located at distance  $\Lambda_j$  from the Fermi surface. The van Hove singularities at the antinodes  $((\pi, 0)$  and  $(0, \pi))$  induces

a logarithmic dependence on the density of states  $l_j = \log \frac{\Lambda_0}{\Lambda_j}$ . The dependence on  $l_j$  in the RG eq.9.63 arises by summing the RG contribution of tangential scattering processes between electronic states in the transverse direction to the Fermi surface [180]. From here, we extract the Umklapp scattering vertex RG flow

$$\frac{\Delta V_{(j)}}{\Delta \log \Lambda / \Lambda_0} = \frac{2l_j V_{(j)}^2}{h - l_j^2 V_{(j)}} , \quad (7.60)$$

where  $\Delta \log \Lambda / \Lambda_0 = 1$ . In the continuum, this RG equation attains the form ( $\bar{V} = V/h$ )

$$\frac{d\bar{V}}{d \log \Lambda} = \frac{2l(\Lambda)\bar{V}}{1 - l^2(\Lambda)\bar{V}} . \quad (7.61)$$

For weak coupling  $V \ll 1/l^2(\Lambda)$ , the above RG equation has the perturbative one-loop RG equation form  $\frac{d\bar{V}}{d \log \Lambda} = 2 \log \frac{\Lambda_0}{\Lambda} \bar{V}^2$ . This leads to the gap function  $\Lambda^*/\Lambda_0 = \exp\left(-\sqrt{\frac{2}{V_0}}\right)$ , where  $\bar{V}_0 = V_0/h$  and corresponds to the Neél SDW phase [227]. From the non-perturbative RG formulation of eq.7.60 for the passage between the Mott liquid phase and SDW phase, we can construct the effective Hamiltonian at the RG fixed point

$$H^* = \frac{h}{2}(D_{*,\uparrow}^x - D_{*,\downarrow}^x) + V^* \sum_{\Lambda < \Lambda^*, \hat{s}} \mathbf{D}_{\Lambda,\hat{s},\uparrow} \cdot \mathbf{D}_{\Lambda,-\hat{s},\downarrow} , \quad V^* = \frac{h}{2 \log \frac{\Lambda_0}{\Lambda^*}} . \quad (7.62)$$

The form of the paired electron-hole pseudospin operators are as follows

$$\begin{aligned} D_{\Lambda,\hat{s},\sigma}^x &= \frac{1}{2}(c_{\mathbf{k}_{\Lambda\hat{s}},\sigma}^\dagger c_{\mathbf{k}_{-\Lambda,-T\hat{s}},\sigma} + h.c.) , \\ D_{\Lambda,\hat{s},\sigma}^y &= \frac{i}{2}(c_{\mathbf{k}_{\Lambda\hat{s}},\sigma}^\dagger c_{\mathbf{k}_{-\Lambda,-T\hat{s}},\sigma} - h.c.) , \\ D_{\Lambda,\sigma}^z &= \frac{1}{2}(\hat{n}_{\mathbf{k}_{\Lambda\hat{s}},\uparrow} - \hat{n}_{\mathbf{k}_{-\Lambda,-T\hat{s}},\uparrow}) , \end{aligned} \quad (7.63)$$

and  $\mathbf{D}_{*,\sigma} = \sum_{\Lambda \leq \Lambda^*} \mathbf{D}_{\Lambda,\sigma}$ . For the case  $D_{*,\sigma} = 1/2$ , the ground state of the  $H^*$  has the form

$$\begin{aligned} |\Psi\rangle &= \cos \frac{\theta}{2} |\uparrow\downarrow\rangle - \sin \frac{\theta}{2} |\downarrow\uparrow\rangle , \\ |\uparrow\rangle &= \frac{1}{\sqrt{2}} [|1_{\mathbf{k}_{\Lambda^*\hat{s}},\uparrow} 0_{\mathbf{k}_{-\Lambda^*,-T\hat{s}},\uparrow} 0_{\mathbf{k}_{\Lambda^*\hat{s}},\downarrow} 0_{\mathbf{k}_{-\Lambda^*,-T\hat{s}},\downarrow}\rangle - |0_{\mathbf{k}_{\Lambda^*\hat{s}},\uparrow} 1_{\mathbf{k}_{-\Lambda^*,-T\hat{s}},\uparrow} 0_{\mathbf{k}_{\Lambda^*\hat{s}},\downarrow} 0_{\mathbf{k}_{-\Lambda^*,-T\hat{s}},\downarrow}\rangle] , \\ |\downarrow\rangle &= \frac{1}{\sqrt{2}} [|1_{\mathbf{k}_{\Lambda^*\hat{s}},\uparrow} 0_{\mathbf{k}_{-\Lambda^*,-T\hat{s}},\uparrow} 0_{\mathbf{k}_{\Lambda^*\hat{s}},\downarrow} 0_{\mathbf{k}_{-\Lambda^*,-T\hat{s}},\downarrow}\rangle + |0_{\mathbf{k}_{\Lambda^*\hat{s}},\uparrow} 1_{\mathbf{k}_{-\Lambda^*,-T\hat{s}},\uparrow} 0_{\mathbf{k}_{\Lambda^*\hat{s}},\downarrow} 0_{\mathbf{k}_{-\Lambda^*,-T\hat{s}},\downarrow}\rangle] , \end{aligned} \quad (7.64)$$

where

$$\cos \theta = \frac{h}{\sqrt{h^2 + \frac{(V^*)^2}{4}}} = \frac{1}{\sqrt{1 + \frac{1}{16 \log^2 \frac{\Lambda_0}{\Lambda^*}}}} . \quad (7.65)$$

For an IR fixed-point with a momentum-space width around the Fermi surface of  $\Lambda^* < \Lambda_0$ , the superposition coefficient  $\cos \frac{\theta}{2} \rightarrow 1$  results in a highly polarized Neél antiferromagnetic configuration [180]. Upon simulating the RG equation for bare  $V \equiv U_0 = 8$  on a  $512 \times 512$  momentum-space grid, we found that the magnitude of the coupling at RG fixed point is  $V^* = 8 \times 10^{-5}t$ , the fixed point width  $\Lambda^*/\Lambda_0 = 0.988$  and polarization coefficient given by  $\cos \theta/2 = 0.999$ . From here, we can perform the MERG scheme using the inverse unitary transformations  $U_{j+1}^\dagger |\Psi_{(j)}\rangle = |\Psi_{(j+1)}\rangle$  (see Fig.9.7.2), and obtain the many-body states across RG scales from UV to IR.

## 7.D Effective Cooper pair Hamiltonian obtained from the Mott liquid fixed point at half filling

We begin by writing the effective Hamiltonian for the spin-type Mott liquid (eq.7.2)

$$\hat{H}_2^* = \sum_{\Lambda, \hat{s}} \epsilon_{\Lambda, \hat{s}} \hat{n}_{\Lambda, \hat{s}, \sigma} - \sum_{\hat{s}} K_{\hat{s}}^* \mathbf{S}_{*, \hat{s}} \cdot \mathbf{S}_{*, -\hat{s}}, \quad (7.66)$$

where the spin-type pseudospins ( $\mathbf{S}_{*, \hat{s}}$ ) within the emergent fixed-point window are defined as

$$\mathbf{S}_{\Lambda, \hat{s}} = f_{\Lambda, \hat{s}}^{s; \dagger} \frac{\boldsymbol{\sigma}}{2} f_{\Lambda, \hat{s}}^s, \quad f_{\Lambda, \hat{s}}^{s; \dagger} = \left[ c_{\Lambda, \hat{s}, \sigma}^\dagger \quad c_{\Lambda - 2\Lambda_s^*, T\hat{s}, -\sigma}^\dagger \right], \quad (7.67)$$

and demonstrate the presence of Cooper pairs within the spin-type Mott liquid. For this, we rewrite the above effective Hamiltonian as  $\hat{H}_2^* = H_0 + H_1$ , where

$$\begin{aligned} H_0 &= \sum_{\Lambda, \hat{s}} \epsilon_{\Lambda, \hat{s}} \hat{n}_{\Lambda, \hat{s}, \sigma} + \sum_{\hat{s}, \Lambda} K_{\hat{s}, \mathbf{p}=0}^* c_{\Lambda, \hat{s}, \sigma}^\dagger c_{\Lambda, -\hat{s}, -\sigma}^\dagger c_{\Lambda - 2\Lambda^*, T\hat{s}, -\sigma} c_{\Lambda - 2\Lambda^*, -T\hat{s}, \sigma}, \\ H_1 &= \sum_{\Lambda \neq \Lambda'} K_{\hat{s}, \mathbf{p}}^* c_{\Lambda, \hat{s}, \sigma}^\dagger c_{\Lambda', -\hat{s}, -\sigma}^\dagger c_{\Lambda - 2\Lambda^*, T\hat{s}, -\sigma} c_{\Lambda' - 2\Lambda^*, -T\hat{s}, \sigma}, \end{aligned} \quad (7.68)$$

and where  $H_0$  denotes the physics of zero-momentum electron pairs ( $|\mathbf{k}_{\Lambda, \hat{s}}, \sigma\rangle, |\mathbf{k}_{\Lambda, -\hat{s}}, -\sigma\rangle$ ),  $H_1$  the physics of non-zero net-momentum electron pairs ( $|\mathbf{k}_{\Lambda, \hat{s}}, \sigma\rangle, |\mathbf{k}_{\Lambda', -\hat{s}}, -\sigma\rangle$ ) and  $\mathbf{p} = \mathbf{k}_{\Lambda_j, \hat{s}} + \mathbf{k}_{\Lambda_j - \delta, -\hat{s}}$ . Here  $\delta > 0$ , such that we account for only the states within the window  $\Lambda' = \Lambda - \delta < \Lambda_j$ , where  $\Lambda_N = \Lambda^* > \Lambda_{N-1} > \dots > 0$ . Also,  $K_{\hat{s}, \mathbf{p}}^* = K_{\hat{s}, \mathbf{p}=0}^* \equiv K_{\hat{s}}^*$  at the bare level. We now perform a second renormalization group analysis of the Hamiltonian  $H_2^*$  in order to study the effect of the non-zero momentum pairs on their zero-momentum counterparts. For this, we write down the unitary disentangling operator

$$U_{\mathbf{k}_{\Lambda \hat{s}}, \sigma} = \frac{1}{\sqrt{2}} \left[ 1 + \eta_{\mathbf{k}_{\Lambda \hat{s}}, \sigma} - \eta_{\mathbf{k}_{\Lambda \hat{s}}, \sigma}^\dagger \right], \quad (7.69)$$

where

$$\eta_{\mathbf{k}_{\Lambda \hat{s}}, \sigma} = \frac{1}{\hat{\omega} - Tr_{\mathbf{k}_{\Lambda \hat{s}}, \sigma}(H_{\mathbf{k}_{\Lambda \hat{s}}, \sigma}^D \hat{n}_{\mathbf{k}_{\Lambda \hat{s}}, \sigma})} c_{\mathbf{k}_{\Lambda \hat{s}}, \sigma}^\dagger Tr_{\mathbf{k}_{\Lambda \hat{s}}, \sigma}(H_{\mathbf{k}_{\Lambda \hat{s}}, \sigma} c_{\mathbf{k}_{\Lambda \hat{s}}, \sigma}). \quad (7.70)$$

From the Hamiltonian RG flow equation  $H_{(j-1)} = U_{(j)} H_{(j)} U_{(j)}^\dagger$ , we obtain the coupling RG equation

$$K_{\hat{s}, \mathbf{p}}^{*(j-1)} - K_{\hat{s}, \mathbf{p}}^{*(j)} = \frac{(K_{\hat{s}, \mathbf{p}}^{*(j)})^2}{\omega - \frac{1}{2}(\epsilon_{\Lambda_j, \hat{s}} + \epsilon_{\Lambda_j - \delta, -\hat{s}}) - \frac{K_{\hat{s}, \mathbf{p}}^{*(j)}}{4}}. \quad (7.71)$$

For  $\omega > 0$ , the denominator  $\omega - \frac{1}{2}(\epsilon_{\Lambda_j, \hat{s}} + \epsilon_{\Lambda_j - \delta, -\hat{s}})$  attains its highest value for  $\mathbf{p} = 0$ , thereby indicating the domination of the  $\mathbf{p} = 0$  pairs under RG. By accounting solely for the dominant scattering processes, the effective Hamiltonian at the IR fixed point ( $V^* = 4(\omega - \epsilon_{\Lambda^{**}, \hat{s}})$ ) is then given by

$$H_0^* = \sum_{\Lambda < \Lambda^{**}, \hat{s}} \epsilon_{\Lambda, \hat{s}} B_{\Lambda, \hat{s}}^z + \epsilon_{\Lambda - 2\Lambda^*, T\hat{s}} B_{\Lambda - 2\Lambda^*, T\hat{s}}^z + \sum_{\hat{s}, \Lambda < \Lambda^{**}} K_{\hat{s}}^{**} B_{\Lambda, \hat{s}}^+ B_{\Lambda - 2\Lambda^*, T\hat{s}}^- , \quad (7.72)$$

where  $B_{\Lambda, \hat{s}}^+ = c_{\mathbf{k}_{\Lambda, -\hat{s}}, -\sigma}^\dagger c_{\mathbf{k}_{\Lambda \hat{s}}, \sigma}^\dagger$ ,  $B_{\Lambda, \hat{s}}^z = \frac{1}{2}(\hat{n}_{\mathbf{k}_{\Lambda, -\hat{s}}, -\sigma} + \hat{n}_{\mathbf{k}_{\Lambda, \hat{s}}, \sigma} - 1)$  etc.

## 7.E Effective Hamiltonian and eigenstates at critical doping

At the QCP of the doped 2D Hubbard model ( $\omega = 4$  and  $\Delta\mu_{eff} = -4$ ) [181], the nodal direction  $(\pi/2, \pi/2)$  is gapless while the antinodal regions centered around  $(0, \pi)$  and  $(\pi, 0)$  are gapped. The effective Hamiltonian for the QCP was derived in Ref.[181] and is given by  $H_{QCP}$

$$\begin{aligned} H_{QCP} = & \sum_{\hat{s}=\hat{s}_{AN}, \Lambda, \Lambda'}^{\hat{s}'} K_{\hat{s}}^*(B_{\Lambda, \hat{s}}^+ B_{\Lambda', -\hat{s}}^- + h.c.) \\ & + \sum_{\Lambda < \Lambda^*} \epsilon_{\Lambda \hat{s}_N} B_{\Lambda \hat{s}_N}^z + \sum_{\Lambda, \hat{s}} R_{\hat{s}}^* \left( B_{\Lambda, \hat{s}_N}^z + \frac{1}{2} \right) \left( B_{-\Lambda, \hat{s}_N}^z + \frac{1}{2} \right) \left( B_{\Lambda', \hat{s}_N}^z + \frac{1}{2} \right) . \end{aligned} \quad (7.73)$$

Note that we have written the two electron-one hole vertices  $R_{ll'}^* \hat{n}_{j,l} \hat{n}_{j',l'} (1 - \hat{n}_{j',l})$  describing the marginal Fermi liquid (eq.7.1) in terms of Anderson pseudospins defined below eq.7.72 with  $l = \hat{s}_N$  (the nodal direction). The first term in eq.7.73 reflects the physics of the off-diagonal backscattering vertices between opposite directions normal to the Fermi surface, and generates a gap in the antinodal region. The ground state wavefunction can be written in terms of the two Fermi points, one near the antinodes  $\hat{s} = (\pi/4, 3\pi/4)$  and another along the nodes  $\pi/2, \pi/2$ , as follows

$$|\Psi\rangle = \frac{1}{2} \prod_{n=[0,3]} \prod_{i=[7n, 7n+2], j=[7n+3, 7n+5]} |0_i 1_j\rangle (|0_6 1_{20}\rangle - |1_6 0_{20}\rangle) |1_{13} 1_{27}\rangle . \quad (7.74)$$

The Cooper pair (Anderson) pseudospins qubits 6 and 20 within the antinodal patch along  $(3\pi/4, \pi/4)$  form a singlet ground state  $|0_6 1_{20}\rangle - |1_6 0_{20}\rangle$  via the backscattering vertex in eq.7.73. Importantly, we note that at the QCP, the Umklapp charge backscattering vertices are RG irrelevant. This is due to the presence of a term for the doublon-holon disparity caused by hole doping in eq.7.2 [181]:  $-\Delta\mu_{eff}(A_{*, \hat{s}}^z + A_{*, -\hat{s}}^z)$ . This can be simply seen from the modified RG equations (eq.7.14) for Umklapp backscattering  $K_l^{(j-1)}$  at the QCP  $\Delta\mu_{eff} = -\omega = 4$

$$\Delta K_l^{(j-1)} = \frac{(K_l^{(j)})^2}{\omega - \frac{1}{2}(\epsilon_{\Lambda_j, \hat{s}} + \epsilon_{\Lambda_j - \delta, -\hat{s}}) + \Delta\mu_{eff} - \frac{1}{4}K_l^{(j)}} . \quad (7.75)$$

The negative signature in the denominator  $\omega - \frac{1}{2}(\epsilon_{\Lambda_j, \hat{s}} + \epsilon_{\Lambda_j - \delta, -\hat{s}}) + \Delta\mu_{eff} < 0$  renders the coupling  $K_l$  RG irrelevant.

# Chapter 8

## Fermionic criticality is shaped by Fermi surface topology: a case study of the Tomonaga-Luttinger liquid

Given the extensive developments in the understanding the many-body correlations [4, 3] and many particle entanglement content [157, 175, 289–293], topological features [368, 291, 369, 292, 370–377] of interacting fermions in one spatial dimension, a unified view is needed of the emergence of the effective low-energy Hamiltonians of quantum liquids and the associated entanglement content of their many-particle Hilbert space. With this as our goal, we turn in this chapter to the unitary tensor network RG (URG) introduced in Chapter 2 for studying the primary instabilities of the Tomonaga Luttinger liquid (TLL) [3]. From the effective Hamiltonians obtained at the gapless and the gapped fixed points, we study the low energy spectrum, transport properties and entanglement content within the ground state.

We now outline the sections of this chapter. In Sec.8.1, we review the symmetries and topological properties of the Hilbert space for the degrees of freedom at the Fermi surface of the 1D tight binding chain. We follow this in Sec.8.2 by showing that, in the presence of a Fermi surface instability arising from the presence of inter-particle interactions, a topological property of the Fermi surface Hilbert space (the first Chern class) imposes a constraint on the condensation of four-fermion vertices. This involves the formation of composite pseudospin  $S = 1/2$  degrees of freedom formed by the pairing of fermions. This is followed in Sec.8.3 by showing that the pseudospin backscattering vertices connecting the Fermi points  $\pm k_F$  lead to a change in the centre of mass (c.o.m) Hilbert space by satisfying a constructive interference condition for scattering processes. We then implement the URG formalism for the case of correlated electrons on the 1D tight-binding chain in Sec.8.4, and demonstrate how the topological features of the Fermi surface Hilbert space guide the RG flows. In Sec.8.5, we study the URG flow of the many-particle entanglement and unveil the role played by the Fermi surface in distinguishing between flows to gapless and gapped quantum liquid phases. We study dynamical spectral weight redistribution between the fundamental and emergent degrees of freedom in Sec.8.6, showing the manifest unitarity of the RG formalism by tracking the flow of the Friedel’s phase shift from the scattering matrix [542]. In Sec.8.7, we unveil signatures of topological order in some of the gapped quantum liquids attained from the URG flow, and design a thought experiment to track its features from the properties of the degrees of freedom at the (erstwhile) Fermi surface. We end by summarising

our results in Sec.8.8.

## 8.1 Symmetries and Topology of the Fermi surface

We recapitulate the symmetries and topological properties of the Fermi volume and Fermi surface of non-interacting electrons in one spatial dimension in this section, as these will be critical in dealing with the case of interacting electrons in later sections. To begin with, the 1D tight binding Hamiltonian in momentum-space for spinful electrons is given by [543]

$$H_t = -2t \sum_{k\sigma} \cos(k) c_{k\sigma}^\dagger c_{k\sigma} , \quad (8.1)$$

and leads to the dispersion spectrum  $E_{k\sigma} = -2t \cos k$ . The parity operation (P)  $P c_{k\sigma}^\dagger P^\dagger = c_{-k\sigma}^\dagger$ ,  $P \in Z_2$  and time reversal transformation (T)  $T c_{k\uparrow}^\dagger T^\dagger = c_{k\downarrow}^\dagger$ ,  $T \in Z_2$  leave the Hamiltonian invariant

$$PH_t P^\dagger = H_t , \quad TH_t T^\dagger = H_t . \quad (8.2)$$

Accordingly, the dispersion has the following symmetries:  $E_{k\sigma} = E_{-k\sigma}$ ,  $E_{k\uparrow} = E_{k\downarrow}$ . The Hamiltonian  $H_t$  commutes with the number operator  $\hat{N} = \sum_{k\sigma} \hat{N}_{k\sigma}$ ,  $[H_t, \hat{N}] = 0$ , admitting a global  $U(1)$  phase-rotation symmetry of the Hamiltonian under the unitary operation  $U(\theta) \in U(1)$ :  $U(\theta) c_{k\sigma}^\dagger U^\dagger(\theta) = e^{i\theta} c_{k\sigma}^\dagger$ . At zero temperature and with a chemical potential  $\mu$ , a description of the low-energy fermionic excitations about the sharp Fermi surface is obtained by linearisation of the dispersion around the two Fermi points,  $k_F$  and  $-k_F$ :  $E_{ak} = -2t \cos k - E_F \approx v_F(k \pm k_F)$ , where the Fermi energy and velocity are  $E_F = -2t \cos k_F$ ,  $v_F = -2t \sin k_F$  and where  $a = R/L$ . The retarded single-particle propagator (Green's function) for states in the window  $W_{\Lambda_0} : [-\Lambda_0/\hbar v_F, \Lambda_0/\hbar v_F]$  around the Fermi points  $(-k_F, k_F)$  is given by

$$G_{a\sigma}^{ret}(z, k) = (z - E_{ak})^{-1}, \quad Im(z) > 0 , \quad (8.3)$$

and the advanced propagator by its complex conjugate:  $G_{a\sigma}^{adv}(\bar{z}, k) = (G_{a\sigma}^{ret}(z, k))^*$ . The retarded Green's function has poles in the complex frequency plane at  $z = \omega_{re} + i\omega_{im}$ , where  $\omega_{im} = 0+$ ,  $\omega_{re,L} = v_F(k - k_F)$  and  $\omega_{re,R} = v_F(k + k_F)$ . For all non-zero momenta, the poles appear in pairs  $(L, R)$  for  $(\uparrow, \downarrow)$  spin-states due to the  $Z_2^P \times Z_2^T$  symmetry mentioned above. For states at the Fermi energy  $(k_F, -k_F)$ , the poles appear at the points  $z_L = 0 = z_R$ . At this point, we recall a topological invariant ( $N_1$ ) associated with number of states at the Fermi energy [544, 453]. This arises from the  $E = 0$  poles of the non-interacting single-particle Green's function (eq.(8.3))

$$N_1 = \int d\omega \partial_\omega Tr(\ln \hat{G}_0) = Tr(\ln \hat{G}_0(0 + i\eta)) - Tr(\ln \hat{G}_0(0 - i\eta)) . \quad (8.4)$$

For the 1D Fermi surface,  $N_1 = 4$  (accounting for spin degeneracy).

We can represent the Hamiltonian of non-interacting electrons as a sum over a set of sub-Hamiltonians, each of which governs a group of four states  $\tilde{k} = (k, -k) \otimes (\uparrow, \downarrow)$  as follows

$$H_t = \sum_{\tilde{k}} H_{\tilde{k}} , \quad H_{\tilde{k}} = E_{\tilde{k}} m_{\tilde{k}}^\dagger I_4 m_{\tilde{k}} , \quad (8.5)$$

where  $m_{\tilde{k}} = [c_{k\uparrow}, c_{k\downarrow}, c_{-k\uparrow}, c_{-k\downarrow}]^t$ ,  $E_{\tilde{k}} = E_{k\sigma}$ ,  $I_4$  is the  $4 \times 4$  unit matrix  $I_4 = I_2^s \times I_2^{L/R}$  and the two  $I_2$  unit matrices are Casimir invariants of the SU(2) groups for the spin (s) and chirality (L/R) sectors respectively. For the poles at  $z = 0$ , the Fermi energy sub-Hamiltonian  $H_{k=0} = 0$  possesses a further particle-hole symmetry ( $C \in Z_2$ ). This unites with the number conservation  $U(1)$  symmetry, leading to an enhanced  $SU_C(2)$  symmetry for states at the Fermi surface. Thus, the complete symmetry group for the two Fermi points is seen to be  $SU_s(2) \times SU_{L/R}(2) \times SU_C(2)$ . The  $S = 1/2$  representation of symmetry group SU(2) is associated with a topological  $CP_1$  space, i.e., the Bloch sphere. The rotations on the Bloch sphere is generated by the set of unitary operations  $U = aI + \boldsymbol{\sigma} \cdot \mathbf{n}$ , where  $\boldsymbol{\sigma}$  is the S=1/2 representative of the SU(2) group and the constraint  $a^2 + |\mathbf{n}|^2 = 1$  represents the compact space  $S_3$ . The homotopy group of the compact space SU(2) (with a constraint  $\mathbf{n}^2 = 1$ ) is given by  $\pi_3(SU(2)) = Z$ . The topological invariants of this space are Chern invariants. The existence of the Fermi surface as a sharp boundary in energy-momentum space at  $T = 0K$  can then be seen as the  $N_1$  topological invariant (eq.(8.4)) arising out of a pole of the single-particle Green's function at zero frequency [545]. Further,  $N_1$  is associated with a non-trivial homotopy group  $\pi_1(S_1) = Z$  characterizing the winding around the sharp Fermi surface.

A pole in the complex frequency plane of the single-particle Green's function  $G_{\sigma a}^{ret}(z, k)$  at a given momentum  $k$  near the left or right Fermi point ( $a = L/R$ ) is also associated with a residue. This residue is picked up by the phase field  $\Phi(k, z)$  of the single-particle Green's function  $G(k, z) = |G(k, z)|e^{i\Phi(k, z)}$  by traversing a non-contractible closed path  $P \equiv S_1$  around the singularity. The number of electrons ( $n_{\sigma,ak}$ )  $n_{\sigma,ak} \in Z$  at a given state  $k\sigma$  belongs to the homotopy group of  $P$ ,  $\pi_1(S(1)) = Z$ , such that

$$n_{\sigma,ak} = \frac{1}{2\pi i} \int dz G_{\sigma a}^{ret}(z, k) \partial_z [G_{\sigma a}^{ret}(z, k)]^{-1}. \quad (8.6)$$

The orientation of the two Fermi points [546, 547] is defined as an integral over the momentum vector at  $T = 0K$  for a sharp Fermi surface within a window  $2\Lambda_0/\hbar v_F$

$$\nu_{\sigma,R} = \frac{1}{2\pi i} \int_{k_F - \frac{\Lambda_0}{\hbar v_F}}^{k_F + \frac{\Lambda_0}{\hbar v_F}} dk \frac{dn_{\sigma,R}(k)}{dk} = -1, \quad \nu_{\sigma,L} = \frac{1}{2\pi i} \int_{-k_F - \frac{\Lambda_0}{\hbar v_F}}^{-k_F + \frac{\Lambda_0}{\hbar v_F}} dk \frac{dn_{\sigma,L}(k)}{dk} = 1. \quad (8.7)$$

Using eq.(8.6) in eq.(8.7), along with compactifying the boundaries of the momentum-space  $[\frac{-\Lambda}{\hbar v_F}, \frac{\Lambda}{\hbar v_F}]$  and frequency-space  $[-\infty + 0i, \infty + 0i]$  windows, the Fermi point singularities lead to first class Chern invariants on the frequency-momentum torus

$$\nu_{a\sigma} = \frac{1}{2\pi i} \oint dk \oint d\omega Tr \left[ \hat{G}_{\sigma a}(\omega, k) \partial_k \hat{G}_{\sigma a}^{-1}(\omega, k) \hat{G}_{\sigma a}(\omega, k) \partial_\omega G_{\sigma a}^{-1}(\omega, k) \right]. \quad (8.8)$$

It can be seen that  $\nu_{\sigma L, R} = \pm 1 \times C$ , where  $C = 2S = 1 \in \pi_3(SU(2))$ . The Atiyah-Singer index [546] is then obtained as  $\nu_{\sigma L} - \nu_{\sigma R} = 2$ , and can be related to the net axial current ( $\Delta J^5$ ) across the gapless Fermi points ( $k_F, -k_F$ ) in the presence of an electric field ( $E$ )

$$\begin{aligned} \Delta J_\sigma^5 &= J_\sigma^5 \left( \frac{\Lambda_0}{\hbar v_F} \right) - J_\sigma^5 \left( -\frac{\Lambda_0}{\hbar v_F} \right) = eE, \quad J_\sigma^5 = J_{\sigma,L} - J_{\sigma,R}, \\ J_{\sigma,a} &= eG_{a\sigma}^{-1}(k, \omega) \partial_k G_{a\sigma}(k, \omega), \quad (a = L/R), \end{aligned} \quad (8.9)$$

where  $e$  is the charge of the electron and  $\Delta J^5$  is related to the anomaly of the axial charge  $Q_5$  [548]

$$\Delta J^5 = \frac{dQ_5}{dt} = e \frac{d}{dt} (\int dx (\psi_L^\dagger \psi_L - \psi_R^\dagger \psi_R)) = \nu_{\sigma L} - \nu_{\sigma R}. \quad (8.10)$$

For fermions on a 1D lattice, the axial current is generated by momentum imparted to the center of mass (c.o.m) spin ( $s$ ) and charge ( $c$ ) degrees of freedom (d.o.f) with positions  $X_s = X_\uparrow - X_\downarrow$ ,  $X_c = X_\uparrow + X_\downarrow$  respectively by a twist operation [549, 379, 522]. Note that  $X_\sigma = 1/(2N) \sum_{j=1}^N j \hat{n}_{j\sigma}$  (here  $\hat{n}_{j\sigma} = \psi_{j\sigma}^\dagger \psi_{j\sigma}$ , and we have kept a factor of 2 for the spin degeneracy). The twist operator is defined in terms of the following unitary operations on the c.o.m

$$\hat{O}_s = U_\uparrow U_\downarrow^\dagger, \quad \hat{O}_c = U_\uparrow U_\downarrow, \quad (8.11)$$

where  $U_\sigma = \exp[i2\pi\phi X_\sigma]$  leads to twisted boundary conditions (TBC) in real space. Thus, the spin twist operator  $\hat{O}_s$  changes boundary conditions for  $\uparrow$  and  $\downarrow$  fermions with opposite phases  $\hat{O}_s \rightarrow \psi_\uparrow(j=N) = e^{i\pi\phi} \psi_\uparrow(j=0)$ ,  $\psi_\downarrow(j=N) = e^{-i\pi\phi} \psi_\downarrow(j=0)$ , causing a shift in center of mass momentum ( $P_{cm}$ ) due to spin excitations of the Fermi sea

$$\hat{O}_s \hat{T} \hat{O}_s^\dagger = T e^{i\phi(\pi/N)(NS - S_{tot}^z)}, \quad (8.12)$$

where  $S_{tot}^z = \sum_j S_j^z$  is the  $z$ -component of the total spin angular momentum and  $\hat{T} = \exp[iP_{cm}]$  is the global translation operator. On the other hand, the charge twist operator  $\hat{O}_c$  causes an equal amount of twist for  $\uparrow$  and  $\downarrow$  fermions, leading to a gain in momentum for the center of mass of the Fermi sea

$$\hat{O}_c \hat{T} \hat{O}_c^\dagger = \hat{T} e^{i\phi(\pi/N)\hat{N}_e}, \quad (8.13)$$

where the total no. of electrons is given by  $\hat{N}_e = \sum_{j\sigma} \hat{n}_{j\sigma}$ . The non-commutativity between  $T$  and the twist operators  $O_{c/s}$  defines Wilson loop operators on a two-tori [523, 86, 522]  $(\phi, X_{c,s}) \mapsto \mathcal{T}^2 \equiv S_1 \times S_1$

$$\hat{Z}_{c/s} = \hat{O}_{c/s} \hat{T} \hat{O}_{c/s}^\dagger \hat{T}^\dagger \quad (8.14)$$

where  $\log \hat{Z}_c = i\hat{N}_e/2N$ ,  $\log \hat{Z}_s = i\hat{S}_{tot}^z/N - S$ . The action of the Wilson loop operators  $\hat{Z}_{c/s}$  on the c.o.m. state  $|P_{cm} = 0, S_{tot}^z\rangle$  gives

$$\hat{Z}_{c/s} |P_{cm} = 0, S_{tot}^z\rangle = e^{i2\pi\nu_{c/s}} |P_{cm} = 0, S_{tot}^z\rangle, \quad (8.15)$$

where  $\nu_c = N_e/2N$  and  $\nu_s = S_{tot}^z/N$  are the net flux in the  $c$  and  $s$  sectors respectively emanating from  $\mathcal{T}^2$ . By taking a state  $|P_{cm} = 0, S_{tot}^z\rangle$  around in a local patch (P) given by  $P \equiv \{\phi \in (0, \alpha_1), \hat{X}_{c/s} \in (0, \alpha_2)\}$ , we obtain the twisted state

$$|\Psi(\alpha_1, \alpha_2)\rangle = \hat{T}_{\alpha_2} \hat{O}_{c/s\alpha_1} |P_{cm} = 0, S_{tot}^z\rangle, \quad (8.16)$$

where  $\hat{T}_{\alpha_2} \hat{X}_{c/s} \hat{T}_{\alpha_2}^\dagger = \hat{X}_{c/s} + \alpha_2$  and  $\hat{O}_{\alpha_1} \hat{P}_{cm} \hat{O}_{\alpha_1}^\dagger = \hat{P}_{cm} + \alpha_1$ . In the space  $\boldsymbol{\alpha} = (\alpha_1, \alpha_2)$ , we define the persistent current vector  $\mathbf{J}_{c/s\alpha} = \langle \Psi(\boldsymbol{\alpha}) | \nabla | \Psi(\boldsymbol{\alpha}) \rangle$ , such that  $\mathbf{J}_{c/s\alpha} = (J_{1c/s\alpha}, J_{2c/s\alpha})$  represents the zero mode of the charge/spin current generated on  $\mathcal{T}^2$  due to TBC. The first Chern class [550, 551] on the torus can now be computed in terms of the curl of the nonlocal current vector in the  $\boldsymbol{\alpha}$  space

$$\gamma = \frac{1}{2i} \int_0^{2\pi} \int_0^{2\pi} d^2\boldsymbol{\alpha} \hat{n} \cdot \nabla \times \mathbf{J}_{c/s\alpha} = 2\pi \frac{p}{q}. \quad (8.17)$$

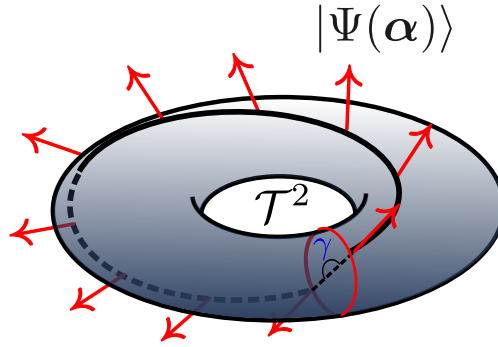


Figure 8.1.1: The red vectors on the torus  $\mathcal{T}^2$  represent the eigenstates  $|\Psi(\alpha)\rangle$  that form a M—"obius strip for the centre of mass (c.o.m.) Hilbert space, where the angle between initial and final vector is  $\gamma = \pi$ .

As shown in Fig.8.1.1, the ray field  $|\Psi(\alpha)\rangle$  (represented by the red vector) gathers a phase as it traverses the torus  $\mathcal{T}^2$  along a Möbius strip. In the above relation,  $p/q = (S - M)$  is the Luttinger's sum for spin excitations of the Fermi sea [86, 549] (where  $S$  and  $M$  are the total spin quantum number and magnetisation of the Fermi sea respectively), while  $p/q = \nu$  is the Luttinger's sum for charge excitations [544, 435, 552, 40]. In the presence of both time-reversal and particle-hole symmetries,  $\nu = 1/2$  (i.e.,  $M = 0, N_e = N/2$ ) such that  $\gamma = \pi$ .

We can now compute experimentally measurable spin/charge Drude conductivities  $D_{c/s}$  from spectral flow arguments [379, 553]. For this, we note that the eigenvalue ( $E_{c/s}(\phi)$ ) of the twisted tight-binding Hamiltonian is given by

$$\hat{O}_{c/s} \hat{H}_t \hat{O}_{c/s}^\dagger |\Psi\rangle = E_{c/s}(\phi) |\Psi\rangle. \quad (8.18)$$

The spin/charge Drude conductivity  $D_{c/s}$  [379, 553] can now be computed from the energy curvature  $d^2E_{c/s}/d\alpha_{1c/s}^2 = \hat{x} \cdot \Delta \mathbf{J}(\alpha_1, 2\pi)/\Delta\alpha_{1c/s}$  (i.e., the change in persistent current in the ring  $\hat{x} \cdot \mathbf{J}(\alpha_1, 2\pi) = e\Delta P_{cm}^{c/s}$  under the twisting of boundary conditions)

$$D_{c/s} = \lim_{\omega \rightarrow 0} \omega \sigma''_{s/c}(\omega) = \frac{d^2E_{c/s}}{d\alpha_{1c/s}^2} = e \frac{\Delta P_{cm}^{c/s}}{\Delta\alpha_{1c/s}} = e \frac{\gamma}{2\pi}, \quad (8.19)$$

where  $\sigma''_{s/c}(\omega)$  is the imaginary part of the longitudinal conductivity,  $\omega$  the probing frequency, and the persistent current momentum generated in the ring is given by

$$J_{c/s} \equiv e\Delta P_{cm}^{c/s} = e\hat{O}_{c/s} P_{cm} \hat{O}_{c/s}^\dagger - eP_{cm}. \quad (8.20)$$

This relation shows that the Drude conductivity is related to the first Chern class  $\gamma$  (eq.(8.17)). Further, it can be shown that a net persistent current  $\Delta J_{1c/s} = J_{1c/s}(\Phi_0, 0) - J_1(0, 0)$  is accumulated by taking the c.o.m on a one-flux quantum circuit of  $\phi = \Phi_{c/s}/\Phi_0 \in [0, 1]$  (where  $\Phi_{c/s}$  is the AB flux), and is connected to the Atiyah-Singer index computed from the Chern numbers (eq.(8.8)) for the states  $(k_{Fc/s}, -k_{Fc/s})$

$$\frac{1}{k_{Fc/s}} \Delta J_{1c/s} = (\nu_L - \nu_R) = 2 \equiv \Delta J^5. \quad (8.21)$$

In the above,  $k_{Fc/s}$  represents the Fermi momentum of the charge ( $k \uparrow, k \downarrow$ ) and spin ( $k \uparrow, -k \downarrow$ ) excitations of the Fermi sea.

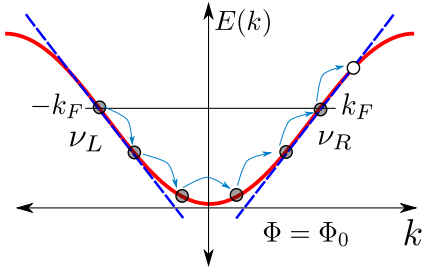


Figure 8.1.2: Chern numbers  $\nu_L$  and  $\nu_R$  around the two Fermi energy points  $\pm k_F$  of the 1D tight-binding electronic chain take part in the spectral flow of the c.o.m spectrum upon changing boundary conditions by a full flux quantum  $\Phi = \Phi_0$ .

The same thought experiment can also be carried out with the persistent current  $J_2$ , i.e., by now taking the c.o.m on a complete circuit of  $X_{c/s} \in [0, 2\pi]$ . The above relation depicts that the net current accumulated by the c.o.m. is associated with an anomaly in the bulk of Fermi sea: the injection of one electron from the left Fermi point ( $\nu_L = -1 \equiv -C$ ), together with the ejection of one electron from the right Fermi point ( $\nu_R = 1 \equiv C$ ), leads to a net transfer of  $2C = 2$  states upon tuning through a complete circuit. At the same time, as shown in Fig.(8.1.2), the relation can also be interpreted as the action of independent monopole sources at the L/R Fermi points (the Chern nos.  $C$ ) in leading to an anomalous current  $\Delta J^5$ . This is the well-known phenomenon of anomalous axial-symmetry breaking [554, 555], seen either from the perspective of the c.o.m or that of the Fermi surface. When taken together, these two anomalies cancel and the apparent anomalous breaking of the symmetry is restored. Finally, the Atiyah-Singer index is directly related to the central charge ( $c$ ) of the conformal field theory for a gapless 1D electronic system [556, 557, 152],  $c = \frac{1}{2}(\nu_L - \nu_R)$  .

While the results presented in this section are for the case of a two-point Fermi surface, the formalism adopted by us is equally applicable to Fermi surfaces of higher dimensional systems of noninteracting electrons. Further, the notion of adiabatic continuity guarantees the existence of a Fermi surface in Landau's formulation of the Fermi liquid even in the presence of electronic correlations. It is, thus, possible to explore various topological properties of the Fermi liquid in an analogous manner. In what follows, many of the ideas introduced in this section will be shown to be useful in understanding the interplay of interactions, symmetry and topology in shaping the many-body instabilities of the Fermi surface. Specifically, we will see in Sec.8.2 that, in the presence of a Fermi surface instability arising from the presence of inter-particle interactions, the first Chern class  $\gamma = \pi$  imposes a topological constraint on the condensation of four-fermion vertices. This involves the formation of composite pseudospin  $S = 1/2 = \gamma/2\pi$  d.o.fs formed by pairing  $1/S = 2$  fermions. We will follow this up in Sec.8.3 by showing that the pseudospin backscattering vertices connecting the Fermi points  $\pm k_F$  lead to a change in the c.o.m Hilbert space by satisfying the constructive interference condition  $2\gamma = 2\pi$ .

## 8.2 Topological constraints on condensation

We will now look into the topological features that arise out of various instabilities of the Fermi surface (e.g., either the spin backscattering or the Umklapp scattering across the Fermi surface [558]) upon adding the Hubbard term (with on-site repulsion strength  $U$ ) to the tight-binding Hamiltonian

$$H = -2t \sum_{k,\sigma} \cos(k) c_{k\sigma}^\dagger c_{k\sigma} + U \sum_i n_{i\uparrow} n_{i\downarrow}, \quad (8.22)$$

where the local electronic density is  $n_{i\sigma} = \psi_{i\sigma}^\dagger \psi_{i\sigma}$ . The Hubbard term has a spin backscattering vertex  $c_{k_1+q\uparrow}^\dagger c_{-k_1-q\downarrow}^\dagger c_{-k_1\uparrow} c_{k_1\downarrow}$ , where  $c_{k\sigma}^\dagger = 1/\sqrt{2N} \sum_j e^{ikj} \psi_{j\sigma}^\dagger$ . This scattering process operates in the low-energy subspace with zero momentum and opposite spin pairs respecting P and TR symmetries, as seen from the application of the following constraint on the many-body fermionic Fock space [413]

$$C_1 : \hat{n}_{k\sigma} = \hat{n}_{-k-\sigma}. \quad (8.23)$$

This constraint can be classified in terms of matching of helicity ( $\eta = \text{sgn}(k)\text{sgn}(\sigma) = \pm 1$ ) across the Fermi surface. Starting with the  $SU(2)_s \otimes SU(2)_{L/R} \otimes U(1)_C$  symmetric many-body fermionic Fock space of the metal (see Sec.8.1), the matching of helicities leads to a locking of spin  $SU(2)_s$  and chirality  $SU(2)_{L/R}$  projected Hilbert spaces (PHS) to form a new helicity  $SU(2)_s \otimes SU(2)_{L/R} \rightarrow SU(2)_{\eta=\pm 1}$  PHS for the emergent degrees of freedom whose condensation characterizes the instability. Time reversal symmetry is respected via the formation of paired-fermion states ( $N_{co} = 2$ ) that are either occupied or unoccupied. The constraint  $C_1$  ensures that each paired-fermion state is equivalent to a two-level system (i.e., isomorphic to  $CP^1$ ). It is important to note the topological origin of  $C_1$ : the Chern class  $\gamma = \pi$  (eq.(8.17)) defining the c.o.m PHS topology of the metal is connected to constraint  $C_1$  via the relation

$$|\hat{n}_{k\sigma} + \hat{n}_{-k-\sigma} - 1| = 2\gamma/2\pi = N_{co}/2. \quad (8.24)$$

As a consequence of the constraint  $C_1$ ,  $\gamma = 2\pi S$  leads to formation of  $SU(2)$   $S = 1/2$  Hilbert spaces from the original many-body fermionic Fock space. Due to TRS, every  $\uparrow$  state has a partner  $\downarrow$ . Hence, the  $4N$  particle antisymmetrized Hilbert space of a 1D system of  $2N$  lattice sites is defined as  $\mathcal{F}_{4N} = A\mathcal{H}^{\otimes 4N}$ , where  $A$  is the antisymmetrizer and  $\mathcal{H}$  is the single-particle projective Hilbert space (PHS) in which the many-body states are represented in the basis  $B_{\mathcal{F}_N} := \{\prod_{l=1}^{N_e} c_{k_l}^\dagger |0\rangle, k_l \in [-\pi, \pi]\}$  and  $N_e$  is the number of electrons. A subspace  $\mathcal{F}_{8N_{\Lambda_0}} = A\mathcal{H}^{\otimes 4N_{\Lambda_0}} \subseteq \mathcal{F}_{4N}$  is constituted of  $8N_{\Lambda_0}$  states in the window  $W_{\Lambda_0} = [-\Lambda_0, \Lambda_0]$  around the two Fermi points( $k_F, -k_F$ ). The momentum wave-vectors in the window are given by  $k_\Lambda = k_{F\hat{s}} + \Lambda\hat{s}$ , where  $\Lambda$  is the normal distance from the two point Fermi surface and  $\hat{s}$  denotes the orientation ( $\hat{s} = 1$  and  $-1$  for right and left Fermi points respectively). The states within  $\mathcal{F}_{8N_{\Lambda_0}}$  transform via imposition of the constraint  $C_1$ : as shown in Fig.(8.2.1), the constraint  $C_1$  maps a subset of four-fermion scattering vertices involving zero-momentum pairs onto  $S = 1/2$  pseudospin vertices.

We now present a precise mathematical formulation of how the symmetries and topology of the Fermi surface guides the constraint  $C_1$  in shaping the PHS of the emergent condensate. In order to carry out the transformation of the Hilbert space, we first obtain a compact notation for the one-electron states:  $|\kappa\rangle \equiv |k_{\Lambda,\hat{s}}, \sigma\rangle$ . In this way, we define partial trace operators  $Tr_{(j,l)}(\dots)$  that

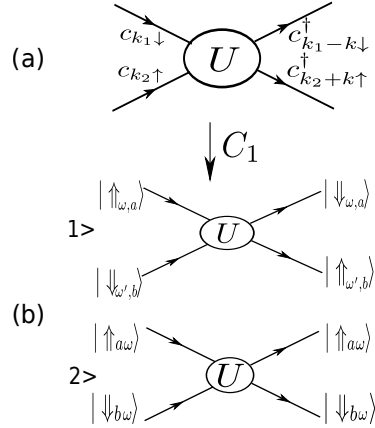


Figure 8.2.1: (a) The four-fermionic vertex (designated by the  $U$  within the oval) is composed of  $c, c^\dagger \in \mathcal{F}_{4N}$ . The constraint  $C_1$  condenses pairs of fermions forming  $S = 1/2$  pseudo-spin  $\mathbf{A}_{\omega_0, \eta} \in SU(2)$ . (b) The pseudo-spins scatter via spin-flip ( $1_c$ ) and non-spin-flip vertices ( $2_c$ ).

extract four-fermion vertices involving  $|\kappa\rangle$  from the Hamiltonian  $H$

$$Tr_\kappa(c_\kappa^\dagger H)c_\kappa + h.c. = \frac{U}{V} \sum_{\kappa_1, \kappa_2, \kappa_3} c_\kappa^\dagger c_{\kappa_1}^\dagger c_{\kappa_2} c_{\kappa_3} . \quad (8.25)$$

The single-electron states  $|\kappa\rangle$  can be grouped into two helicity ( $\eta$ ) classes,  $\eta = 1$  for  $\kappa(\eta = 1) = (\Lambda, 1, 1)$  or  $(\Lambda, -1, -1)$  and  $\eta = -1$  for  $\kappa(\eta = -1) = (\Lambda, 1, -1)$  or  $(\Lambda, -1, 1)$ . The three normal distances  $\Lambda'_i$ s and orientations  $\hat{s}'_i$ s correspond to the momentum wave-vectors  $k_{\Lambda_1 \hat{s}_1}$ ,  $k_{\Lambda_2 \hat{s}_2}$  and  $k_{\Lambda_3 \hat{s}_3}$ , such that  $k_{\Lambda \hat{s}} + k_{\Lambda_1 \hat{s}_1} = 2n\pi + k_{\Lambda_2 \hat{s}_2} + k_{\Lambda_3 \hat{s}_3}$ . Note that if  $k_F = \pm\pi/2$ , the Umklapp process is allowed, implying  $n = 0, 1$ . On the other hand, for  $k_F \neq \pm\pi/2$ , we have only  $n = 0$ . The three spin orientations are given as  $(\sigma_1, \sigma_2, \sigma_3) = (-\sigma, -\sigma, \sigma)$ .

A subset of the four-fermion vertices containing the zero pair-momentum  $p = 0$  TRS-invariant pair  $(\uparrow, \downarrow)$  is extracted as follows

$$Tr_\kappa(c_\kappa^\dagger Tr_{\kappa'}(c_{\kappa'}^\dagger H))c_{\kappa'}c_\kappa + h.c. = \frac{U}{V} \sum_{\kappa_1} c_{\kappa_1}^\dagger c_{\kappa_1}^\dagger c_{\kappa'} c_\kappa + h.c. , \quad (8.26)$$

where  $\kappa = (\Lambda, \hat{s}, \sigma)$ ,  $\kappa' = (\Lambda, -\hat{s}, -\sigma)$ ,  $\kappa_1 = (\Lambda', \hat{s}', \sigma')$  and,  $\kappa'_1 = (\Lambda', -\hat{s}', -\sigma')$ . We can easily see that the sum of momentum wave-vectors belonging to  $\kappa$  and  $\kappa'$  is  $\mathbf{p} = 0$ . Summing over all the  $\kappa$  electronic states, we obtain an effective model containing off-diagonal scattering terms involving  $\mathbf{p} = 0$  net-momentum electronic pairs

$$\sum_\kappa Tr_\kappa(c_\kappa^\dagger Tr_{\kappa'}(c_{\kappa'}^\dagger H))c_{\kappa'}c_\kappa + h.c. = \frac{U}{V} \sum_{\kappa, \kappa_1} c_\kappa^\dagger c_{\kappa'}^\dagger c_{\kappa'_1} c_{\kappa_1} . \quad (8.27)$$

The wavevectors  $\kappa, \kappa', \kappa_1, \kappa'_1$  are defined as earlier. We now define Nambu spinors [559] in the  $CP^1$  representation  $d_{\Lambda, \eta}^\dagger = (c_\kappa^\dagger \ c_{\kappa'})$  for the  $p = 0$  TRS pairs, where  $\eta = sgn(\hat{s})sgn(\sigma)$  is the helicity. From the spinors, we define Anderson pseudospins [413]  $\mathbf{A}_{\Lambda, \eta}$ , with magnitude  $|\mathbf{A}_{\Lambda, \eta}|^2 = S(S+1)(\hat{n}_\kappa + \hat{n}_{\kappa'} - 1)^2$ . Here,  $S = 1/2$  as  $A_{\Lambda, \eta}^{\pm 2} = 0$ . We also note that the Hartree processeses  $n_\kappa n_{\kappa_1}$  within the  $p = 0$  momentum subspace can be written purely in terms of  $A_{\Lambda, \eta}^z A_{\Lambda', \eta'}^z$ .

The instability in the electronic Hilbert space due to the backscattering processes results in the condensation of electronic pairs, as seen from eq.(8.23). The resulting Anderson pseudo-spins [413] ( $\mathbf{A}_{\Lambda,\eta} \in SU(2)$ ) follow the  $SU(2)$  algebra

$$[A_{\Lambda,\eta}^i, A_{\Lambda',\eta'}^j] = \epsilon_{ijk}\delta_{\Lambda,\Lambda'}\delta_{\eta,\eta'}A_{\Lambda,\eta}^k , \quad (8.28)$$

and the Casimir  $|\mathbf{A}_{\Lambda,\eta}|^2 = S(S+1)I$  (where  $I = |\uparrow\rangle\langle\uparrow| + |\downarrow\rangle\langle\downarrow|$ ).  $S = 1/2$  leads to a two-level system ( $|1_{k\uparrow}, 1_{-k\downarrow}\rangle, |0_{k\uparrow}, 0_{-k\downarrow}\rangle$ ). This allows identification of the first Chern class  $\gamma$  (eq(8.17)) on the c.o.m torus  $\mathcal{T}^2$  with a monopole of charge  $2S = \gamma/\pi \Rightarrow \gamma = \pi$ .

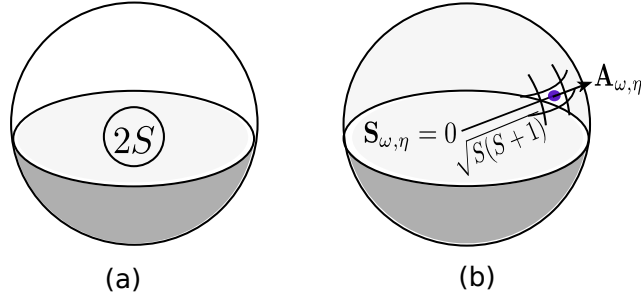


Figure 8.2.2: (a) The unitary operations  $\hat{L}$  ( $\hat{L}\mathbf{A}_\omega\hat{L}^\dagger = \mathbf{A}_\omega$ ) span the space  $S^3$  that wraps around a monopole of charge  $2S$ . (b) A representation of the geometry of the Hilbert space of the angular momentum vectors  $\mathbf{A}_\omega, \mathbf{S}_\omega$ .

Within the PHS enforced via eq.(8.23) arises an emergent symmetry  $SU(2)^{\otimes 2N_{\Lambda_0}}$  of the resulting projected Hamiltonian eq.(8.27). Here,  $\Lambda_0$  is the width around both the Fermi points within which the putative condensation takes place, and  $N(\Lambda_0)$  is the number of electronic states within the window. We will demonstrate this via the unitary RG prescription in a later section. Further, this space of  $SU(2)$  transformations is spanned by

$$\hat{L} = \prod_{j=1}^{N_\Lambda} \exp[i\theta_j \mathbf{S}_{\Lambda_j} \cdot \mathbf{n}_j] , \quad \mathbf{S}_{\Lambda_j,\eta} = S\tilde{c}_{\Lambda_j,\eta}^\dagger \boldsymbol{\sigma} \tilde{c}_{\Lambda_j,\eta} , \quad (8.29)$$

where  $\tilde{c}_{\Lambda_j,\eta}^\dagger = (c_{\Lambda_j,\eta}^\dagger, c_{\Lambda_j,-\eta}^\dagger)$ ,  $S = 1/2$  and with a parameter space  $S^3 \rightarrow (\theta_j, \mathbf{n}_j)$ . As shown by Fig.(8.2.2a), the  $S^3$  spheres explore the topology of the enclosed null vectors at the origin of the angular momentum sphere:  $|\mathbf{S}_{\Lambda,\eta}| = S(S+1)(\hat{n}_{k_{\Lambda},\hat{s}\uparrow} - \hat{n}_{k_{\Lambda},-\hat{s}\downarrow})^2 = 0$ . The non-trivial topology of the symmetry group  $SU(2)^{\otimes 2N_\Lambda}$  is seen, therefore, from the homotopy group  $\pi_3(SU(2)) = \mathbb{Z}$ , and is a reflection of the existence of angular momentum spheres of radius ( $|\mathbf{A}_{\Lambda,\eta}| = \sqrt{S(S+1)}$ ) in the Fock space  $\mathcal{F}_{4N}$ . As shown in Fig.(8.2.2b), the geometry of the angular momentum vector  $\mathbf{A}_{\Lambda,\eta}$  traces a sphere  $S^2$  centred around a monopole of charge  $2S = \gamma/\pi$  coinciding with the null vector  $\mathbf{S}_\omega$ . This symmetry in the PHS reflects in the invariance of the basis  $B \equiv \{\otimes |A_\Lambda^z\rangle\}$  under unitary operation:  $\hat{L}B = B$ .

For  $\mathbf{n}_j = (0, 0, n_z)$ ,  $\theta_j = \delta k_F j$ , the  $U(1)^{\otimes 2N_{\Lambda_0}}$  group generated by the c.o.m. translation operators is

$$U_z = \exp(i \sum_j k_j S_j^z) : \quad \hat{X}_{cm}^{\Lambda_0} \rightarrow \hat{X}_{cm}^{\Lambda_0} + 2\pi S, \quad \hat{X}_{cm}^\Lambda = (1/4N_\Lambda) \sum_{js\sigma} j \hat{n}_{\Lambda_j, \hat{s}, \sigma} , \quad (8.30)$$

where  $U_z \in S^1$  and  $k_j = k_F + \Lambda_j$ , and the number of states within window  $W_{\Lambda_0}$  is given by  $N_\Lambda$ . Further,  $U_z|\Psi\rangle = |\Psi\rangle$  implies the presence of parity, and leads to a vanishing total current for composite objects:  $2eP_{cm}^\Lambda = 0$ . Therefore, a vanishing c.o.m. kinetic energy,  $P_{cm}^{\Lambda 2}/2I = 0$ , ensures the stability of the composite objects. A shift of the c.o.m momentum,  $P_{cm}^\Lambda \neq 0$ , can be generated by applying twisted boundary conditions for the states in the window  $W_{\Lambda_0}$  via the twist operator  $\hat{O}_c$  (eq.(8.11)). The twist operator imparts a net momentum  $p$  to every electronic pair, resulting in the pseudospins  $\mathbf{A}_{p,\Lambda,\eta} = \hat{O}_c \mathbf{A}_{\Lambda,\eta} \hat{O}_c^\dagger$  being constituted of electronic states  $(\Lambda + p, +1, \sigma)$  and  $(\Lambda, -1, -\sigma)$ . This momentum gain creates a collective Cooper-pair persistent current  $P_{cm} = 2N_{\Lambda p}$  with a modified constraint  $C_1 : n_{k,\sigma} = n_{-k+p,-\sigma}$ .

The dynamics of the modified PHS,  $\mathcal{H}_{tot} = (CP^1)^{\otimes 2N_{\Lambda_0}}$ , is governed by the projected Hamiltonian

$$H^{p=0} = v_F \sum_\omega \Lambda A_{\Lambda,\eta}^z + \frac{U}{2N_\Lambda} \mathbf{A}_{+1} \cdot \mathbf{A}_{-1} , \quad (8.31)$$

where  $\mathbf{A}_\eta$  is the total pseudospin vector given by  $\mathbf{A}_\eta = \sum_\Lambda \mathbf{A}_{\Lambda,\eta}$ . The zero mode of the Hamiltonian is given by

$$H_{\Lambda=0}^{p=0} = \frac{U}{2N_\Lambda} \mathbf{A}_{+1} \cdot \mathbf{A}_{-1} , \quad (8.32)$$

and possesses eigenstates and eigenvalues given by [560]

$$|A = p; A_{+1} = A_{-1} = n + 1/2\rangle , \quad E_{n,m,p} = \frac{U}{2N_{\Lambda_0}} [p(p+1) - (2n+1)(n+\frac{3}{2})] . \quad (8.33)$$

The gap  $\Delta E$  around the Fermi energy  $E_F = 0$  between the highest negative energy state ( $E_0 = |U|/(8N_\Lambda)$ , a pseudo-spin triplet ( $|1; 1/2, 1/2\rangle$ )) and the lowest positive energy state ( $E_1 = -3|U|/(8N_\Lambda)$ , a pseudo-spin singlet ( $|0; 1/2, 1/2\rangle$ )) is given by  $\Delta E = E_1 - E_0 = U/2N_\Lambda$ . This shows that  $\Delta E$  gaps the spin excitations around  $E_F$ . We will show subsequently that  $\Delta E$  survives after taking account of divergent fluctuations in a renormalization group (RG) formalism. Unlike back-scattering processes, forward scattering physics given by  $\mathbf{A}_{+1}^2 + \mathbf{A}_{-1}^2$  does not cause the coupling of helicities, and hence does not lead to instabilities of the Fermi surface. The RG irrelevance of forward scattering events in gap opening of the 1D Fermi surface has been confirmed by RG [561, 102] and bosonization [558, 4] methods.

A similar analysis of the Umklapp (charge) scattering instability leads to the constraint  $C_2 : n_\omega = n_{\bar{\omega}}$ , where  $\omega = (\Lambda, \hat{s}, \sigma)$  and  $\bar{\omega} = (-\Lambda, \hat{s}, -\sigma)$ , and which can be classified in terms of the chirality ( $\hat{s} = +1/-1$ ). The Fermi momentum satisfies the condition  $2k_F = \pi$ , such that the particle-hole symmetry enforces the first Chern class for the torus  $\mathcal{T}^2$  in the c.o.m Hilbert space,  $\gamma = \pi$ . In turn, this leads to pairs of fermions from the same side of the Fermi sea forming a  $SU(2)$  PHS of spins with  $S = 1/2 = \gamma/2\pi$ . This PHS is again associated with a  $S = 1/2$  representation of the  $SU(2)$  group for pseudospin operators  $\mathbf{A}_{\Lambda,\hat{s}} = S(c_\omega^\dagger c_{\bar{\omega}}) \boldsymbol{\sigma} (c_\omega^\dagger c_{\bar{\omega}})^\dagger$ , and where  $\hat{s} = +1/-1$  represents the two chiralities  $L/R$ .

The projection mechanism leads to the condensation of spinors representing pairs of fermions with total momentum  $2ak_F$ . The Umklapp instability Hamiltonian is governing the dynamics in the PHS  $SU(2)^{\otimes 2N_{\Lambda_0}}$  is given by

$$H_{\Lambda_0}^{p=\pm 2k_F} = \frac{U}{2N_\Lambda} \mathbf{A}_L \cdot \mathbf{A}_R , \quad (8.34)$$

where  $\mathbf{A}_{\hat{s}} = \sum_{\Lambda} \mathbf{A}_{\Lambda,\hat{s}}$  is the total pseudospin vector that acts as the generator of global rotations in the PHS. The Hamiltonian  $H^{\pm 2k_F}$  has eigenvalues and eigen vectors given by

$$|A_{\Lambda} = p; A_L = A_R = n + 1/2\rangle, E_{n,m,p} = \frac{U}{2N_{\Lambda}}[p(p+1) - (2n+1)(n+\frac{3}{2})]. \quad (8.35)$$

The gap around the Fermi energy for charge excitations exists between pseudospin singlet and triplet states:  $\Delta E = U/2N_{\Lambda}$ . The robust nature of this charge gap will be confirmed via RG in a later section. For the sake of generality, we will study the anisotropic version of this Hamiltonian

$$H_{\Lambda_0}^{p=\pm 2k_F} = \frac{J_{||}}{2N_{\Lambda}} A_{L\Lambda}^z A_{R\Lambda}^z + \frac{J_{\perp}}{4N_{\Lambda}} [A_{L\Lambda}^+ A_{R\Lambda}^- + h.c.] . \quad (8.36)$$

In the next section, we will see the formation of topological objects (with  $\gamma = \pi$ ) at the Fermi surface arising from the constraints  $C_1$  or  $C_2$ . Subsequently, we will study their effect on the c.o.m Hilbert space due to the ensuing instability.

## 8.3 Structure of the Fermi surface pseudospin Hilbert space

In this section, we will see how the instability associated with constraints  $C_1$  and  $C_2$  form  $SU(2)$  PHS at the Fermi surface (FS), supporting topological objects like Dirac strings and magnetic monopoles. Furthermore, the first Chern class  $\gamma = \pi$  on the c.o.m Hilbert space will be seen to characterize the topological objects at FS. The states at the FS are given by

$$\begin{aligned} F \equiv & \{| \uparrow_{F;s,c}^a \rangle = |1_{k_F\uparrow} 1_{\mp k_F\downarrow}\rangle, | \downarrow_{F;s,c}^a \rangle = |0_{k_F\uparrow} 0_{\mp k_F\downarrow}\rangle\} \otimes \\ & \{| \uparrow_{F;s,c}^b \rangle = |1_{k_F\downarrow} 1_{\mp k_F\uparrow}\rangle, | \downarrow_{F;s,c}^b \rangle = |0_{k_F\downarrow} 0_{\mp k_F\uparrow}\rangle\} \end{aligned} \quad (8.37)$$

belonging to PHS  $SU(2)_a \otimes SU(2)_b$ . Here, the indices  $(a/b) \rightarrow s := (+/-)$  and the index  $c := (R/L)$  correspond to the pseudospin PHS of spin and charge instability sectors respectively. The sub-Hamiltonian ( $H_F$ ) operating on  $F$  is given by

$$H_F (\delta k_F = 0) = \frac{U}{2N_{\Lambda}} \mathbf{A}_{Fa} \cdot \mathbf{A}_{Fb} , \quad (8.38)$$

and possesses a resonant backscattering at the FS in terms of the action of the pseudospin flip piece  $1/2(A_{Fa}^+ A_{Fb}^- + h.c.)$  on the subspace  $F_1 \equiv \{| \uparrow_{Fa} \downarrow_{Fb} \rangle, | \downarrow_{Fa} \uparrow_{Fb} \rangle\}$  containing 2 electrons ( $\hat{N}_F = \sum_{a=\pm,\sigma} \hat{n}_{ak_F,\sigma} = 2$ ). The backscattering leads to helicity ( $\eta = +/-$ ) symmetry breaking:  $SU(2)_a \times SU(2)_b \rightarrow SU(2)_{a+b}$ . The subspace  $\hat{N}_F = 2 \equiv A_{Fa}^z + A_{Fb}^z = A_F^z = 0$  allows the identification  $\hat{N}_F = 2C_{F_1}$ , where  $C_{F_1} = 2S$  is the Chern number of the effective monopole charge associated with the homotopy group  $\pi_3(SU(2)_{F_1}) = Z$  and  $SU(2)_{F_1} \subset SU_a(2) \times SU_b(2)$ . The PHS  $SU(2)_{F_1}$  is composed of the states in  $F_1$ , and is associated with a topological  $CP^1$  space. As seen from the c.o.m. PHS, a doubled twist operator  $\hat{O}_{c/s}^2$  causes the total momentum ( $P_{cm}$ , defined on the compact space  $S^1 : P_{cm} \in S^1 : (0, 2\pi]$ ) to shift by a reciprocal lattice vector  $P_{cm} \rightarrow P_{cm} + 2\gamma = P_{cm} + 2\pi$  due to the transfer of 2 electrons [380, 522]. The relation  $2\gamma = 2\pi$  is equivalent to the Lieb-Schultz-Mattis criterion [86], and allows either a gapless unique

ground state or a doubly-degenerate gapped state of matter. The gapped state of matter is associated with constructive interference between paths on a non-simply connected  $P_{cm}$  Hilbert space manifold, and will be discussed further in Sec.8.6. This leads us to conclude that, in basis  $F_1$ , the pseudospin flip term (corresponding to a vertex operator in the equivalent sine-Gordon theory) is equivalent to the double-twist operator  $\hat{O}_{c/s}^2$  [380]

$$(A_{Fa}^+ A_{Fb}^- + h.c.) \equiv \hat{O}_{c/s}^2 + h.c. . \quad (8.39)$$

Tunnelling between the two degenerate levels of the subspace  $F_1$  can be studied via the effective Hamiltonian

$$H_{F_1} = -U/2N_\Lambda D_z^2 + U/2N_\Lambda D_x , \quad (8.40)$$

where  $\mathbf{D} = (\gamma/2\pi) A_F^\dagger \boldsymbol{\sigma} A_F$ , and the spinor  $A_F^\dagger = (A_{Fa}^+ A_{Fb}^+)$  etc.  $H_{F_1}$  is invariant under a Unitary transformation  $U_1 = \exp[i2\pi D_z] \in Z_2$  &  $U_2 = \exp[i\theta D_x] \in U(1)$ . In the parameter space  $S^2$  of radius  $R = |U/2N_\Lambda|$ , a closed path is traced such that the eigenstate  $|\psi(\mathbf{R})\rangle \in CP^1$  traces a great circle on the Bloch sphere described by Fubini-Study metric [411, 562]

$$ds^2 \equiv \langle D\psi | D\psi \rangle = S^2 r^2 (d\theta^2 + \sin^2 \theta d\phi^2) = S^2 d\phi^2 , \quad (r = 1, \theta = \pi/2, \phi = (0, 2\pi)) , \quad (8.41)$$

where  $|D\psi\rangle = |\psi\rangle - |\psi\rangle\langle\psi|d\psi\rangle$  is a gauge-invariant derivative on the PHS. The great circle  $S_1 \rightarrow ds^2 = d\phi^2$  traced by  $U_2$  winds around the Dirac-string associated with the monopole of charge  $2S = 2\gamma/2\pi$  ( $R = 0 \rightarrow E_+ = E_-$ ) arising from the energy degeneracy point. The integrated two-form,  $d\mathbf{F} = \langle D\psi | \wedge | D\psi \rangle = \mathcal{F}_{\mu\nu} dx_\mu \wedge dx_\nu$ , can be written in terms of the Berry curvature [563]  $\mathcal{F}_{\mu\nu} = \text{Im}(\langle D_\mu \psi | D_\nu \psi \rangle)$  for a hemisphere of the Bloch sphere (with solid angle  $\Omega = 2\pi$ ). Parametrizing the Bloch sphere by the angles  $(\theta, \phi)$  gives the non-commutativity between the unitary operators  $\hat{T}_1 = \exp[i(\pi/2)\hat{D}_\theta]$  and  $\hat{T}_2 = \exp[i2\pi\hat{D}_\phi]$

$$\hat{T}_1 \hat{T}_2 \hat{T}_1^\dagger \hat{T}_2^\dagger = e^{i\gamma_b} , \quad (8.42)$$

where, following Schwinger [564], we define the generators  $D_\theta = (1/2i)(D_+ e^{-i\phi} - e^{i\phi} D_-)$  and  $D_\phi = (1/i)\partial_\phi$ . The topological phase accrued by the closed circuit ( $\gamma_b$ ) is then given by

$$\gamma_b = \frac{\gamma}{2\pi} \int_{\theta<\pi/2} d\mathbf{F} = \frac{\gamma}{2\pi} \Omega = \gamma . \quad (8.43)$$

This shows that the nesting instability associated with  $\gamma_b$  arises from a monopole of charge  $2S = \gamma/\pi$  [565], where  $\gamma$  is the first Chern class of the gapless FS. This leads to the equivalence:  $\hat{T}_1 \hat{T}_2 \hat{T}_1^\dagger \hat{T}_2^\dagger = e^{i\gamma_b} \equiv \hat{O}_{c/s} \hat{T} \hat{O}_{c/s}^\dagger \hat{T}^\dagger = e^{i\gamma}$ . The Dirac string [565] (see Fig.(8.3.1a)) carries an effective flux  $\Phi = \gamma/2\pi\Phi_0$ , punctures the XZ plane from the North/South pole ( $\gamma_{bN} = -\gamma_{bS}$ ), and is revealed by using Gauss' law

$$\gamma_b = \pm \oint dA , \quad dA = d\mathbf{l} \cdot \hat{\phi} \frac{\gamma}{2\pi} . \quad (8.44)$$

The associated  $\Theta$ -term,  $\gamma_b/\gamma \in \pi_1(U(1)) = Z$ , acts as a half-flux quantum  $\Phi_0/2$  Dirac string for the Möbius strip PHS encircling the great circle of the Bloch sphere made by the subspace  $F_1$ .

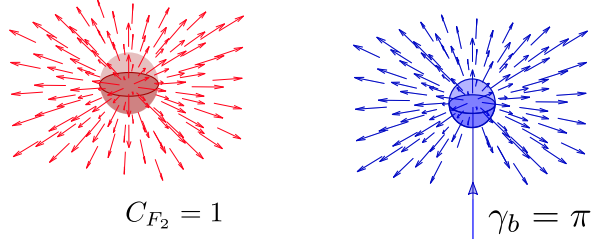


Figure 8.3.1: Topological object in (a) subspace  $F_2$ , the WZNW topological term and (b)  $F_1$ , the  $\Theta$ -term for a monopole with a Dirac string.

By making the two-spin interaction of the Hamiltonian eq.(8.38) anisotropic

$$H_F = \frac{J_{||}}{2N_\Lambda} A_{Fa}^z A_{Fb}^z + \frac{J_\perp}{4N_\Lambda} (A_{Fa}^+ A_{Fb}^- + h.c.) , \quad (8.45)$$

we extend our arguments to a two-dimensional coupling space:  $(J_{||}, J_\perp)$ . Now,  $H_F$  lowers the symmetry associated with its PHS from  $SU(2)_a \otimes SU(2)_b \rightarrow U(1)_{a+b} \otimes Z_{2a+b}$ . Along two special lines on the  $(J_{||}, J_\perp)$  plane,  $J_{||} = \pm J_\perp$ , the Hamiltonian  $H_F$  has the enhanced symmetry  $SU(2)_{a+b}$ . Further, precisely at the crossing point of the two lines,  $J_{||} = \pm J_\perp$ , the Hamiltonian vanishes ( $H_F = 0$ ) and the symmetry group is emergently restored to  $SU(2)_a \otimes SU(2)_b$ . The  $H_F$  Hamiltonian can be block decomposed as  $H_F = H_{F_1} \oplus H_{F_2}$ , where  $H_{F_1}$  is given in eq.(8.40) and the Hamiltonian  $H_{F_2} = J_{||} S^2 I_{F_2}$  is represented by subspace  $F_2 \equiv \{|\uparrow_a\uparrow_b\rangle, |\downarrow_a\downarrow_b\rangle\} \subset F$  and  $I_{F_2} = |\uparrow_a\uparrow_b\rangle\langle\uparrow_a\uparrow_b| + |\downarrow_a\downarrow_b\rangle\langle\downarrow_a\downarrow_b|$ . The family of unitary operations that keep  $H_{F_2}$  invariant is  $U_{\delta k_F=0, F_2}(\theta, \hat{n}) = \exp[i\theta \mathbf{S}_1 \cdot \hat{n}] \in S^3$ , where  $\mathbf{S}_1 = S \bar{A}_F^+ \boldsymbol{\sigma} \bar{A}_F^-$ ,  $\bar{A}_F^\pm = (A_{Fa}^\pm A_{Fb}^\pm)$  and  $S = 1/2$ . This  $S^3$  wraps the FS metric singularity of the PHS  $F_2$ :  $ds^2 = S^2 r^2 (d\theta^2 + \sin^2 \theta d\phi^2) = 0$  as  $r = 0$ . The density matrix  $\rho_{F_2} = \frac{1}{2}[I + \mathbf{r} \cdot \boldsymbol{\sigma}]|_{r=0}$  lies at the origin of the Bloch sphere, reaffirming the  $SU(2)$  symmetry of  $F_2$ . The  $\hat{n}$  vectors form a unit sphere  $S^2$  homeomorphic to  $CP^1$  (i.e., once again a Bloch sphere with a monopole of charge  $2S$ ). The topological term associated with the homotopy group of this  $SU(2)$  PHS is the  $0 + 1D$  Wess-Zumino-Novikov-Witten term [227]

$$C_{F_2} = 2S \int d^2 \mathbf{x} \mathbf{n} \cdot (\partial_\theta \mathbf{n} \times \partial_\phi \mathbf{n}) , \quad (8.46)$$

where the Chern numbers  $C_{F_2} \in \pi_3(SU(2)_{A_F^z=\pm 1}) \in \mathbb{Z}$ . The monopole charge  $2S = 1$  is shown in Fig.(8.3.1(a)), and arises from an equivalence of the PHS  $F_2$  to a two-level system formed by pairing of two pseudospins of  $S = 1/2$  representation.

We have seen earlier that  $H_{F_1} = -\frac{J_{||}}{4} D_z^2 + \frac{J_\perp}{2} D_x$  acts in sub-basis  $F_1$  for which we have computed the topological  $\Theta$ -term associated with a Dirac string is given by  $\gamma_b = \gamma \frac{\Omega}{2\pi}$ ,  $\Omega = 2\pi(1-\cos\theta)$ ,  $\theta = \pi/2$ . By varying the coupling values  $(J_{||}, J_\perp)$ , the four energy eigenvalues ( $E_{\uparrow_a\uparrow_b} = E_{\downarrow_a\downarrow_b} = J_{||}/4$ ), ( $E_{\uparrow\downarrow\pm\uparrow} = -J_{||}/4 \pm J_\perp/2$ ) rearrange themselves. Thus, the existence of topological objects like magnetic monopoles or Dirac strings in the lowest energy subspace ( $LES : \{\psi_i\}$  such that  $H_F \psi_i = E \psi_i$ ,  $E = \min[E_{\uparrow_a\uparrow_b}, E_{\downarrow_a\downarrow_b}, E_{\uparrow\downarrow\pm\uparrow}, E_{\uparrow\downarrow\pm\downarrow}]$ ) is determined by whether  $LES \in F_1$  or  $F_2$ . A compact form for  $\gamma_b$  can be written down in terms of  $(J_{||}, J_\perp)$

$$\gamma_b = f + \text{sgn}(f)(\gamma - |f|) \quad (8.47)$$

where  $f = \text{sgn}(J^\perp)(\gamma/2(1 + \text{sgn}(r))\text{sgn}(J^{\parallel}) + \gamma/4(1 - \text{sgn}(r))(1 + \text{sgn}(J^{\parallel}))$  and  $r = J^{\perp 2} - J^{\parallel 2}$ . Fig.(8.3.2a) is a skeletal phase diagram that depicts the topological objects residing in the LES of the Fermi surface PHS for anisotropic couplings characterized by  $r \neq 0$ . For  $J_{\parallel} < 0$  and  $r < 0$ , the  $\text{LES} = F_2$  is associated with a monopole with strength given by Chern number  $C_{F_2} = 2S$  (eq.(8.46)). On the other hand, for either  $r > 0$  or  $J_{\parallel} > 0$ , the  $\text{LES} = F_1$  possesses a Dirac string whose  $\Theta$ -term coefficient is given by  $\gamma_b$  (eq.(8.44))). Two special half-lines  $J^\perp = \pm J^{\parallel} = J < 0$  where  $r = 0$  lead to the  $\text{LES}$

$$\begin{aligned}\text{LES}_{\gamma_b=\pm\pi, J<0} &= \{|\uparrow_{Fa}\uparrow_{Fb}\rangle, |\downarrow_{Fa}\downarrow_{Fb}\rangle, |\gamma_b\rangle\} \quad \text{where} \\ |\gamma_b\rangle &= |\mathbf{A}_F = 1/2(1 + e^{i\frac{(\gamma-\gamma_b)}{2}}), A_F^z = 0\rangle.\end{aligned}\quad (8.48)$$

This special  $\text{LES}$  contains states belonging to both  $F_1$  and  $F_2$ . As depicted in the skeletal phase diagram of Fig.(8.3.2b), the topological objects describing this  $\text{LES}$  is a monopole associated with PHS  $F_2$  (with Chern number  $C_{F_2} = 2S = 1 \in \pi_3(SU(2)_{F_2})$ ) and a Dirac string associated with  $F_1$  (with  $\Theta$  term  $\gamma_b/\gamma \in \pi_1(U(1))$ ). The co-existence of two topological objects in the  $\text{LES}$  for  $r = 0, J_{\parallel} < 0$  is an outcome of an emergent  $SU(2)_{a+b}$  seen from a  $2 \otimes 2 = 3 \oplus 1$  block decomposition of the Hamiltonian

$$H_F = J/4I_{\text{LES}}^{\gamma_b=\pm\pi} - 3J/4|\gamma_b\rangle\langle\gamma_b|,\quad (8.49)$$

where  $I_{\text{LES}}^{\gamma_b=\pm\pi}$  is a  $n \times n, n = 3$  Casimir invariant under  $SU(2)$  rotations of spin representation  $S = (n-1)/2 = 1$ . For  $J > 0, r = 0$ , the  $\text{LES}_{\gamma_b=\pm\pi, J<0}$  switches to  $\text{LES}_{\gamma_b=\mp\pi, J>0} = \{|\gamma_b\rangle\}$ . Precisely at the critical point  $J^{\parallel} = J^\perp = 0$ , the  $\text{LES} = F_1 \cup F_2 = F$  and possesses both the Chern numbers  $C_{F_1} \in \pi_3(SU(2)_{F_2})$  and  $C_{F_2} \in \pi_3(SU(2)_{F_1})$  given earlier, displaying the enhanced symmetry of  $SU(2)_a \times SU(2)_b$ . In the following section, we will treat the instabilities of the Fermi surface via a renormalization group (RG) procedure. We will see there that the RG flows are characterized by the quantity  $r$  shown above, such that the relevance or irrelevance of a flow is decided by the quantities  $(\text{sgn}(J_{\parallel}), \text{sgn}(r), \text{sgn}(J_{\perp}))$ . In this way, RG flows will be dictated by the discontinuous changes in boundary conditions accounted for by the topological object at the FS ( $\gamma_b$ ).

## 8.4 URG for Fermi surface instabilities: a topological viewpoint

In Sec.8.2, we showed that the constraints  $C_1$  and  $C_2$  lead to the condensation of four-fermion vertices into  $SU(2)^{\otimes 2N_{\Lambda_0}}$  PHS associated with the putative BCS and Mott instabilities respectively. This way, the first Chern class  $\gamma = \pi$  associated with the Fock space  $\mathcal{F}_{8N_{\Lambda_0}}$  of the gapless FS became the Chern number belonging to the homotopy group of the  $SU(2)$  condensate PHS, i.e.,  $C = 2S = 2\gamma/2\pi \in \pi_3(SU(2)) \equiv Z$ . Further, in Sec.8.3, the first Chern class  $C$  was observed to be a monopole of charge  $(2\gamma/\pi)$ , possessing a Dirac string given by the  $\Theta$ -term  $\gamma_b = \gamma$  acting on the Fermi surface PHS  $F$ . In this section, we will show how FS topology shapes the instabilities via a renormalization group (RG) formalism. For this, we start with an electronic model for strong correlations, and perform the unitary renormalization group (URG) method by decoupling electronic states starting from the UV. In this way, we show the emergence of IR fixed

points governed by the topological constraints  $C_1, C_2$  of Sec.8.2. Furthermore, we show that the essential features of the RG phase diagram obtained via URG is dictated by a topological term  $\gamma_b$ , and reflects the qualitative accuracy of the skeletal phase diagrams shown in Figs.(8.3.2a) and (b).

### URG algorithm

In the URG scheme [180, 181, 184, 182, 183], the Hamiltonian  $H$  is iteratively block-diagonalized by a succession of unitary maps  $U_{(N)}, U_{(N-1)}, \dots, U_{(j)}$ , leading to the flow equation

$$H_{(j-1)} = U_{(j)} H_{(j)} U_{(j)}^\dagger, \quad [H_{(j)}, \hat{n}_j] = 0, \quad (8.50)$$

where  $j$  is the  $j$ -th electronic state that is disentangled and  $H_{(N)} = H$  is the bare Hamiltonian. The occupancies of the disentangled electronic states become good quantum numbers, as they commute with the Hamiltonian,  $[H_{(j)}, \hat{n}_i] = 0$  for  $i \geq j$ . The  $N$  electronic states are labelled as  $j \in [1, N]$ , in increasing order of bare one-particle energy  $\epsilon_1 \leq \epsilon_2 \leq \dots \leq \epsilon_N$ . Electronic states in the UV are disentangled first, eventually scaling towards the IR. Concomitantly, this involves the entanglement renormalization within the eigenstates  $|\Psi_{(j)}\rangle$  of  $H_{(j)}$

$$|\Psi_{(j-1)}\rangle = U_{(j)} |\Psi_{(j)}\rangle, \quad \hat{n}_i |\Psi_{(j-1)}\rangle = |\Psi_{(j-1)}\rangle. \quad (8.51)$$

This guarantees the preservation of the many-body eigenspectrum

$$H_{(j)} |\Psi_{(j)}\rangle = E(|\Psi\rangle) |\Psi_{(j)}\rangle, \quad (8.52)$$

where the initial (bare) eigenstate is  $|\Psi\rangle = |\Psi_{(N)}\rangle$ . The unitary operation  $U_{(j)}$  [180, 181, 184, 182, 183] is given by

$$U_{(j)} = \frac{1}{\sqrt{2}} (1 + \eta_{(j)} - \eta_{(j)}^\dagger), \quad \eta_{(j)}^\dagger = \frac{1}{\hat{\omega}_{(j)} - Tr_j(H_{(j)}^D \hat{n}_j) \hat{n}_j} c_j^\dagger Tr_j(H_{(j)} c_j). \quad (8.53)$$

The operators  $\eta_{(j)}, \eta_{(j)}^\dagger$  in the above expression satisfy the algebra  $\{\eta_{(j)}, \eta_{(j)}^\dagger\} = 1, [\eta_{(j)}, \eta_{(j)}^\dagger] = 1 - 2\hat{n}_{(j)}$ . The operator  $\hat{\omega}_{(j)}$  accounts for the residual quantum fluctuations due to renormalized off-diagonal blocks, and is defined as

$$\hat{\omega}_{(j)} = H_{(j-1)}^D + H_{(j-1)}^X - H_{(j)}^X. \quad (8.54)$$

$H_{(j)}^D$  and  $H_{(j)}^X$  represents the diagonal and the off-diagonal components of  $H_{(j)}$ . Note that eq.(8.54) is essentially a rewriting of the Hamiltonian RG flow equation:  $\Delta H_{(j)} = H_{(j-1)} - H_{(j)} = \hat{\omega}_{(j)} - H_{(j)}^D$ . In terms of  $\eta_{(j)}$ , the Hamiltonian renormalization  $\Delta H_{(j)}$  is given by

$$\Delta H_{(j)} = \tau_j \{Tr(c_j^\dagger H_{(j)}) c_j, \eta_j^\dagger\}, \quad (8.55)$$

where  $\{A, B\} = AB + BA$  represents the anticommutator and  $\tau_j = n_j - \frac{1}{2}$  represents the disentangled degree of freedom. Associated with the quantum fluctuation operator  $\hat{\omega}_{(j)}$  are eigenstates  $|\Phi(\omega_{(j)})\rangle$  and eigenvalues  $\omega_{(j)}$ . These constitute the natural quantum energyscales arising from the off-diagonal blocks. For each of the  $\omega_{(j)}$ s, an effective Hamiltonian RG flow is obtained, describing the renormalization of a sub-part of the many-body energy spectrum. The condition for reaching a RG fixed point is obtained from vanishing of the matrix element

$$\langle \Phi_{(j)} | (\hat{\omega}_{(j)} - H_{(j)}^D) | \Psi_{(j)} \rangle = \langle \Phi_{(j)} | (\omega_{(j)} - H_{(j)}^D) | \Psi_{(j)} \rangle = \langle \Phi_{(j)} | \Delta H_{(j)} | \Psi_{(j)} \rangle = 0. \quad (8.56)$$

This implies that the projected subspace generated by  $|\Phi_{(j)}\rangle\langle\Phi_{(j)}|$ ,  $\hat{\omega}_{(j)}$  is number diagonal:  $[\omega_{(j)}|\Phi_{(j)}\rangle\langle\Phi_{(j)}|, H_{(j)}^D] = 0$ .

### **URG study of the BCS and Mott instabilities of 1D correlated electrons**

We adapt the URG procedure to a 1D model of strongly correlated electrons. We first address the BCS instability by starting from the model

$$H_1 = \sum_{\kappa} \epsilon_{\kappa} \hat{n}_{\kappa} + \sum_{\kappa, \kappa', p, \eta} \left[ K c_{\kappa(p, \eta)}^{\dagger} c_{\kappa'(p, \eta)}^{\dagger} c_{\kappa'_1(p, -\eta)} c_{\kappa_1(p, -\eta)} \right. \\ \left. + V c_{\kappa(p, \eta)}^{\dagger} c_{\kappa'(p, \eta)}^{\dagger} c_{\kappa'_1(p, \eta)} c_{\kappa_1(p, \eta)} \right], \quad (8.57)$$

where  $p$  is the pair momentum and  $\eta$  is the helicity. We have included the spin-backscattering process (with coupling  $K$ ) and forward scattering processes for the various opposite spin,  $p$  momentum pairs (with coupling  $V$ ). The redefinition of momentum wavevectors  $k_{\Lambda\hat{s}} = k_{F\hat{s}} + \Lambda\hat{s}$  in Sec.8.2 unveils a natural labelling scheme for states in terms of normal distances from Fermi points  $\Lambda_N > \dots > \Lambda_j > \Lambda_{j-1} > \dots > 0$ . The RG transformations then disentangle electronic states farthest from the Fermi points, while scaling gradually towards it. At RG step  $j$ , two electronic states with spins  $(\uparrow, \downarrow)$  at a distance  $\Lambda_j$  from both the  $L$  and  $R$  Fermi points are simultaneously disentangled. The net unitary transformation at the step  $j$  is  $U_{(j)} = \prod_{\hat{s}=\pm 1, \sigma=\pm 1} U_{j, \hat{s}, \sigma}$ , where  $U_{j, \hat{s}, \sigma}$  (eq.(8.53)) disentangles the electronic state  $|k_{\Lambda_j \hat{s}}, \sigma\rangle$ . The rotated Hamiltonian  $H_{(j-1)} = U_{(j)} H_{(j)} U_{(j)}^{\dagger}$  thus obtained is off-diagonal with respect to electronic states at distances  $\Lambda < \Lambda_j$ . Next, from the Hamiltonian RG flow equation, we extract the vertex RG flow equations for all the  $p = 0$  and  $p \neq 0$  pair momentum vertices (see Appendix 8.A for details)

$$\Delta K^{(j)}(p) = \frac{K^{(j)}(p)V^{(j)}(p)}{\omega - \frac{1}{2}(\epsilon_{\kappa_j} + \epsilon_{\kappa'_j}) - \frac{V^{(j)}(p)}{4}}, \quad \Delta V^{(j)}(p) = \frac{(K^{(j)}(p))^2}{\omega - \frac{1}{2}(\epsilon_{\kappa_j} + \epsilon_{\kappa'_j}) - \frac{V^{(j)}(p)}{4}}, \quad (8.58)$$

where  $\kappa_j = (\Lambda_j, \hat{s}, \sigma)$  and  $\kappa'_j = (\Lambda_j + p, -\hat{s}, -\sigma)$ . In obtaining the above equations, we have chosen the intermediate configuration  $\tau_{\kappa_j} = \tau_{\kappa'_j} = \frac{1}{2}$ . It is important to note that for arriving at the above RG equations, we have accounted only for the quantum fluctuation energy scales  $\omega$  at the one-particle level. Also, we have not accounted for the feedback of the renormalized vertices in the  $\omega$ 's (eq.(8.54)). We investigate the RG equation in the regime

$$\omega < \frac{1}{2}(\epsilon_{\kappa_j} + \epsilon_{\kappa'_j}), \quad (8.59)$$

as it corresponds to the vicinity of Fermi energy. Note that the only set of non-trivial fixed points of the above RG equations (eq.(8.58)) exists for  $V, V^{(j)}(p) < 0$ . Further, in those cases, the two-particle vertices scattering  $p = 0$  momentum pairs constitute the dominant RG flows

$$|\omega - \hbar v_F(\Lambda_j + \frac{p}{2})| > |\omega - \hbar v_F \Lambda_j| \\ \implies |\Delta K^{(j)}(p)| < |\Delta K^{(j)}(0)|, \quad |\Delta V^{(j)}(p)| < |\Delta V^{(j)}(0)|. \quad (8.60)$$

Here, the net kinetic energy for the pair of electronic states near the Fermi surface (about  $E_F$ ) is given by  $(\epsilon_{\kappa_j} + \epsilon_{\kappa'_j}) \approx \hbar v_F(2\Lambda_j + p)$ . We have additionally reasoned that  $|\omega - \hbar v_F(2\Lambda_j + p)| > |V|$ ;

as  $V \propto O(1/L)$  (where  $L$  is the system dimension), the relation is naturally satisfied for large system sizes. Thus, we study the dominant vertex ( $p = 0$  momentum vertices) RG flow equations in the continuum limit

$$\begin{aligned} \frac{dK_1}{d \log \frac{\Lambda}{\Lambda_0}} &= K_1(1 - \omega G(\omega, \Lambda)) + \frac{K_1 V_1}{1 - V_1/4}, \\ \frac{dV_1}{d \log \frac{\Lambda}{\Lambda_0}} &= V_1(1 - \omega G(\omega, \Lambda)) + \frac{K_1^2}{1 - V_1/4}, \end{aligned} \quad (8.61)$$

where  $G(\omega, \Lambda) = \frac{1}{\omega - \hbar v_F \Lambda}$ . In obtaining the continuum RG equations, we have replaced the discrete difference  $\Delta \log \frac{\Lambda_j}{\Lambda_0}$  by the differential  $d \log \frac{\Lambda}{\Lambda_0}$ , and defined the couplings  $K_1 = K(\Lambda)/(\omega - \hbar v_F \Lambda)$  and  $V_1 = V(\Lambda)/(\omega - \hbar v_F \Lambda)$ . In the regime of eq.(8.59), the signatures of  $K_1$  and  $V_1$  are related to those of  $K$  and  $V$ , as  $\text{sgn}(K_1) = -\text{sgn}(K)$  and  $\text{sgn}(V_1) = -\text{sgn}(V)$ . For  $\omega < 0$  and upon scaling towards the Fermi surface  $\Lambda \rightarrow 0$ , the ratio  $\hbar v_F \Lambda / \omega \rightarrow 0-$ , such that  $\omega G(\omega, \Lambda) = (1 - \hbar v_F \Lambda / \omega)^{-1} \rightarrow 1$ . This ensures that both RG equations are eventually dominated by the second term, i.e.,

$$\frac{dK_1}{d \log \frac{\Lambda}{\Lambda_0}} = \frac{K_1 V_1}{1 - V_1/4}, \quad \frac{dV_1}{d \log \frac{\Lambda}{\Lambda_0}} = \frac{K_1^2}{1 - V_1/4}. \quad (8.62)$$

Similarly, in order to study the Mott instability, we study the Hamiltonian that includes Umklapp scattering processes (with coupling  $K'$ ) along with forward scattering processes (with coupling  $V'$ )

$$\begin{aligned} H_2 &= \sum_{\kappa} \epsilon_{\kappa} \hat{n}_{\kappa} + \sum_{\kappa, \kappa', p, \eta} \left[ K' c_{\kappa(p, \hat{s})}^{\dagger} c_{\kappa'(p, \hat{s})}^{\dagger} c_{\kappa'_1(p, -\hat{s})} c_{\kappa_1(p, -\hat{s})} \right. \\ &\quad \left. + V' c_{\kappa(p, \hat{s})}^{\dagger} c_{\kappa'(p, \hat{s})}^{\dagger} c_{\kappa'_1(p, \hat{s})} c_{\kappa_1(p, \hat{s})} \right], \end{aligned} \quad (8.63)$$

where  $\kappa(p, \hat{s}) = (\Lambda, \hat{s}, \sigma)$  and  $\kappa'(p, \hat{s}) = (-\Lambda + p, \hat{s}, -\sigma)$ . The pair of electronic states  $|\kappa\rangle$  and  $|\kappa'\rangle$  scatter onto the opposite side of the Fermi surface, such that net momentum transfer is  $2\pi$ . The resulting electronic states  $|\kappa_1\rangle$  and  $|\kappa'_1\rangle$  are given by  $\kappa_1 = (\Lambda, -\hat{s}, \sigma)$ ,  $\kappa'_1 = (\Lambda, -\hat{s}, \sigma)$  and  $\kappa_1 = (-\Lambda + p, -\hat{s}, -\sigma)$ . By constructing the unitary maps  $U_{(j)}$  (eq.(8.53)), we obtain the coupling RG equations from eq.(8.55) as

$$\Delta K'^{(j)}(p) = \frac{K'^{(j)}(p) V'^{(j)}(p)}{\omega - \frac{1}{2}(\epsilon_{\kappa_j} + \epsilon_{\kappa'_j}) - \frac{V'^{(j)}(p)}{4}}, \quad \Delta V'^{(j)}(p) = \frac{(K'^{(j)}(p))^2}{\omega - \frac{1}{2}(\epsilon_{\kappa_j} + \epsilon_{\kappa'_j}) - \frac{V'^{(j)}(p)}{4}}. \quad (8.64)$$

We again make the choice of electronic states in the vicinity of the Fermi surface,  $\frac{1}{2}(\epsilon_{\kappa_j} + \epsilon_{\kappa'_j}) \approx -\hbar v_F p$ , and investigate the above RG equations in the regime  $\omega + \hbar v_F p > 0$ , where  $V, V^{(j)}(p) > 0$  leads to non-trivial fixed points. In this case, the pairs with net momentum  $k_{\Lambda, \hat{s}} + k_{-\Lambda, \hat{s}} = \pi$  dominate the RG flows as seen below

$$\omega < \omega + \hbar v_F p \Rightarrow |\Delta K'^{(j)}(p)| < |\Delta K'^{(j)}(0)|, \quad |\Delta V'^{(j)}(p)| < |\Delta V'^{(j)}(0)|. \quad (8.65)$$

In the continuum limit, the RG equations attain the form

$$\frac{dK'_1}{d \log \frac{\Lambda}{\Lambda_0}} = \frac{K'_1 V'_1}{1 - V'_1/4}, \quad \frac{dV'_1}{d \log \frac{\Lambda}{\Lambda_0}} = \frac{(K'_1)^2}{1 - \frac{V'_1}{4}}, \quad (8.66)$$

where  $K'_1 = K'(\Lambda)/\omega$ ,  $V'_1 = V'(\Lambda)/\omega$ .

### **RG and Fermi surface topology**

The continuum RG equations for the Mott (eq.(8.66)) and BCS instabilities (eq.(8.61)) can be written in a compact form as

$$\frac{dJ_{||}}{d \ln \frac{\Lambda}{\Lambda_0}} = \frac{J_{\perp}^2}{1 - \frac{J_{||}}{4}}, \quad \frac{dJ_{\perp}}{d \ln \frac{\Lambda}{\Lambda_0}} = \frac{J_{\perp} J_{||}}{1 - \frac{J_{||}}{4}}, \quad (8.67)$$

with  $J_{||} = V'_1$  or  $V_1$  and  $J_{\perp} = K'_1$  or  $K_1$  for the Mott and BCS cases respectively. These equations have the same form as the Berezinskii-Kosterlitz-Thouless (BKT) RG equations [566, 567], and are precisely identical to them at weak coupling (i.e., for  $J_{||} \rightarrow 0$ ). They also possess the same RG invariant labelling each RG trajectory,  $r = J_{\perp}^2 - J_{||}^2$ . However, the presence of the  $(1 - J_{||} S^2)^{-1}$  term in the denominator of both RG equations represents a new non-perturbative feature obtained from the URG formalism, and will be seen to be responsible for the RG flows reaching stable fixed points at intermediate coupling [180, 181, 184, 182, 183]. The critical and intermediate coupling stable fixed point features of the RG phase diagram are depicted in Fig.(8.4.1). Remarkably, the essential structure of this RG phase diagram is captured by the skeletal phase diagrams presented earlier in Fig.(8.3.2a) and (b). We recall that the diagrams in Fig.(8.3.2a) and (b) were obtained purely from the consideration of the topological features of the Fermi surface Hamiltonian.

We can now use the RG invariant  $r$  to write the two RG equations in a combined fashion

$$\frac{dJ_{\perp}}{d \ln \Lambda} = \frac{\text{sgn}(J_{\perp}) \text{sgn}(J_{||}) \sqrt{J_{\perp}^2 - |r| \text{sgn}(r)}}{1 - \frac{\text{sgn}(J_{||})}{4} \sqrt{J_{\perp}^2 - |r| \text{sgn}(r)}}. \quad (8.68)$$

Using eq.(8.47), it is possible to simplify this RG equation for the case of the WZNW lines ( $r = 0$ ,  $J_{||} = \pm J_{\perp} \equiv J$ ) in terms of the topological properties of the Fermi surface, i.e., the first Chern class  $\gamma$  and the  $\Theta$  term  $\gamma_b$

$$\frac{d|J|}{d \ln \Lambda} = e^{i(\gamma - \gamma_b)/2} \frac{|J|^2}{1 - e^{i(\gamma - \gamma_b)/2} \frac{|J|}{4}}, \quad (8.69)$$

where particle-hole/time reversal symmetry leads to  $\gamma = \pi$  (eq.(8.17)). We recall that a change in  $\Theta$ -term (eq.(8.47)) with the sign of  $J$  coupling, i.e.,  $\gamma_b = \gamma \text{sgn}(J)$ , is associated with a change in the Fermi surface LES from  $LES_{\gamma_b, J < 0}$  to  $LES_{-\gamma_b, J > 0}$  (eq.(8.48)). Indeed, as seen from RG flow eq.(8.69), this change in  $\gamma_b$  triggers the back-scattering instability, leading to an irrelevant coupling turning dangerously relevant. Further, the RG equation eq.(8.69) has a  $Z_2$  helicity-inversion symmetry,  $(J_{||}, J_{\perp}) \mapsto (J_{||}, -J_{\perp})$ , given by the unitary operation:  $\hat{K} \equiv \hat{U}_1^{1/2} = \exp[i\pi/2(A_{\Lambda a}^z - A_{\Lambda b}^z)]$ .

The enhanced symmetry of the critical point  $r = 0, J_\perp = 0$  can now be seen as follows. For  $\gamma_b = -\gamma$ ,  $d|J|/d \log \Lambda < 0$  (irrelevant RG flows) and  $\Lambda \rightarrow 0$  leads to the coupling sequence  $\{|J_{\Lambda_{n_0}}| > |J_{\Lambda_{n_0-1}}| > \dots > |J_{\bar{n}}| > |J_{\bar{n}-1}| = 0\}$ . This tracks the passage through a space of  $SU(2)_{a+b}$  symmetric theories ending at a  $SU(2)_a \otimes SU(2)_b$  fixed point theory. The enhanced symmetry of the critical point is associated with two Chern invariants  $C_{F_1}$  and  $C_{F_2}$  in the pseudo-spin composite operator basis  $F$  (see Sec.(8.3)). Remarkably, it is also a consequence of the independent conservation laws for the chiral currents  $J_L$  and  $J_R$  for the gapless Fermi surface. We recall that in eq.(8.8), these conserved currents gave rise to Chern invariants  $\nu_a$  and  $\nu_b$ . In the presence of an electric field, this gapless spectrum will again display the axial anomaly seen earlier the non-interacting metal (eq.(8.10)). Similarly, the relation observed earlier between the central charge ( $c$ ) of the associated conformal field theory and the Atiyah-Singer indices ( $\nu_L - \nu_R$ ) holds here as well.

### **Topological structure of the RG phase diagram**

For RG invariant  $r \neq 0$ , the  $\Theta$ -term ( $\gamma_b = f$  in eq.(8.47)) changes from  $\gamma_b = \gamma$  (for either  $r > 0$  or  $(r < 0, J_{||} > 0)$ ) to  $\gamma_b = 0$  ( $r < 0, J_{||} < 0$ ). This change shows up as a distinction between irrelevant ( $\gamma_b = 0$ ) and relevant ( $\gamma_b = \gamma$ ) RG flows (above and below the  $r = 0$  WZNW separatrices respectively) in the equation

$$\frac{d|J_\perp|}{d \log \Lambda} = e^{i(\gamma-\gamma_b)} \frac{\sqrt{J_\perp^2 - r}}{1 - \frac{1}{4}\sqrt{J_\perp^2 - r}}. \quad (8.70)$$

By combining the isotropic (eq.(8.69)) and anisotropic (eq.(8.70)) RG flows, we obtain the RG equation

$$\frac{d|J_\perp|}{d \log \Lambda} = e^{i\varpi(r)} \frac{\sqrt{J_\perp^2 - r}}{1 - \frac{1}{4}\sqrt{J_\perp^2 - r}} \quad (8.71)$$

where  $\varpi(r)$  is given by

$$\begin{aligned} \varpi(r) &= (\gamma - \gamma_b), r \neq 0, \\ &= (\gamma - \gamma_b)/2, r = 0. \end{aligned} \quad (8.72)$$

Changing  $\varpi$  from  $\theta : 0 \rightarrow \gamma$  leads to constructive interference  $2\varpi = 2\pi$  between clockwise & anticlockwise paths in the c.o.m PHS  $P_{cm} : [0, 2\pi]$ . This causes vortices and anti-vortices in momentum-space,  $\hat{O}_{c/s}^2 = e^{i(2\pi/\gamma)X_{c/s}}$  and  $\hat{O}_{c/s}^{2\dagger} = e^{-i(2\pi/\gamma)X_{c/s}}$  respectively, to bind via the spin/charge backscattering term  $J_\perp(\hat{O}_{c/s}^2 + h.c.) \equiv J_\perp(A_a^+ A_b^- + h.c.)$  [380]. The red dots in Fig.(8.4.1) for the  $J_\perp > 0$  and  $J_\perp < 0$  regime indicate stable fixed points at intermediate coupling, and lead to (charge/spin) vortex-antivortex pseudospin singlet and triplet condensates which are odd and even under (helicity/chirality) exchange respectively. This is equivalent to the unbinding of real space vortex-anti vortex pairs, as is well known for the BKT transition [566, 567]. Instead, for the cases  $(r < 0, J_{||} < 0)$ , there is no Dirac string in the LES (see Fig.(8.3.2a)):  $\gamma_b = 0$ , and the  $e^{i\gamma} = -1$  phase factor in the RG equation, and will lead to destructive interference between paths traversed in clockwise and anticlockwise senses in the c.o.m PHS  $P_{cm} \in [0, \pi]$  (as shown

$\Theta$ -term ( $\gamma_b$ )	LE	ML
0	$J_{1,\parallel}^* = - r $	$J_{1,\parallel}^* = - r $
$\pi$	$J_{\parallel}^* = -4 \omega - \hbar v_F \Lambda^* $	$J_{\parallel}^* = 4\omega$

Table 8.4.1: Magnitude of couplings at critical and non-critical fixed points.

in Fig.(8.4.2)). The irrelevant RG flows then lead to a line of blue dots in Fig.(8.4.1), corresponding to gapless Tomonaga-Luttinger liquid (TLL) metallic system [367, 544]. The dashed line in Fig.(8.4.1) corresponds to a line of Lifshitz transitions of the Fermi surface labelled by the topological angle  $\varpi(r)$  (eq.(8.72)). Finally, note that the unitary RG procedure generates effective Hamiltonian at the gapless fixed points (blue dots) and gapped fixed points (red dots) in Fig.8.4.1. In the next section we present the mathematical forms of the effective Hamiltonians, as well as their eigenstates and eigenvalues.

### **Effective Hamiltonians obtained at the stable fixed points of the RG flow**

We just saw that the appearance of a  $\Theta$ -term with  $\gamma_b$  (eq.(8.47)) in the RG eq.(8.69) governs the nature of stable fixed points, i.e.,  $\gamma_b = \pi$  corresponds to non-critical phases and  $\gamma_b = 0$  corresponds to the critical phases. From the coupling RG flows for these two cases, we can construct the effective Hamiltonians  $H_0^*$  and  $H_\pi^*$  corresponding to the critical and gapped fixed points (blue dots and red dots respectively in Fig.(8.4.1) as

$$H_0^* = J_{1,\parallel}^* A_a^z A_b^z , \quad (8.73)$$

$$H_\pi^* = J_{\parallel}^* A_a^z A_b^z + \frac{J_{\perp}^*}{2} (A_a^+ A_b^- + h.c.) . \quad (8.74)$$

$J_{1,\parallel}^*$ ,  $J_{\parallel}^*$  and  $J_{\perp}^*$  are the magnitudes of the couplings for the Ising and pseudospin scattering terms at the fixed points, and can be reconstructed from their definitions below eqs.(8.61) and (8.66). Note that in obtaining the above fixed point Hamiltonians, we have only accounted for only the dominant RG flows.

The values of the fixed point couplings at the Luther-Emery (LE) and Mott liquid (ML) phases arising from the RG flow of Hamiltonians  $H_1$  eq.(8.57) and  $H_2$  eq.(8.63) are tabulated in Table-8.4.1. Along the WZNW lines ( $r = 0$  and with  $\gamma_b = \pi$ ), the eigenstates at the stable fixed point are given by

$$|\Psi\rangle_\pi = |A_a + A_b = m, A_a^z + A_b^z = 0, A_a = \frac{N_*}{2}, A_b = \frac{N_*}{2}\rangle , \quad (8.75)$$

where  $N_*$  is the number of pseudospins within each emergent window  $[-\Lambda^*, \Lambda^*]$  centered about the Fermi points. From  $H_\pi$  (eq.(8.74)), we obtain the corresponding eigenspectrum as  $E(m) = J^* [m(m+1) - 2N_*(N_*+1)]$ , where  $0 < m < 2N_*$  and  $J^* = -4|\omega - \hbar v_F \Lambda^*|$  for the LE liquid, and  $J^* = 4\omega$  for the Mott liquid phase. As the LE fixed point is reached in the attractive regime  $J^* < 0$ , the eigenfunctions are determined completely from  $m = 2N_*$ ; on the other hand,  $m = 0$  for the ML fixed point. Similarly for the critical phases governed by  $H_0^*$  (eq.(8.73)), the many-body eigenfunctions are given by

$$|\Psi\rangle_0 = |A_a = N_*, A_b = N_*, A_a^z = m, A_b^z = m, A_a^z = m\rangle , \quad (8.76)$$

and the corresponding eigenspectrum is  $E(m) = J_{1,\parallel}^* m^2$ . In subsequent sections, we will show that the electronic states at the Fermi surface are witness to the low energy features of the LE and ML phases.

## 8.5 Holographic entanglement scaling towards the Fermi surface

The Entanglement entropy (EE)  $S(R)$  of an interacting quantum system is a measure of many-particle quantum entanglement that is generated upon isolating a region  $R$  from the rest of the system. It quantifies the information lost with regards to quantum correlations between degrees of freedom in region  $R$  and its complement. Earlier works based on real space entanglement RG [236] revealed distinct scaling features of EE for gapped as against gapless phases. Using the URG formalism, some of us have recently studied entanglement RG flow towards various IR fixed points of the 2D Hubbard model, distinguishing thereby the entanglement scaling features of the normal and Mott insulating states [184]. The URG represents the nonlocal unitary disentanglement transformations as a product of two-local unitary operations, providing thereby a entanglement holographic mapping (EHM) [232, 177] or tensor network representation of URG. The URG method generates Hamiltonian and entanglement RG along the holographic scaling direction of the EHM [161, 241, 232]. Further, Ref.[184] shows that the many-body states generated by the entanglement renormalisation respects the Ryu-Takayanagi EE bound [147, 148], i.e., the entanglement entropy generated upon isolating region  $R$  from its complement is bounded from above by the number of links between them. In this section, we will demonstrate that the RG flow of EE and the holographic EE bound possess distinct features in the TLL phase and Luther Emery phases.

As noted above, upon scaling from UV towards the IR fixed point, the URG generates effective Hamiltonians at each step. Starting with the ground state at the IR fixed point,  $\Psi_{(j^*)}$  (eq.(8.75) and eq.(8.76)) of the effective Hamiltonian  $H_{(j^*)}$  (eq.(8.74) and eq.(8.73) respectively), and performing reverse URG steps using the unitary maps  $U^\dagger$  leads to the reconstruction of the states in the UV energy scale:

$$\begin{aligned} \text{UV} &\xrightarrow{\text{URG}} \text{IR} : \quad H_{(N)} \xrightarrow{U_{(N)}} H_{(N-1)} \xrightarrow{U_{(N-2)}} \dots \xrightarrow{U_{(j^*+1)}} H_{(j^*)}, \\ \text{IR} &\xrightarrow{\text{reverse URG}} \text{UV} : \quad |\Psi_{(N)}\rangle \xleftarrow{U_{(N)}^\dagger} \dots \xleftarrow{U_{(j^*+2)}^\dagger} |\Psi_{(j^*+1)}\rangle \xleftarrow{U_{(j^*+1)}^\dagger} |\Psi_{(j^*)}\rangle. \end{aligned} \quad (8.77)$$

We now discuss some important features of this scheme. Recall that at each step of the URG, two pseudospin degrees of freedom of opposite helicities  $\mathbf{A}_{\Lambda_j,+1}$  and  $\mathbf{A}_{\Lambda_j,-1}$  are disentangled, generating a Hamiltonian flow towards, say, the Luther-Emery fixed point (see Table-8.4.1). On the other hand, along the reverse RG flow, two pseudospins re-entangle at each step, enabling the reconstruction of the eigenstates at high energy scales. Fig.8.5.1 displays the EHM construction for the entanglement RG flow from the UV towards the LE ground state in the IR. Pseudospin states are labelled in descending order of energy, such that pair of pseudospins  $|0\rangle, |10\rangle$  with opposite helicities ( $\eta$ ) are located farthest from the Fermi points and naturally associated with the highest electronic pair-energy. Thus, a succession of pseudospin pairs  $(|1\rangle, |11\rangle), (|2\rangle, |12\rangle), \dots$  carry a decreasing sequence of net electronic energy, such that the pair  $|9\rangle, |19\rangle$  is located

at the Fermi points. The dotted oval in Fig.8.5.1 represents the entangled groundstate  $|\Psi_\pi\rangle$  of the LE phase (eq.(8.75)). Comprised of the pseudospins  $|9\rangle$  with helicity  $\eta = +1$  and  $|19\rangle$  with helicity  $-1$ , it has the form  $|\Psi_\pi\rangle = |A = 1, A_z = 0, A_{+1} = \frac{1}{2}, A_{-1} = \frac{1}{2}\rangle$ . The complete ground state at the IR fixed point can be obtained by performing a tensor product of  $|\Psi_\pi\rangle$  with the disentangled pseudospin states labelled 0 to 8 and 11 to 18,  $|\Psi_{(j*)}\rangle = |\Psi_\pi\rangle \otimes_{i=0}^8 |s_i\rangle \otimes_{i=11}^{18} |s_i\rangle$ . Here, the  $s_i$  are the  $|\uparrow\rangle$  and  $|\downarrow\rangle$  configurations of the individual pseudospins. The reverse unitary operations  $U^\dagger$  (yellow blocks in Fig.8.5.1, eq.(8.77)) map the ground state from IR to UV (with RG step  $j^* = 1$  being the fixed point):  $U_1^\dagger|\Psi\rangle, U_2^\dagger U_1^\dagger|\Psi\rangle, U_3^\dagger U_2^\dagger U_1^\dagger|\Psi\rangle, \dots$ , generating thereby the EHM tensor network.

An essential feature of the EHM network is that it can be represented entirely as a product of two-qubit disentangling gates [232]. Such a decomposition will allow us to interpret the URG as a quantum circuit renormalization group [184]. For the present EHM network shown in Fig.8.5.1, we show some aspects of the equivalent quantum circuit in Fig.8.5.2. The second last yellow block  $U_3$  (connecting states  $|\Psi_2\rangle$  and  $|\Psi_3\rangle = U_3^\dagger|\Psi_2\rangle$ ) can be decomposed as follows

$$U_3 = U_{17,9}U_{17,8}U_{7,19}U_{7,18}U_{7,17} , \quad (8.78)$$

where  $U_{i,j}$  disentangles the pair of pseudospins  $|i\rangle$  and  $|j\rangle$  (orange block in Fig.8.5.2). Note that in the parent Hamiltonian for the RG analysis (eq.(8.57)), we have only accounted for the backscattering diagrams that couple pairs of electronic states with opposite helicity ( $\eta$ ). In the second last RG step, the collection of unitary disentanglers  $U_{7,19}U_{7,18}U_{7,17}$  decouple the pseudospin  $|7\rangle$  with helicity  $\eta = +1$  from the pseudospins  $|17\rangle, |18\rangle, |19\rangle$  of opposite helicity  $\eta = -1$ . This is followed by the next set of unitary maps  $U_{17,9}U_{17,8}$  that disentangle pseudospin  $|17\rangle$  of helicity  $\eta = -1$  from  $|8\rangle$  and  $|9\rangle$  with helicity  $\eta = +1$ . The depth  $d$  of the orange block equals the number of  $U_{a,b}$  operations carried out sequentially (in eq.(8.78)) to complete the disentanglement operation  $U_j$ . For  $U_3$ , as shown in Fig.8.5.2, the circuit depth  $d = 5$ . The form of the individual qubit disentanglers  $U_{a,b}$  in eq.(8.78) are constrained by the analytical form of the complete unitary map  $U_j$  (eq.(8.53)) determined by the renormalized Hamiltonian  $H_{(j)}$ . Many-body states  $U_{7,17}|\Psi_3\rangle, U_{7,18}U_{7,17}|\Psi_3\rangle, \dots$  generated at each sublayer of the circuit composing  $U_3$  (see Fig.8.5.2) involve the vanishing of mutual information  $I(i : j) = S(i) + S(j) - S(i, j)$  [232, 240] for the pair of qubits  $(7, 17), (7, 18)$  and so on [184].  $S(i), S(j)$  is the entanglement entropy associated with isolating qubit  $i$  and  $j$  from the system and  $S(i, j)$  is the joint entropy associated with the isolating pair of qubits  $(i, j)$ .

Upon implementing the reverse URG, we isolate at each RG step  $j$  momentum-space blocks of increasing lengths  $(9), (9, 8), (9, 8, 7), \dots (9, 8, \dots, 0)$ , and obtain therefrom the EE  $S_j(l)$

$$S_j(l) = -Tr(\rho_j(l) \log \rho_j(l)), \quad \rho_j(l) = Tr_{9,\dots,10-l}(|\Psi_{(j)}\rangle\langle\Psi_{(j)}|) , \quad (8.79)$$

where  $l \in [1, 10]$  is the size of the momentum-space block and  $\rho_j(l)$  is the reduced density matrix. For this, the state  $|\Psi_{(j)}\rangle$  is generated from  $|\Psi_{(j*)}\rangle$  by doing reverse URG:  $|\Psi_{(j)}\rangle = U_j^\dagger U_{j-1}^\dagger \dots U_{j^*}^\dagger |\Psi_{(j^*)}\rangle$ . We can also provide a reverse URG formulation for the TLL phase starting from the state  $|\Psi_0\rangle = |A_{+1}^z = \frac{1}{2}, A_{-1}^z = \frac{1}{2}\rangle$  (eq.(8.76)). This allows us to construct a EHM quantum circuit realization of the URG similar to above(Fig. 8.5.1, Fig. 8.5.2) generating an block entanglement entropy RG flow. The left and right panels of Fig.8.5.3 show the entanglement entropy RG flow for different momentum-space block sizes in the LE and TLL phases respectively. Along the forward RG flow, the successive disentanglement of pseudospins leads to a gradual

reduction of block EE: the disentanglement of UV degrees of freedom reduces the entanglement sharing between IR and UV degrees of freedom. It is important to note, however, that in the left panel of Fig.8.5.3 the EE for the lowest block size 9 at the Fermi point increases along the RG flow, terminating at a final value of  $S = \log 2$ . This shows that the entanglement between Fermi points at the IR fixed point is enhanced, leading to formation of the maximally entangled state  $|\Psi_\pi\rangle = \sqrt{2^{-1}}[|\uparrow_{+1}\downarrow_{-1}\rangle - |\downarrow_{+1}\uparrow_{-1}\rangle]$ . On the other hand, for the TLL phase, the momentum-space block EE is observed to decrease monotonically to zero along the RG flow for *all* block sizes, suggesting perfect disentanglement of the pseudospins. In this way, we observe distinct scaling features for the TLL and LE phases.

Finally, we turn to display the holographic feature of the EHM: when computed from the bulk of the EHM tensor network, the EE associated with region  $R$  possesses an upper bound related to the number of degrees of freedom in  $R$  ( $n(R)$ ) that are entangled [241, 161, 232]. To compute the upper bound, we multiply  $n_j(R)$  with the maximum one-pseudospin entanglement entropy  $S_j(i)$  at RG step  $j$ , such that

$$S_j(R) \leq n_j(R) \times \max_{i \in R}(S_j(i)) . \quad (8.80)$$

This leads to the Ryu-Takayanagi formula for entanglement entropy [147, 148]. The grey block ranging from pseudospin 0 to 9 in Fig.8.5.1 represents the region  $R$  at UV, while the dotted blue line is the minimal surface, or, equivalently, the number of links cut to isolate  $R$  from deep within the EHM. Evidently, the minimal surface shrinks as we proceed deeper into the bulk of the EHM such that  $n_j(R)$  reduces. In the present case of Fig.8.5.1,  $n_{j-1}(R) = n_j(R) - 1$ . In Fig.8.5.4, we confirm the holographic entanglement entropy relation (eq.(8.80)) with  $R = \{0, 1, \dots, 9\}$  for both the LE and TLL phases. The blue curve shows the holographic entropy upper bound, while the orange curve shows the entropy computed for the region  $R$  from the bulk of the EHM. Importantly, the distinct holographic entanglement entropy scaling features imply that it is a witness to the entanglement phase transition between the critical TLL phase (blue dots in the phase diagram Fig.8.4.1) and the gapped LE phase (red dots of Fig.8.4.1). First, we note that the  $S_{max}(1)$  leading to the EE upper bound for the LE and TLL phases are distinct: while it arises entirely from the degree of freedom at the Fermi surface (pseudospin 9) along the RG trajectory (step 9 to step 0) for the LE phase, it shifts gradually from UV (pseudospin 0) to the IR (Fermi surface pseudospin 9) for the TLL as the RG proceeds. Second, the shape of the upper bound for the two phases is quite different: while it scales linearly with the logarithmic RG step size for the LE phase, it is clearly non-linear for the TLL phase. While the latter is reminiscent of the rapid expansion of holographically generated entanglement spacetime expected for a gapless phase (i.e., the AdS-CFT conjecture for continuum field theories [568, 569], and its discrete counterpart in lattice field theories [211]), this will need further investigation and will be presented elsewhere. Though we have not shown the analysis here, precisely similar results to those shown for the LE phase are also obtained for the gapped ML phase described earlier.

## 8.6 Observing the instability of the Fermi surface

### *Dynamical spectral weight transfer*

We recall that a topological constraint (eq.(8.24)) ensured that the FS backscattering vertex acts

on the 2-electron subspace

$$N_F = \int_{-\infty}^{\infty} \frac{d\omega}{i\pi} \frac{\partial \text{Tr}_{F_1}(\ln(\hat{G}_0))}{\partial \omega} = 2 , \quad (8.81)$$

where  $\hat{G}_0$  is the non-interacting Greens' function given in eq(8.3). The vertex is described by  $H_{F_1}$  (eq.(8.40)), and satisfies the criterion [86]

$$N_F\gamma = 2\pi , \quad \gamma = 2\pi\nu , \quad 2\pi S = \pi , \quad (8.82)$$

where  $\nu = \gamma/2\pi = 1/2$  and  $S = 1/2$  are the Luttinger sum for the charge and spin excitations (eq.(8.17), in the presence of p-h and TRS symmetries) respectively. As seen earlier, backscattering leads to the formation of composite objects with spectral weight given by Friedel's sum rule [542], relating the scattering phase-shift ( $\delta$ ) to the scattering matrix ( $\hat{S}_{F_1}$ )

$$2\delta = 2\text{Tr}_{F_1}(\ln(\hat{S}_{F_1})) , \quad \hat{S}_{F_1} = 1 - 2\pi\hat{G}_{0F_1} \frac{H_{F_1}}{1 - \hat{G}_{0F_1}H_{F_1}} , \quad (8.83)$$

where  $H_{F_1}$  is given in (eq.(8.40)). The scattering matrix  $\hat{S}_{F_1}$  has the following matrix representation in the basis  $(1/\sqrt{2})[|\uparrow_{Fa}\downarrow_{Fb}\rangle \pm |\downarrow_{Fa}\uparrow_{Fb}\rangle]$

$$\hat{S}_{F_1} = \begin{bmatrix} e^{i\delta_s} & 0 \\ 0 & e^{i\delta_t} \end{bmatrix} , \quad (8.84)$$

where the pseudospin singlet/triplet scattering phase shifts are given respectively by  $\delta_s = \tan^{-1}(3\pi J/4)$ ,  $\delta_t = \tan^{-1}(-\pi J/4)$ . We recall that the change in c.o.m momentum under twist via a full flux-quantum is related to the Luttinger sum  $\gamma/2\pi$  (eq.(8.17)),  $\Delta P_{cm} = \gamma/2\pi$ . Due to Kohn's theorem [570], this relation holds even in the presence of electronic interactions. Thus, in the presence of a putative instability of the FS, the total spectral weight associated with the FS subspace  $F_1$  within the window  $L_{n^*}$  (i.e., of the composite objects, together with that of any remnant fermionic degrees of freedom) is given by a generalized Luttinger's sum rule [448, 278],

$$\frac{2\pi}{\gamma} = \text{Tr}(\ln(\hat{G}_{F_1}(0 + i\eta))) - \text{Tr}(\ln(\hat{G}_{F_1}(0 - i\eta))) + \text{Tr}(\ln((\hat{S})_{F_1})) , \quad (8.85)$$

where the fermionic single-particle Greens' function is given by  $\hat{G}_{F_1}(E) = (\hat{G}_{0F_1}(E)^{-1} - H_{F_1})^{-1}$ . The RG equation for the pseudo-spin singlet scattering phase-shift  $\delta_s$  along the WZNW line  $J_{||} = J_{\perp} = J$  is then given by

$$\frac{d\delta_s}{d \ln \Lambda} = \frac{e^{i(\gamma - \gamma_b)/2}}{1 + \frac{9\pi^2}{4}J^2} \frac{d|J|}{d \ln \Lambda} . \quad (8.86)$$

This relation shows that the Friedel's phase shift changes non-analytically across the critical point  $J = 0$  for the WZNW flows as  $\gamma_b$  changes from  $-\gamma$  to  $\gamma$ . Further, for  $\gamma_b = \gamma$ , unitarity dictates that the increasing dynamical spectral weight transfer between fermions and composite degrees of freedom within the LEB be obtained from

$$\frac{d}{d \ln \Lambda} \text{Tr}(\ln((\hat{S})_{F_1})) + \frac{d}{d \ln \Lambda} \text{Tr}(\ln(\hat{G}_{F_1})) = 0 . \quad (8.87)$$

The dynamical spectral weight transfer stops eventually at the IR fixed point  $J^* = 4$ , where the scattering phase shift  $\delta_s^* = \tan^{-1}(3\pi J^*/4) = \tan^{-1}(3\pi)$ . For the  $N_F = 2$  particle subspace at the Fermi surface, we define a quantity  $\bar{N}_1$  [571] that tracks spectral weight redistribution in terms of  $N_F$  and the Friedel's scattering phase shift ( $\delta_s$ ) [278]

$$\bar{N}_1 = \int_{-\infty}^{\infty} \frac{d\omega}{i\pi} \frac{\partial \text{Tr}_{F_1}(\ln(\hat{G}))}{\partial \omega} = N_F - \frac{2\delta_s}{\pi} = N_F - \frac{2\text{Tr}(\ln \hat{S}_{F_1})}{\pi}. \quad (8.88)$$

### **Measuring full counting statistics for Fermi surface electrons**

We have seen in earlier sections that the electronic degrees of freedom at the FS possess topological attributes that track the two-particle scattering induced instabilities. In this spirit, we now propose a “two-path” thought experiment for a ring-like geometry of the interacting 1D electronic system. This gedanken aims to measure the various moments of the spin/charge backscattering dynamics of FS electrons (full counting statistics (FCS)) in the presence of a putative instability. As shown in Fig.(8.6.1), the setup has two open identical 1D systems that are tunnel coupled to injectors  $I1$  and  $I2$  and detectors  $D1$  and  $D2$  in a ring geometry enclosing a flux  $\lambda = \Phi/\Phi_0$ . The injectors and detectors are momentum resolved, such that they inject and extract electrons in a resonant manner at the Fermi energy  $E_F$ , and with well defined helicity/chirality. Further, the injection and extraction events involve 1-particle superpositions across the two arms of the ring. In order to track the BCS instability in the two 1D systems, injectors  $I1$  and  $I2$  simultaneously inject an electron each with a given helicity  $\eta = \pm 1$ , but with oppositely directed momenta  $-k_F$  and  $+k_F$  respectively. The injectors are switched off immediately after the injection, and the detectors are switched on simultaneously. The injected electrons suffer backscattering in each of the arms, and reach the two detectors through trajectories that involve two-particle interfering pathways between the two arms that together enclose the AB flux  $\lambda$ . This two-particle interference thus provides information related to the correlations accrued from the backscattering processes in the two arms. For the Mott instability, two electrons are instead injected from  $I1$  in superposition between the two arms and are extracted at  $D2$  (while  $I2, D1$  are deactivated). This thought experiment is, therefore, a two-particle fermionic Hanbury-Brown-Twiss setup whose purpose is to expose the interplay of interparticle correlations and Fermi surface topology. An Andreev scattering variant of this gedanken would involve injection of electrons and extraction of holes.

The two-electron scattering matrix at the Fermi surface eq.(8.83) in the basis  $F_1 = \{| \uparrow_{Fa}\downarrow_{Fb} \rangle, | \downarrow_{Fa}\uparrow_{Fb} \rangle\}$  of the composite pseudospin instability operator (see Sec.(8.3)) is given by

$$\hat{S}_{F_1} = \frac{1}{2} \begin{bmatrix} r & t \\ t & r \end{bmatrix}, \quad (8.89)$$

where  $\delta_s, \delta_t$  are the pseudospin singlet/triplet phase shifts defined earlier for the Fermi surface electrons, and  $r = e^{i\delta_s} + e^{i\delta_t}, t = e^{i\delta_s} - e^{i\delta_t}$  are the reflection and transmission coefficients respectively. The  $r$  and  $t$  coefficients can be represented as follows

$$\begin{aligned} r &= \sqrt{\frac{\gamma_s}{2\pi}} e^{i\theta_r}, \quad t = \sqrt{\frac{2\pi - \gamma_s}{2\pi}} e^{i\theta_t}, \\ \theta_r &= \arctan \left( \frac{\sin \delta_s + \sin \delta_t}{\cos \delta_s + \cos \delta_t} \right), \quad \theta_t = \arctan \left( \frac{\sin \delta_s - \sin \delta_t}{\cos \delta_s - \cos \delta_t} \right), \end{aligned} \quad (8.90)$$

where the two-electron wavefunction upon scattering in PHS  $F_1$  acquires a geometric phase

$$\gamma_s = \gamma(1 - \cos(\delta_s - \delta_t)) \quad (8.91)$$

associated with the monopole of charge  $2S = \gamma/\pi$  (see discussion in Sec.(8.3)). The geometric phase  $\gamma_s$  is acquired as follows. The initial state  $|\uparrow_{Fa}\downarrow_{Fb}\rangle$  of the injected electrons is an equal amplitude superposition of the two arms 1 and 2. For instabilities in the the two arms and in the absence of the AB flux  $\lambda$ , this initial state scatters to

$$|\psi(\omega)\rangle = \hat{S}_{F_1} |\uparrow_{Fa}\downarrow_{Fb}\rangle = e^{i\theta_r} (|r||\uparrow_{Fa}\downarrow_{Fb}\rangle + e^{i\omega t} |\downarrow_{Fa}\uparrow_{Fb}\rangle) . \quad (8.92)$$

This scattered state then traverses a closed loop over  $\omega = \theta_t - \theta_r \in [0, 2\pi]$ , acquiring a scattering berry-phase  $\gamma_s$  computed from the berry potential  $\mathbf{A} = i\hat{\phi}\langle\psi(\omega)|\partial_\omega|\psi(\omega)\rangle$  as follows,

$$\gamma_s = \oint d\boldsymbol{\omega} \cdot \mathbf{A}, \quad \boldsymbol{\omega} = \omega\hat{\phi} . \quad (8.93)$$

We define flux-resolved momentum space Wilson loop operators that encode the amount of effective flux observed by charge/spin degrees of freedom

$$\begin{aligned} \hat{Z}_{c/s}^\lambda &= \hat{T}_{c/s} \hat{O}_{c/s}^\lambda \hat{T}_{c/s}^\dagger \hat{O}_{c/s}^{\lambda\dagger}, \\ \hat{Z}_c^\lambda &= \exp[i\gamma\lambda(\hat{n}_{k_F\uparrow} + \hat{n}_{k_F\downarrow} - 1)] , \quad \hat{Z}_s^\lambda = \exp[i\gamma\lambda(\hat{n}_{k_F\uparrow} - \hat{n}_{k_F\downarrow})] . \end{aligned} \quad (8.94)$$

In the above expressions for  $\hat{Z}_{c/s}^\lambda$ , we have used the spin ( $\hat{T}_s$ ) and charge ( $\hat{T}_c$ ) translation operators given by

$$\hat{T}_s = \exp[i \sum_{|k|<|k_F|} k(\hat{n}_{k\uparrow} - \hat{n}_{k\downarrow})] , \quad \hat{T}_c = \exp[i \sum_{|k|<|k_F|} k(\hat{n}_{k\uparrow} + \hat{n}_{k\downarrow} - 1)] , \quad (8.95)$$

and the spin ( $\hat{O}_s$ ) and charge ( $\hat{O}_c$ ) twist operators defined as

$$\hat{O}_c = \exp[i\hat{X}_{cm}] , \quad \hat{O}_s = \exp[i(N/N_e)\hat{X}_{cm}] . \quad (8.96)$$

These Wilson loop operators are the momentum-space duals of the real-space variants shown in eq.(8.14) (and which led to the first Chern class  $\gamma$  eq(8.17)). Further, they track boundary condition changes at the Fermi surface for the spin/charge degrees of freedom. In the scattering problem between the two Fermi points ( $\pm k_F$ ), backscattering processes can be visualized on the ring in terms of interfering clockwise (1) and a anticlockwise (2) paths (see fig8.6.1). Along path-1, a flux is accrued by FS electrons via the Wilson loop operator  $\hat{Z}^{\lambda/2}$ , leading to the modified S-matrix

$$S_{F_1}(\lambda/2) = \hat{Z}_{c/s}^{\lambda/2} S_{F_1} \hat{Z}_{c/s}^{\dagger\lambda/2} . \quad (8.97)$$

This leads to a scattered two-particle wavefunction:  $|\psi_{c/s}^F(\lambda/2)\rangle = S_{F_1}(\lambda/2) |\uparrow_{Fa}\downarrow_{Fb}\rangle$ . Along path-2, the modified S-matrix is

$$S_{F_1}(-\lambda/2) = \hat{Z}_{c/s}^{\dagger\lambda/2} S_{F_1} \hat{Z}_{c/s}^{\lambda/2} , \quad (8.98)$$

and the scattered state is given by  $|\psi_{c/s}^F(-\lambda/2)\rangle = S_{F_1}(-\lambda/2)|\uparrow_{Fa}\downarrow_{Fb}\rangle$ . Superposing these two scattered wavefunctions gives the total wavefunction as  $|\Psi_{c/s}^F(\lambda)\rangle = |\psi_{c/s}^F(\lambda/2)\rangle + |\psi_{c/s}^F(-\lambda/2)\rangle$ , and leads to the following two-particle interference pattern for spin/charge currents carried by the pseudospin composite degrees of freedom (see Sec.8.2)

$$\begin{aligned}\langle \Psi_{c/s}^F(\lambda) | \Psi_{c/s}^F(\lambda) \rangle &= 2 + 2\text{Re}\langle \psi_{c/s}^F(-\lambda/2) | \psi_{c/s}^F(\lambda/2) \rangle , \\ &= 2 + 2|r|^2 + 2|t|^2 \cos \gamma \lambda .\end{aligned}\quad (8.99)$$

We can now define a moment generating function,  $M_{c/s}^F(\lambda)$ , containing the FCS for the two-particle back-scattering at the FS

$$M_{c/s}^F(\lambda) = \langle \psi_{c/s}^F(-\lambda/2) | \psi_{c/s}^F(\lambda/2) \rangle = \langle \psi_{c/s}^F(0) | \hat{Z}_{s/c}^\lambda | \psi_{c/s}^F(0) \rangle . \quad (8.100)$$

The real part of the moment generating function,  $\text{Re}(M_{c/s}^F(\lambda))$ , can be determined from the two-electron interference pattern (eq.(8.99)). Alternatively, the quantity  $\langle \Psi_{c/s}^F(\lambda) | \Psi_{c/s}^F(\lambda) \rangle$  is a measure of the expectation value of the charge operator

$$\begin{aligned}\hat{Q}_{c/s}^F(\lambda) &= \frac{e}{S} \Psi_{c/s}^{F\dagger}(\lambda) \Psi_{c/s}^F(\lambda) , \quad (S = 1/2) \\ \langle \hat{Q}_{c/s}^F \rangle &= \text{Re}(M_{c/s}^F(\lambda)) = 2|r|^2 + 2|t|^2 \cos \gamma \lambda ,\end{aligned}\quad (8.101)$$

where  $\Psi_{c/s}^{F\dagger}(\lambda)$  is given by

$$\Psi_{Fc/s}^\dagger(\lambda) = \hat{S}_{F_1}(\lambda/2) A_{Fa}^+ + \hat{S}_{F_1}(-\lambda/2) A_{Fa}^+ , \quad (8.102)$$

and, as shown earlier,  $A_{Fa}^+ = c_{k_F\uparrow}^\dagger c_{\pm k_F\downarrow}^\dagger$ ,  $A_{Fb}^+ = c_{-k_F\uparrow}^\dagger c_{\mp k_F\downarrow}^\dagger$ . Similarly,  $\text{Im}(M_{c/s}^F(\lambda))$  is evaluated from the expectation value of the composite current operator  $\langle \hat{I}_{c/s}(\lambda) \rangle$  defined as

$$\begin{aligned}\hat{I}_{c/s}^F(\lambda) &= \frac{e}{S} \left[ \psi_{c/s}^{F\dagger}\left(\frac{\lambda}{2}\right) \psi_{c/s}^F\left(-\frac{\lambda}{2}\right) - \psi_{c/s}^{F\dagger}\left(-\frac{\lambda}{2}\right) \psi_{c/s}^F\left(\frac{\lambda}{2}\right) \right] , \\ \langle \hat{I}_{c/s}^F(\lambda) \rangle &= \text{Im}(M_{c/s}^F(\lambda)) = 2|t|^2 \sin \gamma \lambda .\end{aligned}\quad (8.103)$$

Thus, in terms of the charge ( $\langle \hat{Q}_{Fc/s}(\lambda) \rangle$ ) and current ( $\langle \hat{I}_{Fc/s}(\lambda) \rangle$ ) observables, the two-particle FCS generating function can be written as

$$M_{c/s}^F(\lambda) = \langle \hat{Q}_{c/s}^F(\lambda) \rangle + i \langle \hat{I}_{c/s}^F(\lambda) \rangle . \quad (8.104)$$

A cumulant generating function can now be constructed from the moment generating function:  $G^F(\lambda) = \ln M_{c/s}^F(\lambda)$ . By varying the counting field  $\lambda$ , we can generate all cumulants of the spin or charge distributions at the FS. Further, using the Klich-Levitov formula [572] together with eq.(8.91), the even cumulants yield the entanglement entropy  $S_{FS}$  between the helicity/chirality sectors (see Sec.(8.2))

$$\begin{aligned}S_{FS} &= \sum_{m>0} \frac{\alpha_{2m}}{(2m)!} \frac{d^{2m}}{d\lambda^{2m}} G^F(\lambda) |_{\lambda=0} \\ &= -\frac{\gamma_s}{2\pi} \ln \frac{\gamma_s}{2\pi} - (1 - \frac{\gamma_s}{2\pi}) \ln(1 - \frac{\gamma_s}{2\pi}) \\ &= -\ln \frac{\gamma}{2\pi} + \frac{\gamma}{2\pi} \cos(\delta_s - \delta_t) \ln \tan \frac{\delta_s - \delta_t}{2} ,\end{aligned}\quad (8.105)$$

where we have used eq(8.91) in the final line. The first piece of this entanglement entropy is purely topological, i.e.,  $S_{top} = -\ln \frac{\gamma}{2\pi} = \ln 2$  depends purely on the first Chern class  $\gamma$  and accounts for dimension of PHS  $F_1$  ( $d = 2$ ). We will see in the next section that this topological piece of the entanglement entropy ( $S_{top}$ ) reappears in the c.o.m. Hilbert space. The second piece ( $S_{dyn}$ ) is a function of the pseudospin singlet and triplet scattering phase shifts, and is dependent on the geometry of the PHS  $F_1$ . This reflects on the additional entanglement content of the many-body wavefunction arising from the dynamical spectral weight transfer. This second piece renormalizes incrementally as the instability hits the Fermi surface ( $\gamma_b = \gamma$ , and  $d|J|/d\ln \lambda > 0$ ), leading to a value at the IR stable fixed point ( $J^* = 4$ ) given by

$$S_{dyn}^* = \frac{\gamma}{2\pi} \cos(\phi) \ln\left\{\tan \frac{\phi}{2}\right\}, \quad \phi = \tan^{-1}(3\pi) - \tan^{-1}(-\pi). \quad (8.106)$$

Note that  $S_{FS} \rightarrow 0$  as  $\delta_s = \pi/2 = -\delta_t$  (unitary limit). Interestingly, for  $J = 4/(\sqrt{3}\pi)$ ,  $\delta_s - \delta_t = \pi/2$ , such that  $S_{FS} = -\ln \frac{\gamma}{2\pi}$  is purely topological. In this way, a measurement of the FCS should enable that of the associated many-particle entanglement entropy [572].

## 8.7 Topological order and its observables

We begin by clarifying how the c.o.m. Hilbert space topology is shaped by the instability. Recall that for  $J_{||} < 0$ ,  $\text{sgn}(r)$  jumps across the  $SU(2)$  WZNW lines from  $-1$  to  $+1$ , together with a jump in the Berry phase  $\gamma_b = (\gamma/2)(1 + \text{sgn}(r))$  from  $0 \rightarrow \pi$  (eq.(8.47)). These changes are associated with a modification of the c.o.m Hamiltonian from  $H_{cm}^0 = P_{cm}^2/2M$  to

$$H_{cm} = \frac{P_{cm}^2}{2M} + \Delta E_{s/c} \cos\left(\frac{2\pi}{\gamma} X_{c/s}\right), \quad (8.107)$$

where  $M$  is the total mass of the system and the cosine potential arises from the pseudospin-flip operation (eq.(8.39)). This changes the gauge symmetry of the state manifold from  $Z_N \simeq S_1$  (in the thermodynamic limit  $N \rightarrow \infty$ ) to  $Z_2$  (where  $Z_2$  is the  $X_{c/s} : 0 \rightarrow \pi$  symmetry of the cosine potential). The translation- and gauge-invariant wavefunction basis  $\mathcal{B}_{\gamma_b=0}$  for the metal (described by  $H_{cm}^0$ ) and basis  $\mathcal{B}_{\gamma_b=\pi}$  for the (spin/charge) gapped insulator (described by  $H_{cm}$ ) are given by

$$\begin{aligned} \mathcal{B}_0 &= \{|k\rangle = \frac{1}{\sqrt{N}} \sum_j e^{ikj} |X_{c/s} = j\rangle, k = \frac{2\pi j}{N}\}, \quad \mathcal{B}_\pi = \{|P_{cm} = 0, \pi\rangle\} \\ |P_{cm} = 0, \pi\rangle &= \sqrt{\gamma/2\pi} [|X_{c/s} = 0\rangle \pm |X_{c/s} = \gamma\rangle], \end{aligned} \quad (8.108)$$

where  $|P_{cm} = 0, \pi\rangle$  represents the two degenerate states in c.o.m spectrum. That this degeneracy is not lifted due to tunneling (via the kinematic term  $P_{cm}^2/2M$ ) arises from the destructive interference in the manifold of quantum states within  $\mathcal{B}_\pi$  (eq.(8.114)). The Hamiltonian  $H_{cm}$  projected onto the basis  $\mathcal{B}_\pi$  vanishes, where the projection operator  $P_\pi = |P_{cm} = 0\rangle\langle P_{cm} = 0| + |P_{cm} = \pi\rangle\langle P_{cm} = \pi|$ . Thus,  $P_\pi H_{cm} P_\pi = 0$  leads to purely topological dynamics governed by a  $0 + 1D$  WZNW term (of the form shown in eq.(8.46)) with Chern coefficient  $C_{cm} = 1$  for  $\gamma = \pi$ . The two-fold ground state degeneracy ( $d = 2$ ) is directly related to the Chern coefficient

as  $d = C + 1$ . We will shortly see how this establishes topological order.

### Two spectral gaps and topological order

We have seen already that the  $\Theta$ -term,  $\gamma_b = \gamma$ , leads to an increasing  $J_\perp$  coupling under RG, eventually ending at an asymptotically safe stable fixed point  $J_{||}(\Lambda_{n*}) = 4$  in the IR. The fixed point theory resides in the low-energy window  $L_{n*} : [-\Lambda_{n*}, \Lambda_{n*}]$  with a width given by the many-body gap ( $\Delta E_{MB}$ )

$$\Delta E_{MB} = 2\Lambda_{n*} = 2\Lambda_0 \left( \frac{J_{||}^0}{4} \right)^{1/4} \exp \left[ \frac{1}{4} - \frac{1}{J_{||}^0} \right], \quad (8.109)$$

where  $J_{||}^0$  is the bare coupling. This gap is the analogue of that obtained from the one-loop BKT RG for the 1D superconducting Luther-Emery liquid and 1D Mott insulator [558, 4]. The asymptotically free nature of the one-loop RG leads, in contrast, to an exponentially small gap  $\Delta E_{MB}^{1\text{-loop}} \sim \exp[-1/J_{||}^0]$ .

Within the window  $L_{n*}$ , the FS pseudo-spin degrees of freedom ( $F$ ) undergo backscattering and lead to an *additional (spin/charge) gap* between the two states  $|\mathbf{A}_a + \mathbf{A}_b = (1, 0)\rangle = 1/\sqrt{2} |\uparrow_a \downarrow_b\rangle \pm |\downarrow_a \uparrow_b\rangle$  around the Fermi energy  $E_F = 0$ . In the previous section, we have already obtained the effective Hamiltonians for the LE and MI phases. From there, we determine the spin/charge gap in ( $\Delta E_{s/c} = J_\perp^*/N_{\Lambda^*}$ ) between the pseudospin singlet and triplet states ( $|\mathbf{A}_{\Lambda_{n*}a} + \mathbf{A}_{\Lambda_{n*}b}|^2 = 0, 2$ ) as

$$\Delta E_{s/c} = \left( \frac{4}{J_{||}^0} \right)^{1/4} \frac{(\sqrt{J_{||}^*})^2 + r^2}{2\Lambda_0} \exp \left[ \frac{1}{J_{||}^0} - \frac{1}{4} \right], \quad (8.110)$$

where  $J_{||}^*$  is determined from the Table 8.4.1 for the MI and LE phases. That this spin/charge gap at the intermediate coupling fixed point ( $J_{n*||} = 1/S^2$ ) is equivalent to the gap between  $|\mathbf{A}_a + \mathbf{A}_b = 1\rangle$  and  $|\mathbf{A}_a + \mathbf{A}_b = 0\rangle$  at the FS can be attributed to the fact that the Hamiltonians eq.(8.45) and eq.(8.36) possess the same couplings. Following Ambegaokar et al. [573], we can now define the coherence length  $\xi_{coh}$  for the BKT transition in terms of the RG invariant

$$\xi_{coh}(J_\perp^*) = l_c e^{1/\sqrt{r}} = l_c e^{(16 - J_\perp^{*2})^{-1/4}}, \quad (8.111)$$

where  $l_c$  is the vortex core size and we have used the relation between the RG invariant  $r$  and the final fixed point coupling  $J_\perp^*$ .

The modified c.o.m PHS has a emergent  $Z_2$  symmetry and associated doubly-degenerate ground states

$$\begin{aligned} |P_{cm} = 0, A_{a+b} = 0\rangle &\quad , \quad \hat{O}_{c/s}|P_{cm} = 0, A_{a+b} = 0\rangle = |P_{cm} = \gamma, A_{a+b} = 0\rangle , \\ \hat{O}_{c/s}^2|P_{cm} = 0, A_{a+b} = 0\rangle &= |P_{cm} = 2\gamma, A_{a+b} = 0\rangle , \end{aligned} \quad (8.112)$$

separated from the lowest-lying excited states with  $|A_{a+b} = 1\rangle$  by the (spin/charge) gap  $\Delta E_{s/c}$  given above. We recall that the commutation relation between the twist ( $\hat{O}_{c/s}$ ) and translation ( $\hat{T}$ ) operators was shown in Sec.(8.1) to be

$$\hat{O}_{c/s}\hat{T} = \hat{T}\hat{O}_{c/s}e^{\gamma[X_{c/s}, P_{cm}]}, \quad (8.113)$$

where  $[X_{c/s}, P_{cm}] = i$ ,  $\gamma = \pi$ . This leads to destructive interference in a multiply-connected geometry ( $S^1 \equiv [0, 2\pi]$ ) involving path-1 ( $X_{c/s} = [0, \pi]$  traversed in clockwise sense) and path-2 ( $X_{c/s} = [0, \pi]$  traversed in anti-clockwise sense) between the two degenerate states  $|\Psi_1\rangle = |X_{c/s} = 0, A_{a+b} = 0\rangle$  and  $|\Psi_2\rangle = |X_{c/s} = \pi, A_{a+b} = 0\rangle$ ,

$$|\Psi_1|^2 + |\Psi_2|^2 + 2|\Psi_1||\Psi_2| \cos \gamma = 0 , \quad (8.114)$$

where  $\Psi_1 = e^{i\gamma}\Psi_2$ . The Aharonov-Bohm phase  $e^{i\gamma}$  arises from charge  $e/2$  objects encircling the Dirac string in the FS PHS. Indeed, the finding of topological degeneracy with a gap  $\Delta E_{s/c}$  for  $\gamma = \pi$  corresponds to one of the possible conclusions of the LSM-type criterion [86] discussed in Sec.8.3. The zero mode of the square-root of the vertex operator  $\hat{O}_{c/s}^2$  [380] is a nonlocal gauge transformation with an associated  $Z_2$  Wilson loop given by eq.(8.14). This Wilson loop operator reveals the presence of a vortex condensed topological state of matter at the intermediate coupling fixed point  $J_\perp^*$  [574, 258]. The modified Hilbert space  $\mathcal{B}_\pi$ , topological degeneracy, topological excitations and *spin/charge* gap are depicted pictorially in Fig.(8.7.1). On the other hand, for  $\gamma_b = 0$ , the gapless TLL metal corresponds to the second conclusion of the LSM-type criterion (see Sec.8.3).

### **Observables for changes in Hilbert space geometry and topology**

We now identify observables associated with the c.o.m twist operator  $\hat{O}_{c/s}$  (eq.(8.11)) that probe changes in Hilbert space geometry and topology across the RG phase diagram. The modification in c.o.m Hilbert space as the sign of the RG invariant  $\text{sgn}(r)$  changes from  $-1$  to  $+1$  can be tracked by the cumulants  $\mathcal{C}_n$  of the c.o.m. position operator  $X_{c/s}$ . The cumulants  $\mathcal{C}_n$  are defined as the  $n$ th derivative of the gauge-invariant cumulant generating function  $G(\lambda)$

$$G(\lambda) = \ln\langle\hat{O}_{s/c}^\lambda\rangle , \quad \mathcal{C}_n = \frac{(-i)^n}{(2\pi)^n} \lim_{L \rightarrow \infty} \frac{d^n}{d\lambda^n} G(\lambda)|_{\lambda=0} . \quad (8.115)$$

The first cumulant,

$$\mathcal{C}_1 = \frac{\gamma_b}{2\pi} = \frac{\gamma}{4\pi}(1 + \text{sgn}(r))\text{sgn}(J_{||}) \quad (8.116)$$

is related to the  $\Theta$ -term associated with the Dirac string in the PHS [575, 380]. Now, for  $r > 0$ , as  $J_{||}$  changes sign,  $\gamma_b : \gamma \rightarrow -\gamma$ . Nelson and Kosterlitz [576] have shown that for crossover RG flows  $r > 0$ , the superfluid stiffness  $\chi$  for the classical 2D XY model is related to the coupling  $J_{||}$  in the Hamiltonian eq.(8.45)

$$\chi = \frac{m^2 k_B T}{\hbar^2 \rho_s} = \frac{\pi}{\pi J_{||} - 2} . \quad (8.117)$$

They then employ the asymptotically free nature of the weak coupling perturbative RG for the BKT transition to show that for  $r > 0$ ,  $J_{||} : 0 \rightarrow \infty$ , there exists a universal jump in the superfluid stiffness across the transition given by  $\Delta\chi = \chi(J_{||} = 0) - \chi(J_{||} \rightarrow \infty) = \pi/2$  [576]. Our asymptotically safe RG equations eq.(8.67) show that for  $r > 0$ ,  $J_{||} : 0 \rightarrow 4\pi^2/\gamma^2 = 4 = 1/S^2$  and  $\Delta\chi = \chi(J_{||} = 0) - \chi(J_{||} = 1/S^2) = \pi/(4\pi - 2)$ . In this light, the asymptotic safety of our RG results arise from the intermediate coupling fixed point at  $S = 1/2$  discussed earlier and are indicative of fermionic criticality, while the asymptotically free BKT RG equations are obtained

for the limit of  $S \rightarrow 0$ . Importantly, we see that the crossover RG flow is also associated with a jump in the Berry phase  $\Delta\gamma_b = 2\pi$ , as well as a jump in the first cumulant  $\mathcal{C}_1$

$$\Delta\mathcal{C}_1 = \frac{\Delta\gamma_b}{2\pi} = 1 . \quad (8.118)$$

The second cumulant  $\mathcal{C}_2$  is related to the localization length ( $\xi$ ) [575]

$$\mathcal{C}_2 = \xi^2 = \langle \hat{X}_{c/s}^2 \rangle - \langle \hat{X}_{c/s} \rangle^2 . \quad (8.119)$$

For  $J_{||} < 0$ , the change in the localization length is  $\xi : \infty \rightarrow (\gamma/2\pi)$ , as the change in  $\text{sgn}(r)$  depicts the transition from a metal to a (spin/charge) gapped state. The localization length  $\xi$  has an interpretation as a geometric distance on the c.o.m. Hilbert space. To see this, we define the quantum metric of the c.o.m. Hilbert space as

$$g_{\lambda\lambda} = \langle \partial_\lambda \Psi(\lambda) | \partial_\lambda \Psi(\lambda) \rangle - |\langle \Psi(\lambda) | \partial_\lambda \Psi(\lambda) \rangle|^2 , \quad (8.120)$$

where  $|\Psi(\lambda)\rangle \in \hat{O}\mathcal{B}_\pi$  or  $|\Psi(\lambda)\rangle \in \hat{O}\mathcal{B}_0$ . By performing an average over the gauge  $\lambda$ , we obtain

$$d\xi^2 = \frac{1}{4\pi^2} d\lambda^2 g_{\lambda\lambda} \Rightarrow \xi = \frac{1}{2\pi} \int_0^{2\pi} d\lambda \sqrt{g_{\lambda\lambda}} . \quad (8.121)$$

We can now relate the imaginary part of the (spin/charge) conductivity at zero frequency  $\lim_{\omega \rightarrow 0} \text{Im } \sigma_{s/c}(\omega)$  to the fluctuations encoded in the quantum metric [577]  $g_{\lambda\lambda}$  via the fluctuation-dissipation and Kramers-Kronig relations

$$g_{\lambda\lambda} = \lim_{\omega \rightarrow 0} \text{Im } \sigma_{s/c}(\omega) = \int_0^\infty d\omega' \frac{\text{Re } \sigma_{s/c}(\omega')}{\omega'} . \quad (8.122)$$

Thus, the drastic jumps in both  $\xi$  and  $\text{Im } \sigma_{s/c}(\omega = 0)$  are both topological in origin. The cumulant generating function  $G(\lambda)$  in the (spin/charge) gapped phase  $J_{||} < 0, r < 0$  is given by  $G(\lambda) = \ln(\gamma/2\pi) + \ln(1 + e^{i2\gamma\lambda})$ . In the light of the arguments presented above, we can conclude that all cumulants ( $M_n$ ) are functions of the quantum metric  $g_{\lambda\lambda}$  and Berry phase  $\gamma$  of the c.o.m. Hilbert space. Further, they will all show universal jumps across the transition.

### **Entanglement entropy and noise in the center of mass Hilbert space**

The center of mass Hilbert space  $\mathcal{H}_{cm}$  for  $\gamma_b = \gamma$  is spanned by a  $SU(2), S = 1/2$  representation basis  $\mathcal{B}_\pi$  (eq.(8.108)) embedded on a circle ( $S_1$ )  $S_{cm} : X_{c/s} = [0, 2\pi]$ . In order to compute the entanglement entropy, the circle  $S_{cm}$  is cut at diametrically opposite points

$$S_{cm} = S_{1cm} \oplus S_{2cm} , \quad S_{1cm} = \{\pi/2, \dots, 0, \dots, 3\pi/2\} , \quad S_{2cm} = [\pi/2, \dots, \pi, \dots, 3\pi/2] . \quad (8.123)$$

This results in a surgery of the c.o.m. Hilbert space  $\mathcal{H}_{cm} \equiv SU(2)$  into  $\mathcal{H}_1 \otimes \mathcal{H}_2$ , where

$$\mathcal{H}_1 : \mathcal{B}_1 = \{|0_{X_1=0}\rangle, |1_{X_1=0}\rangle, X_1 \in S_{1cm}\} , \quad \mathcal{H}_2 : \mathcal{B}_2 = \{|0_{X_2=\pi}\rangle, |1_{X_2=\pi}\rangle, X_2 \in S_{2cm}\} , \quad (8.124)$$

where  $|0_{0,\pi}\rangle, |1_{0,\pi}\rangle$  are labelled by eigenvalues of the number operators  $\hat{n}_0$  and  $\hat{n}_\pi$ . As both  $\mathcal{H}_1$  and  $\mathcal{H}_2$  represent two-level systems ( $SU(2), S = 1/2$ ), the combined Hilbert space  $\mathcal{H}_1 \otimes \mathcal{H}_2$  is isomorphic to  $SU(2) \otimes SU(2)$ . The c.o.m. coordinate in  $\mathcal{H}_1 \otimes \mathcal{H}_2$  is represented as  $\hat{X}_{c/s} =$

$\hat{n}_0 X_1 + \hat{n}_\pi X_2 = \gamma \hat{n}_\pi$ . Within this formalism, the basis  $\mathcal{B}_\pi \subset \mathcal{B}_1 \times \mathcal{B}_2$  is subject to the constraint  $\hat{n}_0 + \hat{n}_\pi = 1$ . The basis  $\mathcal{B}_\pi$  can then be represented in terms of entangled states

$$|P_{cm} = 0, \pi\rangle = \sqrt{\frac{\gamma}{2\pi}} |1_{X_1} 0_{X_2}\rangle \pm \sqrt{\frac{2\pi - \gamma}{2\pi}} |0_{X_1} 1_{X_2}\rangle . \quad (8.125)$$

Recall that  $\gamma = \pi$  is the first Chern class on the c.o.m. torus  $\mathcal{T}^2$  (eq.(8.17)). Now, by partial tracing over  $\mathcal{H}_2$ , the reduced density matrix for  $\mathcal{H}_1$  is given by

$$\rho_{\mathcal{H}_1} = \frac{\gamma}{2\pi} |0_{X_1}\rangle\langle 0_{X_1}| + \left(1 - \frac{\gamma}{2\pi}\right) |1_{X_1}\rangle\langle 1_{X_1}| . \quad (8.126)$$

The entanglement entropy,  $S = -\text{Tr}(\rho_{\mathcal{H}_1} \ln \rho_{\mathcal{H}_1})$ , is thus dependent on the c.o.m. Hilbert space topology and is given by

$$S = -\frac{\gamma}{2\pi} \log \frac{\gamma}{2\pi} - \left(1 - \frac{\gamma}{2\pi}\right) \log \left(1 - \frac{\gamma}{2\pi}\right) . \quad (8.127)$$

Clearly, the entanglement entropy is  $S_{top} = \ln 2$  [578] for  $\gamma = \pi$ , where the 2 within the log refers to the two-fold topological degeneracy ( $d = 2$ ) on the torus  $\mathcal{T}_2$  observed earlier. We recall that the same topological entanglement entropy was derived in an earlier section by the scattering dynamics at the Fermi surface. As seen earlier, there exists a relation [572] between the even cumulants  $\mathcal{C}_{2m}$  in eq.(8.115) (i.e. fluctuation associated with the center of mass position vector) and the entanglement entropy

$$S_{top} = \sum_{m>0} \frac{\alpha_{2m}}{(2m)!} \mathcal{C}_{2m} , \quad (8.128)$$

where  $\alpha_{2m} = (2\pi)^{2m} |B_{2m}|$ , and  $B_{2m}$  are the Bernoulli numbers. The cumulant generating function (eq.(8.115)) can therefore be written in terms of basis states of eq.(8.125)

$$G(\lambda) = \ln \langle \exp [i\lambda \gamma \hat{n}_\pi] \rangle . \quad (8.129)$$

This shows that changing boundary conditions via operator  $\hat{O}^\lambda$  tracks the number fluctuations associated with the state of the c.o.m. position  $X_{c/s} = \pi$ .

## 8.8 Discussions and Outlook

In summary, we have applied the unitary renormalization group (URG) technique to the problem of interacting electrons in 1D, unveiling thereby the role played by emergent topological features in guiding the RG flow towards critical (TLL) and stable (LE and MI) fixed points. While the nature of critical RG flows comprising the BKT RG phase diagram is preserved, the nonperturbative nature of the URG formalism shows the emergence of non-Abelian constraints leading to a family of gapped intermediate coupling fixed points. We also perform a quantum mechanical analysis of scattering processes at the Fermi surface, and compute topological terms induced by interactions. In doing so, we obtain a skeletal phase diagram that shares the essential features characteristic of the BKT phase diagram. This skeletal phase diagram highlights regions possessing different symmetries, and which are separated by transitions involving changes in topological quantities related to the projected Hilbert space at the Fermi surface. In this way,

we observe an interaction driven Fermi surface topology-changing (Lifshitz) transition of the 1D metal across the critical point, similar to the transitions observed in the 2D Hubbard [180, 181] and other models of correlated lattice electrons [182, 183]. Given the simplicity of the two-point Fermi surface at hand, we expect that these insights into the nature of fermionic criticality are universal, i.e., they shed light also on the instabilities of regular connected [183], as well as Dirac point-like [185], Fermi surfaces in higher dimensions. In this sense, fermionic criticality appears to be shaped by the global (topological) features of the Fermi surface.

The many-particle entanglement renormalization comprising the EHM tensor network show distinct features for the critical and gapped phases. Thus, the topological phase transition across the critical point of the BKT phase diagram also corresponds to a entanglement phase transition. By verifying the Ryu-Takayanagi holographic entropy bound for the EHM network, we demonstrate the emergence of two distinct spacetimes across the critical point in the dual gravity theory (i.e., corresponding to the gapless TLL and gapped LE/MI phases respectively), such that the critical point appears to act as a horizon in the holographic dual spacetime generated from entanglement RG flow [579]. We also demonstrate the important role played by the degrees of freedom at the Fermi surface in guiding the entanglement RG flows from UV to IR for both the gapped and gapless phases. It is tempting to speculate that these are again universal findings, and will be explored in future works.

The MI and LE phases emerge respectively from the charge gapping and spin gapping of the Fermi surface and its neighbourhood. We find that these phases possess the essential features of topological order: ground state degeneracy (for the system placed on a periodic manifold) protected by a many body gap, charge fractionalization etc. An important feature of emergent phases is the phenomena of dynamical spectral weight transfer between the emergent pairs of electronic states and the fundamental electrons. Using the URG analysis of the scattering phase shift, we compute nonperturbatively the net Friedel phase shift and quantify the dynamical spectral weight transferred from UV to IR. Finally, by treating the degrees of freedom at the two-point Fermi surface as a “quantum impurity” coupled to other (“bath”) degrees of freedom at higher energies, we present a scattering matrix thought-experiment for the topological and entanglement features of the Fermi surface. In this way, we track the entanglement entropy generated by isolating the Fermi surface from the rest of the system. We also suggest ways of measuring this entanglement entropy by studying the quantum noise and higher order cumulants generated by two-electron scattering between the Fermi surface and the excitations. An experimental verification of the results obtained from our gedanken would pave the way towards systematic studies of many-particle entanglement and the Fermi surface.

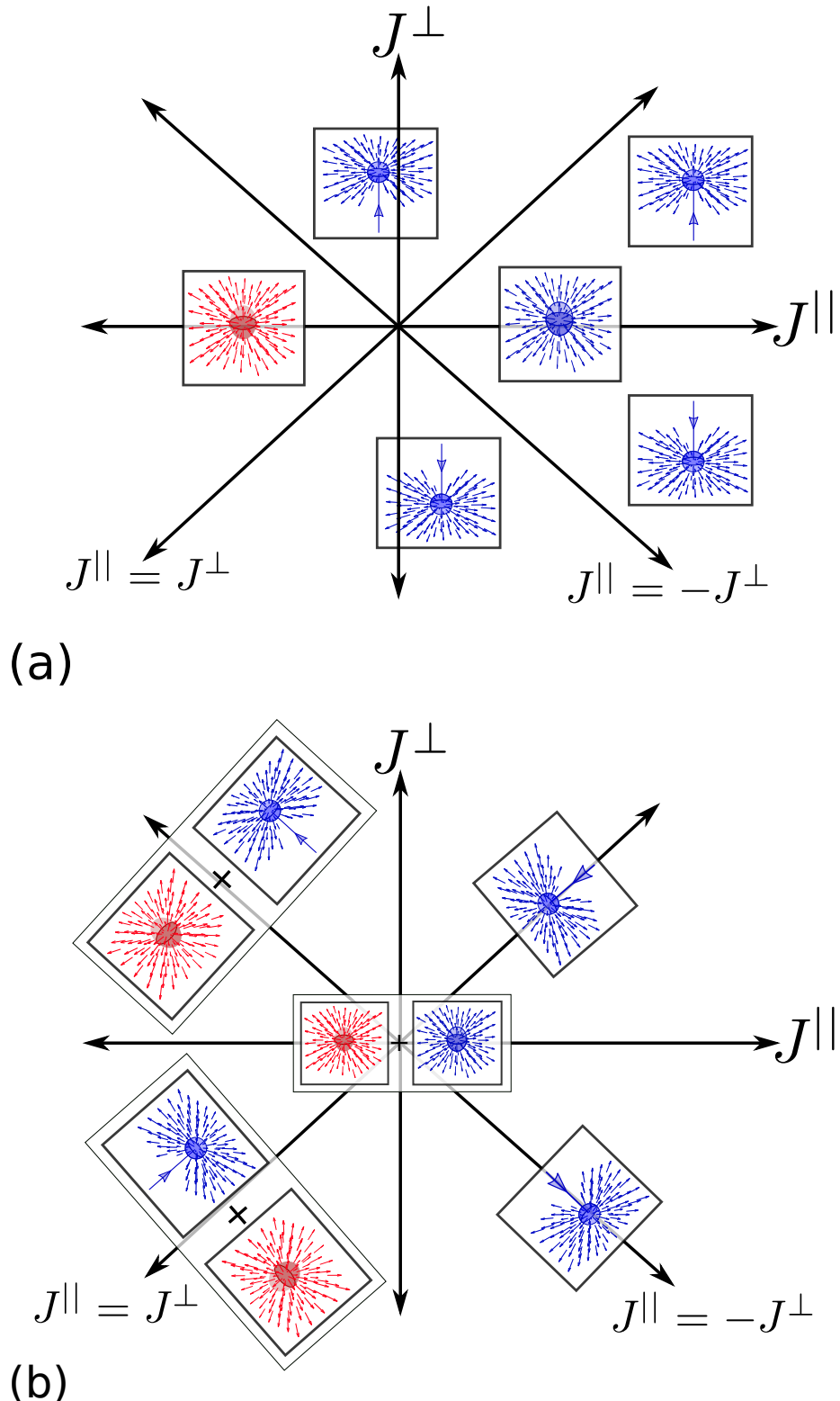


Figure 8.3.2: Fig.(a) corresponds to topological objects lying between the separatrices of the coupling ( $J^{\parallel}, J^{\perp}$ ) phase diagram obtained by studying the effective problem at the Fermi surface. Fig.(b) corresponds to the topological objects living on the separatrices, and at the critical point (the origin). Together, these two diagrams reveal the shape of the BKT RG phase diagram. See main text for detailed discussions.

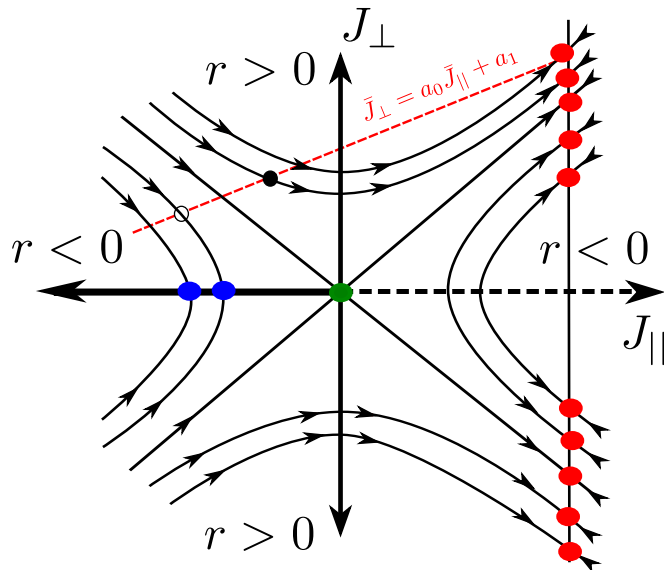


Figure 8.4.1: Nonperturbative BKT RG phase diagram for the LE/Mott instabilities of the TLL. The WZNW transitions are depicted by the separatrices (i.e., the  $r = 0$  trajectories). The red line drawn across trajectories shows the transition from the TLL fixed points (blue circles) to the LE/Mott phases (red circles). The dashed line (including the origin) corresponds to a line of interaction driven Fermi surface topology changing (Lifshitz) transitions of the Fermi surface.

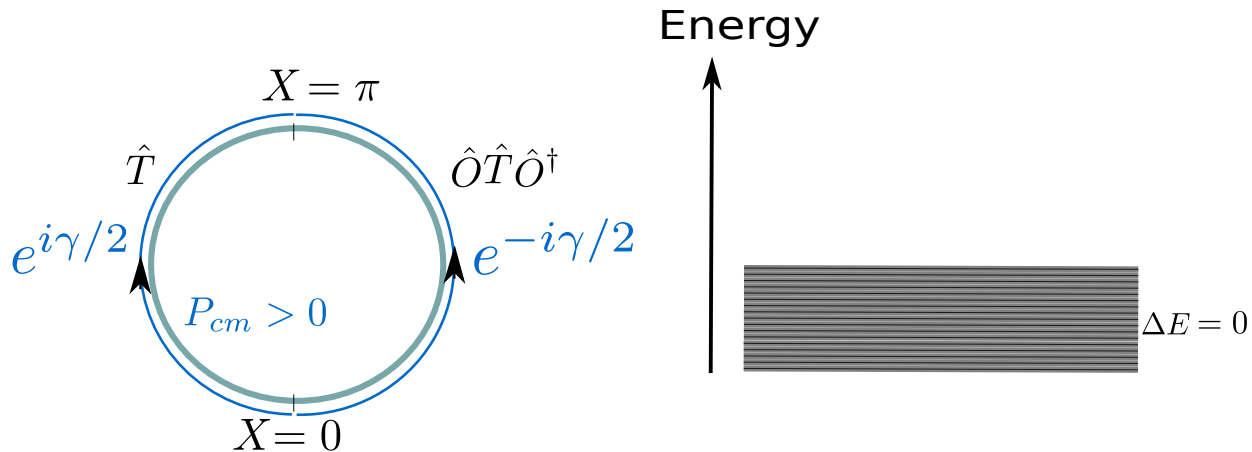


Figure 8.4.2: Destructive interference in the scattering processes involving the center of mass Hilbert space (left) leads to a gapless TLL metal (right). The interference shows up between two opposing trajectories involving the twist ( $\hat{O}$ ) and translation ( $\hat{T}$ ) operations of the c.o.m. position  $X$ , with phases  $\pm\gamma/2$  respectively.

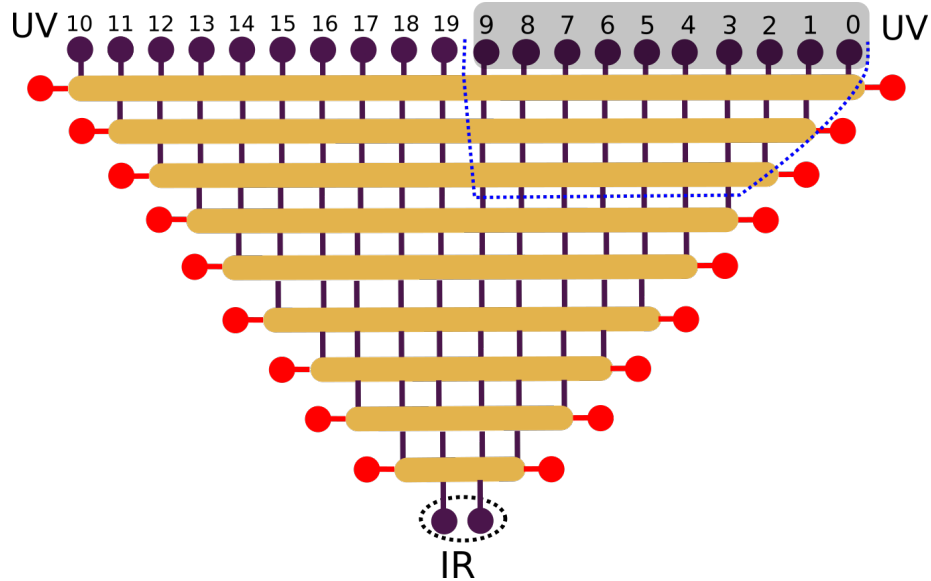


Figure 8.5.1: EHM representation of URG flow towards the LE ground state. The black nodes  $0, \dots, 9$  represent pseudospins with helicity  $\eta = +1$ , while  $10, \dots, 19$  represent pseudospins with  $\eta = -1$ . Together, they comprise the holographic boundary in the UV. Pseudospins are labelled in descending order of energy, such that the pair  $(0, 9)$  is associated with the highest energy. The energy of the pairs  $(1, 10), (2, 11), \dots$ , forms a monotonically decreasing sequence such that the  $(9, 19)$  pair is located at the Fermi energy. The yellow block represents the unitary map  $U_{(j)}$  that, at every step, disentangles the highest energy pair of pseudospins (represented by red nodes in the bulk of the EHM). The dotted circle around the pair of black nodes  $(9, 19)$  comprise the entangled ground state emergent in the IR. The grey box represents the region (nodes 0 to 9) in the UV that is being isolated by the blue dotted *minimal curve* from within the bulk of the network.

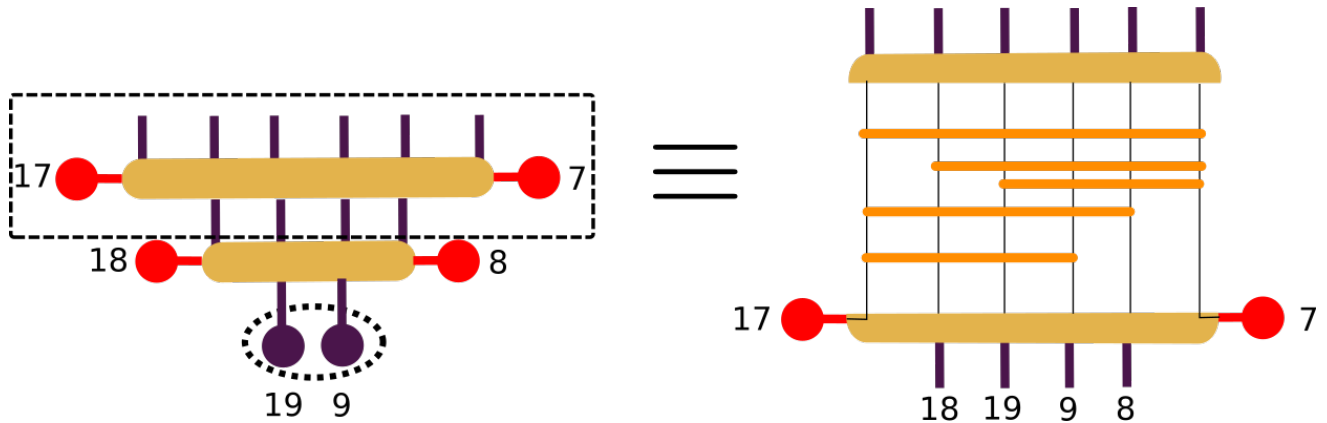


Figure 8.5.2: Decomposition of nonlocal unitary disentanglement map  $U_2$  into two-qubit disentanglers represented as orange blocks (within the right figure).  $U_2$  decouples the pseudospins/qubits  $|17\rangle$  and  $|7\rangle$  (red nodes) from the pseudospins  $|8\rangle, |9\rangle, |18\rangle, |19\rangle$  and has depth (d=number of orange blocks acting sequentially)  $d = 5$ . An orange block operates on the two pseudospins demarcated by the lines crossing its edges.

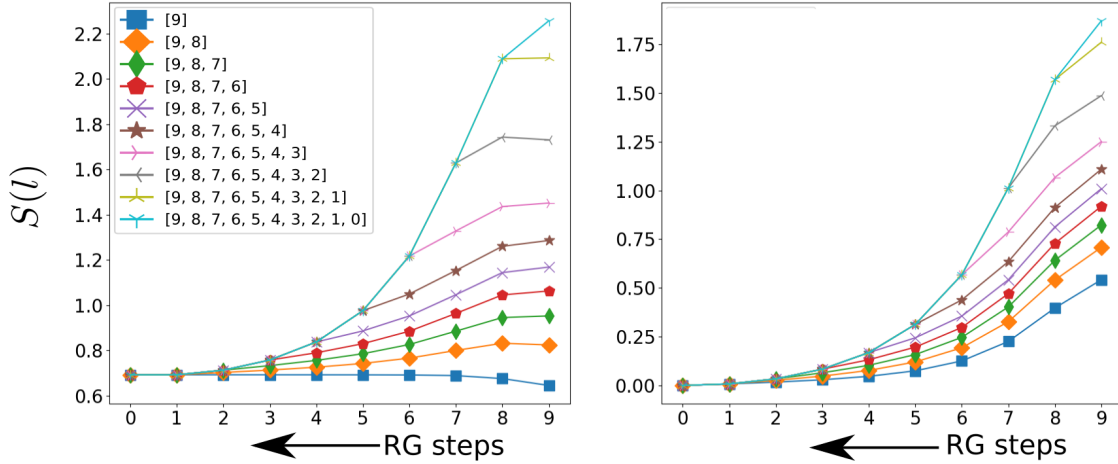


Figure 8.5.3: Entanglement Entropy  $S(l)$  renormalization for varying sizes of momentum-space blocks  $(9), (9, 8), (9, 8, 7), \dots, (9, 8, \dots, 0)$  (i.e.g, block size  $l$  ranging from 1 to 10) for (a) the LE and (b) the TLL phases. See discussion in main text.

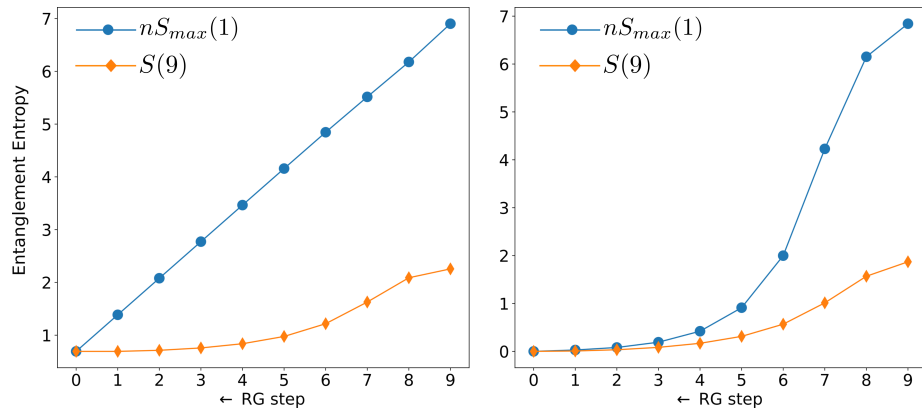


Figure 8.5.4: Blue and orange curves show the RG scaling of the holographic entanglement entropy bound and the entropy scaling of the the momentum-space block  $(9, \dots, 0)$ . Left panel represents the curves for the LE phase, and right panel for the TLL phase. The legend  $S(9)$  is the entanglement entropy generated by isolating block of size 9 units,  $S_{max}(1)$  is the maximum single-pseudospin EE and  $n$  the size of the minimal surface in the bulk of the EHM (varies with the RG step). See discussion in main text.

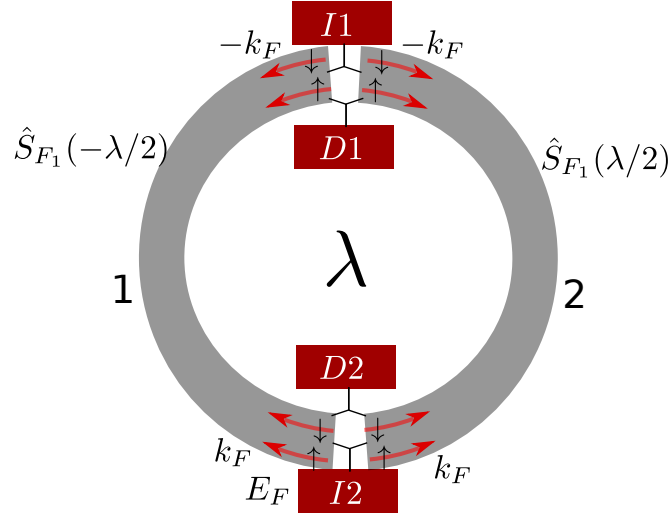


Figure 8.6.1: Thought experiment for probing the entanglement entropy related to two-particle scattering through transport measurements. Two open 1D systems 1 and 2 (at the brink of LE/Mott instability) are coupled to electron injectors  $I_1, I_2$  and detectors  $D_1, D_2$  via Y junctions. The ring geometry encloses a flux  $\lambda$ . The Y junctions of injectors  $I_1$  and  $I_2$  feed two electrons ( $|\uparrow_{Fa}\downarrow_{Fb}\rangle$ ) to either system 1 or 2. This results in a superposition state  $\Psi_s^F(\lambda)$  created by the scattering process described by matrices  $S_{F_1}(\lambda/2)$  and  $S_{F_1}(-\lambda/2)$ . See main text for discussions.

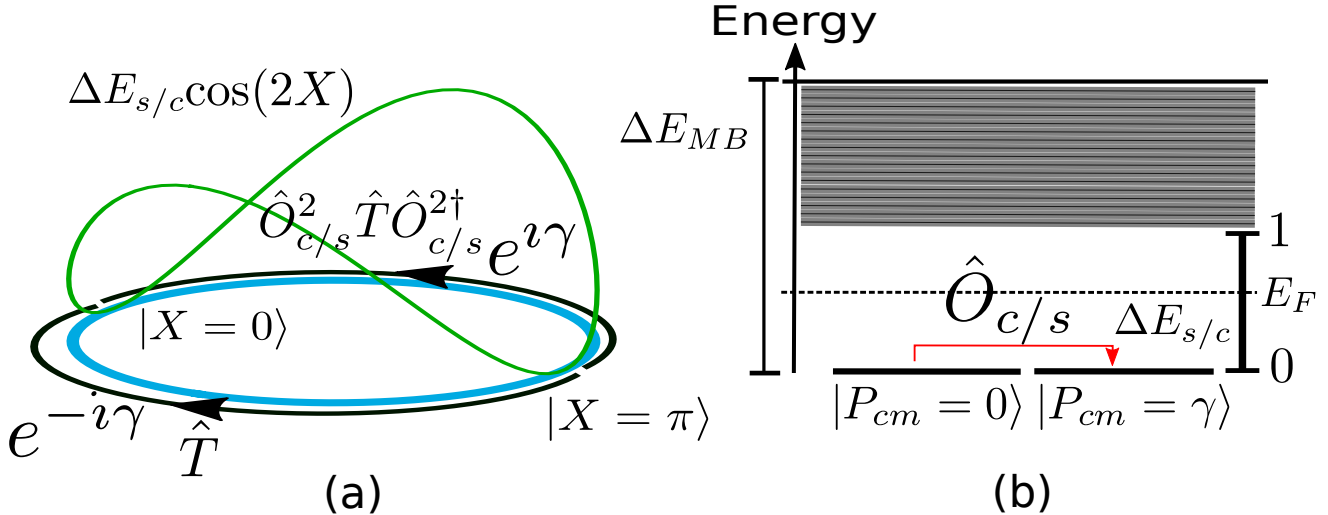


Figure 8.7.1: Constructive interference phenomenon for scattering processes on the center of mass Hilbert space described by basis  $\mathcal{B}_\pi$  in eq.(8.108) (left). The interference shows up between two opposing trajectories involving the twist ( $\hat{O}^2$ ) and translation ( $\hat{T}$ ) operations of the c.o.m. position  $X$ , with phases  $\pm\gamma$  respectively. This leads to a *spin/charge gap* ( $\Delta E_{s/c}$ ) around the Fermi energy  $E_F$ , along with the standard many-body gap  $\Delta E_{MB}$  demarcating the low energy window  $L_{n^*}$  (right). The green curve within the left figure corresponds to the interaction induced potential ( $\Delta E_{s/c} \cos(2X)$ ) within the c.o.m. Hamiltonian. See main text for discussions.

# Appendix

## 8.A RG equation for the BCS instability

Starting from the Hamiltonian RG flow eq.(8.55), and accounting only for two-particle vertices in the Hamiltonian given in eq.(8.57), we obtain the renormalisation of the Hamiltonian as

$$\begin{aligned} \Delta H_{(j)} &= \sum_{\kappa, \kappa_1, p, \eta} \left[ c_{\kappa(p, \eta)}^\dagger c_{\kappa'(p, \eta)}^\dagger c_{\kappa'_1(p, \eta)} c_{\kappa_1(p, \eta)} \frac{(K^{(j)}(p))^2 \tau_{\kappa_j(p, -\eta)} \tau_{\kappa'_j(p, -\eta)}}{[G_{j,p}]^{-1} - V^{(j)}(p) \tau_{\kappa_j(p, -\eta)} \tau_{\kappa'_j(p, -\eta)}} \right. \\ &\quad \left. + c_{\kappa(p, \eta)}^\dagger c_{\kappa'(p, \eta)}^\dagger c_{\kappa'_1(p, -\eta)} c_{\kappa_1(p, -\eta)} \frac{K^{(j)}(p) V^{(j)}(p) \tau_{\kappa_j(p, -\eta)} \tau_{\kappa'_j(p, -\eta)}}{[G_{j,p}]^{-1} - V^{(j)}(p) \tau_{\kappa_j(p, -\eta)} \tau_{\kappa'_j(p, -\eta)}} \right]. \end{aligned} \quad (8.130)$$

Here,

$$G_{j,p}^{-1} = \omega - \epsilon_{\kappa_j} \tau_{\kappa_j(p, -\eta)} - \epsilon_{\kappa'_j} \tau_{\kappa'_j(p, -\eta)}. \quad (8.131)$$

Importantly, we note that in obtaining the denominator of the above RG equation, we have limited the study of the quantum fluctuation scale  $\hat{\omega}_{(j)}$  to only the one-particle dispersion

$$\begin{aligned} \hat{\omega}_{(j)} &= \sum_i (\epsilon_i + \Sigma_i^{(j-1)}) \left( \hat{n}_i - \frac{1}{2} \right) + \sum_{a,b} \Gamma_{a,b}^{4,(j-1)} \left( \hat{n}_a - \frac{1}{2} \right) \left( \hat{n}_b - \frac{1}{2} \right) + \dots + \Delta H_{(j)}^X \\ &\approx \sum_i (\epsilon_i + \Sigma_i^{(j-1)}) \left( \hat{n}_i - \frac{1}{2} \right). \end{aligned} \quad (8.132)$$

We interpret the various quantum fluctuation eigenvalues  $\omega$  of the operator  $\hat{\omega}_{(j)}$  as an inherent quantum parameter arising out of the renormalization of the interaction vertices, and study thereby the RG equations as a function of  $\omega$ .

The vertex RG flow equations for the forward ( $K$ ) and backscattering ( $V$ ) vertices are then obtained as

$$\begin{aligned} \Delta K^{(j)}(p) &= \frac{4K^{(j)}(p)V^{(j)}(p)\tau_{\kappa_j(p, -\eta)}\tau_{\kappa'_j(p, -\eta)}}{[G_{j,p}]^{-1} - V^{(j)}(p)\tau_{\kappa_j(p, -\eta)}\tau_{\kappa'_j(p, -\eta)}}, \\ \Delta V^{(j)}(p) &= \frac{4(K^{(j)}(p))^2\tau_{\kappa_j(p, -\eta)}\tau_{\kappa'_j(p, -\eta)}}{[G_{j,p}]^{-1} - V^{(j)}(p)\tau_{\kappa_j(p, -\eta)}\tau_{\kappa'_j(p, -\eta)}}. \end{aligned} \quad (8.133)$$



# Chapter 9

## URG study of the Kondo model: unveiling the Kondo cloud

In this chapter we will study the single channel Kondo problem via the URG approach, i.e., the physics of screening of a magnetic impurity via coupling with a conduction electron bath. The thermodynamic properties and universal characteristics of the single channel Kondo problem has been extensively studied in the past using various methods, starting from Kondo's perturbation theory solution [300], the Coulomb gas approach [397, 398], the poor man scaling approach [301], Bethe Ansatz calculations [401, 400], Wilson's numerical RG approach [93, 281] and the conformal field theory (CFT) approach [402, 403]. Another important strong coupling approach based on arguments of scattering phase shifts is that of the local Fermi liquid theory [399, 580]. We have already reviewed the extensive literature on this celebrated problem in Sec.9 of the introduction (Chapter1).

However, the form of the effective Hamiltonian governing the low- energy physics of the Kondo cloud, and the form of the many-body singlet wavefunction, has remained a challenge. Further, the entanglement properties of the constituents of the Kondo cloud [581] is a matter of recent studies. The rest of the chapter is outlined as follows. In Sec.9.1, we introduce the single channel Kondo model, and perform a URG analysis of it in Sec.9.2. Sec.9.3 constitutes results on the scaling of the Kondo coupling, various low-energy fixed points and their respective effective Hamiltonians and ground state wavefunction. In Sec.9.4, we derive the local Fermi liquid theory. In Sec.9.5 and Sec.9.6, we compute various well studied thermodynamics signatures for the Kondo problem and benchmark them with the literature. In Sec.9.7, we study the entanglement features and many-body correlations of the Kondo cloud. Finally, we conclude in Sec.9.8.

### 9.1 The Model

The Kondo model [300, 301] describes the coupling between a magnetic quantum impurity localized in real space with a bath of conduction electrons

$$\hat{H} = \sum_{\mathbf{k}\sigma} \epsilon_{\mathbf{k}} \hat{n}_{\mathbf{k}\sigma} + \frac{J}{2} \sum_{\mathbf{k}, \mathbf{k}'} \mathbf{S} \cdot c_{\mathbf{k}\alpha}^\dagger \boldsymbol{\sigma}_{\alpha\beta} c_{\mathbf{k}'\beta} . \quad (9.1)$$

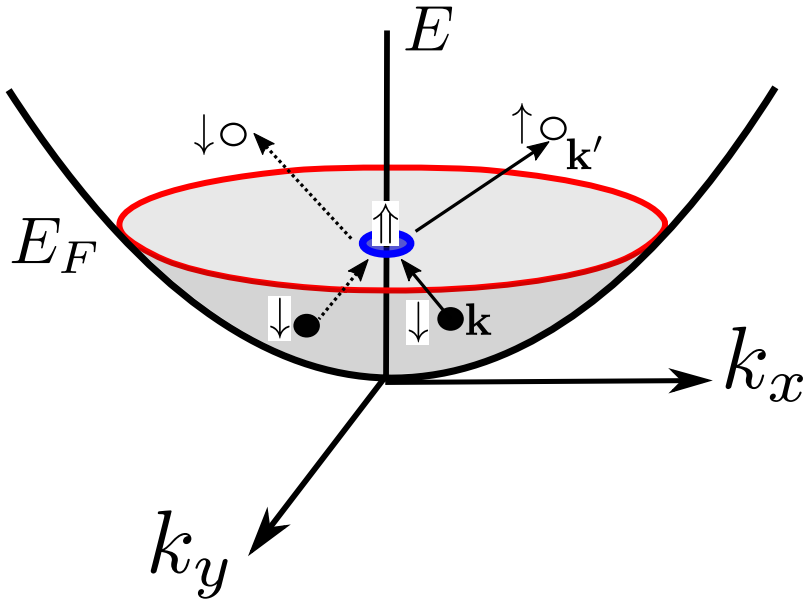


Figure 9.2.1: The Kondo model is composed of a two-dimensional conduction electron bath (Fermi liquid) coupled to a magnetic impurity via a spin-flip (solid) / non spin-flip (dashed) scattering coupling.

Here, we consider a 2D electronic bath  $\epsilon_{\mathbf{k}} = -2t(\cos k_x + \cos k_y)$  with the Fermi energy  $E_F = \mu$ .  $J$  is the Kondo scattering coupling between the impurity and the conduction electrons. An important feature of the Kondo coupling is the two different classes of scattering processes: one involving spin-flip scattering processes for the bath electrons ( $c_{\mathbf{k}\uparrow}^\dagger c_{\mathbf{k}'\downarrow} + h.c.$ ), and the other not (i.e., simple potential scattering processes). In the antiferromagnetic regime  $J > 0$ , the spin-flip scattering processes generates quantum entanglement between the impurity spin and a macroscopic number of bath electrons (called the “Kondo cloud”), resulting in the complete screening of the impurity via the formation of a singlet spin state. It is clear that the dynamical Kondo cloud corresponds to an effective single spin-1/2, such that the screening is an example of macroscopic quantum entanglement arising from electronic correlations. It is the nature of this entanglement, and the underlying quantum liquid that forms the Kondo cloud, that we seek to learn more of.

## 9.2 URG Theory for the Kondo model

In constructing an effective low-energy theory for the Kondo singlet, we employ the unitary RG formalism to the Kondo model such that electronic states from the non-interacting conduction bath are stepwise disentangled, starting with the highest energy electrons at the bandwidth and eventually scaling towards the FS. While this aspect is similar to Anderson’s poor man’s scaling [301], we shall see that several other aspects of the unitary RG formalism are different from those adopted in the poor man’s scaling approach. The electronic states are labelled in terms of the normal distance  $\Lambda$  from the FS and the orientation unit vectors (Fig.9.2.2)  $\hat{s}$ :  $\mathbf{k}_{\Lambda\hat{s}} = \mathbf{k}_F(\hat{s}) + \Lambda\hat{s}$ , where  $\hat{s} = \frac{\nabla\epsilon_{\mathbf{k}}}{|\nabla\epsilon_{\mathbf{k}}|}|_{\epsilon_{\mathbf{k}}=E_F}$ . The states are labelled as  $|j, l, \sigma\rangle = |\mathbf{k}_{\Lambda_j\hat{s}}, \sigma\rangle$ ,  $l := (\hat{s}_m, \sigma)$ .

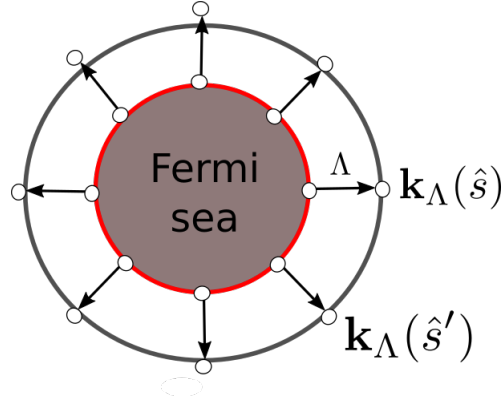


Figure 9.2.2: Fermi surface geometry for a circular Fermi volume of non-interacting electrons in 2 spatial dimensions.

The  $\Lambda$ 's are arranged as follows:  $\Lambda_N > \Lambda_{N-1} > \dots > 0$ , where the electronic states farthest from FS  $\Lambda_N$  are disentangled first, eventually scaling towards the FS. This leads to the Hamiltonian flow equation

$$H_{(j-1)} = U_{(j)} H_{(j)} U_{(j)}^\dagger , \quad (9.2)$$

where the unitary operation  $U_{(j)}$  is the unitary map at RG step  $j$ .  $U_{(j)}$  disentangles all the electronic states  $|\mathbf{k}_{\Lambda_j \hat{s}_m}, \sigma\rangle$  on the isogeometric curve and has the form[180]

$$U_{(j)} = \prod_l U_{j,l}, U_{j,l} = \frac{1}{\sqrt{2}} [1 + \eta_{j,l} - \eta_{j,l}^\dagger] , \quad (9.3)$$

where  $\eta_{j,l}$  are electron-hole transition operators following the algebra

$$\{\eta_{j,l}, \eta_{j,l}^\dagger\} = 1 , \quad [\eta_{j,l}, \eta_{j,l}^\dagger] = 1 . \quad (9.4)$$

The transition operator can be represented in terms of the diagonal ( $H^D$ ) and off-diagonal ( $H^X$ ) parts of the Hamiltonian as follows

$$\eta_{j,l} = Tr_{j,l}(c_{j,l}^\dagger H_{j,l}) c_{j,l} \frac{1}{\hat{\omega}_{j,l} - Tr_{j,l}(H_{j,l}^D \hat{n}_{j,l}) \hat{n}_{j,l}} . \quad (9.5)$$

We note that in the numerator of the expression for  $\eta_{j,l}$ , the operator  $Tr_{j,l}(c_{j,l}^\dagger H_{j,l}) c_{j,l} + h.c.$  is composed of all possible scattering vertices that modify the configuration of the electronic state  $|j, l\rangle$ . The generic forms of  $H_{j,l}^D$  and  $H_{j,l}^X$  are as follows

$$\begin{aligned} H_{j,l}^D &= \sum_{\Lambda \hat{s}, \sigma} \epsilon^{j,l} \hat{n}_{\mathbf{k}_{\Lambda \hat{s}}, \sigma} + \sum_{\alpha} \Gamma_{\alpha}^{4,(j,l)} \hat{n}_{\mathbf{k}_{\sigma}} \hat{n}_{\mathbf{k}'_{\sigma'}} + \sum_{\beta} \Gamma_{\beta}^{8,(j,l)} \hat{n}_{\mathbf{k}_{\sigma}} \hat{n}_{\mathbf{k}'_{\sigma'}} (1 - \hat{n}_{\mathbf{k}''_{\sigma''}}) + \dots , \\ H_{j,l}^X &= \sum_{\alpha} \Gamma_{\alpha}^2 c_{\mathbf{k}_{\sigma}}^\dagger c_{\mathbf{k}'_{\sigma'}} + \sum_{\beta} \Gamma_{\beta}^2 c_{\mathbf{k}_{\sigma}}^\dagger c_{\mathbf{k}'_{\sigma'}}^\dagger c_{\mathbf{k}'_{\sigma'_1}} c_{\mathbf{k}_1 \sigma_1} + \dots . \end{aligned} \quad (9.6)$$

The operator  $\hat{\omega}_{j,l}$  accounts for the quantum fluctuations arising from the non-commutativity between different parts of the renormalized Hamiltonian and has the following form [182]

$$\hat{\omega}_{j,l} = H_{j,l}^D + H_{j,l}^X - H_{j,l-1}^X . \quad (9.7)$$

Upon disentangling electronic states  $\hat{s}, \sigma$  along a isogeometric curve at distance  $\Lambda_j$ , the following effective Hamiltonian  $H_{j,l}$  is generated

$$H_{j,l} = \prod_{m=1}^l U_{j,m} H_{(j)} \left[ \prod_{m=1}^l U_{j,m} \right]^\dagger. \quad (9.8)$$

We note that  $H_{j,2n_j+1} = H_{(j-1)}$  is the Hamiltonian obtained after disentangling all the electronic states on the isogeometric curve  $j$ . Below we depict the different terms generated upon successive disentanglement of the states  $|\mathbf{k}_{\Lambda_j \hat{s}_l}, \sigma\rangle$  on a given curve,

$$\begin{aligned} H_{j,l+1} &= Tr_{j,l}(H_{(j,l)}) + \{c_{j,l}^\dagger Tr_{j,l}(H_{(j,l)} c_{j,l}), \eta_{j,l}\} \tau_{j,l}, \tau_{j,l} = \hat{n}_{j,l} - \frac{1}{2} \\ H_{j,l+2} &= Tr_{j,l+1}(Tr_{j,l}(H_{(j,l)})) + Tr_{j,l+1}(\{c_{j,l}^\dagger Tr_{j,l}(H_{(j,l)} c_{j,l}), \eta_{j,l}\} \tau_{j,l}) \\ &\quad + \{c_{j,l+1}^\dagger Tr_{j,l+1}(Tr_{j,l}(H_{(j,l)} c_{j,l+1}), \eta_{j,l+1}\} \tau_{j,l+1} \\ &\quad + \{c_{j,l+1}^\dagger Tr_{j,l+1}(\{c_{j,l}^\dagger Tr_{j,l}(H_{(j,l)} c_{j,l}), \eta_{j,l}\} c_{j,l+1}), \eta_{j,l+1}\} \tau_{j,l} \tau_{j,l+1}. \\ H_{j,l+3} &= \dots \text{terms with } \tau_{j,l}, \tau_{j,l+1}, \tau_{j,l+2} \dots \\ &\quad + \dots \text{terms with } \tau_{j,l} \tau_{j,l+1}, \tau_{j,l+1} \tau_{j,l+2}, \tau_{j,l} \tau_{j,l+2} \dots \\ &\quad + \dots \text{terms with } \tau_{j,l} \tau_{j,l+1} \tau_{j,l+2}. \end{aligned} \quad (9.9)$$

Upon disentangling multiple electronic states placed in the tangential direction on a given momentum shell at distance  $\Lambda_j$  generates RG contribution from leading order scattering processes (terms multiplied with  $\tau_{j,l}, \tau_{j,l+1}$ , etc.) that goes as  $\text{Area}/\text{Vol} = 1/L$  and higher order processes like terms multiplied with  $\tau_{j,l} \tau_{j,l+1}$  that goes as  $(\text{Area})^2/\text{Vol}^2 = 1/L^2$ ,  $\tau_{j,l} \tau_{j,l+1} \tau_{j,l+2}$  that goes as  $(\text{Area})^3/\text{Vol}^3 = 1/L^3$ . Here, each factor of area arises from decoupling an entire shell of single-particle states ( $\tau_{j,l}$ ) at every RG step, and every factor of volume arises from the Kondo coupling. Accounting for only the leading tangential scattering processes, as well as other momentum transfer processes along the normal direction  $\hat{s}$ , the renormalized Hamiltonian has the form

$$H_{(j-1)} = Tr_{j,(1,\dots,2n_j)}(H_{(j)}) + \sum_{l=1}^{2n_j} \{c_{j,l}^\dagger Tr_{j,l}(H_{(j)} c_{j,l}), \eta_{j,l}\} \tau_{j,l}. \quad (9.10)$$

Here,  $2n_j$  are the number of electronic states on the isogeometric curve at distance  $\Lambda_j$ , and  $\tau_{j,l} = n_{j,l} - \frac{1}{2}$ .

### 9.3 RG flow to the IR fixed point

The unitary RG process generates the effective Hamiltonian's  $\hat{H}_{(j)}(\omega)$ 's for various eigen directions  $|\Phi(\omega)\rangle$  of the  $\hat{\omega}$  operator. Note the associated eigenvalue  $\omega$  identifies a subspectrum in the interacting many body eigenspace. The form of  $\hat{H}_{(j)}(\omega)$  is given by,

$$\hat{H}_{(j)}(\omega) = \sum_{j,l,\sigma} \epsilon_{j,l} \hat{n}_{j,l} + \frac{J^{(j)}(\omega)}{2} \sum_{\substack{j_1,j_2 < j, \\ m,m'}} \mathbf{S} \cdot c_{j_1, \hat{s}_m, \alpha}^\dagger \boldsymbol{\sigma}_{\alpha\beta} c_{j_2, \hat{s}_{m'}, \beta} + \sum_{a=N, m=1}^{j,n_j} J^{(a)} S^z s_{a, \hat{s}, m}^z, \quad (9.11)$$

where  $s_{l,\hat{s},m}^z = \frac{1}{2}(\hat{n}_{l,\hat{s}_m,\uparrow} - \hat{n}_{l,\hat{s}_m,\downarrow})$ . The Kondo coupling RG equation for the RG steps (Appendix 9.A) has the form,

$$\frac{\Delta J^{(j)}(\omega)}{\Delta \log \frac{\Lambda_j}{\Lambda_0}} = \frac{n_j(J^{(j)})^2 \left[ (\omega - \frac{\hbar v_F \Lambda_j}{2}) \right]}{(\omega - \frac{\hbar v_F \Lambda_j}{2})^2 - \frac{(J^{(j)})^2}{16}}, \quad (9.12)$$

where  $n_j = \sum_{\hat{s}} 1$  is the number of states on the isogeometric shell at distance  $\Lambda_j$  from the Fermi surface. Note that the denominator  $\Delta \log \frac{\Lambda_j}{\Lambda_0} = 1$  for the RG scale parameterization  $\Lambda_j = \Lambda_0 \exp(-j)$ . We now redefine Kondo coupling as a dimensionless parameter

$$K^{(j)} = \frac{J^{(j)}}{\omega - \frac{\hbar v_F}{2} \Lambda_j}, \quad (9.13)$$

and operate in the regime  $\omega > \frac{\hbar v_F}{2} \Lambda_j$ . With the above parametrization of eq.(9.13), we can convert the difference RG relation (eq.(9.12)) into a continuum RG equation

$$\frac{dK}{d \log \frac{\Lambda}{\Lambda_0}} = \left( 1 - \frac{\omega}{\omega - \hbar v_F \Lambda} \right) K + \frac{n(\Lambda) K^2}{1 - \frac{K^2}{16}} \quad (9.14)$$

Upon approaching the Fermi surface  $\Lambda_j \rightarrow 0$ ,  $\left( 1 - \frac{\omega}{\omega - \hbar v_F \Lambda} \right) \rightarrow 0$  and  $n(\Lambda)$  can be replaced by density of states on the Fermi surface  $n(0)$ :

$$\frac{dK}{d \log \frac{\Lambda}{\Lambda_0}} = \frac{n(0) K^2}{1 - \frac{K^2}{16}} \quad (9.15)$$

At this point, we observe an important aspect of the RG equation: for  $K \ll 1$ , the RG equation

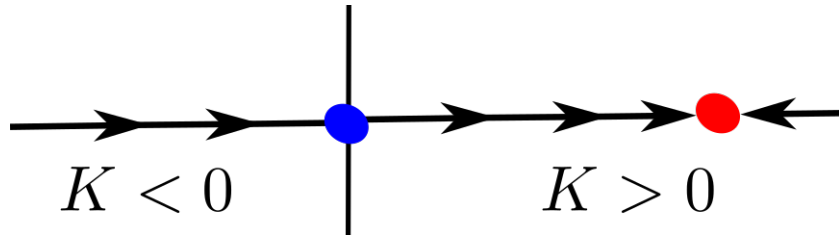


Figure 9.3.1: Schematic RG phase diagram for the Kondo problem. The red dot represents intermediate coupling fixed point at  $K^* = 4$  for the case of the AFM Kondo coupling. The blue dot represents the critical fixed point at  $K^* = 0$  for the case of the FM Kondo coupling.

reduces to the one loop form:  $\frac{dK}{d \log \frac{\Lambda}{\Lambda_0}} = K^2$  [301]. On the other hand, the nonperturbative form of the flow equation obtained from the URG formalism shows the presence of intermediate coupling fixed point at  $K^* = 4$  in the antiferromagnetic regime  $K > 0$ . Upon integrating the RG equation and using the fixed point value  $K^* = 4$  we obtain the Kondo energy scale ( $T_K$ ) and thence the

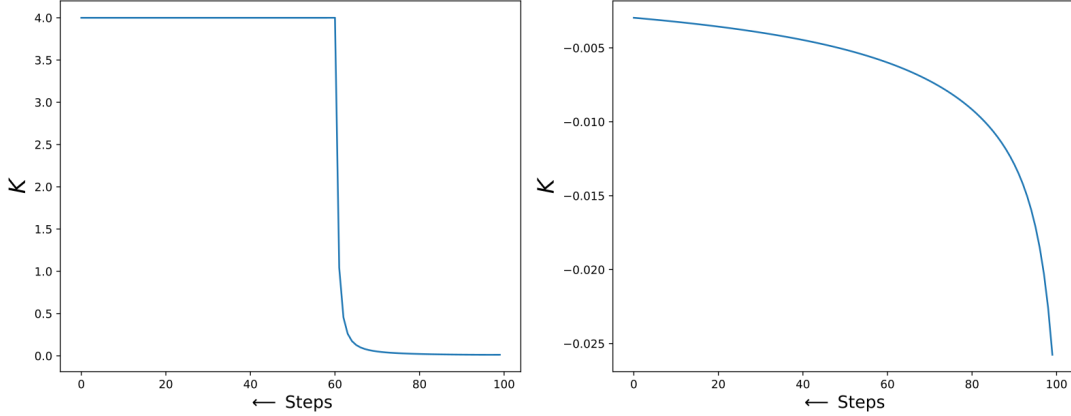


Figure 9.3.2: Renormalized dimensionless Kondo coupling  $K$  with RG steps ( $\log \Lambda_j / \Lambda_0$ ) for left panel:  $K > 0$ , and right panel:  $K < 0$ . The growth of the Kondo coupling to a finite value of the intermediate coupling fixed point is evident in the left panel, while the decay to zero at the critical fixed point can be seen in the right panel. For these plot, we chose  $\omega = \hbar v_F \Lambda_j$ .

effective length of the Kondo cloud ( $\xi_K$ )

$$\frac{1}{K_0} - \frac{1}{2} + \frac{K_0}{16} = -n(0) \log \frac{\Lambda^*}{\Lambda_0}, \quad (9.16)$$

$$\Lambda^* = \Lambda_0 \exp \left( \frac{1}{2n(0)} - \frac{1}{n(0)K_0} - \frac{K_0}{n(0)16} \right), \quad (9.17)$$

$$T_K = \frac{\hbar v_F \Lambda^*}{k_B} = \frac{\hbar v_F \Lambda_0}{k_B} \exp \left( \frac{1}{2n(0)} - \frac{1}{n(0)K_0} - \frac{K_0}{n(0)16} \right), \quad (9.18)$$

$$\xi_K = \frac{2\pi}{\Lambda^*} = \frac{hv_F}{k_B T_K} = \frac{2\pi}{\Lambda_0} \exp \left( -\frac{1}{2n(0)} + \frac{1}{n(0)K_0} + \frac{K_0}{n(0)16} \right). \quad (9.19)$$

At the IR fixed point in the AF regime the effective Hamiltonian is given by,

$$H^* = \sum_{|\Lambda| < \Lambda^*} \hbar v_F \Lambda \hat{n}_{\Lambda, \hat{s}, \sigma} + \frac{J^*}{2} \sum_{\substack{j_1, j_2 \leq j^*, \\ m, m'}} \mathbf{S} \cdot c_{j_1, \hat{s}_m, \alpha}^\dagger \boldsymbol{\sigma}_{\alpha\beta} c_{j_2, \hat{s}_{m'}, \beta} + \sum_{j'=N, m=1}^{j^*, n_{j'}} J^{j'} S^z s_{j', m}^z, \quad (9.20)$$

where  $m$  refers to the various normal directions  $\hat{s}_m$  of the Fermi surface. In the above equation, the second term is the effective Hamiltonian for the coupling of the Kondo cloud to the impurity spin, while the third encodes the interaction between the impurity spin moment and the decoupled electronic degrees of freedom that do not belong to the Kondo cloud (lying on radial shells in momentum-space indexed by the RG step  $j$ ). When taken together with the first term (the kinetic energy/dispersion of the lattice conduction electrons), the third gives rise to the local Fermi liquid of Nozieres. In this way, it can be viewed as a (mean-field) self-energy for the decoupled electrons in the  $j'$  shell arising from their interaction with the impurity spin

$$\Sigma_{j'}^{dec} = J^{j'} \langle S^z \rangle. \quad (9.21)$$

As shown in Fig.9.3.2 (left panel), the local nature of the Fermi liquid can be seen by the rapid rise of the coupling  $J^j = 2K_j\epsilon_j$  with RG step/shell index  $j$  only very near to where the Kondo coupling saturates (signalling the Kondo cloud formation). For this plot, we chose  $\omega = \hbar v_F \Lambda_j$ , i.e., the energy cost for the spin-flip scattering of a single electron. We will see the exact derivation in detail in a subsequent section.

We can now extract a zero mode from the above Hamiltonian that captures the low energy theory near the Fermi surface,

$$\begin{aligned} H_{coll} &= \frac{1}{N} \sum_{|\Lambda| < \Lambda^*} \hbar v_F \Lambda \sum_{|\Lambda| < \Lambda^*} \hat{n}_{\Lambda, \hat{s}, \sigma} + \frac{J^*}{2} \sum_{\substack{j_1, j_2 < j^*, \\ m, m'}} \mathbf{S} \cdot c_{j_1, \hat{s}_m, \alpha}^\dagger \boldsymbol{\sigma}_{\alpha\beta} c_{j_2, \hat{s}_{m'}, \beta} + \sum_{j'=N, m=1}^{j^*, n_{j'}} J^{j'} S^z s_{j', m}^z \\ &= \frac{J^*}{2} \sum_{\substack{j_1, j_2 < j^*, \\ m, m'}} \mathbf{S} \cdot c_{j_1, \hat{s}_m, \alpha}^\dagger \boldsymbol{\sigma}_{\alpha\beta} c_{j_2, \hat{s}_{m'}, \beta} + \sum_{j'=N, m=1}^{j^*, n_{j'}} J^{j'} S^z s_{j', m}^z, \end{aligned} \quad (9.22)$$

where the first term vanishes as the sum over wavevector  $\Lambda$  within the symmetric window  $\Lambda^*$  around the Fermi surface itself vanishes.

Indeed, we observe that the zero mode Hamiltonian at the IR fixed point is responsible for the formation of the Kondo singlet ground state

$$|\Psi^*\rangle = \frac{1}{\sqrt{2}} \left[ |\uparrow\rangle \sum_{\Lambda, \hat{s}} |1_{\Lambda, \hat{s}, \downarrow}\rangle \otimes_{\Lambda' \neq \Lambda, \hat{s}' \neq \hat{s}} |\Lambda', \hat{s}'\rangle - |\downarrow\rangle \sum_{\Lambda, \hat{s}} |1_{\Lambda, \hat{s}, \uparrow}\rangle \otimes_{\Lambda' \neq \Lambda, \hat{s}' \neq \hat{s}} |\Lambda', \hat{s}'\rangle \right]. \quad (9.23)$$

Note that this state will be in direct product with the wavefunction for the decoupled electronic degrees of freedom.

### 9.3.1 Variation of the Kondo cloud size $\xi_K$ and effective Kondo coupling $J^*$ as function of bare coupling $J_0$

In Fig.9.3.3, we show the variation of the Kondo cloud size  $\xi_K$  and effective Kondo coupling  $J^*$  as function of bare coupling  $J$  (in units of  $t$ ) in the range  $5.7 \times 10^{-5} < J < 5.4$ . All plots below are obtained for momentum-space grid  $100 \times 100$  and with RG scale factor  $\Lambda_j = b\Lambda_{j+1}$  ( $b = 0.9999 = 1 - 1/N * N$ ,  $N = 100$ ). The  $E_F$  for the 2d tight binding band  $-W/2 < E_k = -2t(\cos k_x + \cos k_y) < W/2$  ( $W = 4t$ ) is chosen at  $E_F = -3.9t$ , and the bare  $k$ -space cutoff is set at  $\Lambda_0 \simeq 2.83$ .

The variation of the renormalised Kondo coupling  $J^*$  with the bare  $J$  shown in Fig.9.3.3 clearly indicates the flow under RG towards saturation at a strong coupling value of  $J_{sat}^* \sim 16$ . Similarly, the variation of the Kondo screening length  $\xi_K$  with  $J$  shows a fall to an asymptotic value of  $\xi_K \sim 3$  lattice sites at the strong coupling fixed point. We recall that Wilson's NRG calculation for the Kondo problem (for a bath of conduction electrons in the continuum with linear dispersion and a very large UV cutoff  $D$ ) shows that the renormalised Kondo coupling  $J^* \rightarrow \infty$  under flow to strong coupling. This can be reconciled from our URG results by noting that the value of  $J_{sat}^*$  increases upon rescaling the conduction bath bandwidth  $D$  to larger values (by rescaling the nearest neighbour hopping strength  $t$ ). This is shown in Fig.9.3.4, where we see that  $J_{sat}^*$

increases from a value of  $\mathcal{O}(1)$  (in units of  $t$ ) to  $\mathcal{O}(10^9)$  as  $t$  is increased from  $\mathcal{O}(1)$  to  $\mathcal{O}(10^4)$ . Thus, taking the limit of  $D \rightarrow \infty$  will lead to  $J_{sat}^* \rightarrow \infty$ .

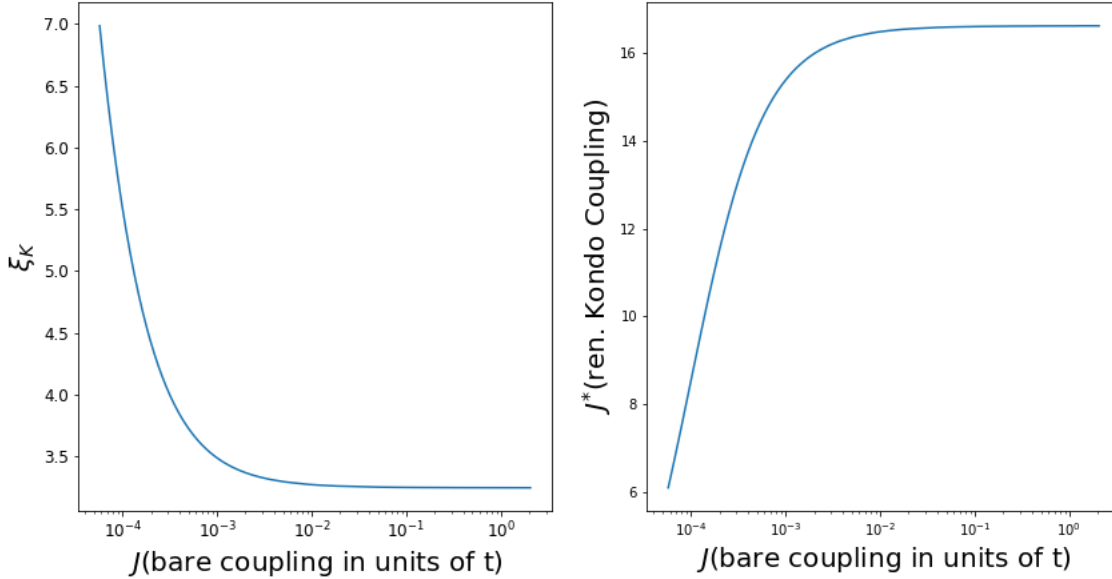


Figure 9.3.3: Left panel: Kondo cloud length  $\xi$  vs. bare Kondo coupling  $J$  (x-axis in log scale) in , right panel: renormalized Kondo coupling  $J^*$  vs.  $J$  (x-axis in log scale). The bare Kondo coupling  $J$  is chosen to lie within the range  $5.7 \times 10^{-5} < J < 5.4$ .

## 9.4 Derivation of the local Fermi liquid effective Hamiltonian

We begin by recalling the effective collective Hamiltonian obtained from the URG at the IR fixed point

$$H_{coll} = J^* \mathbf{S} \cdot \mathbf{s} + \sum_{l=N, m=1}^{j^*, n_l} J_l S^z s_{l,m}^z + \sum_{l=N, m=1}^{j^*, n_l} \epsilon_l (\hat{n}_{l,m,\uparrow} + \hat{n}_{l,m,\downarrow}) \quad (9.24)$$

The thermal density matrix at finite temperatures is then

$$\rho = \exp(-\beta H_{coll}) = \prod_{l=N, m=1}^{j^*, n_l} \exp(-\beta \epsilon_l (\hat{n}_{l,m,\uparrow} + \hat{n}_{l,m,\downarrow})) \times \exp(-\beta (J^* \mathbf{S} \cdot \mathbf{s} + \sum_{l=N, m=1}^{j^*, n_l} J_l S^z s_{l,m}^z)) \quad (9.25)$$

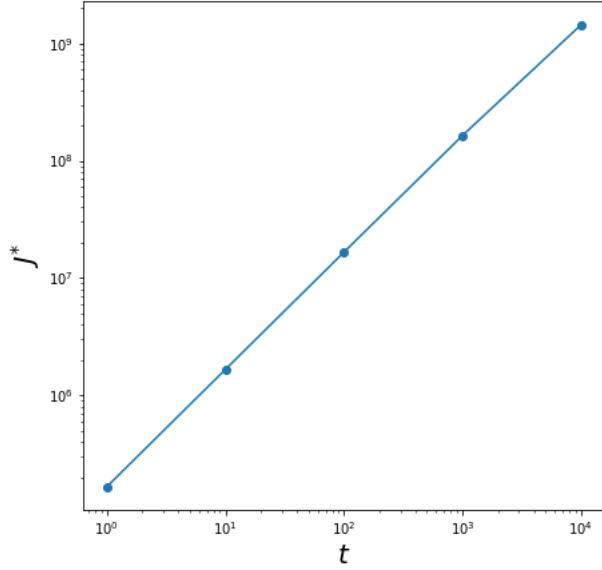


Figure 9.3.4: Left panel: Variation of the renormalized Kondo coupling  $J^*$  with the hopping parameter  $\mathcal{O}(1) < t < \mathcal{O}(10^4)$  of the electronic bath (and hence the conduction band width).

We now rewrite  $H_{coll}$  in the projected basis of the impurity spin and Kondo cloud ( $|\uparrow\downarrow\rangle, |\downarrow\uparrow\rangle$ )

$$\begin{aligned}
 PH_{coll}P &= \begin{pmatrix} -\frac{J^*}{4} + \sum_{l=N,m=1}^{j^*,n_l} \frac{J_l}{2} s_{l,m}^z & \frac{J^*}{2} \\ \frac{J^*}{2} & -\frac{J^*}{4} - \sum_{l=N,m=1}^{j^*,n_l} \frac{J_l}{2} s_{l,m}^z \end{pmatrix} \\
 &= -\frac{J^*}{4} + \sigma^z h_z + \frac{J^*}{2} \sigma_x = -\frac{J^*}{4} + A \boldsymbol{\sigma} \cdot \hat{\mathbf{n}}, \\
 A &= \sqrt{h_z^2 + \frac{(J^*)^2}{4}}, \quad \cos \theta = \frac{h_z}{\sqrt{h_z^2 + \frac{(J^*)^2}{4}}}, \quad h_z = \sum_{l=N,m=1}^{j^*,n_l} \frac{J_l}{2} s_{l,m}^z. \tag{9.26}
 \end{aligned}$$

Thus, the thermal density matrix can be rewritten as

$$\begin{aligned}
 \rho &= \rho_0 \times \exp(-\beta(J^* \mathbf{S} \cdot \mathbf{s} + \sum_{l=N,m=1}^{j^*,n_l} J_l S^z s_{l,m}^z)) \\
 &= \rho_0 \times \left[ 2 \exp(-\beta \frac{J^*}{4}) \cosh \left( \sum_{l=N,m=1}^{j^*,n_l} \frac{\beta J_l}{2} s_{l,m}^z \right) + \exp(\beta \frac{J^*}{4}) \exp(-\beta A \boldsymbol{\sigma} \cdot \hat{\mathbf{n}}) \right] \\
 &= \rho_0 \times \left[ 2 \exp(-\beta \frac{J^*}{4}) \cosh \left( \sum_{l=N,m=1}^{j^*,n_l} \frac{\beta J_l}{2} s_{l,m}^z \right) + \exp(\beta \frac{J^*}{4}) [\cosh(\beta A) + \boldsymbol{\sigma} \cdot \hat{\mathbf{n}} \sinh(\beta A)] \right]. \tag{9.27}
 \end{aligned}$$

where  $\rho_0 = \prod_{l=N,m=1}^{j^*,n_l} \exp(-\beta \epsilon_l (\hat{n}_{l,m,\uparrow} + \hat{n}_{l,m,\downarrow}))$  is the thermal density matrix for the disentangled electrons.

In order to obtain the effective Hamiltonian for just the disentangled electrons, we trace out the impurity and Kondo cloud degrees of freedom from the thermal density matrix ( $\rho$ )

$$\begin{aligned}\bar{\rho} &= Tr_{imp+cloud}(\rho) \\ &= Tr_{imp+cloud}(\rho_0 \times \exp(-\beta(J^* \mathbf{S} \cdot \mathbf{s} + \sum_{l=N,m=1}^{j^*,n_l} J_l S^z s_{l,m}^z))) \\ &\approx \rho_0 \times \exp(\beta \frac{J^*}{4}) \exp(\beta A), \text{ for } \beta \rightarrow \infty\end{aligned}\quad (9.28)$$

Thus, we obtain the effective Hamiltonian for the disentangled electrons

$$\begin{aligned}H_{eff} = -k_B T \log(Tr_{imp+cloud}(\exp(-\beta H_K^*))) &\approx \sum_{l,m} \epsilon_l (\hat{n}_{l,m,\uparrow} + \hat{n}_{l,m,\downarrow}) - \frac{J^*}{4} - \frac{J^*}{2} \sqrt{1 + \frac{4h_z^2}{(J^*)^2}} \\ &\approx \sum_{l,m} \epsilon_l (\hat{n}_{l,m,\uparrow} + \hat{n}_{l,m,\downarrow}) - \frac{3J^*}{4} - \frac{h_z^2}{J^*},\end{aligned}\quad (9.29)$$

where we recall that  $h_z = \sum_{l=N,m=1}^{j^*,n_l} \frac{J_l}{2} s_{l,m}^z$  contains spin density density interactions between the disentangled electrons of various shells  $\Lambda \geq \Lambda^*$ . Importantly, we see that the ground state energy of the Kondo singlet ( $-3J^*/4$ ) appears, signalling that  $H_{eff}$  governs the dynamics of quasiparticle excitations.

Now, upon expanding the square root term within  $H_{eff}$  in leading orders of  $\frac{h_z}{J^*}$ , we obtain the Fermi liquid fixed point theory

$$H_{FL} = \sum_{l,m} \epsilon_l (\hat{n}_{l,m,\uparrow} + \hat{n}_{l,m,\downarrow}) - \sum_{l,l',m,m'} f_{ll'} s_{l,m}^z s_{l',m'}^z, f_{ll'} = \frac{J_l J_{l'}}{J^*}, s_{l,m}^z = \frac{1}{2} (\hat{n}_{l,m,\uparrow} - \hat{n}_{l,m,\downarrow}). \quad (9.30)$$

Given that the interaction strength  $f_{ll'} = \frac{J_l J_{l'}}{J^*}$  falls off sharply compared to  $\epsilon_{\Lambda^*}$  with increasing distances  $\Lambda > \Lambda^*$  (see left panel of Fig.9.3.2) with the highest magnitude being that for electronic states on shell  $\Lambda^*$  ( $f_{j^*} = J_* = 4\epsilon_{\Lambda^*}$ ), we obtain the “local” Fermi liquid Hamiltonian for the disentangled electrons of the shell  $\Lambda^*$  as

$$H_{LFL} = \epsilon_* \sum_m (\hat{n}_{*,m,\uparrow} + \hat{n}_{*,m,\downarrow}) - J^* \sum_{m,m'} s_{*,m}^z s_{*,m'}^z, s_{*,m}^z = \frac{1}{2} (\hat{n}_{\Lambda^*,m,\uparrow} - \hat{n}_{\Lambda^*,m,\downarrow}). \quad (9.31)$$

#### 9.4.1 Wilson ratio ( $R$ ) for the local Fermi liquid

By following the steps shown in Refs.[399, 396], we now obtain the Wilson ratio for the local Fermi liquid we have derived above. For this, we note that the energy cost for quasiparticle excitations with density  $\delta n_{*,m,\sigma}$  is given by

$$\mathcal{E} = \mathcal{E}_0 + \epsilon_* \sum_{m,\sigma} \delta n_{*,m,\sigma} + \frac{J^*}{4} \sum_{m,m',\sigma} \delta n_{*,m,\sigma} \delta n_{*,m',-\sigma} + \frac{J^*}{4} \sum_{m,m',\sigma} n_{*,m,\sigma} \delta n_{*,m',-\sigma}. \quad (9.32)$$

Then, it is easily seen that

$$\begin{aligned}\frac{\delta\mathcal{E}}{\delta n_{*,m,\sigma}} &= \epsilon_* + \frac{J^*}{4} \sum_{m'} \delta n_{*,m',-\sigma} + \frac{J^*}{4} \sum_{m'} n_{*,m',-\sigma} , \\ &= \epsilon_* + \frac{\Delta\epsilon}{\pi} \delta_\sigma(\{n_{*,m',-\sigma}\}, \epsilon_*) ,\end{aligned}\quad (9.33)$$

where we have taken

$$\begin{aligned}E_k - E_F &= -2t \cos(k_{Fx} + \Lambda^*) - 2t \cos(k_{Fy} + \Lambda^*) + 2t \cos k_{Fx} + 2t \cos k_{Fy} \\ &= 2t(\sin k_{Fx} + \sin k_{Fy})\Lambda^* \approx 2t(k_{Fx} + k_{Fy})\Lambda^* .\end{aligned}\quad (9.34)$$

Therefore, we obtain

$$\frac{\Delta E}{\Delta\Lambda^*} = 2t(k_{Fx} + k_{Fy}) , \quad \Delta\epsilon = 2t(k_{Fx} + k_{Fy})\frac{\pi}{L} . \quad (9.35)$$

This leads to the quasiparticle (Friedel's) scattering phase shift

$$\delta_\sigma(\{n_{*,m',-\sigma}\}, \epsilon_*) = \frac{\pi J^*}{4\Delta\epsilon} \sum_{m'} \delta n_{*,m',-\sigma} + \frac{\pi}{2} + \alpha(\epsilon_* - E_F) , \quad (9.36)$$

where  $\delta_0 = \frac{\pi}{2}$  is the phase shift accounting for the absorption of an effective single electron (corresponding to the Kondo cloud) into the singlet. The quantity  $\alpha(\epsilon^* - E_F) = \frac{\pi J^*}{4\Delta\epsilon} \sum_{m'} n_{*,m',-\sigma} - \frac{\pi}{2}$  accounts for the quasiparticle self energy generated by potential scattering with the impurity-cloud singlet [582, 399, 396]. Following Ref.[399, 396], we obtain the zero temperature specific heat coefficient (in units of  $k_B = 1$ ) as

$$\gamma = \frac{2\pi}{3} \alpha(\epsilon_* - E_F) , \quad (9.37)$$

and the impurity spin susceptibility as

$$\chi = \frac{4\alpha(\epsilon_* - E_F)}{\pi} . \quad (9.38)$$

This leads to Wilson's ratio ( $R$ )

$$R = \frac{\chi}{\gamma} \frac{\pi^2}{3} = 2 . \quad (9.39)$$

## 9.5 Impurity susceptibility at finite temperatures

The complete effective Hamiltonian for the impurity spin ( $\mathbf{S}$ ), Kondo cloud spin ( $\mathbf{s}$ ) and the electrons that comprise the local Fermi liquid has the form,

$$H_2 = \epsilon_* \sum_{m,\sigma} \hat{n}_{*,m,\sigma} + J^* \mathbf{S} \cdot \mathbf{s} + J^* S^z \sum_m s_{*,m}^z . \quad (9.40)$$

The Hamiltonian  $H_2$  has several conserved quantities which we depict below,

$$[H_2, S^z + s^z] = 0 , \quad [H_2, s_{*,m}^z] = 0 \quad \forall 1 \leq m \leq n_j , \quad (9.41)$$

such that  $[H^*, S_{tot}^z] = 0$  where  $S_{tot}^z = S^z + s^z + \sum_m s_{*,m}^z$ . Therefore, the eigenvalues of  $|s_{*,m}^z = \uparrow / \downarrow\rangle$  are good quantum numbers; this is simply an outcome of the URG method. We can now extract the effective Kondo impurity-electron cloud Hamiltonian by treating the effect of local Fermi liquid electrons as an effective field  $B = J^* \sum_m \langle s_{*,m}^z \rangle$  (note that this is the eigenvalue of the LFL spins) on the impurity spin,

$$H_K^* = J^* \mathbf{S} \cdot \mathbf{s} + BS^z . \quad (9.42)$$

It is also important to note that the URG procedure did not lead to the generation of spin density density interaction between the electrons of the Kondo cloud and those of the LFL.

We now obtain the impurity magnetization and susceptibility from this effective Hamiltonian. The four state eigenspectrum of  $H_K^*$  is given by

$$\begin{aligned} E_1 &= \frac{1}{2} \left( -\frac{J^*}{2} + \sqrt{B^2 + J^{*2}} \right) , \quad E_2 = \frac{1}{2} \left( -\frac{J^*}{2} - \sqrt{B^2 + J^{*2}} \right) , \\ E_3 &= E_4 = \frac{J^*}{4} . \end{aligned} \quad (9.43)$$

The partition function for this Hamiltonian (with  $\beta = \frac{1}{k_B T}$ ) is given by

$$Z(B) = 2 \exp\left(\beta \frac{J^*}{4}\right) \left[ \cosh\left(\beta \frac{B}{2}\right) + \cosh\left(\frac{\beta}{2} (\sqrt{B^2 + J^{*2}})\right) \right] . \quad (9.44)$$

The magnetization is then given by,

$$M = \frac{k_B T}{Z(B)} \frac{dZ(B)}{dB} = \frac{k_B T}{Z(B)} \exp\left(\beta \frac{J^*}{4}\right) \beta \left[ \sinh\left(\beta \frac{B}{2}\right) + \frac{B}{\sqrt{B^2 + J^{*2}}} \sinh\left(\frac{\beta}{2} \sqrt{B^2 + J^{*2}}\right) \right] , \quad (9.45)$$

and the susceptibility is obtained by taking the effective field  $B \rightarrow 0$

$$\chi = \lim_{B \rightarrow 0} \frac{dM}{dB} = \frac{\frac{\beta}{4} + \frac{1}{2J^*} \sinh\left(\frac{\beta}{2} J^*\right)}{1 + \cosh\left(\frac{\beta}{2} J^*\right)} . \quad (9.46)$$

We can now make several important observations based on eq.9.46. First, the saturation value of  $4T_K \chi$  as  $\beta \rightarrow \infty$  (i.e.,  $T \rightarrow 0$ ) is given by

$$\chi(T = 0) = \frac{1}{2J^*} . \quad (9.47)$$

We find that the Wilson number  $W = 4T_k \chi(T = 0) = \frac{2T_k}{J^*}$ . For values of  $J^* \simeq 16.612t$  and  $T_k \simeq 3.433t$  we obtain  $W = 0.413$ . This is in excellent agreement with the value for  $W$  obtained from NRG [583] and Bethe Ansatz solution of the Kondo problem [584, 585]. This is shown in Fig.9.5.1 (upper panel). Further, we show the variation of  $W$  with the bare Kondo coupling  $J$  in Fig.9.5.1 (lower panel). The figure clearly shows the saturation of  $W$  to the value mentioned above as  $J$  flows to the strong coupling fixed point.

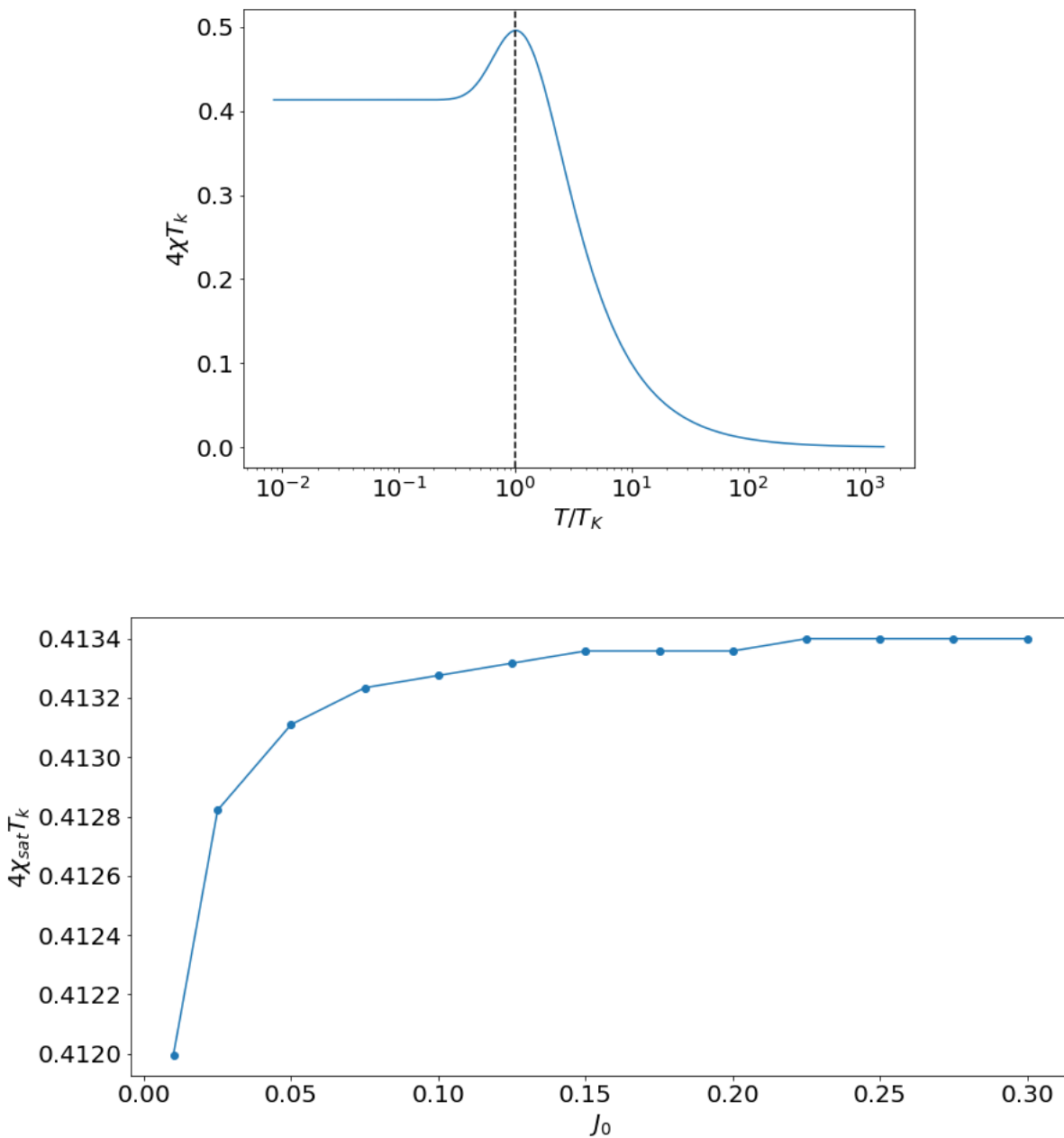


Figure 9.5.1: Upper panel: Variation of  $4T_K\chi$  with  $T/T_K$ . Dashed line shows  $T = T_K$ . Lower panel: Variation of Wilson number  $W$  with bare Kondo coupling  $J_0$ . See discussion in text.

Second, the  $T_K\chi$  vs temperature curve shown in Fig.9.5.1 has a non-monotonic behaviour, i.e.,

we find a maxima obtained from the transcendental equation

$$\begin{aligned} \frac{d\chi}{d\beta} &= \frac{1}{4} - \frac{1}{4} \frac{(1 + \frac{2}{J^*\beta} \sinh \frac{\beta J^*}{2})(\frac{J^*\beta}{2} \sinh \frac{\beta J^*}{2})}{(1 + \cosh \frac{\beta J^*}{2})^2} \\ \implies (1 + \cosh \frac{\beta J^*}{2})^2 &= \frac{J^*\beta}{2} \sinh \frac{\beta J^*}{2} + \sinh^2 \frac{\beta J^*}{2}. \end{aligned} \quad (9.48)$$

We confirm from our numerical studies that the temperature ( $T_{max}$ ) corresponding to the maximum value of  $T_K\chi$  varies as  $T_{max} \rightarrow T_k$  as  $J$  flows to strong coupling. Further, we find that the maximum value of  $T_K\chi$  does not vary with the bare  $J$  in the range  $\mathcal{O}(10^{-5}) < J < \mathcal{O}(1)$ .

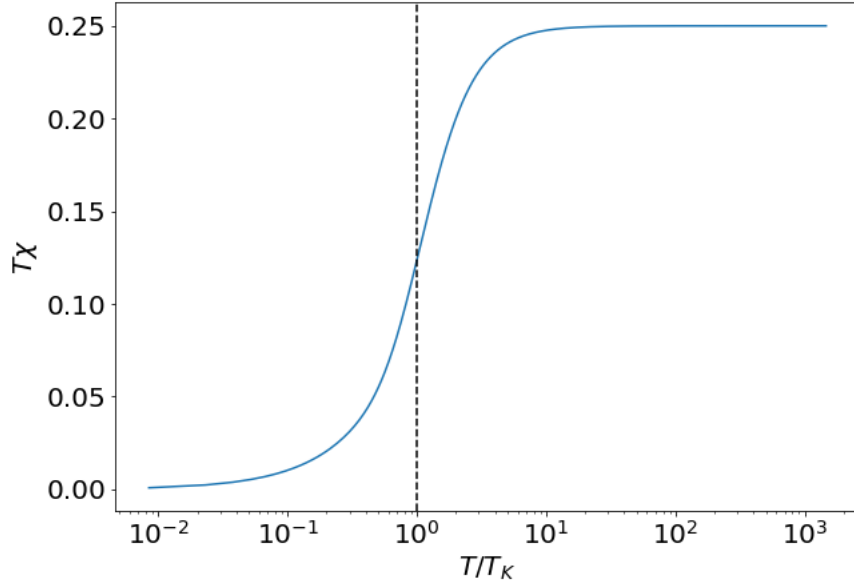


Figure 9.5.2: Variation of  $T\chi$  with  $T/T_K$ . See discussion in text.

Finally, we find that the saturation value of  $T \times \chi$  for  $\beta \rightarrow 0$  is given by the universal value

$$k_B T \chi(T = \infty) = \frac{1}{4}, \quad (9.49)$$

as shown in Fig.9.5.2.

## 9.6 Excitations of the Kondo cloud and the Sommerfield coefficient

In this section we will study the effect of the renormalized Kondo coupling on the self energy of the electrons comprising the Kondo cloud. We integrate out the decoupled electronic states to obtain the effective Hamiltonian  $H^*$  of the impurity + electronic cloud system. In this Hamiltonian we

have additionally kept the electronic dispersion to study the effect of electronic density fluctuation due to the inter-electronic interaction mediated by the impurity spin,

$$H^* = H_0^* + \frac{J^*}{2} \sum_{\substack{j_1, j_2 < j^*, \\ m, m'}} \mathbf{S} \cdot c_{j_1, \hat{s}_m, \alpha}^\dagger \boldsymbol{\sigma}_{\alpha\beta} c_{j_2, \hat{s}_{m'}, \beta} \quad (9.50)$$

$$H_0^* = \sum_{|\Lambda_j| < \Lambda^*, \sigma} \epsilon_j \hat{n}_{j, \hat{s}, \sigma}. \quad (9.51)$$

In order to study the inter-electronic interaction we need to isolate the quantum impurity from the Kondo cloud. This can be done by first recasting the many body eigenstate  $|\Psi\rangle$  of  $H^*$  in the  $\uparrow / \downarrow$  basis of the impurity and the associated configuration of the rest electronic states,

$$|\Psi\rangle = a_0 |\uparrow_{imp}\rangle |\Phi_0\rangle + a_1 |\downarrow_{imp}\rangle |\Phi_1\rangle, \quad (9.52)$$

here  $|\Phi_0\rangle$  and  $|\Phi_1\rangle$  refer to the electronic configurations of the remnant electrons. With the above decomposed state we can rewrite the eigen value relation for  $H_K^*$  as a set of two coupled equations ( $E_1$  is the eigenvalue),

$$\begin{aligned} a_0(H_0^* + \frac{J^*}{2}s_z)|\Phi_0\rangle + a_1 \frac{J^*}{2}s_+|\Phi_1\rangle &= a_0 E_1 |\Phi_0\rangle \\ a_0 \frac{J^*}{2}s_-|\Phi_0\rangle + a_1(H_0^* - \frac{J^*}{2}s_z)|\Phi_1\rangle &= a_1 E_1 |\Phi_1\rangle. \end{aligned} \quad (9.53)$$

Combining this two equations we can obtain,

$$a_0(\frac{J^*}{2}s_z)|\Phi_0\rangle + s_+ \frac{\frac{(J^*)^2}{4}}{E + \frac{J^*}{2}s_z - H_0^*} s_- |\Phi_0\rangle = a_0(E - H_0^*)|\Phi_0\rangle \quad (9.54)$$

From here we obtain the form of the effective Hamiltonian accounting for the leading order density-density and off-diagonal four Fermi interaction terms,

$$\begin{aligned} H_{eff} &= \frac{J^*}{2}s_z + s_+ \frac{\frac{(J^*)^2}{4}}{(E_1 + \frac{J^*}{2}s_z)(1 - \frac{1}{E_1 + \frac{J^*}{2}s_z} H_0^*)} s_- \\ &\approx \frac{J^*}{2}s_z + s_+ \frac{\frac{(J^*)^2}{4}}{E_1 + \frac{J^*}{2}s_z} (1 + \frac{1}{E_1 + \frac{J^*}{2}s_z} H_0^* + \frac{1}{E + \frac{J^*}{2}s_z} H_0^* \frac{1}{E + \frac{J^*}{2}s_z} H_0^*) s_- + O((H_0^*)^3) \\ &\approx \frac{J^*}{2}s_z + s_+ \frac{\frac{(J^*)^2}{4}}{E + \frac{J^*}{2}s_z} s_- + s_+ \frac{\frac{(J^*)^2}{4}}{(E_1 + \frac{J^*}{2}s_z)^2} H_0^* s_- + s_+ \frac{\frac{(J^*)^2}{4}}{(E_1 + \frac{J^*}{2}s_z)^2} H_0^* \frac{1}{E + \frac{J^*}{2}s_z} H_0^* s_-, \\ &\approx \frac{J^*}{2}s_z + (\frac{1}{2} + s_z) \frac{\frac{(J^*)^2}{4}}{E_1 - \frac{J^*}{2}s_z} + s_+ \frac{\frac{(J^*)^2}{4}}{(E_1 + \frac{J^*}{2}s_z)^2} (s_- H_0^* + [H_0^*, s_-]) + \\ &+ s_+ \frac{\frac{(J^*)^2}{4}}{(E_1 + \frac{J^*}{2}s_z)^2} H_0^* \frac{1}{E_1 + \frac{J^*}{2}s_z} (s_- H_0^* + [H_0^*, s_-]). \end{aligned} \quad (9.55)$$

Finally we obtain the effective Hamiltonian upon setting  $E_1 = 0$  in the equation above and choosing  $s_z = \frac{1}{2}$  (this is the spin configuration associated with the wave function eq.(9.52) in eq.(9.54), from which the effective Hamiltonian is derived),

$$H_{Eff} = -\frac{3J^*}{4} + 4(H_0^* + H_0^*\frac{4}{J^*}H_0^*) + \sum_{k_1, k_2, k_3, k_4} \frac{4\epsilon_k \epsilon_{k_1}}{J^*} c_{k_4\uparrow}^\dagger c_{k_1\downarrow}^\dagger c_{k_2\downarrow} c_{k_1\uparrow}. \quad (9.56)$$

The first represents the ground state energy of the singlet configuration, the second term the kinetic energy (eq.(9.51)) density-density correlation (see eq.(9.57) below), and the third term the spin-fluctuation mediated electron-electron scattering process respectively.

In order to study the thermodynamic properties of the Fermi liquid we restrict our attention to the density-density terms only, at a later point we will see the effect of non-Fermi liquid corrections due to the off-diagonal terms. From the density terms we obtain the low excitation energy functional accounting for the quasiparticle interaction

$$E = E_0 + \sum_{\mathbf{k}_\Lambda \hat{s}, \Lambda < \Lambda^*} \epsilon_\Lambda \delta n_{\mathbf{k}\sigma} + \sum_{\mathbf{k}, \mathbf{k}'} \frac{4\epsilon_\mathbf{k} \epsilon_{\mathbf{k}'}}{J^*} \delta n_{\mathbf{k}\sigma} \delta n_{\mathbf{k}'\sigma'}. \quad (9.57)$$

This leads to the renormalized one-particle dispersion, where the self energy term has the following form

$$\bar{\epsilon}_\Lambda = \epsilon_\Lambda + \Sigma_\Lambda, \Sigma_\Lambda = \left( \sum_{\Lambda', \hat{s}, \sigma'} \frac{4\epsilon_\Lambda \epsilon_{\Lambda'}}{J^*} \delta n_{\Lambda', \hat{s}, \sigma'} \right) \text{ for } \Lambda < \Lambda^*. \quad (9.58)$$

Note that as  $\Lambda \rightarrow 0$ ,  $\Sigma_\Lambda \rightarrow 0$ . Next, we compute the specific heat of the impurity from the Fermi Dirac distribution of the renormalized quasiparticles

$$\begin{aligned} C_{imp} &= C(J^*) - C(0) \\ &= \sum_{\Lambda, \hat{s}, \sigma} \left( \frac{(\bar{\epsilon}_\Lambda)^2 \exp(\beta \bar{\epsilon}_\Lambda)}{(\exp(\beta \bar{\epsilon}_\Lambda) + 1)^2} - \frac{(\epsilon_\Lambda)^2 \exp(\beta \epsilon_\Lambda)}{(\exp(\beta \epsilon_\Lambda) + 1)^2} \right), \end{aligned} \quad (9.59)$$

where  $C(J^*)$  is the specific heat for the electronic system with the Kondo impurity, and  $C(0)$  is the specific heat for the free electronic system without coupling to Kondo impurity. The specific heat coefficient is given by  $\gamma_{imp} = \frac{C_{imp}}{k_B T}$ . Fig.9.6.1(left panel) shows that  $\gamma_{imp} T_K$  rises from 0 at high temperatures  $T > 10^2 T_K$  and saturates at a value  $\gamma_{imp}(0) T_K = 0.0519$  for  $T < 10^{-2} T_K$ . The Wilson ratio in Fig.9.6.1(right panel) obtained from the ratio of the saturation values of the susceptibility and specific heat coefficient saturates to a value  $W = \chi(0)/\gamma_{imp}(0) = 2.012$  for  $T < 10^{-2} T_K$ .

## 9.7 Many body correlations and entanglement properties of the Kondo cloud

In order to study the effect of the off-diagonal terms eq.(9.56) on the constituents of the Kondo cloud we perform a reverse URG treatment (shown in Fig.9.7.2) starting from the Kondo model ground state  $|\Psi^*\rangle$  at the IR fixed point eq.(9.23).

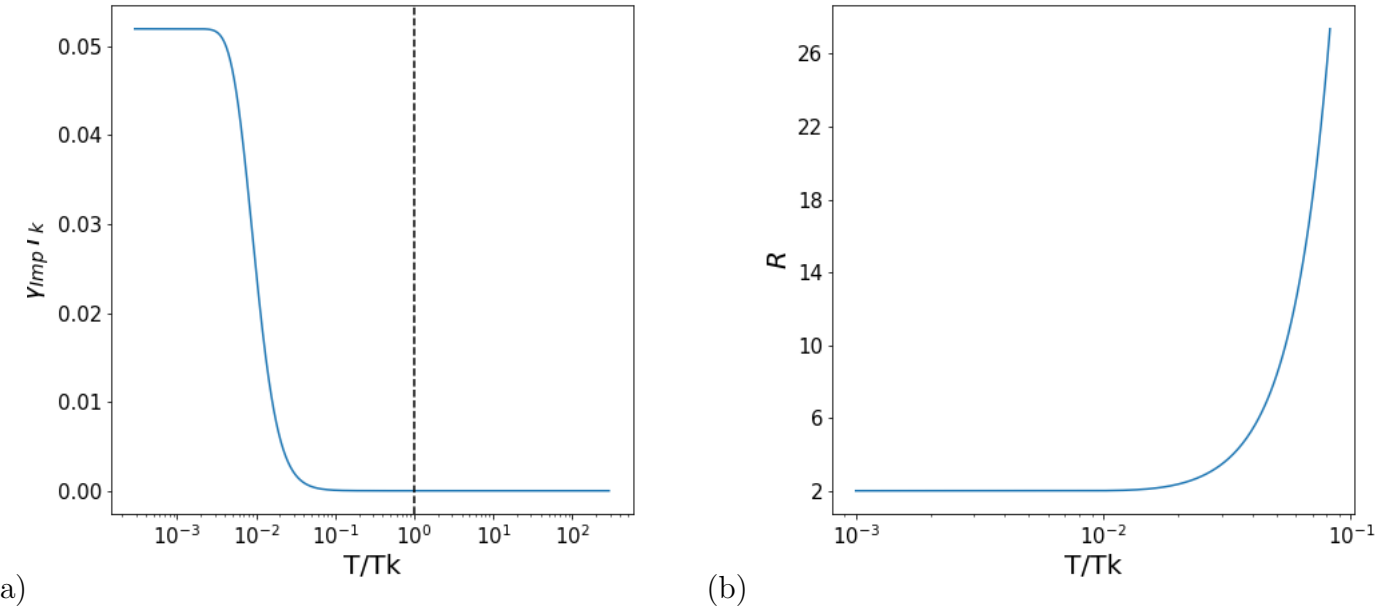


Figure 9.6.1: (a) Variation of  $\gamma_{imp} T_K$  with  $T/T_K$ , dashed line shows  $T = T_k$ . (b) Variation of  $R$  Wilson ratio with  $T/T_K$ .

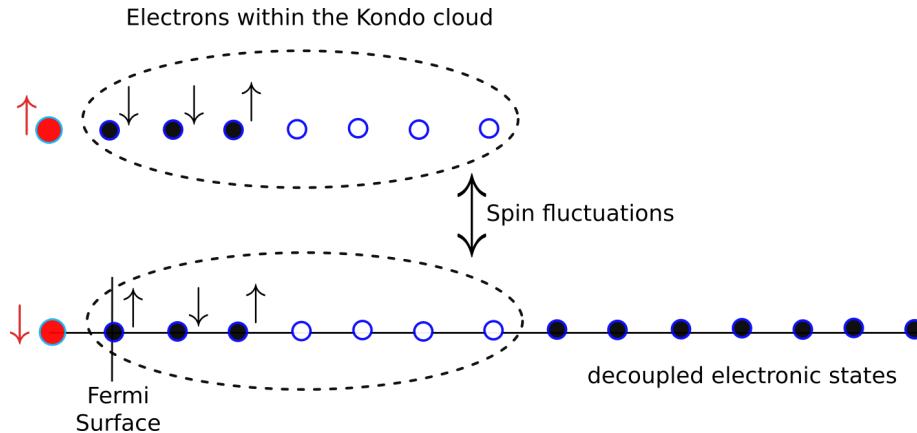


Figure 9.7.1: Figure describes the electronic Kondo cloud (dashed oval) coupled to the impurity spin (red arrow).

For the present study we take a toy model construction of the ground state wavefunction  $|\Psi^*\rangle$  eq.(9.23) at IR, the Kondo impurity couples to 12 electronic states  $|\mathbf{k}\sigma\rangle$  of which three are occupied and 9 are unoccupied. The net spin of the electrons comprising the Kondo cloud is oppositely aligned to that of the Kondo impurity. The Kondo cloud system is in tensor product with 14 separable electronic states. This construction is represented in Fig.9.7.1. At each URG step  $U_{j,\uparrow}U_{j,\downarrow}$  two electronic states  $|k_j, \uparrow\rangle$ ,  $|k_j, \downarrow\rangle$  are disentangled in reaching the IR fixed point. Upon performing reverse RG at each step two electrons are re-entangled into the eigenstates via the inverse unitary maps  $U_{j,\uparrow}^\dagger U_{j,\downarrow}^\dagger$ , Fig.9.7.2, all total we perform seven reverse RG steps. This

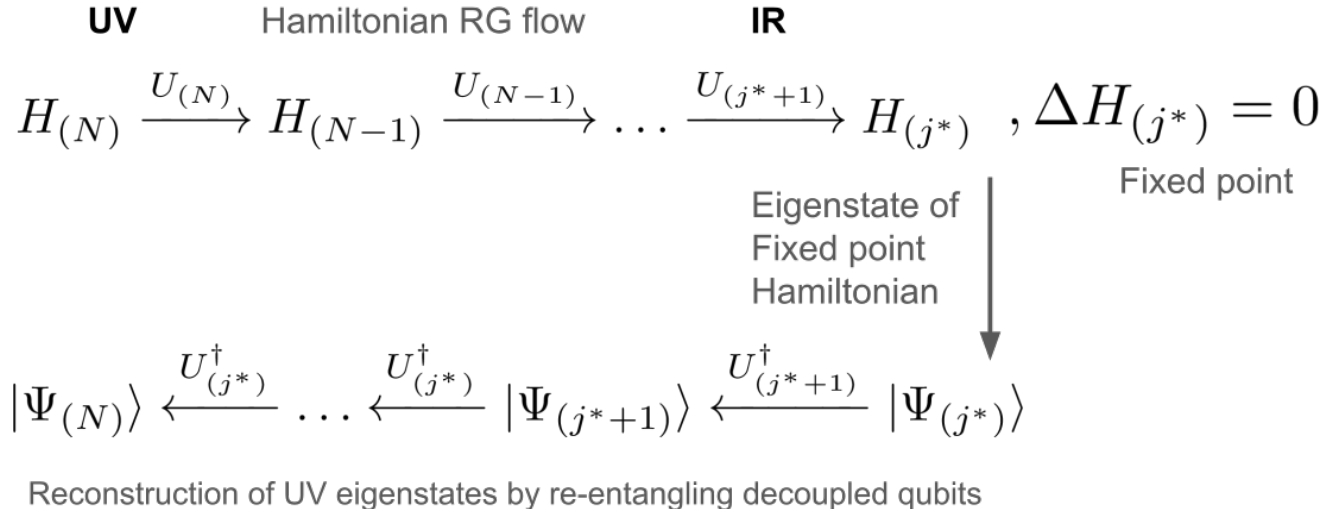


Figure 9.7.2: The first line represent the Hamiltonian RG flow via the unitary maps. Upon reaching the Kondo IR fixed point, reverse RG will re-entangled decoupled electronic states with the Kondo singlet. This will result in generation of the many body eigenstates at UV.

reverse RG program is numerically implemented using python.

We use the wavefunctions generated under the reverse RG to compute the mutual information between (a) an electron in the Kondo cloud and the impurity electron, and (b) two electrons within the cloud. MI measures the total amount of quantum and classical correlations in a system [239]. The mutual information between two electrons is given by

$$I(i:j) = -Tr(\rho_i \ln \rho_i) - Tr(\rho_j \ln \rho_j) + Tr(\rho_{ij} \ln \rho_{ij}) , \quad (9.60)$$

where  $\rho_i$  or  $\rho_j$  and  $\rho_{ij}$  are the 1- and 2-electron reduced density matrices respectively obtained from the wavefunctions obtained at each step of the reverse RG simulation. In Fig.9.7.3, we present the RG flow of both types of mutual information mentioned above. The orange curve in Fig.9.7.3(a) represents the plot for the maximum mutual information  $I(e:e)$  (eq.(9.60)) between any two of the electrons comprising the Kondo cloud, and shows that the maximum entanglement content/quantum correlation increases under RG flow from UV to IR. This implies that the electrons within the Kondo cloud is not simply a separable state in momentum space expected of a local Fermi liquid. This is a strong indication of the fact that the two-particle off-diagonal ( $c_{k_4\uparrow}^\dagger c_{k_1\downarrow}^\dagger c_{k_2\downarrow} c_{k_1\uparrow}$ ) scattering term in eq.(9.56) is playing a role in the electronic entanglement within the Kondo cloud. Further, the blue curve in Fig.9.7.3(a) shows that the maximum mutual information between the Kondo impurity and any one member of the electronic cloud also increases under RG and to a higher value compared to that between electrons. This originates from the maximally entangled singlet state that is formed between the impurity and the electronic cloud. In this manner, the Kondo impurity mediates the entanglement between electrons (orange curve) in the Kondo cloud.

In order to understand this further, we also study (i) the maximum density-density correlations  $\max_{k,k_1} \langle \hat{n}_{k\uparrow} \hat{n}_{k_1\downarrow} \rangle$  (blue curve in Fig.9.7.3(b)), and (ii) the maximum two-particle off-diagonal correlations  $\max_{k,k_1} \langle c_{k\uparrow}^\dagger c_{k_1\downarrow}^\dagger c_{k_2\downarrow} c_{k_3\uparrow} \rangle$  (orange curve in Fig.9.7.3(b)) between electrons within the

Kondo cloud. The plots show clearly that both the correlations grow under RG from UV to IR, finally reach the same value at the IR fixed point. Given that the amplitude of the number diagonal term in the effective Hamiltonian for the Kondo cloud ( $\frac{4\epsilon_k\epsilon_{k_1}}{J^*}$ , eq.(9.56)) is much smaller than that for the decoupled electronic degrees of freedom ( $\frac{J^*}{4}$ , eq.(9.32)) at strong coupling ( $J^* \gg 1$ ), we see that the local Fermi liquid is formed predominantly by the latter. On the other hand, the large values of the off-diagonal correlations reinforce our observation of a non-zero mutual information content between the cloud electrons. This implies that the electronic cloud is, in general, a non-Fermi liquid with non-zero entanglement content. Further studies of the many body entanglement content and transport properties are required to understand the physics of these non-Fermi liquid metal.

## 9.8 Conclusions

The Kondo problem [300] is one of the oldest and well studied problem of electronic correlations in condensed matter [301, 93], and represents a set of benchmarking exercises for verifying the accuracy of the URG method. The RG analysis of the Kondo Hamiltonian leads to a zero temperature phase diagram revealing a intermediate coupling fixed point for an antiferromagnetic Kondo coupling. At the IR fixed point, we obtained the effective Hamiltonian, the ground state wavefunction and the energy eigenspectrum. This enabled the computation of various thermodynamic quantities such as the impurity susceptibility, specific heat coefficient, Wilson ratio, Wilson number, all of which are found to be in excellent agreement with that obtained from the NRG studies [583].

Furthermore, we found that the effective Hamiltonian for the Kondo cloud, obtained by integrating out the impurity spin, contains a density-density repulsion (corresponding to the local Fermi liquid) as well as a four-fermion interaction term description. In order to understand the roles of the two types of electronic correlations better, we performed a comparative study of the RG evolution of four-point number diagonal and number off-diagonal correlators. By using the singlet IR ground state wavefunction obtain from the URG analysis, we also studied the RG evolution of the mutual information (an entanglement based measure) between (a) the impurity and an electron in the cloud and (b) two electrons in the cloud. The results show strong inter-electronic as well as electron-impurity entanglement upon approaching the IR fixed point. This is in agreement with the presence of both types of two-particle correlators at the IR ground state. We find that both the number diagonal and number off-diagonal correlators reach same value at the IR fixed point, indicating that the electronic configuration within the Kondo cloud is not simply a local Fermi liquid. Indeed, our analysis lays bare the fact that the local Fermi liquid is formed primarily from the decoupled electrons lying outside the cloud, while the large entanglement within the Kondo cloud is an indication of the spin singlet it forms together with the impurity spin. Future studies need to be performed for investigating the nature of the correlated non-Fermi liquid metal comprising the Kondo cloud, e.g., various observables like spectral function, resistivity of the electronic system need to be quantified. Such studies should help in providing predictions that can be tested experimentally.

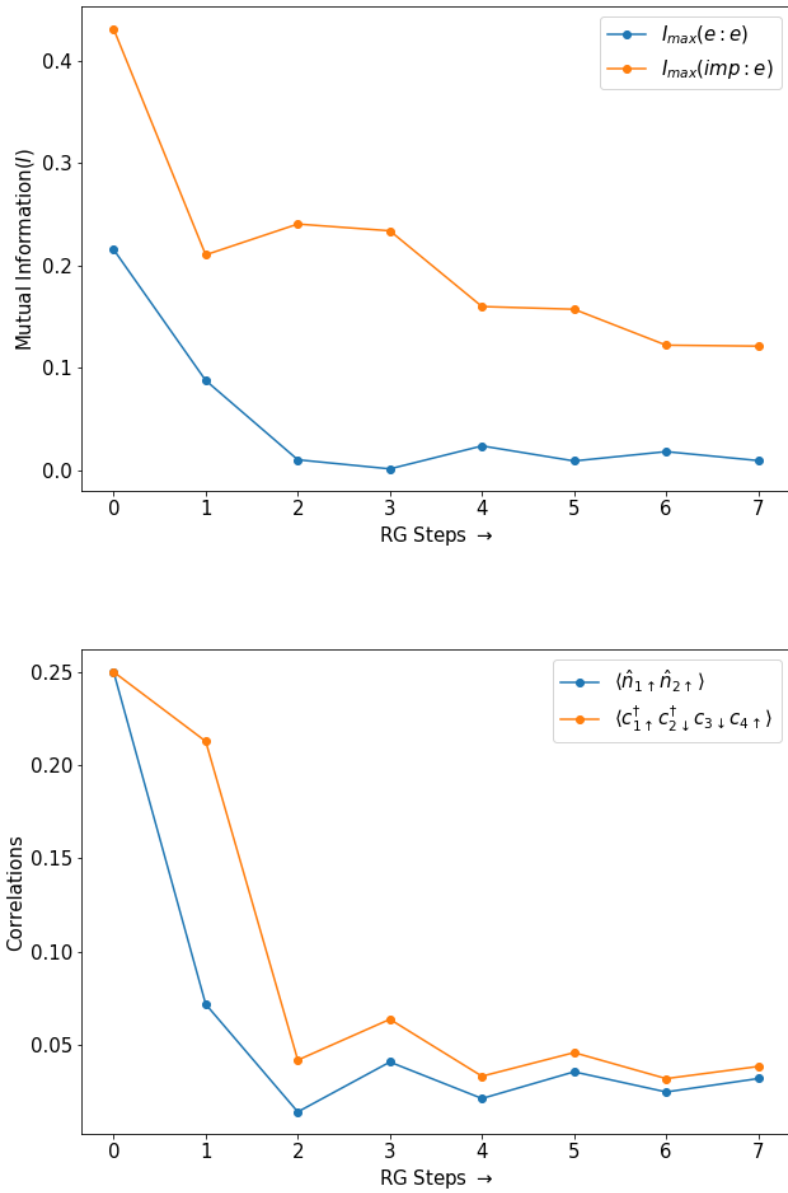


Figure 9.7.3: Figure(a) shows the RG flows for the maximum mutual information between the impurity and electron (orange curve) and diagonal correlations (blue curve). Figure(b) shows the RG flows for the off-diagonal (orange curve) and diagonal correlations (blue curve).

# Appendix

## 9.A Calculation of effective Hamiltonian from URG

Starting from the Kondo Hamiltonian eq.(9.1) and using the URG based Hamiltonian RG equation eq.(9.10), we obtain the renormalised Hamiltonian

$$\begin{aligned}
\Delta \hat{H}_{(j)} &= \sum_{\substack{m=1, \\ \beta=\uparrow/\downarrow}}^{n_j} \frac{(J^{(j)})^2 \tau_{j,\hat{s}_m,\beta}}{2(2\omega \tau_{j,\hat{s}_m,\beta} - \epsilon_{j,l} \tau_{j,\hat{s}_m,\beta} - J^{(j)} S^z s_{j,\hat{s}_m}^z)} \\
&\times \left[ S^a S^b \sigma_{\alpha\beta}^a \sigma_{\beta\gamma}^b \sum_{\substack{(j_1,j_2 < j), \\ n,o}} c_{j_1,\hat{s}_n,\alpha}^\dagger c_{j_2,\hat{s}_o,\gamma} (1 - \hat{n}_{j,\hat{s}_m,\beta}) + S^b S^a \sigma_{\beta\gamma}^b \sigma_{\alpha\beta}^a \sum_{\substack{(j_1,j_2 < j), \\ n,o}} c_{j_2,\hat{s}_o,\gamma} c_{j_1,\hat{s}_n,\alpha}^\dagger \hat{n}_{j,\hat{s}_m,\beta} \right] \\
&+ \sum_{\substack{m=1, \\ \beta=\uparrow/\downarrow}}^{n_j} \frac{(J^{(j)})^2}{2(2\omega \tau_{j,\hat{s}_m,\beta} - \epsilon_{j,l} \tau_{j,\hat{s}_m,\beta} - J^{(j)} S^z s_{j,\hat{s}_m}^z)} \left[ S^x S^y \sigma_{\alpha\beta}^x \sigma_{\beta\alpha}^y c_{j,\hat{s}_m,\alpha}^\dagger c_{j,\hat{s}_m,\beta} c_{j,\hat{s}_m,\beta}^\dagger c_{j,\hat{s}_m,\alpha} \right. \\
&\left. + S^y S^x \sigma_{\alpha\beta}^x \sigma_{\beta\alpha}^y c_{j,\hat{s}_m,\beta}^\dagger c_{j,\hat{s}_m,\alpha} c_{j,\hat{s}_m,\alpha}^\dagger c_{j,\hat{s}_m,\beta} \right]. \tag{9.61}
\end{aligned}$$

The first term in eq.(9.61) corresponds to the renormalization of the Kondo coupling and describes the s-d exchange interactions for the entangled degrees of freedom

$$\begin{aligned} \Delta H_{(j)}^1 &= \sum_{m=1, \beta=\uparrow/\downarrow}^{n_j} \frac{(J^{(j)})^2 \tau_{j,\hat{s}_m,\beta}}{(2\omega\tau_{j,\hat{s}_m,\beta} - \epsilon_{j,l}\tau_{j,\hat{s}_m,\beta} - J^{(j)}S^z s_{j,\hat{s}_m}^z)} \sum_{\substack{(j_1,j_2 < j), \\ n,o}} \mathbf{S} \cdot c_{j_1,\hat{s}_n,\alpha}^\dagger \frac{\sigma_{\alpha\beta}}{2} c_{j_2,\hat{s}_o,\beta} \\ &= \frac{1}{2} \sum_{m=1, \beta=\uparrow/\downarrow}^{n_j} \frac{\tau_{j,\hat{s}_m,\beta}(J^{(j)})^2 [(2\omega\tau_{j,\hat{s}_m,\beta} - \epsilon_{j,l}\tau_{j,\hat{s}_m,\beta}) + J^{(j)}S^z s_{j,m}^z]}{(\omega - \frac{\epsilon_{j,l}}{2})^2 - \frac{(J^{(j)})^2}{16}} \sum_{\substack{(j_1,j_2 < j), \\ n,o}} \mathbf{S} \cdot c_{j_1,\hat{s}_n,\alpha}^\dagger \frac{\sigma_{\alpha\beta}}{2} c_{j_2,\hat{s}_o,\beta} \\ &= \frac{1}{2} \sum_{m=1, \beta=\uparrow/\downarrow}^{n_j} \frac{(J^{(j)})^2 \left[ \left( \frac{\omega}{2} - \frac{\epsilon_{j,l}}{4} \right) \right]}{(\omega - \frac{\epsilon_{j,l}}{2})^2 - \frac{(J^{(j)})^2}{16}} \sum_{\substack{(j_1,j_2 < j), \\ n,o}} \mathbf{S} \cdot c_{j_1,\hat{s}_n,\alpha}^\dagger \frac{\sigma_{\alpha\beta}}{2} c_{j_2,\hat{s}_o,\beta} \\ &+ \frac{1}{2} \sum_{m=1}^{n_j} \frac{(J^{(j)})^3 S^z s_{j,m}^z (\tau_{j,\hat{s}_m,\uparrow} + \tau_{j,\hat{s}_m,\downarrow})}{(\omega - \frac{\epsilon_{j,l}}{2})^2 - \frac{(J^{(j)})^2}{16}} \sum_{\substack{(j_1,j_2 < j), \\ n,o}} \mathbf{S} \cdot c_{j_1,\hat{s}_n,\alpha}^\dagger \frac{\sigma_{\alpha\beta}}{2} c_{j_2,\hat{s}_o,\beta} \end{aligned} \quad (9.62)$$

$$= \frac{n_j (J^{(j)})^2 \left[ (\omega - \frac{\epsilon_{j,l}}{2}) \right]}{(\omega - \frac{\epsilon_{j,l}}{2})^2 - \frac{(J^{(j)})^2}{16}} \mathbf{S} \cdot \sum_{\substack{(j_1,j_2 < j), \\ n,o}} c_{j_1,\hat{s}_n,\alpha}^\dagger \frac{\sigma_{\alpha\gamma}}{2} c_{j_2,\hat{s}_o,\gamma}. \quad (9.63)$$

In the second last step of the calculation (eq.(9.62)), we have used the result  $\tau_{j,\hat{s}_m,\uparrow}^2 = \frac{1}{4}$ , where  $\tau_{j,\hat{s}_m,\uparrow} = \hat{n}_{j,\hat{s}_m,\uparrow} - \frac{1}{2}$ . In obtaining the last step of the calculation we have assumed  $\epsilon_{j,l} = \epsilon_j$  for a circular Fermi surface geometry. Further, we have replaced  $\tau_{j,\hat{s}_m,\uparrow}$  and  $\tau_{j,\hat{s}_m,\downarrow}$  by their eigenvalues,  $\tau_{j,\hat{s}_m,\uparrow} = -\tau_{j,\hat{s}_m,\downarrow} = \frac{1}{2}$ , i.e., the resulting decoupled electronic wave vector  $|j, \hat{s}_m\rangle$  carries a non-zero spin angular momentum. This configuration promotes the spin scattering between the Kondo impurity and the fermionic bath.

The second term in eq.(9.61) corresponds to the renormalization of the number diagonal Hamiltonian for the immediately disentangled electronic states  $|j, \hat{s}_m, \sigma\rangle$

$$\begin{aligned} \Delta H_{(j)}^2 &= \sum_{m=1, \beta=\uparrow/\downarrow}^{n_j} \frac{(J^{(j)})^2}{(2\omega\tau_{j,\hat{s}_m,\beta} - \epsilon_{j,l}\tau_{j,\hat{s}_m,\beta} - J^{(j)}S^z s_{j,\hat{s}_m}^z)} \left[ S^x S^y \sigma_{\alpha\beta}^x \sigma_{\beta\alpha}^y c_{j,\hat{s}_m,\alpha}^\dagger c_{j,\hat{s}_m,\beta} c_{j,\hat{s}_m,\beta}^\dagger c_{j,\hat{s}_m,\alpha} \right. \\ &\quad \left. + S^y S^x \sigma_{\alpha\beta}^x \sigma_{\beta\alpha}^y c_{j,\hat{s}_m,\beta}^\dagger c_{j,\hat{s}_m,\alpha} c_{j,\hat{s}_m,\alpha}^\dagger c_{j,\hat{s}_m,\beta} \right] \\ &= \sum_{m=1, \beta=\uparrow/\downarrow}^{n_j} \frac{(J^{(j)})^2}{(2\omega\tau_{j,\hat{s}_m,\beta} - \epsilon_{j,l}\tau_{j,\hat{s}_m,\beta} - J^{(j)}S^z s_{j,\hat{s}_m}^z)} S^z \frac{\sigma_{\alpha\alpha}^z}{2} \left[ \hat{n}_{j,\hat{s}_m,\alpha} (1 - \hat{n}_{j,\hat{s}_m,\beta}) - \hat{n}_{j,\hat{s}_m,\beta} (1 - \hat{n}_{j,\hat{s}_m,\alpha}) \right] \\ &= \sum_{m=1}^{n_j} \frac{(J^{(j)})^2}{(2\omega\tau_{j,\hat{s}_m,\beta} - \epsilon_{j,l}\tau_{j,\hat{s}_m,\beta} - J^{(j)}S^z s_{j,\hat{s}_m}^z)} S^z s_{j,\hat{s}_m}^z, \end{aligned} \quad (9.64)$$

where we have used  $\hat{n}_{j,\hat{s}_m,\alpha} (1 - \hat{n}_{j,\hat{s}_m,\beta}) - \hat{n}_{j,\hat{s}_m,\beta} (1 - \hat{n}_{j,\hat{s}_m,\alpha}) = \hat{n}_{j,\hat{s}_m,\alpha} - \hat{n}_{j,\hat{s}_m,\beta}$  in the last step, and the spin density for the state  $|j, \hat{s}_m\rangle$  is given by  $s_{j,\hat{s}_m}^z = \frac{1}{2}(\hat{n}_{j,\hat{s}_m,\uparrow} - \hat{n}_{j,\hat{s}_m,\downarrow})$ .

In obtaining the above RG equation we have replaced  $\hat{\omega}_{(j)} = 2\omega\tau_{j,\hat{s}_m,\beta}$ . We set the electronic configuration  $\tau_{j,\hat{s}_m,\uparrow} = -\tau_{j,\hat{s}_m,\downarrow} = \frac{1}{2}$  to account for the spin scattering between the Kondo impurity

and the fermionic bath. The operator  $\hat{\omega}_{(j)}$  (eq.(9.7)) for RG step  $j$  is determined by the occupation number diagonal piece of the Hamiltonian  $H_{(j-1)}^D$  attained at the next RG step  $j - 1$ . This demands a self-consistent treatment of the RG equation to determine the  $\omega$ . In this fashion, two-particle and higher order quantum fluctuations are automatically encoded into the RG dynamics of  $\hat{\omega}$ . In the present work, however, we restrict our study by ignoring the RG contribution in  $\omega$ . The electron/hole configuration ( $|1_{j,\hat{s}_m,\beta}\rangle / |0_{j,\hat{s}_m,\beta}\rangle$ ) of the disentangled electronic state (and associated with energy  $\pm\epsilon_{j,l}$ ) is accounted by the fluctuation energy scales  $\pm\omega$ .

From the above Hamiltonian RG equations eq.(9.63), we can obtain the form of the Kondo coupling RG equation

$$\Delta J^{(j)} = \frac{n_j(J^{(j)})^2 [\omega - \frac{\epsilon_{j,l}}{2}]}{(\frac{\epsilon_{j,l}}{2} - \omega)^2 - \frac{(J^{(j)})^2}{16}}. \quad (9.65)$$



# Chapter 10

## Conclusion and Future Directions

We present here some of the important takeaways from the work presented in this thesis, as well as point to some directions for future work. This thesis develops a unitary renormalisation group (URG) formalism for a system of interacting electrons on a lattice and described by the Hamiltonian framework. The unitary transformation disentangles an electronic state from the rest, generating thereby a block-diagonal Hamiltonian in the occupation number basis of the state. The electronic states are arranged typically in descending order of their bare values from high to low, making such an arrangement scheme dependent. The Hamiltonian RG flow (from high to low energies) is then a recursion sequence of Hamiltonians generated via the unitary transformations. The effective Hamiltonians generated at each RG step are stacked across various spectral frequencies that account for retardation effects, and tracks different parts of the many-body spectrum. These retardation effects arise from the quantum fluctuations due to non-commuting terms in the Hamiltonian. In this way, the renormalisation procedure outlined above is a multireference method [219–221]: the RG steps resolve the multiple energy scales for quantum fluctuations in an iterative fashion. The multireference nature of the approach allows for the treatment of dynamical fluctuations associated with the occupation number configurations of the coupled states, i.e., it enables the exploration of the ground state(s) as well as excited states of the Hamiltonian spectrum. At each RG step, the effective Hamiltonians can enable the construction of the density matrix for a given temperature scale  $k_B T$ , such that one can compute the finite temperature partition function [586]. As a future direction, we can take up this path to study the RG flow of various finite temperature correlation functions, and classify thereby the finite temperature phase transitions of a given electronic model. In this manner, we can extend the URG formalism to finite temperatures.

The collection of  $2n$ -point scattering vertex tensors that flow under RG lead to a vertex tensor network description of the Hamiltonian. As a consequence, the Hamiltonian RG flow equation obtained from URG generates a hierarchy of  $2n$ -point vertex RG flow equations, where all loop-contributions are re-summed. The form of the RG equations involves the various  $2n$ -point Green's functions made out of  $p$ -particle  $2n - p$ -hole self/correlation energies. The appearance of the frequency-dependent correlation energies within the RG equations (via the appropriate Green's functions) has two major effects. First, the interplay of the multireference quantum fluctuation scale and the correlation energies in the vertex RG flows enables the distillation of the relevant vertices from the irrelevant ones. Secondly, the poles of the RG equations for the vertices (that stem from the poles of the Green's function) are nontrivial stable fixed point solutions that yield

effective Hamiltonians. Further, the appearance of such poles are linked to either bound state formation of electronic pairs leading to a many-body gap, or the emergence of a new composite of electrons and holes that have a long lifetime near the Fermi surface. The latter circumstance leads to a non-Fermi liquid metal arising from the breakdown of Landau quasiparticles comprising the Fermi liquid theory, and can be observed from the breakdown of the Luttinger's sum [544] defined solely in terms of single-particle Green's function. For the case of marginal Fermi liquid phase derived from a URG analysis, we have shown that the two-electron one-hole Green's function has a well defined spectral weight that can restore the Luttinger's sum. A future direction would be to characterize non-Fermi liquid metals in terms of sum rules involving the many-body Green's function. For the case of bound-state formation, we find zeros in the single-particle Green's function (i.e. the Luttinger surface of zeros)[276], arising from a divergent self-energy. We have also shown that the zeros of the single-particle Green's function leads to a vanishing spectral weight in the f-sum rule. However, the net spectral weight is restored upon accounting for the poles in the appropriate two-particle Green's function. Apart from the pole structure, the sign of the Green's function has two essential features. First, it distills the relevant scattering vertices in the RG equations. Second, the sign emerges as a topological number describing the various gapped, pseudogapped and gapless phases of an interacting electronic model (e.g., as observed in our studies of the 2d Hubbard model). In future, a systematic characterization of various correlation driven insulators can be carried out in terms of such topological numbers.

An important aspect of the URG approach is the generation of a tractable effective Hamiltonian  $H^*(\omega)$  at the IR fixed point for a given retardation energy scale  $\omega$ . Upon solving this Hamiltonian, we can obtain low energy eigenspectrum and eigenstates. We have performed such analyses for the effective Hamiltonians obtained from URG study of the 2D Hubbard model, the Kondo model, 1D Hubbard model etc. From the ground state  $|\Psi^*\rangle$  obtained at the RG fixed point, we have computed various frequency-resolved many-body measurables like the spectral function, two-particle correlations, ODLRO, resistivity, structure factor, susceptibilities etc. These have assisted in signalling the breakdown of Fermi liquid paradigm, revealing an exotic array of phases of emergent quantum matter, e.g., d-wave superconductivity, non-Fermi liquids, pseudogap, etc. In the future, we plan to study the finite temperature  $T = k_B^{-1}\beta^{-1}$  counterparts of these measures by initially performing an imaginary-time evolution of the ground state  $\exp(-\beta H^*(\omega))|\Psi^*\rangle$ , and then subsequently computing the correlations. This will allow us to study the temperature scales up to which the quantum phases can remain coherent. Furthermore, such an approach can reveal the interplay between the thermal fluctuation scale  $k_B T$  and the multireference quantum retardation energy scales ( $\omega$ 's) that naturally emerge from the URG procedure.

The many-body wavefunction is a storehouse of quantum information encoded within various entanglement-based features like mutual information [239], entanglement entropy[529] etc. that can be extracted by isolating subregions within it. In this regard, we have constructed a quantum circuit architecture for the ground state wavefunction in terms of one qubit and two-qubit gates, i.e., a sequence of gates that takes a separable state as input such that the desired entangled state is obtained at the output. The efficiency of the state preparation protocol can be quantified by comparing the entanglement features of the target state and the state produced by the circuit. A future goal would be to prepare the ground state on a cloud-based quantum processing unit such as IBM Q [587], Rigetti quantum device [588] etc. If such a protocol can be carried out, we can study the quantum advantage for computing various correlation functions and constructing

---

phase diagrams over traditional methods for computing the same on classical computers. The main idea is the following: URG leads to a simplified representation of the ground state, i.e., it will have lesser entangled qubits than the undetermined parent wavefunction. Implementing such a refined ground state on a quantum computer should naturally require a lower depth circuit (number of one and two-qubit gates that prepare the entangled state). Finally, upon performing a reverse RG flow using the inverse unitary RG transformations, we have constructed the ground state wavefunction for various parent Hamiltonian models such as the 2d Hubbard model, 1d Hubbard model, Kondo model. In this manner, URG is observed to function as a quantum processor of information. In earlier chapters, we have already discussed in detail the holographic nature of the tensor network representation of the many-body wavefunctions we have obtained. Thus, we will not dwell on that aspect any further here, except to say that such URG studies open a pathway by which to characterise the hitherto elusive many-particle entanglement content of various states of quantum matter.

The quantum circuit representation of the URG possesses different architectures for gapless and gapped states. This is seen from the qualitative difference between the URG scaling of mutual information and entanglement entropy for gapped and gapless phases, and corresponds to an entanglement phase transition between them. Furthermore, the entanglement features associated with the quantum circuit are found to be very different for topologically ordered gapped phases and symmetry broken phases. An interesting possibility exists in quantifying the varied nature of many-particle entanglement for different phases based on their quantum circuit representations. From the URG studies of various electronic models, we have observed either the pairing of electronic states leading to a gapped state or gapless states that are separable in momentum-space. Importantly, we do not need to account for the fermion exchange signatures in both types of IR ground states, as their effects are observed to be mitigated along the URG flow from UV to IR. However, the superposition coefficients comprising the wavefunction have a non-trivial dependence on fermion exchange signatures at the high-energy (UV) boundary of the RG flow. Thus, further study is required in order to understand the role played by fermion exchange signatures on the RG flow of entanglement entropy.

For the topologically ordered insulating ground states of the 2d Hubbard model at half-filling, we have tracked the entanglement properties and the emergence of topological quantum numbers along the RG flow. Using studies based on nonlocal twist operators, we have shown the existence of fractional excitations in this phase of matter. A future study could involve employing the mathematics of modular matrices [375], K-matrices [586] and topological entanglement entropy [227] for the classification of these topologically ordered states based. Importantly, can the URG scaling of these quantities show the emergence of topological order? How do topological attributes interplay with many-particle entanglement? An additional attribute of the topologically ordered states revealed by URG is the connection to a topological stabilizer code. Given this connection, can URG flow for topologically ordered ground states be useful for a quantum error-correction protocol? Can we quantify the robustness of topological order under URG flow in the background of single-qubit error introduced at UV energyscales? Can we study how the error introduced at the UV boundary of the URG quantum circuit/tensor network propagates along with the URG flow?

We have shown the usage of the URG wavefunction coefficient tensor network in constructing a deep learning neural network (DNN) [537, 535, 538] that can distinguish between topologically

ordered gapped states and gapless states based on their entanglement features. Specifically, URG has been shown to satisfy the information bottleneck principle [538], i.e., the entanglement feature data is compressed from one layer to the next layer of URG transformations (from UV to IR) such that the essential information is preserved. We have constructed an optimal DNN from the URG flow in this manner. A future direction would be to upgrade the DNN architecture for classifying different kinds of topological ordered ground states by studying different model Hamiltonians on frustrated lattices, including the physics of spin-orbit coupling etc. By studying some of the well-known problems with topological order from the URG approach, we can construct a database of entanglement features including mutual information, entanglement entropy, purity etc. We can then construct a deep neural network for learning from the entanglement data, and relevant labels that group different types of topological order based on the nature of their fractional excitations, modular matrices, topological entanglement entropy etc. Finally, we can use such a DNN to predict the accuracy of detecting a particular type of topological order in the ground states of unexplored models of interacting fermions.

Finally, we will discuss some concluding points and future directions with regards to the phenomenology of various models studied in this thesis. We have studied the 2d Hubbard model with only nearest neighbour hopping, and have observed a quantum critical point associated with the collapse of Mottness upon doping the Mott insulating ground state at half-filling. A future direction would be to observe how the critical doping depends upon the introduction of frustration in the hopping (e.g., next-nearest neighbour hopping). How does this affect the critical temperature for d-wave superconductivity that arises from the QCP? Another future direction would be to study the interplay of stripes and d-wave superconductivity within the URG approach. [79] For the Kondo model, we have shown that the metallic state comprising the Kondo singlet cloud has non-zero four-point correlators and finite mutual information between the electronic qubits, suggesting that this gapless quantum liquid is a non-Fermi liquid. The impurity thermodynamics of the Kondo model, including the Wilson ratio, Wilson number, impurity specific heat coefficient, impurity spin susceptibility, is in agreement with results from various existing methods (e.g., NRG, local Fermi liquid theory, Bethe ansatz, CFT etc.). However, the novel entanglement and correlation features of the non-Fermi liquid metal found by us are novel to the URG approach. Thus, a future work could be to calculate the complete impurity spectral function, and identify how its features are correlated with the entanglement features we have observed here. Further, an important extension would be to study the implications of the non-Fermi liquid electronic cloud for the Kondo lattice model: does it influence the nature of gapless excitations at the QCP in this model [589]?

We end by discussing the impact of the developments presented in this thesis on the subject of fermionic criticality. The results gathered from studying various models of interacting fermions outline clearly the importance of the topological quantum numbers associated with the Fermi surface. Our studies also describe the changes in these topological numbers via (interacting Lifshitz) quantum phase transitions that lead, for instance, to emergent gauge theories describing topologically ordered gapped quantum liquid ground states. Such transitions lie well beyond the Landau Ginzburg Wilson (LGW) paradigm of phase transitions, as they rely on a non-perturbative description of order parameters that are real-space non-local in nature. Further, our studies have unveiled the qualitative and quantitative description of a varied array of phases of interacting quantum matter in the form of effective Hamiltonians, ground state (and some-

---

times excited state) wavefunctions and various experimental measurables. Equally important is the fact that the URG enables a systematic analysis of the many-particle entanglement content of the eigenspectrum. Wherever possible, we have numerically benchmarked our results against the literature, and obtained very good agreement. We have also extended the URG formalism to be able to account for various symmetry broken states of matter. In several instances, our efforts have yielded microscopic explanations for existing experimental phenomenologies, as well as offered completely fresh insight into challenging open problems. While our focus has been primarily in understanding the emergence of new phenomena at low-energies, we have occasionally also unveiled the physics of excited states (e.g., many-body localisation), suggesting that a systematic approach towards non-equilibrium dynamics can be obtained by extending the URG formalism. Further, following the approach of Refs.[590, 591] to the study of the low-energy physics of open quantum systems, it appears possible to include the effects of dissipation within the URG formalism. In this way, URG appears to provide a framework for the qualitative and quantitative study of fermionic criticality and the emergence of new forms of interacting quantum matter that lie beyond the LGW paradigm. It appears safe to conclude that these developments herald exciting times ahead.



# Bibliography

- [1] Nevill F Mott. The basis of the electron theory of metals, with special reference to the transition metals. *Proceedings of the Physical Society. Section A*, 62(7):416, 1949.
- [2] Masatoshi Imada, Atsushi Fujimori, and Yoshinori Tokura. Metal-insulator transitions. *Reviews of modern physics*, 70(4):1039, 1998.
- [3] Thierry Giamarchi. *Quantum physics in one dimension*, volume 121. Clarendon press, 2003.
- [4] Alexander O Gogolin, Alexander A Nersesyan, and Alexei M Tsvelik. *Bosonization and strongly correlated systems*. Cambridge university press, 2004.
- [5] Bernhard Keimer, Steven A Kivelson, Michael R Norman, Shinichi Uchida, and J Zaanen. From quantum matter to high-temperature superconductivity in copper oxides. *Nature*, 518(7538):179, 2015.
- [6] Daijiro Yoshioka. *The quantum Hall effect*, volume 133. Springer Science & Business Media, 2013.
- [7] JMB Lopes Dos Santos, NMR Peres, and AH Castro Neto. Continuum model of the twisted graphene bilayer. *Physical Review B*, 86(15):155449, 2012.
- [8] Alexander Cyril Hewson. *The Kondo problem to heavy fermions*, volume 2. Cambridge university press, 1997.
- [9] Dmytro Pesin and Leon Balents. Mott physics and band topology in materials with strong spin-orbit interaction. *Nature Physics*, 6(5):376–381, 2010.
- [10] Patrick A Lee and TV Ramakrishnan. Disordered electronic systems. *Reviews of Modern Physics*, 57(2):287, 1985.
- [11] D Belitz and TR Kirkpatrick. The anderson-mott transition. *Reviews of modern physics*, 66(2):261, 1994.
- [12] William Witczak-Krempa, Gang Chen, Yong Baek Kim, and Leon Balents. Correlated quantum phenomena in the strong spin-orbit regime. *Annu. Rev. Condens. Matter Phys.*, 5(1):57–82, 2014.
- [13] Kliment I Kugel and Khomskii. The jahn-teller effect and magnetism: transition metal compounds.
- [14] LD Landau. The theory of a fermi liquid. *Soviet Physics Jetp-Ussr*, 3(6):920–925, 1957.
- [15] John Bardeen, Leon N Cooper, and John Robert Schrieffer. Theory of superconductivity. *Physical Review*, 108(5):1175, 1957.
- [16] Johannes Knolle and Roderich Moessner. A field guide to spin liquids. *Annual Review of Condensed Matter Physics*, 10:451–472, 2019.
- [17] Sung-Sik Lee. Low-energy effective theory of fermi surface coupled with u (1) gauge field in 2+ 1 dimensions. *Physical Review B*, 80(16):165102, 2009.

- [18] Max A Metlitski and Subir Sachdev. Quantum phase transitions of metals in two spatial dimensions. i. ising-nematic order. *Physical Review B*, 82(7):075127, 2010.
- [19] Max A Metlitski and Subir Sachdev. Quantum phase transitions of metals in two spatial dimensions. ii. spin density wave order. *Physical Review B*, 82(7):075128, 2010.
- [20] David F Mross, John McGreevy, Hong Liu, and T Senthil. Controlled expansion for certain non-fermi-liquid metals. *Physical Review B*, 82(4):045121, 2010.
- [21] Xiao-Gang Wen. Topological orders and edge excitations in fractional quantum hall states. *Advances in Physics*, 44(5):405–473, 1995.
- [22] Xie Chen, Zheng-Cheng Gu, and Xiao-Gang Wen. Local unitary transformation, long-range quantum entanglement, wave function renormalization, and topological order. *Physical review b*, 82(15):155138, 2010.
- [23] Dmitry A Abanin, Ehud Altman, Immanuel Bloch, and Maksym Serbyn. Colloquium: Many-body localization, thermalization, and entanglement. *Reviews of Modern Physics*, 91(2):021001, 2019.
- [24] Xiao-Gang Wen. Choreographed entanglement dances: Topological states of quantum matter. *Science*, 363(6429), 2019.
- [25] Román Orús. A practical introduction to tensor networks: Matrix product states and projected entangled pair states. *Annals of Physics*, 349:117–158, 2014.
- [26] Román Orús. Tensor networks for complex quantum systems. *Nature Reviews Physics*, 1(9):538–550, 2019.
- [27] Robert B Laughlin. Anomalous quantum hall effect: an incompressible quantum fluid with fractionally charged excitations. *Physical Review Letters*, 50(18):1395, 1983.
- [28] Lev Davidovich Landau, Evgenij Mihajlovič Lifšic, Evgenii Mikhailovich Lifshitz, and LP Pitaevskii. *Statistical physics: theory of the condensed state*, volume 9. Butterworth-Heinemann, 1980.
- [29] Kenneth G Wilson and John Kogut. The renormalization group and the expansion. *Physics reports*, 12(2):75–199, 1974.
- [30] John A Hertz. Quantum critical phenomena. *Physical Review B*, 14(3):1165, 1976.
- [31] AJ Millis. Effect of a nonzero temperature on quantum critical points in itinerant fermion systems. *Physical Review B*, 48(10):7183, 1993.
- [32] Toru Moriya. *Spin fluctuations in itinerant electron magnetism*, volume 56. Springer Science & Business Media, 2012.
- [33] Andrey V Chubukov, Catherine Pépin, and Jerome Rech. Instability of the quantum-critical point of itinerant ferromagnets. *Physical review letters*, 92(14):147003, 2004.
- [34] D Belitz, TR Kirkpatrick, and Thomas Vojta. How generic scale invariance influences quantum and classical phase transitions. *Reviews of modern physics*, 77(2):579, 2005.
- [35] T Senthil, Leon Balents, Subir Sachdev, Ashvin Vishwanath, and Matthew PA Fisher. Quantum criticality beyond the landau-ginzburg-wilson paradigm. *Physical Review B*, 70(14):144407, 2004.
- [36] Xiao Yan Xu, Kai Sun, Yoni Schattner, Erez Berg, and Zi Yang Meng. Non-fermi liquid at (2+ 1) d ferromagnetic quantum critical point. *Physical Review X*, 7(3):031058, 2017.
- [37] Max A Metlitski, David F Mross, Subir Sachdev, and T Senthil. Cooper pairing in non-fermi liquids. *Physical Review B*, 91(11):115111, 2015.
- [38] FDM Haldane. 'luttinger liquid theory'of one-dimensional quantum fluids. i. properties of

- the luttinger model and their extension to the general 1d interacting spinless fermi gas. *Journal of Physics C: Solid State Physics*, 14(19):2585, 1981.
- [39] T Senthil and Matthew PA Fisher. Z 2 gauge theory of electron fractionalization in strongly correlated systems. *Physical Review B*, 62(12):7850, 2000.
- [40] Masaki Oshikawa. Topological approach to luttinger's theorem and the fermi surface of a kondo lattice. *Physical Review Letters*, 84(15):3370, 2000.
- [41] Masaki Oshikawa. Insulator, conductor, and commensurability: A topological approach. *Physical review letters*, 90(23):236401, 2003.
- [42] Masaki Oshikawa and T Senthil. Fractionalization, topological order, and quasiparticle statistics. *Physical review letters*, 96(6):060601, 2006.
- [43] A Legros, S Benhabib, W Tabis, F Laliberté, M Dion, M Lizaire, B Vignolle, D Vignolles, H Raffy, ZZ Li, et al. Universal  $t$ -linear resistivity and planckian limit in overdoped cuprates. *arXiv preprint arXiv:1805.02512*, 2018.
- [44] CC Homes, SV Dordevic, M Strongin, DA Bonn, Ruixing Liang, WN Hardy, Seiki Komiya, Yoichi Ando, G Yu, N Kaneko, et al. A universal scaling relation in high-temperature superconductors. *Nature*, 430(6999):539, 2004.
- [45] Wei Pan, JS Xia, HL Stormer, DC Tsui, C Vicente, ED Adams, NS Sullivan, LN Pfeiffer, KW Baldwin, and KW West. Experimental studies of the fractional quantum hall effect in the first excited landau level. *Physical Review B*, 77(7):075307, 2008.
- [46] Richard Blankenbecler, DJ Scalapino, and RL Sugar. Monte carlo calculations of coupled boson-fermion systems. i. *Physical Review D*, 24(8):2278, 1981.
- [47] Shiwei Zhang, Joseph Carlson, and James E Gubernatis. Constrained path monte carlo method for fermion ground states. *Physical Review B*, 55(12):7464, 1997.
- [48] Shiwei Zhang and Henry Krakauer. Quantum monte carlo method using phase-free random walks with slater determinants. *Physical review letters*, 90(13):136401, 2003.
- [49] JPF LeBlanc, Andrey E Antipov, Federico Becca, Ireneusz W Bulik, Garnet Kin-Lic Chan, Chia-Min Chung, Youjin Deng, Michel Ferrero, Thomas M Henderson, Carlos A Jiménez-Hoyos, et al. Solutions of the two-dimensional hubbard model: benchmarks and results from a wide range of numerical algorithms. *Physical Review X*, 5(4):041041, 2015.
- [50] Mario Motta, David M Ceperley, Garnet Kin-Lic Chan, John A Gomez, Emanuel Gull, Sheng Guo, Carlos A Jiménez-Hoyos, Tran Nguyen Lan, Jia Li, Fengjie Ma, et al. Towards the solution of the many-electron problem in real materials: Equation of state of the hydrogen chain with state-of-the-art many-body methods. *Physical Review X*, 7(3):031059, 2017.
- [51] Walter Metzner and Dieter Vollhardt. Correlated lattice fermions in  $d=$  dimensions. *Physical review letters*, 62(3):324, 1989.
- [52] Antoine Georges, Gabriel Kotliar, Werner Krauth, and Marcelo J Rozenberg. Dynamical mean-field theory of strongly correlated fermion systems and the limit of infinite dimensions. *Reviews of Modern Physics*, 68(1):13, 1996.
- [53] Gabriel Kotliar, Sergej Y Savrasov, Kristjan Haule, Viktor S Oudovenko, O Parcollet, and CA Marianetti. Electronic structure calculations with dynamical mean-field theory. *Reviews of Modern Physics*, 78(3):865, 2006.
- [54] Thomas Maier, Mark Jarrell, Thomas Pruschke, and Matthias H Hettler. Quantum cluster theories. *Reviews of Modern Physics*, 77(3):1027, 2005.

- [55] MH Hettler, AN Tahvildar-Zadeh, M Jarrell, Th Pruschke, and HR Krishnamurthy. Non-local dynamical correlations of strongly interacting electron systems. *Physical Review B*, 58(12):R7475, 1998.
- [56] MH Hettler, M Mukherjee, M Jarrell, and HR Krishnamurthy. Dynamical cluster approximation: Nonlocal dynamics of correlated electron systems. *Physical Review B*, 61(19):12739, 2000.
- [57] Ehsan Khatami, Karlis Mikelsons, D Galanakis, A Macridin, J Moreno, RT Scalettar, and Mark Jarrell. Quantum criticality due to incipient phase separation in the two-dimensional hubbard model. *Physical Review B*, 81(20):201101, 2010.
- [58] NS Vidhyadhiraja, A Macridin, C Şen, M Jarrell, and Michael Ma. Quantum critical point at finite doping in the 2d hubbard model: A dynamical cluster quantum monte carlo study. *Physical review letters*, 102(20):206407, 2009.
- [59] Karlis Mikelsons, Ehsan Khatami, Dimitrios Galanakis, Alexandru Macridin, Juana Moreno, and Mark Jarrell. Thermodynamics of the quantum critical point at finite doping in the two-dimensional hubbard model studied via the dynamical cluster approximation. *Physical Review B*, 80(14):140505, 2009.
- [60] Emanuel Gull, Olivier Parcollet, and Andrew J Millis. Superconductivity and the pseudo-gap in the two-dimensional hubbard model. *Physical review letters*, 110(21):216405, 2013.
- [61] AI Lichtenstein and MI Katsnelson. Antiferromagnetism and d-wave superconductivity in cuprates: A cluster dynamical mean-field theory. *Physical Review B*, 62(14):R9283, 2000.
- [62] Gabriel Kotliar, Sergej Y Savrasov, Gunnar Pálsson, and Giulio Biroli. Cellular dynamical mean field approach to strongly correlated systems. *Physical review letters*, 87(18):186401, 2001.
- [63] Marcello Civelli, Massimo Capone, A Georges, K Haule, O Parcollet, TD Stanescu, and G Kotliar. Nodal-antinodal dichotomy and the two gaps of a superconducting doped mott insulator. *Physical review letters*, 100(4):046402, 2008.
- [64] Michel Ferrero, Pablo S Cornaglia, Lorenzo De Leo, Olivier Parcollet, Gabriel Kotliar, and Antoine Georges. Pseudogap opening and formation of fermi arcs as an orbital-selective mott transition in momentum space. *Physical Review B*, 80(6):064501, 2009.
- [65] Shiro Sakai, Yukitoshi Motome, and Masatoshi Imada. Doped high-t c cuprate superconductors elucidated in the light of zeros and poles of the electronic green's function. *Physical Review B*, 82(13):134505, 2010.
- [66] Shiro Sakai, Yukitoshi Motome, and Masatoshi Imada. Evolution of electronic structure of doped mott insulators: Reconstruction of poles and zeros of green's function. *Phys. Rev. Lett.*, 102:056404, Feb 2009.
- [67] Emanuel Gull, Michel Ferrero, Olivier Parcollet, Antoine Georges, and Andrew J Millis. Momentum-space anisotropy and pseudogaps: A comparative cluster dynamical mean-field analysis of the doping-driven metal-insulator transition in the two-dimensional hubbard model. *Physical Review B*, 82(15):155101, 2010.
- [68] G Sordi, Kristjan Haule, and A-MS Tremblay. Finite doping signatures of the mott transition in the two-dimensional hubbard model. *Physical review letters*, 104(22):226402, 2010.
- [69] Steven R White. Density matrix formulation for quantum renormalization groups. *Physical review letters*, 69(19):2863, 1992.
- [70] Ian P McCulloch and Miklós Gulácsi. The non-abelian density matrix renormalization

- group algorithm. *EPL (Europhysics Letters)*, 57(6):852, 2002.
- [71] Ulrich Schollwöck. The density-matrix renormalization group. *Reviews of modern physics*, 77(1):259, 2005.
- [72] Garnet Kin-Lic Chan and Sandeep Sharma. The density matrix renormalization group in quantum chemistry. *Annual review of physical chemistry*, 62:465–481, 2011.
- [73] Mark Fannes, Bruno Nachtergaelle, and Reinhard F Werner. Finitely correlated states on quantum spin chains. *Communications in mathematical physics*, 144(3):443–490, 1992.
- [74] Stellan Östlund and Stefan Rommer. Thermodynamic limit of density matrix renormalization. *Physical review letters*, 75(19):3537, 1995.
- [75] Frank Verstraete and J Ignacio Cirac. Renormalization algorithms for quantum-many body systems in two and higher dimensions. *arXiv preprint cond-mat/0407066*, 2004.
- [76] Frank Verstraete, Valentín Murg, and J Ignacio Cirac. Matrix product states, projected entangled pair states, and variational renormalization group methods for quantum spin systems. *Advances in Physics*, 57(2):143–224, 2008.
- [77] G. Ehlers, S. R. White, and R. M. Noack. Hybrid-space density matrix renormalization group study of the doped two-dimensional hubbard model. *Phys. Rev. B*, 95:125125, Mar 2017.
- [78] Bo-Xiao Zheng, Chia-Min Chung, Philippe Corboz, Georg Ehlers, Ming-Pu Qin, Reinhard M Noack, Hao Shi, Steven R White, Shiwei Zhang, and Garnet Kin-Lic Chan. Stripe order in the underdoped region of the two-dimensional hubbard model. *Science*, 358(6367):1155–1160, 2017.
- [79] Mingpu Qin, Chia-Min Chung, Hao Shi, Ettore Vitali, Claudius Hubig, Ulrich Schollwöck, Steven R White, Shiwei Zhang, et al. Absence of superconductivity in the pure two-dimensional hubbard model. *Physical Review X*, 10(3):031016, 2020.
- [80] Gerald Knizia and Garnet Kin-Lic Chan. Density matrix embedding: A simple alternative to dynamical mean-field theory. *Physical review letters*, 109(18):186404, 2012.
- [81] Gerald Knizia and Garnet Kin-Lic Chan. Density matrix embedding: A strong-coupling quantum embedding theory. *Journal of chemical theory and computation*, 9(3):1428–1432, 2013.
- [82] Ireneusz W Bulik, Gustavo E Scuseria, and Jorge Dukelsky. Density matrix embedding from broken symmetry lattice mean fields. *Physical Review B*, 89(3):035140, 2014.
- [83] Sebastian Wouters, Carlos A Jiménez-Hoyos, Qiming Sun, and Garnet K-L Chan. A practical guide to density matrix embedding theory in quantum chemistry. *Journal of chemical theory and computation*, 12(6):2706–2719, 2016.
- [84] Bo-Xiao Zheng and Garnet Kin-Lic Chan. Ground-state phase diagram of the square lattice hubbard model from density matrix embedding theory. *Physical Review B*, 93(3):035126, 2016.
- [85] Bo-Xiao Zheng and Garnet Kin-Lic Chan. Ground-state phase diagram of the square lattice hubbard model from density matrix embedding theory. *Physical Review B*, 93(3):035126, 2016.
- [86] Elliott Lieb, Theodore Schultz, and Daniel Mattis. Two soluble models of an antiferromagnetic chain. *Annals of Physics*, 16(3):407–466, 1961.
- [87] Masaki Oshikawa, Masanori Yamanaka, and Ian Affleck. Magnetization plateaus in spin chains: “haldane gap” for half-integer spins. *Phys. Rev. Lett.*, 78:1984–1987, Mar 1997.

- [88] Kazuhiro Seki and Seiji Yunoki. Topological interpretation of the luttinger theorem. *Physical Review B*, 96(8):085124, 2017.
- [89] Kenneth G Wilson. Model of coupling-constant renormalization. *Physical Review D*, 2(8):1438, 1970.
- [90] Kenneth G Wilson. Renormalization group and critical phenomena. i. renormalization group and the kadanoff scaling picture. *Physical review B*, 4(9):3174, 1971.
- [91] Kenneth G Wilson. Renormalization group and critical phenomena. ii. phase-space cell analysis of critical behavior. *Physical Review B*, 4(9):3184, 1971.
- [92] Kenneth G. Wilson and J. Kogut. The renormalization group and the  $\epsilon$ -expansion. *Physics Reports*, 2(2):75 – 199, 1974.
- [93] Kenneth G. Wilson. The renormalization group: Critical phenomena and the kondo problem. *Rev. Mod. Phys.*, 47:773–840, Oct 1975.
- [94] Leo P Kadanoff. Lp kadanoff et al., rev. mod. phys. 39, 395 (1967). *Rev. Mod. Phys.*, 39:395, 1967.
- [95] L. P. Kadanoff, A. Houghton, and M. C. Yalabik. Variational approximations for renormalization group transformations. *Journal of Statistical Physics*, 14:171, 1976.
- [96] Michael E. Fisher. Renormalization group theory: Its basis and formulation in statistical physics. *Rev. Mod. Phys.*, 70:653–681, Apr 1998.
- [97] Leo P Kadanoff, Wolfgang Götze, David Hamblen, Robert Hecht, EAS Lewis, V V Palciauskas, Martin Rayl, J Swift, David Aspnes, and Joseph Kane. Static phenomena near critical points: theory and experiment. *Reviews of Modern Physics*, 39(2):395, 1967.
- [98] Franz Wegner. Flow-equations for hamiltonians. *Annalen der physik*, 506(2):77–91, 1994.
- [99] G Benfatto and G Gallavotti. Renormalization-group approach to the theory of the fermi surface. *Physical Review B*, 42(16):9967, 1990.
- [100] Joel Feldman and Eugene Trubowitz. The flow of an electron-phonon system to the supercomputing state. *Helvetica Physica Acta*, 64(3):213–357, 1991.
- [101] Rev Shankar. Renormalization-group approach to interacting fermions. *Reviews of Modern Physics*, 66(1):129, 1994.
- [102] Joseph Polchinski. Effective field theory and the fermi surface. *arXiv preprint hep-th/9210046*, 1992.
- [103] Philip W Anderson et al. More is different. *Science*, 177(4047):393–396, 1972.
- [104] Elbio Dagotto. Complexity in strongly correlated electronic systems. *Science*, 309(5732):257–262, 2005.
- [105] Leon Balents. Spin liquids in frustrated magnets. *Nature*, 464(7286):199, 2010.
- [106] C Castelnovo, R Moessner, and Shivaji Lal Sondhi. Spin ice, fractionalization, and topological order. *Annu. Rev. Condens. Matter Phys.*, 3(1):35–55, 2012.
- [107] A Banerjee, CA Bridges, J-Q Yan, AA Aczel, L Li, MB Stone, GE Granroth, MD Lumsden, Y Yiu, Johannes Knolle, et al. Proximate kitaev quantum spin liquid behaviour in a honeycomb magnet. *Nature materials*, 15(7):733, 2016.
- [108] Walter Metzner, Manfred Salmhofer, Carsten Honerkamp, Volker Meden, and Kurt Schönhammer. Functional renormalization group approach to correlated fermion systems. *Reviews of Modern Physics*, 84(1):299, 2012.
- [109] Christian Platt, Werner Hanke, and Ronny Thomale. Functional renormalization group for multi-orbital fermi surface instabilities. *Advances in Physics*, 62(4-6):453–562, 2013.

- [110] Christof Wetterich. Exact evolution equation for the effective potential. *Physics Letters B*, 301(1):90–94, 1993.
- [111] Christoph J Halboth and Walter Metzner. d-wave superconductivity and pomeranchuk instability in the two-dimensional hubbard model. *Physical review letters*, 85(24):5162, 2000.
- [112] Walter Metzner, Manfred Salmhofer, Carsten Honerkamp, Volker Meden, and Kurt Schönhammer. Functional renormalization group approach to correlated fermion systems. *Reviews of Modern Physics*, 84(1):299, 2012.
- [113] Manfred Salmhofer and Carsten Honerkamp. Fermionic renormalization group flows: Technique and theory. *Progress of Theoretical Physics*, 105(1):1–35, 2001.
- [114] Peter Kopietz and Tom Busche. Exact renormalization group flow equations for nonrelativistic fermions: Scaling toward the fermi surface. *Physical Review B*, 64(15):155101, 2001.
- [115] Fabian B Kugler and Jan von Delft. Multiloop functional renormalization group that sums up all parquet diagrams. *Physical review letters*, 120(5):057403, 2018.
- [116] Agnese Tagliavini, Cornelia Hille, Fabian Kugler, Sabine Andergassen, Alessandro Toschi, and Carsten Honerkamp. Multiloop functional renormalization group for the two-dimensional hubbard model: Loop convergence of the response functions. *SciPost Physics*, 6(1):009, 2019.
- [117] Stefan Uebelacker and Carsten Honerkamp. Self-energy feedback and frequency-dependent interactions in the functional renormalization group flow for the two-dimensional hubbard model. *Physical Review B*, 86(23):235140, 2012.
- [118] Demetrio Vilardi, Ciro Taranto, and Walter Metzner. Nonseparable frequency dependence of the two-particle vertex in interacting fermion systems. *Physical Review B*, 96(23):235110, 2017.
- [119] Christoph Husemann and Manfred Salmhofer. Efficient parametrization of the vertex function,  $\Omega$  scheme, and the t, t hubbard model at van hove filling. *Physical Review B*, 79(19):195125, 2009.
- [120] Kay-Uwe Giering and Manfred Salmhofer. Self-energy flows in the two-dimensional repulsive hubbard model. *Physical Review B*, 86(24):245122, 2012.
- [121] Wan-Sheng Wang, Zheng-Zhao Li, Yuan-Yuan Xiang, and Qiang-Hua Wang. Competing electronic orders on kagome lattices at van hove filling. *Physical Review B*, 87(11):115135, 2013.
- [122] Fabian B Kugler and Jan von Delft. Multiloop functional renormalization group for general models. *Physical Review B*, 97(3):035162, 2018.
- [123] Cornelia Hille, Fabian B Kugler, Christian J Eckhardt, Yuan-Yao He, Anna Kauch, Carsten Honerkamp, Alessandro Toschi, and Sabine Andergassen. Quantitative functional renormalization-group description of the two-dimensional hubbard model. *arXiv preprint arXiv:2002.02733*, 2020.
- [124] AA Katanin and AP Kampf. Quasiparticle anisotropy and pseudogap formation from the weak-coupling renormalization group point of view. *Physical review letters*, 93(10):106406, 2004.
- [125] Daniel Rohe and Walter Metzner. Pseudogap at hot spots in the two-dimensional hubbard model at weak coupling. *Physical Review B*, 71(11):115116, 2005.

- [126] Cornelia Hille, Daniel Rohe, Carsten Honerkamp, and Sabine Andergassen. Pseudogap opening in the two-dimensional hubbard model: a functional renormalization group analysis. *arXiv preprint arXiv:2003.01447*, 2020.
- [127] Fa Wang, Hui Zhai, and Dung-Hai Lee. Antiferromagnetic correlation and the pairing mechanism of the cuprates and iron pnictides: A view from the functional renormalization group studies. *EPL (Europhysics Letters)*, 85(3):37005, 2009.
- [128] Demetrio Vilardi, Ciro Taranto, and Walter Metzner. Antiferromagnetic and d-wave pairing correlations in the strongly interacting two-dimensional hubbard model from the functional renormalization group. *Physical Review B*, 99(10):104501, 2019.
- [129] S. D. Glazek and Kenneth G. Wilson. Renormalization of hamiltonians. *Phys. Rev. D*, 48:5863–5872, Dec 1993.
- [130] S. D. Glazek and Kenneth G. Wilson. Perturbative renormalization group for hamiltonians. *Phys. Rev. D*, 49:4214–4218, Apr 1994.
- [131] H Krull, NA Drescher, and GS Uhrig. Enhanced perturbative continuous unitary transformations. *Physical Review B*, 86(12):125113, 2012.
- [132] Samuel Savitz and Gil Refael. Stable unitary integrators for the numerical implementation of continuous unitary transformations. *Physical Review B*, 96(11):115129, 2017.
- [133] I Grote, E Körding, and F Wegner. Stability analysis of the hubbard model. *Journal of low temperature physics*, 126(3-4):1385–1409, 2002.
- [134] Kenji Suzuki and Ryoji Okamoto. Degenerate perturbation theory in quantum mechanics. *Progress of Theoretical Physics*, 70(2):439–451, 1983.
- [135] Kenji Suzuki and Ryoji Okamoto. Effective interaction theory and unitary-model-operator approach to nuclear saturation problem. *Progress of Theoretical Physics*, 92(6):1045–1080, 1994.
- [136] Bruce R Barrett, Petr Navrátil, and James P Vary. Ab initio no core shell model. *Progress in Particle and Nuclear Physics*, 69:131–181, 2013.
- [137] Isaiah Shavitt and Lynn T Redmon. Quasidegenerate perturbation theories. a canonical van vleck formalism and its relationship to other approaches. *The Journal of Chemical Physics*, 73(11):5711–5717, 1980.
- [138] Kenji Suzuki and Shyh Yuan Lee. Convergent theory for effective interaction in nuclei. *Progress of Theoretical Physics*, 64(6):2091–2106, 1980.
- [139] Kenji Suzuki. Construction of hermitian effective interaction in nuclei:-general relation between hermitian and non-hermitian forms. *Progress of Theoretical Physics*, 68(1):246–260, 1982.
- [140] Paul Westhaus. Connections between perturbation theory and the unitary transformation methods of deriving effective hamiltonians. *International Journal of Quantum Chemistry*, 20(6):1243–1253, 1981.
- [141] Amir H Rezaeian and Niels R Walet. Renormalization of hamiltonian field theory; a non-perturbative and non-unitarity approach. *Journal of High Energy Physics*, 2003(12):040, 2003.
- [142] Amir H Rezaeian and Niels R Walet. Linked-cluster tamm–dancoff field theory. *Physics Letters B*, 570(1-2):129–136, 2003.
- [143] Hui Li and F Duncan M Haldane. Entanglement spectrum as a generalization of entanglement entropy: Identification of topological order in non-abelian fractional quantum hall

- effect states. *Physical review letters*, 101(1):010504, 2008.
- [144] Hong Yao and Xiao-Liang Qi. Entanglement entropy and entanglement spectrum of the kitaev model. *Physical review letters*, 105(8):080501, 2010.
- [145] Ronny Thomale, DP Arovas, and B Andrei Bernevig. Nonlocal order in gapless systems: Entanglement spectrum in spin chains. *Physical review letters*, 105(11):116805, 2010.
- [146] Pasquale Calabrese and John Cardy. Entanglement entropy and quantum field theory. *Journal of Statistical Mechanics: Theory and Experiment*, 2004(06):P06002, 2004.
- [147] Shinsei Ryu and Tadashi Takayanagi. Aspects of holographic entanglement entropy. *Journal of High Energy Physics*, 2006(08):045, 2006.
- [148] Shinsei Ryu and Tadashi Takayanagi. Holographic derivation of entanglement entropy from the anti-de sitter space/conformal field theory correspondence. *Physical review letters*, 96(18):181602, 2006.
- [149] Guifre Vidal. Entanglement renormalization. *Physical review letters*, 99(22):220405, 2007.
- [150] Luigi Amico, Rosario Fazio, Andreas Osterloh, and Vlatko Vedral. Entanglement in many-body systems. *Reviews of modern physics*, 80(2):517, 2008.
- [151] Nicolas Laflorencie. Quantum entanglement in condensed matter systems. *Physics Reports*, 646:1–59, 2016.
- [152] Brian Swingle. Entanglement entropy and the fermi surface. *Physical review letters*, 105(5):050502, 2010.
- [153] Benjamin J Brown, Daniel Loss, Jiannis K Pachos, Chris N Self, and James R Wootton. Quantum memories at finite temperature. *Reviews of Modern Physics*, 88(4):045005, 2016.
- [154] Tatsuma Nishioka. Entanglement entropy: holography and renormalization group. *Reviews of Modern Physics*, 90(3):035007, 2018.
- [155] Andreas Osterloh, Luigi Amico, Giuseppe Falci, and Rosario Fazio. Scaling of entanglement close to a quantum phase transition. *Nature*, 416(6881):608–610, 2002.
- [156] Tobias J Osborne and Michael A Nielsen. Entanglement in a simple quantum phase transition. *Physical Review A*, 66(3):032110, 2002.
- [157] Guifre Vidal, José Ignacio Latorre, Enrique Rico, and Alexei Kitaev. Entanglement in quantum critical phenomena. *Physical review letters*, 90(22):227902, 2003.
- [158] Román Orús. Universal geometric entanglement close to quantum phase transitions. *Physical review letters*, 100(13):130502, 2008.
- [159] Guifré Vidal. Class of quantum many-body states that can be efficiently simulated. *Physical review letters*, 101(11):110501, 2008.
- [160] Glen Evenbly and Guifré Vidal. Algorithms for entanglement renormalization. *Physical Review B*, 79(14):144108, 2009.
- [161] Glen Evenbly and Guifré Vidal. Tensor network states and geometry. *Journal of Statistical Physics*, 145(4):891–918, 2011.
- [162] Luca Tagliacozzo, Glen Evenbly, and Guifré Vidal. Simulation of two-dimensional quantum systems using a tree tensor network that exploits the entropic area law. *Physical Review B*, 80(23):235127, 2009.
- [163] Valentin Murg, Frank Verstraete, Örs Legeza, and Reinhard M Noack. Simulating strongly correlated quantum systems with tree tensor networks. *Physical Review B*, 82(20):205105, 2010.
- [164] Vittorio Giovannetti, Simone Montangero, and Rosario Fazio. Quantum multiscale entan-

- lement renormalization ansatz channels. *Physical review letters*, 101(18):180503, 2008.
- [165] Robert NC Pfeifer, Glen Evenbly, and Guifré Vidal. Entanglement renormalization, scale invariance, and quantum criticality. *Physical Review A*, 79(4):040301, 2009.
- [166] Brian Swingle, John McGreevy, and Shenglong Xu. Renormalization group circuits for gapless states. *Physical Review B*, 93(20):205159, 2016.
- [167] Miguel Aguado and Guifré Vidal. Entanglement renormalization and topological order. *Physical review letters*, 100(7):070404, 2008.
- [168] Brian Swingle and John McGreevy. Renormalization group constructions of topological quantum liquids and beyond. *Physical Review B*, 93(4):045127, 2016.
- [169] Xueda Wen, Gil Young Cho, Pedro LS Lopes, Yingfei Gu, Xiao-Liang Qi, and Shinsei Ryu. Holographic entanglement renormalization of topological insulators. *Physical Review B*, 94(7):075124, 2016.
- [170] Yingfei Gu, Ching Hua Lee, Xueda Wen, Gil Young Cho, Shinsei Ryu, and Xiao-Liang Qi. Holographic duality between (2+ 1)-dimensional quantum anomalous hall state and (3+ 1)-dimensional topological insulators. *Physical Review B*, 94(12):125107, 2016.
- [171] Matthias Gerster, Matteo Rizzi, Pietro Silvi, Marcello Dalmonte, and Simone Montangero. Fractional quantum hall effect in the interacting hofstadter model via tensor networks. *Physical Review B*, 96(19):195123, 2017.
- [172] Robert NC Pfeifer, Glen Evenbly, and Guifré Vidal. Entanglement renormalization, scale invariance, and quantum criticality. *Physical Review A*, 79(4):040301, 2009.
- [173] Jacob C Bridgeman, Aroon O’Brien, Stephen D Bartlett, and Andrew C Doherty. Multi-scale entanglement renormalization ansatz for spin chains with continuously varying criticality. *Physical Review B*, 91(16):165129, 2015.
- [174] Brian Swingle and John McGreevy. Renormalization group constructions of topological quantum liquids and beyond. *Physical Review B*, 93(4):045127, 2016.
- [175] Philippe Corboz and Guifré Vidal. Fermionic multiscale entanglement renormalization ansatz. *Physical Review B*, 80(16):165129, 2009.
- [176] Thomas Barthel, Carlos Pineda, and Jens Eisert. Contraction of fermionic operator circuits and the simulation of strongly correlated fermions. *Physical Review A*, 80(4):042333, 2009.
- [177] Ching Hua Lee and Xiao-Liang Qi. Exact holographic mapping in free fermion systems. *Physical Review B*, 93(3):035112, 2016.
- [178] Jutho Haegeman, Brian Swingle, Michael Walter, Jordan Cotler, Glen Evenbly, and Volkher B Scholz. Rigorous free-fermion entanglement renormalization from wavelet theory. *Physical Review X*, 8(1):011003, 2018.
- [179] Glen Evenbly and Guifré Vidal. Entanglement renormalization in noninteracting fermionic systems. *Physical Review B*, 81(23):235102, 2010.
- [180] Anirban Mukherjee and Siddhartha Lal. Scaling theory for mott-hubbard transitions-i: T=0 phase diagram of the 1/2-filled hubbard model. *New J. Phys.*, 2020.
- [181] Anirban Mukherjee and Siddhartha Lal. Scaling theory for mott-hubbard transitions-ii: Quantum criticality of the doped mott insulator. 2019.
- [182] Anirban Mukherjee and Siddhartha Lal. Unitary renormalisation group for correlated electrons-i: a tensor network approach. 2020.
- [183] Anirban Mukherjee and Siddhartha Lal. Unitary renormalisation group for correlated electrons-ii: insights on fermionic criticality. 2020.

- [184] Anirban Mukherjee and Siddhartha Lal. Holographic entanglement renormalisation of topological order in a quantum liquid. *arXiv preprint arXiv:2003.06118*, 2020.
- [185] Santanu Pal, Anirban Mukherjee, and Siddhartha Lal. Correlated spin liquids in the quantum kagome antiferromagnet at finite field: a renormalization group analysis. *New Journal of Physics*, 21(2):023019, 2019.
- [186] JH Van Vleck. On  $\sigma$ -type doubling and electron spin in the spectra of diatomic molecules. *Physical Review*, 33(4):467, 1929.
- [187] Simen Kvaal. Geometry of effective hamiltonians. *Physical Review C*, 78(4):044330, 2008.
- [188] Paul Westhaus. Cluster expansions of canonically transformed hamiltonians and effective interactions. *International Journal of Quantum Chemistry*, 7(S7):463–477, 1973.
- [189] Debashis Mukherjee, Raj Kumar Moitra, and Atri Mukhopadhyay. Correlation problem in open-shell atoms and molecules: A non-perturbative linked cluster formulation. *Molecular Physics*, 30(6):1861–1888, 1975.
- [190] Werner Kutzelnigg. Pair correlation theories.
- [191] Sourav Pal, M Durga Prasad, and Debasish Mukherjee. On certain correspondences among various coupled-cluster theories for closed-shell systems. *Pramana*, 18(3):261–270, 1982.
- [192] Arijit Pal and David A Huse. Many-body localization phase transition. *Physical review b*, 82(17):174411, 2010.
- [193] S. K. Ma, C. Dasgupta, and C. K. Hu. *Phys. Rev. Lett.*, 43:1434, 1979.
- [194] Chandan Dasgupta and Shang-keng Ma. Low-temperature properties of the random heisenberg antiferromagnetic chain. *Physical review b*, 22(3):1305, 1980.
- [195] Hideo Aoki. Decimation method of real-space renormalization for electron systems with application to random systems. *Physica A: Statistical Mechanics and its Applications*, 114(1-3):538–542, 1982.
- [196] Daniel S Fisher. Random transverse field ising spin chains. *Physical review letters*, 69(3):534, 1992.
- [197] Daniel S Fisher. Random antiferromagnetic quantum spin chains. *Physical review b*, 50(6):3799, 1994.
- [198] Daniel S Fisher. Critical behavior of random transverse-field ising spin chains. *Physical review b*, 51(10):6411, 1995.
- [199] Daniel S Fisher. Phase transitions and singularities in random quantum systems. *Physica A: Statistical Mechanics and its Applications*, 263(1-4):222–233, 1999.
- [200] Louk Rademaker and Miguel Ortuno. Explicit local integrals of motion for the many-body localized state. *Physical review letters*, 116(1):010404, 2016.
- [201] Louk Rademaker, Miguel Ortúñ, and Andres M Somoza. Many-body localization from the perspective of integrals of motion. *Annalen der Physik*, 529(7):1600322, 2017.
- [202] Cécile Monthus. Strong disorder renormalization for the dynamics of many-body-localized systems: iterative elimination of the fastest degree of freedom via the floquet expansion. *Journal of Physics A: Mathematical and Theoretical*, 51(27):275302, 2018.
- [203] Cécile Monthus. Many-body-localization: strong disorder perturbative approach for the local integrals of motion. *Journal of Physics A: Mathematical and Theoretical*, 51(19):195301, 2018.
- [204] Cécile Monthus. Many-body-localization transition: sensitivity to twisted boundary conditions. *Journal of Physics A: Mathematical and Theoretical*, 50(9):095002, 2017.

- [205] Steven R White. Numerical canonical transformation approach to quantum many-body problems. *The Journal of chemical physics*, 117(16):7472–7482, 2002.
- [206] Carl Gustav Jacob Jacobi. Ueber ein leichtes verfahren, die in der theorie der sacularstörungen vorkommenden gleichungen numerisch aufzulösen. *J. reine angew. Math.*, pages 51–94, 1846.
- [207] Claude Bloch. *Nuclear Physics*, 6:329 – 347, 1958.
- [208] Claude Bloch. *Nuclear Physics*, 7:451 – 458, 1958.
- [209] Baird H Brandow. Linked-cluster expansions for the nuclear many-body problem. *Reviews of Modern Physics*, 39(4):771, 1967.
- [210] Susumu Okubo. Diagonalization of hamiltonian and tamm-dancoff equation. *Progress of Theoretical Physics*, 12(5):603–622, 1954.
- [211] Brian Swingle. Entanglement renormalization and holography. *Physical Review D*, 86(6):065007, 2012.
- [212] Sung-Sik Lee. Holographic description of quantum field theory. *Nuclear Physics B*, 832(3):567–585, 2010.
- [213] Ki-Seok Kim, Miok Park, Jaeyoon Cho, and Chanyong Park. Emergent geometric description for a topological phase transition in the kitaev superconductor model. *Phys. Rev. D*, 96:086015, Oct 2017.
- [214] Ki-Seok Kim, Suk Bum Chung, Chanyong Park, and Jae-Ho Han. Emergent holographic description for the kondo effect: Comparison with bethe ansatz. *Phys. Rev. D*, 99:105012, May 2019.
- [215] Ingvar Lindgren and Debashis Mukherjee. On the connectivity criteria in the open-shell coupled-cluster theory for general model spaces. *Physics Reports*, 151(2):93–127, 1987.
- [216] Debashis Mukherjee and Sourav Pal. Use of cluster expansion methods in the open-shell correlation problem.
- [217] Jozef Mášik and Ivan Hubač. Multireference brillouin-wigner coupled-cluster theory. single-root approach.
- [218] Ivan Hubač and Stephen Wilson. Brillouin-wigner methods for many-body systems.
- [219] Wolfgang Wenzel and Kenneth G Wilson. Basis set reduction in hilbert space. *Physical review letters*, 69(5):800, 1992.
- [220] Wolfgang Wenzel, Matthew M Steiner, and Kenneth G Wilson. Multireference basis-set reduction. *International journal of quantum chemistry*, 60(7):1325–1330, 1996.
- [221] Jozef Mášik and Ivan Hubač. Multireference brillouin—wigner coupled-cluster theory: Hilbert space approach.
- [222] Gregory Breit. The effect of retardation on the interaction of two electrons. *Physical Review*, 34(4):553, 1929.
- [223] Stefan Uebelacker and Carsten Honerkamp. Self-energy feedback and frequency-dependent interactions in the functional renormalization group flow for the two-dimensional hubbard model. *Physical Review B*, 86(23):235140, 2012.
- [224] D Boyanovsky, HJ De Vega, R Holman, and M Simionato. Dynamical renormalization group resummation of finite temperature infrared divergences. *Physical Review D*, 60(6):065003, 1999.
- [225] D Boyanovsky and HJ De Vega. Non-fermi-liquid aspects of cold and dense qed and qcd: Equilibrium and nonequilibrium. *Physical Review D*, 63(3):034016, 2001.

- [226] D Boyanovsky and HJ De Vega. Dynamical renormalization group approach to relaxation in quantum field theory. *Annals of Physics*, 307(2):335–371, 2003.
- [227] Eduardo Fradkin. *Field theories of condensed matter physics*. Cambridge University Press, 2013.
- [228] Ingvar Lindgren, Sten Salomonson, and Daniel Hedendahl. Many-body procedure for energy-dependent perturbation: Merging many-body perturbation theory with qed. *Physical Review A*, 73(6):062502, 2006.
- [229] Yi-Zhuang You, Xiao-Liang Qi, and Cenke Xu. Entanglement holographic mapping of many-body localized system by spectrum bifurcation renormalization group. *Physical Review B*, 93(10):104205, 2016.
- [230] Tobias Baier, Eike Bick, and Christof Wetterich. Temperature dependence of antiferromagnetic order in the hubbard model. *Physical Review B*, 70(12):125111, 2004.
- [231] Xiao-Liang Qi. Exact holographic mapping and emergent space-time geometry. *arXiv preprint arXiv:1309.6282*, 2013.
- [232] Xiao-Liang Qi. Exact holographic mapping and emergent space-time geometry. *arXiv preprint arXiv:1309.6282*, 2013.
- [233] Daniel Gottesman. The heisenberg representation of quantum computers. *arXiv preprint quant-ph/9807006*, 1998.
- [234] A Mukherjee, S Patra, and S Lal. Fermionic criticality is shaped by fermi surface topology: a case study of the tomonaga-luttinger liquid. *arXiv:2005.02332*, 2020.
- [235] A Mukherjee, N. S. Vidhyadhiraja, A Taraphder, and S Lal. Urg analysis of the kondo effect. *arXiv:*, 2020.
- [236] Guifre Vidal. Entanglement renormalization. *Physical review letters*, 99(22):220405, 2007.
- [237] Glen Evenbly and Guifre Vidal. Tensor network renormalization. *Physical review letters*, 115(18):180405, 2015.
- [238] Glen Evenbly and Guifre Vidal. Tensor network renormalization yields the multiscale entanglement renormalization ansatz. *Physical review letters*, 115(20):200401, 2015.
- [239] Berry Groisman, Sandu Popescu, and Andreas Winter. Quantum, classical, and total amount of correlations in a quantum state. *Phys. Rev. A*, 72:032317, Sep 2005.
- [240] Katharine Hyatt, James R Garrison, and Bela Bauer. Extracting entanglement geometry from quantum states. *Physical review letters*, 119(14):140502, 2017.
- [241] Brian Swingle. Constructing holographic spacetimes using entanglement renormalization. *arXiv preprint arXiv:1209.3304*, 2012.
- [242] Xiao-Gang Wen. A systematic construction of gapped non-liquid states. *arXiv preprint arXiv:2002.02433*, 2020.
- [243] David P DiVincenzo. Two-bit gates are universal for quantum computation. *Physical Review A*, 51(2):1015, 1995.
- [244] Jacob Biamonte and Ville Bergholm. Tensor networks in a nutshell. *arXiv preprint arXiv:1708.00006*, 2017.
- [245] Jutho Haegeman, Tobias J Osborne, Henri Verschelde, and Frank Verstraete. Entanglement renormalization for quantum fields in real space. *Physical review letters*, 110(10):100402, 2013.
- [246] Yi-Zhuang You, Xiao-Liang Qi, and Cenke Xu. Entanglement holographic mapping of many-body localized system by spectrum bifurcation renormalization group. *Physical Re-*

- view B, 93(10):104205, 2016.
- [247] Isaac H Kim and Brian Swingle. Robust entanglement renormalization on a noisy quantum computer. *arXiv preprint arXiv:1711.07500*, 2017.
- [248] Adam R Brown and Leonard Susskind. Second law of quantum complexity. *Physical Review D*, 97(8):086015, 2018.
- [249] Cedric Beny. Causal structure of the entanglement renormalization ansatz. *New Journal of Physics*, 15(2):023020, 2013.
- [250] Michael M Wolf, Frank Verstraete, Matthew B Hastings, and J Ignacio Cirac. Area laws in quantum systems: mutual information and correlations. *Physical review letters*, 100(7):070502, 2008.
- [251] M Dolev, M Heiblum, V Umansky, Ady Stern, and D Mahalu. Observation of a quarter of an electron charge at the  $\nu = 5/2$  quantum hall state. *Nature*, 452(7189):829–834, 2008.
- [252] Parsa Bonderson, Alexei Kitaev, and Kirill Shtengel. Detecting non-abelian statistics in the  $\nu = 5/2$  fractional quantum hall state. *Physical review letters*, 96(1):016803, 2006.
- [253] Eun-Ah Kim, Michael Lawler, Smitha Vishveshwara, and Eduardo Fradkin. Signatures of fractional statistics in noise experiments in quantum hall fluids. *Physical review letters*, 95(17):176402, 2005.
- [254] Zhihuang Luo, Jun Li, Zhaokai Li, Ling-Yan Hung, Yidun Wan, Xinhua Peng, and Jiangfeng Du. Experimentally probing topological order and its breakdown through modular matrices. *Nature Physics*, 14(2):160–165, 2018.
- [255] A Yu Kitaev. Fault-tolerant quantum computation by anyons. *Annals of Physics*, 303(1):2–30, 2003.
- [256] F Duncan M Haldane. Model for a quantum hall effect without landau levels: Condensed-matter realization of the “parity anomaly”. *Physical review letters*, 61(18):2015, 1988.
- [257] Gregor Jotzu, Michael Messer, Rémi Desbuquois, Martin Lebrat, Thomas Uehlinger, Daniel Greif, and Tilman Esslinger. Experimental realization of the topological haldane model with ultracold fermions. *Nature*, 515(7526):237–240, 2014.
- [258] TH Hansson, Vadim Oganesyan, and SL Sondhi. Superconductors are topologically ordered. *Annals of Physics*, 313(2):497–538, 2004.
- [259] Shou Cheng Zhang. The chern–simons–landau–ginzburg theory of the fractional quantum hall effect. *International Journal of Modern Physics B*, 6(01):25–58, 1992.
- [260] Xiao-Gang Wen and Anthony Zee. Classification of abelian quantum hall states and matrix formulation of topological fluids. *Physical Review B*, 46(4):2290, 1992.
- [261] Huan He, Heidar Moradi, and Xiao-Gang Wen. Modular matrices as topological order parameter by a gauge-symmetry-preserved tensor renormalization approach. *Physical Review B*, 90(20):205114, 2014.
- [262] Daniel Gottesman. Stabilizer codes and quantum error correction. *arXiv preprint quant-ph/9705052*, 1997.
- [263] Ahmed Almheiri, Xi Dong, and Daniel Harlow. Bulk locality and quantum error correction in ads/cft. *Journal of High Energy Physics*, 2015(4):163, 2015.
- [264] Fernando Pastawski, Beni Yoshida, Daniel Harlow, and John Preskill. Holographic quantum error-correcting codes: Toy models for the bulk/boundary correspondence. *Journal of High Energy Physics*, 2015(6):149, 2015.
- [265] Isaac H Kim and Michael J Kastoryano. Entanglement renormalization, quantum error

- correction, and bulk causality. *Journal of High Energy Physics*, 2017(4):40, 2017.
- [266] Andrew J Ferris and David Poulin. Tensor networks and quantum error correction. *Physical review letters*, 113(3):030501, 2014.
- [267] H Bombin and MA Martin-Delgado. Topological quantum error correction with optimal encoding rate. *Physical Review A*, 73(6):062303, 2006.
- [268] Héctor Bombin, Ruben S Andrist, Masayuki Ohzeki, Helmut G Katzgraber, and Miguel A Martín-Delgado. Strong resilience of topological codes to depolarization. *Physical Review X*, 2(2):021004, 2012.
- [269] Isaac H Kim. Noise-resilient preparation of quantum many-body ground states. *arXiv preprint arXiv:1703.00032*, 2017.
- [270] EY Loh Jr, JE Gubernatis, RT Scalettar, SR White, DJ Scalapino, and RL Sugar. Sign problem in the numerical simulation of many-electron systems. *Physical Review B*, 41(13):9301, 1990.
- [271] Matthias Troyer and Uwe-Jens Wiese. Computational complexity and fundamental limitations to fermionic quantum monte carlo simulations. *Physical review letters*, 94(17):170201, 2005.
- [272] David M Ceperley. Fermion nodes. *Journal of statistical physics*, 63(5-6):1237–1267, 1991.
- [273] Frank Krüger and Jan Zaanen. Fermionic quantum criticality and the fractal nodal surface. *Physical Review B*, 78(3):035104, 2008.
- [274] N Kaplis, F Krüger, and J Zaanen. Entanglement entropies and fermion signs of critical metals. *Physical Review B*, 95(15):155102, 2017.
- [275] Shiro Sakai, Marcello Civelli, and Masatoshi Imada. Hidden-fermion representation of self-energy in pseudogap and superconducting states of the two-dimensional hubbard model. *Physical Review B*, 94(11):115130, 2016.
- [276] Tudor D Stanescu, Philip Phillips, and Ting-Pong Choy. Theory of the luttinger surface in doped mott insulators. *Physical Review B*, 75(10):104503, 2007.
- [277] Philip Phillips, Tudor Stanescu, and Ting-Pong Choy. Much ado about zeros: The luttinger surface and mottness. *APS*, pages V16–001, 2007.
- [278] Richard M Martin. Fermi-surface sum rule and its consequences for periodic kondo and mixed-valence systems. *Physical Review Letters*, 48(5):362, 1982.
- [279] J Friedel. Electronic structure of primary solid solutions in metals. *Advances in Physics*, 3(12):446–507, 1954.
- [280] N Levinson. Kgl. danske videnskab selskab mat.-fys. medd. 25 (1949), no. 9. m. ida. *Prog. Theor. Phys.*, 21:625, 1959.
- [281] Ralf Bulla, Theo A Costi, and Thomas Pruschke. Numerical renormalization group method for quantum impurity systems. *Reviews of Modern Physics*, 80(2):395, 2008.
- [282] T Giamarchi and C Lhuillier. Phase diagrams of the two-dimensional hubbard and t-j models by a variational monte carlo method. *Physical Review B*, 43(16):12943, 1991.
- [283] Subir Sachdev and Jinwu Ye. Gapless spin-fluid ground state in a random quantum heisenberg magnet. *Physical review letters*, 70(21):3339, 1993.
- [284] Samuel Moukouri and Mark Jarrell. Absence of a slater transition in the two-dimensional hubbard model. *Physical review letters*, 87(16):167010, 2001.
- [285] J Merino and O Gunnarsson. Pseudogap and singlet formation in organic and cuprate superconductors. *Physical Review B*, 89(24):245130, 2014.

- [286] Hyowon Park, Kristjan Haule, and Gabriel Kotliar. Cluster dynamical mean field theory of the mott transition. *Physical review letters*, 101(18):186403, 2008.
- [287] DJ Blankenbecler. Scalapino, and rl sugar. *Phys. Rev. D*, 24:2278, 1981.
- [288] Thomas Schäfer, Faruk Geles, Daniel Rost, Georg Rohringer, Enrico Arrigoni, Karsten Held, Nils Blümer, Markus Aichhorn, and Alessandro Toschi. Fate of the false mott-hubbard transition in two dimensions. *Physical Review B*, 91(12):125109, 2015.
- [289] Mark Fannes, Bruno Nachtergaele, and Reinhard F Werner. Finitely correlated states on quantum spin chains. *Communications in mathematical physics*, 144(3):443–490, 1992.
- [290] Matthew B Hastings. An area law for one-dimensional quantum systems. *Journal of Statistical Mechanics: Theory and Experiment*, 2007(08):P08024, 2007.
- [291] Frank Pollmann, Ari M Turner, Erez Berg, and Masaki Oshikawa. Entanglement spectrum of a topological phase in one dimension. *Physical review b*, 81(6):064439, 2010.
- [292] Norbert Schuch, David Pérez-García, and Ignacio Cirac. Classifying quantum phases using matrix product states and projected entangled pair states. *Physical review b*, 84(16):165139, 2011.
- [293] Yohei Fuji. Effective field theory for one-dimensional valence-bond-solid phases and their symmetry protection. *Physical Review B*, 93(10):104425, 2016.
- [294] Daniel F. Agterberg, J.C. Séamus Davis, Stephen D. Edkins, Eduardo Fradkin, Dale J. Van Harlingen, Steven A. Kivelson, Patrick A. Lee, Leo Radzihovsky, John M. Tranquada, and Yuxuan Wang. The physics of pair-density waves: Cuprate superconductors and beyond. *Annual Review of Condensed Matter Physics*, 11(1):231–270, 2020.
- [295] GR Stewart. Addendum: Non-fermi-liquid behavior in d-and f-electron metals. *Reviews of Modern Physics*, 78(3):743, 2006.
- [296] Sung-Sik Lee. Recent developments in non-fermi liquid theory. *Annual Review of Condensed Matter Physics*, 9(1):227–244, 2018.
- [297] V. Ros, M. Muller, and A. Scardicchio. *Nuclear Physics B*, 891:420, 2015.
- [298] SA Parameswaran and S Gopalakrishnan. Non-fermi glasses: Localized descendants of fractionalized metals. *Physical review letters*, 119(14):146601, 2017.
- [299] Rahul Nandkishore and David A. Huse. Many-body localization and thermalization in quantum statistical mechanics. *Annual Review of Condensed Matter Physics*, 6(1):15–38, 2015.
- [300] Jun Kondo. Resistance minimum in dilute magnetic alloys. *Progress of theoretical physics*, 32(1):37–49, 1964.
- [301] PW Anderson. A poor man’s derivation of scaling laws for the kondo problem. *Journal of Physics C: Solid State Physics*, 3(12):2436, 1970.
- [302] S.-S. B. Lee, Jinhong Park, and H.-S. Sim. Macroscopic quantum entanglement of a kondo cloud at finite temperature. *Phys. Rev. Lett.*, 114:057203, Feb 2015.
- [303] Gwangsu Yoo, S.-S. B. Lee, and H.-S. Sim. Detecting kondo entanglement by electron conductance. *Phys. Rev. Lett.*, 120:146801, Apr 2018.
- [304] Elliott H. Lieb and F. Y. Wu. Absence of mott transition in an exact solution of the short-range, one-band model in one dimension. *Phys. Rev. Lett.*, 20:1445, Jun 1968.
- [305] Philip W Anderson. The resonating valence bond state in la<sub>2</sub>cuo<sub>4</sub> and superconductivity. *science*, 235(4793):1196–1198, 1987.
- [306] Bernhard Edegger, Vangal N Muthukumar, and Claudius Gros. Gutzwiller-rvb theory

- of high-temperature superconductivity: Results from renormalized mean-field theory and variational monte carlo calculations. *Advances in Physics*, 56(6):927–1033, 2007.
- [307] Arun Paramekanti, Mohit Randeria, and Nandini Trivedi. High-t c superconductors: a variational theory of the superconducting state. *Physical Review B*, 70(5):054504, 2004.
- [308] PHILIP W Anderson, PA Lee, M Randeria, TM Rice, N Trivedi, and FC Zhang. The physics behind high-temperature superconducting cuprates: the ‘plain vanilla’version of rvb. *Journal of Physics: Condensed Matter*, 16(24):R755, 2004.
- [309] Y Kuroasaki, Y Shimizu, K Miyagawa, K Kanoda, and G Saito. Mott transition from a spin liquid to a fermi liquid in the spin-frustrated organic conductor  $\kappa$ -(et) 2 cu 2 (cn) 3. *Physical review letters*, 95(17):177001, 2005.
- [310] JS Helton, Kittiwit Matan, MP Shores, EA Nytko, BM Bartlett, Yiming Qiu, DG Nocera, and YS Lee. Dynamic scaling in the susceptibility of the spin-1 2 kagome lattice antiferromagnet herbertsmithite. *Physical review letters*, 104(14):147201, 2010.
- [311] Bastien Dalla Piazza, M Mourigal, Niels Bech Christensen, GJ Nilsen, P Tregenna-Piggott, TG Perring, Mechtilde Enderle, Desmond Francis McMorrow, DA Ivanov, and Henrik Moodysson Rønnow. Fractional excitations in the square-lattice quantum antiferromagnet. *Nature physics*, 11(1):62, 2015.
- [312] Mauro Iazzi, Alexey A Soluyanov, and Matthias Troyer. Topological origin of the fermion sign problem. *Physical Review B*, 93(11):115102, 2016.
- [313] Antoine Georges, Gabriel Kotliar, Werner Krauth, and Marcelo J Rozenberg. Dynamical mean-field theory of strongly correlated fermion systems and the limit of infinite dimensions. *Reviews of Modern Physics*, 68(1):13, 1996.
- [314] Antoine Georges and Gabriel Kotliar. Hubbard model in infinite dimensions. *Physical Review B*, 45(12):6479, 1992.
- [315] P. Werner and A. J. Millis. Doping-driven mott transition in the one-band hubbard model. *Phys. Rev. B*, 75:085108, 2007.
- [316] J. Joo and V. Oudovenko. Quantum monte carlo calculation of the finite temperature mott-hubbard transition. *Phys. Rev. B*, 64:193102, 2001.
- [317] Alessandro Toschi, AA Katanin, and Karsten Held. Dynamical vertex approximation: A step beyond dynamical mean-field theory. *Physical Review B*, 75(4):045118, 2007.
- [318] Karsten Held, Andrey A Katanin, and Alessandro Toschi. Dynamical vertex approximationan introduction. *Progress of Theoretical Physics Supplement*, 176:117–133, 2008.
- [319] Erik GCP van Loon, Hartmut Hafermann, and Mikhail I Katsnelson. Precursors of the insulating state in the square-lattice hubbard model. *Physical Review B*, 97(8):085125, 2018.
- [320] Y. Yu, L. Ma, P. Cai, R. Zhong, C. Ye, J. Shen, G. D. Gu, X. H. Chen, and Y. Zhang. High-temperature superconductivity in monolayer  $\text{bi}_2\text{sr}_2\text{cacu}_2\text{o}_{8+\delta}$ . *Nature*, doi:10.1038/s41586-019-1718-x, 2019.
- [321] S. Chakravarty, A. Sudbo, P. W. Anderson, and S. Strong. Interlayer tunneling and gap anisotropy in high-temperature superconductors. *Science*, 261:337, 1993.
- [322] S Martin, AT Fiory, RM Fleming, LF Schneemeyer, and JV Waszczak. Normal-state transport properties of  $\text{bi}_{2+x}\text{sr}_{2-y}\text{cu}_{6+\delta}$  crystals. *Physical Review B*, 41(1):846, 1990.
- [323] A Legros, S Benhabib, W Tabis, F Laliberté, M Dion, M Lizaire, B Vignolle, D Vignolles,

- H Raffy, Z Li, et al. Universal  $t$ -linear resistivity and planckian dissipation in overdoped cuprates. *Nature Physics*, 15(2):142–147, 2019.
- [324] Utpal Chatterjee, Dingfei Ai, Junjing Zhao, Stephan Rosenkranz, Adam Kaminski, Helene Raffy, Zhizhong Li, Kazuo Kadowaki, Mohit Randeria, Michael R Norman, et al. Electronic phase diagram of high-temperature copper oxide superconductors. *Proceedings of the National Academy of Sciences*, 108(23):9346–9349, 2011.
- [325] JL Tallon and JW Loram. The doping dependence of  $t^*$ —what is the real high- $t_c$  phase diagram? *Physica C: Superconductivity*, 349(1-2):53–68, 2001.
- [326] Subir Sachdev. Colloquium: Order and quantum phase transitions in the cuprate superconductors. *Reviews of Modern Physics*, 75(3):913, 2003.
- [327] Philip W Anderson. The resonating valence bond state in  $\text{La}_2\text{Cu}_3\text{O}_6$  and superconductivity. *science*, 235(4793):1196–1198, 1987.
- [328] AC Cosentini, Massimo Capone, L Guidoni, and GB Bachelet. Phase separation in the two-dimensional hubbard model: A fixed-node quantum monte carlo study. *Physical Review B*, 58(22):R14685, 1998.
- [329] Federico Becca, Massimo Capone, and Sandro Sorella. Spatially homogeneous ground state of the two-dimensional hubbard model. *Physical Review B*, 62(19):12700, 2000.
- [330] HJM Van Bemmel, DFB Ten Haaf, W Van Saarloos, JMJ Van Leeuwen, and Guozhong An. Fixed-node quantum monte carlo method for lattice fermions. *Physical review letters*, 72(15):2442, 1994.
- [331] Shiwei Zhang, J Carlson, and JE Gubernatis. Constrained path monte carlo method for fermion ground states. *Physical Review B*, 55(12):7464, 1997.
- [332] Chia-Chen Chang and Shiwei Zhang. Spatially inhomogeneous phase in the two-dimensional repulsive hubbard model. *Physical Review B*, 78(16):165101, 2008.
- [333] Chia-Chen Chang and Shiwei Zhang. Spin and charge order in the doped hubbard model: Long-wavelength collective modes. *Physical review letters*, 104(11):116402, 2010.
- [334] Hisatoshi Yokoyama and Hiroyuki Shiba. Variational monte-carlo studies of hubbard model. i. *Journal of the Physical Society of Japan*, 56(4):1490–1506, 1987.
- [335] David Eichenberger and Dionys Baeriswyl. Superconductivity and antiferromagnetism in the two-dimensional hubbard model: A variational study. *Physical Review B*, 76(18):180504, 2007.
- [336] Kunihiko Yamaaji, Takaashi Yanagisawa, Takeshi Nakanishi, and Soh Koike. Variational monte carlo study on the superconductivity in the two-dimensional hubbard model. *Physica C: Superconductivity*, 304(3-4):225–238, 1998.
- [337] Steven R White and DJ Scalapino. Phase separation and stripe formation in the two-dimensional  $t$ -  $j$  model: A comparison of numerical results. *Physical review B*, 61(9):6320, 2000.
- [338] Douglas J Scalapino and Steven R White. Numerical results for the hubbard model: implications for the high  $t_c$  pairing mechanism. *Foundations of Physics*, 31(1):27–39, 2001.
- [339] Steven R White and DJ Scalapino. Stripes on a 6-leg hubbard ladder. *Physical review letters*, 91(13):136403, 2003.
- [340] Michael Potthoff, Markus Aichhorn, and Christopher Dahnken. Variational cluster approach to correlated electron systems in low dimensions. *Physical review letters*, 91(20):206402, 2003.

- [341] Christopher Dahnken, Markus Aichhorn, Werner Hanke, Enrico Arrigoni, and Michael Potthoff. Variational cluster approach to spontaneous symmetry breaking: The itinerant antiferromagnet in two dimensions. *Physical Review B*, 70(24):245110, 2004.
- [342] Sebastian Schmitt. Non-fermi-liquid signatures in the hubbard model due to van hove singularities. *Physical Review B*, 82(15):155126, 2010.
- [343] Edwin W Huang, Ryan Sheppard, Brian Moritz, and Thomas P Devereaux. Strange metallicity in the doped hubbard model. *arXiv preprint arXiv:1806.08346*, 2018.
- [344] Jan Kaczmarczyk, Tobias Schickling, and Jörg Bünemann. Coexistence of nematic order and superconductivity in the hubbard model. *Physical Review B*, 94(8):085152, 2016.
- [345] David Sénéchal, P-L Lavertu, M-A Marois, and A-MS Tremblay. Competition between antiferromagnetism and superconductivity in high-t c cuprates. *Physical review letters*, 94(15):156404, 2005.
- [346] Markus Aichhorn, Enrico Arrigoni, Michael Potthoff, and Werner Hanke. Antiferromagnetic to superconducting phase transition in the hole-and electron-doped hubbard model at zero temperature. *Physical Review B*, 74(2):024508, 2006.
- [347] HJ Schulz. Incommensurate antiferromagnetism in the two-dimensional hubbard model. *Physical review letters*, 64(12):1445, 1990.
- [348] Steven R White, Douglas J Scalapino, Robert L Sugar, EY Loh, James E Gubernatis, and Richard T Scalettar. Numerical study of the two-dimensional hubbard model. *Physical Review B*, 40(1):506, 1989.
- [349] Andrey V Chubukov and Karen A Musaelian. Magnetic phases of the two-dimensional hubbard model at low doping. *Physical Review B*, 51(18):12605, 1995.
- [350] Massimo Capone and G Kotliar. Competition between d-wave superconductivity and anti-ferromagnetism in the two-dimensional hubbard model. *Physical Review B*, 74(5):054513, 2006.
- [351] Masatoshi Imada, Shiro Sakai, Youhei Yamaji, and Yukitoshi Motome. Theory of pseudo-gap in underdoped cuprates.
- [352] N. Lin, E. Gull, and A. J. Millis. Physics of the pseudogap in eight-site cluster dynamical mean-field theory: Photoemission, raman scattering, and in-plane and c-axis=is conductivity. *Phys. Rev. B*, 82:045104, 2010.
- [353] E. Gull and A. J. Millis. Energetics of superconductivity in the two-dimensional hubbard model. *Phys. Rev. B*, 86:241106, 2012.
- [354] T. A. Maier, M. Jarrell, T. C. Schulthess, P. R. C. Kent, and J. B. White. Systematic study of d-wave superconductivity in the 2d repulsive hubbard model. *Phys. Rev. Lett.*, 95:237001, 2005.
- [355] Henry Fu and Dung-Hai Lee. Dichotomy between the nodal and antinodal excitations in high-temperature superconductors. *Physical Review B*, 74(17):174513, 2006.
- [356] AI Lichtenstein and MI Katsnelson. Antiferromagnetism and d-wave superconductivity in cuprates: A cluster dynamical mean-field theory. *Physical Review B*, 62(14):R9283, 2000.
- [357] Hiroyuki Yamase, Andreas Eberlein, and Walter Metzner. Coexistence of incommensurate magnetism and superconductivity in the two-dimensional hubbard model. *Physical review letters*, 116(9):096402, 2016.
- [358] Christoph Husemann and Walter Metzner. Incommensurate nematic fluctuations in the two-dimensional hubbard model. *Physical Review B*, 86(8):085113, 2012.

- [359] Roland Zeyher and Andrés Greco. Competition between spin-induced charge instabilities in underdoped cuprates. *Physical Review B*, 98(22):224504, 2018.
- [360] Tuomas I Vanhala and Päivi Törmä. Dynamical mean-field theory study of stripe order and d-wave superconductivity in the two-dimensional hubbard model. *Physical Review B*, 97(7):075112, 2018.
- [361] Philipp Lange, Oleksandr Tsyplyatyev, and Peter Kopietz. Critical pairing fluctuations in the normal state of a superconductor: Pseudogap and quasiparticle damping. *Physical Review B*, 96(6):064506, 2017.
- [362] Ye-Hua Liu, Wan-Sheng Wang, Qiang-Hua Wang, Fu-Chun Zhang, and Thomas M Rice. Transformation of the superconducting gap to an insulating pseudogap at a critical hole density in the cuprates. *Physical Review B*, 96(1):014522, 2017.
- [363] Gordon Baym and Christopher Pethick. *Landau Fermi-liquid theory: concepts and applications*. John Wiley & Sons, 2008.
- [364] G Benfatto and G Gallavotti. Renormalization-group approach to the theory of the fermi surface. *Physical Review B*, 42(16):9967, 1990.
- [365] Michael Tinkham. *Introduction to superconductivity*. Courier Corporation, 2004.
- [366] André LeClair, José María Román, and Germán Sierra. Russian doll renormalization group and superconductivity. *Phys. Rev. B*, 69:020505, Jan 2004.
- [367] Sin-itiro Tomonaga. Remarks on bloch's method of sound waves applied to many-fermion problems. *Progress of Theoretical Physics*, 5(4):544–569, 1950.
- [368] Zheng-Cheng Gu and Xiao-Gang Wen. Tensor-entanglement-filtering renormalization approach and symmetry-protected topological order. *Physical Review B*, 80(15):155131, 2009.
- [369] Xie Chen, Zheng-Cheng Gu, and Xiao-Gang Wen. Classification of gapped symmetric phases in one-dimensional spin systems. *Physical review b*, 83(3):035107, 2011.
- [370] Huaiming Guo and Shun-Qing Shen. Topological phase in a one-dimensional interacting fermion system. *Physical Review B*, 84(19):195107, 2011.
- [371] Frank Pollmann, Erez Berg, Ari M Turner, and Masaki Oshikawa. Symmetry protection of topological phases in one-dimensional quantum spin systems. *Physical review b*, 85(7):075125, 2012.
- [372] Zheng-Cheng Gu and Xiao-Gang Wen. Symmetry-protected topological orders for interacting fermions: Fermionic topological nonlinear  $\sigma$  models and a special group supercohomology theory. *Physical Review B*, 90(11):115141, 2014.
- [373] Arianna Montorsi, Fabrizio Dolcini, Rita C Iotti, and Fausto Rossi. Symmetry-protected topological phases of one-dimensional interacting fermions with spin-charge separation. *Physical Review B*, 95(24):245108, 2017.
- [374] Ruben Verresen, Ryan Thorngren, Nick G Jones, and Frank Pollmann. Gapless topological phases and symmetry-enriched quantum criticality. *arXiv preprint arXiv:1905.06969*, 2019.
- [375] Bei Zeng, Xie Chen, Duan-Lu Zhou, and Xiao-Gang Wen. *Quantum information meets quantum matter*. Springer, 2019.
- [376] Alexander Altland and Martin R Zirnbauer. Nonstandard symmetry classes in mesoscopic normal-superconducting hybrid structures. *Physical Review B*, 55(2):1142, 1997.
- [377] Ching-Kai Chiu, Jeffrey CY Teo, Andreas P Schnyder, and Shinsei Ryu. Classification of topological quantum matter with symmetries. *Reviews of Modern Physics*, 88(3):035005, 2016.

- [378] EN Bogachev, IV Krive, IO Kulik, and AS Rozhavsky. Instanton aharonov-bohm effect and macroscopic quantum coherence in charge-density-wave systems. *Physical Review B*, 42(12):7614, 1990.
- [379] Walter Kohn. Theory of the insulating state. *Physical Review*, 133(1A):A171, 1964.
- [380] Masaaki Nakamura and Johannes Voit. Lattice twist operators and vertex operators in sine-gordon theory in one dimension. *Physical Review B*, 65(15):153110, 2002.
- [381] Horacio Casini, C D Fosco, and Marina Huerta. Entanglement and alpha entropies for a massive dirac field in two dimensions. *Journal of Statistical Mechanics: Theory and Experiment*, 0507:007, 2005.
- [382] C Holzhey, F Larsen, and F Wilczek. Geometric and renormalized entropy in conformal field theory. *Nuclear Physics B*, 424:443, 1994.
- [383] A R Its, B Q Jin, and V E Korepin. Entanglement in xy spin chain. *Journal Phys. A: Math. Gen.*, 38:2975, 2005.
- [384] B Q Jin and V E Korepin. Quantum spin chain, toeplitz determinants and the fisher-hartwig conjecture. *Journal of Statistical Physics*, 116:79, 2004.
- [385] Michael M Wolf. Violation of the entropic area law for fermions. *Physical review letters*, 96:010404, 2006.
- [386] D Gioev and I Klich. Entanglement entropy of fermions in any dimension and the widom conjecture. *Physical Review Letters*, 96:100503, 2006.
- [387] Vijay Balasubramanian and Per Kraus. Spacetime and the holographic renormalization group. *Physical Review Letters*, 83(18):3605, 1999.
- [388] Jan De Boer, Erik Verlinde, and Herman Verlinde. On the holographic renormalization group. *Journal of High Energy Physics*, 2000(08):003, 2000.
- [389] Idse Heemskerk, Joao Penedones, Joseph Polchinski, and James Sully. Holography from conformal field theory. *Journal of High Energy Physics*, 2009(10):079, 2009.
- [390] Horacio Casini, Marina Huerta, and Robert C Myers. Towards a derivation of holographic entanglement entropy. *Journal of High Energy Physics*, 2011(5):36, 2011.
- [391] Idse Heemskerk and Joseph Polchinski. Holographic and wilsonian renormalization groups. *Journal of High Energy Physics*, 2011(6):31, 2011.
- [392] Sung-Sik Lee. Quantum renormalization group and holography. *Journal of High Energy Physics*, 2014(1):76, 2014.
- [393] Román Orús. Advances on tensor network theory: symmetries, fermions, entanglement, and holography. *The European Physical Journal B*, 87(11):280, 2014.
- [394] Freek Witteveen, Volkher Scholz, Brian Swingle, and Michael Walter. Quantum circuit approximations and entanglement renormalization for the dirac field in 1+ 1 dimensions. *arXiv preprint arXiv:1905.08821*, 2019.
- [395] Philip Phillips. *Advanced solid state physics*. Cambridge University Press, 2012. Discussion regarding f-sum rule and dynamical spectral weight transfer in pages 394-395, section 12.4 on Cooper pairs and computation of effective two particle energy.
- [396] Piers Coleman. *Introduction to many-body physics*. Cambridge University Press, 2015. Chapter:18.
- [397] Philip W Anderson and Gideon Yuval. Exact results in the kondo problem: equivalence to a classical one-dimensional coulomb gas. *Physical Review Letters*, 23(2):89, 1969.
- [398] Philip W Anderson, G Yuval, and DR Hamann. Exact results in the kondo problem.

- ii. scaling theory, qualitatively correct solution, and some new results on one-dimensional classical statistical models. *Physical Review B*, 1(11):4464, 1970.
- [399] Philippe Nozieres. A “fermi-liquid” description of the kondo problem at low temperatures. *Journal of low temperature physics*, 17(1-2):31–42, 1974.
- [400] PB Wiegmann. Exact solution of the sd exchange model (kondo problem). *Journal of Physics C: Solid State Physics*, 14(10):1463, 1981.
- [401] Natan Andrei, K Furuya, and JH Lowenstein. Solution of the kondo problem. *Reviews of modern physics*, 55(2):331, 1983.
- [402] Ian Affleck. Conformal field theory approach to the kondo effect. *arXiv preprint cond-mat/9512099*, 1995.
- [403] Ian Affleck and Andreas WW Ludwig. Exact conformal-field-theory results on the multi-channel kondo effect: Single-fermion green’s function, self-energy, and resistivity. *Physical Review B*, 48(10):7297, 1993.
- [404] Per-Olov Löwdin. A note on the quantum-mechanical perturbation theory. *The Journal of Chemical Physics*, 19(11):1396–1401, 1951.
- [405] Per-Olov Löwdin. Studies in perturbation theory. iv. solution of eigenvalue problem by projection operator formalism. *Journal of Mathematical Physics*, 3(5):969–982, 1962.
- [406] Per-Olov Löwdin. Partitioning technique, perturbation theory, and rational approximations. *International Journal of Quantum Chemistry*, 21(1):69–92, 1982.
- [407] Herman Feshbach. Unified theory of nuclear reactions. *Annals of Physics*, 5(4):357–390, 1958.
- [408] Herman Feshbach. A unified theory of nuclear reactions. ii. *Annals of Physics*, 19(2):287 – 313, 1962.
- [409] Stanisław D Głazek and Kenneth G Wilson. Universality, marginal operators, and limit cycles. *Physical Review B*, 69(9):094304, 2004.
- [410] R. Haag, N. M. Hugenholtz, and M. Winnink. On the equilibrium states in quantum statistical mechanics. 5(3):215–236, 1967.
- [411] J Anandan and Yakir Aharonov. Geometry of quantum evolution. *Physical review letters*, 65(14):1697, 1990.
- [412] Abner Shimony. Degree of entanglement. *Annals of the New York Academy of Sciences*, 755(1):675–679, 1995.
- [413] Philip W Anderson. Random-phase approximation in the theory of superconductivity. *Physical Review*, 112(6):1900, 1958.
- [414] Ryszard Horodecki, Paweł Horodecki, Michał Horodecki, and Karol Horodecki. Quantum entanglement. *Reviews of modern physics*, 81(2):865, 2009.
- [415] Tzu-Chieh Wei and Paul M Goldbart. Geometric measure of entanglement and applications to bipartite and multipartite quantum states. *Physical Review A*, 68(4):042307, 2003.
- [416] Paolo Zanardi and Nikola Paunković. Ground state overlap and quantum phase transitions. *Physical Review E*, 74(3):031123, 2006.
- [417] Shiraz Minwalla, Mark Van Raamsdonk, and Nathan Seiberg. Noncommutative perturbative dynamics. *Journal of High Energy Physics*, 2000(02):020, 2000.
- [418] Philip Phillips. Colloquium: Identifying the propagating charge modes in doped mott insulators. *Reviews of Modern Physics*, 82(2):1719, 2010.
- [419] Philip W Anderson. Infrared catastrophe in fermi gases with local scattering potentials.

- Physical Review Letters*, 18(24):1049, 1967.
- [420] Kosaku Yamada and Kei Yosida. Orthogonality catastrophe for a system of interacting electrons. ii. *Progress of Theoretical Physics*, 62(2):363–369, 1979.
- [421] Grigory E Volovik. *The universe in a helium droplet*, volume 117. Oxford University Press on Demand, 2003.
- [422] J Sperling and W Vogel. The schmidt number as a universal entanglement measure. *Physica Scripta*, 83(4):045002, 2011.
- [423] A Brooks Harris and Robert V Lange. Single-particle excitations in narrow energy bands. *Physical Review*, 157(2):295, 1967.
- [424] H Eskes, MBJ Meinders, and GA Sawatzky. Anomalous transfer of spectral weight in doped strongly correlated systems. *Physical review letters*, 67(8):1035, 1991.
- [425] Mark S Hybertsen, EB Stechel, WMC Foulkes, and M Schlüter. Model for low-energy electronic states probed by x-ray absorption in high-t c cuprates. *Physical Review B*, 45(17):10032, 1992.
- [426] MBJ Meinders, H Eskes, and GA Sawatzky. Spectral-weight transfer: Breakdown of low-energy-scale sum rules in correlated systems. *Physical Review B*, 48(6):3916, 1993.
- [427] Antoine Georges, Olivier Parcollet, and Subir Sachdev. Quantum fluctuations of a nearly critical heisenberg spin glass. *Physical Review B*, 63(13):134406, 2001.
- [428] Tudor D Stănescu and Gabriel Kotliar. Fermi arcs and hidden zeros of the green function in the pseudogap state. *Physical Review B*, 74(12):125110, 2006.
- [429] Shiro Sakai, Yukitoshi Motome, and Masatoshi Imada. Evolution of electronic structure of doped mott insulators: Reconstruction of poles and zeros of green's function. *Physical review letters*, 102(5):056404, 2009.
- [430] Ipsita Mandal and Sung-Sik Lee. Ultraviolet/infrared mixing in non-fermi liquids. *Physical Review B*, 92(3):035141, 2015.
- [431] Igor Dzyaloshinskii. Some consequences of the luttinger theorem: The luttinger surfaces in non-fermi liquids and mott insulators. *Physical Review B*, 68(8):085113, 2003.
- [432] Henk Eskes, Andrzej M Oleś, Marcel BJ Meinders, and Walter Stephan. Spectral properties of the hubbard bands. *Physical Review B*, 50(24):17980, 1994.
- [433] AE Ruckenstein and CM Varma. A theory of marginal fermi-liquids. *Physica C: Superconductivity*, 185:134–140, 1991.
- [434] AF Ho and P Coleman. Marginal fermi liquid in a lattice of three-body bound states. *Physical Review B*, 58(8):4418, 1998.
- [435] Joaquin Mazdak Luttinger and John Clive Ward. Ground-state energy of a many-fermion system. ii. *Physical Review*, 118(5):1417, 1960.
- [436] Brian Swingle. Conformal field theory approach to fermi liquids and other highly entangled states. *Physical Review B*, 86(3):035116, 2012.
- [437] J Friedel. Xiv. the distribution of electrons round impurities in monovalent metals. *The London, Edinburgh, and Dublin Philosophical Magazine and Journal of Science*, 43(337):153–189, 1952.
- [438] Norman Levinson. On the uniqueness of the potential in a schrodinger equation for a given asymptotic phase. *Kgl. Danske Videnskab Selskab. Mat. Fys. Medd.*, 25, 1949.
- [439] P Coleman, I Paul, and J Rech. Sum rules and ward identities in the kondo lattice. *Physical Review B*, 72(9):094430, 2005.

- [440] Leon N Cooper. Bound electron pairs in a degenerate fermi gas. *Physical Review*, 104(4):1189, 1956.
- [441] Richard A Ferrell and Rolfe E Glover III. Conductivity of superconducting films: A sum rule. *Physical Review*, 109(4):1398, 1958.
- [442] Claudius Gros, Bernhard Edegger, VN Muthukumar, and PW Anderson. Determining the underlying fermi surface of strongly correlated superconductors. *Proceedings of the National Academy of Sciences*, 103(39):14298–14301, 2006.
- [443] Rajdeep Sensarma, Mohit Randeria, and Nandini Trivedi. Can one determine the underlying fermi surface in the superconducting state of strongly correlated systems? *Physical review letters*, 98(2):027004, 2007.
- [444] A Rosch. Breakdown of luttinger’s theorem in two-orbital mott insulators. *The European Physical Journal B*, 59(4):495–502, 2007.
- [445] J Dukelsky, S Pittel, and G Sierra. Colloquium: Exactly solvable richardson-gaudin models for many-body quantum systems. *Reviews of modern physics*, 76(3):643, 2004.
- [446] Å Bohr, BR Mottelson, and D Pines. Possible analogy between the excitation spectra of nuclei and those of the superconducting metallic state. *Physical Review*, 110(4):936, 1958.
- [447] ST Belyaev. *Mat. Fys. Medd. Dan. Vid. Selsk.*, 31:11, 1959.
- [448] JS Langer and V Ambegaokar. Friedel sum rule for a system of interacting electrons. *Physical Review*, 121(4):1090, 1961.
- [449] Matthew D Schwartz. *Quantum field theory and the standard model*. Cambridge University Press, 2014.
- [450] E Dagotto, A Moreo, F Ortolani, Poilblanc, and J Riera. Statis and dynamical properties of doped hubbard clusters. *Physical Review B*, 45(18):10741, 1992.
- [451] HR Krishnamurthy, C Jayaprakash, Sanjoy Sarker, and Wolfgang Wenzel. Mott-hubbard metal-insulator transition in nonbipartite lattices. *Physical review letters*, 64(8):950, 1990.
- [452] G Kemeny and Laurent G Caron. Self-consistent pair correlations in mott-type insulators. *Physical Review*, 159(3):768, 1967.
- [453] Grigory E Volovik. *The universe in a helium droplet*, volume 117. Oxford University Press on Demand, 2003.
- [454] AE Ruckenstein and CM Varma. A theory of marginal fermi-liquids. *Physica C: Superconductivity*, 185:134–140, 1991.
- [455] Masatoshi Imada, Takahiro Misawa, and Youhei Yamaji. Unconventional quantum criticality emerging as a new common language of transition-metal compounds, heavy-fermion systems, and organic conductors. *Journal of Physics: Condensed Matter*, 22(16):164206, mar 2010.
- [456] PW Anderson. A re-examination of concepts in magnetic metals: the ‘nearly antiferromagnetic fermi liquid’. 46:3, 1997.
- [457] Samuel Moukouri and Mark Jarrell. Absence of a slater transition in the two-dimensional hubbard model. *Physical review letters*, 87(16):167010, 2001.
- [458] MJ Rozenberg, G Kotliar, and XY Zhang. Mott-hubbard transition in infinite dimensions. ii. *Physical Review B*, 49(15):10181, 1994.
- [459] Antoine Georges, Gabriel Kotliar, Werner Krauth, and Marcelo J Rozenberg. Dynamical mean-field theory of strongly correlated fermion systems and the limit of infinite dimensions. *Reviews of Modern Physics*, 68(1):13, 1996.

- [460] CM Varma, P Be Littlewood, S Schmitt-Rink, E Abrahams, and AE Ruckenstein. Phenomenology of the normal state of cu-o high-temperature superconductors. *Physical Review Letters*, 63(18):1996, 1989.
- [461] A. R. EDMONDS.
- [462] Xiao-Gang Wen. Topological orders in rigid states. *International Journal of Modern Physics B*, 4(02):239–271, 1990.
- [463] Anirban Mukherjee and Siddhartha Lal. Codes for ground state properties. 2019. Codes available at "<https://github.com/anirban-m/anirban-m.github.io/blob/master/unitary-disentanglement-RG/benchmarking2DHubbard/GroundStateEnergyDensity.ipynb>".
- [464] Manfred Salmhofer, Carsten Honerkamp, Walter Metzner, and Oliver Lauscher. Renormalization group flows into phases with broken symmetry. *Progress of theoretical physics*, 112(6):943–970, 2004.
- [465] Nobuo Furukawa, TM Rice, and Manfred Salmhofer. Truncation of a two-dimensional fermi surface due to quasiparticle gap formation at the saddle points. *Physical review letters*, 81(15):3195, 1998.
- [466] B Binz, D Baeriswyl, and B Douçot. Wilson’s renormalization group applied to 2d lattice electrons in the presence of van hove singularities. *The European Physical Journal B-Condensed Matter and Complex Systems*, 25(1):69–87, 2002.
- [467] V Yu Irkhin, AA Katanin, and MI Katsnelson. Effects of van hove singularities on magnetism and superconductivity in the t- t hubbard model: a parquet approach. *Physical Review B*, 64(16):165107, 2001.
- [468] Luca F Tocchio, Federico Becca, and Sandro Sorella. Hidden mott transition and large-u superconductivity in the two-dimensional hubbard model. *Physical Review B*, 94(19):195126, 2016.
- [469] S Kawasaki, C Li, P. L. Kuhns, A. P. Reyes, and G. Zhang. Carrier-constriction dependence of the pseudogap ground state of superconducting  $\text{bi}_2\text{sr}_{2-x}\text{la}_x\text{cuo}_{6+\delta}$  revealed by  $^{63,65}\text{cu}$ -nuclear magnetic resonance in very high magnetic fields. *Phys. Rev. Lett.*, 105:137002, 2010.
- [470] Anirban Mukherjee and Siddhartha Lal. Scaling theory for mott-hubbard transitions- ii : Quantum criticality of the doped mott insulator. 2020.
- [471] M. Randeria and E. Taylor. *Annu. Rev. Condens. Matter Phys.*, 5:209, 2014.
- [472] B. Mukherjee, P. B. Patel, Z. Yan, J. Struck, and M. W. Zwierlein. Spectral response and contact of the unitary fermi gas. *Physical Review Letters*, 122:203402, 2019.
- [473] Assa Auerbach. *Interacting electrons and quantum magnetism*. Springer Science & Business Media, 2012.
- [474] Christoph J Halboth and Walter Metzner. Renormalization-group analysis of the two-dimensional hubbard model. *Physical Review B*, 61(11):7364, 2000.
- [475] Philip Phillips. Mottness collapse and t-linear resistivity in cuprate superconductors. *Philosophical Transactions of the Royal Society A: Mathematical, Physical and Engineering Sciences*, 369(1941):1574–1598, 2011.
- [476] J Zaanen and BJ Overbosch. Mottness collapse and statistical quantum criticality. *Philosophical Transactions of the Royal Society A: Mathematical, Physical and Engineering Sciences*, 369(1941):1599–1625, 2011.
- [477] Shiladitya Chakraborty, Dimitrios Galanakis, and Philip Phillips. Emergence of particle-

- hole symmetry near optimal doping in high-temperature copper oxide superconductors. *Physical Review B*, 82(21):214503, 2010.
- [478] Nobuo Furukawa and Masatoshi Imada. Charge gap, charge susceptibility and spin correlation in the hubbard model on a square lattice. *Journal of the Physical Society of Japan*, 60(11):3604–3607, 1991.
- [479] S-X Yang, Herbert Fotso, S-Q Su, Dimitrios Galanakis, Ehsan Khatami, J-H She, Juana Moreno, Jan Zaanen, and Mark Jarrell. Proximity of the superconducting dome and the quantum critical point in the two-dimensional hubbard model. *Physical review letters*, 106(4):047004, 2011.
- [480] Yang He, Yi Yin, M Zech, Anjan Soumyanarayanan, Michael M Yee, Tess Williams, MC Boyer, Kamalesh Chatterjee, WD Wise, I Zeljkovic, et al. Fermi surface and pseudogap evolution in a cuprate superconductor. *Science*, 344(6184):608–611, 2014.
- [481] K Fujita, Chung Koo Kim, Inhee Lee, Jinho Lee, MH Hamidian, IA Firsov, S Mukhopadhyay, H Eisaki, S Uchida, MJ Lawler, et al. Simultaneous transitions in cuprate momentum-space topology and electronic symmetry breaking. *Science*, 344(6184):612–616, 2014.
- [482] Fedor F Balakirev, Jonathan B Betts, Albert Migliori, S Ono, Yoichi Ando, and Gregory S Boebinger. Signature of optimal doping in hall-effect measurements on a high-temperature superconductor. *Nature*, 424(6951):912, 2003.
- [483] Lei Wang, Ye-Hua Liu, Jakub Imriška, Ping Nang Ma, and Matthias Troyer. Fidelity susceptibility made simple: A unified quantum monte carlo approach. *Physical Review X*, 5(3):031007, 2015.
- [484] Wen-Long You, Ying-Wai Li, and Shi-Jian Gu. Fidelity, dynamic structure factor, and susceptibility in critical phenomena. *Physical Review E*, 76(2):022101, 2007.
- [485] Philip W Anderson. The resonating valence bond state in la<sub>2</sub>cu<sub>3</sub>O<sub>4</sub> and superconductivity. *science*, 235(4793):1196–1198, 1987.
- [486] VJ Emery and SA Kivelson. Importance of phase fluctuations in superconductors with small superfluid density. *Nature*, 374(6521):434, 1995.
- [487] A Kanigel, MR Norman, M Randeria, U Chatterjee, S Souma, A Kaminski, HM Fretwell, S Rosenkranz, M Shi, T Sato, et al. Evolution of the pseudogap from fermi arcs to the nodal liquid. *Nature Physics*, 2(7):447, 2006.
- [488] Yayu Wang, Lu Li, and NP Ong. Nernst effect in high-t c superconductors. *Physical Review B*, 73(2):024510, 2006.
- [489] Dirk Van Der Marel, HJA Molegraaf, J Zaanen, Z Nussinov, Fabrizio Carbone, A Damascelli, H Eisaki, M Greven, PH Kes, and M Li. Quantum critical behaviour in a high-t c superconductor. *Nature*, 425(6955):271, 2003.
- [490] Aakash Pushp, Colin V Parker, Abhay N Pasupathy, Kenjiro K Gomes, Shimpei Ono, Jinsheng Wen, Zhijun Xu, Genda Gu, and Ali Yazdani. Extending universal nodal excitations optimizes superconductivity in bi<sub>2</sub>sr<sub>2</sub>cacu<sub>2</sub>o<sub>8+</sub> δ. *Science*, 324(5935):1689–1693, 2009.
- [491] Suchitra E Sebastian, N Harrison, MM Altarawneh, CH Mielke, Ruixing Liang, DA Bonn, and GG Lonzarich. Metal-insulator quantum critical point beneath the high tc superconducting dome. *Proceedings of the National Academy of Sciences*, 107(14):6175–6179, 2010.
- [492] MR Presland, JL Tallon, RG Buckley, RS Liu, and NE Flower. General trends in oxygen stoichiometry effects on tc in bi and tl superconductors. *Physica C: Superconductivity*,

- 176(1-3):95–105, 1991.
- [493] J-H Ma, Z-H Pan, FC Niestemski, M Neupane, Y-M Xu, P Richard, K Nakayama, T Sato, T Takahashi, H-Q Luo, et al. Coexistence of competing orders with two energy gaps in real and momentum space in the high temperature superconductor  $\text{Bi}_2\text{Sr}_2\text{Ca}_x\text{Cu}_6+\delta$ . *Physical Review Letters*, 101(20):207002, 2008.
- [494] B Fauqué, Y Sidis, V Hinkov, S Pailhes, CT Lin, Xavier Chaud, and Ph Bourges. Magnetic order in the pseudogap phase of high-t c superconductors. *Physical Review Letters*, 96(19):197001, 2006.
- [495] V Hinkov, D Haug, B Fauqué, P Bourges, Y Sidis, A Ivanov, Christian Bernhard, CT Lin, and B Keimer. Electronic liquid crystal state in the high-temperature superconductor  $\text{YBa}_2\text{Cu}_3\text{O}_6.45$ . *Science*, 319(5863):597–600, 2008.
- [496] Yoichi Ando, Kouji Segawa, Seiki Komiya, and AN Lavrov. Electrical resistivity anisotropy from self-organized one dimensionality in high-temperature superconductors. *Physical review letters*, 88(13):137005, 2002.
- [497] R Daou, J Chang, David LeBoeuf, Olivier Cyr-Choiniere, Francis Laliberté, Nicolas Doiron-Leyraud, BJ Ramshaw, Ruixing Liang, DA Bonn, WN Hardy, et al. Broken rotational symmetry in the pseudogap phase of a high-t c superconductor. *Nature*, 463(7280):519, 2010.
- [498] V Hinkov, Ph Bourges, S Pailhes, Y Sidis, A Ivanov, CD Frost, TG Perring, CT Lin, DP Chen, and B Keimer. Spin dynamics in the pseudogap state of a high-temperature superconductor. *Nature Physics*, 3(11):780, 2007.
- [499] Motoaki Hirayama, Youhei Yamaji, Takahiro Misawa, and Masatoshi Imada. Ab initio effective hamiltonians for cuprate superconductors. *Physical Review B*, 98(13):134501, 2018.
- [500] Tom Timusk and Bryan Statt. The pseudogap in high-temperature superconductors: an experimental survey. *Reports on Progress in Physics*, 62(1):61, 1999.
- [501] FC Zhang and TM Rice. Effective hamiltonian for the superconducting cu oxides. *Physical Review B*, 37(7):3759, 1988.
- [502] E Pavarini, I Dasgupta, T Saha-Dasgupta, O Jepsen, and OK Andersen. Band-structure trend in hole-doped cuprates and correlation with  $t_c$  max. *Physical review letters*, 87(4):047003, 2001.
- [503] Xiao-Jia Chen, Viktor V Struzhkin, Yong Yu, Alexander F Goncharov, Cheng-Tian Lin, Ho-kwang Mao, and Russell J Hemley. Enhancement of superconductivity by pressure-driven competition in electronic order. *Nature*, 466(7309):950, 2010.
- [504] L Gao, YY Xue, F Chen, Q Xiong, RL Meng, D Ramirez, CW Chu, JH Eggert, and HK Mao. Superconductivity up to 164 k in  $\text{HgBa}_2\text{Ca}_m\text{Cu}_m\text{O}_{2m+2+\delta}$  ( $m=1, 2$ , and 3) under quasihydrostatic pressures. *Physical Review B*, 50(6):4260, 1994.
- [505] T Muramatsu, D Pham, and CW Chu. A possible pressure-induced superconducting-semiconducting transition in nearly optimally doped single crystalline  $\text{YBa}_2\text{Cu}_3\text{O}_{7-\delta}$ . *Applied Physics Letters*, 99(5):052508, 2011.
- [506] C Pépin. Selective mott transition and heavy fermions. *Physical Review B*, 77(24):245129, 2008.
- [507] J Feldman and E Trubowitz. Perturbation theory for many fermion systems. *Helvetica Physica Acta*, 63(1):157–260, 1990.

- [508] G Benfatto and G Gallavotti. Perturbation theory of the fermi surface in a quantum liquid. a general quasiparticle formalism and one-dimensional systems. *Journal of Statistical Physics*, 59(3-4):541–664, 1990.
- [509] G Benfatto, G Gallavotti, A Procacci, and B Scoppola. Beta function and schwinger functions for a many fermions system in one dimension. anomaly of the fermi surface. *Communications in mathematical physics*, 160(1):93–171, 1994.
- [510] R Shankar. Renormalization group for interacting fermions in  $d \geq 1$ . *Physica A: Statistical Mechanics and its Applications*, 177(1-3):530–536, 1991.
- [511] Manfred Salmhofer. Continuous renormalization for fermions and fermi liquid theory. *Communications in mathematical physics*, 194(2):249–295, 1998.
- [512] Giuseppe Benfatto, Alessandro Giuliani, and Vieri Mastropietro. Fermi liquid behavior in the 2d hubbard model at low temperatures.
- [513] Manfred Salmhofer. Renormalization in condensed matter: Fermionic systems—from mathematics to materials. *Nuclear Physics B*, 941:868–899, 2019.
- [514] Andreas Eberlein and Walter Metzner. Superconductivity in the two-dimensional t-t-hubbard model. *Physical Review B*, 89(3):035126, 2014.
- [515] Shao-Kai Jian and Hong Yao. Solvable sachdev-ye-kitaev models in higher dimensions: from diffusion to many-body localization. *Physical review letters*, 119(20):206602, 2017.
- [516] Matthew B Hastings. Lieb-schultz-mattis in higher dimensions. *Physical review b*, 69(10):104431, 2004.
- [517] Peter Fulde and Richard A Ferrell. Superconductivity in a strong spin-exchange field. *Physical Review*, 135(3A):A550, 1964.
- [518] AI Larkin and Yu N Ovchinnikov. Sov. phys. jett 20, 762 (1965). *Sov. Phys. JETP*, 20:762, 1965.
- [519] CM Varma, Z Nussinov, and Wim Van Saarloos. Singular or non-fermi liquids. *Physics Reports*, 361(5-6):267–417, 2002.
- [520] CC Homes, SV Dordevic, M Strongin, DA Bonn, Ruixing Liang, WN Hardy, Seiki Komiya, Yoichi Ando, G Yu, N Kaneko, et al. A universal scaling relation in high-temperature superconductors. *Nature*, 430(6999):539, 2004.
- [521] Jan Zaanen. Superconductivity: Why the temperature is high. *Nature*, 430(6999):512, 2004.
- [522] Masanori Yamanaka, Masaki Oshikawa, and Ian Affleck. Nonperturbative approach to luttinger’s theorem in one dimension. *Physical review letters*, 79(6):1110, 1997.
- [523] Ehud Altman and Assa Auerbach. Haldane gap and fractional oscillations in gated josephson arrays. *Physical review letters*, 81(20):4484, 1998.
- [524] Santanu Pal and Siddhartha Lal. Magnetization plateaus of the quantum pyrochlore heisenberg antiferromagnet. *Physical Review B*, 100(10):104421, 2019.
- [525] Santanu Pal, Anirban Mukherjee, and Siddhartha Lal. Topological approach to quantum liquid ground states on geometrically frustrated heisenberg antiferromagnets. *Journal of Physics: Condensed Matter*, 32(16):165805, 2020.
- [526] Kenzo Ishikawa and Toyoki Matsuyama. A microscopic theory of the quantum hall effect. *Nuclear Physics B*, 280:523–548, 1987.
- [527] Xue-Yang Song, Chao-Ming Jian, and Leon Balents. Strongly correlated metal built from sachdev-ye-kitaev models. *Phys. Rev. Lett.*, 119:216601, Nov 2017.

- [528] Zhen Bi, Chao-Ming Jian, Yi-Zhuang You, Kelly Ann Pawlak, and Cenke Xu. Instability of the non-fermi-liquid state of the sachdev-ye-kitaev model. *Physical Review B*, 95(20):205105, 2017.
- [529] Michael A Nielsen and Isaac Chuang. Quantum computation and quantum information, 2002.
- [530] Xun Gao and Lu-Ming Duan. Efficient representation of quantum many-body states with deep neural networks. *Nature communications*, 8(1):1–6, 2017.
- [531] Yi-Zhuang You, Zhao Yang, and Xiao-Liang Qi. Machine learning spatial geometry from entanglement features. *Physical Review B*, 97(4):045153, 2018.
- [532] Xiao-Gang Wen. Topological orders in rigid states. *International Journal of Modern Physics B*, 4(02):239–271, 1990.
- [533] Steven A Kivelson, Daniel S Rokhsar, and James P Sethna. Topology of the resonating valence-bond state: Solitons and high- $t_c$  superconductivity. *Physical Review B*, 35(16):8865, 1987.
- [534] Cédric Bény. Deep learning and the renormalization group. *arXiv preprint arXiv:1301.3124*, 2013.
- [535] Pankaj Mehta and David J Schwab. An exact mapping between the variational renormalization group and deep learning. *arXiv preprint arXiv:1410.3831*, 2014.
- [536] Hong-Ye Hu, Shuo-Hui Li, Lei Wang, and Yi-Zhuang You. Machine learning holographic mapping by neural network renormalization group. *arXiv preprint arXiv:1903.00804*, 2019.
- [537] Ruslan Salakhutdinov and Geoffrey Hinton. Deep boltzmann machines.
- [538] Naftali Tishby and Noga Zaslavsky. Deep learning and the information bottleneck principle.
- [539] Ravid Shwartz-Ziv and Naftali Tishby. Opening the black box of deep neural networks via information. *arXiv preprint arXiv:1703.00810*, 2017.
- [540] Terence Parr and Jeremy Howard. The matrix calculus you need for deep learning. *arXiv preprint arXiv:1802.01528*, 2018.
- [541] E. Cocchi, L. A. Miller, J. H. Drewes, C. F. Chan, D. Pertot, F. Brennecke, and M. Köhl. Measuring entropy and short-range correlations in the two-dimensional hubbard model. *Phys. Rev. X*, 7:031025, Aug 2017.
- [542] Steven Weinberg. *Lectures on quantum mechanics*. Cambridge University Press, 2015.
- [543] F. Bloch. Bremsvermögen von atomen mit mehreren elektronen. *Zeitschrift für Physik*, 81(5):363–376, 1933.
- [544] JM Luttinger. Fermi surface and some simple equilibrium properties of a system of interacting fermions. *Physical Review*, 119(4):1153, 1960.
- [545] GE Volovik. An analog of the quantum hall effect in a superfluid  $^3\text{He}$  film. 1988.
- [546] Michael F Atiyah and Isidor M Singer. The index of elliptic operators on compact manifolds. *Bulletin of the American Mathematical Society*, 69(3):422–433, 1963.
- [547] FDM Haldane. Luttinger’s theorem and bosonization of the fermi surface. *arXiv preprint cond-mat/0505529*, 2005.
- [548] NS Manton. The schwinger model and its axial anomaly. *Annals of Physics*, 159(1):220–251, 1985.
- [549] Masaki Oshikawa, Masanori Yamanaka, and Ian Affleck. Magnetization plateaus in spin chains: “haldane gap” for half-integer spins. *Physical review letters*, 78(10):1984, 1997.
- [550] Rongjia Tao and FDM Haldane. Impurity effect, degeneracy, and topological invariant in

- the quantum hall effect. *Physical Review B*, 33(6):3844, 1986.
- [551] Qian Niu and DJ Thouless. Quantised adiabatic charge transport in the presence of substrate disorder and many-body interaction. *Journal of Physics A: Mathematical and General*, 17(12):2453, 1984.
- [552] Masaki Oshikawa. Commensurability, excitation gap, and topology in quantum many-particle systems on a periodic lattice. *Physical review letters*, 84(7):1535, 2000.
- [553] Douglas J Scalapino, Steven R White, and Shoucheng Zhang. Insulator, metal, or superconductor: The criteria. *Physical Review B*, 47(13):7995, 1993.
- [554] John S Bell and Roman Jackiw. A pcac puzzle:  $\pi 0 \rightarrow \gamma\gamma$  in the  $\sigma$ -model. *Il Nuovo Cimento A*, 60(1):47–61, 1969.
- [555] Stephen L Adler. Axial-vector vertex in spinor electrodynamics. *Physical Review*, 177(5):2426, 1969.
- [556] Michael Stone. Edge waves in the quantum hall effect. *Annals of Physics*, 207(1):38–52, 1991.
- [557] Pasquale Calabrese and John Cardy. Entanglement entropy and quantum field theory. *Journal of Statistical Mechanics: Theory and Experiment*, 2004(06):P06002, 2004.
- [558] Thierry Giamarchi. *Quantum physics in one dimension*. Clarendon Oxford, 2004.
- [559] Yoichiro Nambu and Giovanni Jona-Lasinio. Dynamical model of elementary particles based on an analogy with superconductivity. i. *Physical Review*, 122(1):345, 1961.
- [560] Jasper van Wezel and Jeroen van den Brink. Spontaneous symmetry breaking and decoherence in superconductors. *Physical Review B*, 77(6):064523, 2008.
- [561] Rev Shankar. Renormalization-group approach to interacting fermions. *Reviews of Modern Physics*, 66(1):129, 1994.
- [562] Samuel L Braunstein and Carlton M Caves. Statistical distance and the geometry of quantum states. *Physical Review Letters*, 72(22):3439, 1994.
- [563] Michael V Berry. Quantal phase factors accompanying adiabatic changes. In *Proceedings of the Royal Society of London A: Mathematical, Physical and Engineering Sciences*, volume 392, pages 45–57. The Royal Society, 1984.
- [564] Julian Schwinger. *Quantum Theory of Angular Momentum*. Academic Press, New York, 1965.
- [565] Paul AM Dirac. Quantised singularities in the electromagnetic field. In *Proceedings of the Royal Society of London A: Mathematical, Physical and Engineering Sciences*, volume 133, pages 60–72. The Royal Society, 1931.
- [566] VL Berezinskii. Destruction of long-range order in one-dimensional and two-dimensional systems having a continuous symmetry group i. classical systems. *Soviet Journal of Experimental and Theoretical Physics*, 32:493, 1971.
- [567] JM Kosterlitz and David J Thouless. Two-dimensional physics. *Progress in low temperature physics*, 7:371–433, 1978.
- [568] Juan Maldacena. The large-n limit of superconformal field theories and supergravity. *International journal of theoretical physics*, 38(4):1113–1133, 1999.
- [569] Edward Witten. Anti de sitter space and holography. *arXiv preprint hep-th/9802150*, 1998.
- [570] Walter Kohn. Cyclotron resonance and de haas-van alphen oscillations of an interacting electron gas. *Physical Review*, 123(4):1242, 1961.
- [571] Victor Gurarie. Single-particle green's functions and interacting topological insulators.

- Physical Review B*, 83(8):085426, 2011.
- [572] Israel Klich and Leonid Levitov. Quantum noise as an entanglement meter. *Physical review letters*, 102(10):100502, 2009.
- [573] Vinay Ambegaokar, BI Halperin, David R Nelson, and Eric D Siggia. Dynamics of superfluid films. *Physical Review B*, 21(5):1806, 1980.
- [574] Eduardo Fradkin and Stephen H Shenker. Phase diagrams of lattice gauge theories with higgs fields. *Physical Review D*, 19(12):3682, 1979.
- [575] Ivo Souza, Tim Wilkens, and Richard M Martin. Polarization and localization in insulators: Generating function approach. *Physical Review B*, 62(3):1666, 2000.
- [576] David R Nelson and JM Kosterlitz. Universal jump in the superfluid density of two-dimensional superfluids. *Physical Review Letters*, 39(19):1201, 1977.
- [577] JP Provost and G Vallee. Riemannian structure on manifolds of quantum states. *Communications in Mathematical Physics*, 76(3):289–301, 1980.
- [578] Wenxin Ding. Entanglement entropy in many-fermion system. *arXiv preprint arXiv:0908.2418*, 2009.
- [579] Sung-Sik Lee. Horizon as critical phenomenon. *Journal of High Energy Physics*, 2016(9):44, 2016.
- [580] Masahiro Nozaki, Shinsei Ryu, and Tadashi Takayanagi. Holographic geometry of entanglement renormalization in quantum field theories. *Journal of High Energy Physics*, 2012(10):193, 2012.
- [581] Gwangsu Yoo, S-SB Lee, and H-S Sim. Detecting kondo entanglement by electron conductance. *Physical review letters*, 120(14):146801, 2018.
- [582] Richard M Martin. Fermi-surface sum rule and its consequences for periodic kondo and mixed-valence systems. *Physical Review Letters*, 48(5):362, 1982.
- [583] R Bulla, T Costi, and T Pruschke. Numerical renormalisation group method for quantum impurity systems. *Rev. Mod. Phys.*, 80:395, 2008.
- [584] N Andrei, K Furuya, and J H Lowenstein. Solution of the kondo problem. *Rev. Mod. Phys.*, 55:331, 1983.
- [585] A M Tsvelick and P B Wiegmann. Exact results in the theory of magnetic alloys. *Adv. in Phys.*, 32:453, 1983.
- [586] Wen Xiao Gang. *Quantum field theory of many-body systems: from the origin of sound to an origin of light and electrons*. Oxford University Press, 2007.
- [587] Alwin Zulehner, Alexandru Paler, and Robert Wille. An efficient methodology for mapping quantum circuits to the ibm qx architectures. arxiv. *arXiv preprint arXiv:1712.04722*, 2017.
- [588] Eyob A Sete, William J Zeng, and Chad T Rigetti. A functional architecture for scalable quantum computing. In *2016 IEEE International Conference on Rebooting Computing (ICRC)*, pages 1–6. IEEE, 2016.
- [589] Yi-feng Yang, David Pines, and Gilbert Lonzarich. Quantum critical scaling and fluctuations in kondo lattice materials. *Proceedings of the National Academy of Sciences*, 114(24):6250–6255, 2017.
- [590] E M Kessler. Schrieffer-wolff formalism for dissipative systems. *Phys. Rev. A*, 86:012126, 2012.
- [591] F Reiter and A S Sorenson. Effective operator formalism for open quantum systems. *Phys. Rev. A*, 85:032111, 2012.